PROCEEDINGS
of the

6th RARE EARTH RESEARCH CONFERENCE

MAY 3-5, 1967

AF-OSR-1-67 new

ARCHIVE COPY

Gatlinburg, Tennessee

D D C

JUN 21 1967

A

F
757

FOREWORD

The Sixth Rare Earth Research Conference was held at Gatlinburg, Tennessee in the foothills of the Great Smoky Mountains in May 1967. This booklet contains the preprints of papers presented at the technical sessions, and it is prepared for the convenience of the Conferees. The issuance of this booklet is in no way intended to take the place of the publication of its contents in the scientific literature.

As usual in these Rare Earth Research Conferences we have tried to bring together scientists of all disciplines whose interests lie in the study of the properties of the rare earth metals, compounds, and alloys, and we have made a special effort this year to have a session devoted exclusively to Industrial Processes. (For the organization of this session we are indebted to Mark M. Woyski and Howard E. Kremers.)

The response to the call for papers was overwhelming--so much so that parallel sessions were required in order to conduct the business of the Conference in a three day period. We tend to view the increasing popularity of these conferences with mixed feelings, for, as they become larger, they necessarily become more formal and unwieldy.

The Conference was made possible by the generous support of the Oak Ridge National Laboratory, operated for the U. S. Atomic Energy Commission by Union Carbide Corporation, and by the Air Force Office of Scientific Research - Directorate of Chemical Sciences. To them go our sincere thanks.

We wish to acknowledge with thanks the generous support the Conference has received from its industrial sponsors. Their assistance has enabled us to make the Conference a more pleasant occasion. They are:

American Potash and Chemical Corporation, Los Angeles, California
Lunex Company, Pleasant Valley, Iowa
Michigan Chemical Corporation, Saint Louis, Michigan
Molybdenum Corporation of America, New York, New York
ORTEC, Oak Ridge, Tennessee
Ronson Metals Corporation, Newark, New Jersey
Tennelec Instrument Company, Oak Ridge, Tennessee
Union Carbide Corporation, Nuclear Division, Oak Ridge, Tennessee.

Finally we wish to express our appreciation to Alvin Weinberg, Director of the Oak Ridge National Laboratory, for his after-dinner address "New Vistas in Transuranium Research," to all the Session Chairmen (whose names appear in the Table of Contents), to the speakers, and to the Conferees themselves for helping to make the Sixth Conference a stimulating and interesting one.

The Committee

TABLE OF CONTENTS

i

TABLE OF CONTENTS

SESSION D - CHEMISTRY I

Chairman: AMOS G. HORNEY, Air Force Office of Scientific
           Research

SESSION E - CHEMISTRY II

Chairman: L. L. QUILL, Michigan State University

TABLE OF CONTENTS

TABLE OF CONTENTS

TABLE OF CONTENTS

TABLE OF CONTENTS

SESSION I - CHEMISTRY V

Chairman: C. J. HARDY, AERE, Harwell

SESSION J - METALLURGY

Chairman: CARL J. McHARGUE, Oak Ridge National Laboratory

TABLE OF CONTENTS

SESSION K - SOLID STATE IV

Chairman: J. S. FAULKNER, Oak Ridge National Laboratory

TABLE OF CONTENTS

SESSION L - SOLID STATE V

Chairman: R. M. BOZORTH, IBM Watson Research Center

TABLE OF CONTENTS

TABLE OF CONTENTS

x

RARE EARTH USES

Howard E. Kremers
Manager, Market Development and Technical Services
American Potash & Chemical Corporation
New York, New York   10016

Abstract

The rare earth producing industry is now about 75 years old. It has
gone through several cycles of end-use patterns, and these will be re-
viewed as they relate to technical progress made by industry.

This is not a dry list of the many uses for rare earth, but
instead is a sort of history of the development of both uses and the
rare earth supplying industry. There are also some misconceptions
about our industry which this paper should help to clear up.

For example, with all respect to Frank Spedding and the
Atomic Energy Commission, they did not invent rare earths! And, the
gas mantle industry is not obsolete!

Many scientists are not aware that we are an old industry by
today's standards for chemicals. Seventy five years is a pretty good
record, and the industry has gone through many changes and many de-
grees of technical competence.

If you have wondered why the rare earth producers have not
directly participated in the past Rare Earth Research Conferences as
much as they appear to have, the reason is quite clear. Most of the
research we do is supported by our own funding. We are generally not
government-business oriented, and we are not patent prolific. We owe
a debt of gratitude to the works of hundreds of academic and govern-
ment researchers who have contributed basic process information. We
have devoted most of our efforts to making rare earths available, and
the processes by which we do this are our carefully guarded secrets,
and the sources of our income.

The producers have relied heavily on the users to develop
uses, and the users in turn have relied on fundamental research, some
of which they have had to do themselves.

There are three underlying patterns for the development of
rare earth uses. The first relates to the availability of materials
for research and ultimate use. The second involves a need for a

material which can be filled by a specific inherent property of the rare earths. The third did not become significant until the last couple of decades; it involves the point of view of looking at rare earths not as a group of similar elements, and from the standpoint of their relationship with other materials rather than consideration of them for their own obvious properties.

The use of rare earths in ceramic colors is an example of the third pattern. Both neodymium and praseodymium have intense, sharp absorption bands in the visible spectrum. Their dichroic red and green colors are obvious clues to use in coloring glass and ceramic pieces. But the fact that praseodymium in particular can cause defect structures in zirconium oxide leading to brillant yellow colors is the basis for one of the largest coloring uses for rare earths, the praseodymium-vanadium stains used for porcelan enamel coloring.

Traditionally, the rare earth producers' technical people were largely old timers who "grew up in the business." The smallness of the industry did not particularly attract graduates. By the mid 1940's, however, a change was beginning to take place. Demands for more technical competence, and spin offs from the Manhattan Project led to new people coming into the industry. Many of these didn't know it couldn't be done, so they did it!

The invention of the incandescent gas mantle about 75 years ago, was the start of the rare earth industry. The thorium nitrate required for gas mantles was obtained from monazite ore, and there is about ten times as much rare earth content in the ore as there is thorium. In the 1890's to the 1920's, the main rare earth stream from the processing of monazite was discarded, and the rare earth materials needed for use were obtained from the purification of crude thorium.

Although a great deal of work was done in characterizing the rare earths-even in the late 1700's-no real efforts were made to find uses for them until Auer von Welsbach's studies in Germany led to the development of the incandescent gas mantle. His device was so well received that an industry rapidly developed, and within a few years it was consuming several thousand tons of monazite ore annually.

The fact that there were ten times as much rare earths in the ore as thorium did not bother the mantle producers. They simply threw the rare earths away.

The discovery that small amounts of cerium were needed in the thorium oxide mantle created the first demand for a rare earth, and for a pure one at that. Cerous nitrate was required to make the 1% CeO_2-99% ThO_2 Welsbach oxide mixture. The by-product from the cerium separation was didymium, and this was used for trademarking gas mantles.

The 1890's mantle production also provided by-product rare earths for exploitation, and the first uses of crude neodymium and praseodymium concentrate for glass coloring were soon developed. The Nernst glower was patented in 1898, and this was the first use for yttrium oxide, although the crude yttria used was not obtained from monazite by-products but from the now flooded Barringer Hill, Texas pegmatite deposits.

Welsbach patented misch metal in 1903, and within a few years production of misch metal and ferrocerium reached a few hundred tons a year. In this country Ronson began lighter flint production in 1915.

Incidentally, in spite of what some authors say, gas mantles are not dead. In fact, there are more mantles in service today than at the height of the old gas lighting era. As a commercial use for thorium insofar as present industry sales of thorium nitrate are concerned, gas mantles are still the largest market.

Other uses were developed in the early 1900's, but many of these never became important because the rare earth properties being utilized were also common to those of more abundant and better known materials. Examples are oxidation catalysis of sulfur dioxide to sulfuric acid, and hydrogen chloride to chlorine in 1910, textile and leather dying (1904-1911), silk weighing (1914), photographic reducers (1910), etc.

Rare earth cored arc carbons for lighting were invented in 1909-1911, and consumption of mixed oxides and fluorides soon increased to a few hundred tons per year, not unlike today's consumption.

Except for cerium, the only rare earth materials available from industry for many years were mixtures. This is completely understandable if you remember that most rare earth separation was tedious and extremely expensive until the commercial development of ion exchange technology a little over a decade ago. Even into the 1940's, if a researcher wanted a pure rare earth to play with, the only convenient reliable sources were academic friends who loaned or donated small amounts of materials of doubtful purity.

In this country, the rare earth producing industry did not really develop until the Allied blockade in World Ware I cut off supplies of German thorium nitrate. The war ended the dominance of European rare earth ore processors. American mantle manufacturers then learned the technology of processing monazite ore, but they soon found that the demand for gas mantles was decreasing. Development of uses for the previously discarded rare earth stream 'ed to American markets which still exist: ferrocerium for lighter lints, arc carbon cores, misch metal, and the start of metallurgical uses for rare earths, ceramic and glass coloring, etc.

In the post World War I period, the only commercially available purified rare earths were cerium, and some crude neodymium compounds. However, without waiting for commercial availability, Eastman Kodak in the 1930's developed lanthanum oxide-based optical glasses, and the Second World War spurred commercial production of very high purity lanthanum oxide. Lanthanum was separated from cerium-free rare earths by fractional crystallization of the double ammonium nitrates, a process which even today has some merit. Production of lanthanum oxide having rare earth impurities below 10 ppm was routine by the early 1940's.

The availability of modern tools for spectrophotometric analysis in the 1940's took the guess work out of classical fractional crystallization processes, and better neodymium materials for coloring glass became available.

World War II also created demands for rare earths which today are still the bread and butter of much of the industry. Cerium oxide-based optical glass polishes were developed in this country after European success with these was demonstrated in the late 1930's. These faster acting polishes increased the production rate of optical polishing machinery, and after the war they became important in opthalmic lens and plate glass polishing.

Barium titanate capacitors containing neodymium, lanthanum, and praseodymium to control the temperature coefficient of capacitance became important as communication devices became more sophisticated.

The need to identify and know more about fission product rare earths in the 1940's led to the development of ion exchange separation technology, and as we are all aware, the continued practical development of this by Spedding and his people at Ames led to commercially usable ion exchange separation processes.

The neutron absorption characteristics of the four high cross section rare earths were interesting for nuclear poison use, and although there is still a modest use for gadolinium, the only significant use that has been developed was that for europium oxide in control rods. The ability of industry to meet this need paved the way for subsequent use of europium in television phosphors in 1963-1964.

As significant as the development of a practical ion exchange technique to the promotion of rare earths was the aircraft nuclear propulsion project in the mid 1950's. The need for large amounts of very high purity yttrium in a short time was the real start of appreciable rare earth separation work.

The availability of reasonably priced high purity rare earths from commercial sources, coupled with advertising to let people know they were available, opened opportunities for industrial basic research. In the last decade we have seen the extrordinary development of ferrite garnets and phosphors, new ceramic materials and colorants, and new catalysts.

In the early 1950's, the large AEC demand for thorium necessitated enlargement of existing ore processing facilities and the creation of new ones. Again, monazite was the thorium source, and considerable quantities of semi-refined by-product rare earths were produced. The availability of these, as well as decreasing dependence on foreign-ore sources, were further stimulations to large scale use of both cheap mixtures and purified materials.

The Socony development of Durabead rare earth catalysts for petroleum cracking in 1960 came from a great deal of research by Socony and from some marketing skill and the promotion of availability by the rare earth industry.

In the 1960's, the rare earth producers stretched their capacities to keep up with the rising demands for high purity materials for television phosphors, and in response to needs dramatically increased ion exchange production rates, and began finally to capitalize on the capabilities of liquid-liquid extraction.

Now for some statistics: The capacity to convert rare earth ore to rare earth products has increased in this country from about 1,000 tons per year in the 1910's and 1920's to about 14,000 tons rare earth oxide equivalent in the 1950's and 1960's. Due to the relatively high demand for thorium in the early 1900's for gas mantles, and again in the early 1950's for atomic energy, the industry ore handling capacity in these periods was based largely on thorium demand. There were ups and downs, of course, but it is axiomatic with the producers that by-products do not remain by-products very long. Eventually a use is found for everything.

Commercial ion exchange separation of all of the rare earths began on a modest scale in the mid 1950's and has increased rapidly ever since. Aside from cerium and lanthanum products, total yearly production of high purity rare earths grew from a few hundred pounds yearly in the mid 1950's to more than a quarter of a million pounds per year now. But do not be misled by these numbers: mixed rare earths have shown a steady growth in use from about 2 million pounds per year in the early 1900's to about 8 million pounds per year rare earth oxide equivalent now. Installed USA capacity to process rare earth ores will soon reach about 20 thousand tons per year, and production of rare earth ore concentrates in this country has approached 25 to 30 thousand tons per year.

The bar graphs compare the 1946 and 1966 production and value of the American primary producers' products. Mixtures of rare earths account for about 80 per cent of the volume of rare earths used.
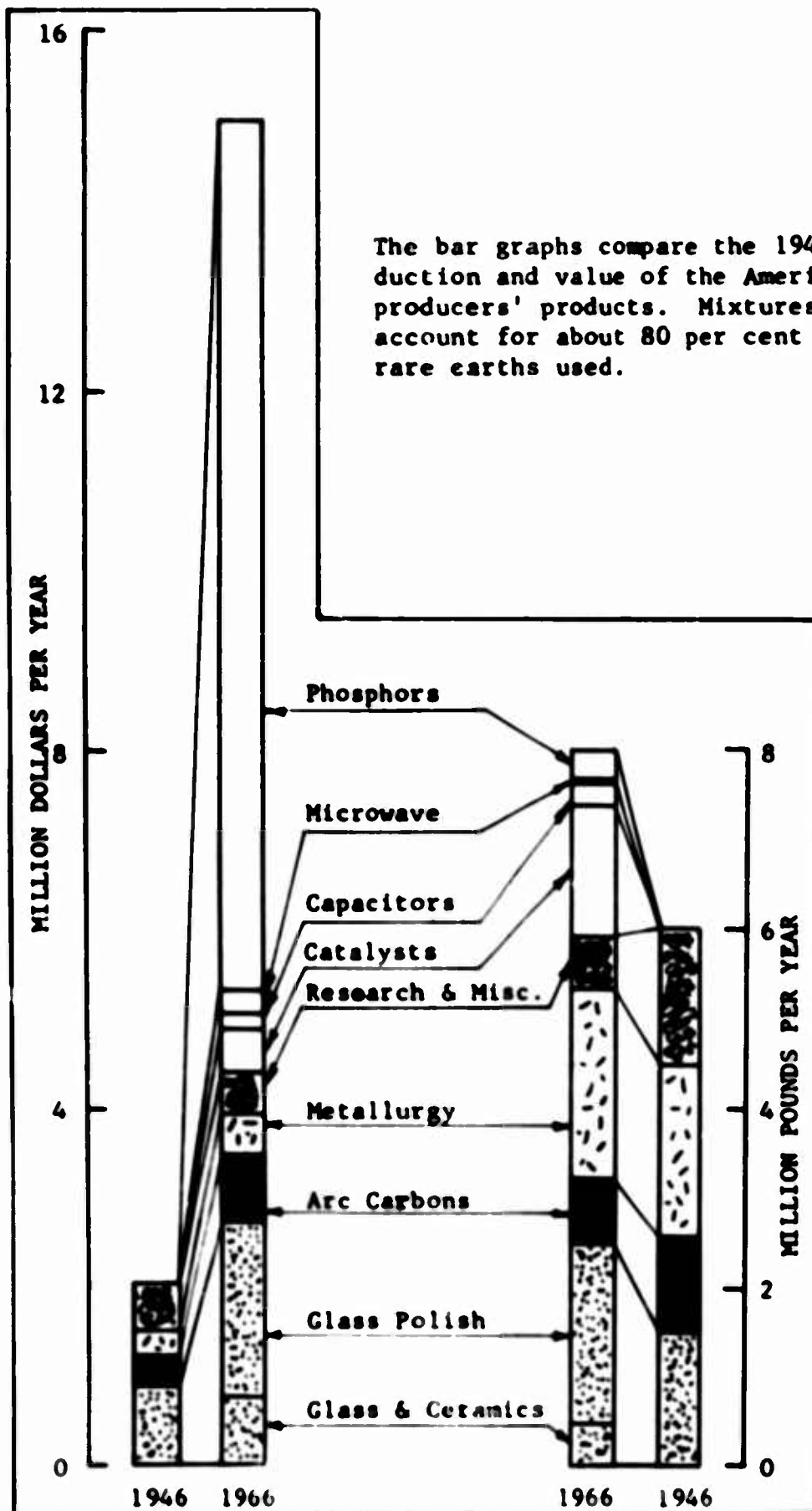
OPTICAL AND MAGNETIC PROPERTIES OF RARE EARTH COMPOUNDS

K. H. Hellwege, S. Hüfner and G. Weber

Institut für Technische Physik, Darmstadt

A survey of the optical and magnetic investigations going on in this Laboratory will be given.

The optical studies are mainly concerned with some magnetically ordered compounds. The rare earth iron perovskites of erbium, holmium and dysprosium have been investigated. The ground state splitting in these compounds and its temperature dependence have been deduced from the spectra and compared with the values expected from other, magnetic measurements. For dysprosium aluminum perovskite a triplet structure of all lines was found up to 20°K. This structure is interpreted as the result of an almost exact Ising type of interaction in this compound. An exchange integral of $/J/ = 6.2$ cm^{-1} is deduced from the spectroscopic measurements. The Néel temperature of this compound has been determined as $3.55 \pm 0.10^{\circ}$K by a magnetic measurement.

Hyperfine structure investigations in rare earth compounds have been performed using a grating spectrograph and a Fabry Pérot interferometer. The hyperfine structure of various lines in holmium ethylsulfate and holmium chloride have been resolved. In the ethylsulfate the Zeeman splitting has been measured carefully in the region where various

levels overlap. An isotope shift has been observed in the absorption spectrum of Eu^{2+} (CaF_2).

The frequency dependent magnetic susceptibility has been measured for several compounds in the frequency range from 2 c/s to 40.10^6 c/s.

For holmium ethylsulfate the susceptibility reveals one- and two-spin cross relaxation processes at points in the energy level scheme which are expected from the optical hyperfine structure measurements. The one-spin relaxation times show a strong dependence on the change of nuclear spin quantum number of the levels involved in the processes: for $\Delta I_z = 0$ the cross relaxation times T are $T < 10^{-9}$ sec whereas for $\Delta I_z > 0$ the relaxation times are $T \approx 10^{-6}$ sec. Cross relaxation processes have also been found in $CeCl_3 \cdot 6H_2O$. In this compound the multilevel ground term scheme arises from exchange coupled ion pairs, where the interaction is of the Heisenberg type. Cross relaxation processes of very high order have been detected.

CRYSTAL FIELD SPLITTINGS OF Nd^{3+} IN

$NdAlO_3$ and Nd^{3+}: $LaAlO_3$

P. Sitaram*, S. R. Polo** and W. B. White*

*Materials Research Laboratory
**Department of Physics
Pennsylvania State University
University Park, Pennsylvania

As part of an investigation of the optical spectra of ions in 12 coordinated sites, the spectra of Nd^{3+} in $NdAlO_3$ and $LaAlO_3$ have been obtained. Both $NdAlO_3$ and $LaAlO_3$ have a rhombohedrally distorted perovskite structure in which the rare earth ion has 12 oxygen neighbors with site symmetry C_{3v}.

Spectra have been measured on single crystals (grown from a PbC PbF_2 - B_2O_3 flux by Remeika's method) and on powders pressed with KBr pellets over the spectra range of 3.2 to 0.35 microns and at temperatures down to 4^0K.

The energy states are defined by the set of quantum numbers $f^3WUSLJ'_z$ where W and U are irreducible representations of the groups of R_7 and G_2. Matrix elements of the type.

$\langle 1^3TSLJJ_z|U_q^k|1^3T'S'L'J'J_z'\rangle$. where T and T' are additional quantum numbers and U_q^k is the tensor operator for the appropriate symmetry at the Nd^{3+} site, have been calculated. The crystal-field parameters, the three Slater integrals F_2, F_4 and F_6, and the spin-orbit coupling constant ζ have been evaluated.

Magnetism of some rare earth elements and ionic compounds under pressure

R. PAUTHENET, D. BLOCH, F. CHAISSE
Laboratoire d'Electrostatique et de
Physique du Métal - GRENOBLE - France

Abstract : Experiment results and discussion of the effect of the pressure on the magnetic ordering points and on the saturation magnetization of several polycristalline rare earth elements and rare earth iron garnets.

. . . .

The problem of the variation of the exchange interaction of magnetic substances as a function of volume is of great interest for the understanding of magnetic phenomena. A large amount of information on this subject can be obtained by the study of the influence of pressure upon certain magnetic properties. In this article, we present briefly the results of our studies on the effect of hydrostatic pressure upon the magnetic properties of several rare earth elements and rare earth ferrite garnets.

I - The rare earth elements

The Curie point θ_f of gadolinium and the Néel point θ_N of terbium, dysprosium, and holmium decrease when the temperature increases[1][2][3] (table 1).

At 77°K, in a field of 29,000 Oe, the amplitudes of the magnetization M of the elements gadolinium, terbium, or dysprosium are very close to those of the spontaneous magnetization M_s for these elements at the same temperature; it follows that the relative variation of the magnetization in a field of 29,000 Oe as a function of pressure represents to a good approximation, the corresponding variation of the spontaneous magnetization. The values of $(1/M_s)(\partial M_s/\partial p)$ at 77°K are negative. The experiment could not be made with holmium.

T A B L E 1

	θ_f (°K)	$\dfrac{d\theta_f}{dp}$ (10^{-3}d°.bar^{-1})	θ_N °K	$\dfrac{d\theta_N}{dp}$ (10^{-3}d°.bar^{-1})	$\dfrac{1}{M_s}\dfrac{\partial M_s}{\partial p}$ 77°K (10^{-6} bar^{-1})
Gd	294.5	- 1.56 ± 0.05			-1.1 ± 0.3
Tb			231	- 0.82 ± 0.10	-3.8 ± 0.4
Dy			172	- 0.6 ± 0.1	-0.15 ± 0.20
Ho			110	- 0.45 ± 0.15	

Discussion of Results

In the molecular field model, the magnetization M, in an external field H, at a temperature T, obeys a law of the form

$$\frac{M}{M_o} = f\left(M_o \cdot \frac{H + nM}{T}\right) \qquad (1)$$

where M_o designates the moment at absolute saturation and the molecular field coefficient. In the absence of an external field, the substance is spontaneously magnetized and relation (1) becomes

$$\frac{M_s}{M_o} = f\left(\frac{M_s/M_o}{T/\theta}\right), \qquad (2)$$

where θ designates the ordering temperature.

When the ordering temperature varies by an amount $d\theta$ under the application of a pressure dp, the difference between the spontaneous magnetizations at these temperatures is evidently zero, and there results the relation

$$\left(\frac{\partial M_s}{\partial p}\right)_\theta dp + \left(\frac{\partial M_s}{\partial T}\right)_{p=1\ atm.} d\theta = 0 \qquad (3)$$

In addition, since it is necessary to apply a magnetic field in order to bring about a magnetization, the experiments made at constant field satisfy the relation

$$\left(\frac{\partial M}{\partial p}\right)_{\theta, H} dp + \left(\frac{\partial M}{\partial T}\right)_{p=1\ atm, H} \cdot d\theta = dM \qquad (4)$$

When the variations of the pressure and the temperature are small, the magnetization measured in a field H, at a temperature θ, and at atmospheric pressure is, to the first approximation, equal to that measured in the same field, but at a temperature $\theta + d\theta$ and a pressure dp. Thus $dM \approx 0$, and from relations (3) and (4),

$$\frac{d\theta}{dp} = -\frac{(\partial M_s/\partial p)_\theta}{(\partial M_s/\partial T)_{p=1\ atm}} \approx -\frac{(\partial M/\partial p)_{\theta, H}}{(\partial M/\partial T)_{p=1\ atm, H}} \qquad (5)$$

For gadolinium, in a field of 20,000 Oe, $\left(\frac{\partial M}{\partial T}\right)_{p=1\ atm, 20,000\ Oe} = -2$ e.m.u. $\times$ degree^{-1} gm^{-1} and

$\left(\frac{\partial M}{\partial p}\right)_{\theta, 20,000\ Oe} = -3.3 \cdot 10^{-3}$ e.m.u. $\times$ bar^{-1} gm^{-1}; from relation (5), $\frac{d\theta}{dp} = -1.65 \times 10^{-3}$ degree $\times$ bar^{-1}, in good agreement with the experimental value.

From the thermodynamic potential, the relation

$$\left(\frac{\partial V}{\partial H}\right)_{p, T} = -\left(\frac{\partial M}{\partial p}\right)_{H, T} \qquad (6)$$

is established, in which V represents the volume of the substance relative to a constant number of carriers; this relation is expressed, as a function of the coefficient of magnetostriction at saturation λ, in the form

$$\lambda/H = -1/3V \left(\frac{\partial M}{\partial p}\right)_{H,T} \qquad (7)$$

At $293°K$, for gadolinium, $\partial M/\partial p$ is of the order -3.85×10^{-3} e.m.u. x bar^{-1} x gm^{-1} for fields between 6,000 and 11,000 Oe and -2.85×10^{-3} for H between 11,000 and 23,000 Oe; λ/H is calculated to be 103×10^{-10} and 70×10^{-10}, respectively. The experimental values are 90×10^{-10} and 60×10^{-10} (4).

The variation of magnetic properties induced by the application of pressure can result from the variation of the moment at absolute saturation and the variation of the exchange interactions. After having neglected certain terms, the relative variation of the magnetization at absolute saturation can be deduced from relation (2), as follow

$$\frac{1}{M_o} \cdot \left(\frac{\partial M_o}{\partial p}\right)_T = \frac{1}{M_s} \cdot \left(\frac{\partial M_s}{\partial p}\right)_T + \frac{1}{M_s} \cdot \frac{T}{\theta} \cdot \left(\frac{\partial M_s}{\partial T}\right)_p \cdot \left(\frac{\partial \theta}{\partial p}\right)_T \qquad (8).$$

For gadolinium, at $77°K$, $(\partial M_s/\partial T)_{p=1\ atm}$ is of the order -0.3 e.m.u. x degree^{-1} x gm^{-1}; letting the value of $(\partial\theta/\partial p)_{77°K}$ be equal to that measured in the neighborhood of the Curie point, $\frac{1}{M_s} \frac{T}{\theta} \left(\frac{\partial M_s}{\partial T}\right)_{p=1\ atm} \cdot \left(\frac{\partial \theta}{\partial p}\right)_{77°K}$ is of the order $+ 0.5 \times 10^{-6}$; with $\frac{1}{M_s} \cdot \left(\frac{\partial M_s}{\partial p}\right)_{77°K}$ equal to $(-1.1 \pm 0.3) \times 10^{-6}$, the value of $1/M_o (\partial M_o/\partial p)_{77°K}$ is calculated to be of the order $(-0.6 \pm 0.3) \times 10^{-6}$ bar^{-1}. The same calculation gives $1/M_o (\partial M_o/\partial p)_{77°K} = (-3.6 \pm 0.5) \times 10^{-6}$ bar^{-1} for terbium and $(0.1 \pm 0.25) \times 10^{-6}$ for dysprosium.

In the rare earth elements, the magnetic interactions are indirect[5], through the intermediary of the conduction electrons; if Γ designates the constant of coupling between the spin of a conduction electron, of effective mass m^*, and the spin of a 4 f electron, the following relations can be established.

$$-\frac{1}{R} \cdot \frac{1}{\theta} \cdot \left(\frac{\partial \theta}{\partial p}\right)_{H,T} = -\frac{4}{3} + 2\left(\frac{\partial \log \Gamma}{\partial \log V}\right)_{H,T} + \left(\frac{\partial \log m^*}{\partial \log V}\right)_{H,T} \qquad (9)$$

$$- \frac{1}{K} \cdot \frac{1}{\rho_m} \cdot \left(\frac{\partial \rho_m}{\partial p}\right)_{H,T} = -\frac{1}{3} + 2 \left(\frac{\partial \log \Gamma}{\partial \log V}\right)_{H,T} + 2 \left(\frac{\partial \log m^*}{\partial \log V}\right)_{H,T} \quad (10)$$

$$- \frac{1}{K} \cdot \frac{1}{\Delta M} \cdot \left(\frac{\partial \Delta M}{\partial p}\right)_{H,T} = \frac{2}{3} + \left(\frac{\partial \log \Gamma}{\partial \log V}\right)_{H,T} + \left(\frac{\partial \log m^*}{\partial \log V}\right)_{H,T} \quad (11)$$

K is the compressibility, ρ_m the magnetic contribution to
the resistivity, and ΔM the contribution of the conduction
electrons to the magnetization.

From the experimental data on the variation of the ordering
temperature and of the resistivity with pressure, the follo
wing values can be calculated.

	$\frac{\partial \log \Gamma}{\partial \log V}_{H,T}$	$\frac{\partial \log m^*}{\partial \log V}_{H,T}$	$\frac{1}{\Delta M} \frac{\partial \Delta M}{\partial p}_{H,T}$
Gd	2.6	- 1.7	- 4.1
Tb	1.2	0.3	- 4.1
Dy	1.9	- 1.1	- 3.9
Ho	2.3	- 1.2	- 4.6

Γ varies approximately as the square of the volume.

The experimental value for the moment at absolute satura-
tion for gadolinium is 7.55 μ_B; if the excess value 0.55 μ_B
is attributed to the moment of the conduction electrons by
comparison to the moment of the spin, $(\partial \Delta M / \partial p)_{H,T}$ is
determined as - 2.2 x 10^{-6} μ_B x bar^{-1} x gm^{-1}, in acceptable
agreement with the value $(- 4 \pm 2)$ x 10^{-6} μ_B x bar^{-1}
calculated from the preceding experiments. A similar result
is obtained for dysprosium.

In view of the above discussion, it appears that the
variation with pressure of the magnetization of gadolinium
and of dysprosium can be uniquely attributed to the
variation of the magnetization of the conduction electrons.

II - The rare earth ferrite garnets

The magnetic ions in the rare earth ferrite garnets,
$5Fe_2O_3.3T_2O_3$, are classified into three categories of
crystallographic sites : 4 Fe^{3+} ions occupy the 16 a-sites,
6 Fe^{3+} ions the 24 d-sites, and 6 T^{3+} ions the 24 c-sites.
A ferrimagnetic model permits the interpretation of the
magnetic properties. Between the moments of sub-lattices
a and d there exist strong negative interactions which
orient the moments of the iron ions on the 16 a sites
antiparallel to those on the 24 d sites; the a-c and d-c

interactions tend to polarize the moments of the rare earth
ions in the sense opposite to that of the resultant magne-
tization of the iron ions. The interactions relative to a
rare earth ion are about 10 times as weak as the
interactions with an iron ion; apparently the ferro-
magnetic Curie points θ_f are principally determined by the
interactions between the iron ions of the sub-lattices a
and d. Since the Curie points vary little from one ferrite
to the other , the interactions between the iron ions
vary equally little. It follows that the effect of pressure
upon the Curie point should be the same for the various
ferrites. The experiments have confirmed this hypothesis;
$\frac{d\theta_f}{dp}$ is of the order 1.22×10^{-3} degree bar^{-1}.

The magnetic interactions are of the superexchange type;
they depend on the distances between the ions $Fe^{3+} - O^{2-}$,
that is, on the volume of the lattice as well as the
angles of the bonds $Fe^{3+} - O^{2-} - Fe^{3+}$, the values of which
are related equally to the volume of the lattice. Since
magnetoelastic effects shall be neglected in what follows,
the interactions are considered to be a function of the
volume V_T of the specimen at a temperature T, in the
absence of spontaneous magnetization. The molecular field
coefficient representing the interactions between the ions
of the sub-lattice a with those of the sub-lattice d is
represented as n_{ad}; the coefficient corresponding to the
interactions between the ions on the same sub-lattice are
represented as n_{aa} and n_{dd} for sub-lattices a and d
respectively. At constant pressure and field, the magnetic
interaction depends only on the temperature; generally the
thermal variation of the molecular field coefficient is
represented by an expression of the form

$$n_{ij}^{T} = n_{ij}^{\circ} (1 + \gamma_{ij} T) \tag{12}$$

in which n_{ij}^{T} represents the value of one of the coeffi-
cients n_{aa}, n_{dd}, or n_{ad} at the temperature T. This
expression is applicable only for sufficiently high tempera
tures; in particular, it has allowed (upon assuming
$\gamma_{aa} = \gamma_{dd} = \gamma_{ad} = \gamma$), the interprétation of the
paramagnetic properties of spinel ferrites and garnets.
Rigorously, the γ_{ij} are not all equal, although they are
of the same order of magnitude. In effect, when T varies,
only the distances $Fe^{3+} - O^{2-}$ vary, with the angles
remaining constant. These distances are of the same order
of magnitude for the Fe^{3+} ions on the a - sites as for
those on the d - sites, so that the effects upon the

coupling of the variations of the distances with temperature can be comparable . The equality of the τ_{ij} leads to [6]

$$\frac{d(\log n_{aa})}{d(\log V)_{\theta_f}} = \frac{d(\log n_{dd})}{d(\log V)_{\theta_f}} = \frac{d(\log n_{ad})}{d(\log V)_{\theta_f}} = \frac{\gamma}{3\alpha_{\theta_f}} \cdot \frac{1}{1 + \gamma\theta_f} \quad (13)$$

where α_{θ_f} designates the coefficient of linear dilatation for the sample at the Curie temperature θ_f, in the absence of spontaneous magnetization. For yttrium ferrite, $\gamma = - 1 \times 10^{-4}$, α_{θ_f} is of the order 9.9×10^{-6}, and $\frac{d(\log n_{ij})}{d(\log V)_{\theta_f}}$ is calculated to be $- 3.5$, a value close to $-10/3$.

The Curie temperature is expressed as a function of the molecular field coefficients by the relation

$$\theta_f = \frac{C}{2} \left[\lambda n_{aa}^{\theta_f} + \mu n_{dd}^{\theta_f} + \sqrt{(\lambda n_{aa}^{\theta_f} - \mu n_{dd}^{\theta_f})^2 + 4 \lambda\mu (n_{ad}^{\theta_f})^2} \right] \quad (14)$$

where λ and μ are the proportions of iron ions on the a - sites and the d - sites, respectively, and C is the Curie constant of an Fe^{3+} ion. The moment of an Fe^{3+} ion is well defined by its spin, sothat the Curie constant does not vary with pressure. Taking into account the preceding results, the following relation can then be established

$$\frac{d(\log \theta_f)}{d(\log V)} = \frac{d(\log n_{ij}^{\theta_f})}{d(\log V)} \quad . \quad (15)$$

Upon considering that during the course of an experiment the variation of the volume is due to the application of pressure and to the elevation of the temperature, the above relation can be expressed in terms of the results $\frac{d\theta_f}{dp}$ as follows

$$\frac{d(\log \theta_f)}{d(\log V)} = \frac{- \frac{1}{K_{\theta_f}} \cdot \frac{1}{\theta_f} \cdot \frac{d\theta_f}{dp}}{1 - \frac{3\alpha_{\theta_f}}{K_{\theta_f}} \cdot \frac{d\theta_f}{dp}} \quad . \quad (16)$$

K_{θ_f} is taken to be the value of the compressibility of yttrium ferrite at ambient temperature, 0.68×10^{-6} bar^{-1}; $d(\log \theta_f)/d(\log V)$ is calculated to be of the order

- 3.4, in good agreement with the value determined above.

This law of the variation of the exchange interaction with the volume is contrary in sign to that which one might expect from the variation of the Curie point of the different ferrite garnets as a function of their parameters It appears that from one ferrite to the other, the variation of the angle of the bond $Fe^{3+} - O^{2-} - Fe^{3+}$ plays the important role in the variation of the magnetic interactions.

The compensation temperature θ_c of a ferrite garnet is expressed as a function of the molecular field coefficient n, representing the interactions between the ensemble of iron ions of the a - and of the d - sites and the rare earth ions of the c - sites, by the relation

$$\theta_c = - n\nu\, C_T \qquad (17)$$

ν is the proportion of rare earth ions on the c - sites and C_T the Curie constant for a rare earth ion. From the above relation it follows that

$$\frac{d(\log \theta_c)}{d(\log V)} = \frac{d(\log (-n))}{d(\log V)} \qquad (18)$$

$\frac{d(\log \theta_c)}{d(\log V)}$ can be calculated by an expression analogous to (16), relative to the compensation temperature; it is found that $\frac{d(\log (-n))}{d(\log V)}_{\theta_c}$ is of the order - 4.

These studies of the magnetic properties under pressure allow to obtain progressively the variations of the local exchange interactions with distance.

R E F E R E N C E S

1 - L. PATRICK - Phys. Rev. 1954, 93, p. 384

2 - L.B. ROBINSON, F. MILSTEIN, A. JAYARAMAN -
    Phys. Rev. 1964, A 134, p. 187

3 - D. BLOCH, R. PAUTHENET -
    International Conference on Magnetism. Nottingham 1964

4 - R.M. BOZORTH, T. WAKIYAMA -
    J. Phys. Soc. Japan. 1963, 18, p. 97

5 - P.G. de GENNES - J. Phys. Rad. 1962, 23, p. 510

6 - D. BLOCH, F. CHAISSE, R. PAUTHENET -
    C.R. Acad. Sci. 1966, 262, p. 404

PROPERTIES OF THE RARE-EARTH METALS
AND ALLOYS AT HIGH PRESSURES

D. B. McWhan
Bell Telephone Laboratories
Murray Hill, New Jersey

ABSTRACT

A review of recent measurements of the pressure
dependence up to 85 kbar of the Néel and Curie tempera-
tures, and crystal structures will be given. The mate-
rials which have been studied include (1) the elements
Eu, Gd, Tb, Dy, and Ho, (2) the Tb-Y alloy system, and
(3) a series of alloys with equal average DeGennes func-
tion. The initial slopes (dT/dP) are approximately
proportional to the average DeGennes function. A poly-
morphic transition from a hexagonal-close-packed structure
to a Sm-type structure is found with increasing pressure
in many of these alloys. The Sm-type phase does not ex-
hibit ferromagnetism but has two ordering temperatures.
The higher ordering temperature of the Sm-type phase is
10% lower than that of the hcp phase, and the two order-
ing temperatures in the Sm-type phase differ by 17%.

Can measurements at high pressures help us to
understand the properties of the rare earth metals at
1 atm? At present only fairly simple measurements have
been made, and these include x-ray diffraction, electri-
cal resistivity, ordering temperatures (from the relative
initial susceptibility), and melting point and solid-
solid transition temperatures (from differential thermal
analysis). Unfortunately, these properties are not

easily interpreted unambiguously, but they do neverthe-
less provide some guidelines for discussing the prop-
erties of the rare earths at 1 atm and for suggesting
under what conditions of pressure and temperature such
experiments as neutron scattering, positron annihlation,
and Mössbauer studies should be done. Below, the crys-
tal structures of the rare earth metals and alloys at
high pressures will be summarized and the effect of
changes of volume and crystal structure on the magnetic
ordering temperatures of the heavy rare earths will be
discussed. For the most part the measurements cover
the range of pressure from ~ 5 to ~ 100 kbar and of
temperature from 77° to 298°K. More detailed discus-
sions can be found in references 1-4 and references
therein.

At 1 atm and room temperature the rare earth
metals have a series of different crystal structures.
For the present discussion the metals Ce, Eu, and Yb
will be excluded because of their anomalous properties.
The sequence of structures in the trivalent metals is
face-centered-cubic (fcc) (La at T > 300°C), double
hexagonal-close-packed (dhcp) (La, Pr, Nd), samarium
type (Sm), and hexagonal-close-packed (hcp) (Gd through

Lu and Y). These structures may be viewed as a stepwise
progression from cubic to hexagonal nearest neighbor
symmetry. If each structure is considered as stacking
sequences of close-packed layers with the B layer being
cubic (C) in the sequence ABC and hexagonal (H) in the
sequence ABA, then the crystal structures become
$3C \rightarrow 2(CH) \rightarrow 3(CHH) \rightarrow 2H$. The opposite sequence has
been found to exist with increasing pressure.[5] Figure 1
compares the regions of stability of the different
structures as a function of atomic number or the number
of 4f electrons. The figure was constructed from com-
pression measurements by Bridgman,[6] and x-ray measure-
ments by Perez-Albuerne, et al.[7], Piermarini and Weir[8]
and ourselves, and our initial susceptibility studies.
As a first approximation, the critical volume at which
a structure change will occur is given by the following
equations

$$V = A - 0.78n$$
$$A = 20.7 \text{ cm}^3/\text{mole} \quad \text{for} \quad \text{fcc} \rightarrow \text{dhcp}$$
$$23.5 \text{ cm}^3/\text{mole} \quad \text{for} \quad \text{dhcp} \rightarrow \text{Sm-type}$$
$$24.4 \text{ cm}^3/\text{mole} \quad \text{for} \quad \text{Sm-type} \rightarrow \text{hcp}$$

where n is the number of 4f electrons and V is the
volume at the transition. The line for the dhcp -
Sm-type boundary is poorly defined, and the figure

only shows the general trend which might be expected. If one assumes that Y is close to Lu in its properties, then the data for some Tb - Y alloys and some alloys of the heavy rare earths with each other also fall on the appropriate line. The transitions become very sluggish in the alloys and the observed critical volumes are subject to large errors. At 1 atm the sequence of crystal structures dhcp → Sm-type → hcp is found in many alloy systems of the light rare earth metals with the heavy rare earth metals or Y. In these cases the composition range for the Sm-type structure seems to be correlated with the c/a ratio. In trying to understand the origin of this sequence of structures from a theoretical point of view it may be more profitable to carry out band structure calculations on say Gd as a function of volume than to cope with alloys. It seems reasonable to speculate that the negative slope of the phase boundaries reflects the decreasing radius of the $4f$ shell with increasing atomic number. As a result of this the volume at which the core perturbs the conduction bands sufficiently to make another structure more stable decreases with increasing atomic number.

Turning to the pressure dependence of the highest ordering temperature, the average slope (dT/dP)

in the hcp phase of the different materials which have
been studied is plotted against the average DeGennes
function

$$\left(X_1 = \sum_1 \, c_1(g_1-1)^2 J_1(J_1+1) \right)$$

in Fig. 2. Roughly, the magnitude of the slopes in-
creases linearly with X_1 and in all cases dT/dP is
negative. The data include the elements Ce, Nd and
Gd through Er and a series of Tb - Y alloys. The
ordering temperature is dependent on a large number of
variables and it would be difficult to ascribe the
pressure dependence to a variation of one or two of
them unambiguously. Only recently have detailed cal-
culations begun to show the real complexity of the band
structures of the heavy rare earth metals and the im-
portance of anisotropy in the s-f exchange. Because
of this, only two general statements will be made.
First from Fig. 2 it would appear that the gross fea-
tures of the pressure dependence can be expressed by
an equation of the form

$$(dT/dP) = - (0.092 \pm 0.014) \sum_1 c_1(g_1-1)^2 J_1(J_1+1)$$

This equation is compatible with a relation for the
ordering temperature of the form $T = AX$, but it is not
compatible with the relation $T = AX^{\frac{2}{3}}$ which has been
found empirically to fit the observed ordering temper-
atures at 1 atm. Secondly, the magnitude of the
logarithmic derivative (d log T/d log V) is consistent
with the expected change in the density of states with
volume. Liu has shown that for a free electron model
with isotropic exchange the following relation applies:

$$\frac{d \log T_c}{d \log V} = \frac{\partial \log N(E_F)}{\partial \log V} + 2 \frac{\partial \log |I|}{\partial \log V}$$

where $N(E_F)$ is the density of states at the fermi surface
per atom and $|I|$ is an s-f exchange integral.[9] The
quantity $\dfrac{\partial \log N(E_F)}{\partial \log V}$ is approximately equal to the
electronic Grüneisen parameter γ_e. Typical values of
γ_e for the transition metals range from 1 to 2.5 and the
observed values of (d log T/d log V) are from 2.2 to 0.8.
This is consistent with the bulk of d log T/d log V re-
sulting from the volume dependence of the density of
states, and, therefore, the volume dependence of $|I|$
may be very small.

The effect on the magnetic properties of the
change in crystal structure from hcp $\rightarrow$ Sm-type is quite

pronounced. In all of the materials where the transition was observed the highest magnetic ordering temperature decreased $\sim$ 10% on going to the Sm-type phase. As the volume change at the transition is less than 1%, the bulk of the decrease in the ordering temperature must result from the change in symmetry.

Another feature of the magnetic properties of the Sm-type phase is the apparent disappearance of ferromagnetism in the temperature range studied. In Gd or the Tb_xY_{1-x} alloys (with $x > 0.8$) in the hcp phase a sharp rise in magnetic susceptibility indicative of ferromagnetism is observed with decreasing temperature. In the Tb_xY_{1-x} alloys of course this is preceded by a small cusp as the material first becomes antiferromagnetic. In the Sm-type phase only small cusps are observed suggesting that only some type of antiferromagnetic ordering occurs. Magnetic studies at 1 atm of alloys with the Sm-type structure and for lighter rare earth metals have only revealed antiferromagnetic ordering but this might have been a property of the $4f$ electron configuration. The high pressure studies suggest that the structure is the dominant factor. It will be interesting to investigate the heavy rare earth metals in the Sm-type structure down to liquid helium temperatures to see if this conclusion is still valid.

The most striking effect observed in the
studies of the relative initial susceptibility as a
function of temperature in the Sm-type phase is the
occurrence of two symmetrical cusps differing in
temperature by $\sim$ 17%. This suggests that two inde-
pendent ordering temperatures exist. One is tempted
to draw an analogy to the magnetic properties of Nd
metal. In both the dhcp (Nd) and Sm-type structures
there are two types of crystallographic sites, and
the neutron diffraction studies on Nd suggest that
the cubic and hexagonal sites order independently
and at different temperatures. Perhaps this is a
far more general phenomenon which is not necessarily
associated with the beginning of the rare earth series
where the crystal field effects are fairly important.
However, until experiments such as neutron diffraction
can be done at high pressure (P > 30 kbar) a definitive
answer cannot be given.

In conclusion, the variation of the size of
the 4f electron cloud with atomic number leads to dif-
ferences in crystal structure which in turn lead to
striking differences in the magnetic properties. Pres-
sure induced lattice parameter changes appear to affect
the ordering temperatures through changes in the density

of states, which gives strong evidence for a magnetic coupling through interaction of the conduction electrons. It appears that ferromagnetism can never be achieved in the Sm-structure, but further work will be needed at low temperatures to check this. In this connection, we have recently started to make measurements which extend down to temperatures of $4°K$ and up to pressures of ~ 100 kbar. It is hoped that in addition to further initial susceptibility studies it will be possible to investigate the pressure dependence of the electrical resistivity and in particular the spin disorder scattering.

REFERENCES

1. D. B. McWhan and A. L. Stevens, Phys. Rev. 139, A682 (1965).

2. D. B. McWhan, P. C. Souers and G. Jura, Phys. Rev. 143, 385 (1966).

3. D. B. McWhan, E. Corenzwit and A. L. Stevens, J. Appl. Phys. 37, 1355 (1966).

4. D. B. McWhan and A. L. Stevens, Phys. Rev. (Feb.1967).

5. A. Jayaraman and R. C. Sherwood, Phys. Rev. 134, A691 (1964).

6. P. W. Bridgman, Collected Experimental Papers, (Harvard University Press, 1964).

7. E. A. Perez-Albuerne, R. L. Clendenen, R. W. Lynch and H. G. Drickamer, Phys. Rev. 142, 392 (1966).

8. G. J. Piermarini and C. E. Weir, Science 144, 575 (1964).

9. J. H. Liu, Phys. Rev. 127, 1889 (1962).

FIGURE CAPTIONS

Fig. 1   Generalized phase diagram for the rare earth
         metals at $98°K$. x and ● are the volume per
         mole at which the phase change occurs for the
         elements; Δ are points for some alloys of
         heavy rare earth metals with each other and
         with Y (Y assumed equivalent to Lu), and O
         are limiting points for the Sm-type to dhcp
         transition.

Fig. 2   The pressure dependence of the highest magnetic
         ordering temperature as a function of X_t.

         + and ● are from Ref. 4; ∇ D. Bloch, Ann.
         Phys., series 14, 1, 93 (1966); ◻ J. E. Milton
         and T. A. Scott, Bull. Amer. Phys. Soc. 11,
         527 (1966); x L. Patrick, Phys. Rev. 93, 384
         (1954); ▼ L. B. Robinson, F. Milstein, and
         A. Jayaraman, Phys. Rev. 134, A187 (1964);
         ◇ K. Andres, Phys. Kondensienten Materie 2,
         294 (1964); ◆ P. Landry and R. Stevenson,
         Can. J. Phys. 41, 1273 (1963); ▲ P. C. Souers
         and G. Jura, Science 145, 575 (1964); ■ L. D.
         Livshits and Yu S. Genshaft, Zhur. Eksper. i
         Teoret. Fiz. 48, 1050 (1965).
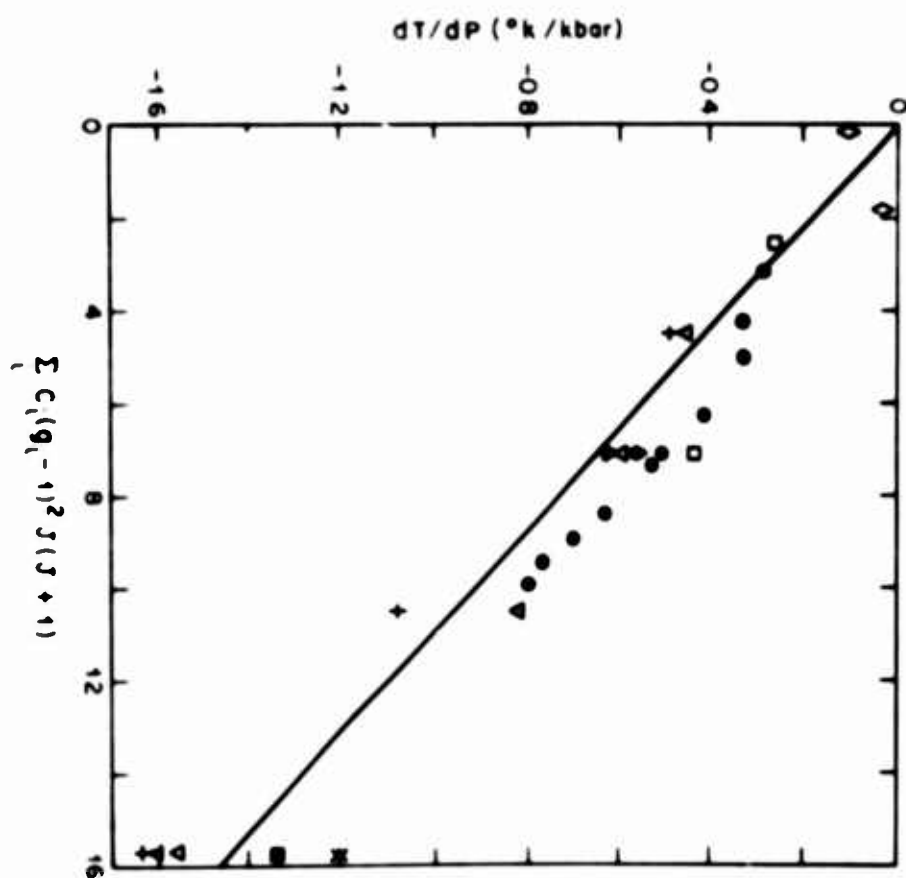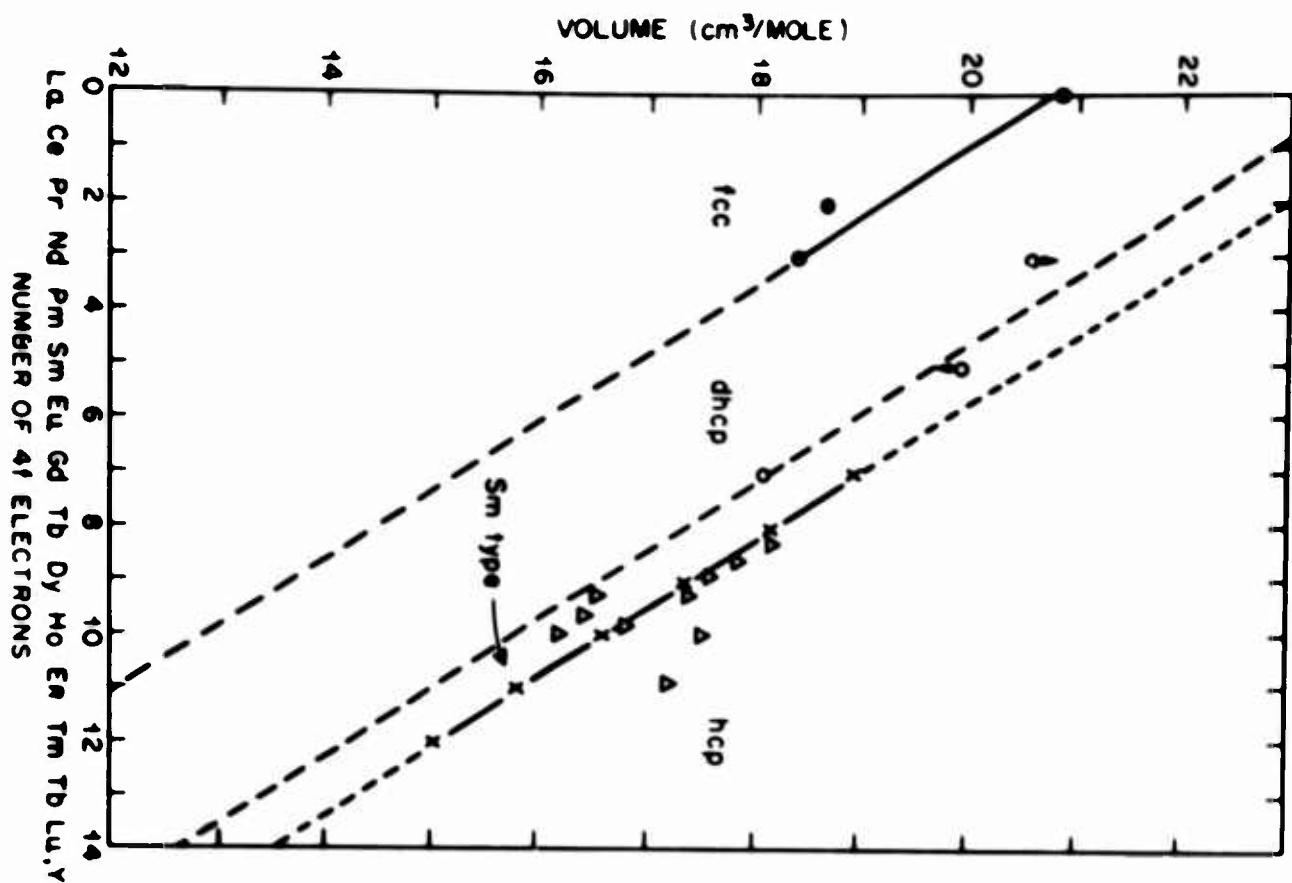
Magnetic and Electrical Properties of Some Yb-Sb Phases [1]

R. E. Bodnar[2], H. Steinfink, and K. S. V. Narasimhan
Department of Chemical Engineering
The University of Texas
Austin, Texas

Introduction

Recently we reported (3) on the crystal chemistry of seven
stable intermediate phases in the ytterbium-antimony binary system.
In addition to characterizing the new alloys as to electrical and mag-
netic properties, a study of ytterbium valence variations in the alloys
has been made based on magnetic susceptibility data. The rare earth,
ytterbium, in addition to being trivalent as the other lanthanides, also
exhibits divalent behavior. In the divalent state, all the 4f electrons
are paired and hence the atom will not be magnetic, whereas in the triva-
lent state, an unpaired 4f electron generates a theoretical magnetic
moment of 4.5 Bohr Magnetons. From the magnetic susceptibility data,
the actual moment can be calculated, and the statistical number of
Yb atoms in each valence state can be deduced for each alloy.

Experimental Procedure

The magnetic susceptibility measurements were made in the
range 325°K to 1.70°K using the Faraday technique. Samples ranging
from two to ten milligram in weight were placed in a pyrex sample
bucket and suspended in an inhomogeneous field produced by a four inch
electromagnet. The vertical forces exerted on the specimens were
measured with a Cahn R-G electrobalance. Corrections for the sample
holder were determined in advance and applied in each case. Measure-
ments were made at several field strengths in the order of five to eight
kilogauss. The system was checked by measuring the magnetic sus-
ceptibility of Hg $[Co(CSN)_4]$ and 99.999% pure antimony, both of
which have well documented susceptibilities. (4, 5).

Corrections for ferromagnetic impurities commonly found in rare earth metals were made by the susceptibility-magnetic field extrapolation first suggested by Honda and Owen (6). Samples which exhibited more than five percent of their susceptibility as being due to ferromagnetic impurities were discarded. Since most of the alloys exhibited weak paramagnetic behavior, corrections for the diamagnetic part of the atom cores were applied. Commonly accepted values are (7) -0.41×10^{-6} emu/g for antimony and -0.116×10^{-6} emu/g for ytterbium. For the more electrically conductive samples, a correction (8) of 0.24×10^{-6} emu/g was applied to account for the paramagnetism of each conduction electron in the alloy. Electrical conductivity measurements were made on pressed and sintered polycrystalline blocks using a four-probe d.c. method. These were made over the range 350°K to 4.2°K; thermoelectric power measurements were made at 25°C. The interatomic separation of Yb and Sb and Yb radii, where possible, were obtained from single crystal X-ray diffraction work reported previously (3).

Results

a) Magnetic Data

The magnetic susceptibility vs. temperature curves for the seven alloys are shown in Figure 1. Both the Weiss constant, θ, and effective magnetic moment, μ, were obtained using the linear portions of the curves and assuming Curie-Weiss behavior. The distributions of electrons in the 4f shells were obtained by considering the observed susceptibility (after corrections) to be attributable to unpaired 4f electrons. Hence, one can say that

$$\chi_{obs} = a \, \chi(4f^{14}) + b \, \chi(4f^{13})$$

where a and b represent the number of Yb atoms in each of the two respective electronic configurations. Since $\chi(4f^{14})$ is zero, the fraction of atoms with an unpaired electron is simply $\chi_{obs}/\chi(4f^{13})$. The theoretical

- 30 -

moment for an unpaired 4f electron in Yb is 4.50 Bohr Magnetons, so that

$$b = [\frac{\lambda_{obs}}{4.50}]^2$$

These results along with representative susceptibility values and Weiss constants for each phase are shown in Table I. Only YbSb exhibits near trivalent Yb with an observed moment of 4.24 Bohr Magnetons. This value is somewhat higher than the 3.74 B.M. reported for YbSb by Iandelli (9), but is presumed to be more reliable since purer YbSb material was produced in this investigation. Almost an entire electron has been promoted out of the 4f shell, and thus one should expect the Yb radius to decrease because of the reduced nuclear screening. In general, 1:1 ratio compounds of Yb with group V elements snow normal trivalent behavior, but at the expense of thermal stability, as indicated by the low melting point of YbSb, (3) for example.

The relationship between atom separation and observed magnetic moment or number of 4f electrons removed out of the 4f shell is shown in Figure 1 for the alloys for which interatomic distances are available. The phase Yb_4Sb_3 exhibits a valence between two and three with 0.26 electrons promoted out of the 4f shell. This is consistent with the observed Yb-Sb atom separation for this alloy. The remaining two phases for which interatomic distances are available, Yb_5Sb_3 and $YbSb_2$, are seen to be divalent both by the low magnetic moment and by the large atom separations. This large atom separation is due mainly to the larger effective diameter of the Yb atom in these alloys. The effective radius of the antimony atom is not expected to vary greatly in these metal-like alloys.

The remaining three phases exhibit low moments indicating divalent Yb behavior, but no crystallographic data exist to compare magnetic moments with atom separation. All of these remaining unsolved structures are complex and could contain Yb atoms in several valence states.

The molecular field constant W was calculated using the expression[10]

$$\theta = NW \, g^2 \mu_\beta^2 \, J(J+1)/3k$$

$$= NW \, \mu_{exp}^2 / 3k$$

where N is Avagadro's number and k is the Boltzmann constant and they are -31 for YbSb and -593 for Yb_4Sb_3. In the case of YbSb which exhibits a strong antiferromagnetism $\dfrac{J_{ex}}{k}$ was calculated using the expression of Domb and Sykes (11),

$$\frac{k}{J_{ex}} = \frac{0.68 \, (S+1) \, q}{3 \, S \, \theta}$$

where q = 12 is the lattice coordination number. The value of J_{ex}/k obtained for YbSb is -8.5.

The molecular field constant W is intimately connected with the paramagnetic Curie temperature and the Neel temperature, T_N. In the case of an antiferromagnetic substance with two identical sublattices this is given by (10)

$$\frac{\theta}{T_N} = \frac{1+W}{1-W} \; .$$

In the case of YbSb and Yb_4Sb_3 the ratio on the left is 4.7 and 3.7 respectively. If the type of magnetic ordering were known in these two cases it would be possible to calculate the molecular field constant. The value $\dfrac{\theta}{T_N} \sim 5$ could imply that ordering of the third kind for a f.c.c. structure exists for YbSb.

The shape of the $1/\chi$ vs T curves for the nearly diamagnetic phases is similar to that of pure Yb metal as shown by Locke (12). The magnetic susceptibility data on the Yb metal used in this investigation agreed very closely with those reported by Locke. Since Sb is diamagnetic, the observed susceptibility is simply a reflection of the magnetism of the divalent Yb atoms in the alloys.

TABLE I

Phase	$\chi_g \times 10^6$ emu/g(25°C)	θ°K	μ_{eff} B.M.	No. of electrons removed from 4f shell
$YbSb_2$	0.371	5	0.60	0.018
$YbSb$	20.57	-70	4.24	0.887
α-Yb_5Sb_4	0.70	-42	0.72	0.026
β-Yb_5Sb_4	1.35	-159	1.15	0.065
Yb_4Sb_3	3.65	-389	2.29	0.260
Yb_5Sb_3	1.35	-53	0.97	0.046
Yb_5Sb_2	0.917	-46	0.75	0.028
Yb metal	0.41	-50	0.46	0.010
Sb metal	-0.81	--	---	---
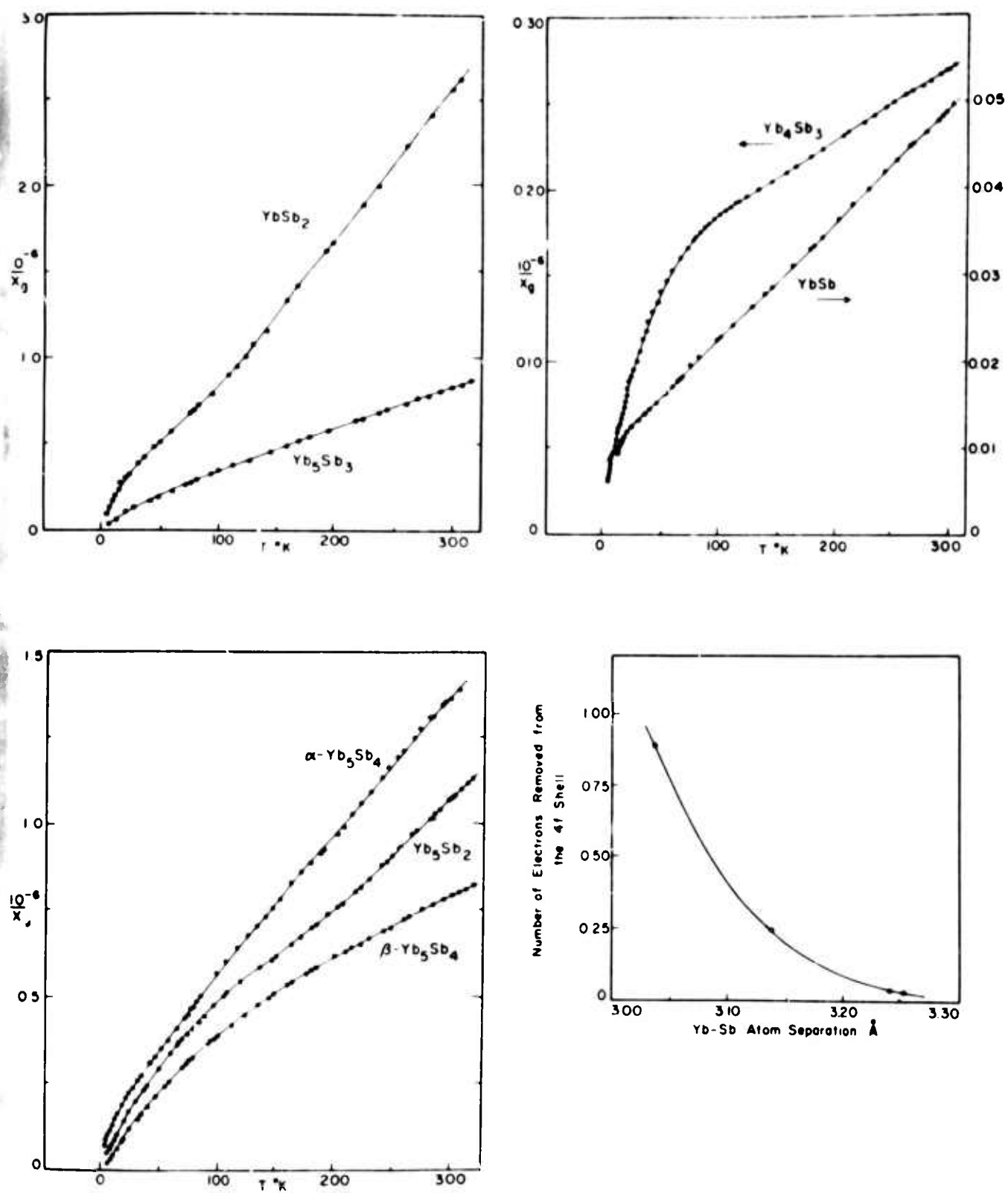
Figure 1

Magnetic Susceptibility vs. temperature for Yb-Sb phases and relationship of interatomic distance to oxidation state of ytterbium.

References

1) Research sponsored by National Science Foundation Grant GK 1236.

2) Present address: Central Research, 3M Company, 2501 Hudson Road, St. Paul, Minnesota.

3) Bodnar, R. E., and H. Steinfink, Inorg. Chem. 6, 327,   7

4) Gschneidner, K. A. and R. Smoluchowski, J. Less Common Metals, 5, 374 (1963).

5) Figgis, B. N., and R. S. Nyholm, J. Chem. Soc., 4190 (1958).

6) Bates, L. F., Modern Magnetism, 4th Edition, Cambridge University Press, London (1961).

7) Selwood, P. W., Magnetochemistry, Interscience Publishers, Inc., New York (1956).

8) McClure, J. W., J. Phys. Chem. Solids, Vol. 24, 871, (1963).

9) Iandelli, A., Rare Earth Research, The Macmillan Co., New York (1961).

10) Goodenough, J. B., "Magnetism and the Chemical Bond", Interscience Publishers, New York, 1963.

11) Domb, C. and Sykes, M. F., Phys. Rev. 128, 168(1962).

12) Locke, J. M. Proc. Soc. London, 870, 476 (1957).

Magnetic and Crystallographic Characteristics of Praseodymium[*] Hydrides

K. H. Mader and W. E. Wallace
Department of Chemistry, University of Pittsburgh, Pittsburgh, Pa.
15213

ABSTRACT

The susceptibilities (X) and lattice parameters are reported for a series of praseodymium hydrides represented by the formula PrH_x in which x varies from .99 to 2.57. X was measured from 4 to 300°K and at field strengths up to 21 kOe. The samples are two phase for $x < 1.85$. Curie-Weiss behavior is observed for all samples above 100°K with slopes in fairly good agreement with that expected for an assemblage of free tripositive ions. Deviations occur below 100°K. These are two kinds -- negative for $x < 2.1$ and positive for $x > 2.1$. The deviations in the first case are small and are thought to result from the crystal field interaction. The positive deviations are ascribed to a change of valence for Pr from +3 to +4. Magnetic, electrical and crystallographic evidence is in accord with this postulate. There is no indication of magnetic ordering in the Pr hydrides at 4.2°K. This is attributed to weakness of the interactions and to the valence changes which reduce the atomic moment.

I. INTRODUCTION

The lanthanide hydrides were studied by Kubota and Wallace[1-4] in this laboratory several years ago. Results were obtained for only a few Pr hydrides and these were anomalous. The present study was undertaken in an attempt to clarify the situation. To anticipate that which follows somewhat different results have now been obtained. The behavior can now be logically accounted for on the basis of a change in valence or crystal field quenching.

II. RESULTS AND DISCUSSION

The results are largely summarized in Table I and Figs. 1-5. At room temperature and at 4.2°K all samples listed in Table I were paramagnetic; their X values were independent of field up to 20 kOe. The lattice parameters (Fig. 1) indicate that the hydride phase extends from x = 1.85 to the highest concentrations studied. The break in the lattice parameter is in agreement with the sharp rise of the

electrical resistance at H/Pr = 1.85 found by Daou,[6] also evidence
for the occurring of the one phase-region. At lower hydrogen content
the system is two-phase (hydride plus the terminal phase based on Pr)
in keeping with the findings of Pebler and Wallace.[7] X versus temp-
erature results were obtained for x = 0.99 and 1.47, which are in the
two-phase region. These are included in Table I but are not dis-
played graphically. The data plotted in Figs. 2 and 3 are representa-
tive of all the hydrides listed in Table I.

The effective moments for the 11 single phase samples average
3.76 μ_B, which is slightly higher (3.9%) than the free tripositive ion
moment (3.62 μ_B).[8] This is the value obtained from the slope of the
1/X versus T curves for the region 100 to 300°K. The most noteworthy
feature of the curves in Figs. 2 and 3 is the deviation from C-W
behavior for T < 100°K. With hydrides having x < 2.10 this deviation
is monotonously negative. For the more hydrogen-rich samples there
is a region of positive deviations, then a plateau which is followed
by a new C-W region with another effective moment. This low tempera-
ture moment, μ_{eff}, cannot be established precisely but the values
(Column 6, Table I) accord reasonably well with the moment of quadri-
positive Pr, 2.56 μ_B.[8] The low temperature behavior noted for the most
hydrogen-rich samples is in marked contrast with the 1/X-T behavior
for elemental Pr.[3,9] The latter material behaves as a Van Vleck
paramagnet with X becoming essentially temperature-independent be-
low about 10°K.

It is also of interest to note (Fig. 4) that X measured at
4.2°K decreases approximately tenfold over the range of the dihydride
phase. The data given in Fig. 5 show that X varies with temperature
in the presumed "plateau" region and that, moreover, X exhibits a
weak maximum near 55°K, the actual temperature of the maximum being
slightly field dependent.

The unusual 1/X versus T behavior below 100°K is ascribed
largely to a valence change. Above 100°K the Pr ions are predominantly
in the tripositive state. When x > 2.10 and the lattice is somewhat
contracted, cooling promotes partial conversion of the ions into the

+4 state. The valence change and the accompanying reduction in average Pr moment produces the positive deviations from C-W behavior. Below about 20°K the conversion is largely complete and the 1/X versus T behavior is that of an assemblage of quadripositive ions. For samples with x < 2.10 the situation is different. Since a valence change introduces positive deviations from C-W behavior, the non-linearity of 1/X with T for these materials must stem from another source. The small, negative deviations is probably due to crystal field quenching effects. [10-14] The μ_{eff} values for hydrides with x between 1.85 and 2.10 are about the same as those for x > 2.10. However, this is regarded as fortuitous. The unimportance of valence changes for hydrogen-poor samples is a result of the distention of the lattice for these materials. The maximum in X near 56°K for $PrH_{2.57}$ is, on this basis, due to the decline in moment caused by the ionization of Pr^{+3} into Pr^{+4}. The rise in X below 40°K is associated with improved alignment of the Pr^{+4} ions in the field as thermal agitation is diminished.

The postulate of the valence change near 56°K is supported by conductivity data inferred from the behavior of the equipment for measuring X. The magnetic balance by its time response indicates whether or not the sample under investigation is a good (i.e. metallic) conductor. If it is, the balance is sluggish when field is altered due to the effects of eddy currents. The lanthanide hydrides near room temperature are known to be poor conductors. [15] Their valence band is either filled or empty. Thus $PrH_{2.57}$ above 60°K acts in the magnetic measurements as a non-conductor. Near 55°K its behavior changes; it begins to act as a metallic conductor as expected if ionization of the Pr ion into a higher valence state is occurring with the released electron going into a previously empty conduction band.

The deviation from C-W behavior, which is associated with the valence change is concentration dependent (Fig. 3). This follows from the dependence of the lattice spacing or composition. The more

hydrogen-rich sample has a more compact lattice. It experiences the valence change at a higher temperature than a sample which is poorer in hydrogen and more distended. The composition dependence of X at 4.2°K reflects this same effect. The sharp fall in X between x = 2 and 2.25 is associated with the conversion of Pr^{+3} ions into Pr^{+4} ions as the hydrogen concentration is increased.

The behavior of Pr in these hydrides is very similar to that observed by Kern[16] for Pr oxide systems.

The results obtained have been carefully examined to ascertain what type of magnetic order, if any, the Pr hydrides develop at lowest temperatures studied. NdH_2 becomes ferromagnetic below 9.5°K. X values are unavailable for CeH_2 but Schreiber[17] reports on the basis of NMR results that it becomes antiferromagnetic in the liquid helium range. There is no indication of magnetic ordering of the Pr hydrides. This is perhaps not surprising since on the basis of de Gennes factor,[18] $(g-1)^2 J(J+1)$, the interactions are weakened fourfold in Pr as compared to Nd compounds. Thus ordering might not be expected at temperatures in excess of 2.5°K.

The observed Weiss constant ranges from -25 to -75°K, suggesting antiferromagnetic interactions. However, conclusions based on θ values in systems in which there is a valence shift with temperature can be misleading if viewed uncritically. All the hydrides studied probably contain a small fraction of Pr in the quadripositive state, which increases with decreasing temperature. This shift of valence will decrease the slope of the 1/X versus T plots and make the intercept more negative. Thus the valence change will affect θ and μ_{eff}, negatively and positively, respectively. On this basis the large negative Weiss constants and excess of μ_{eff} over $g\sqrt{J(J+1)}$ both represent additional evidence in favor of the +3 to +4 valence change. There is no indication of antiferromagnetic exchange (nor for that matter of ferromagnetic exchange) in the effect of field on X at 4.2°K. From the considerations in the preceding paragraph ordering would not be expected unless temperature were reduced to about 2°K. This is

the case if all ions were tripositive. If some or all of the ions are quadripositive, even lower temperatures would be required. Thus it is not surprising that a cooperative phase was not detected at $4.2°K$.

Table I

Summary of Magnetic Measurements on Pr Hydrides

PrH_x	χ_g $[10^{-6}]$		μ_{eff}*	θ	μ'_{eff}
x	$4.2°K$	$298°K$	(μ_B)	$(°K)$	(μ_B)
0.99**	1170	37.2	3.69	-26	3.4
1.47**	1140	35.0	3.59	-25	2.8
1.85	1145	35.5	3.77	-37	2.5
2.01	940	36.0	3.69	-33	2.6
2.03	989	35.1	3.62	-32	2.7
2.10	352	35.9	3.75	-43	3.0
2.16	355	35.8	3.74	-44	2.3
2.19	270	37.5	3.86	-51	2.4
2.24	125	34.5	3.73	-50	3.2
2.33	122	36.5	3.85	-60	2.8
2.53	142	34.5	3.90	-85	2.2
2.57	90	34.0	3.76	-75	2.8
2.57	94	33.5	3.72	-75	2.8

* μ_{eff} is the moment for $T > 100°K$.

μ'_{eff} applies to the region between 4 and $20°K$.

** These samples are in the two-phase region.

1. Y. Kubota and W. E. Wallace, J. Appl. Phys. Suppl. 33, 1348 (1962).

2. W. E. Wallace, Y. Kubota and R. L. Zanowick, Advances in Chemistry
    Series issue on "Non-Stoichiometric Compounds," Vol. 39, 122 (1963).

3. Y. Kubota and W. E. Wallace, J. Appl. Phys. 34, 1348 (1963).

4. Y. Kubota and W. E. Wallace, J. Chem. Phys. 39, 1285 (1963).

5. R. A. Butera, R. S. Craig and L. V. Cherry, Rev. Sci. Instruments
    32, 708 (1961).

6. J N. Daou, Compt. Rend. 247, 1595 (1958).

7. A. Pebler and W. E. Wallace, J. Phys. Chem. 66, 148 (1962).

8. J H. Van Vleck, The Theory of Electric and Magnetic Suscepti-
    bilities, Oxford University Press, New York, 1932, p. 248.

9. J. M. Lock, Proc. Phys. Soc. (London) 70B, 566 (1957).

10. E. A. Skrabek and W. E. Wallace, J. Appl. Phys. 34, 1356 (1963).

11. B. Bleaney, Proc. Roy. Soc. 276, 28 (1963).

12. T. Tsuchida and W. E. Wallace, J. Chem. Phys. 43, 2087 (1965).

13. David P. Schumacher and W. E. Wallace, Inorg. Chem. 5, 1563 (1966).

14. W. E. Wallace in Progress in Rare Earth Science and Technology,
    Ed. by L. Eyring, Vol. 3, to appear.

15. B. Stalinski, Bull. acad. plon. sci. 5, 1001 (1957) and 7, 269
    (1959).

16. S. Kern, J. Chem. Phys. 40, 208 (1964).

17. D. S. Schreiber, private communication.

18. P. G. de Gennes, Compt. Rend. 247, 1836 (1958).

Captions for Diagrams

Fig. 1. Lattice Spacing Versus the H/Pr Ratio. The dashed curve
represents the data of Pebler and Wallace, ref. 7.

Fig. 2. Inverse susceptibility per gram versus temperature for
$PrH_{1.85}$ ($\triangle$), $PrH_{2.01}$ (o) and $PrH_{2.10}$ (x). For clarity the
$1/\chi_g$ values for the latter two samples have been displaced
upward by 10 and 20 units, respectively.

Fig. 3. Inverse susceptibility per gram versus temperature for
$PrH_{2.24}$ ($\triangle$), $PrH_{2.33}$ (o) and $PrH_{2.57}$ (x). The $1/\chi_g$ for
$PrH_{2.33}$ and $PrH_{2.57}$ have been displaced upward by 10
units and 20 units, respectively.

Fig. 4. Susceptibility per gram (at $4.2°K$) versus composition for
praseodymium hydrides.

Fig. 5. Field and temperature dependence of the susceptibility for
$PrH_{2.57}$ in the "plateau" region.

Figure 1

Figure 5

Figure 1

$\chi_g \times 10^6 \left(\frac{emu}{g}\right)$ vs H/Pr ratio

Figure 5

- 47 -
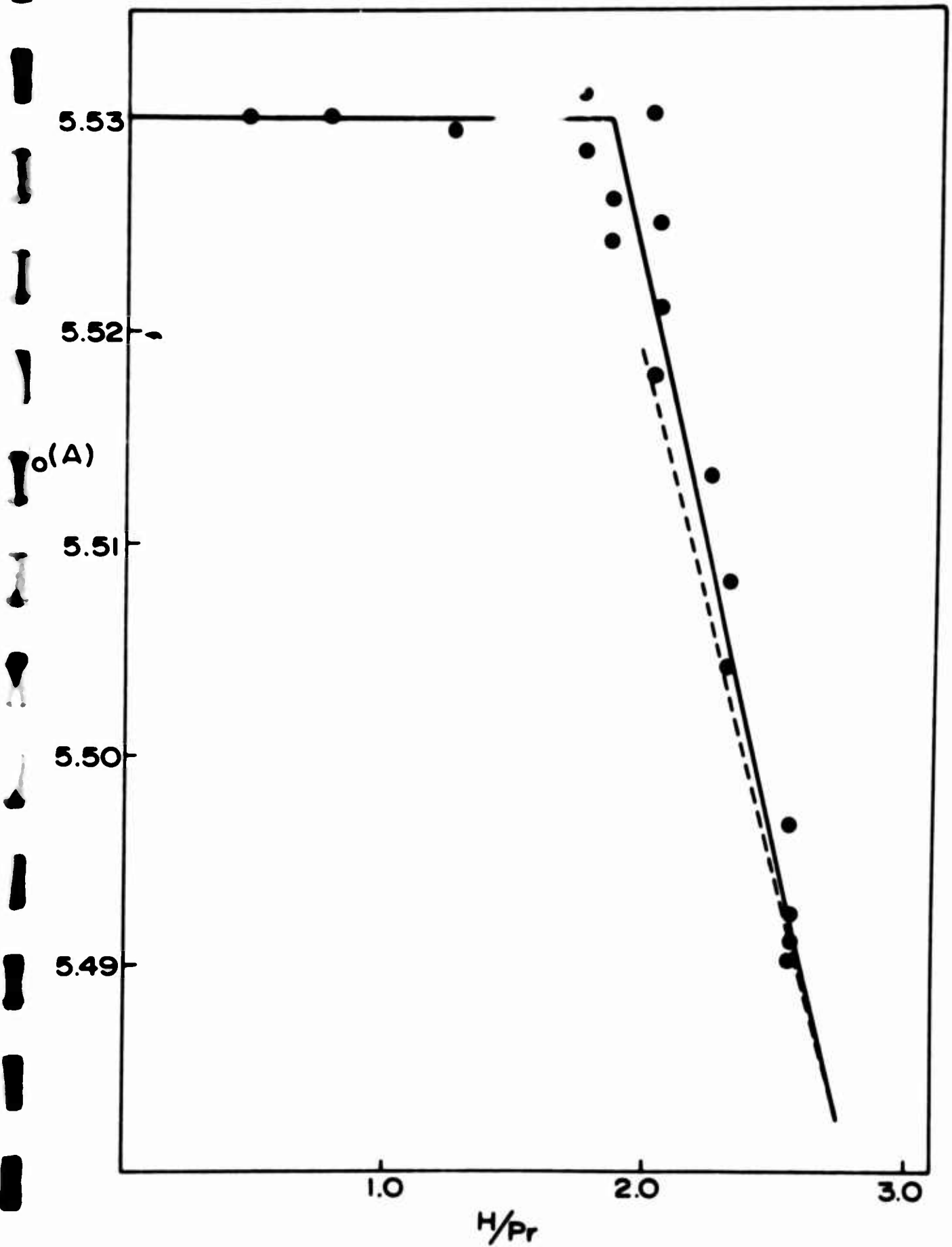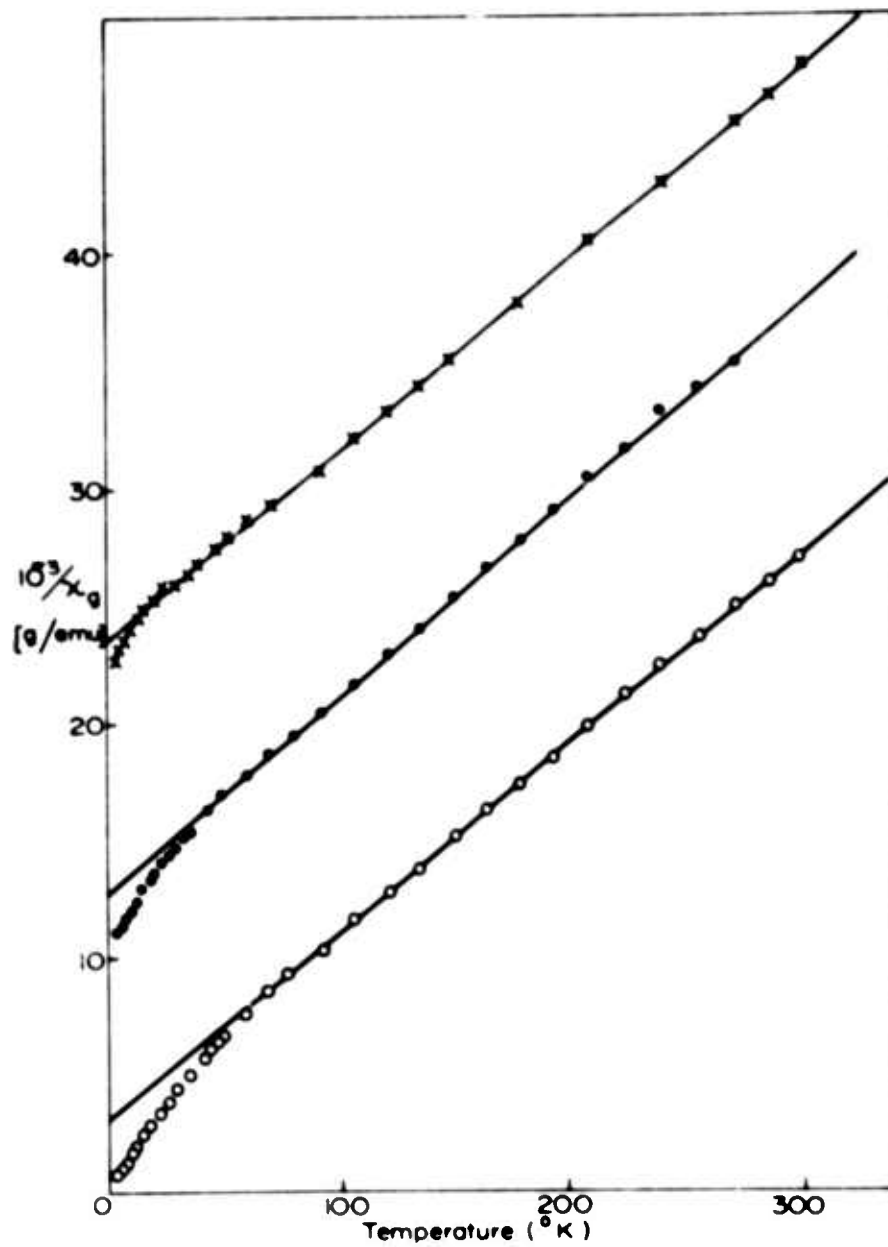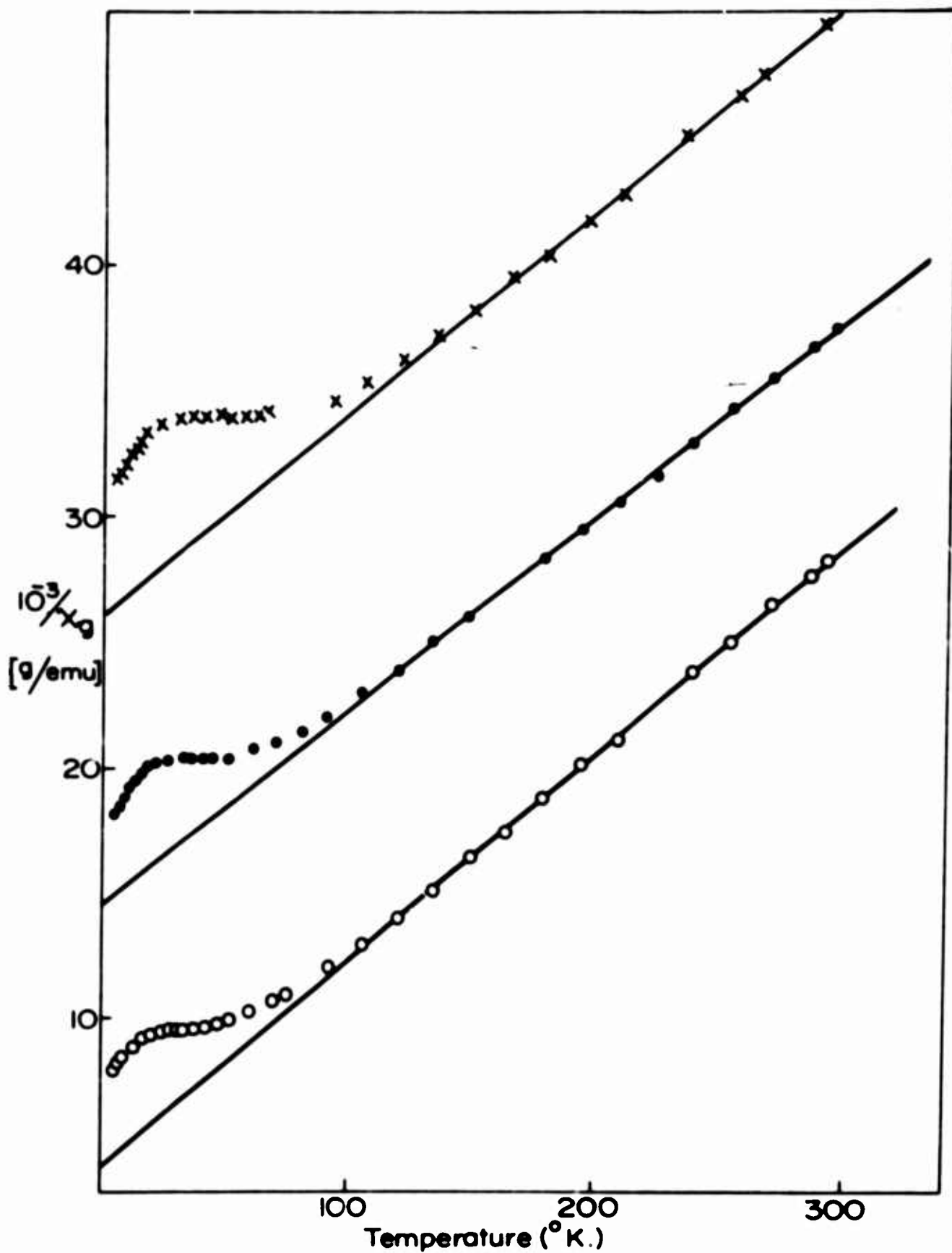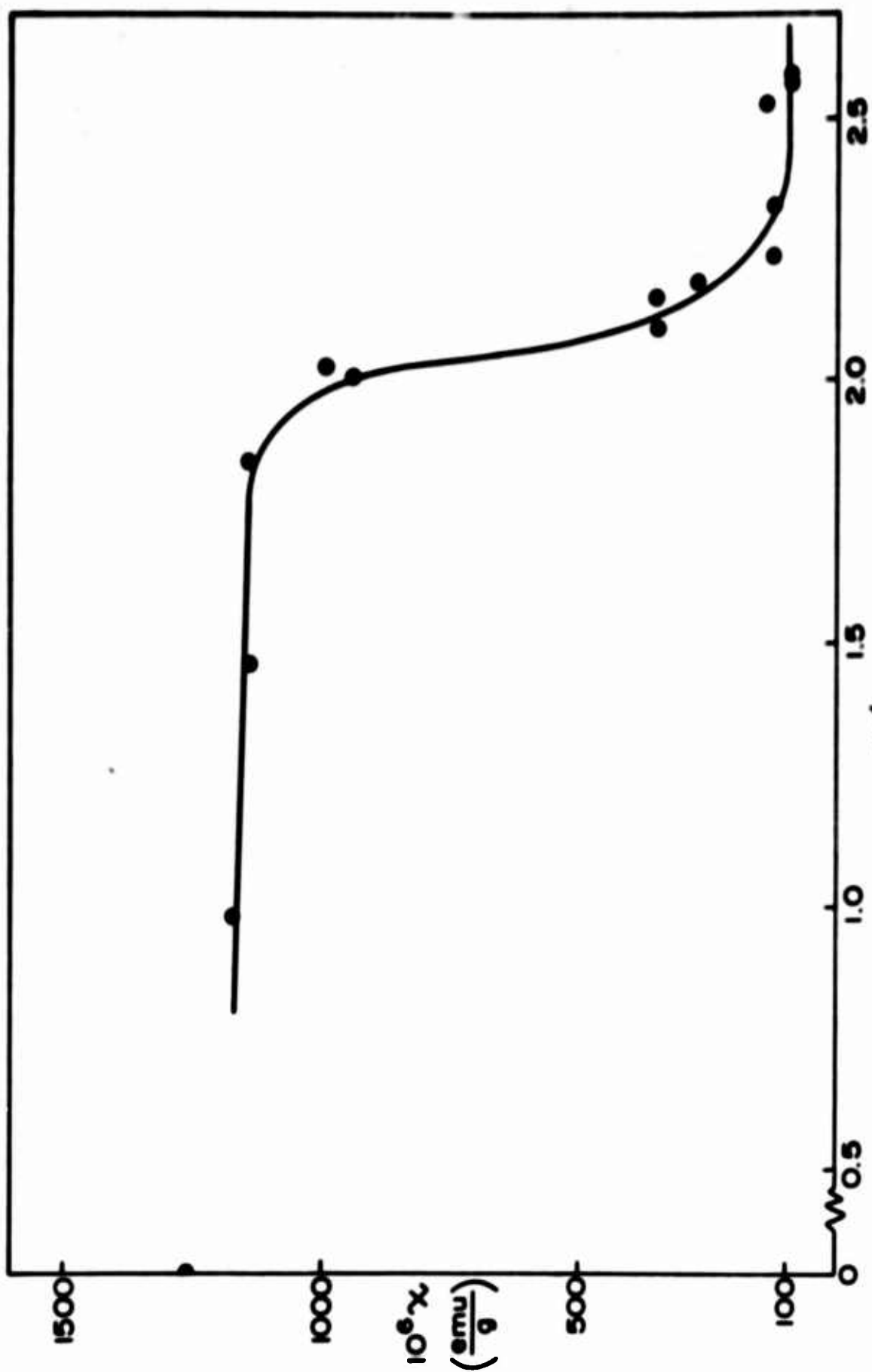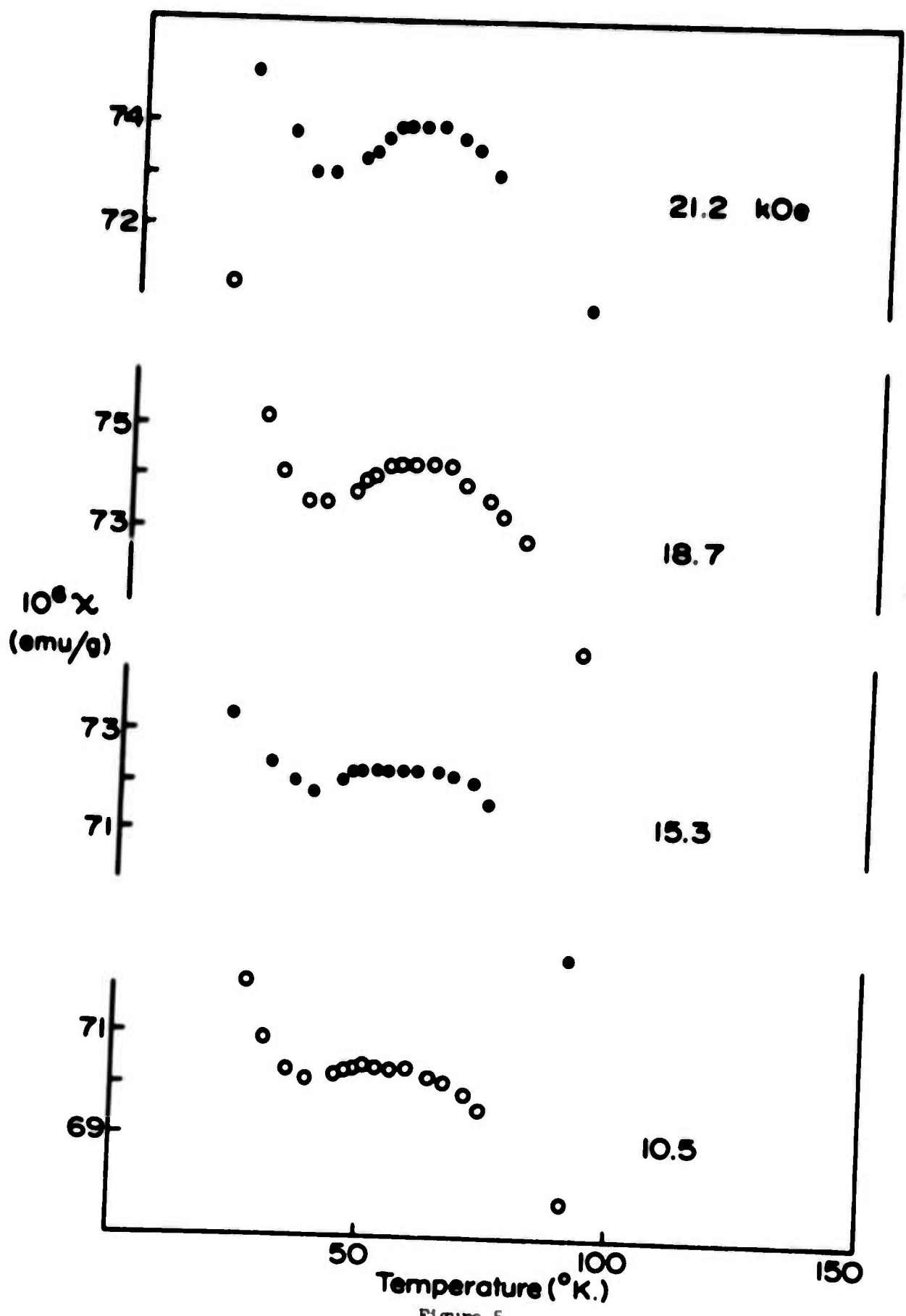
MAGNETIC BEHAVIOR OF RARE EARTH COMPOUNDS WITH SINGLET CRYSTAL FIELD GROUND STATE

Bernard R. Cooper
General Electric Research and Development Center
Schenectady, New York

ABSTRACT: The susceptibility and high field magnetization expected for rare earth compounds with singlet crystal field ground state are discussed. In particular, we discuss the limitations of molecular field theory in treating exchange effects on the susceptibility, non-linear magnetization, and criterion for magnetic ordering in such systems.

There is much current interest[1-6] in the magnetic properties of rare earth compounds where the crystal field ground state of the rare earth ion is a singlet. For crystal field effects large compared with exchange, the ionic moment is completely quenched and consequently there is no magnetic ordering.[7] This situation occurs, for example, for the Tm and Pr compounds of NaCl structure with group V anions. Such compounds have some quite interesting properties. The susceptibility at low temperature is of a Van Vleck type brought about by the polarization of the singlet ground state. At high fields the magnetization becomes nonlinear,[3,4] and the present author[3,5,6] predicted the development of a large anisotropy in the nonlinear region. This has now been observed experimentally in TmSb.

For such singlet ground state systems, it is interesting to consider the effects of exchange as it increases from zero toward the value necessary for magnetic ordering. For compounds such as those of Tm and Pr, one often

observes departures from the simple crystal field only sus-
ceptibility and high field magnetization. It is a simple
matter to include exchange effects on these properties
within the molecular field approximation. However, the
molecular field calculations often do not explain the ob-
served behavior. The question then arises as to whether
this lack of agreement reflects inadequacies of the molec-
ular field model for treating the effect of a given ex-
change interaction; or whether the discrepancies must be
attributed to a change of the exchange mechanism with tem-
perature and high magnetic fields, or to some other mech-
anism not yet considered. This has led us to consider
the question of corrections to the molecular field behav-
ior arising from correlation effects. The calculations on
which most of our discussion will be based are of a con-
stant coupling type. The theory obtained should also be
useful in discussing experiments on magnetic systems
where the exchange increases so that the threshold value
for magnetic ordering is approached and exceeded. Such
experiments could be done on mixed rare earth compounds
with group V anions (e.g., mixed Tb-Tm or mixed Tb-Lu
compounds). We choose Tm rather than Pr to treat in the
numerical calculations. We do this because for those
materials investigated as yet, the predicted and observed
effect of greatest interest, the nonlinear anisotropic
magnetization, is much larger in Tm for experimentally
attainable fields.

The level scheme for Tm^{3+} in an octahedral crystal
field is shown in Fig. 1(a). Exchange correlation effects

vanish with increasing temperature and magnetic field. Thus, as shown in Fig. 1(b), we can consider such effects quite adequately by considering a two level model for each ion, where the ground state is a Γ_1 singlet and the excited state is a Γ_4 triplet. Then the theory we develop could be used as part of an interpolation scheme for real materials. The results of the present calculation would be used at low temperature and field, while the molecular field calculation would be used at higher temperature and field where the present calculation indicated negligible correlation effects.

The constant coupling approximation proceeds in the following way. We first consider a single ion Hamiltonian where the exchange effects of each neighbor are incorporated in an effective field H'.

$$\mathcal{X}_1 = V_c - \lambda B(H + zH')J_z \tag{1}$$

We can find a magnetization per ion for this Hamiltonian and this magnetization, $\bar{M}_1$, will be a function of $H + zH'$. Next we consider a two ion Hamiltonian for ions a and b, where the exchange effects of all neighbors other than a and b are given by the effective field H'.

$$\mathcal{X}_2 = V_{ca} + V_{cb} - \lambda B[H+(z-1)H'](J_{za}+J_{zb}) - 2\mathcal{J}\vec{J}_a \cdot \vec{J}_b \tag{2}$$

Again we can find a magnetization per ion, $\bar{M}_2$, which is a function of $H + (z-1)h'$. Then the condition

$$M(H) = \bar{M}_1(H + zH') = \bar{M}_2(H + [z-1]H') \tag{3}$$

self consistently determines the effective field H' and hence the magnetization.

The critical value of $\Lambda = \mathcal{J}/\Delta$ necessary for magnetic ordering at $T = 0$ is increased in magnitude by the correlation effects as shown in Table I. Correlation effects are relatively more important for decreasing number of nearest neighbors.

For both ferromagnetic and antiferromagnetic exchange, the curves of $1/\chi$ versus T including correlation effects lie above the molecular field curves. This is shown in Fig. 2 for ferromagnetic exchange. The difference in χ from the molecular field value arises from higher order terms in Λ. Thus, as Λ decreases from the critical value, the difference between the molecular field and constant coupling curves for $1/\chi$ decreases more rapidly than the difference between either of those curves and the zero exchange curve. At high temperatures, correlation effects disappear and the molecular field curve becomes exact. Corresponding results for the antiferromagnetic case will also be shown. Such correlation effects also enter into the high field magnetization as illustrated in Fig. 3.

To the extent that time allows we will relate these results to the current experimental situation. Also, we will critically discuss the pertinence of boson-like excitations in treating the present paramagnetic case.

REFERENCES

1. H.R. Child, M.K. Wilkinson, J.W. Cable, W.C. Koehler, and E.O. Wollan, Phys. Rev. 131, 922 (1963).

2. D.P. Schumacher and W.E. Wallace, J. Appl. Phys. 36, 984 (1965).

3. B.R. Cooper, I.S. Jacobs, R.C. Fedder, J.S. Kouvel, and D.P. Schumacher, J. Appl. Phys. 37, 1384 (1966).

4. G. Busch, P. Junod, F. Levy, A. Menth, and O. Vogt, Phys. Letters 14, 264 (1965).

5. B.R. Cooper, Phys. Letters 22, 24 (1966).

6. B.R. Cooper, Phys. Letters 22, 244 (1966).

7. G.T. Trammell, Phys. Rev. 131, 932 (1963).

8. O. Vogt, private communications.

TABLE I

Values of $\Lambda = \ell/\Delta$ for Magnetic Ordering at $T = 0$

z	6	8	12
Ferromagnetic molecular field	2.976×10^{-3}	2.232×10^{-3}	1.488×10^{-3}
Ferromagnetic constant coupling	3.663×10^{-3}	2.584×10^{-3}	1.632×10^{-3}
Antiferromagnetic molecular field	-2.976×10^{-3}	-2.232×10^{-3}	
Antiferromagnetic constant coupling	-3.654×10^{-3}	-2.579×10^{-3}	

FIGURE CAPTIONS

1(a) Level scheme for Tm^{3+} in octahedral crystal field;

  (b) Model two level scheme.

2(a) Variation of $1/\chi$ with T for A equal to constant coupling critical value for ferromagnetic ordering at $T = 0$ with $z = 6$;

  (b) Variation of $1/\chi$ with T for A equal to half the critical value.

3.   High field magnetization for A equal to molecular field critical value for ferromagnetic ordering at $T = 0$ with $z = 6$.

Tm^{3+} IN TmV(J=6)

TWO LEVEL MODEL

Γ_3 (2)

$\Gamma_5^{(1)}$ (3)

Γ_2 (1)

$\Gamma_5^{(2)}$ (3)

Γ_4 (3)

Γ_1 (1)

(a)

Γ_4 a b c

Δ

Γ_1

(b)

(a)
ZERO EXCHANGE
CONSTANT COUPLING
MOLECULAR FIELD

$Z=6$, $A=3.663 \times 10^{-3}$

(b)
ZERO EXCHANGE
CONSTANT COUPLING
MOLECULAR FIELD

$Z=6$, $A=1.831 \times 10^{-3}$

Z=6
$\Delta = 28.16°K$, $A = 2.976 \times 10^{-3}$
T=0

—— MOLECULAR FIELD
----- CONSTANT COUPLING
— — ZERO EXCHANGE

H (kOe)

BOHR MAGNETONS/MOLECULE
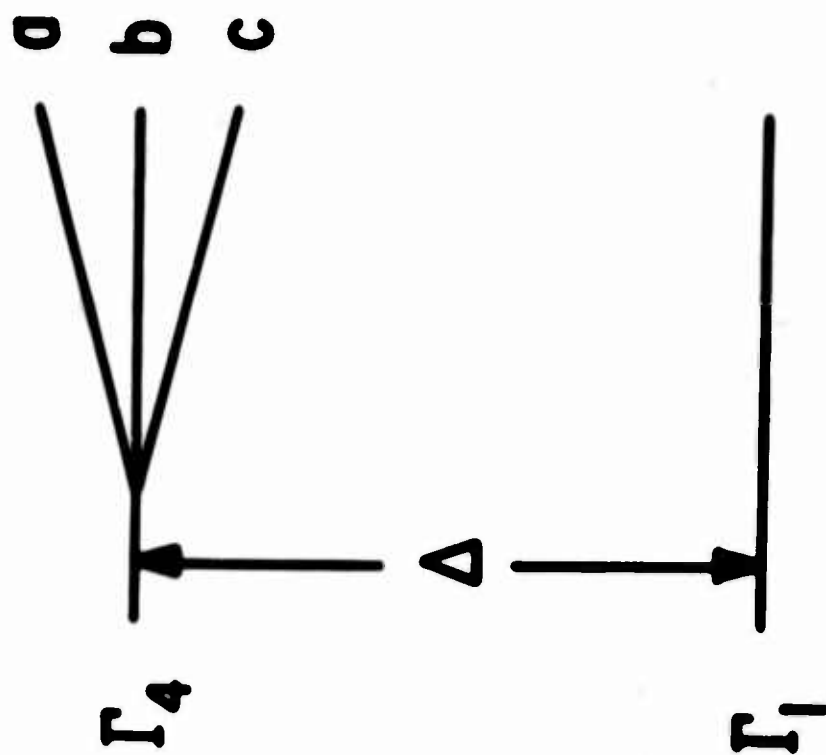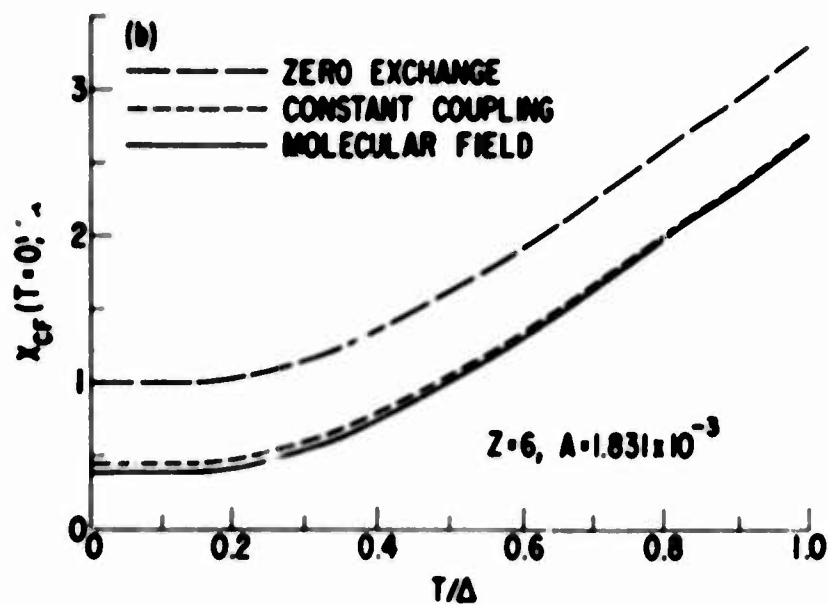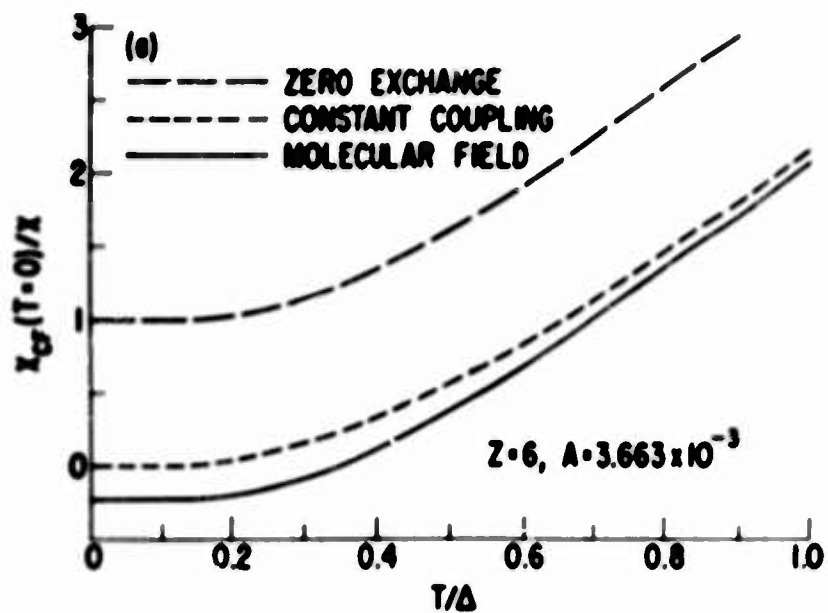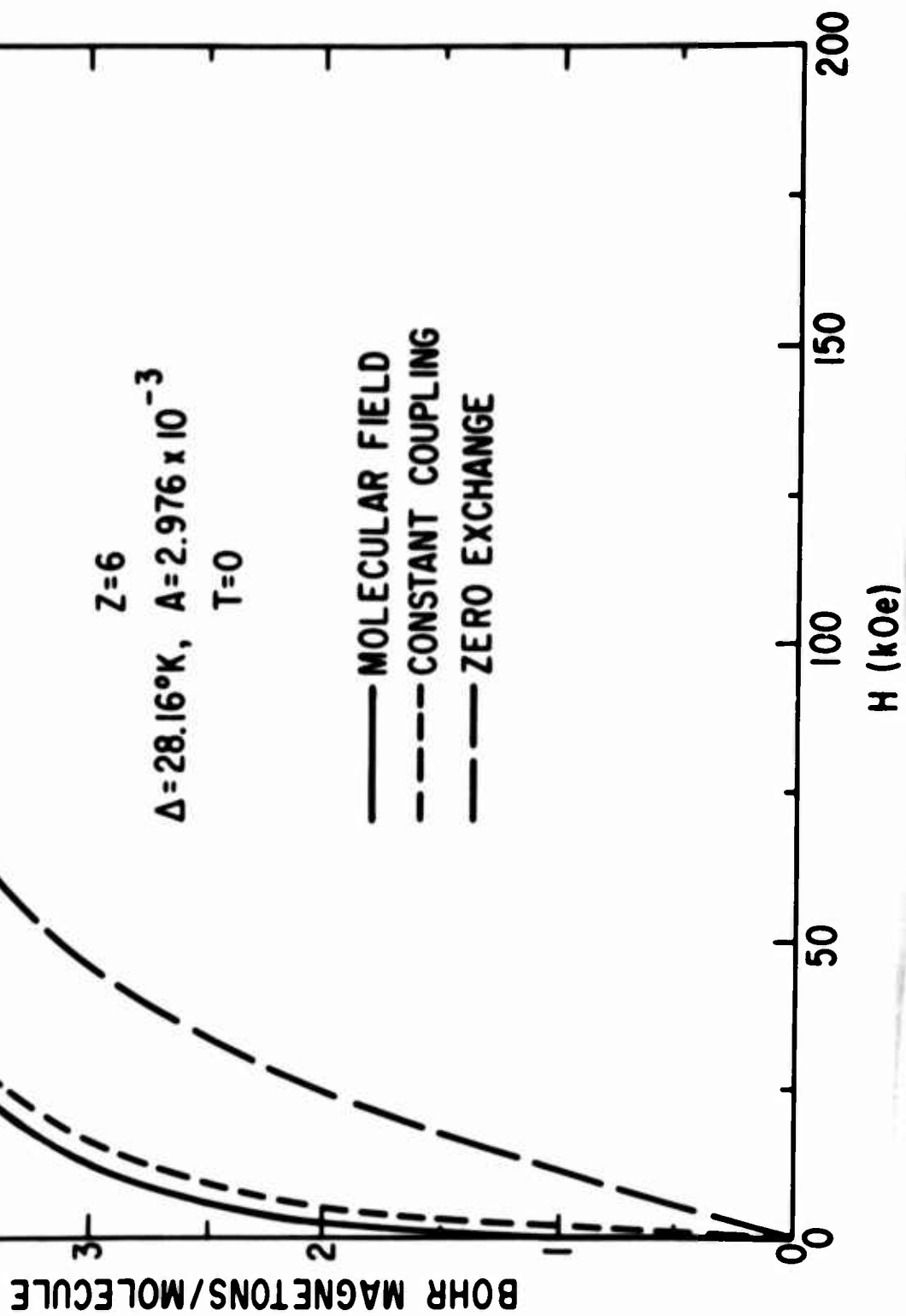
Microwave Absorption in Dysprosium Single Crystals*

H.A. Blackstead´ and P.L. Donoho

William Marsh Rice University, Houston, Texas 77001

ABSTRACT

We have observed microwave power absorption at a frequency of 9.8 GHz in single-crystal c-plane platelets of dysprosium at temperatures from 40°K to 179°K. The rf magnetic field was aligned parallel to an a-axis (easy axis), and the dc magnetic field was aligned along a b-axis (hard axis), either perpendicular to the rf field or at an angle of thirty degrees to it.

At temperatures below 85°K, and for temperatures from 85°K to approximately 110°K with $H_{dc} > H_c$, a strong resonance line with a width of approximately 1 kOe was observed. This resonance, predicted from spin-wave analysis, is apparently related to the strong six-fold basal-plane anisotropy which is important below 110°K. With the dc field perpendicular to the rf field, and for temperatures above 110°K, there was no apparent field-dependence of the absorption for $H_{dc} < H_c$. At higher fields, however, the absorption increased rapidly, reaching a maximum at H_f, the field at which the fan structure has collapsed to ferromagnetic alignment. With further increase of the field, the absorption then decreased linearly. No absorption was observed above 179°K, the temperature for the transition from the helicoidal spin structure to the paramagnetic state. Frequency-dependence studies are in progress in the range 8 to 25 GHz.

I. INTRODUCTION

For dysprosium in the temperature range from 85°K to 179°K the magnetic ordering is a helicoidal structure with the moments confined to the c-plane by a very large axial anisotropy. Below 85°K the moments are ferromagnetically aligned along a basal-plane a-axis. The antiferromagnetic helicoid can be collapsed by a magnetic field applied in the basal plane: at a critical field, denoted by H_c, the helicoid collapses into a fan-like structure; with further increase of the field, the fan closes continuously, reaching nearly complete ferromagnetic alignment at a value of the field denoted by H_f.

Cooper and Elliott[1] have theoretically studied the microwave resonance properties of the heavy rare earths in terms of spin-wave expansions. Their predicted values of resonant frequencies were originally very high, near the infrared, but in a recent correction to their work[2] they show that the dispersion curve does have a branch extending to zero frequency at k=0. Cooper and Elliott also suggest that at temperatures where the basal-plane anisotropy is large (T < 110°K) the high-frequency resonance can be brought to zero frequency by the application of a field along a hard axis of a value approximately $36H_h$, where H_h is the effective anisotropy field. Such a resonance has been apparently observed by Rossol and Jones[3] and in the work reported here, although the qualitative features of our observations, described below, differ in several respects from those of Rossol and Jones. In addition, Cooper and Elliott also predict a resonance at H_c, with H_{dc} parallel to an easy axis. This resonance has also been observed by Rossol, Cooper,

and Jones[4], but it has not been observed reproducibly
in our work, possibly because of the lower frequency of
observation. Several of the features of our observations
can be deduced theoretically without recourse to a spin-
wave treatment, and the details of such a calculation are
given below.

II. EXPERIMENTAL DETAILS

Initial measurements were performed on single-crystal
platelets of dysprosium furnished by Dr. J. L. Moriarity of
the Lunex Company, Pleasant Valley, Iowa. These platelets
were roughly hexagonal, about 2 mm in diameter and 0.5 mm
thick. X-ray analysis showed angular dispersion of about
5 degrees. The samples currently being studied were cut
from a single crystal approximately 6 mm in diameter and
12 mm long obtained from a commercial source. Surface
preparation was found to be very important in obtaining
reproducibility because of the small microwave skin depth.
The most satisfactory technique for surface preparation
seems to be spark-planing of the surface, followed by a
light acid etch. It has also been found necessary to pro-
tect the surface by means of a vacuum-evaporated film of
SiO deposited immediately after etching the surface. The
angular dispersion of X-ray Laue patterns obtained from
crystals prepared by this method is less than one degree.

A standard X-band spectrometer using a reflection-
type cavity, with the klystron stabilized to the cavity
resonance, was employed. The sample was placed in the
cavity so that the rf magnetic field at the sample lay in

a horizontal plane, which was also the plane of the dc mag-
netic field. The sample could be rotated about a vertical
axis (the c-axis) to permit alignment of the rf field along
any desired direction in the basal plane. The dc field,
which could be varied from zero to 20 kOe, could also be
adjusted to any desired direction in the basal plane.

The cryogenic system consisted of a continuous-flow
cryostat which permitted operation at any temperature be-
tween 20°K and room temperature. The temperature could be
stabilized to approximately 15 millidegrees at any tempera-
ture in this range.

III. RESULTS AND DISCUSSION

At temperatures from approximately 115°K to 179°K the
absorption curves are nearly identical in shape, as seen in
figures 1 and 2. The absorption rises sharply at H_c,
reaching a maximum at H_f. For $H > H_f$, the absorption de-
creases nearly linearly with increasing field. The curves
of figure 2 are all normalized to the same peak absorption,
although the signal intensity increases as temperature is
increased. As temperature decreases below approximately
115°K, the sixth-order basal-plane anisotropy becomes im-
portant, and begins to modify the shapes of the absorption
curves. The initial experiments on one of the small Lunex
platelets showed in this region two resonant peaks of
approximately 1 kOe width superimposed on a much broader
absorption curve. These peaks occurred at increasing
values of the field as temperature was raised from 86°K to
115°K. This behavior has not, however, been reproduced
precisely in later measurements on crystals of better

Reflected Power (arb. units)

Dy T = 140°K

$H_{dc} \parallel b$

$H_{ac} \parallel a$

9.18 GHz

H (kOe)

Figure 2: Absorption as a function of field, showing behavior at H_c and H_f.

Reflected Power (arb. units)

Dy
$H_{dc} \parallel b$
$H_{rf} \parallel a$
9.18 GHz

139.8°K

130°K

140°K

130°K

120°K

110°K

H (kOe)

Figure 1: High-temperature absorption as a function of field and temperature.

quality, although similar effects have been observed.

The absorption observed from 115°K to 179°K may be studied theoretically without resort to the use of a spin-wave treatment or even the equation of motion. Consider the following Hamiltonian:

$$H = H_{mag} + H_{anisotropy} + H_{magnetoelastic} + H_{elastic}.$$

The magnetoelastic and elastic contributions, although probably quite significant[5], will be neglected in the simple treatment considered here. The anisotropy term can be treated by assuming that the moments are confined to the basal plane. These approximations leave an oversimplified Hamiltonian which can, nevertheless, provide an insight into the behavior of the material in applied dc and rf fields. We now have:

$$H = H_{mag} = -(g-1)^2 J^2 \sum_{i,j} I_{ij} \cos(\varphi_i - \varphi_j) + g\beta H_{dc} \sum_i \cos \varphi_i$$

$$+ g\beta J |H_{rf}| e^{-i\omega t} \sum_i \sin \varphi_i$$

Assuming H_{rf} small, and considering only nearest and next-nearest neighbors, minimization of the free energy in the zero-degree approximation yields a difference equation for the direction of the pth moment. Let

$$\varphi_p = p\varphi + \epsilon_p(H_{dc}) + \epsilon_p'(H_{dc}, H_{rf})$$

where φ is the pitch angle, and ϵ_p and ϵ_p' are the dc- and rf-field induced deviations respectively. Assuming that $\varphi \gg \epsilon_p > \epsilon_p'$, and making a small-angle approximation

to the difference equation, one can find a solution for $\epsilon_p(H)$ [6]:

$$\epsilon_p(H_{dc}) = \frac{g\beta H_{dc} \sin(\theta_0 + p\varphi)}{16 J (g-1)^2 I_z \sin^4\frac{\varphi}{2}[1 + 2\cos\varphi(1+\cos\varphi)]}$$

But, the susceptibility χ is given by:

$$\chi = -\frac{g^2 \beta^2}{32 (g-1)^2 I_z \sin^4\frac{\varphi}{2}[1 + 2\cos\varphi(1+\cos\varphi)]}$$

so that

$$\epsilon_p(H_{dc}) = -\frac{2\chi H}{g\beta J} \sin(\theta_0 + p\varphi)$$

where θ_0 is a phase angle. Now, inserting this term back
into the difference equation, and retaining the ϵ_p' terms,
one can find a solution

$$\epsilon_p'(H_{dc}, H_{rf}) = -\frac{2\chi}{g\beta J} |H_{rf}| \cos(\theta_0 + p\varphi) e^{-i\omega t}$$

This approximation, valid only for ϵ_p' proportional to H,
suggests that the moments vibrate in the basal plane about
their equilibrium position at the rf frequency. Further-
more, this absorption mechanism should be independent of
frequency. Measurements by Rossol, Cooper, and Jones[4] at
37 GHz apparently verify this conclusion. A more accurate
approach would require keeping all the terms in the
Hamiltonian, and to perform a numerical calculation without
making a small-angle approximation. Such a calculation is
in progress, but has as yet yielded only preliminary
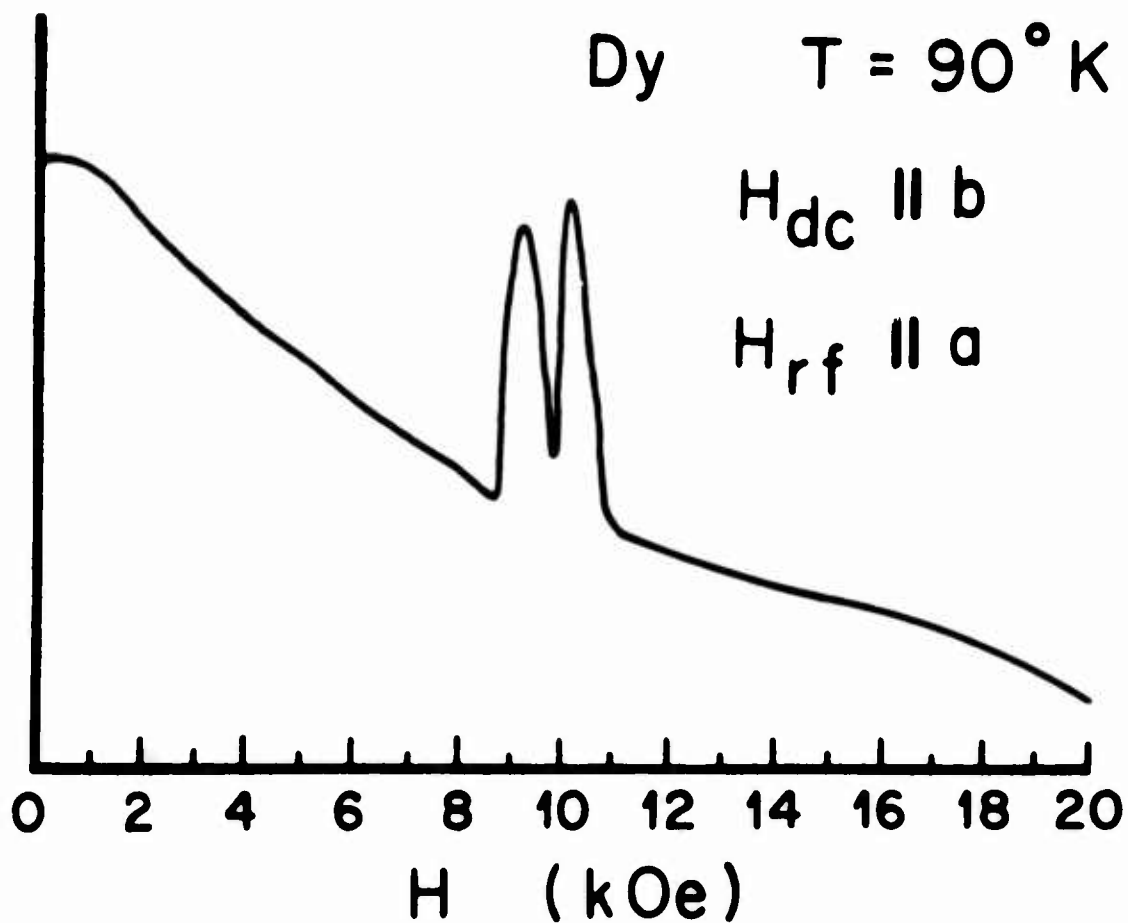
Figure 3: Low-temperature absorption as a function of field.

results.

We have also observed a fairly sharp resonance, of approximately 1 kOe width in the lower temperature range from about 40°K to 95°K. In this case, H_{dc} must be aligned along a hard axis lying 30 degrees from the easy axis along which the rf field is aligned. Figure 3 shows this resonance, which is resolved into two closely-spaced peaks. The above-mentioned alignment of the dc and rf fields must be closely maintained: for a rotation of the dc field of approximately 0.3 degrees, the resonance disappears. The rf-field alignment seems to be almost as important. This resonance appears to be that predicted by Cooper and Elliott[1], which was described above. The position of the two lines depends upon the magnitude of the basal-plane anisotropy in this effect, and our experimental results show the expected temperature dependence of the resonance field. The resonance appears, however at a smaller field than one would expect from the result of Cooper and Elliott, namely $H = 36H_h$. A similar resonance was also observed by Rossol and Jones[3] at a frequency of 37 GHz, but they observed line widths of 5-10 kOe, and saw only a single peak. Our results on this resonance are, however, in a rather preliminary state, and require considerable further work. We expect to extend this work to higher frequencies shortly.

IV. ACKNOWLEDGMENTS

REFERENCES

1. B.R. Cooper and R.J. Elliott, Phys. Rev. 131, 1043 (1963).

2. B.R. Cooper and R.J. Elliott, Phys. Rev. 153, 654 (1967).

3. F.C. Rossol and R.V. Jones, J. Appl. Phys. 36, 1209 (1965).

4. F.C. Rossol, B.R. Cooper, and .V. Jones, J. Appl. Phys. 37, 1227 (1966).

5. M.P. Maley, H.A. Blackstead, and P.L. Donoho, J. Appl. Phys. 37, 1006 (1966).

6. A. Herpin and P. Meriel, J. Phys. Rad. 22, 337 (1961).

NUCLEAR MAGNETIC RESONANCE MEASUREMENTS IN THE NaCl-TYPE RARE-EARTH GROUP VA INTERMETALLIC COMPOUNDS[*]

E. D. Jones

Sandia Laboratory, Albuquerque, New Mexico

ABSTRACT

The phosphorus nuclear magnetic resonance (nmr) has been observed in the paramagnetic state of the NaCl-type rare-earth intermetallic compounds REP (RE=rare-earth). The phosphorus Knight shifts were measured in the temperature range of 100-600°K. Analyzing the temperature dependent Knight shifts in terms of a uniform-conduction electron spin polarization model yields values for the s-f exchange energy Γ. The arsenic, antimony and bismuth Knight shift data in SmAs, SmSb and SmBi are also presented. For the Sm^{3+} compounds, it is shown that theoretical predictions concerning the behavior of the temperature dependence of the Sm^{3+} spin $\langle S(T) \rangle$ are verified.

I. INTRODUCTION

The indirect (s-f) exchange interaction via the conduction electrons is believed to be the important mechanism for providing magnetic coupling between the 4-f spins in rare-earth metals and rare-earth intermetallic compounds. Nuclear magnetic resonance (nmr) techniques have been employed[1-5] on a variety of rare-earth intermetallic compounds in order to study the resulting conduction electron spin polarization due to the s-f exchange interaction. The first application of this technique was performed by Jaccarino, et. al.[1] who measured aluminum Knight shifts in a series of $REAl_2$ compounds (RE=rare-earth) having

the cubic Laves crystal structure. Jaccarino, et al. were able to determine the sign and magnitude of the s-f exchange energy Γ for these intermetallic compounds by using a uniform-conduction electron spin polarization model to interpret their Knight shift data.

This paper will present and discuss the results of phosphorus Knight shift measurements in the intermetallic rare-earth monophosphides which have the NaCl-type crystal structure. Paramagnetic susceptibility[6-13] measurements indicate that the number of 4-f electrons corresponds to a +3 valence for each rare-earth ion. In addition to the phosphorus nmr data, results of arsenic, antimony and bismuth Knight shift measurements in SmAs, SmSb and SmBi will also be presented.

II. EXPERIMENTAL

The nmr measurements were performed in powdered samples using a variable frequency induction spectrometer and a conventional laboratory electromagnet. Sample temperatures were controlled by use of a calibrated variable temperature unit. The phosphorus Knight shifts were determined at a fixed frequency by measuring the magnetic field with respect to the phosphorus nmr frequency in red phosphorus. The arsenic, antimony and bismuth Knight shifts in SmAs, SmSb and SmSb were determined in the same manner, except that the reference used to measure the magnetic field was the aluminum nmr frequency in a saturated solution of $Al_2(SO_4)_3$.

The samples were prepared by mixing correct proportions of phosphorus and rare-earth metal in a quartz pressure bomb and heating to approximately 600°C for several days. The samples were then pressed in pellets and reheated in order to achieve sample uniformity. Standard x-ray powder

diffraction techniques were used to confirm that the
samples had the NaCl-type crystal structure and correct
lattice constants.

III. KNIGHT SHIFTS IN REP

There have been several calculations[1,14,15] for the
Knight shift of a nonmagnetic constituent in a magnetically
dense paramagnetic rare-earth intermetallic compound. All
of these calculations predict that the Knight shift has a
term proportional to the time averaged value of the rare-
earth 4-f spin $\langle S \rangle$. For simplicity the uniform-conduction
electron spin polarization model will be used in the
analysis of the Knight shift data presented in this paper.
The resulting expression for the Knight shift $K(T)$ is
given by

$$K(T) = K_o \left[1 - \Gamma \langle \vec{S} \rangle \cdot \vec{H} / 2\beta H^2 \right] \quad , \tag{1}$$

where K_o is the ordinary Knight shift found in a nonmagnetic
isomorph such as P^{31}:LaP etc., Γ is the s-f exchange energy
resulting from the interaction (of the form $-\Gamma S \cdot s$) between
the rare-earth 4-f spin S and the conduction electron spins,
$\langle S \rangle$ is the time averaged value of the rare-earth spin, β is
the Bohr magneton and H is the applied magnetic field. Ex-
cluding Eu^{3+} and Sm^{3+} compounds (the Sm^{3+} data will be
discussed in Section IV), $\langle S \rangle$ is given by

$$\frac{\langle S \rangle}{H} = - \frac{(g_J - 1) \chi_f}{g_J N \beta} \quad , \tag{2}$$

where g_J is the Landé g-factor, N is Avogadro's number and
$\chi_f(T)$ is the rare-earth paramagnetic susceptibility ex-
pressed in emu per mole.

In the temperature range (100-600°K) for which the
Knight shift measurements were performed, the paramagnetic

susceptibilities of the REP compounds exhibited Curie-Weiss behavior,[6-13] i.e.,

$$\chi_f(T) = C(T-\theta)^{-1} \tag{3}$$

where C is the appropriate Curie-Weiss constant for each RE^{3+} ion and θ is the Curie-Weiss temperature for each compound. From Eqs. (2) and (3), Eq. (1) can be rewritten as

$$K(T) = K_o\left[1 + \frac{\Gamma(g_J-1)C}{2g_JN\beta^2(T-\theta)}\right] \tag{4}$$

It is evident from Eq. (4) that a graph of K(T) vs $(T-\theta)^{-1}$ should give a straight line with a slope which is proportional to the s-f exchange energy Γ. Equation (4) also predicts that the slope should reverse sign in going from rare-earth intermetallics with $g_j<1 (Ce^{3+}, Pr^{3+}$ and $Nd^{3+})$ to the compounds with $g_j>1 (Gd^{3+}, Tb^{3+}, Dy^{3+}, Ho^{3+}, Er^{3+}, Tm^{3+}$ and $Yb^{3+})$. The Curie-Weiss temperature θ for each REP compound can be obtained from a graph of $(K(T)-K_o)^{-1}$ vs temperature.

The phosphorus Knight shifts in the REP intermetallic compounds were measured between 100 and 600°K and the results of plotting the observed K(T) vs $(T-\theta)^{-1}$ are shown in Fig. 1. The Curie-Weiss temperatures for each REP compound used are also tabulated in Fig. 1. The values of K_o obtained from such a graph are consistent with the value $K_o = +0.06\%$ measured[16] in ScP, YP, LaP and LuP. Inspection of Fig. 1 also shows that the slopes do indeed reverse sign for those compounds with $g_J<1$ compared to those with $g_J>1$. From the data shown in Fig. 1, the s-f exchange energies Γ were obtained and are listed in Table 1.

TABLE 1. Values of the s-f exchange energies in the REP intermetallic compounds obtained from phosphorus Knight shift measurements.

RE^{3+}	g_J	C^*	$\Gamma(ev)$
Ce	6/7	0.804	-1.00
Pr	4/5	1.60	-0.66
Nd	8/11	1.64	-0.54
Gd	2	7.88	-0.38
Tb	3/2	11.81	-0.29
Dy	4/3	14.17	-0.27
Ho	5/4	14.06	-0.23
Er	6/5	11.48	-0.23
Tm	7/6	7.15	-0.18
Yb	8/7	2.57	-0.26

*The Curie-Weiss constant used was the free ion value.

These values for the s-f exchange energies compare favorably with those obtained from the aluminum Knight shift measurements in $REAl_2$ compounds.[17] The minus sign for the s-f exchange energy Γ indicates that the s-f exchange interaction is antiferromagnetic when the uniform-conduction electron spin polarization model is used to analyze the Knight shift data.

IV. KNIGHT SHIFTS IN SmP, SmAs, SmSb AND SmBi

Since the energy separation between the two lowest Sm^{3+} spin-orbit states is approximately 1500°K, Eq. (2) is not valid. Hence Eq. (1) must be used together with a calculation $\langle S \rangle/H$ for the Sm^{3+} energy level system. Neglecting crystalline field interactions, a calculation of $\langle S \rangle/H$, to first order gives

$$\frac{\langle S \rangle}{\beta H} = \left\{ \frac{25}{42kT} - \frac{120}{42E_{7/2}} \right\} \tag{5}$$

where $E_{7/2}/k \simeq 1500°K$ is the energy separation between the first excited state and the $J = 5/2$ ground state. The sign convention used in Eq. (5) is for $\langle S \rangle$ parallel to H to be positive.

White and Van Vleck[18] were the first to note that the expectation value of the Sm^{3+} spin S should have a sign reversal at $T \simeq 300°K$. This reversal in the sign of the $Sm^{3+}\langle S \rangle$ results from the fact that the spin of the $J = 5/2$ ground state points in the same direction as the applied magnetic field and is temperature dependent, while the component of $\langle S \rangle$ which arises from the (temperature-independent) field-induced admixture of the $J = 7/2$ state into the $J = 5/2$ ground state is antiparallel to the magnetic field. Hence, as White and Van Vleck[18] mention, these two components of $\langle S \rangle$ will cancel at some temperature.

The effect of an octahedral crystalline-field interaction is to split the $^6H_{5/2}Sm^{3+}$ ground state into a doublet (Γ_7) and a quartet (Γ_8). To first order, the crystalline field interaction modifies Eq. (5) by multiplying the T^{-1} term by a function $f(T)$, where

$$f(T) = [5 + 26e^{-x} + (32/x)(1-e^{-x})]/21 \, (1+2e^{-x}) \tag{6}$$

with $x = \Delta/kT$ (where Δ is the energy separation between the Γ_7 and Γ_8 levels). If the doublet Γ_7 lies lowest in energy, x is poxitive, while if the quartet Γ_8 is lowest, x is negative.

The results of the Knight shift measurements in SmP, SmAs, SmSb and SmBi for the temperature range of 100-600°K are shown in Fig. 2. The appropriate values for the Knight

shift K_o are given in Ref. 16. The solid lines shown in Fig. 2 are smooth curves drawn through the data. From Fig. 2, it can be seen that the spin dependent part of the Knight shift reverses sign at T ≃ 300°K in agreement with the prediction of White and Van Vleck[18] (Eq. (5)). Furthermore, within experimental error, after normalizing the Knight shifts at 100°K, the data shown in Fig. 2 all exhibit the same temperature dependence.

Jones and Hesse[19] have reported the phosphorus Knight shift measurements in SmP for the temperature range of 4-600°K. By fitting the data to Eqs. (1), (5) and (6) they find a crystal field splitting of $\Delta \simeq$ 150°K with the Γ_7 level lowest in energy. Jones and Hesse[19] also obtained a value for the s-f exchange energy Γ in SmP to be Γ = -0.40 ev which is in good agreement with the values reported in Table 1 for the other REP intermetallic compounds.

ACKNOWLEDGMENTS

REFERENCES

* This work was supported by the U. S. Atomic Energy Commission.

1. V. Jaccarino, B. T. Matthias, M. Peter, H. Suhl and J. H. Wernick, Phys. Rev. Letters $\underline{5}$, 251 (1960).

2. V. Jaccarino, J. Appl. Phys. $\underline{32}$, 102S (1961).

3. A. C. Gossard and V. Jaccarino, Proc. Phys. Soc. (London) $\underline{80}$, 877 (1962).

4. R. G. Barnes, F. Borsa and D. Peterson, J. Appl. Phys. $\underline{36}$, 940 (1965).

5. E. D. Jones and J. I. Budnick, J. Appl. Phys. $\underline{37}$, 1250 (1966).

6. A. Iandelli, Rare Earth Research, edited by V. Kleber (MacMillian Corp., New York 1961).

7. G. Busch, P. Junod, O. Vogt and F. Hulliger, Phys. Letters $\underline{6}$, 79 (1963).

8. G. Busch, O. Marincek, A. Menth and O. Vogt, Phys. Letters $\underline{14}$, 262 (1965).

9. G. Busch and O. Vogt, Phys. Letters $\underline{20}$, 152 (1966).

10. T. Tsuchida and W. E. Wallace, J. Chem. Phys. $\underline{43}$, 2087 (1965).

11. T. Tsuchida and W. E. Wallace, J. Chem. Phys. $\underline{43}$, 2885 (1965).

12. G. Busch, P. Schwob, O. Vogt and F. Hulliger, Phys. Letters $\underline{11}$, 100 (1964).

13. G. Busch, O. Vogt and F. Hulliger, Phys. Letters $\underline{15}$, 301 (1965).

14. K. Yosida, Phys. Rev. $\underline{106}$, 893 (1957).

15. P. G. deGennes, J. Phys. Radium $\underline{23}$, 510 (1962).

16. E. D. Jones and J. E. Hesse, Bull. Am. Phys. Soc. $\underline{11}$, 172 (1966).

17. R. G. Barnes and E. D. Jones, Solid State Communs. (to be published).

18. J. A. White and J. H. Van Vleck, Phys. Rev. Letters <u>6</u>, 512 (1961).

19. E. D. Jones and J. E. Hesse, J. Appl. Phys. March 1967.
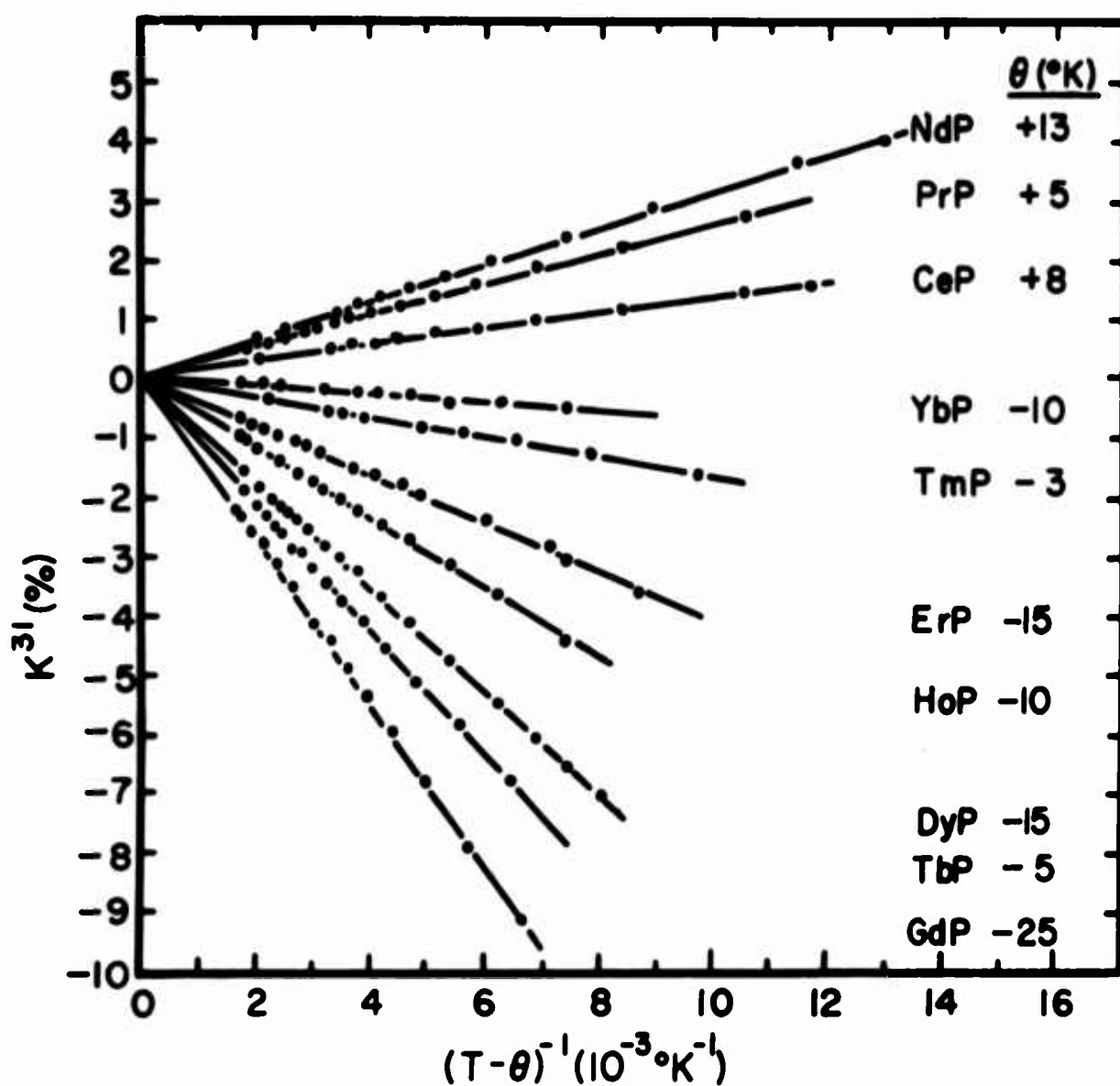
Fig. 1 Phosphorus Knight Shifts as a function of $(T-\theta)^{-1}$

Fig 2   Knight shifts in SmP, SmAs, SmSb and SmBi plotted as a function of temperature. (● - SmBi, ◻ - SmSb, ⬡ - SmAs and ○ - SmP)
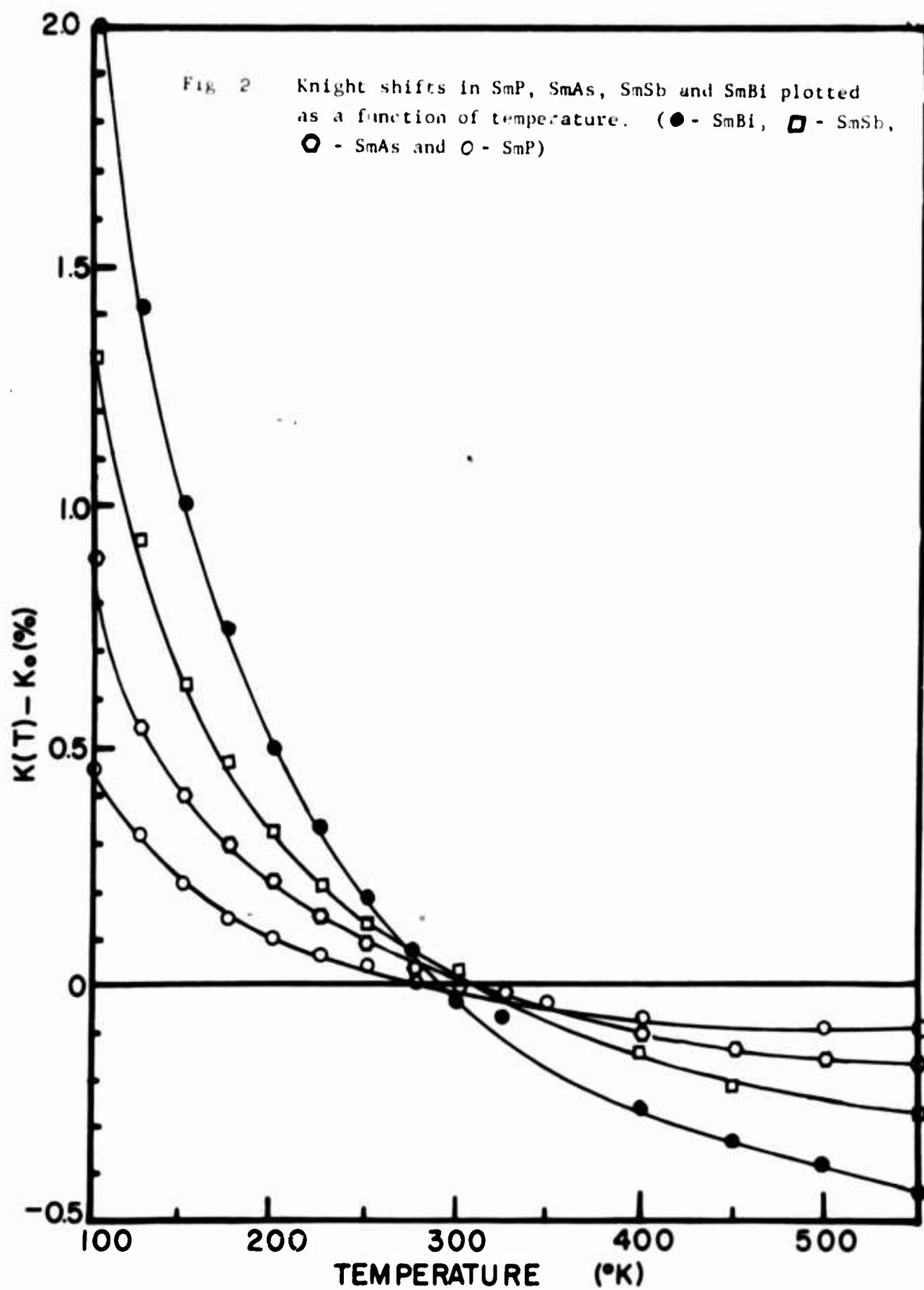
EPR ANGULAR SPECTRA OF GADOLINIUM IN RARE-EARTH
DOUBLE NITRATE SINGLE CRYSTALS

H. A. Buckmaster, J. C. Dering and D. J. I. Fry

Physics Department, University of Calgary

Calgary, Alberta, Canada.

ABSTRACT

A systematic study of the 10GHz electron paramagnetic resonance (EPR) spectra of the gadolinium ion (Gd^{3+}; ^8S) in isomorphic, diamagnetic lattices of hydrated, rare-earth double nitrate single crystals is reported. These lattices are of the form $M_2''' \, M_3'' \, (NO_3)_{12} \cdot 24 \, H_2O$ where M''' is bismuth or lanthanum and M'' is zinc or magnesium. The ratio of Gd^{3+} to M''' ions was $\simeq 0.1\%$. The experimental data for temperatures of 290°K and 77°K are fitted to the phenomenological spin-Hamiltonian for C_{3i} symmetry. The angular dependence of the spectra shows substantial variations from that predicted, which have not been reported previously. These variations are not inconsistent with C_{3i} symmetry but cannot be completely described by any spin-Hamiltonian of the above form. This raises doubts as to the usefulness of the spin-Hamiltonian formalism because the intrinsic symmetry of the terms is too high to describe the variations.

I INTRODUCTION

The hydrated double-nitrates of the rare-earth elements form an interesting series of salts for EPR studies. Their general formula is $M_2''' \, M_3'' \, (NO_3)_{12} \cdot 24H_2O$ where M''' is a trivalent rare-earth element or bismuth and M'' is a divalent metal. Trenam (1953) obtained the crystal field parameters for gadolinium in magnesium bismuth nitrate using EPR, by assuming C_{3h} symmetry. Judd (1955) attempted a theoretical analysis of the crystal field using the operator equivalent formalism. He deduced that the symmetry could not be C_{3h} and suggested C_{3v}. Judd and Wong (1958) made a series of measurements with crystals of lanthanum magnesium nitrate containing erbium and holmium as paramagnetic impurities. They interpreted the results in terms of a crystalline electric field of predominantly icosahedral symmetry. Previously, Judd (1957) had shown that a crystal field with this symmetry is consistent with the requirements of the C_{3v} point-group. He suggested that either the water molecules or the nitrate ions were clustered around the rare-earth ions in

an icosahedral arrangement. He also showed that this was not very likely and noted that the agreement of the sixth order terms with the requirements of icosahedral symmetry might be fortuitous.

The complexity of the unit cell, which contains three formula units, discouraged X-ray crystallographers from determining the structure of the double-nitrate crystals. Culvahouse, Unruh and Sapp (1961) deduced the point-group to be C_{3v} from X-ray data. Later Zalkin, Forrester and Templeton (1963) analyzed the complete lattice for cerium magnesium nitrate. The other hydrated double nitrates can be expected to have similar structures. Zalkin et al. showed that the nearest neighbours of the rare-earth ions were the oxygens of the nitrate ions, arranged at the corners of an irregular icosahedron. They claimed that oxygens did not have mirror symmetry, so the nearest-neighbour symmetry was much closer to C_{3i} than C_{3r}. They also found that the symmetry at the site of a M''' ion was C_3 when the complete unit cell was taken into account.

II THEORY

The spin-Hamiltonian for a paramagnetic ion situated in a point charge lattice with trigonal symmetry is

$$H = \beta \vec{B} \cdot \underline{g} \cdot \vec{S} + B_2^0 T_{20} + B_4^0 T_{40} + B_4^3 (T_{43} - T_{4-3})$$
$$+ B_6^0 T_{60} + B_6^3 (T_{63} - T_{6-3}) + B_6^6 (T_{66} + T_{6-6}) \tag{1}$$

where β is the Bohr magneton,

$\vec{B}$ is the applied magnetic flux density,

$\underline{g}$ is the spectroscopic splitting factor which is a symmetric tensor of second rank,

$\vec{S}$ is the spin angular momentum,

B_i^j are the crystal field parameters

and T_{ij} are the angular momentum tensor operators.

The crystal field parameters B_4^3 and B_6^3 are identically zero for C_{3h} or C_{3i} symmetry and not zero for C_{3v} symmetry. The operators T_{ij} are identical to the operator equivalents O_ℓ^m of Bleaney and Stevens (1953) and others except for the normalization factors which conform with the definition of angular momentum tensor operators given by Edmonds (1957).

This normalization is defined such that $T_{kk} = (T_{11})^k$ which is equivalent to using k 1-dimensional spaces to construct a k-dimensional space.

III EXPERIMENTAL TECHNIQUE

The measurements reported in this paper were carried out using a 10GHz, magnetic-field-modulation, synchrodyne EPR spectrometer. The microwave power source was simultaneously phase-locked to a MHz crystal oscillator and frequency-locked to the sample cavity. This instrumentation has been described by Buckmaster and Dering (1967).

IV EXPERIMENTAL RESULTS

The results of the measurements of the EPR spectra of the S-state Gd^{3+} ion in the isomorphic, diamagnetic lattices of hydrated lanthanum magnesium nitrate, lanthanum zinc nitrate, bismuth magnesium nitrate and bismuth zinc nitrate at 290°K and 77°K are given in Tables Ia and Ib. The results of Trenam (1953) for bismuth magnesium nitrate at 90°K are appended, converted to the normalization of this paper. The crystal field parameters are expressed in the experimentally useful units of GHz

$$B_\ell^m \bigg|_{GHz} = (29.97925 \pm 0.00003)B_\ell^m \bigg|_{cm^{-1}}$$

The "best-fit" values of the crystal field parameters are those which gave the least mean square deviation Δ between the magnetic field values of the seven transitions of the calculated spectrum and the measured spectrum. They were calculated by an electronic computer iteration procedure using a program for exact matrix diagonalization. The g-value and each parameter in turn was varied to minimize Δ, and the sequence repeated until consistent values resulted. The errors given in the Tables were calculated from the rate of convergence of each crystal field parameter, the sensitivity of Δ to changes in the parameter, and Δ for the final set of values. The g-value and the crystal-field parameters were calculated independently when magnetic field was parallel and perpendicular to the trigonal axis. The angular variation of the spectra reported in the next section raises doubts as to the meaning of $g_\perp$.

The crystal field parameters for bismuth magnesium nitrate were calculated using the field values corresponding to the maximum separation

of the symmetrical pairs of transitions near the perpendicular direction. This numerical exercise is of interest because the "best fit" values of the major parameters in the spin-Hamiltonian lie between these values of the parameters calculated in the parallel and perpendicular directions. The value of Δ for this artificial spectrum is an order of magnitude smaller than that obtained using the measured spectrum in the perpendicular direction. These parameters are listed on the bottom line of Table Ib.

V ANGULAR VARIATION OF SPECTRA

A qualitative description of the angular variation of the EPR spectra is given in this section. No theoretical explanation of this variation has been attempted because it was obvious from the data that the variations could not be explained by the spin-Hamiltonian (1).

Figure 1 shows the angular variation of the seven EPR transitions of Gd^{3+} in the lattice of bismuth zinc nitrate at room temperature, for a rotation of $\pm 20°$ about the perpendicular axis. Points of interest in the angular variation of the spectra are

(a) The maximum field separation of the absorption lines occurs when the field is parallel to the trigonal axis of the crystal. This axis can be located accurately from the external characteristics of the crystal.

(b) The subsidiary maxima occur when the magnetic field is approximately perpendicular to the trigonal axis of the crystal. The maxima A corresponding to the transitions $|\pm\frac{7}{2}> \leftrightarrow |\pm\frac{5}{2}>$ are displaced to one side of the perpendicular to the trigonal axis while the other pairs, B and C, are displaced to the other side. The maximum D of the central transition $|\pm\frac{1}{2}> \leftrightarrow |\mp\frac{1}{2}>$ occurs perpendicular to the trigonal axis, within experimental error.

(c) The conservation of parity is not violated by this variation. The spectrum observed at an angle of $+\frac{\pi}{2}$ radians from the trigonal axis is identical with the spectrum observed at an angle of $-\frac{\pi}{2}$ radians. The spectrum is not repeated at angles of $+\theta$ and $-\theta$ for arbitrary values of θ.

These three characteristics were present in the angular variation of the spectra of Gd^{3+} in the four lattices studied at 290°K and 77°K.

Characteristic (c) indicates that the symmetry of the Gd^{3+} lattice site is not C_{3v}. It is not inconsistent with C_{3i} symmetry. Characteristic (b) is not explained. An angular variation of this type has not been reported previously, although angular spectra in Geschwind (1961) and Culvahouse and Olsen (1961) indicate its existance. It was not observed by Scovil [quoted by Bleaney and Stevens (1953)] in the angular variation of the $\Delta M = \pm 1$ transitions of Gd^{3+} in the rare-earth ethyl-sulphate crystals, or in the $\Delta M = \pm 2, \pm 3$ transitions of this ion in the same crystal reported by Buckmaster (1963). The angular resolution of Scovil's measurements was $2.5°$ and the effect may have been unnoticed; however, the angular resolution of Buckmaster's measurement was $\pm 1°$ and the effect would have been detectable if it had been present to the same extent as in the double-nitrate crystals. Table 2 shows the angular displacement of the maxima A, B, C, D from a direction perpendicular to the trigonal axis for each crystal at 290°K and 77°K.

VI DISCUSSION OF RESULTS

The values of the crystal field parameters are given in Tables Ia and Ib for the Gd^{3+} ion in four double-nitrate lattices at temperatures of 290°K and 77°K. These results are in good agreement with Trenam (1953) who investigated Gd^{3+} in bismuth magnesium nitrate at 20°K and 90°K. The discussion of the anomalous angular variation of the EPR spectra reported in V is incomplete because the problem of explaining this type of variation is not yet fully understood. The signs of the values assigned to the angular anomalies tabulated in Table 2 are chosen so that A is positive. The sign of A is indeterminate if parity is conserved. Parity conservation requires that a reversal of the magnetic field direction does not change the spectrum. This, together with trigonal symmetry, leads to a periodicity of $\frac{\pi}{3}$ radians in the angular variation of the spectrum in a plane perpendicular to the trigonal axis. This is the x-y plane, or in polar coordinates, the plane defined by $\theta = \frac{\pi}{2}$ and $0 < \phi < 2\pi$. The anomalous angular variation occurs when the magnetic field direction is varied in a plane containing the z-axis. If the subsidiary maximum in the angular spectrum occurs when $\theta = \frac{\pi}{2} + \Delta$ in vertical planes for which $\phi = 0$ or $\pm\frac{2\pi}{3}$

then it occurs when $\theta = \frac{\pi}{2} - \Delta$ in vertical planes for which $\phi = \pm \frac{\pi}{3}$ or
$\pm \pi$. ϕ is measured from the normal to an edge of the hexagonal plates.
The periodicity and inversion of the anomalous variation of the spectrum
is consistent with C_{3i} symmetry. It is inconsistent with C_{3h} symmetry,
which has symmetry about the x-y plane and with C_{3v} symmetry, which has
a periodicity of $\frac{\pi}{3}$ radians in the x-y plane. The conclusion is that
the site symmetry of the trivalent ion in the double-nitrate salts is
predominantly C_{3i} in agreement with the nearest-neighbour symmetry found
by Zalkin, Forrester and Templeton (1963). This disagrees with C_{3v}
symmetry deduced by Judd (1955) from optical spectra and by Culvahouse
Unruh and Sapp (1961) from X-ray analysis. It also disagrees with the
C_{3h} symmetry assumed by Trenam (1953) but it is interesting to observe
that the spin-Hamiltonian for the latter symmetry can be shown to be
identical with that for C_{3i} symmetry although the terms arise in a
different manner.

The spin-Hamiltonian (1) cannot predict this type of anomaly be-
cause it contains only angular momentum tensor operators of even parity.
The generalized tensor formalism of Grant and Strandberg (1964) intro-
duces products of odd parity tensors into the spin-Hamiltonian. It has
not been determined if this generalized Hamiltonian can predict the un-
usual angular variations reported in this paper. The further measure-
ments required before the coefficients in this generalized Hamiltonian
can be evaluated are being carried out.

REFERENCES

Bleaney, B. and Stevens, K. W. H., 1953, Rep. Progr. Phys. 16, 108.

Buckmaster, H. A., 1963, Proc. I.U.P.A.P. Conference on Paramagnetic
    Resonance, Editor, W. Low (Academic Press, New York), Vol. 1, 217.

_____ and Dering, J. C., 1967, Can. J. Phys. 45, 107.

Culvahouse, J. W., Unruh, W. and Sapp, R. C., 1961, Phys. Rev. 121, 1370.

_____ and Olsen, L. C., 1965, J. Chem. Phys. 43, 1145.

Edmonds, A. R., 1957, Angular Momentum in Quantum Mechanics, (Princeton University Press, Princeton, N.J.).

Geschwind, S., 1961, Phys. Rev. 121, 363.

Grant, W. J. C. and Strandberg, M. W. P., 1964, J. Phys. Chem. Solids 25, 635.

Judd, B. R., 1955, Proc. Roy. Soc. A232, 458.

_____, 1957, Proc. Roy. Soc. A241, 122.

_____ and Wong, E., 1958, J. Chem. Phys. 28, 1097.

Trenam, R. S., 1953, Proc. Phys. Soc. A66, 118.

Zalkin, A., Forrester, J. D. and Templeton, D. H., 1963, J. Chem. Phys. 39, 2881.

TABLE Ia

CRYSTAL FIELD PARAMETERS FOR EPR SPECTRA OF Gd^{3+} IN RARE-EARTH DOUBLE NITRATE CRYSTALS
Calculated in Parallel Direction

	TEMPERATURE	g	B_2^0	B_4^0	B_6^0	B_6^6	Δ
Lanthanum Magnesium Nitrate	290°K	1.9917 ±0.0001	0.2704 ±0.0001	0.00029 ±0.00001	0.000065 ±0.000002	0.000037 ±0.000001	0.000055
	77°K	1.9917 ±C.0001	0.2827 ±0.0001	0.00076 ±0.00001	0.000063 ±0.000003	0.00046 ±0.00001	0.00035
Lanthanum Zinc Nitrate	290°K	1.9918 ±0.0001	0.2846 ±0.002	0.00052 ±0.00002	0.0000707 ±0.0000001	0.0000001 ±0.0000001	0.0000074
	77°K	1.9928 ±0.0001	0.2980 ±0.0001	0.0010 ±0.0001	0.0000907 ±0.0000001	0.000045 ±0.000001	0.00017
Bismuth Magnesium Nitrate	290°K	1.9917 ±0.0001	0.2886 ±0.0001	0.00032 ±0.00002	0.0000610 ±0.0000001	0.000051 ±0.000001	0.000034
	77°K	1.9926 ±0.0001	0.3166 ±0.0001	0.00099 ±0.00001	0.000085 ±0.000002	0.000052 ±0.000002	0.00011
Bismuth Zinc Nitrate	290°K	1.9914 ±0.0001	0.2830 ±0.0001	0.00044 ±0.00001	0.0000435 ±0.0000001	0.000046 ±0.000002	0.0023
	77°K	1.9912 ±0.0001	0.3059 ±0.0001	0.00094 ±0.00002	0.0000464 ±0.0000001	0.000044 ±0.000002	0.0026
Bismuth Magnesium Nitrate	90°K	1.992 ±0.003	0.302 ±0.003	0.00075 ±0.00007	0.000087 ±0.000010	0.0023 ±0.0002	Trenam (1953)

Units of crystal field parameters are GHz. Δ is the sum of the squares of the differences between the calculated transitions and the observed transitions in units of $(GHz)^2$.

TABLE Ib

CRYSTAL FIELD PARAMETERS FOR EPR SPECTRA OF Gd^{3+}
IN RARE-EARTH DOUBLE NITRATE CRYSTALS
Calculated in Perpendicular Direction

	TEMPERATURE	g	B_2^0	B_4^0	B_6^0	B_6^6	Δ
Lanthanum Magnesium Nitrate	290°K	1.9922 ±0.0001	0.2722 ±0.0001	0.0000286 ±0.00001	0.0000464 ±0.000002	0.000005 ±0.000001	0.00022
	77°K	1.9930 ±0.0001	0.2775 ±0.0001	0.002148 ±0.000121	0.000121 ±0.000002	0.000154 ±0.00001	0.0035
Lanthanum Zinc Nitrate	290°K	1.9924 ±0.0001	0.2636 ±0.0002	0.000138 ±0.00002	0.0000944 ±0.0000001	0.0000948 ±0.000001	0.00012
	77°K	1.9914 ±0.0001	0.2972 ±0.0001	0.000938 ±0.0001	0.0000373 ±0.0000001	0.000091 ±0.000001	0.000044
Bismuth Magnesium Nitrate	290°K	1.9983 ±0.0001	0.2872 ±0.0001	0.000202 ±0.00002	0.0000992 ±0.0000001	0.0000814 ±0.000001	0.000043
	77°K	1.9919 ±0.0001	0.3157 ±0.0001	0.000855 ±0.00001	0.000020 ±0.000002	0.000068 ±0.000002	0.00019
Bismuth Zinc Nitrate	290°K	1.19889 ±0.0001	0.2928 ±0.0001	0.00024 ±0.00001	0.0000848 ±0.0000001	0.000076 ±0.000002	0.0000091
	77°K	1.9886 ±0.0001	0.3196 ±0.0001	0.001316 ±0.00002	0.000101 ±0.000001	0.0000818 ±0.000002	0.000020
Bismuth Magnesium Nitrate (Peak Value)	77°K	1.9905 ±0.003	0.3177 ±0.003	0.000817 ±0.00007	0.0000896 ±0.000010	0.000104 ±0.0002	0.000027

Units of crystal field parameters are GHz. Δ is the sum of the squares of the differences between the calculated transitions and the observed transitions in units of $(GHz)^2$.

TABLE 2

ANGULAR DISPLACEMENT OF POSITIONS OF MAXIMUM FIELD
SEPARATION FROM AN AXIS PERPENDICULAR TO THE TRIGONAL AXIS OF CRYSTALS

Angular Displacement (degrees)

Designation in Text			Lanthanum Magnesium Nitrate		Lanthanum Zinc Nitrate		Bismuth Zinc Nitrate		Bismuth Magnesium Nitrate	
$\|\pm\frac{7}{2}> \leftrightarrow \|\pm\frac{5}{2}>$	A	290°K	+3.5	±0.5	+5.0	±0.5	+3.5	±0.5	+4.0	±0.5
		77°K	+3.0	±0.5	+5.0	±0.5	+3.5	±0.5	+3.5	±0.5
$\|\pm\frac{5}{2}> \leftrightarrow \|\pm\frac{3}{2}>$	B	290°K	-4.0	±0.5	-2.5	±0.5	-3.5	±0.5	-4.0	±0.5
		77°K	-4.5	±0.5	-3.5	±0.5	-3.5	±0.5	-4.0	±0.5
$\|\pm\frac{3}{2}> \leftrightarrow \|\pm\frac{1}{2}>$	C	290°K	-7.5	±1.0	-2.5	±1.0	-11.5	±1.0	+0.0	±2.0
		77°K	-6.0	±1.0	-5.0	±1.0	-11.75	±1.0	-2.5	±2.0
$\|\pm\frac{1}{2}> \leftrightarrow \|\mp\frac{1}{2}>$	D	290°K	-2.5	±2.0	-1.0	±2.0	-2.5	±2.0	+0.0	±2.0
		77°K	-1.5	±2.0	-1.0	±2.0	-2.5	±2.0	-1.0	±2.0
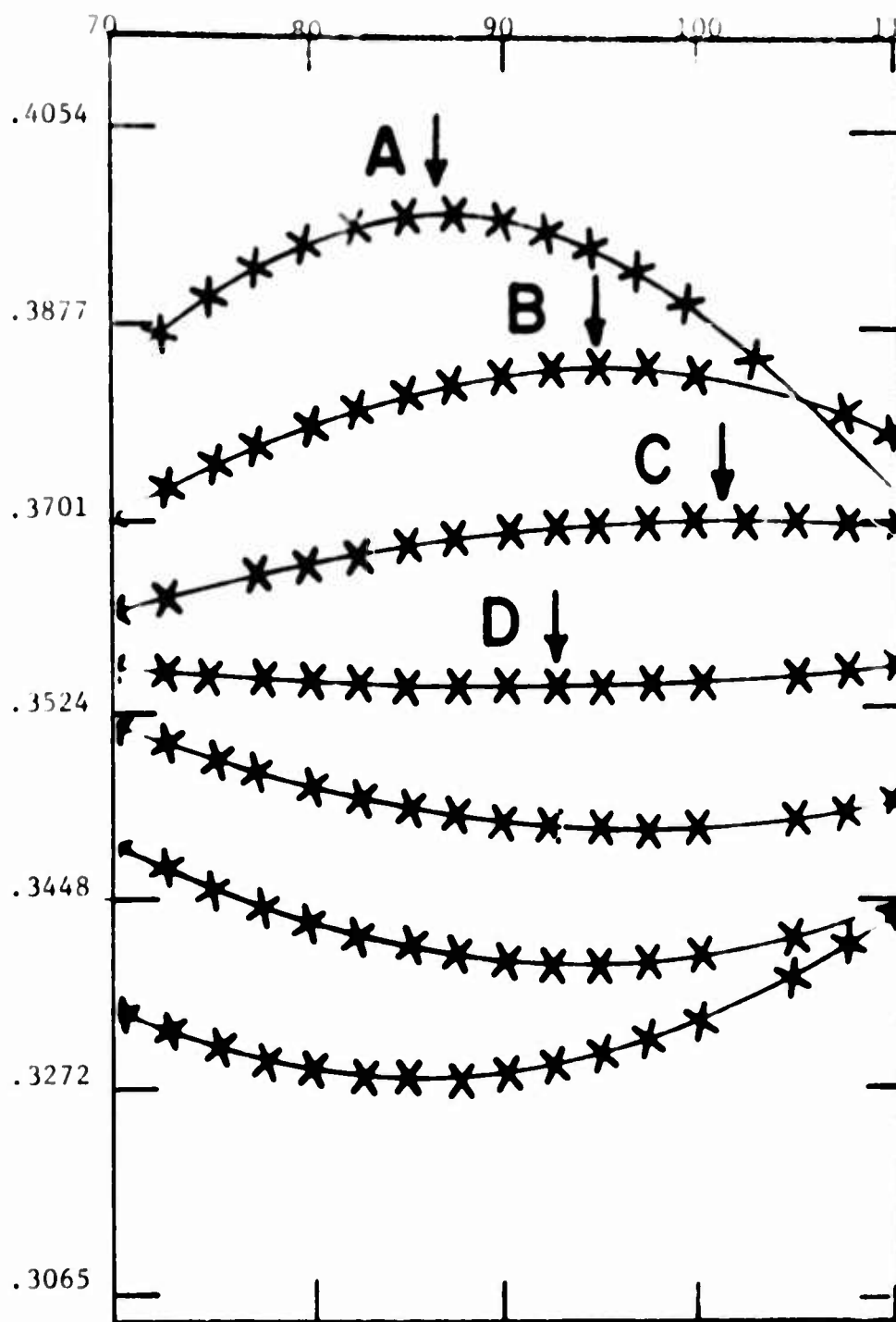
FIGURE I

Angular Variation of EPR Spectrum of

Gd^{3+} in Bismuth Zinc Nitrate at 290°K

$\nu = 9.88207$ GHz

TEMPERATURE VARIATION OF Gd ESR SPECTRA IN CUBIC AND AXIAL CRYSTALS[*]

M. M. Abraham, L. A. Boatner,[†] E. J. Lee and R. A. Weeks

*Solid State Division, Oak Ridge National Laboratory
Oak Ridge, Tennessee*

The electron spin resonance of gadolinium was observed and the temperature variation of the splitting was studied in single crystals of CeO_2, ThO_2, CaF_2, and CaO, where the symmetry of the local crystalline field was cubic. Similar measurements were made on single crystals of $La(C_2H_5SO_4)_3 \cdot 9H_2O$, $LaCl_3$, and $LaBr_3$ in which the symmetry of the local field was axial. Absolute signs of "spin" Hamiltonian parameters have been determined from the relative intensity of the resonance lines at low temperature.

The ground state degeneracy of a paramagnetic ion in a diamagnetic host is usually decreased or completely removed by the interaction of the surrounding crystalline electric field with its orbital angular momentum. Although S-state ions have no net orbital angular momentum, they still experience some removal of degeneracy by the crystal fields. This may be due to some intermediary interaction such as spin-spin or spin-orbit effects, or to small admixtures of non S-state configurations in the ground configuration. Such mechanisms have been proposed by many authors[1] as possible explanations for this S-state splitting.

Although the nature of the interaction causing S-state splitting is not understood, the experimentally observed spectrum may be fitted by a "spin" Hamiltonian which has the same symmetry as the crystalline electric field. For cubic symmetry the "spin" Hamiltonian operators

---

are of the fourth and sixth degree only, whereas for axial symmetry, terms of the second degree are also needed. The parameters of the "spin" Hamiltonian will naturally vary from crystal to crystal depending upon the strength of the interaction. In any given crystal they will vary with temperature and pressure as well, and knowledge of this dependence might be useful in understanding the form of the interaction. The ESR of various crystals doped with Gd were observed at several discrete temperatures in order to study the temperature dependence of the splitting.

Of the four most commonly observed S-state ions in electron spin resonance, Mn^{2+}, Fe^{3+}, Eu^{2+}, and Gd^{3+}, the latter was chosen as the S-state ion to be studied for two reasons. There is a very small hyperfine term and the ion almost always appears in the trivalent state when incorporated into a crystal. The electron spin resonance of gadolinium was observed and the temperature variation of the splitting was studied in single crystals of CeO_2,[1] ThO_2,[2] CaF_2, and CaO, where the symmetry of the local crystalline field was cubic. Similar measurements were made on single crystals of $La(C_2H_5SO_4)_3 \cdot 9H_2O$,[2] $LaCl_3$, and $LaBr_3$ in which the symmetry of the local field was axial.

The $^8S_{7/2}$ ground state of Gd^{3+} with eight-fold degeneracy is split by the action of the crystalline field into two doublets and a quartet for a cubic field, or into four doublets for an axial field. In either case the application of a magnetic field results in eight energy levels and seven strongly allowed transitions, $\Delta M_s = \pm 1$, may then be observed. The symmetry of the crystal field may be determined

from the intensity and position of the lines. Figures 1 and 2 show the appropriate Hamiltonians used for the cubic and axial fields respectively.

The spectra were observed using an x-band superheterodyne spectrometer. Mounting the crystals in the cavity on a gear, which could be rotated in a vertical plane (in addition to the horizontal rotation plane of the magnetic field), allowed accurate alignment of the crystal axes with the field. The magnetic field positions of the electron resonance lines were measured with a nuclear resonance probe (protons in H_2O) using a dual-beam oscilloscope display of both the electron resonance lines and the nuclear resonance. The nuclear and electronic frequencies were measured with a Hewlett Packard 524-C electronic counter and transfer oscillator model 540-B.

The results for the spin Hamiltonian parameters are tabulated in References (1) and (2) and in Tables I and II.

The absolute signs of the parameters were determined by observing the temperature dependence of the outer lines. In Figure 3 the spectrum in cubic CaO is shown and in Fig. 4 and 5 the spectra in the axial crystals $LaCl_3$ and $LaBr_3$, respectively, are shown.

For a point charge model the d value would be positive for both eight-fold and six-fold cubic coordination, while the c value would be negative and positive, respectively. It is interesting to note that both c and d are negative in the fluorite structures of ThO_2, CeO_2 and CaF_2, but in the six-fold coordinated CaO, it is the d parameter that becomes positive while the c value remains negative. This is contrary

to the situation expected for the point charge model, which has been successful in predicting the signs of c and d for non S-state 4f configurations.

In $LaCl_3$ the second order term is dominant and the relative intensities of the lines are 7:12:15:16:15:12:7 with approximately equal spacings between the lines. The parameters are in substantial agreement with Hutchison, Judd and Pope.[3] The fourth order term is appreciable in LaBr and at room temperature the relative intensities of the lines are 7:15:12:16:12:15:7 with uneven spacings between the lines. The temperature variation of the second order term in the presence of a comparatively large fourth order term is sufficient to change the relative positions of the lines between 77° and room temperature. Our results on this crystal differ somewhat from Johnson, Wong and Stafsudd.[4]

REFERENCES

1. A brief summary is given in M. M. Abraham, L. A. Boatner, C. B. Finch, E. J. Lee and R. A. Weeks, J. Phys. Chem. Solids 28, 81 (1967), with references cited therein.

2. M. M. Abraham, E. J. Lee and R. A. Weeks, J. Phys. Chem. Solids 26, 1249 (1965).

3. C. A. Hutchison, Jr., E. R. Judd and D. F. O. Pope, Proc. Phys. Soc. B70, 514 (1957).

4. D. R. Johnson, E. Y. Wong and O. M. Stafsudd, J. Chem. Phys. 44, 2693 (1966).

FIGURE CAPTIONS

Figure 1. Spin Hamiltonian for cubic crystal field. For positive c the transition $M_s = -\frac{5}{2} \rightarrow M_s = -\frac{7}{2}$ is the lowest energy difference (highest field).

Figure 2. Spin Hamiltonian for axial crystal field. For positive b_2^o, the transition $M_s = -\frac{5}{2} \rightarrow M_s = -\frac{7}{2}$ is the lowest energy difference (highest field).

Figure 3. Temperature dependence of the Gd^{3+} spectrum in CaO. At low temperature, the line at the lowest field is more intense than the line at the highest field showing c is negative.

Figure 4. Temperature variation of Gd^{3+} spectrum in $LaCl_3$. At low temperature the line at the highest field is more intense than the line at the lowest field showing b_2^o is positive.

Figure 5. Temperature variation of Gd^{3+} spectrum in $LaBr_3$. At low temperature the line at the highest field is more intense than the line at the lowest field showing b_2^o is positive.

CUBIC CRYSTAL FIELD

$$\mathcal{H}_{C.F.} = B_4[O_4^0 + 5O_4^4] + B_6[O_6^0 - 21O_6^4]$$

Zero field energies for $S = 7/2$

Γ_7 doublet $\qquad E = -18b_4 - 12b_6$

Γ_8 quartet $\qquad E = 2b_4 + 16b_6$

Γ_6 doublet $\qquad E = 14b_4 - 20b_6$

where $b_4 = 60B_4$ and $b_6 = 1260B_6$

Setting the zero level at the Γ_7 doublet the energies are

$\Gamma_7 \qquad E = 0$

$\Gamma_8 \qquad E = 20b_4 + 28b_6 = 5c + 7d$

$\Gamma_6 \qquad E = 32b_4 - 8b_6 = 8c - 2d$

with $H \parallel [100]$

$$E_{\pm 7/2} = \frac{13c + 5d \pm 3G}{2} \pm \frac{1}{2}\left[\left(3c - 9d \mp \frac{2G}{3}\right)^2 + \frac{140G^2}{9}\right]^{1/2}$$

$$E_{\pm 5/2} = \frac{5c + 7d \pm G}{2} \pm \frac{1}{2}[(5c + 7d \mp 2G)^2 + 12G^2]^{1/2}$$

$$E_{\pm 3/2} = \frac{5c + 7d \mp G}{2} \pm \frac{1}{2}[(5c + 7d \pm 2G)^2 + 12G^2]^{1/2}$$

$$E_{\pm 1/2} = \frac{13c + 5d \mp 3G}{2} \pm \frac{1}{2}\left[\left(3c - 9d \pm \frac{2G}{3}\right)^2 + \frac{140G^2}{9}\right]^{1/2}$$

$G = g\beta H \qquad c = 4b_4 = 240B_4$

$\qquad\qquad\qquad d = 4b_6 = 5040B_6$

AXIAL CRYSTAL FIELD

$$\mathcal{H} = B_2^0 O_2^0 + B_4^0 O_4^0 + B_6^0 O_6^0 + B_6^6 O_6^6$$

$$b_2^0 = 3B_2^0 \qquad b_4^0 = 60B_4^0 \qquad b_6^0 = 1260B_6^0 \qquad b_6^6 = 1260B_6^6$$

For $S = 7/2$ there will be four doublets at zero field.

With H $\parallel$ Z (crystal axis) the energies are

$$E_{\pm 7/2} = \pm 7/2\, g\beta H + 7b_2^0 + 7b_4^0 + b_6^0$$

$$E_{\pm 5/2} = \pm 5/2\, g\beta H + b_2^0 - 13b_4^0 - 5b_6^0$$

$$E_{\pm 3/2} = \pm 3/2\, g\beta H - 3b_2^0 - 3b_4^0 + 9b_6^0$$

$$E_{\pm 1/2} = \pm 1/2\, g\beta H - 5b_2^0 + 9b_4^0 - 5b_6^0$$

Transitions $\qquad M_S \longrightarrow (M_S - 1)$

$7/2 \to 5/2$	$G + 6b_2^0 + 20b_4^0 + 6b_6^0$
$5/2 \to 3/2$	$G + 4b_2^0 - 10b_4^0 - 14b_6^0$
$3/2 \to 1/2$	$G + 2b_2^0 - 12b_4^0 + 14b_6^0$
$1/2 \to -1/2$	G
$-1/2 \to -3/2$	$G - 2b_2^0 + 12b_4^0 - 14b_6^0$
$-3/2 \to -5/2$	$G - 4b_2^0 + 10b_4^0 + 14b_6^0$
$-5/2 \to -7/2$	$G - 6b_2^0 - 20b_4^0 - 6b_6^0$

$G = g\beta H$

TABLE I

Temp. (°K)	g	c	d	Total Spread*
		Gd³⁺ in CaF₂		
294	1.9919±0.0005	-560.0±0.6 Mc	-1.44±0.14 Mc	8.533 Mc
77	1.9917±0.0005	-580.9±0.6 Mc	-1.22±0.12 Mc	8.843 Mc
20	1.9918±0.0005	-581.6±0.6 Mc	-1.26±0.13 Mc	8.861 Mc
~10	1.9911±0.0005	-582.5±0.6 Mc	-1.69±0.17 Mc	8.870 Mc
4.2	1.9915±0.0005	-581.7±0.6 Mc	-1.35±0.14 Mc	8.861 Mc
~2	1.9906±0.0005	-582.3±0.6 Mc	-1.67±0.17 Mc	8.861 Mc
		Gd³⁺ in CaO		
294.5	1.992±0.001	-159.3±0.2 Mc	+13.9±0.14 Mc	2.061 Mc
77	1.992±0.001	-146.8±0.2 Mc	+14.1±0.14 Mc	2.175 Mc
20	1.993±0.001	-147.2±0.2 Mc	+14.3±0.14 Mc	2.181 Mc
~10	1.992±0.001	-147.2±0.2 Mc	+14.1±0.14 Mc	2.174 Mc
4.2	1.993±0.001	-147.3±0.2 Mc	+14.1±0.14 Mc	2.182 Mc
~2	1.994±0.001	-147.4±0.2 Mc	+14.1±0.14 Mc	2.184 Mc

*Distance between outer lines 7/2 ↔ 5/2 and - 7/2 ↔ - 5/2 with H∥[100] (measured with proton resonance 42.576 Mc = 10,000 G).

TABLE II

Temperature (°K)	g	b_2^o ($\times 10^{-4}$ cm^{-1})	b_4^o ($\times 10^{-4}$ cm^{-1})	b_6^o ($\times 10^{-4}$ cm^{-1})	Total Spread H‖z (Mc)
		Gd^{3+} in LaCl$_3$			
293.5	1.9923±0.0005	+8.15±0.10	+1.72±0.02	+0.71±0.02	0.802
77	1.9919±0.0005	+16.36±0.10	+2.14±0.02	+0.21±0.02	1.302
20	1.9924±0.0005	+17.81±0.10	+2.13±0.02	+0.21±0.02	1.381
~10	1.9917±0.0005	+17.81±0.10	+2.13±0.02	+0.21±0.02	1.381
4	1.9927±0.0005	+17.68±0.10	+2.16±0.02	+0.23±0.02	1.380
~2	1.9926±0.0005	+17.62±0.10	+2.18±0.02	+0.24±0.02	1.380
		Gd^{3+} in LaBr$_3$			
294	1.9920±0.0005	+44.27±0.10	+13.92±0.02	-0.336±0.020	4.964
77	1.9922±0.0005	+59.36±0.10	+14.17±0.02	-0.345±0.020	5.840
4	1.9922±0.0005	+61.76±0.10	+14.22±0.02	-0.339±0.020	5.978
~2	1.9922±0.0005	+61.22±0.10	+13.45±0.02	-0.325±0.020	5.807

Gd³⁺ in Site with Cubic Symmetry in CaO.

100 gauss

H ∥ [100]

~2°K

4.2°K

77.3°K

294.5°K

Gd^{3+} in Site with Axial Symmetry in LaCl$_3$ H ‖ Z

293.5°K

~273°K

232.4°K

77.3°K

4.2°K

~2°K

100 gauss

H →

Gd^{3+} in Site with Axial Symmetry in LaBr$_3$.

H ∥ Z

100 gauss

~2°K

4.2°K

77.3°K

232.4°K

294.7°K

H →
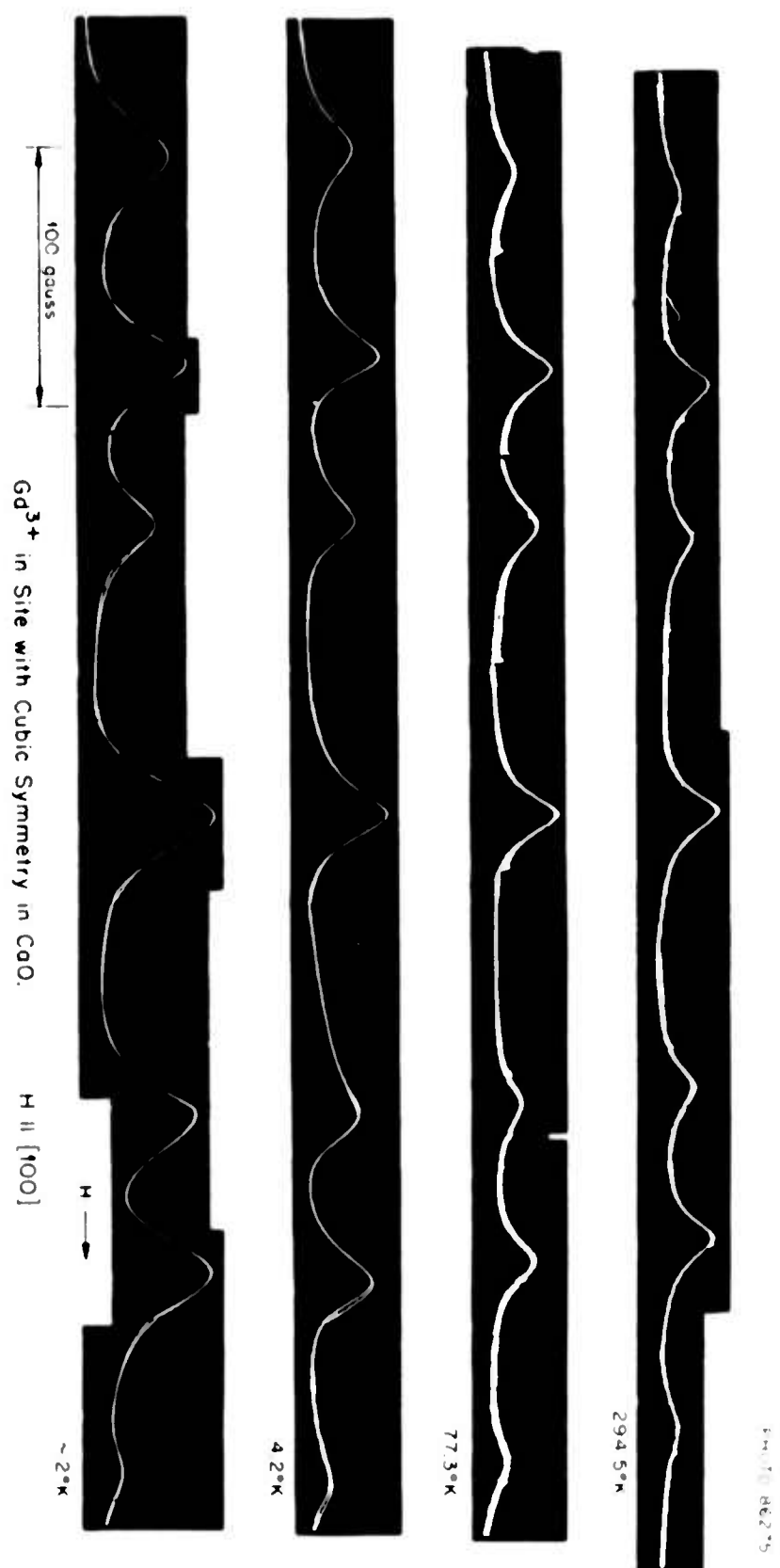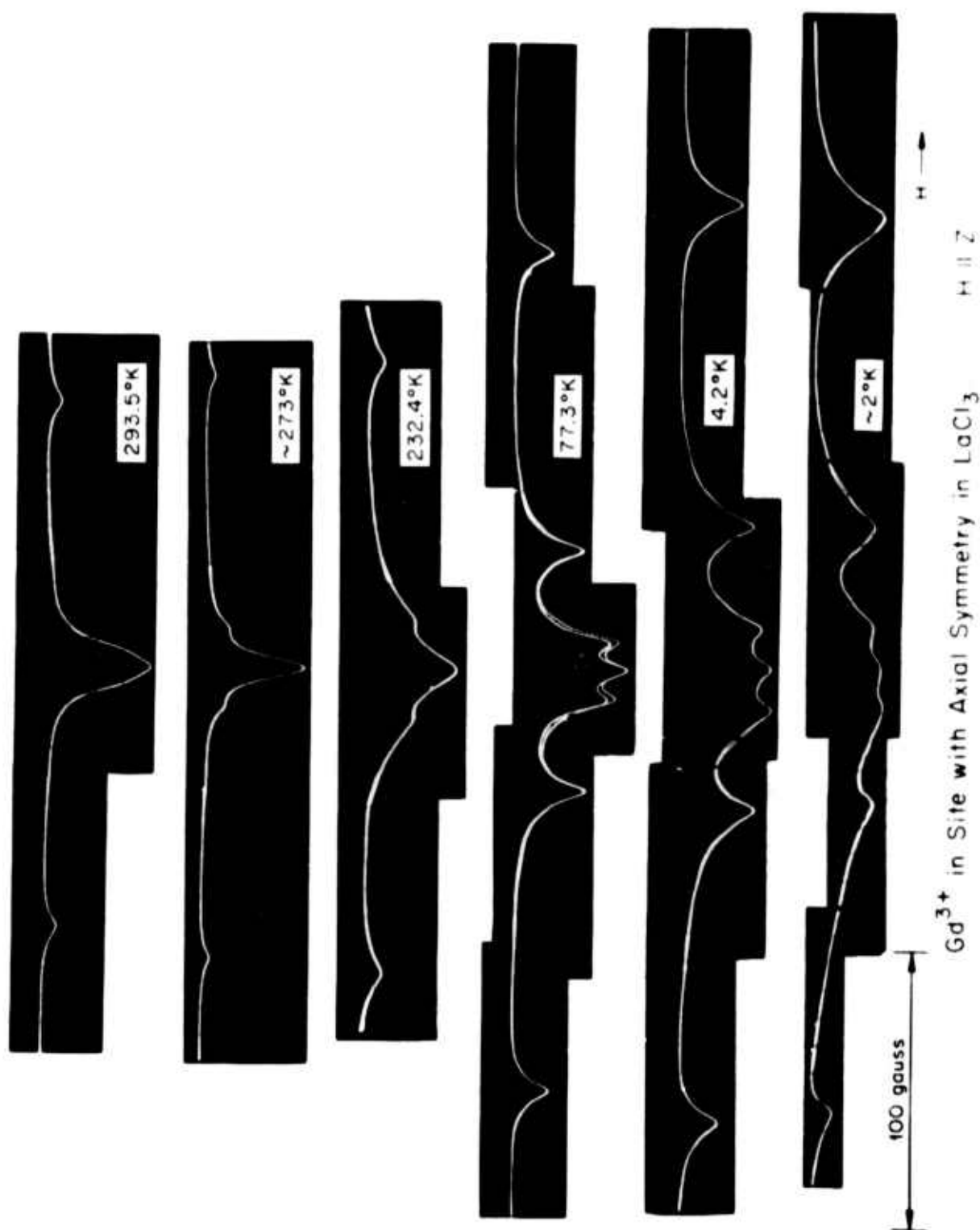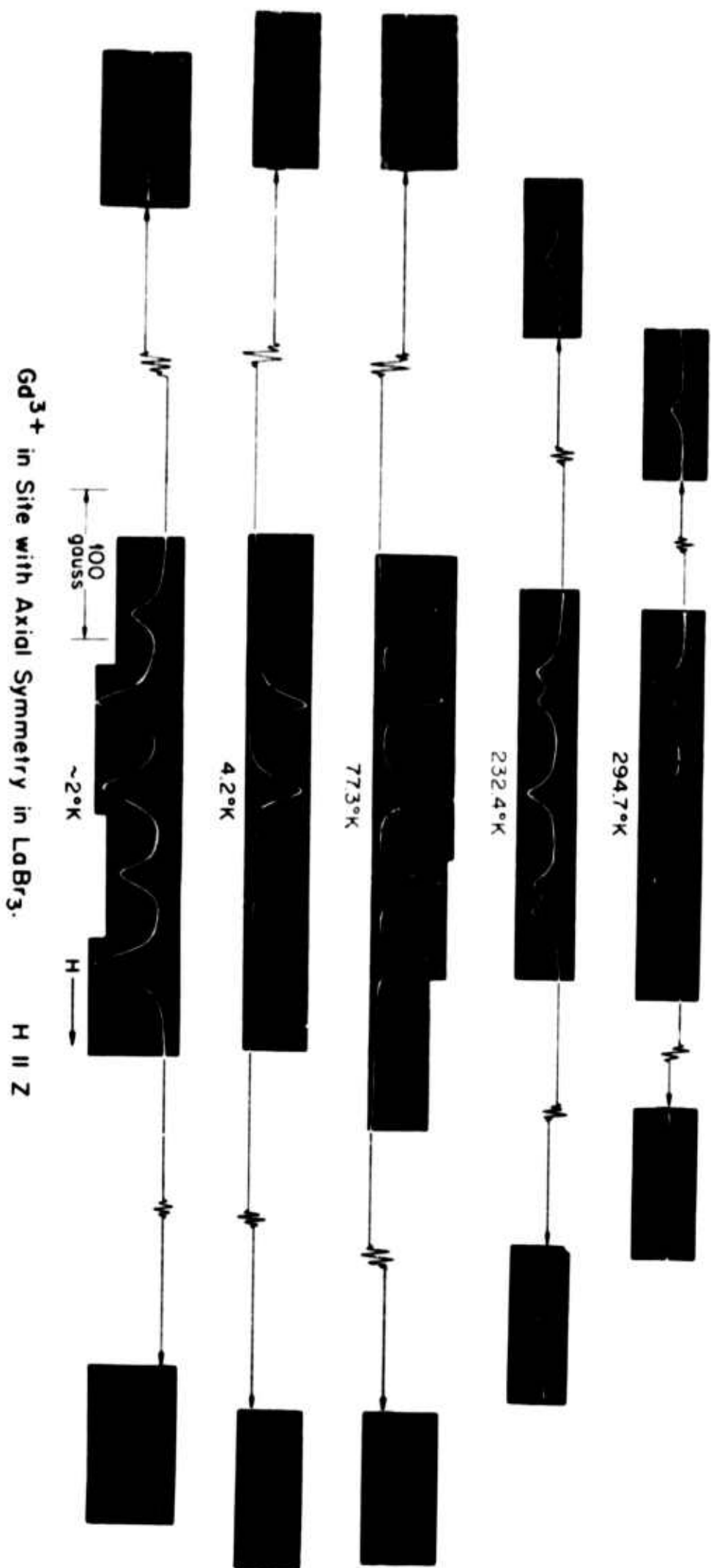
The M Series X-Ray Emission Lines of the Rare Earths*

A. F. Burr
New Mexico State University

Abstract

A review of the wavelengtns and energy levels assigned to the M series x-ray transitions of the rare earths shows that the width and pronounced structure of the Mα line has made the determination of its wavelength difficult and has introduced some uncertainty in the value to be given to the $N_{VI, VII}$ energy level. This study has extended a program of selecting the most probable values for energy levels and wavelengths of x-ray lines by using modified Moseley diagrams to include the information contained in adjacent elements. Revised Mα and Mβ wavelengths are given for a number of rare earths as well as revised $N_{VI, VII}$ energy levels. This study also gives further information on the origin of the structure of the Mα line in the rare earth region of the periodic table.

Introduction

The energy levels and radiative transitions between them involved in the M series of x-ray emission lines are illustrated in Fig. 1, which is a partial energy level diagram of a typical rare earth based on the one electron model. The levels are identified on the right by their x-ray notation and on the left by their spectroscopic notation. A few of the possible dipole transitions between levels are indicated by arrows; the two on the left are the most important.

In the rare earths, the M series transitions cover the range from 7 to 19 Å; hence to study them one must have a vacuum spectrometer and crystals with large lattice spacings as KAP or ADP with spacings of 13.3 and 5.3 Å respectively. Early measurements of these lines were made by van der Tuuk[1] in 1927 and an extensive series of measurements were completed by Lindberg[2] in 1931. More recent measurements have confirmed the findings of these early workers.

These findings include the information that the Mα line (and to a lesser extent the Mβ line) takes on a special character in the rare earths. As one goes down the periodic table through the rare earths, the Mα line becomes progressively broader and breaks up into several peaks. Furthermore its intensity relative to the nearby Mβ line markedly decreases.

Some of these special characteristics are illustrated in Fig. 2, where the Mα line of terbium is superimposed on a more typical Mα line, in this case that of mercury[3]. The intensity of both lines has been normalized to an arbitrary value of 100, and the wavelength scales normalized to the center value and superimposed. In this figure the multiple peaks and the broadness of the rare earth Mα line are plainly evident.

Objective

The objective of this particular study was to obtain from the currently available information the best possible wavelength values

for all possible x-ray lines near the Mα line regardless of the transition probabilities. The best way to accomplish this task is to use all the information for a given element to obtain values of the energy levels and get the desired wavelengths by taking differences.

Method Used

The basic method is to take all the x-ray wavelengths for an element--the K and L series measurements as well as the M measurements-- and obtain relative values of the energy levels by a least squares adjustment. This method, which is described in detail elsewhere[4,5], yields more accurate values for a given energy level difference than any single experimental measurement of the corresponding wavelength. However, this method does not make use of the information contained in the adjacent elements. To obtain this information, modified Moseley diagrams are constructed. This procedure is particularly applicable to the rare earth region of the periodic table since here the physical structure of the elements change little with the change in atomic number.

The Modified Moseley Diagram

Modified Moseley diagrams are based on Moseley's Law which states that

$$\sqrt{E} = k \, Z \tag{1}$$

where E represents the energy of a given transition, Z the atomic number, and k a proportionality constant. In practice a plot of the square root of energy vs Z does not yield a straight line. In order to emphasize the difference from a straight line, a straight line closely approximating the original curve is subtracted from the data

and the resulting modified Moseley curve plotted on a greatly expanded scale. One then has a graph of

$$\sqrt{E} - Y = k Z \qquad (2)$$

where

$$Y = a Z + b \qquad (3)$$

with a and b emperical constants chosen to make the range of the left side of (2) as small as possible. Thus one is enabled to more easily recognize any deviation from a smooth curve. The interpretation of any deviation is a more difficult matter.

A preliminary study showed that only four transitions would be of interest; the $M_{IV}O_{II, III}$, $M_{V}O_{III}$, $M_{V}N_{VI, VII}$, and $M_{IV}N_{VI}$ lines. Figure 3 shows the modified Moseley diagrams constructed for the $M_{IV}O_{II, III}$ and $M_{V}O_{III}$ transitions respectively. The data points, shown with their probable errors, are taken from the previously mentioned least squares study[4]. In only three cases in the rare earth region did the plotted points differ from the smoothing curve by more than two probable errors.

Fig. 4 shows the diagrams constructed for the Mα ($M_{V}N_{VI, VII}$) and Mβ ($M_{IV}N_{VI}$) lines. Note that the vertical scale is quite a bit larger here than in the previous figure. This scale difference indicates that these lines fit the Moseley Law more closely as is typical of the strongest lines in a given series. Note also the great similarity in position of the data points. This similarity is due to the fact that the value of the $N_{VI, VII}$ level was almost solely determined by the Mα line. The Mβ was not used in the basic study[4] since it connected only with the N_{VI} level. The only other line connecting with the $N_{VI, VII}$ level was a N line which carries a large probable error and hence has little influence on the value of the level. The particular smoothing curve shown would not have been selected if it were not that experimental values for the Mβ line as listed by Bearden[6] lie close to it.

Results

Using the smoothed curves, one obtains wavelength values for the
Mα and Mβ lines which differ significantly from the values given in
the least squares adjustment[4,5] for rare earths with atomic numbers
between 62 and 71. It should be noted, however, that the change is
only a fraction of the line width. Revised values for the $N_{VI,VII}$
energy level are also obtained. These revised values are listed in
Table I along with previous values for comparison. A summary of the
results of this study is shown in Fig. 5, where the wavelength of all
the four lines studied are shown on one graph by plotting the differ-
ence from the Mβ line against atomic number Z.

Table I. Comparison of revised values with previous values.

Z	Mβ			Mα		$N_{VI,VII}$	
	a	b	d	b	d	c	d
	Å	Å	Å	Å	Å	ev	ev
63	10.750	10.682	10.744	10.963	11.012	0.0	5.0
64	10.254	10.186	10.257	10.462	10.521	0.1	7.6
65	9.792	9.744	9.801	10.010	10.063	2.6	9.6
66	9.357	9.334	9.374	9.606	9.632	4.2	8.8
67	8.965	8.933	8.974	9.199	9.229	3.7	8.9
68	8.592	8.556	8.597	8.824	8.846	4.3	9.5
69	8.249	8.214	8.244	8.478	8.493	5.3	8.3
70	7.909	7.897	7.911	8.148	8.157	6.3	8.5

a Data from ref. 6
b Data from ref. 4
c Data from ref. 4,5
d Results of this study

Application

These results have been applied to the problem of interpreting the unusual characteristics of the Mα line in the rare earth region. The reason for the lack of intensity in the Mα line compared to the Mβ line has long been recognized as due to the fact that in the rare earths the $N_{VI, VII}$ shell is being filled with electrons and the N_{VI} level fills first. However there has been much dissatisfaction with the usual explanation which ascribes the multiple peaks of the Mα line to splitting caused by the unfilled nature of the $N_{VI, VII}$ shell[2,7]. The $N_{VI, VII}$ level is broad and can possibly account for the unusual width of that line but not the pronounced structure and relative wide spacing of the peaks. Some people have suggested that the various peaks might be due to dipole transitions from the O shell which were for various reasons unexpectedly strong in the rare earth region. The above study appears to rule out this possibility since the best information obtainable on the expected wavelength for these lines does not agree on the whole with the number or location of the multiple peaks. In particular the peaks are much closer together than one would expect if the above explanation were true.

At the present time the best explanation of these multiple peaks appears to be that they are due to self-absorption caused by the use of a large excess voltage to generate measurable intensity in the emission lines and an overlapping of the structure from the nearby absorption edges. This explanation was first proposed by Stewardson[8] and has been supported by more recent work[9]. The difficulty of obtaining good absorption spectra from the same chemical compound as the material used to obtain the emission line spectra is great and makes the investigation of self-absorption more complicated. The question of the possible influence of bound ejected electron states on the absorption spectra and of satellites on the width of the emission lines is a very interesting one. Particularly needed are some low voltage wavelength measurements to give as clear a picture as possible of the position and shape of the emission line uninfluenced by other factors.

Acknowledgements

References

[1] J. H. van der Tuuk, Z. Physik 44, 737 (1927).

[2] E. Lindberg, Nova Acta Reg. Soc. Sci. Upsal. 7, No. 7 (1931).

[3] A. F. Burr, Bull. Am. Phys. Soc. 11, 389 (1966).

[4] J. A. Bearden and A. F. Burr, Atomic Energy Levels, NYO 2543-1 (Federal Sci. and Tech. Inf., U.S. Dept. of Commerce, Springfield, Va. 22151)

[5] J. A. Bearden and A. F. Burr, Rev. Mod. Phys. To be published (1967).

[6] J. A. Bearden, X ray Wavelengths, NYO 10586 (Federal Sci. and Tech. Inf. U.S. Dept. of Commerce, Springfield, Va. 22151).

[7] A. E. Sandström, Handbook der Physik XXX, 78 (1957).

[8] E. A. Stewardson and J. E. Wilson, Proc. Phys. Soc. (London) 69A, 93 (1956).

[9] W. L. Baun and D. W. Fischer, private communication.

SPECTROSCOPIC
NOTATION

X-RAY
NOTATION
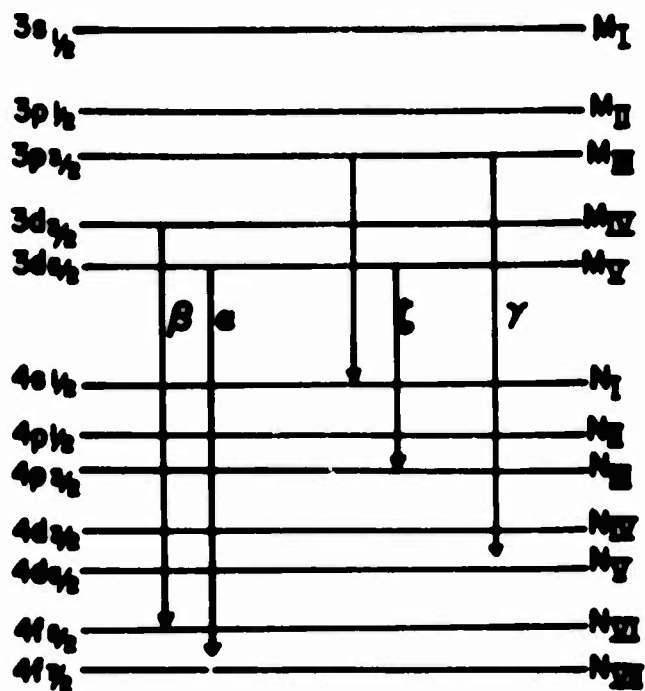
FIG. I PARTIAL ENERGY LEVEL DIAGRAM
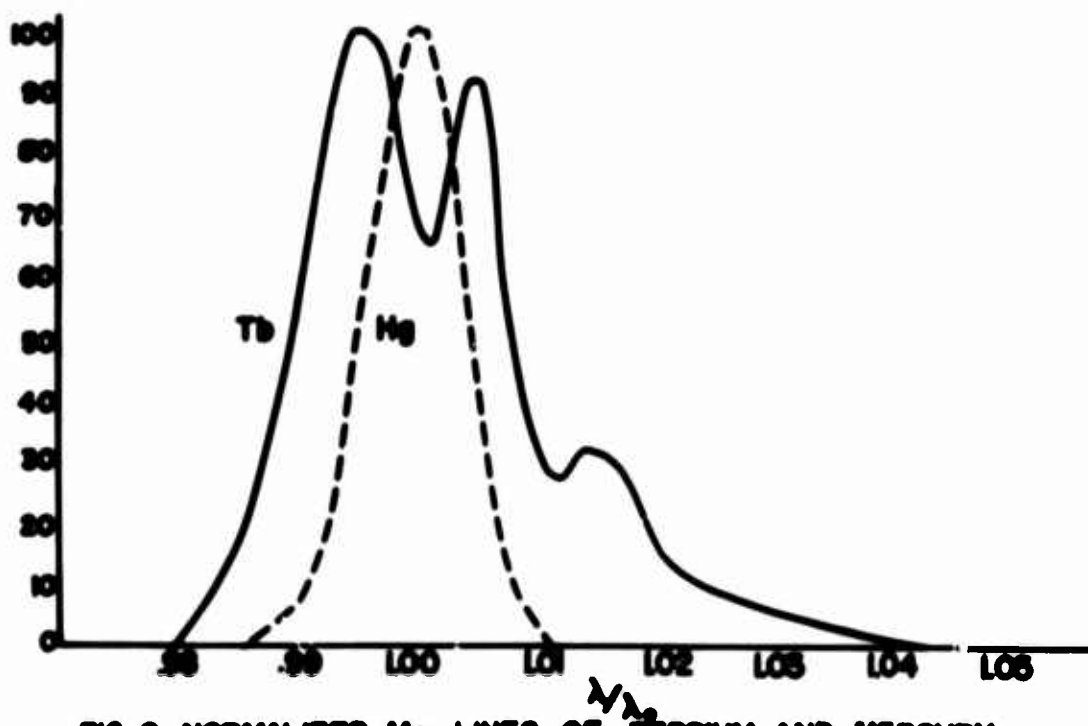
FIG. 2 NORMALIZED Mα LINES OF TERBIUM AND MERCURY
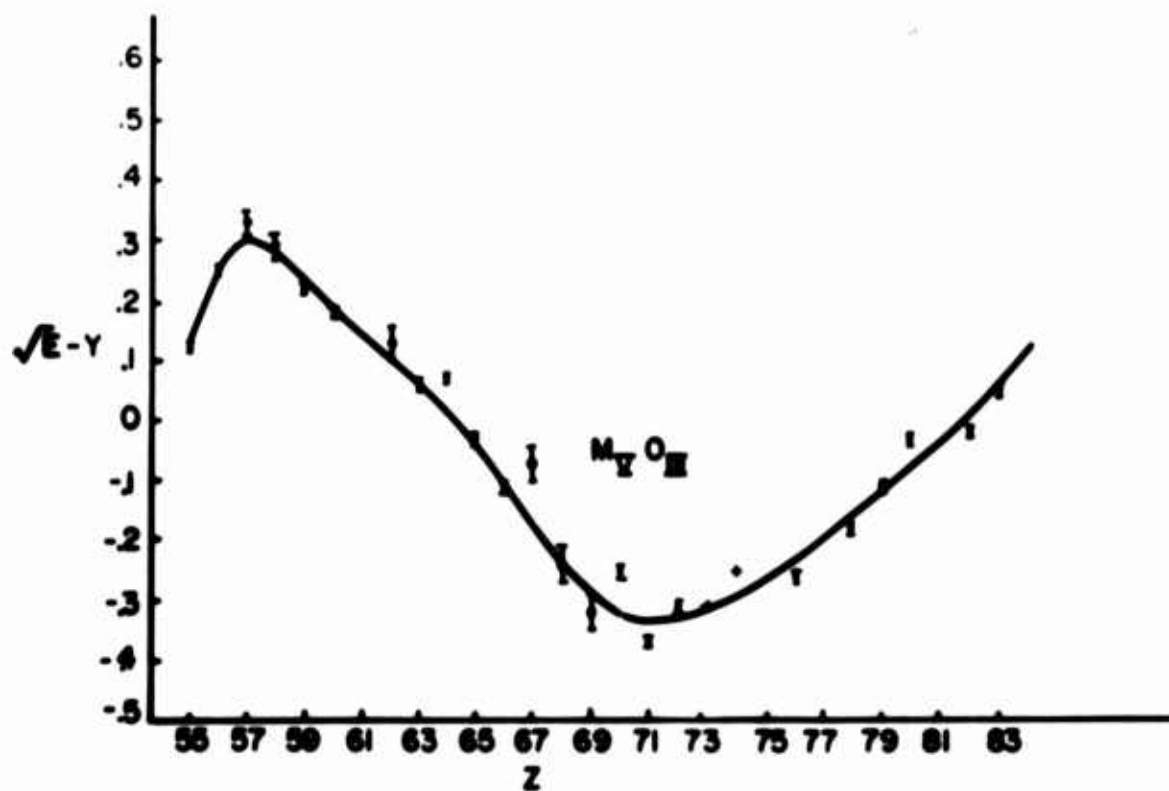
FIG. 3. MODIFIED MOSELEY DIAGRAMS OF $M_{IV}O_{II,III}$ AND $M_{V}O_{III}$ LINES
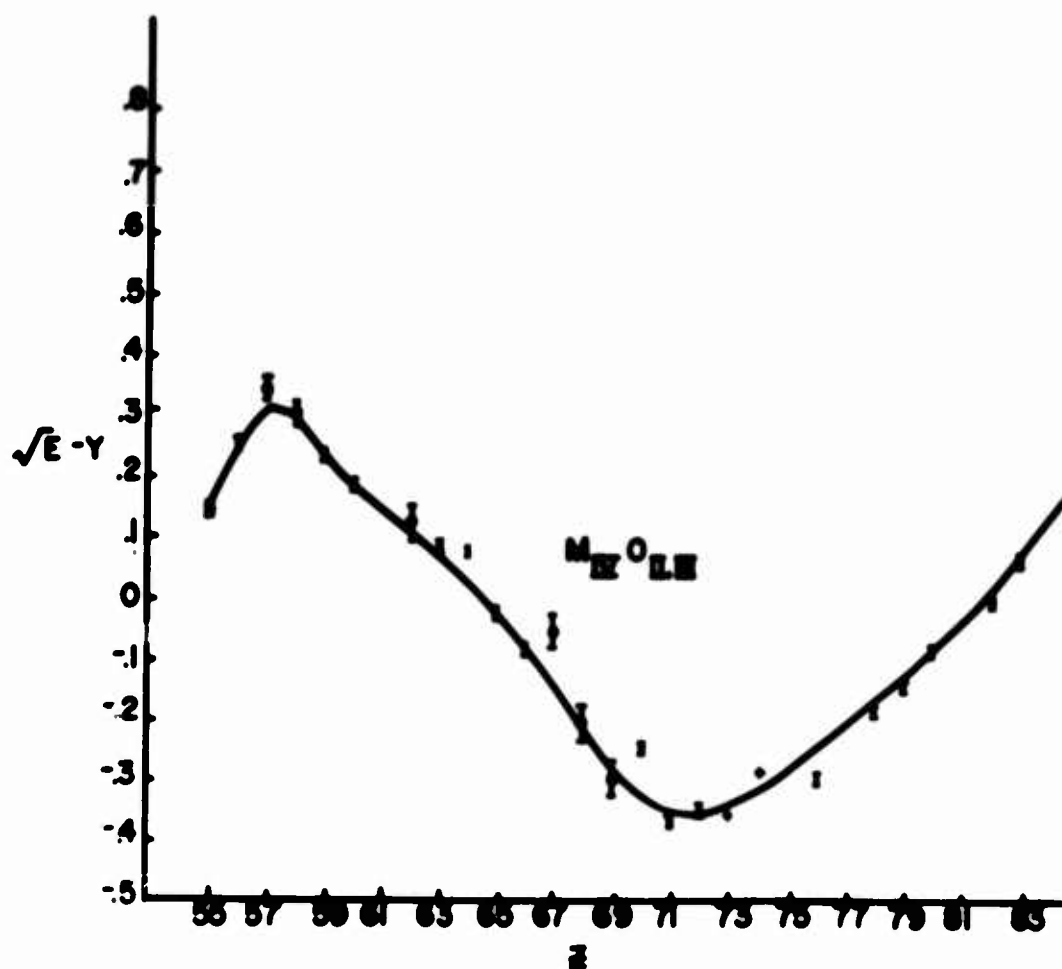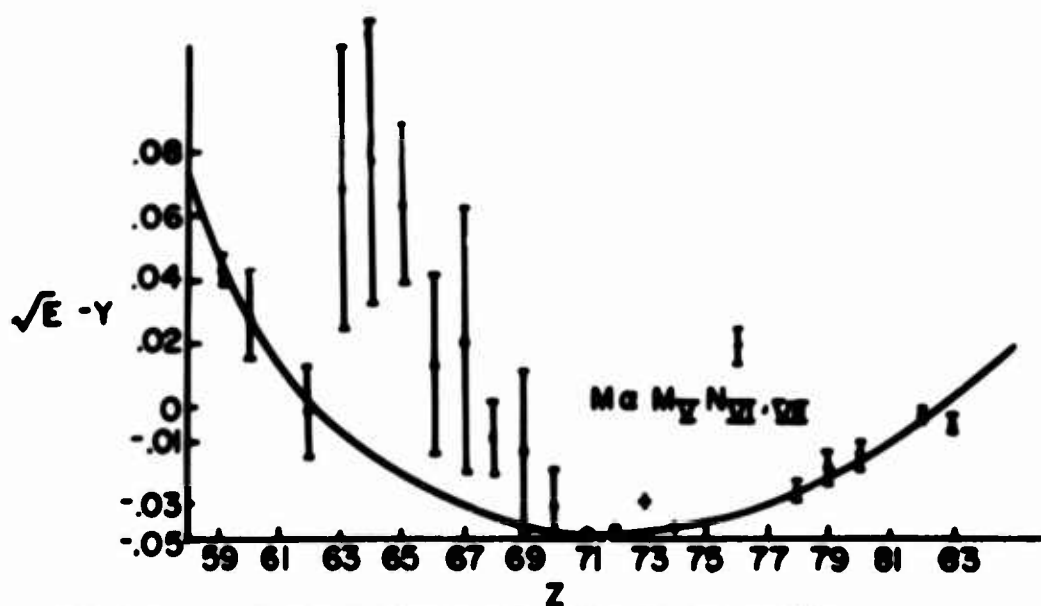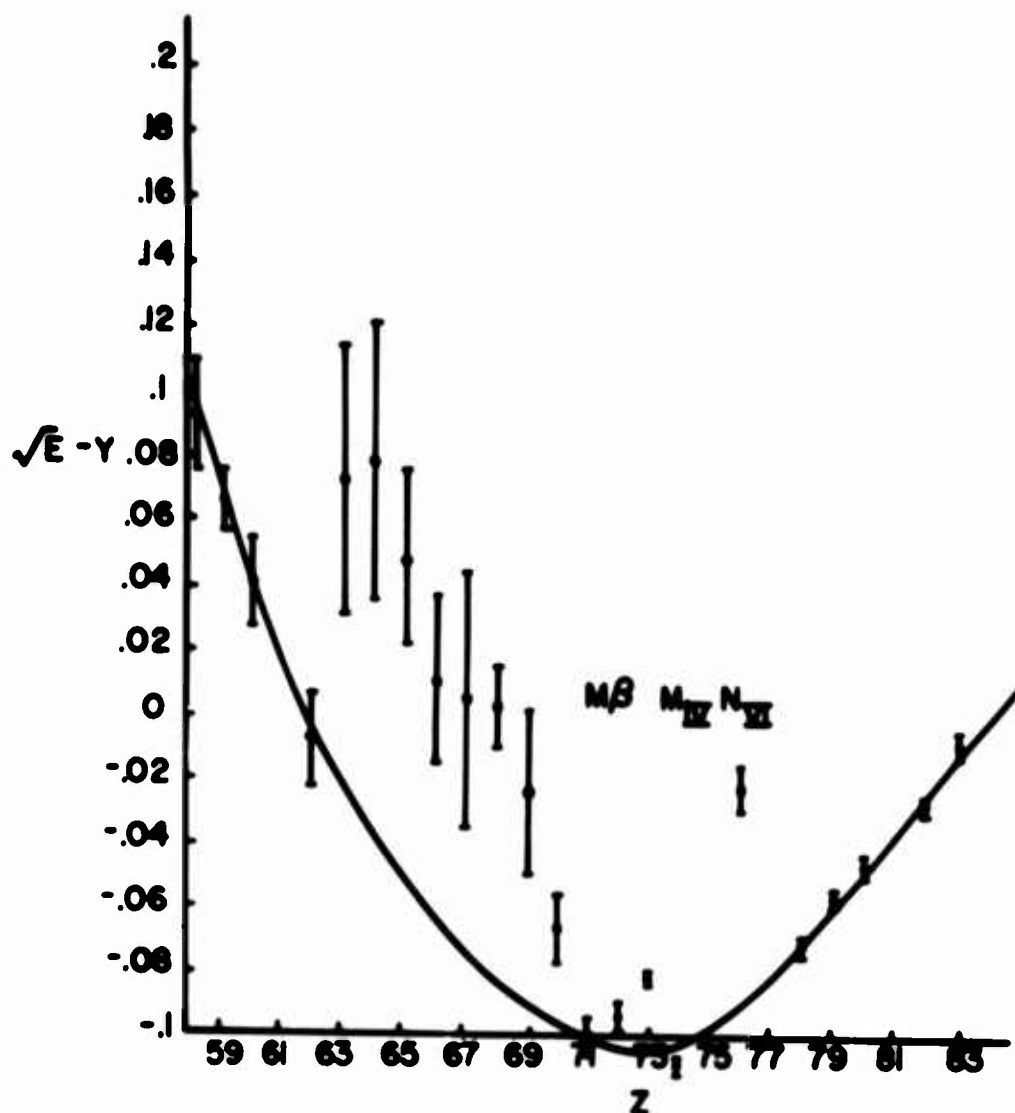
G. 4. MODIFIED MOSELEY DIAGRAM OF Mβ AND Mα LINES
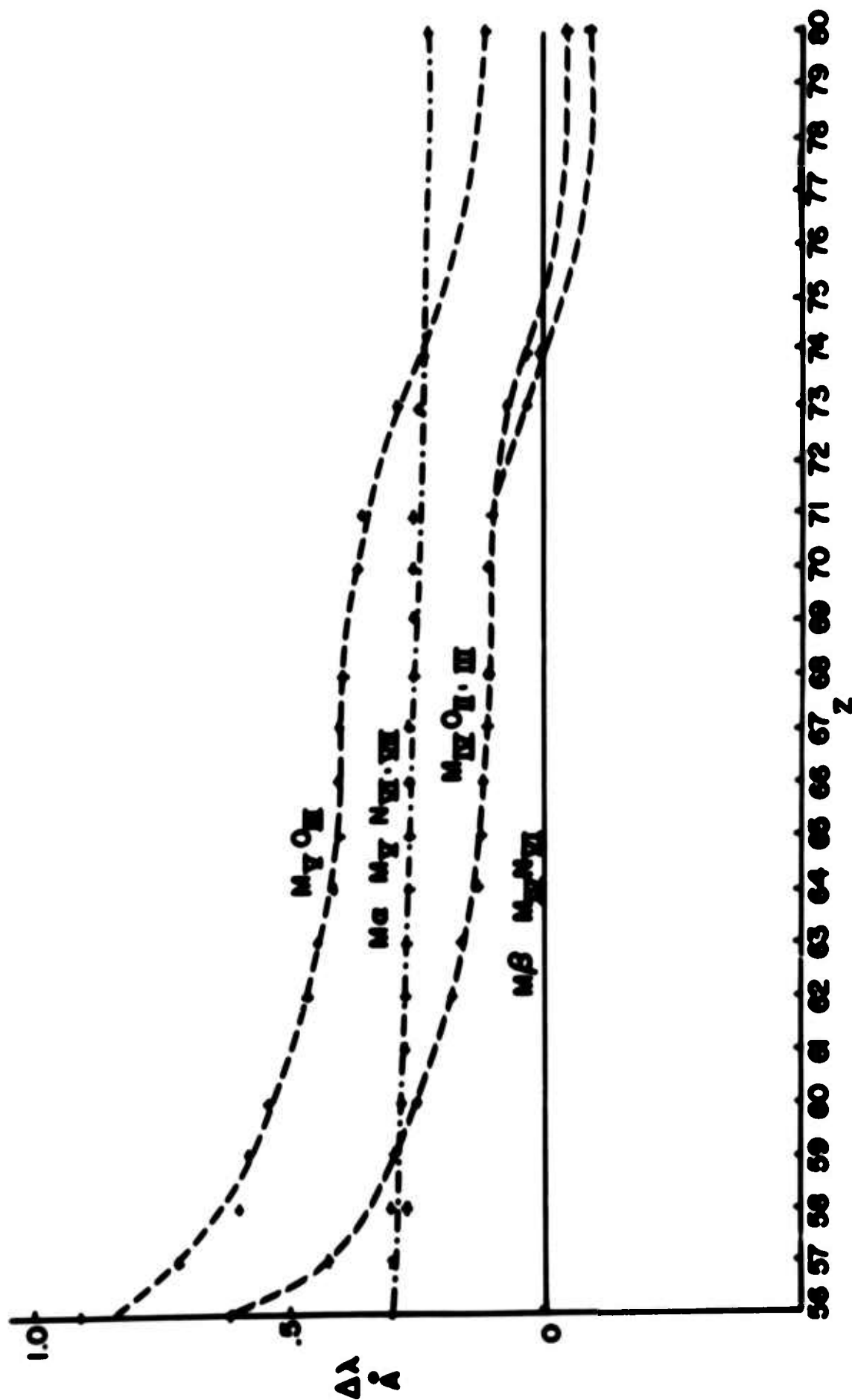
FIG. 5 WAVELENGTH SEPARATIONS

NON-STOICHIOMETRY AND CRYSTAL DEFECTS IN THE SOLID
STATE CHEMISTRY OF THE LANTHANIDES

J. S. Anderson
University of Oxford

It is not the purpose of this paper to make a complete survey of the non-stoichiometric compounds of the lanthanides, but rather to examine how far some of their well investigated classes of compounds shed light on one of the central problems of solid state chemistry. This problem is the real constitution of grossly non-stoichiometric phases: the structural principles that must be postulated to account for them, and the conditions under which stoichiometric variability is observed.

The questions raised by the existence of non-stoichiometric phases have been discussed by the author and others in several publications[1] and will not be elaborated here. It is sufficient to recall that the theory of point defects, as originated by Schottky and Wagner, runs into difficulties in accounting for phases with a very high apparent concentration of vacancies or interstitial atoms. Unacceptable assumptions have to be made about the equilibrium constants for intrinsic disorder in crystals: in general, native disorder of the Schottky-Wagner type is likely to be at a very low concentration (at temperatures significantly below the melting point of ionic crystals, at least). Crystallographers have pointed out that relaxation around 'defects' - especially interstitials - may not only be necessary, but may generate new patterns of short range order (see, especially, Wadsley, ref 1), and that there is a considerable gain in lattice energy in fully ordering vacant sites, or the rearranged configurations around 'interstitials', so that they become structural components of the crystal and generate series of new structures - intermediate phases of fixed composition. Nevertheless, preparative and thermodynamic studies have proved beyond question that non-stoichiometric phases represent real equilibrium states of numerous systems, and that, over appropriate temperature ranges, the real situation may embrace either ordered intermediate phases or random non-stoichiometric phases with a wide range of composition. The work of Hyde, Bevan and Eyring[2] on the praseodymium oxides is one of the most elegant and convincing pieces of evidence on this subject.

Attention has therefore been directed   alternative
viewpoint, first formulated by Ariya[3]:   n-stoichiometric
phases are "submicroheterogeneous," consi   of regions or
microdomains, of small and uncertain exten but perhaps 5-20
unit cells in linear dimension, of two perfectly ordered struc-
tures, which are coherently intergrown with one another. Cer-
tain thermodynamic considerations arise if we are to postulate
that this situation represents an equilibrium state, rather
than continued growth of the microdomains into viable nuclei
and macroscopic crystals in a biphasic mixture, and if we are
to account for the chemical potentials in non-stoichiometric
systems. These implications have not been explored in print:
they may be formulated in the near future. The relevant
point for present discussion is that for the occurrence of
non-stoichiometric compounds two conditions may have to be
fulfilled:

(a) suitable relations between the energetics of
the mixed valence states that are involved in
a non-stoichiometric phase and

(b) appropriate structural and dimensional relations
between the two types of ordered microdomain,
to permit of coherent intergrowth and to minimize
strain and surface free energy at the transition
from one microdomain to the next.

The lanthanide elements provide useful and suggestive
evidence on these points. They provide a series of cations
of similar, but graded, ionic radius; their ionisation ener-
gies are relatively low and the trivalent cations are large
enough to have a low effective electrostatic potential, so
that the L^{3+} cations are the usual structural units in their
solid compounds. Variable valency is effectively restricted
to the well known and regularly behaved members of the
series. The 4 f electrons are well screened so that core-
core interactions are minimized, though there are specific
and graduated ligand field effects along the series[4]. We
therefore have the familiar situation that lanthanide atoms
or ions - subject to the gradations in atomic or ionic radius -
can fully replace one another in mixed crystal systems. It
must be noted, however, that there are two considerations
that are frequently overlooked in dealing with ternary or
more complex lanthanide phases.

1. That a random distribution of lanthanide
cations may be metastable as compared with
an ordered distribution, but the driving
force behind any ordering process is likely
to be small. Many observations on ternary

systems, or made with other than the purest
lanthanide preparations, may relate to meta-
stable conditions.

2. In ternary phases involving the mixed valence
    states Ce^{III}/Ce^{IV}, Pr^{III}/Pr^{IV}, Tb^{III}/Tb^{IV},
    Eu^{II}/Eu^{III} etc. the electron transfer process,
    needed to bring about an ordering of ions in
    the two valence states, may be blocked by the
    random distribution of fixed-valence and
    variable-valence lanthanide ions. In conse-
    quence, vacancies etc. may be locked in a
    random, but essentially metastable, distribu-
    tion.

We may proceed to correlate the evidence obtained by
several groups of workers on (a) the chemistry of the lantha-
nide oxides, (b) the chalcogenides; and (c) the nitrides and
carbides, in relation to the problem outlined at the beginning.

A. Oxide Chemistry

The first point of interest is that the lanthanide
oxides display properties consistent with the presence of a
small degree of native disorder, on the Schottky-Wagner model.
The kind of native disorder found in the Type A sesquioxides
is not known. In the type C oxides, as derivatives of the
fluorite structure, the native disorder undoubtedly consists
of vacant anion sites and interstitial anions, the latter
term being used in a special sense that is more fully considered
below.

At sufficiently high temperatures, and at a low chemical
potential of oxygen, the native defect equilibrium is dis-
turbed and the equilibrium state corresponds to a significant
stoichiometric excess of metal. Studies of the vaporisation
behaviour indicate that oxygen is lost and that the congruently
vaporising oxide - with a composition within the evidence
range - is of the metal-excess type[5]. Daane and Miller[6]
found that the oxides of the elements from gadolinium to
lutecium were reduced when melted in vacuum at 2350-2500°C,
or distilled at 2100°C in presence of the metal, the products
ranging from $GdO_{1.495}$ to $LuO_{1.485}$ (with some trend towards
increasing reducibility as the ionic radius decreased).
Reduction of Type A neodymium oxide at much lower tempera-
tures proceeds only as far as $NdO_{1.4996}$[7]. The existence
of the lower valence state of europium does not markedly in-
fluence the reducibility and existence range of the sesqui-
oxide; in dry hydrogen at 650° it is reduced only to $EuO_{1.493}$,
strictly comparable with the other lanthanides.

Similarly, the dual valence properties of europium do not lead to a wide existence range for the NaCl-structure monoxide, EuO. Morish[8] finds evidence for a composition range from a small excess of metal, $Eu_{1+x}O$, to $Eu_{1.02}$ at $1200^\circ C$.

These facts point to a special structural basis for the wide composition ranges found for the mixed III/IV valence oxides of cerium, praseodymium and terbium, based on the fluorite structure with vacant sites in the anion sub-lattice. These systems have high oxide ion diffusion coefficients and display true equilibrium behaviour down to remarkably low temperatures. At the upper composition limit, the structure is of the fluorite type, involving cubic $[MO_8]$ coordination polyhedra; at the lower composition limit the Type C sesqui-oxides can be regarded as a superstructure on the fluorite type, with 1/4 of the anion sites vacant in a strictly ordered pattern, placing each cation in a coordination polyhedron $[MO_6V_2]$, with two vertices vacant. These vacant sites must be treated as pseudo components of the structure. Oxygen-deficient fluorite oxides, Mo_{2-x}, have occasional vacancies at anion sites within the fluorite structures, giving local coordination $[MO_7V]$ or (if vacancy-vacancy interaction is strong) $[MO_6V_2]$. Oxygen excess Type C oxides, $MO_{1.5+x}$, have additional oxide ions substituted for vacancies, giving local coordination $[MO_7V]$ or $[MO_8]$. Such excess oxide ions thus represent a particular type of 'interstitial' oxygen which is, however, mobile in diffusion processes (by switching to an adjacent potential anion site). It has been clearly shown, however[2,9] that the fluorite-based and Type C-based non-stoichiometric phases are distinct. At low temperatures in these systems there is a 'homologous series' of ordered inter-mediate phases with very narrow composition ranges. At higher temperatures these pass, by peritectoid reactions, into two broad-range phases, based on the fluorite structure (α phase) and the Type C structure (σ phase) respectively, which show no sign of miscibility up to the highest tempera-ture investigated.

The essential feature both of the Type C sesquioxide structure and of the intermediate oxide Pn_7O_{12}, of which the structure has been determined, is the alignment of vacant fluorite sites - i.e. of $[MO_6]$ coordination polyhedra - along the <111> cube diagonal directions. In the Type C structure they are lined up along all four diagonals. In Pr_7O_{12} and in the isostructural compounds $3L2O_3 \cdot WO_3$ $3L_2O_3 \cdot Y_2O_3$[10] they are lined up along one direction, and location of the oxygen positions by neutron crystallography shows that there is considerable relaxation from the idealised fluorite sites. Nevertheless, the formal relation of the structures is valid and it is a reasonable inference[11] that the other inter-mediate oxide phases, with a lower total concentration of

vacant fluorite sites, involve the same kind of ordering
process. On this basis, Hyde, Bevan and Eyring suggest that
the transition from stoichiometric ordered phases in the Ce-O
and R-O systems to the non-stoichiometric, high temperature
α phase leaves a considerable degree of local order. Their
postulate is that the vacancies are not randomised, but are
largely segregated in strips of finite length, oriented with
equal probability along each of the <111> directions. The
mean length of the ordered configuration must depend on the
total vacancy concentration (i.e. on the composition) and on
the temperature. Because the cation sublattice is but little
modified, relaxation in the oxygen sublattice can smooth out
strain and the structures are dimensionally compatible. This
enables such ordered regions to be coherently grown within
the fluorite structure matrix, and the whole is in dynamical
equilibrium because of the facility with which oxygen ions
are exchanged between complete and incomplete coordination
polyhedra.

Further information about ordering processes and struc-
tural relations in defective phases based on the fluorite
type has been derived from ternary oxide systems. These
present a rich variety of solid solutions, ordered intermedi-
ate phases, high and variable apparent concentrations of
defects and order-disorder phenomena in phases based on the
fluorite structure. The simplest of these are of the type
L_2O_3 - CeO_2 or L_2O_3 - ThO_2. Intermediate phases are hardly
to be expected in these systems, since they would presuppose
an ordering of cations within the cation sublattice. Cation
diffusion rates in fluorite structures are very low (e.g.
$D = 2.9 \times 10^{-10}$ cm^2/sec for Y^{3+} in Y_2O_3 at $1400°C$[12]); at
temperatures where diffusion could establish equilibrium it
is not likely that site preference energies are great enough
to lead to complete ordering. It has been clearly estab-
lished[13,14] that the range of oxygen deficient structures
does not extend from $MO_{1.5}$ to MO_2; there is limited misci-
bility between oxygen-deficient fluorite and oxygen-excess
type C phases. With too great a disparity in cation radius -
i.e. too great dimensional difference between the fluorite
unit cell and the pseudo-fluorite Type C unit cell - the
solubility is small.

(Cf Table 1). Furthermore, although the crystal chemis-
try of lanthanide compounds usually conforms rather well to
the hard sphere approximation, using radius ratios based on
the average cation size (i.e. lattice strain can be averaged),[15]
the fluorite-type phase in these ternary systems does not
approximate to Vegard's law. The nonlinear variation of cell
dimension with content of tervalent cations (+ vacancies)
strongly suggests a specific association between L^{3+} and
vacant anion sites, which may be connected with the tendency
for short range ordering considered above.

Ternary oxide systems involving smaller +4 cations -
e.g. Zr^{4+}, Ti^{4+} - have been extensively studied by Collongues
and his colleagues[16] and by Russian workers[17]. With
increasing difference in ionic radii between the constituent
cations, the extent of mutual replaceability diminishes, but
in all cases the solid solutions and intermediate phases ob-
served are those that are formally derivable from the fluorite
structure. As is commonly found, the larger rare earth cat-
ions, at low mole-fractions, stabilized defect tetragonal and
defect fluorite type zirconia, $L_xZr_{1-x}O_{2-x}$; between these two
structures there is said to be a continuous transition above
some critical temperature (Table II). TiO_2 with the oxides
of the lanthanides from praseodymium to ytterbium, and ZrO_2
with the oxides from La_2O_3 to Gd_2O_3, forms intermediate
phases in which the vacancies and coordination are ordered
in a superstructure of the pyrochlore type. These pyrochlores,
nominally $L_2M_2O_7$, are themselves non-stoichiometric, due to
mutual replacement of L^{3+} and M^{4+} on the two types of cation
site, with accompanying defects in the anion lattice, and
have the general formula $L_{2-x}M_{2+x}O_{7+\frac{1}{2}x}$ $(X \gtrless O)$. The existence
range of these phases tends to broaden at high temperatures
(Table III), but whereas the pyrochlore phases formed from
the larger cations are stable up to their melting points,
$Sm_2Zr_2O_7$ and $Gd_2Zr_2O_7$ undergo an order-disorder transforma-
tion into a random defect fluorite structure. Whether (as
would appear from Collongue's work) this involves randomisa-
tion of cations, or only the disappearance of long range
order (as between oxide ions and vacancies) in the anion lat-
tice is not certain. For lanthanide cations smaller in ionic
radius than Gd^{3+}, the pyrochlore $\rightleftharpoons$ fluorite order-disorder
temperature appears to be lower than the temperature of free
diffusion and possible attainment of order. These systems
therefore display a very wide range of existence of a non-
stoichiometric, random fluorite-type solid solution.

The relevance of these ternary oxide systems to the
present discussion is that they combine evidence for a strong
site preference and vacancy-ordering with the existence,
under apparent equilibrium conditions, of defect-rich struc-
tures with variable composition. They emphasise the same
problems of structure and stability as do the binary oxides
LO_{2-x}, and again raise the question whether the wide range
non-stoichiometric phases are truly random in structure, or
whether they are based on microdomains of well developed short
range order. Such an interpretation might account for a
peculiar feature of the pyrochlore $\rightleftharpoons$ defect fluorite trans-
formation which, although requiring both a structural rear-
rangement and a change of symmetry, is stated to be a contin-
uous transformation rather than a normal first order or
higher order phase change.

B. Chalcogenide Chemistry

Chalcogen compounds of the lanthanide elements display
a particularly interesting pattern of nonstoichiometric proper-
ties, in that stoichiometric variability is of rather general
occurrence but is completely independent of the valence proper-
ties of the cations. It occurs in the same structures and to
the same extent both for compounds of the immutably tervalent
elements and for those of potentially variable valency. For
each element there is a succession of sulphide, selenide and
telluride phases, the same compound types occurring broadly
throughout the series, with structures that are determined
principally by geometrical packing considerations - i.e. by
the cation: anion radius ratio. In these structures, the
cations have been shown from their magnetic susceptibility to
be uniformly the +3 cations, and nonstoichiometry is associated
with one of two origins:

(a) variable filling of the band structure of the
    solid, within a crystal structure determined
    by the persistence and sensible perfection of
    the anion sublattice, or

(b) arising from the manner in which the anion
    sublattice may incorporate structural defects
    without disturbance of the charge balance.

During the past few years, the chalcogenides have been
extensively investigated - notably by Flahaut and his col-
leagues[18], by Yarembash, Kuznetsor et al[19], by Dismukes
and White[20] and by Steinfurt and Weiss[21]. The principal
recurring types of compounds have been established and some
regularities that are pertinent to the present discussion
have emerged. Nevertheless, complete knowledge of phase
equilibria is available for only a few of the elements and
there are serious deficiencies in our knowledge of the crys-
tal structure of most of the phases. The particular struc-
tures adopted depend on the radius ratio $R = r_{cation}/r_{anion}$,
and so change fairly regularly along the series. In general
terms, the succession of phases comprises (i) monochalcogenide
LX; (ii) a phase that includes the sesquichalcogenide compo-
sition L_2X_3, expected for ionic systems, and (iii) one or
more phases LX_m (m > 1.5) properly classed as polychalcogenide
compounds and containing X_n^{2-} anions (n = 2, 3...). It appears
from magnetic susceptibility measurements that (except for
some Sm, Eu and Yb phases) the lanthanide elements are present
as L^{3+} cations in all the compounds.

The monochalcogenides LX have the sodium chloride struc-
ture, and are metallic solids with one electron per atom in
the conduction band. They have been usually regarded as 'line

phases' in the equilibrium diagram, though Yarembash et al.[19a] consider that LaSe may extend to the metal-rich composition La $Se_{0.95}$. For the smaller cations, there is a structural relation between the LX and $LX_{1.5}$ phases and, if the behaviour found for ErTe[21a] is at all representative, there may be a wide composition range for the monochalocogenide phase (see below).

Seven crystal structures have been reported for the sesquichalocogenides, as shown in Table IV (based on Flahaut). The α and β phases in sulphide systems are the low temperature forms, transforming reversibly: $\alpha \rightleftharpoons \beta \rightleftharpoons \gamma$ into the high temperature γ phase. Their crystal structure has not been reported; it would be of particular interest to know whether they have any non-reconstructive, topological relationship with the γ phase structure. The δ phase (monoclinic) is also of unknown structure. η is of the U_2S_3 type, ϵ of the corundum type. The most important structures are clearly of the γ and ζ phases, which display considerable stoichiometric variability. The other structures do not seem to have been fully studied in this respect.

The $\gamma L_2 X_3$ structure is an inherently defective structure of the Th_3P_4 type. The 16 anions in the unit cell provide 12 8-coordinated cation positions; in the L_2X_3 phase, 8/9 of the cation sites - i.e. 10.2/3 per unit cell - are statistically and randomly occupied. In some other structures with fractional occupancy of cation sites, the statistical occupancy is essentially a time-averaged figure, corresponding to high cation mobility and high diffusion rates. There is no evidence whether this is true of the γ-type chalcogenides, nor whether there is any tendency to clustering or ordering of the vacant sites as the cation diffusion rate becomes negligible. It is in this respect that the crystal structure of the α and β phases would be of great interest. At the composition L_2X_3, the sesquichalcogenides are ionic solids. The vacant cation sites can incorporate additional L^{3+} ions, up to the composition L_3X_4, the additional valence electrons entering the conduction band of the solid. There is thus a continuous phase range from L_2X_3 to L_3X_4. Flahaut et al. have also shown that 2-valent cations of appropriate size (from Yb^{2+}, $r = 1.01A$ to Ba^{2+}, $r = 1.36 Å$) can also be built into the Th_3P_4 structure. With 4 M^{2+} + 8 L^{3+} ions per unit cell, fully randomised over the cation positions, the composition ML_2X_4 is attained as the limiting (but apparently fully disordered) stoichiometric phase. There is thus a wide range of composition in the system L_2S_3 - L_3S_4 - ML_2S_4, subject to quite stringent restrictions on the mean cation radius, $\bar{r}$. Thus, in the sulphide system for formation of the full range of ternary phase, $\bar{r} > 0.93 A$; the difference in radius of M^{2+}, L^{3+} must be < 28%. These are essentially packing requirements. Provided that the stability of the anion sublattice

is not impaired by inefficient packing of ions, there is non-stoichiometry arising from the assignment of a variable population of electrons to an apparently non-bonding band, the availability of additional cation sites, and an apparently random distribution of cation vacancies. This last may reflect a dynamical situation rather than genuine randomness.

The other interesting sesquichalcogenide structure is that found for small values of the radius ratio R: the ζ phase or Sc_2S_3 structure, found for R ~ 0.414 (range of R for selenides 0.370 - 0.453; for tellurides 0.404 - 0.422).[20] The Sc_2S_3 structure is itself a derivative of the NaCl structure, with 1/3 of the cation sites vacant in a strictly ordered fashion. Sc_2S_3 itself appears to have, at most, a very narrow composition range, although it loses sulphur at high temperatures to give a phase of irrational formula around $Sc_{0.685}S$. This is also a defect NaCl phase, probably with some statistical occupation of cation sites, with a superstructure cell approximating in composition to $Sc_{33}S_{48}$. It would seem likely that in the sulphides, at least, there is a strong tendency for defect ordering in phases based on these cation-deficient Na-Cl structures.

In the selenides and tellurides, the ζ phase can accommodate excess cations in the vacant cation sites. The full series of smaller lanthanide cations has not been studied in detail, but for erbium 'sesquiselenide' there is a complete phase range $Er_{0.667}Se$ to $Er_{0.75}Se$ (Er_2Se_3 - Er_3Se_4). At the lower phase limit 1/4 of the vacant cation sites have been occupied. Haase, Steinfurt and Weiss[21] considered that they were filled statistically but that each occupied site excluded three neighbour vacancies from occupation; their paper suggests that there might be some measure of ordering in the filling of vacant sites. The corresponding telluride phase has a much wider existence range, from $Er_{0.667}Te$ to $Er_{1.0}Te$, corresponding to the possibility of complete filling of the vacant sites in the Sc_2S_3 structure. There is, however, a remarkable discontinuity in the dimensions of the NaCl sub cell around the composition $Er_{0.75}Te$ (or Er_3Te_4) which may be due to change of bond character, from ionic to metallic, but which may reflect a discontinuity in the equilibrium diagram, rather than an unbroken composition range.

The polychalcogenides present an interesting problem for which there is, as yet, inadequate structural evidence. Compounds with the idealised formula LS_2, LSe_2 are readily formed. These are ionic solids, with magnetic susceptibilities indicative of the presence of L^{3+} cations, and react with acids to give H_2S + S or H_2Se + Se. Flahaut therefore formulates them as L_2X_4 with, presumably both X^{2-} and X_2^{2-} anionic species.

Although Flahaut et al.[22] report the formation and cell
dimensions of the stoichiometric polysulphides of La, Ce, Lr,
and Nd, other workers[23] state that the polysulphides are
always deficient in sulphur. They are certainly phases of
variable composition and, as the cation radius decreases
along the lanthanide series, the maximum attainable chalcogen
contact progressively decreases below the ideal formula. No
polysulphide L_2S_4 phase is known for cations smaller than
yttrium, no polyselenide L_2Se_4 for cations smaller than gado-
linium (Table V).

These compounds clearly need further study. It seems
likely, from the small changes in cell dimensions, that non-
stoichiometry arises from the presence of sulphur vacancies -
e.g. from the replacement of S_2^- ions by S^{2-} ions. The ques-
tion then arises whether these are randomly distributed,
although present in quite high concentration, or whether they
are aggregated into regions of stacking fault. The alterna-
tive hypothesis, that interstitial cations are incorporated,
cannot be dismissed. The crystal structures of polysulphides
and polyselenides have not been reported. If they contain
double sheets of sulphur atoms ($\frac{2}{2}^-$ sheets - see the tritel-
lurides, below), suitable interstitial sites may be available
and such an explanation would, indeed, favour the non-
stoichiometry of the compounds of the smaller cations, as
is observed. There may be some doubt whether the highly non-
stoichiometric phases represent equilibrium states. Yarembash
et al.[19a] found a nearly stoichiometric tetragonal compound
La_2Se_4 in the La-Se system (cf Table V), together with an
essentially isostructural phase, formulated as La_4Se_7 which
presumably represents a superstructure ordering of defects
and which may, indeed, be the stable lower limit in the series
of compounds described by Flahaut and others.

In contrast, the ditellurides $L Te_2$ are metallic solids,
do not have the chemical properties of polychalcogenide salts
and are stated by Flahaut et al. to have the Fe_2As structure.[24]
They are thus essentially layer structures, built up by the
stacking of sheets of the composition: (LTe). Te . Te . (LTe).
Te .., in a square array. All these compounds are variable in
composition, and with lanthanide atoms smaller than cerium it
would appear that the existence range does not include the
phase of ideal composition. (Table VI). With decrease in
tellurium content there is a slight shrinkage of the a axis
of the tetragonal cell. According to Yarembash et al.[19b]
the departure from stoichiometry arises from the presence of
vacant Te sites, which order at around the composition $L Te_{1.78}$
to give another non-stoichiometric phase, with a sub-cell of
very similar dimensions, with a composition range around

L $Te_{1.75}$ - L $Te_{1.60}$ based on an ideal composition L_4Te_7 or L_7Te_{12}. The tendency for ordering of vacancies is strong enough to be reflected in a marked departure of the sub stoichiometric ditellurides from Vegard's law[21b].

In addition to the ditellurides, the lanthanides up to erbium, at least, form metallic tritellurides L Te_3. These have also been assigned to tetragonal layer structure, with sheets stacked in the sequence (LTe) Te_2 Te_2 (LTe) (LTe) Te_2 Te_2 (LTe) .... There is some doubt whether these are phases of invariant composition[21] or whether they have a significant existence range[19b]. There is certainly an intermediate phase L_2Te_5 with a closely related layer structure arising from the ordered omission of one quarter of the tellurium-only sheets from the stacking sequence. This is the sort of topochemical relationship that lends itself to the generation of stacking faults and to the formation of coherently intergrown structures that have a variable composition, but actually involve a strict preservation of local order.

C. Nitrides

Phases with the sodium chloride structure have been reported in most types of binary lanthanide systems, and the evidence points to a very limited homogeneity range for the oxides LO (L = Eu, Sm and Yb only) and the chalcogenides LX (X = S, Se, Te). In the case of the nitrides LN it seems to have been assumed by many workers that the compounds are stoichiometrically ideal, without adequate investigation.

The nitrides present an interesting situation in that magnetic susceptibility measurements have shown that (as in the chalcogenides) the lanthanide metals are present as L^{3+} ions. In the energy balance sheet for the formation of ionic nitrides, the electron affinity for the N^{3-} ion is very unfavourable, and consideration of the defect-forming reaction

$$N^{3-} \mid \square_- \rightleftharpoons \tfrac{1}{2} N_2 + \square + 3 \quad \text{(band)}$$
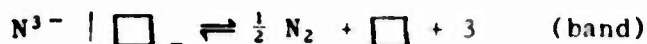
suggests that equilibrium might favour the presence of a significant concentration of vacant anion sites if (a) the electron affinity term ΣEa is high and (b) electrons can be accommodated in an appropriate energy band not too high above the valence bond. Consideration (a) constitutes the important difference encountered in passing from the chalcogenides to the nitrides; (b) seems likely in view of the formation and stability of the isostructural monochlacogenides, with one electron per atom in a band defined by the tervalent state of all the elements except Sm, Eu and Yb in those compounds. It might therefore be inferred that the nitrides should display some measure, at least, of nitrogen deficiency.

The evidence on this point, from the literature, is indecisive. Von Essen and Klemm[25] found that CeN obtained by nitriding the metal with ammonia at 800° gave theoretical analyses for $CeN_{1.0}$ and concluded that there was no stoichiometric variability. Anselin[26] observed that the nitrides had a measurable dissociation pressure above $1600^{\circ}C$ and found a slight variation in the cell dimensions of NdN and YN annealed at 800°, 1400° and 1600°. A metallographic examination of nitrides prepared above $2000^{\circ}C$ by reactive arc melting, reported by Gambino and Cuomo[27] suggests that the homogeneity range is broader near the melting point than at lower temperatures and that an exsolution process deposits metal within the nitride crystals during cooling. On the other hand, they found no difference in cell dimensions between the arc melted material and authentic one-phase samples; the X-ray method may, indeed, be an insensitive detector for stoichiometric variability in these systems.

Some workers, however, have found the nitrides to be markedly sub stoichiometric. In their study of SeN, Samsonov et al.[28] found that direct reaction of nitrogen with scandium yielded $ScN_{0.89}$; they do not state the composition of the products obtained similarly from lanthanium and cerium at 800°. Sclar[29] has concluded that the good metallic conductivity of the nitrides is entirely attributable to marked deviation from ideal stoichiometry. Optical properties indicate a 2 e.v. band gap, consistent with the ionic character of an ideal crystal $L^{3+} N^{3+}$; a gross stoichiometric excess of metal converts the solid into a degenerate semi-conductor or a metal. The implication is that, as normally obtained, the nitrides are invariably sub-stoichiometric.

One difficulty in resolving this question is the possible role of minor properties of oxygen and the possibility that most observations relate to ternary nitride-oxide phases. Lanthanide metals, as usually available, contain significant amounts of oxygen; in processes using the oxides as starting materials, it is not easy to establish that oxygen is completely eliminated. Some workers who have matched preparative work with careful analyses have therefore concluded that lanthanide:nitrogen ratios about $1:0.95 - 0.97$ were due to the presence of impurities (oxygen or carbon), not to nitrogen vacancies[30]. Gambino and Cuomo[27] showed that addition of gadolinium oxide in the preparation of GdN by reactive arc melting yielded a nitride-oxide phase $Gd N_{1-x} O_x$ ($0 < x < 0.12$), with slightly contracted cell dimensions. In addition to the wide-range oxide-nitride phase (with few structural defects but with a variable quasi-free electron population) suggested by these results, interpretation of results, for the Ce-N system at least, can be complicated by the appearance of the

peculiar and unidentified γ^1 phase reported by Gschneidner and Waber[31]. This is a face centered cubic phase, with erratically and widely variable cell dimensions (a = 5.1186 - 5.1347A), quite distinct from γ- Ce (a = 5.1600A), which appears when cerium is heated above 550° in silica vessels. It was thought by Gschneidner and Waber to be the CeO phase, stabilised by varying content of Si or B derived from the container by vapour transport as SiO etc.

With these uncertainties in mind, and as part of another investigation, Drs. I. J. McColm and N. J. Clark, in my laboratory, have re-examined the Ce-N and La-N systems. The evaluation of their results is not complete, but the following results point to a rather wide stoichiometric variability of the lanthanide nitrides. The maximum uptake of nitrogen by metallic cerium at 900-950°C gave a product $CeN_{0.968}$. In these experiments, the metal was generally melted under argon before use; most of the oxygen content is thereby separated as a skin of cerium oxides, which can be removed. The starting material should therefore have an oxygen content little higher than the - unknown, and probably significant - limiting concentration of oxygen in the Ce(O) solid solution. This is certainly less than 3 atom-%, and it can be inferred that the $CeN_{0.97}$ phase was definitely sub-stoichiometric. In preparative experiments at 900-1000°C that were stopped before uptake of nitrogen was complete, monophasic products (as judged by X-ray diffraction) were obtained for compositions CeN with x > 0.6; a biphasic product was found at x = 0.45, the second phase having a cell dimension close to that reported for the peculiar γ^1 phase. Reactive arc melting, in a cold-hearth furnace with N_2 + A atmosphere, invariably gave highly nitrogen-deficient products in the range $CeN_{0.55 - 0.65}$. Preparation at 1800°C by a levitation method, thereby avoiding contamination problems, gave nitride around $CeN_{0.6}$. The nearly stoichiometric preparations lost nitrogen, down to $CeN_{0.8}$ when they were arc melted in nitrogen, or down to $CeN_{0.55}$ when arc melted in argon. Conversely, high temperature preparations (0.55 < x < 0.65) readily reacted with nitrogen at 950° up to compositions around $CeN_{0.95}$.

As has been noted by other workers, lanthanide nitride preparations are rarely well crystallised enough to permit of very precise cell dimension measurements. Our value for $CeN_{0.968}$ (a = 5.0262 A) accords well with Anselin's figure of 5.0263 - 5.0265 A. With decreasing nitrogen content there is a small decrease in unit cell size. The X-ray method is therefore an insensitive one for detecting variations, in stoichiometry and measurements on samples quenched from 2000° show an occasional wide scatter.

The inferences to be drawn from these results are probably (a) that cerium nitride in equilibrium with 1 atm N_2 at 90C-1000° is definitely sub stoichiometric. The deviation from ideal composition appears too large to be accounted for by residual impurities and the inference is consistent with the behaviour at higher temperatures. (b) the dissociation pressure of nitrogen is a function of composition, as would be expected. At ca. 1800° and 2200° respectively, phases around $CeN_{0.6}$ and $CeN_{0.55}$ respectively appear to be in equilibrium with 1 atm. N_2. (c) The phase range may well broaden at high temperatures, both the scattered results of quenched highly sub-stoichiometric specimens and the monophasic character of highly nitrogen-deficient, incompletely reacted products obtained below 1000° corresponding to metastable states.

The apparent degree of imperfection in these sub stoichiometric nitrides is very great. It is comparable with what has been found in the NaCl-type Group IV carbides, and in the high-temperature TiO and VO phases, and it raises the same structural problem: the extent to which such high vacancy concentrations can be genuinely random. We suspect that there must be a considerable degree of vacancy ordering, and that further investigation may reveal another ordered phase, of lower N:Ce ratio.

The results obtained so far in the La-N system are very comparable. Nitride prepared at 900° attains a composition $LaN_{0.97}$; that formed by reactive arc melting is $LaN_{0.55}$. The resolution of the problem is complicated by the breakdown of X-ray methods to discriminate between phases of different composition. There is a very small change in cell dimensions of apparently monophasic lanthanide nitrides ($LaN_{0.90}$: a = 5.291A; $LaN_{0.507}$: a = 5.296 A). In addition, the high temperature f.c.c. modification of lanthanum appears to be stabilised in the limiting La(N) solid solution and this has very similar cell dimensions. It will be impossible to establish the true phase equilibria in such a system without using some other methods - e.g. metallographic techniques, which have not yet been applied.

Conclusion -

In summary, this review has considered three classes of lanthanide compounds, all largely ionic in character, which display a wealth of non-stoichiometric phenomena. The nitrides appear to come into that group of phases with such a high defect concentration that a completely random model is hardly acceptable. In the oxides and chalcogenides there are indications of strong tendencies to the maintenance of strict

local ordering. All these compounds are therefore of particular interest in the present stage of defect theory, for which the central problem is to see how the one viewpoint - existence of regions of perfect local order in some coherent structural relationship to each other - can be fully harmonized with the experimental thermodynamics and the statistical thermodynamics of solids.

REFERENCES

1. J. S. Anderson, A.C.S. Advances in Chemistry No. 39, 1 (1963); Proc. Chem. Soc. 166 (1964).
   A. D. Wadsley, A.C.S. Advances in Chemistry No. 39, 23 (1963); chapter in R. Mandelcorn, 'Non Stoichiometric Compounds' (1964).

2. B. G. Hyde, D. J. M. Bevan and L. Eyring, Phil. Trans. 259, 583, (1966).

3. S. M. Ariya and M. P. Morozova, J. Gen. Chem. 28, 2647, (1958) (English). S. M. Ariya and Y. G. Popov, J. Gen. Chem. 32, 2077 (1962) (English).

4. C. Klixbüll-Jørgensen, R. Pappalardo and E. Rittershaus, Cyanamid Report CERI-TIC-P60 (1964).

5. D. White, P. N. Walsh, W. Ames and H. W. Goldstein, Thermodynamics of Nuclear Materials, Proc. Symposium Vienna 1962, p. 417 (1963); J. Phys. Chem. 65, 1400, 1410 (1961).

6. A. E. Miller and A. H. Daane, J. Inorg. Nucl. Chem. 27, 1955 (1965).

7. M. F. Barrett and T. I. Barry, J. Inorg. Nucl. Chem. 27, 1483 (1965).

8. A. H. Morrish, J. Applied Phys. 36, 1145 (1965).

9. D.J.M. Bevan and J. Kordis, J. Inorg. Nucl. Chem. 26, 1509 (1964).

10. E. A. Aitken, S. F. Bartram and E. F. Juenke, Inorg. Chem. 3, 949 (1964); W. L. Roth and R. Ramanczuk, G.E. Report 66-C-245 (1966).

11. J. O. Sawyer, B. G. Hyde and L. Eyring, Bull. Soc. Chim. France 1190 (1963).

12. M. F. Berard and D. R. Wilder, J. Applied Phys. 34, 2318 (1963).

13. K. A. Gingerich and G. Brauer, Z. anorg. Chem. 324, 48 (1963).

14. D.J.M. Bevan, W. W. Barker, R. L. Martin and T. C. Parks, Proc. 4th Conference on Rare Earth Research, Phoenix, 1964, 441.

15. Compare references 16, 18.

16. M. Perez y Jorba and R. Collongues, Bull. Soc. Chim. (France) 1967, 1969 (1959). R. Collongues, M. Perez y Jorba and J. Lefevre, ibid. 70 (1961). R. Collongues, F. Queyroux, M. Perez y Jorba and J. C. Gilles, ibid, 1141 (1965).

17. V. B. Glushkova, I. A. Davtyan and E. K. Keler, Inorganic Materials (USSR) $\underline{1}$, 1766, (1965).

18. M. Picon, L. Domange, J. Flahaut, M. Guittard and M. Patrie, Bull. Soc. Chim. France 221 (1960). J. Flahaut, L. Domange, M. Patrie, ibid, 2048 (1962). S. M. Golabi, J. Flahaut, L. Domange, Compt. rend. $\underline{259}$, 820 (1964). J. Flahaut, M. Guittard, M. Patrie, M. P. Pardo, S. M. Golabi and L. Domange, Acta Cryst. $\underline{19}$, 14. (1965). V. Tien, J. Flahaut, L. Domange, Compt. rend. $\underline{262}$, 278 (1966).

19a. E. I. Yarembash, E. S. Vigileva, A. A. Eliseev and A. A. Reschikova, Inorganic Materials (U.S.S.R.) $\underline{1}$, 306 (1965).

   b. A. A. Eliseev, E. I. Yarembash, V. G. Kuznetsov, L. I. Antonova and Z. P. Stovantsova, ibid, $\underline{1}$, 943 (1965).

20. J. P. Dismukes and J. G. White, Inorganic Chemistry $\underline{3}$, 1220 (1964); $\underline{4}$, 970 (1965).

21. D. J. Haase, H. Steinfurt and E. J. Weiss, Inorganic Chem. 4, 538, 541, (1965). W. Lin, H. Steinfurt, and E. J. Weiss, ibid, $\underline{4}$, 877 (1965). T. H. Ramsay, H. Steinfurt and E. J. Weiss, ibid. $\underline{4}$, 1154 (1965).

22. J. Flahaut, M. Guittard and M. Patrie, Bull. Soc. Chim. France 1917 (1959). A. Benacerraf, L. Domange and J. Flahaut, Compt. rend. $\underline{248}$, 1672 (1959).

23. S. A. Ring and M. Tecotzky, Inorg. Chem. $\underline{3}$, 182 (1964).

24. J. Flahaut et al. Compt. rend. $\underline{250}$, 857 (1960). M. P. Pardo, J. Flahaut and L. Domange Bull. Soc. Chim. France 3267 (1964).

25. U. von Essen and W. Klemm. Z. anorg. Chem. $\underline{317}$, 25 (1962).

26. F. Anselin, Compt. rend, $\underline{256}$, 2616 (1963).

27. R. J. Gambino and J. J. Cuomo, J. Electrochem. Soc. $\underline{113}$, 401 (1966).

28. G. V. Samsonov, T. Y. Kosolopova, M. D. Lyaitaya and G. N. Makarenko, Redkozem Elementy Akad Nauk SSSR Inst. Geokhim. 8(1963). Chem. Abs. $\underline{61}$ 3892f (1964).

29. N. Sclar, J. Applied Phys. $\underline{35}$, 1534 (1964).

30. M. K. Wilkinson, J. Applied Phys. 31, 3585 (1960), Lavalle, J. Inorg. Nucl. Chem. $\underline{24}$, 930 (1962).

31. K. A. Gschneidner and J. T. Waber, J. Less Common Met. $\underline{6}$, 354 (1963).

Table I

Existence ranges of fluorite phases $M^{4+}_{1-x}L^{3+}_xO_{2-\frac{1}{2}x}$ and Type C phases $M^{4+}_yL^{3+}_{1-y}O_{1.5+\frac{1}{2}y}$

System	Temp., °C	Limit of fluorite phase	Limit of Type C phase
ThO$_2$ – Yb$_2$O$_3$	1400	Th$_{0.92}$Yb$_{0.08}$O$_{1.96}$	Th$_{0.01}$Yb$_{0.99}$O$_{1.505}$
ThO$_2$ – Eu$_2$O$_3$	1200	Th$_{0.64}$Eu$_{0.36}$O$_{1.82}$	Th$_{0.08}$Eu$_{0.92}$O$_{1.54}$
	1400	Th$_{0.53}$Eu$_{0.47}$O$_{1.765}$	Th$_{0.13}$Eu$_{0.87}$O$_{1.565}$
	1500	Th$_{0.47}$Eu$_{0.53}$O$_{1.735}$	Th$_{0.16}$Eu$_{0.84}$O$_{1.58}$
CeO$_2$ – Y$_2$O$_3$	1100	Ce$_{0.58}$Y$_{0.42}$O$_{1.70}$	Ce$_{0.40}$Y$_{0.60}$O$_{1.70}$
	1400	Ce$_{0.52}$Y$_{0.48}$O$_{1.76}$	Ce$_{0.31}$Y$_{0.69}$O$_{1.655}$
	1600	Ce$_{0.47}$Y$_{0.53}$O$_{1.735}$	Ce$_{0.27}$Y$_{0.73}$O$_{1.655}$
	1700	Ce$_{0.46}$Y$_{0.54}$O$_{1.73}$	Ce$_{0.24}$Y$_{0.76}$O$_{1.62}$
CeO$_2$–Yb$_2$O$_3$	1100	Ce$_{0.68}$Yb$_{0.32}$O$_{1.84}$	Ce$_{0.05}$Yb$_{0.95}$O$_{1.525}$
	1400	Ce$_{0.59}$Yb$_{0.41}$O$_{1.795}$	Ce$_{0.08}$Yb$_{0.92}$O$_{1.54}$
	1600	Ce$_{0.52}$Yb$_{0.48}$O$_{1.76}$	Ce$_{0.08}$Yb$_{0.92}$O$_{1.54}$
CeO$_2$–Dy$_2$O$_3$	1500	Ce$_{0.42}$Dy$_{0.58}$O$_{1.71}$	Ce$_{0.30}$Dy$_{0.70}$O$_{1.65}$
	1600	Ce$_{0.40}$Dy$_{0.60}$O$_{1.70}$	Ce$_{0.29}$Dy$_{0.71}$O$_{1.645}$

TABLE III

Existence of pyrochlore phase $L_2Zr_2O_7$ ($La_{2+x}Zr_{2-x}O_{7-\frac{1}{2}x}$, $x \geq 0$)

L	$r_{L^{3+}}$	$r_{L^{3+}}/r_{Zr^{4+}}$	Temp.	Existence range	Pyrochlore fluorite order-disorder transformation.
La	1.14 Å	1.42	2000°C 1400°C	$La_{1.60}Zr_{2.40}O_{7.20}$ $La_{2.28}Zr_{1.72}O_{6.86}$ $La_{1.98}Zr_{2.02}O_{7.01}$ $La_{2.24}Zr_{1.76}O_{6.83}$	Stable to melting pt. 2180°C
Nd	1.04	1.30	2000° 1500°	$Nd_{1.16}Zr_{2.84}O_{7.42}$ $Nd_{2.60}Zr_{1.40}O_{6.70}$ $Nd_{1.16}Zr_{2.84}O_{7.42}$ $Nd_{2.28}Zr_{1.72}O_{6.86}$	Stable to melting point 2280°C. Transition continuous for x outside limits given.
Sm	1.00	1.25	1450°	$Sm_{1.50}Zr_{2.50}O_{7.25}$ $Sm_{2.40}Zr_{1.60}O_{6.70}$	2400°C
Gd	0.97	~1	1450°	$Gd_{1.90}Zr_{2.10}O_{7.05}$ $Gd_{2.16}Zr_{1.84}O_{6.92}$	1550°C
Dy to Yb	0.92 0.86	1.2		No pyrochlore phases formed	Disordered at all temps.

TABLE IV

	La	Ce	Pr	Nd	Sm		Gd	Tb	Dy	Ho	Y	Er	Tm	Yb	Lu	Sc

S, Se, Te rows with bracketed ranges labeled γ, β, δ, α, ε, ζ, η

TABLE V

Reported existence ranges of some polysulphides and polyselenides

La	La_2S_4 (cub. $a = 8.20A$) (22)	$La_2S_{3.6}$ – (tetrag. $a = 8.16$, $c = 16.65A$) (23)
	La_2Se_4 (tetrag. $a = 8.47A$, $c = 8.54A$)	$La_2Se_{3.6}$ – (tetrag. $a = 8.38$, $c = 8.54A$)
Pr	Pr_2S_4 (cub. $a = 8.08A$)	$Pr_2S_{3.4}$ – (tetrag. $a = 7.98$, $c = 8.07A$)
	Pr_2Se_4 (tetrag. $a = 8.37$, $c = 8.44A$)	$Pr_2Se_{3.6}$ – (tetrag. $a = 8.33$, $c = 8.44A$)
Sm	$Sm_2S_{3.88}$ (cub. $a = 7.96A$)	
	Sm_2Se_{4-x}	$Sm_2Se_{3.6}$ – (tetrag. $a = 8.16$, $c = 6.34A$)
Gd	$Gd_2S_{3.80}$ (tetrag. $a = 7.83$, $c = 7.96A$)	$Gd_2S_{3.5\pm0.1}$ – (tetrag. $a = 7.79$, $c = 7.92$)
	Gd_2Se_{4-x}	$Gd_2Se_{3.63}$ – (tetrag. $a = 8.13$, $c = 8.37A$)
Y	$Y_2S_{3.80}$ (tetrag. $a = 7.71$, $c = 7.89$)	$Y_2S_{2.5\pm0.1}$ – (tetrag. $a = 7.73$, $c = 7.90A$)

POINT DEFECTS IN SOME RARE EARTH DIHYDRIDES

G. G. Libowitz and J. B. Lightstone

Ledgemont Laboratory, Kennecott Copper Corporation
Lexington, Massachusetts 02173

Abstract

The rare earth dihydrides exhibit large positive and negative deviations from stoichiometry. By comparing experimental data for lanthanum, cerium, and gadolinium dihydrides with previously derived thermodynamic expressions relating chemical activities with deviations from stoichiometry, the defects responsible for the non-stoichiometry in these compounds may be identified. It is shown that the predominant defects in the stoichiometric rare earth dihydrides are Frenkel defects, with excess hydrogen interstitials causing positive deviations from stoichiometry and excess hydrogen vacancies causing negative deviations from stoichiometry.

The derived equations also permitted calculation of the intrinsic Frenkel defect concentrations and energies and entropies of defect formation. Intrinsic defect concentrations ranged from 2 to 5% over the temperature range 300-800°C. The vibrational entropy change for Frenkel defect formation was found to be negative and to contribute at least as much to the free energy of defect formation as does the enthalpy term.

Introduction

The rare earth metals react with hydrogen to form dihydrides, which may exhibit unusually wide deviations from stoichiometry[1]. At room temperature, the existence range of a hydride having the stoichiometric formula MH_2 may vary from $MH_{1.8}$ to MH_3, and this range usually increases with temperature. Neutron diffraction[2] and NMR studies[3] have fairly well established that the excess hydrogen in $MH_{2+\delta}$ is due to hydrogen situated in the octahedral interstices of the fluorite-type lattice. It is generally believed that the hydrogen deficiency in $MH_{2-\delta}$ is due to hydrogen vacancies.

It has recently been shown[4] that the type of defect responsible for nonstoichiometry may be deduced from measurements of thermodynamic activities. Thus, existing data on hydrogen equilibrium pressures (hydrogen activities) may be used to confirm that the predominant defects in the rare earth dihydride are those mentioned above. Furthermore, comparison of the experimental data with the theoretically derived relation between activity and nonstoichiometry permits computation of the energies and entropies of defect formation.

Identification of Defects

For a binary compound $MX_{s\pm\delta}$, where s is the ideal stoichiometric ratio and δ is the deviation from stoichiometry, positive deviations from stoichiometry may be due to X interstitials, M vacancies, or X substitutionals (X atoms on M sites), while negative deviations from stoichiometry may be due to X vacancies, M interstitials or M substitutionals (M atoms on X sites). The following relations between X activity, a_X, and δ have been derived[4] from considerations of the configurational entropy for each possible type of point defect in the crystal. The assumption was made that the concentration of one type of defect is predominant at large deviations from stoichiometry.

For X interstitials: $\quad a_X = C_{IX}\left(\dfrac{\delta}{a-\delta}\right)$ (1)

For M vacancies: $\quad a_X = C_{VM}\left(\dfrac{\delta}{s+\delta}\right)^{1/s}$ (2)

For X substitutionals: $\quad a_X = C_{X(M)}\left(\dfrac{\delta}{s+\delta+1}\right)^{1/(s+1)}$ (3)

For X vacancies: $\quad a_X = C_{VX}\left(\dfrac{s-\delta}{\delta}\right)$ (4)

For M interstitials: $\quad a_X = C_{IM}\left[\dfrac{(as-a\delta-\delta)^{a+1}}{\delta(as-a\delta)^{a}}\right]^{1/s}$ (5)

For M substitutionals: $\quad a_X = C_{M(X)}\dfrac{s(s+1-\delta)-\delta}{\{[s(s+1-\delta)]^{s}\delta\}^{1/(s+1)}}$ (6)

where a is the ratio of interstices to M atom sites in the particular structure under consideration and C_{IX}, C_{VM}, $C_{X(M)}$, C_{VX}, C_{IM}, $C_{M(X)}$ are temperature dependent constants containing the free energy of defect formation.

For the case of the rare earth dihydrides, $s=2$ and $a=1$ for the fluorite-type structure. If the nonstoichiometric hydride is in equilibrium with hydrogen gas, we may write:

$$\mu_H(\text{hydride}) = \tfrac{1}{2}\mu_{H_2}(\text{gas})$$

where μ_H and μ_{H_2} are the chemical potentials of hydrogen in the hydride and hydrogen in the gaseous phase, respectively. Therefore, for the same standard state (e.g., hydrogen gas at 1 torr pressure):

$$RT \ln a_H = \tfrac{1}{2}RT \ln a_{H_2} = \tfrac{1}{2}RT \ln P$$

where hydrogen pressure, P, is measured in torr. Thus:

$$a_H = P^{\frac{1}{2}}$$

Eqs. (1) through (6) may now be rewritten as follows for rare earth dihydrides:

For H interstitials: $P^{\frac{1}{2}} = C_{IH}\left(\dfrac{\delta}{1-\delta}\right)$ (7)

For M vacancies: $P^{\frac{1}{2}} = C_{VM}\left(\dfrac{\delta}{2+\delta}\right)^{\frac{1}{2}}$ (8)

For X substitutionals: $P^{\frac{1}{2}} = C_{H(M)}\left(\dfrac{\delta}{3+\delta}\right)^{\frac{1}{3}}$ (9)

For H vacancies: $P^{\frac{1}{2}} = C_{VH}\left(\dfrac{2-\delta}{\delta}\right)$ (10)

For M interstitials: $P^{\frac{1}{2}} = C_{IM}\dfrac{2(1-\delta)}{[\delta(s-\delta)]^{\frac{1}{2}}}$ (11)

For M substitutionals: $P^{\frac{1}{2}} = C_{M(H)}\dfrac{3(2-\delta)}{[4\delta(3-\delta)^2]^{\frac{1}{3}}}$ (12)

By comparing Eqs. (7), (8), and (9) with equilibrium hydrogen pressure data for rare earth dihydrides containing excess hydrogen, the defect responsible for the deviation from stoichiometry may be deduced. This was done for lanthanum, cerium, and gadolinium dihydrides using the equilibrium pressure data of Korst and Warf[5], Streck and Dialer[6] and Sturdy and Mulford[7]. The agreement was always best for the interstitial hydrogen case as illustrated by the three representative cases shown in Figs. 1 to 3. The calculated curves were obtained from Eqs. (7), (8) and (9) by determining the value of the constants, C_{VM}, C_{IH}, and $C_{H(X)}$ which gave the best fit with the data in each case. The value of the constant merely determines the relative height of each curve; the shape (or slope) is determined by the particular function of δ in each case.

A similar treatment was made for negative deviations from stoichiometry using Eqs. (10), (11) and (12). Unfortunately, there

are less experimental data available for this case, but the results for LaH$_{2-\delta}$ shown in Figs. (4) and (5) indicate that hydrogen vacancies are the predominant defects.

The deviations of the calculated curve from the experimental points at low deviations from stoichiometry seen in Figures 1, 3, 4 and 5 are due to the assumption made when deriving the equations that only one type of defect is predominant. The stoichiometric composition does not imply a perfect crystal, but rather that there are two opposite types of defects present in equal concentrations; in this case, hydrogen vacancies and hydrogen interstitials or Frenkel defects. Thus, as the stoichiometric composition is approached, the concentration of the second type of defect becomes significant and the assumption that only one type of defect is present no longer is valid.

Calculation of Defect Energies

It has been shown[4] that the constants C_{IH} and C_{VH} represent the following functions:

$$C_{IH} = \exp\left[-\left(E_{IH} - T\Delta S_H - T\Delta S_{IH}^{v}\right)/kT\right]$$

$$C_{VH} = \exp\left[-\left(E_{VH} + T\Delta S_H - T\Delta S_{VH}^{v}\right)/kT\right]$$

where E_{IH} is the enthalpy of formation of a hydrogen interstitial by addition of an H atom to the crystal from some standard state of hydrogen (in this case hydrogen gas at one torr pressure), E_{VH} is the enthalpy of formation of a hydrogen vacancy by removal of an H atom from the crystal to hydrogen gas at one torr, ΔS_H is the change in entropy of the crystal due to the presence of an excess H atom, ΔS_{IH}^{v} is the change in vibrational entropy of the crystal caused by the presence of an interstitial, and ΔS_{VH}^{v} is the change in vibrational entropy due to the presence of a vacancy. Thus:

$$C_{VH}/C_{IH} = \exp\left[-\left(E_F - T\Delta S_F^{v}\right)/kT\right] = \exp\left(-\Delta G_F/kT\right) \quad (13)$$

where E_F is the enthalpy of formation of a Frenkel defect, i.e., it is in the enthalpy necessary to remove an H atom from its normal site and place it into an interstitial position. ΔS_F^{v} is the change of vibrational entropy of a crystal due to the presence of a Frenkel defect, and ΔG_F is the free energy of formation of a Frenkel defect.

Using Eq. (13), free energies of defect formation in rare earth dihydrides may be calculated from the values of C_{VH} and C_{IH} obtained by comparing Eqs. (7) and (10) with experimental data. From the

variation of ln (C_{VH}/C_{IH}) with reciprocal temperature, the enthalpy and vibrational entropy of Frenkel defects may also be deduced from Eq. (13). Unfortunately, in most cases, the data were too sparse at large deviations from stoichiometry, to give reliable values for both C_{VH} and C_{IH}. For example, for those temperatures at which C_{IH} could be reliably calculated, there were insufficient data at large negative deviations from stoichiometry to calculate C_{VH} (and vice versa). However, as mentioned above, the shapes of the calculated P vs δ curves are determined by both types of defects in the vicinity of the stoichiometric composition. Consequently, a more exact expression for P as a function δ which takes into account the simultaneous existence of both types of defects should permit calculation of both C_{VH} and C_{IH} at each temperature. A general expression for all possible types of defects has been derived rigorously in a previous paper[4]. For the special case under consideration here, Frenkel defects in dihydrides, a simple mass action law derivation will suffice

The formation of H vacancies may be written:

$$H \text{ (site)} \rightleftharpoons \tfrac{1}{2}H_2 \text{ (gas)} + \square_H$$
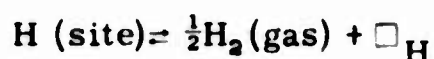
where the symbol $\square_H$ represents an H vacancy. The equilibrium constant for the reaction is:

$$K_{VH} = \frac{n_{VH}P^{\frac{1}{2}}}{n_{H(H)}} = \frac{\left(N_{VH}/2N\right)P^{\frac{1}{2}}}{\left(2N-N_{VH}\right)/2N}$$

$$P^{\frac{1}{2}} = K_{VH}\left(\frac{2N-N_{VH}}{N_{VH}}\right) \tag{14}$$

where n_{VH} and $n_{H(H)}$ are the mole fractions of H vacancies and H atoms on H sites, respectively. N_{VH} is the number of H vacancies in the lattice, and N the number of metal atom sites.

For H interstitials:

$$\tfrac{1}{2}H_2 \text{ (gas)} + \Delta \rightleftharpoons H_I$$
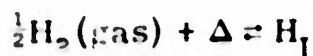
where the symbol Δ represents an unoccupied interstice.

$$K_{IH} = \frac{n_{IH}}{n_\Delta P^{\frac{1}{2}}} = \frac{N_{IH}/aN}{\left[\left(aN-N_{IH}\right)/aN\right]P^{\frac{1}{2}}}$$

where n_{IH} and n_Δ are mole fractions of interstitial hydrogen and unoccupied interstices, respectively, and N_{IH} is the number of H interstitials in the lattice. Therefore:

$$P^{\frac{1}{2}} = \frac{1}{K_{IH}} \left(\frac{N_{IH}}{N-N_{IH}} \right) \tag{15}$$

It can be shown[4] that $K_{VH} = C_{VH}$ and $1/K_{IH} = C_{IH}$. Eq. (14) may be rewritten:

$$\frac{N_{VH}}{N} = \frac{2C_{VH}}{P^{\frac{1}{2}}+C_{VH}} \tag{16}$$

and Eq. (15) may be rewritten:

$$\frac{N_{IH}}{N} = \frac{P^{\frac{1}{2}}}{P^{\frac{1}{2}}+C_{IH}} \tag{17}$$

The deviation from stoichiometry may be defined:

$$\delta \equiv \frac{N_{IH}-N_{VH}}{N} \tag{18}$$

Substituting Eqs. (16) and (17) into (18) and rearranging terms yields:

$$\left(1-\delta\right) P - \left(\delta C_{IH}+\delta C_{VH}+C_{VH}\right)P^{\frac{1}{2}} - \left(2+\delta\right)C_{VH}C_{IH} = 0 \tag{19}$$

Eq. (19) now relates P and δ when both H vacancies and H interstitials are present, and it should be applicable over the whole range of composition from large positive deviations through the stoichiometric composition to large negative deviations from stoichiometry. It may be mentioned at this point that at large deviations from stoichiometry, particularly at compositions close to the existence boundary of the compound, interaction between defects will also lead to deviations between calculated curves and the experimental data. This was observed in several cases, and was especially true in the cases of yttrium[8,9] and scandium[10] dihydrides where negative deviations from stoichiometry as high as 50% have been observed. The effect of interactions among defects is dealt with in a subsequent paper[11].

The constants C_{VH} and C_{IH} were obtained by determining the values which gave the best fit between Eq. (19) and the experimental data over the whole composition range for which data were available. This was done in each case by finding the values of C_{VH} and C_{IH} which gave the minimum average deviation between calculated and measured values for both P and δ using a GE-235 computer. The agreement between Eq. (19) and experimental data is illustrated by the case of LaH_2 at 706°C in Fig. 6, which may be compared with Figs. 1 and 4. It can be seen that the experimental points which deviated from the calculated curve at δ = 0.05, 0.07, and 0.08 in Fig. 1 and at δ = -0.02 and -0.01 in Fig. 4 fall on or closer to the calculated curve in Fig. 6. Similarly, Fig. 7 shows that that at 756°C agreement between the data and Eq. (19) is quite good over the whole range of measured compositions from δ = -0.20 to δ = 0.12. The points at δ = -0.02 and -0.01 which deviated from the curve in Fig. 5 now fall almost directly on the curve. The application of Eq. (19) to $GdH_{2+\delta}$ at 400°C is illustrated in Fig. 8 which may be compared with Fig. 3.

At equilibrium, Eqs. (14) and (15) may be equated to give:

$$C_{VH}/C_{IH} = \frac{N_{VH} N_{IH}}{\left(2N - N_{VH}\right)\left(N - N_{IH}\right)}$$

At the stoichiometric composition: $\dfrac{N_{VH}}{N} = \dfrac{N_{IH}}{N} \equiv n_i$

where n_i is defined as the intrinsic defect concentration or the concentration of Frenkel defects at stoichiometry. Thus, the intrinsic defect concentration may be calculated from the determined values of C_{VH} and C_{IH} using the relation:

$$C_{VH}/C_{IH} = \frac{n_i^2}{(2-n_i)(1-n_i)} \tag{20}$$

The relation between n_i and the energy of Frenkel defect formation may be seen from a comparison of Eqs. (13) and (20).

Eqs. (19), (13) and (20) were applied to hydrogen pressure-composition data for the lanthanum-hydrogen[5], cerium-hydrogen[5,6] and gadolinium-hydrogen[7] systems. The results for lanthanum dihydride are shown in Table I. It can be seen that n_i and ΔG_F appear to be constant with temperature (the apparent increase in ΔG_F is within experimental error). This indicates a value for E_F, the enthalpy of defect formation, which is too low to be calculated over the small temperature range of the data. If E_F were zero, the entropy change as calculated from Eq. (13) would be about -13 cal/deg mole. Thus we can say that ΔS_F^v is somewhat less negative than this value.

Table I - Intrinsic Concentrations and Free Energies of
Formation of Frenkel Defects in LaH_2 (from
Data of Korst and Warf[5])

Temp.(^{O}C)	n_i	ΔG_F (kcal/mole)
606	0.06	11
656	0.05	12
706	0.05	13
756	0.05	14

An analysis of the cerium hydride data of Korst and Warf[5] yields
the results shown in Table II. Here again, there are insufficient data
over the relatively narrow temperature range to give a reliable value

Table II - Intrinsic Concentrations and Free Energies of
Formation of Frenkel Defects in CeH_2 (from
Data of Korst and Warf[5])

Temp.(^{O}C)	n_i	ΔG_F (kcal/mole)
600	0.02_4	$14._1$
650	0.02_6	$14._5$
700	0.02_6	$15._3$
750	0.03_1	$15._4$

for E_F. However, a rough estimate of about 7 kcal/mole can be made
(see dashed curve in Fig. 9). This would give a value of about
-9 cal/deg mole for ΔS_F^V.

Table III gives the results of the application of Eqs. (19), (13) and
(20) to Streck and Dialer's[6] data. Although their equilibrium hydrogen

Table III - Intrinsic Concentrations, Free Energies of
Formation, and Entropy Changes for Frenkel
Defects in CeH_2 (from the Data of Streck and
Dialer[6])

Temp.(^{O}C)	n_i	ΔG_F (kcal/mole)	ΔS_F^V (cal/deg mole)
300	$.015_5$	10.3	-9.0
400	.022	11.0	-8.8
500	.027	12.1	-9.1
600	.033	13.0	-9.0
700	.039	13.8	-8.9
800	.043	14.7	-8.9
		Av.	-8.9

pressures were consistently higher than those of Korst and Warf, the
temperature dependence was about the same in the two cases. Streck
and Dialer's study was carried out over a sufficiently wide temper-
ature range to obtain a value of E_F by plotting $\ln(C_{VH}/C_{IH})$ vs

reciprocal temperature according to Eq. (13). The slope of the line shown in Fig. 9 yielded a value of 5.1 kcal/mole for E_F which permitted calculation of the value -8.9 cal/deg for ΔS_F^V in CeH_2.

Finally, an analysis of the data of Sturdy and Mulford on $GdH_{2\pm\delta}$ yielded the results shown in Table IV. Again, there were insufficient

Table IV - Intrinsic Concentrations and Free Energies of Formation of Frenkel Defects in GdH_2 (from Data of Sturdy and Mulford[7])

Temp. (^{O}C)	n_i	ΔG_F (kcal/mole)
400	.024	10.8
500	.027	12.1

data to calculate E_F. However, the results for n_i and ΔG_F are close to those for cerium hydride as shown in Table II. Therefore, one may assume that the enthalpy and entropy values are similar to those of cerium hydride.

Discussion

The low free energies of defect formation partially account for the large deviations from stoichiometry observed in these compounds. The correspondingly large intrinsic defect concentrations of 2 to 5% in the range 300-800°C are unusually high for defect compounds. For example, the intrinsic concentration of Schottky defects in KCl at 700°C is 4×10^{-5}, while AgBr, which is usually considered to be a highly defective compound, has an n_i value of 0.004 at 300°C. This is still an order of magnitude lower than the rare earth dihydrides.

The negative change in vibrational entropy of about -9 cal/deg mole implies an increased frequency of vibration in the crystal on defect formation. This is usually the case for interstitial defects where a crowding of atoms occurs. In addition, in the case of the rare earth dihydrides, interstitial hydrogen causes contraction of the lattice[1,5]. Apparently, these two effects are sufficient to more than overcome the effect of any possible relaxation of the lattice due to the hydrogen vacancies.

Finally, it is of interest to note that because of the unusually low enthalpy of formation of the Frenkel defects in these dihydrides (~ 5 kcal/mole), the contribution of the entropy term to the free energy of defect formation is at least as large as the enthalpy contribution. For example, at 300°C, $-T\Delta S_F^V = -(573^O K)(-9 \text{ e.u.}) \simeq 5$ kcal/mole which is comparable to the value for E_F, while at 800°C, the value of $-T\Delta S_F^V$ becomes approximately twice that of E_F.

References

1. G. G. Libowitz, The Solid State Chemistry of Binary Metal Hydrides, W. A. Benjamin, Inc., New York, 1965, pp. 38-40.

2. C. E. Holley, R. N. R. Mulford, F. H. Ellinger, W. C. Koehler, and W. H. Zachariasen, J. Phys. Chem. 59, 1226 (1955).

3. D. S. Schreiber and R. M. Cotts, Phys. Rev. 131, 1118 (1963).

4. G. G. Libowitz and J. B. Lightstone, J. Phys. Chem. Solids, to be published 1967.

5. W. L. Korst and J. C. Warf, Inorg. Chem. 5, 1719 (1966).

6. R. Streck and K. Dialer, Z. anorg. Allgem. Chem. 306, 141 (1960).

7. G. E. Sturdy and R. N. R. Mulford, J. Am. Chem. Soc. 78, 1083 (1956).

8. C. E. Lundin and J. P. Blackledge, J. Electrochem. Soc. 109, 838 (1962).

9. L. N. Yannopoulos, R. K. Edwards, and P. G. Wahlbeck, J. Phys. Chem. 69, 2510 (1965).

10. M. L. Lieberman and P. G. Wahlbeck, ibid 69, 3515 (1965).

11. J. B. Lightstone and G. G. Libowitz, paper presented at Chicago meeting of the Am. Phys. Soc., March 1967.

Acknowledgment
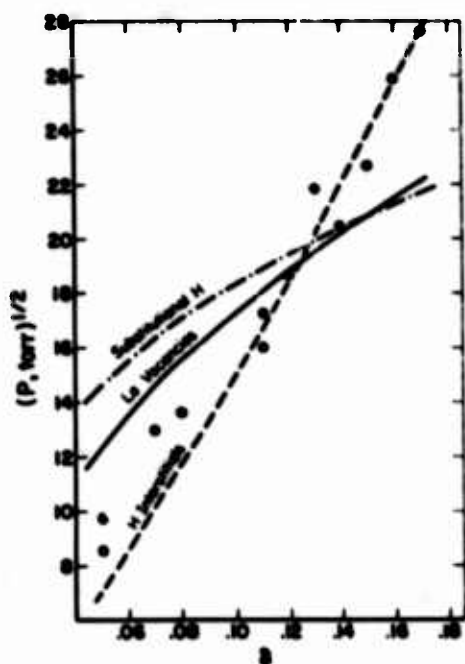
Fig. 1. Activity of hydrogen in $LaH_{2+\delta}$ as a function of deviation from stoichiometry at $706^{\circ}C$. ――――― calculated curve for La vacancies; - - - - calculated curve for H interstitials; ―..―..― calculated curve for H substitutionals; -data of Korst and Warf[5].
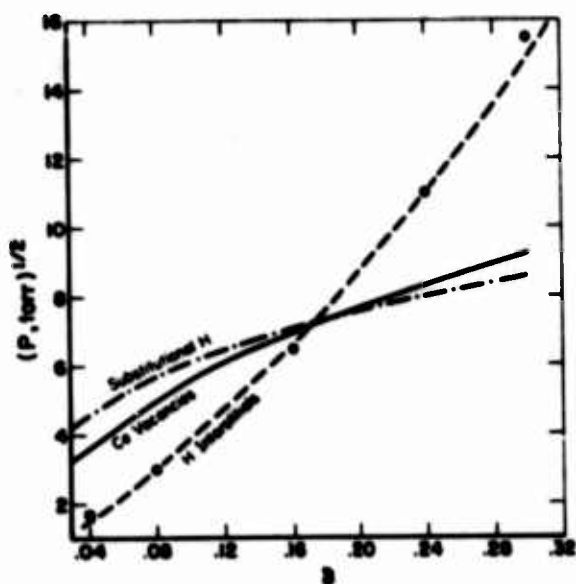
Fig. 2. Activity of hydrogen in $CeH_{2+\delta}$ as a function of deviation from stoichiometry at 500° ――――― calculated curve for Ce vacancies; ― ― ― ― calculated curve for H interstitials; ―..―..― calculated curve for H substitutionals; ●-data of Streck and Dialer[6].
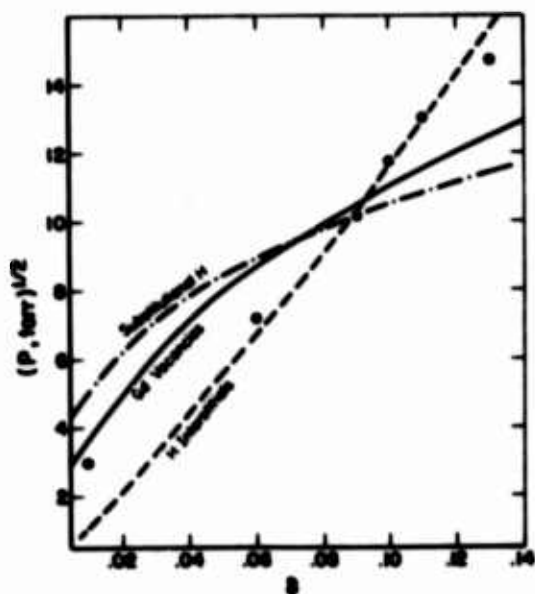
Fig. 3. Activity of hydrogen in $GdH_{2+\delta}$ as a function of deviation from stoichiometry at $400^{\circ}C$. ――――― calculated curve for Gd vacancies; ― ― ― ― calculated curve for H interstitials; ―..―..― calculated curve for H substitutionals; ●-data of Sturdy and Mulford[7].
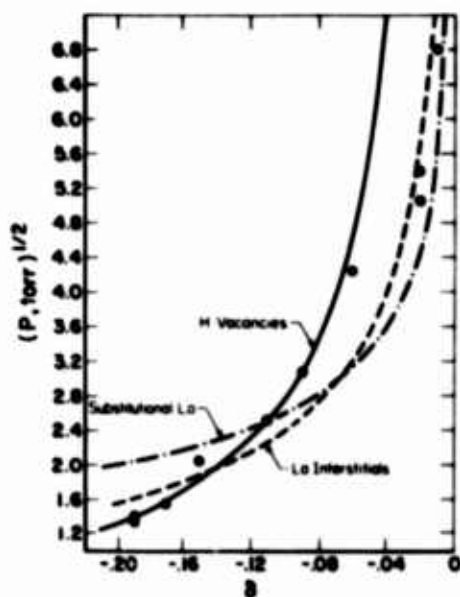
Fig. 4. Activity of hydrogen in $LaH_{2-\delta}$ as a function of deviation from stoichiometry at $706^{O}C$. ——— calculated curve for H vacancies; — — — calculated curve for La interstitials; —.—.— calculated curve for La substitutionals; ●-data of Korst and Warf[5].

Fig. 5. Activity of hydrogen in $LaH_{2-\delta}$ as a function of deviation from stoichiometry at $756^{O}C$. ——— calculated curve for H vacancies; — — — calculated curve for La interstitials; —.—.— calculated curve for La substitutionals; ●-data of Korst and Warf[5].
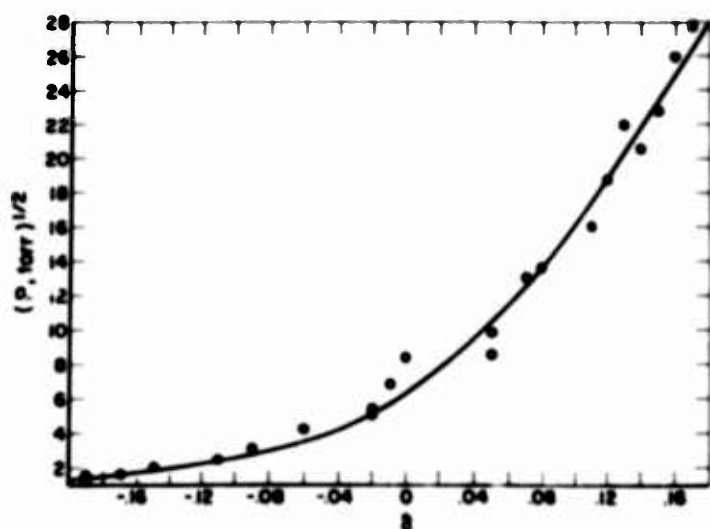
Fig. 6. Comparison of activity data[5] for $LaH_{2\pm\delta}$ at $706^{O}C$ with the corresponding curve calculated from Eq. (19)

- 143 -
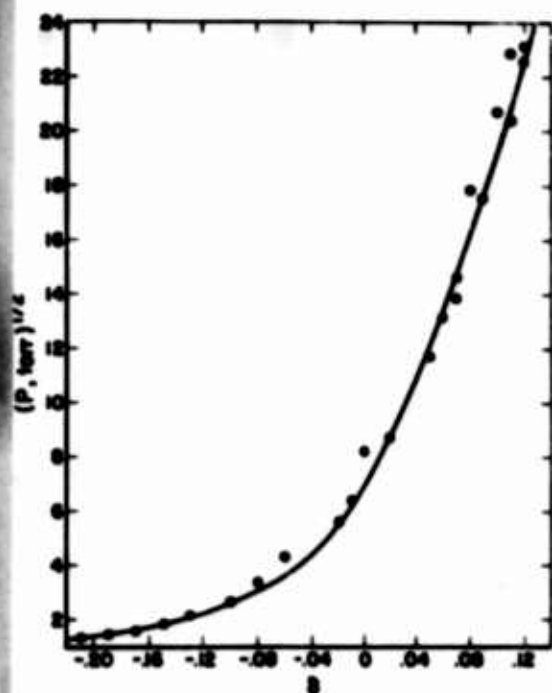
Fig. 7. Comparison of activity data[5] for LaH$_{2\pm\delta}$ at 756°C with the corresponding curve calculated from Eq. (19).
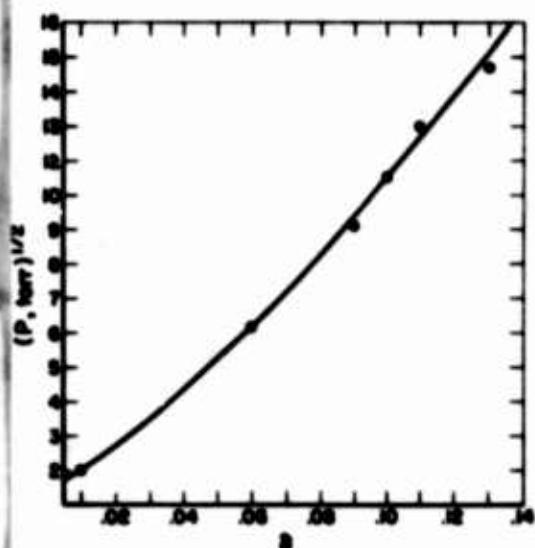
Fig. 8. Comparison of activity data[7] for GdH$_{2+\delta}$ at 400°C with the corresponding curve calculated from Eq. (19).
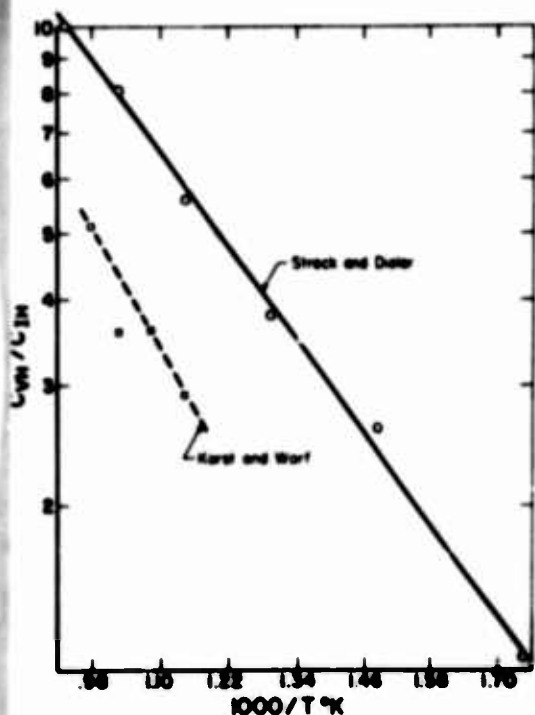
Fig. 9. Variation in energy constant ratio with reciprocal temperature for CeH$_2$.

The Crystal Chemistry of Selected AB_2 Rare Earth Compounds with Se, Te, and Sb. [1]

by

R. Wang [2] and H. Steinfink
Department of Chemical Engineering
The University of Texas
Austin, Texas

Introduction

The stoichiometry REB_2 where RE is a rare earth element and B an element of groups V and VI is widely encountered in such alloys. A structural investigation of these phases was undertaken, using single crystal X-ray diffraction techniques wherever feasible, to determine their crystal structures and resolve any ambiguities which have arisen because of previous work which was based only on powder diffraction diagrams.

Experimental

The ditellurides $LaTe_2$, $CeTe_2$, $NdTe_2$, $SmTe_2$, $GdTe_2$, $DyTe_2$, and $YbTe_2$ were prepared by methods previously described (3) and both single crystal and powder diffraction data showed that they are all iso-structural and have the Fe_2As type structure. The phases $ErTe_2$, and $HoTe_2$ were absent and attempts to synthesize them produced mixtures of RETe and $RETe_3$.

The compounds $LaSe_2$, $CeSe_2$, $NdSe_2$, $SmSe_2$, $GdTe_2$, $DySe_2$, $HoSe_2$ and $ErSe_2$ were prepared from the elements by sealing the stoichio-metric amounts in evacuated vycor tubes and heating at reaction temperatures below 800°C. The compounds thus obtained are labelled with the formula $RESe_2$ even though they may exhibit non-stoichiometric composi-tions, i. e. they may be selenium deficient. $GdSe_2$ was also prepared at a temperature under 300°C. The reaction was very slow and two weeks were required to carry it to completion. The low temperature product gave a homogeneous X-ray powder pattern which displayed no difference when

compared with the pattern from the high temperature preparation and we consider that $GdSe_2$ does not have a high-low temperature phase transition at least to 800°C. All attempts to prepare $YbSe_2$ by preheating the metal with the proper amount of selenium in a vycor tube below 400°C for two days and at final reaction temperatures between 400°C to 800°C were unsuccessful and the diffraction patterns of the products showed the existence of two phases, cubic YbSe and Se.

Crystals of $LaSb_2$, $CeSb_2$, $NdSb_2$, $SmSb_2$ and $YbSb_2$ were prepared by reacting the rare earth elements and antimony in evacuated vycor tubes. The samples were preheated below 500°C for 48 hours and kept later at $700 \sim 750$°C for about a week. Good crystalline phases were obtained. The compounds $LaSb_2$, $NdSb_2$, and $YbSb_2$ were also successfully prepared by a liquid-liquid reaction in tantalum tubes at about 1500°C. These compounds are very stable under atmospheric conditions. Crystals of $LaSb_2$ were heated to 1000°C for 24 hours and quenched in water. No phase transition occurred.

Results

Well formed single crystals suitable for X-ray diffraction studies could be found for $SmSe_2$, $GdSe_2$, $DySe_2$, $HoSe_2$ and $ErSe_2$ and their patterns were essentially identical. Approximately 80% of the hkl reflections whose intensities ranged from weak to strong had indices $h = 2n$, $k = 4n$, and $l = 3n$; the other 20% were very weak and had indices $h + k = 2n$, and all values of l were present. For hk0 reflections only those with indices $h = 2n$, $k = 4n$ were observed, $0kl$ reflection $k = 4n$, $l = 3n$ existed, and $h0l$, $h = 2n$, $l = 3n$ could be seen. The true diffraction symmetry, considering all reflections, was mmmC--a, although the large number of absent reflections places doubt on the a glide, and it was evident that an orthorhombic superstructure cell existed as well as a tetragonal subcell which were related by $a_{super} = 2c_{sub}$, $b_{super} = 4a_{sub}$, $c_{super} = 3a_{sub}$. The subcell was tetragonal and the space group $P\frac{4}{n}mm$ could be derived from the observed extinctions.

The preparative conditions used here produced only very small crystals for the compounds $LaSe_2$, $CeSe_2$, and $NdSe_2$ which were not suitable for single crystal techniques. Their powder patterns resembled each other as well as the powder patterns of the other phases except that several very faint lines which occur in the $ErSe_2$ type pattern, and which are indexed on the basis of an orthorhombic cell, were not observed. The complete powder patterns of $LaSe_2$, $CeSe_2$ and $NdSe_2$ can be indexed by a smaller superstructure cell having two basic $RETe_2$ unit cells stacked along both the a and b axes and the space group $P4/nmm$ is still valid. Table 1 lists the crystallographic data for the diselenides as determined in this investigation.

Refinement of the Structure of $ErSe_2$

A single crystal of $ErSe_2$ with dimensions 0.08 x 0.04 x 0.01 mm was selected and three dimensional hkℓ intensities were measured from multiple film Weissenberg exposures using MoK_α and CuK_α radiation; 227 reflections were obtained with CuK_α radiation, among them 45 very weak reflections from the superlattice.

The space group Cmma was used in the attempt to solve the complete structure of $ErSe_2$. More than twenty trial models were tested and none of them gave an R factor below 0.45. The superstructure need not have the assumed space group; the large number of non space group extinctions is due to either small changes in the atomic arrangement in the various subcells which make up the supercell or to an ordering of vacancies in some of the sites which can be occupied by selenium. The inability to solve the superstructure does not affect the understanding of the basic structure and of the bonding character among the atoms.

The assumption of the same space group and atomic positions as found in $RETe_2$ (4), permitted the subcell structure to be refined to an R factor of 0.13 for 157 independent reflections obtained with MoK_α radiation. The final atomic parameters for the subcell are given in Table 2.

TABLE 2

Final Parameters and their Standard Deviations for $ErSe_2$ Substructure

	x	y	z	$B_{11} = B_{22}$	B_{33}
Er	0	0.5	0.7270 ± 0.0005	0.0074 ± 0.0016	0.0081 ± 0.0008
Se(1)	0	0.5	0.3672 ± 0.0011	0.0044 ± 0.0027	0.0080 ± 0.0015
Se(2)	0	0	0	0.1161 ± 0.0127	0.0057 ± 0.0019

Discussion

The z parameters of the atoms in the $ErSe_2$ subcell have almost the same values as those for $LaTe_2$ and $NdTe_2$ (4). The thermal motions in both structures are quite similar; the Se(2) atoms in the basal plane have also larger temperature factors along the x and y directions than in the z direction.

The Se(2) - Se(2) distance in the basal plane is quite short, the atomic radius of Se calculated from this separation is 1.405 Å which indicates that the bonding is partially ionic and partially covalent in character, (the covalent radius for Se is 1.17 Å).

The observed atomic radius for Er is 1.576 Å and if the metallic radius for Er is taken as 1.770 Å then the bonding can be considered to be 77% metallic in character.

The $RESb_2$ Structures

The structure of $YbSb_2$ is isostructural with $ZrSi_2$ and a detailed discussion has been given elsewhere, (5). The lattice parameters of $LaSb_2$, $CeSb_2$, $NdSb_2$ and $SmSb_2$ are shown in Table 3 and were calculated by a least-squares refinement of their powder diffraction data obtained with CuK_α radiation.

Table 3: Crystal Data of $LaSb_2$, $CeSb_2$, $NdSb_2$ and $SmSb_2$

	a Å	b Å	c Å	Vol. Å^3	D_m g/cc	D_x g/cc
$LaSb_2$	6.314 ± 0.005	6.175 ± 0.005	18.56 ± 0.01	725.1	6.68	7.00
$CeSb_2$	6.295 ± 0.006	6.124 ± 0.006	18.21 ± 0.02	702.2	6.69	7.25
$NdSb_2$	6.207 ± 0.004	6.098 ± 0.004	18.08 ± 0.01	684.3	6.82	7.53
$SmSb_2$	6.171 ± 0.006	6.051 ± 0.006	17.89 ± 0.02	668.0	7.56	7.83

The volumes permit the placement of 8 formula weights in the unit cell. The systematic extinctions showed that the most probable space groups were Cmca or C2ca and the structure refinement indicates that the former is correct.

A single crystal of $SmSb_2$ with dimensions 0.05 x 0.06 x 0.02 mm was mounted along the y axis. In order to obtain the maximum number of reflections and smaller absorption errors ($\mu_{CuK_\alpha} = 2470 cm^{-1}$, $\mu_{MoK_\alpha} = 232.0 cm^{-1}$), MoK_α radiation was used. Intensity data for h0l, h1l, h2l, h3l, and h4l were obtained from multiple Weissenberg films. The peak intensities were read by comparison with a standard intensity scale. The reflections were corrected for Lorentz and polarization effects and also for absorption.

The values of the cell constants indicated that the structures of $LaSb_2$ type phases were closely related to both $RETe_2$ (Cu_2Sb) and $YbSb_2$ ($ZrSi_2$) type structures. The following relationships were evident:

$$a_{LaSb_2} \cong b_{LaSb_2} \cong \sqrt{2} a_{LaTe_2}$$

$$c_{LaSb_2} \cong 2 c_{LaTe_2}$$

$$a_{LaSb_2} \cong \sqrt{2} a_{YbSb_2}$$

$$b_{LaSb_2} \cong \sqrt{2}c_{YbSb_2}$$

$$c_{LaSb_2} \cong b_{YbSb_2}$$

The final parameters and anisotropic temperature factors are shown in Table 4; the discrepancy coefficient is 0.109.

TABLE 4

Final atomic parameters for $SmSb_2$. Numbers in parenthesis are the standard deviations.

	x	y	z	B^*_{11}	B_{22}	B_{33}	B_{13}	B_{23}
Sm	0	0.3786 (.0017)	0.3900 (.0003)	0.0031 (.0011)	0.0139 (.0036)	0.0010 (.0002)	--	--
Sb(1)	0	0.8787 (.0022)	0.4361 (.0003)	0.0046 (.0013)	0.0094 (.0042)	0.0008 (.0002)	--	-0.0057 (.0015)
Sb(2)	0.25	0.1252 (.0024)	0.25	0.0062 (.0017)	-0.0042 (.0033)	0.0008 (.0002)	-0.0003 (.0006)	--

*The anisotropic temperature factor expression is $\exp[-(B_{11}h^2 + B_{22}k^2 + B_{33}l^2 + 2B_{12}hk + 2B_{13}hl + 2B_{23}kl)]$

The $LaSb_2$ type structure is essentially derived from the $RETe_2$ (Cu_2Sb) and $YbSb_2$ ($ZrSi_2$) structures. The structure is formed by ten layers of atoms stacked in the order Sb(1), RE, Sb(2), RE, Sb(1), Sb(1), RE, Sb(2), RE, Sb(1). The stacking sequence and the population of atoms in each layer are analogous to those in $YbSb_2$.

The bond distances for $SmSb_2$ are given in Table 5. Each Sm atom has 4 nearest Sb(1) atoms forming a slightly distorted square 0.82 Å below it and by 4 Sb(2) atoms (in Ref. 4 the atom in the basal plane was labelled Te(1); the corresponding Sb atom here is Sb(2) forming a rectangular layer of size $1/2\ a_o \times 1/2\ b_o$ 2.50 Å above it, and rotated 45°

TABLE 5

Interatomic distances and their standard deviations for $SmSb_2$, Å

Sm-Sm	4.198 ± 0.016	Sb(1)-2Sm	3.193 ± 0.018
-2Sb(1)	3.193 ± 0.018	-Sm	3.136 ± 0.018
-Sb(1)	3.134 ± 0.018	-Sm	3.134 ± 0.018
-Sb(1)	3.136 ± 0.018	-Sm	3.479 ± 0.018
-Sb(1)	3.479 ± 0.018	-Sb(1)	2.720 ± 0.021
-2Sb(2)	3.319 ± 0.018	-2Sb(2)	3.973 ± 0.021
-2Sb(2)	3.300 ± 0.018	-2Sb(2)	3.959 ± 0.021
		Sb(2)-2Sm	3.319 ± 0.018
		-2Sm	3.300 ± 0.018
		-2Sb(1)	3.973 ± 0.021
		-2Sb(1)	3.959 ± 0.021
		-2Sb(2)	3.086 ± 0.021
		-2Sb(2)	3.026 ± 0.021

with respect to the Sb(1) square, Fig. 1(a). The coordination polyhedron around Sm has also one Sb(1) atom at a distance of 3.479 Å and another Sm atom at a distance of 4.198 Å, which lie below the square formed by the Sb(1) layer. Due to the screening effect of this Sb(1) layer, the Sm-Sm distance is too large to assume bonding. Each Sb(1) atom is surrounded by 4 Sm atoms which form a slightly distorted square 0.82 Å above it and at a vertical distance of 3.33 Å are 4 Sb(2) atoms located above the square of Sm atoms, Fig. 1(b). The Sb(1)-Sb(2) distances are about 3.97 Å so that there is no contact between them. The Sb(1) atom is also coordinated by another Sb(1) atom and one Sm atom below it at 2.720 Å and 3.479 Å respectively. The 2.720 Å separation between Sb(1)-Sb(1) is considerably shorter than the 2.87 Å distance found in elemental Sb. One Sb(2) atom is located in the center of 4 nearest Sb(2) atoms within the same layer forming a rectangle of size a_0 x b_0, Fig. 1(c). The Sb(2) atoms are also coordinated by two Sm atoms at a distance of 3.300 Å and two Sm atoms at 3.319 Å.

Table 1: Crystallographic Data of Rare Earth Diselenides

Compound	Structure type	Lattice Constants Å			Number of formula wt/ unit cell	Dimension of subcell Å			Mean Atomic Volume Å³/atom
		a	b	c		a_{sub}	c_{sub}	Vol. Å³	
LaSe$_2$	LaSe$_2$	8.468		8.529	8	4.234	8.529	611.6	25.48
CeSe$_2$	LaSe$_2$	8.439		8.489	8	4.219	8.489	604.5	25.19
NdSe$_2$	LaSe$_2$	8.273		8.330	8	4.137	8.330	570.1	23.75
SmSe$_2$	ErSe$_2$	16.49	16.18	12.14	48	4.046	8.244	3239.1	22.49
GdSe$_2$	ErSe$_2$	15.47	16.08	12.06	48	4.020	8.233	3193.9	22.18
DySe$_2$	ErSe$_2$	16.39	15.94	11.96	48	3.985	8.193	3124.6	21.70
HoSe$_2$	ErSe$_2$	16.37	15.92	11.94	48	3.980	8.188	3111.7	21.61
ErSe$_2$	ErSe$_2$	16.36	15.90	11.92	48	3.975	8.184	3100.7	21.53
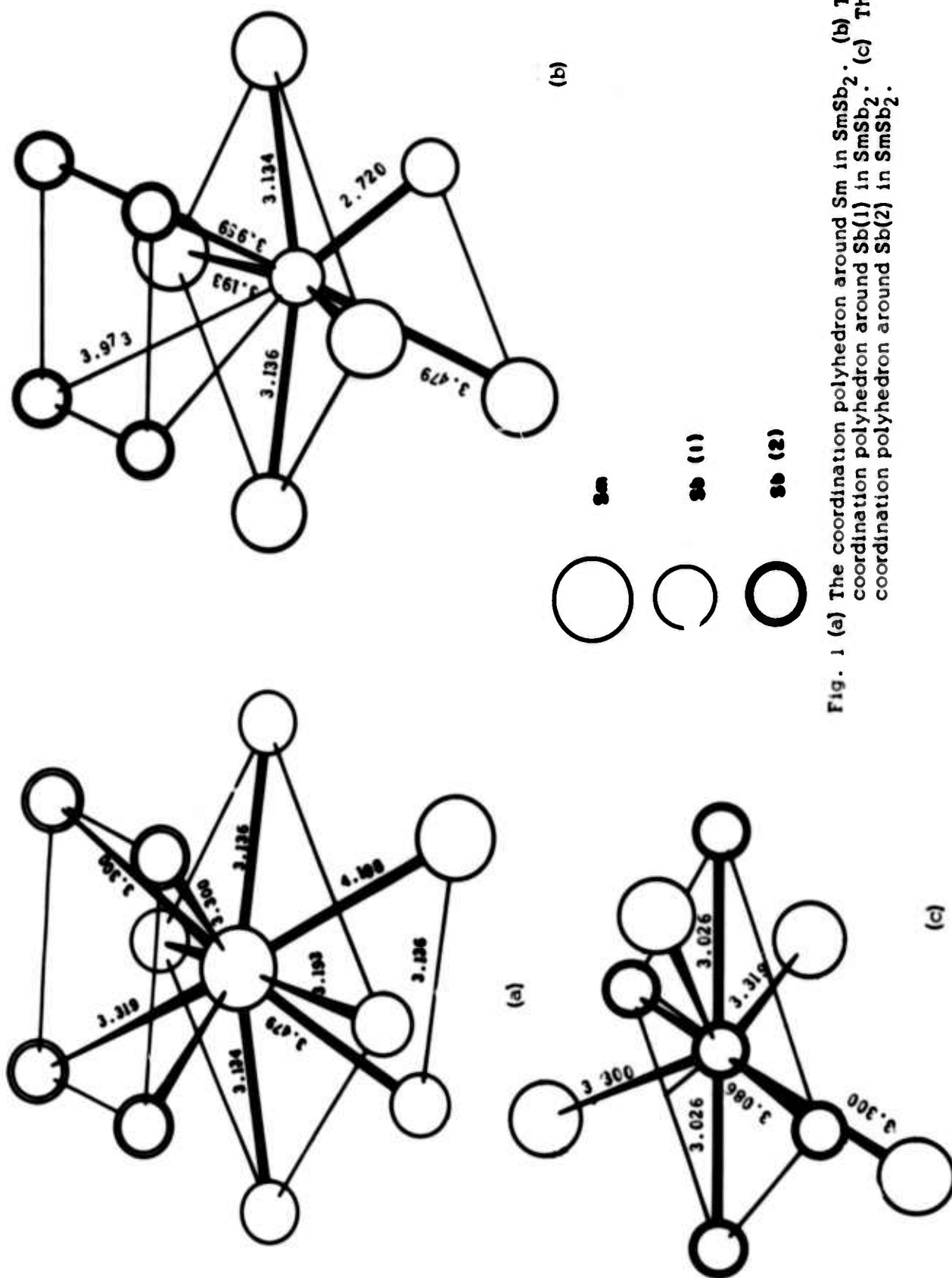
Fig. 1 (a) The coordination polyhedron around Sm in $SmSb_2$. (b) The coordination polyhedron around Sb(1) in $SmSb_2$. (c) The coordination polyhedron around Sb(2) in $SmSb_2$.

References

1) Research sponsored by Air Force Office of Scientific Research, Office of Aerospace Research, U. S. Air Force Grant, Grant No. 806-65.

2) Present address: Organic Division, American Cyanamid Company, 1937 Main W. St., Stamford, Connecticut.

3) D. J. Haase, H. Steinfink, and E. J. Weiss, Inorg. Chem., 4, 538 (1965).

4) R. Wang, H. Steinfink, and W. F. Bradley, Inorg. Chem., 5, 142 (1966).

5) R. Wang, R. E. Bodnar, and H. Steinfink, Inorg. Chem., 5, 1468 (1966).

CRYSTAL CHEMISTRY OF Au-RICH ALLOY PHASES WITH THE HEAVY RARE EARTHS

V. Sadagopan, B. C. Giessen, and N. J. Grant

Department of Metallurgy
Massachusetts Institute of Technology
Cambridge, Massachusetts

Using X-ray powder diffractometry, a comparative study was made of the binary alloy phases formed by Au with the rare earth metals Nd, Sm, Gd, Dy, Ho, Er, and Yb, as well as with Y, covering the concentration range between $(R.E.)Au_2$ and Au. $(R.E.)Au_2$ phases of the $MoSi_2 - Cll_b$ type were found to exist from $GdAu_2$ to $YbAu_2$. $(R.E.)Au_3$ phases of the distorted $TiCu_3 -DO_a$ type exist from $GdAu_3$ to $YbAu_3$ with strongly changing axial ratios. $(R.E.)Au_4$ phases, probably with the $MoNi_4 -Dl_a$ type, exist for $ErAu_4$ and $YbAu_4$. The atomic coordination relationships of all these phases are discussed. Y can be shown to act like a rare earth which is located between Ho and Er; Dy is found to behave like a trivalent rare earth in these alloy phases.

Ternary Compounds having the $CeCu_2$-type Structure

A. E. Dwight

Metallurgy Division
Argonne National Laboratory
Argonne, Illinois 60439

Abstract

The occurrence and unit cell constants of ten ternary compounds are reported. The compounds are formed when Y, Sm, Gd, Tb, Dy, Ho, Er, Tm, Yb or Lu are alloyed with Ni and Ga in equiatomic proportions. These are members of a family of orthorhombic compounds with the $CeCu_2$-type structure. From X-ray diffraction data on powdered specimens, approximate atomic positional parameters and interatomic distances were obtained.

An examination of the structure indicates that the rare earth atoms are aligned parallel to the b axis of the unit cell while the Ni and Ga atoms are aligned parallel to the a axis. The effect on the unit cell dimensions of ternary and quaternary substitutions are discussed.

Introduction:

There are relatively few crystal structures which compete for stability at the AB_2 composition in binary metallic systems. When A is a transition element and B is from the Cu, Zn or Al group, the dominant crystal structures are the Laves phases, $MoSi_2$ and its variant $MoPt_2$, and AlB_2 and its variant $CeCu_2$. The present paper describes a family of ternary compounds in which the $CeCu_2$-type structure is stable.

The occurrence of the $CeCu_2$-type structure in YCu_2 and thirteen rare earth compounds with Cu was reported by Storm and Benson[1]. Also Ryba and coworkers have identified the $CeCu_2$-type

structure in YCu_2[2], $YbZn_2$[3] and $HoZn_2$[4].

Duwell and Baenziger[5] reported the compound KHg_2 and assigned it to the space group Imma with 4 K atoms in e sites and 8 Hg in i sites. This structure differs slightly from that reported for $CeCu_2$[6] in which the 8 Cu atoms are placed in h rather than i sites.

Experimental Procedure:

The alloys for this investigation were prepared by arc melting on a water-cooled copper hearth in a helium-argon atomosphere. After homogenization at 1000°C, powder was prepared by crushing. The powder was then given a short anneal for stress relief. X-ray diffraction patterns were taken on powdered samples with filtered Cr radiation, in Debye-Scherrer cameras. Indexing was accomplished with the aid of the Battelle Indexing Charts[7]. Unit cell constants for all compounds and F^2 value for ErNiGa were obtained by use of a computer program[8]. Intensities were calculated by the relation $I \sim m(L.P.)F^2$.

Results and Discussion:

A perspective view of the unit cell for the HoNiGa compound is shown in Figure 1. The structure is characterized by chains of Ho atoms parallel to the b_o axis and chains of NiGa atoms parallel to the a_o axis. The Ni and Ga atoms are assumed to be in alternate positions in the chain, although the possibility of other arrangements of Ni and Ga on the 8 h sites has not been disproven.

A preliminary intensity calculation was made, assuming the positional parameters reported by Larson and Cromer[6] for CeCu$_2$: for 4 e, 0, 0.25, 0.5377, for 8 h, 0, 0.051, 0.1648. The calculated and observed intensities were in fairly good agreement, but indicated a need for refinement of the positional parameters. We attempted to refine only the Z for Ho, as this is the most sensitive quantity in the structure factor. Calculations were made with Z for Ho taken as 0.55, 0.555 and 0.56. The calculated intensities with Z for Ho equal to 0.555 showed the best agreement with observed intensities, as indicated in Table II, and we estimate Z for Ho to be 0.553 ± .005. This is in good agreement with the value of 0.5503 reported[3] for YbZn$_2$. Interatomic distances for the compound HoNiGa are given in Table III. The agreement between X-ray density and absolute density measurements confirms the assumption that there are four formula weights per unit cell.

The variations in a$_o$, b$_o$, c$_o$ and V/M with atomic number of the rare earth are shown in Figure 2. YbNiGa has a larger volume than its trivalent neighbors, which is to be expected since Yb often exhibits a bivalent state. While the lanthanide cell constants are plotted according to atomic number in Figure 2, Y was located on the plot by placing the V/M value for YNiGa directly on the V/M curve, which is close to the value for TbNiGa. It has been noted repeatedly that Tb is the lanthanide which most nearly resembles Y in alloying behavior.

Another point to be noted from Figure 2 is that the b_o parameter varies with atomic number more steeply than do the a_o and c_o parameters. This reflects the fact that the lanthanide atoms are aligned in chains which run parallel to the b_o axis of the unit cell. Replacement of Gd by Lu, for example, shortens the chain and a concomitant contraction of the lattice occurs predominantly in the b_o direction.

A contrasting trend is shown in Figure 3, in which quaternary substitutions were made in the compound GdNiGa. Four individual alloys were prepared in which the following substitutions were made: 5 at% Th or Hf for Gd, 5 at% Pt for Ni, and 5 at% In for Ga. Th, In and Pt have larger atomic volumes than the respective atoms they replace, while Hf is smaller. The V/M of the compound varies in predictable fashion as a result of the partial substitutions. From Figure 3 it appears that the partial replacement of Ni and Ga by Pt and In results in an expansion of the short Ni-Ga distances. These expansions are reflected by an increase in a_o and c_o, but not b_o because the Ni-Ga-Ni chains are perpendicular to the b_o direction. Partial replacement of Gd by Th results in an expansion of the short interatomic distances between a Gd atom and the neighboring two Ni and two Ga atoms while the substitution with Hf results in a contraction. Since four of these six bonds lie at an angle to all three axes, the resulting expansion or contraction appears in all three axes.

The structure of HoNiGa and the other nine examples depends for its stability upon both relative atomic size and electron concentration

requirements. The size requirement is indicated by the fact Sc, La, Ce, Nd and Pr do not form the $CeCu_2$-type structure with Ni and Ga. Apparently the Sc atoms is too small and the other atoms are too large. A comparison of HoNiGa with the binary $CeCu_2$-type compounds $HoCu_2$ and $HoZn_2$ indicates that a mixture of Ni and Ga can replace Cu or Zn. It is probable that Ni and Ga together contribute the same number of electrons as Cu or Zn, thereby satisfying an electron concentration requirement. It is expected that other ternary $CeCu_2$-type compounds will be found by replacement of Cu,Zn and perhaps Cd with pairs of elements, one lying to the left, the other to the right, of the replaced element.

References:

1. Storm, A. R. and Benson, K. E., Lanthanide-copper Compounds having the $CeCu_2$ and AlB_2 Structures, Acta Cryst. 16, 701 (1963).

2. Kejriwal, P. K. and Ryba, E. The Crystal Structure of YCu_2, Acta Cryst. 16, 687 (1965).

3. Michel, D. J. and Ryba, E. The Crystal Structure of $YbZn_2$, Acta Cryst. 19, 687 (1965).

4. Michel, D. J. and Ryba, E. The Crystal Structure of $HoZn_2$, Acta Cryst. 21, 818 (1966).

5. Duwell, E. J. and Baenziger, N. C., The Crystal Structures of KHg and KHg_2, Acta Cryst. 8, 705 (1955).

6. Larson, A. C. and Cromer, D. J., The Crystal Structure of $CeCu_2$, Acta Cryst. 14, 73, (1961).

7. Bell, J. C. and Austin, A. E. Battelle Indexing Charts for Diffraction Patterns of Tetragonal, Hexagonal and Orthorhombic Crystals, Battelle Memorial Institute, Columbus, Ohio (no date).

8. Mueller, M. H., Heaton, L., and Miller, K. T., Determination of lattice parameters with the aid of a computer, Acta Cryst. 13, 828 (1960).

Table I

Ternary Compounds with the CeCu$_2$-type Structure

Compound	$a_o \pm$ (Å)	$b_o \pm$ (Å)	$c_o \pm$ (Å)	V/M(Å)^3
YNiGa[*]	4.296	6.901	7.319	54.2
SmNiGa	4.347	6.972	7.413	56.2
GdNiGa	4.322	6.931	7.367	55.2
TbNiGa	4.302	6.884	7.347	54.4
DyNiGa	4.284	6.850	7.343	53.9
HoNiGa	4.279	6.829	7.329	53.5
ErNiGa	4.262	6.789	7.315	52.9
TmNiGa	4.247	6.750	7.305	52.4
YbNiGa	4.25	6.76	7.33	52.6
LuNiGa	4.216	6.678	7.290	51.3

[*]The cell constants have an uncertainty of $\pm$ 0.001 Å except those for YbNiGa, which have a uncertainty of $\pm$ 0.01 Å.

Table II

Calculated and observed d spacings and intensities for ErNiGa

Wavelength of radiation: CrK_{α_1} = 2.28962 Å

hkl	d_c	d_o	I_c	I_o	hkl	d_c	d_o	I_c	I_o
011	4.976		2	-	042	1.539		4	-
101	3.683	3.68	25	m	231	1.518	1.53	13	ms
002	3.658	3.65	6	vvw	015	1.430	1.43	12	ms
020	3.394	3.39	4	vw	301	1.395	1.395	3	vw
112	2.569	2.565	51	s	204	1.388		0	-
121	2.496 }	2.495	100 }	vs	105	1.384	1.385	2	vw
022	2.488 }		36 }		134	1.349	1.348	39	ms
013	2.295	2.295	18	m	051	1.335		1	-
031	2.162	2.16	16	m	240	1.328	1.327	13	w
200	2.131	2.13	31	ms	143	1.324	1.325	10	w
103	2.117	2.115	32	s	233	1.309	1.309	15	mw
211	1.959	1.957	1	vvw	312	1.300	1.300	14	mw
202	1.841	1.84	2	vw	321	1.290	1.289	31	ms
004	1.829		0	-	224	1.285	1.284	5	w
220	1.805	1.80	2	vw	125	1.281		0	-
123	1.796		0	-	242	1.248	1.2475	10	w
132	1.754		0	-	044	1.244		0	-
040	1.697	1.698	8	m	035	1.229		2	-
033	1.659	1.66	8	mw	303	1.228	1.227	20	ms
114	1.631	1.632	12	m	152	1.220	1.219	45	ms
222	1.619	1.62	21	ms	006	1.219		0	-
024	1.610	1.61	3	v	215	1.188	1.1878	50	s
213	1.562	1.564	13	ms	053	1.186		12	-
141	1.541	1.544	12	ms	116	1.155	1.155	53	m
					323	1.154		0	-

Table III

Interatomic Distances and Coordination Numbers for ErNiGa

Space Group: Imma, No. 74

Er in 4e: 0, 1/2, z, with z assumed to be 0.553 Ni and
Ga in 8h: 0, y, z, with y assumed to be 0.051
and z 0.165$^{(3)}$.

Interatomic Distances

Er-2Er	3.48 A	(Ni,Ga)-2Er	2.99 A
Er-2Er	3.58	(Ni,Ga)-1Er	2.90
Er-4(Ni,Ga)	2.99	(Ni,Ga)-1Er	3.14
Er-2(Ni,Ga)	2.90	(Ni,Ga)-2Er	3.06
Er-2(Ni,Ga)	3.14	(Ni,Ga)-2(Ni,Ga)	2.47
Er-4(Ni,Ga)	3.06	(Ni,Ga)-1(Ni,Ga)	2.41
		(Ni.Ga)-1(Ni,Ga)	2.70
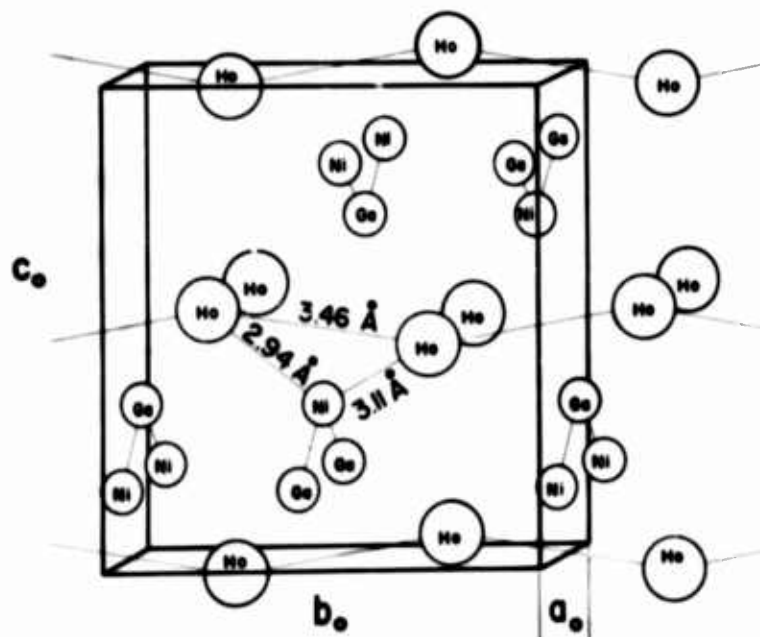
Fig. 1. Unit cell of HoNiGa, a CeCu$_2$-type structure, Imma
with Ho in the 4 e sites, Ni and Ga in the 8 h sites.
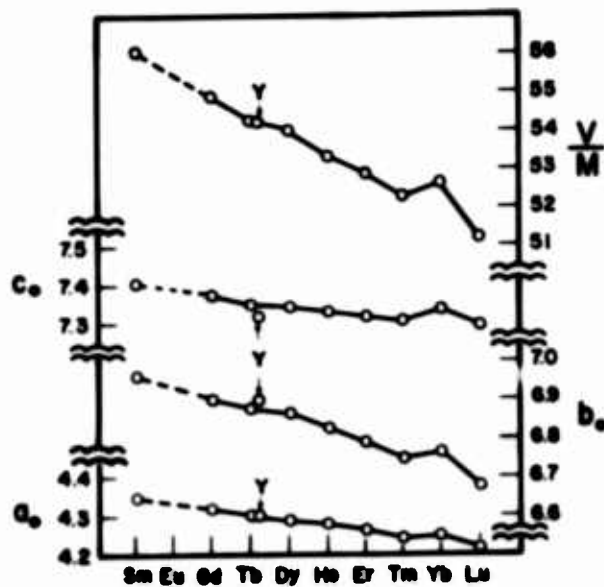
Fig. 2. The unit cell constants of CeCu$_2$-type compounds
stable R.E.-NiGa compositions, in which R.E. in-
cludes Y and the lanthanides Sm, Gd through Lu.

a/o Substitution
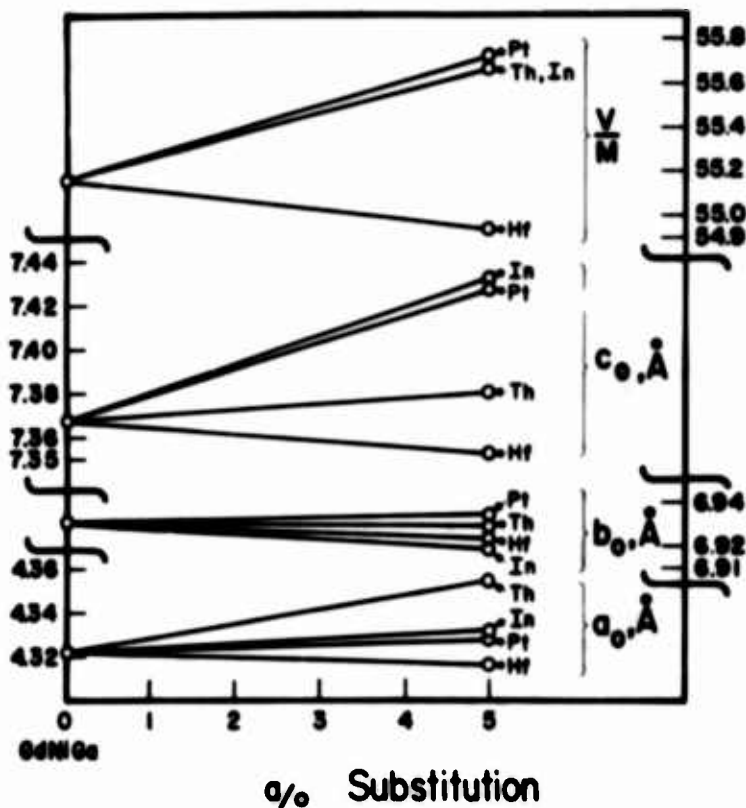
Fig. 3. Unit cell constants of four CeCu$_2$-type compounds
based on GdNiGa in which Th or Hf replaces 5% Gd,
Pt replaces 5% Ni and In replaces 5% Ga.

MAGNETIC PROPERTIES OF DYSPROSIUM

R. G. Jordan
University of Sheffield, England†

ABSTRACT

The magnetic properties of several single crystals of dysprosium
have been investigated along the principal directions of the h. c. p.
structure over the temperature range 4° to 300°K., and in applied
magnetic fields up to 18 Koe. The measurements in the basal plane
agree in general with the previous work. Along the c direction a
small spontaneous moment is observed, appearing at 125 ± 2°K.,
89 ± 3°K. and 88 ± 4°K. for the three crystals studied. The cor-
responding spontaneous moments at 0°K. are 1. 9 ± 0. 4 emu./gm.,
2. 7 ± 0. 3 emu./gm. and 2. 6 ± 0. 3 emu./gm. An analysis of the
results would seem to indicate that the transition from antiferro-
magnetism to ferromagnetism is controlled by the strong dependence
of the indirect exchange interaction with lattice dimensions. On the
basis of this analysis the ferromagnetic c axis lattice parameter has
been calculated for 90°K. $<$ T $<$ 179°K.

EXPERIMENTAL DETAILS

Four disc shaped samples, obtained from Metals Research Ltd.,
Cambridge, England, were used, having dimensions 5 mm. dia. x 1 mm.
One crystal was oriented with the (0001) parallel to the plane of the
disc, and three crystals were oriented with either the (11$\bar{2}$0) or (10$\bar{1}$0)
parallel to the plane of the disc. No details of analysis are available,
except that the crystals were prepared from 99. 9% pure starting
material.

RESULTS

The measurements were made on a vibrating sample magnetometer
using spectroscopically pure nickel as a calibration standard. It is
convenient to consider the experimental results under two headings.

(a) <u>Measurements in the basal plane</u>

The most important parameters are listed in Table I, and they
agree reasonably well with the results of Behrendt, Legvold and
Spedding[1] and Jew and Legvold[2]. The saturation moments, obtained
from plots of magnetic moment against the inverse of the internal
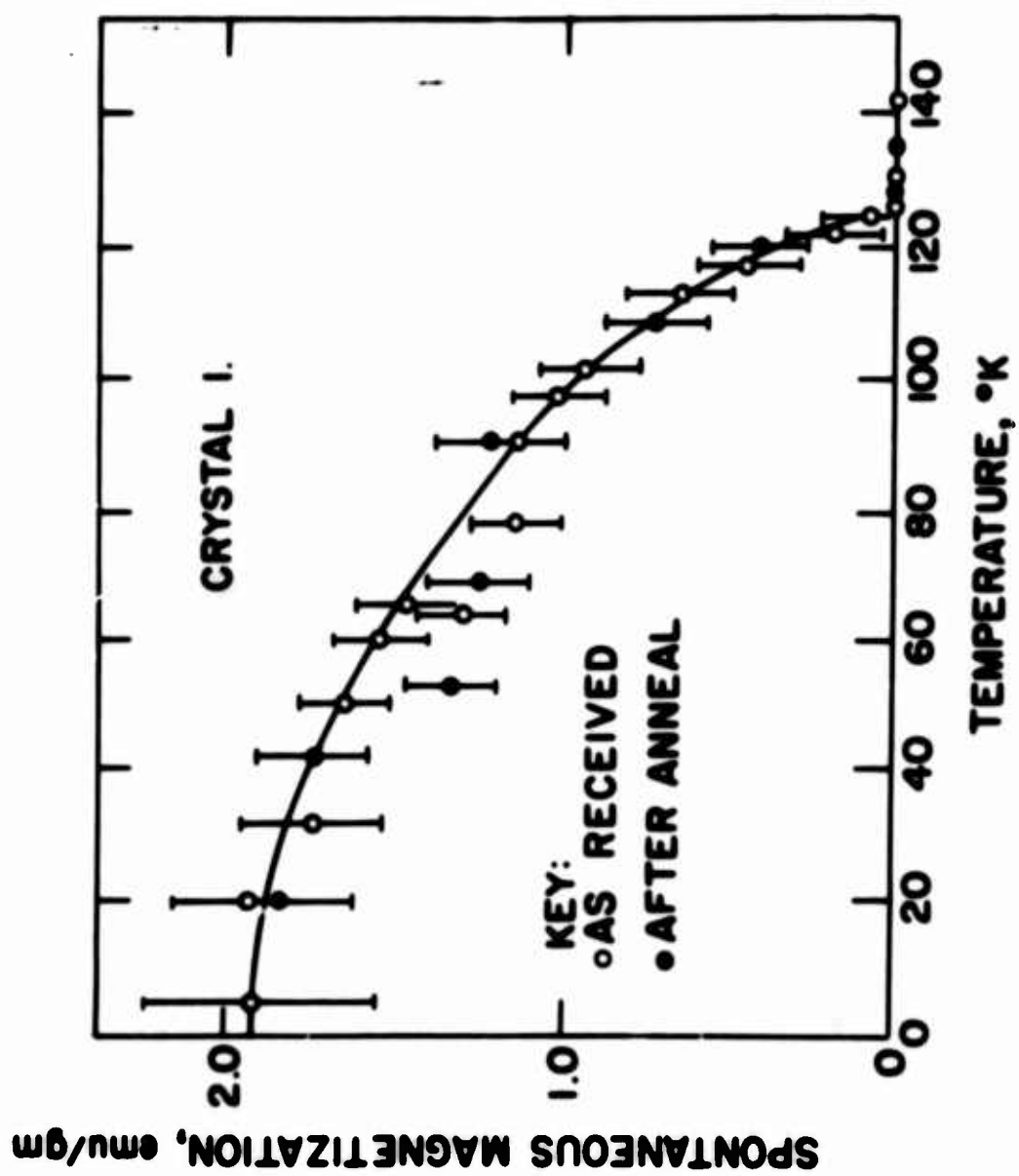
Figure 1.
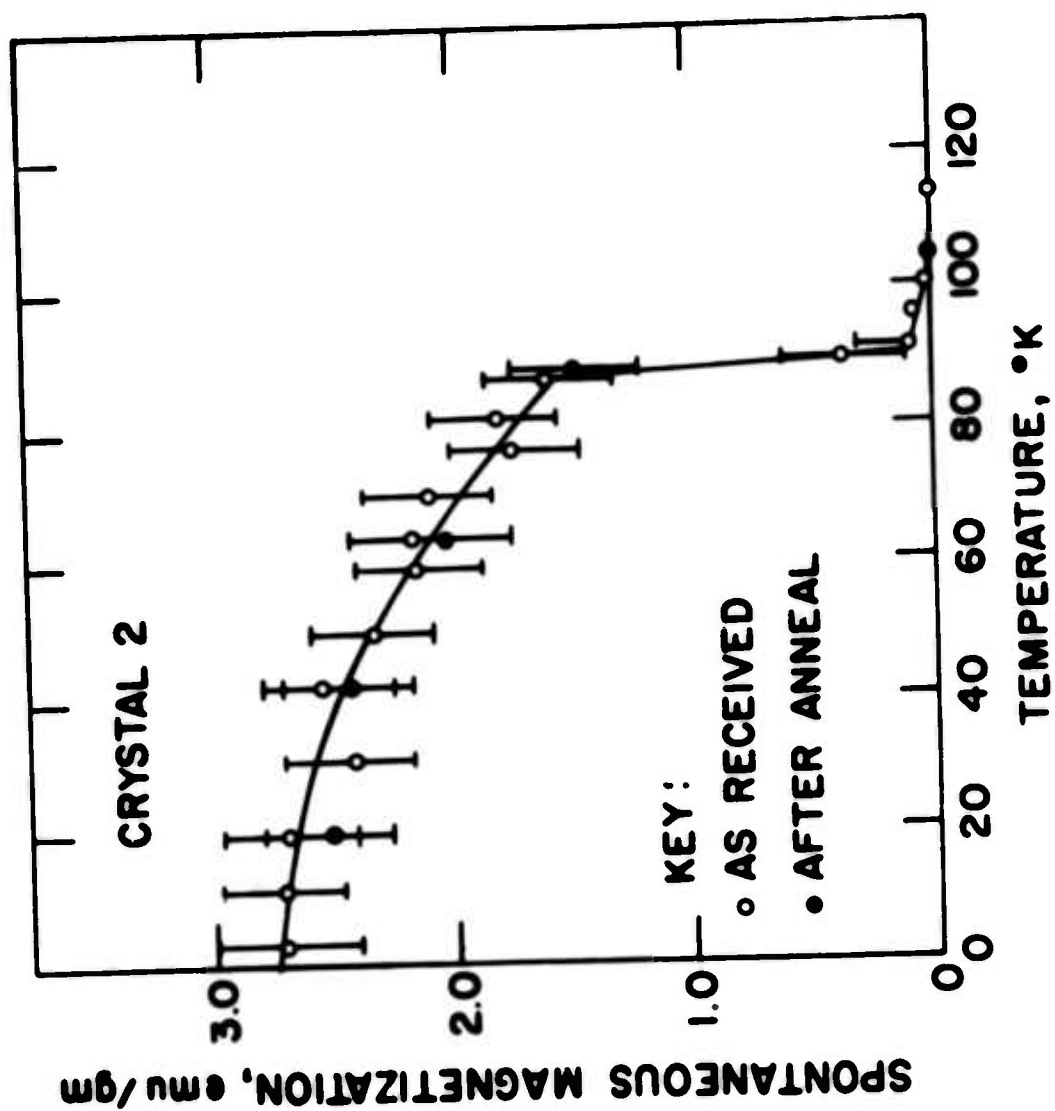
Figure 2.

field, follow a T^2 law.

The extrapolated spontaneous moments agree well with the Mossbauer data of Williams[3], but lie well above the free ion curve for $J = 15/2$.

Magnetic anisotropy exists between the a and b directions below about 140°K., with the a generally preferred. In low fields ($<$500 oe. within the temperature range 78° to 94°K., there is evidence that the b may be preferred, but no real detail could be extracted.

(b) Measurements along the c direction

Each of the 'c direction' crystals showed a small spontaneous moment parallel to the c direction below a certain temperature, T_k. Below this temperature, the magnetization curves were approximately linear above about 3 Koe. allowing one to define a susceptibility from the slope of the linear portion and a spontaneous moment from the intercept of this line on the magnetic moment axis. The variation of this spontaneous moment is shown in figures 1 and 2 for crystals 1 and 2 respectively. Crystal 3 gave results similar to crystal 2. Although the absolute values of the spontaneous moments at 0°K. are different for the two crystals, the reduced curves are identical below 90°K.

This spontaneous moment presumably arises from a canting of the magnetic moments out of the basal plane. This might be due to internal stresses in the samples, a spurious anisotropy providing a mechanism for canting. The crystals were therefore annealed at 750°C. for 24 hours and slow cooled. When remeasured, the characteristics remained the same.

A comparison of the susceptibilities for crystals 1 and 2 showed satisfactory agreement, the susceptibilities being continuous across the canting temperatures. The results obtained for the three crystals are summerized in Table II.

ANALYSIS

The mechanism for canting in the heavy rare earth metals has been dealt with in detail by Miwa and Yosida[4] and will not be considered

TABLE 1

$\sigma_{oo} = 343.2 \pm 3$ emu./gm. $\qquad T_N = 179.9 \pm 0.5°K.$

$\sigma_{oo} = 345.9 \pm 3$ emu./gm. $\qquad \theta_P = 170 \pm 1°K.$

$\mu_o = 10.1 \pm 0.1$ Bohr magnetons $\qquad P_{ef} = 10.6$ Bohr magnetons

$gJ = 10.0 \qquad\qquad\qquad g\sqrt{J(J+1)} = 10.64$

$T_c = 87 \pm 1°K \qquad\qquad \chi_{273} = 816 \pm 10 \times 10^{-6}$ emu./gm.

Basal plane parameters

TABLE II

Crystal	X-ray Details	σ_{oo} emu./gm.	T_k	Behavior at T_k	T_N
1. As received	good	2.0 ± 0.2	125 ± 2	smooth	179.2 ± 0.5
After anneal	"	1.9 ± 0.4	"	"	---
2. As received	c axis wander (5°)	2.8 ± 0.2	89 ± 3	abrupt	178.8 ± 1
After anneal	"	2.7 ± 0.3	"	"	---
3. As received	c axis wander (5°)	2.6 ± 0.3	88 ± 4	abrupt	179 ± 1
After anneal	"	---	"	"	-

c direction parameters
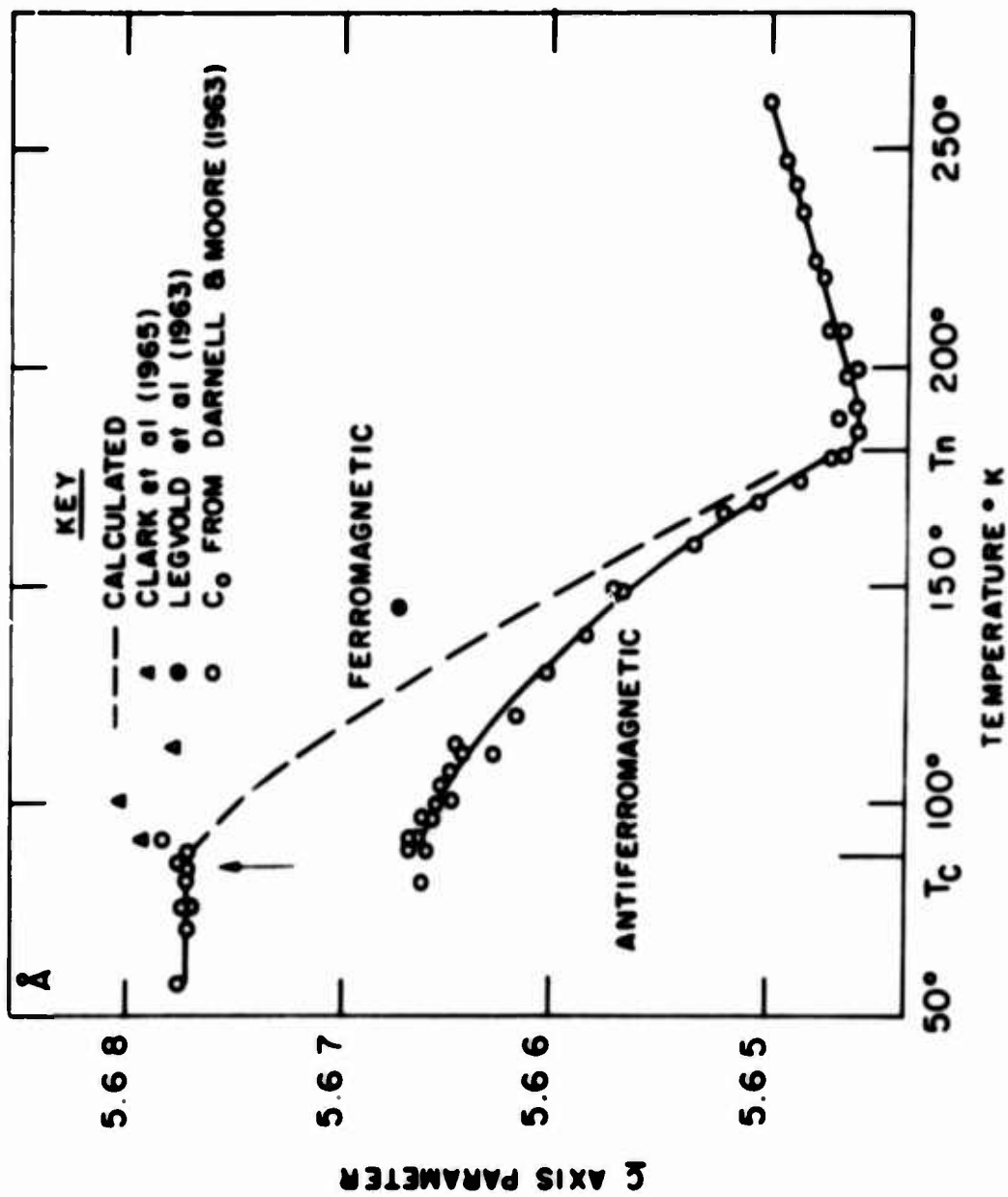
Figure 3.

here.   In this analysis we shall consider only the antiferromagnetic
to ferromagnetic transition.   As the canting is small we shall neglect
it, and assume that the magnetic moments are confined to the basal
plane.

The exchange energy of the antiferromagnetic spiral may be
written:

$$E_{af} = -m^2(J_1 \cos \Theta + J_2 \cos 2\Theta)$$

where J_1 and J_2 are the nearest, next nearest indirect exchange
parameters, m is the reduced moment and Θ is the interplanar turn
angle.   When a magnetic field, H, is applied perpendicularly to the
axis of the spiral, a collapse to ferromagnetism occurs at a critical
field, H_c.   If the field is at an angle, ϕ, to the easy direction of the
ferromagnetic state, we may write the energy of the ferromagnetic
state:

$$E_f = -m^2(J_1 + J_2) - \zeta J - \underline{m}_s \cdot \underline{H} - (K + E_m) \cos 6\phi$$

where m_s is the moment per atom, ζJ is the change of exchange
energy due to the c axis expansion accompanying the transition[5],
K is the hexagonal anisotropy energy and E_m is the energy associated
with the crystal distortion in the basal plane.   It may be shown that:

$$\zeta J > (K + E_m)$$

and

$$\zeta J = \frac{1}{2}(\frac{c - c_o}{c_o})^2 E$$

where $(c - c_o)$ is the c axis expansion at the transition and E is the
elastic modulus.   Values of ζJ have been obtained from an analysis
of the experimental results, and in figure 3 the calculated values of
c, the ferromagnetic lattice parameter, are shown with $E = 3 \times 10^{12}$
dynes/cm.[2], using the c_o values obtained by Darnell and Moore[5].
Estimates of c from thermal expansion data[6] and magnetostriction
data[7] are also shown for comparison.

CONCLUSION

The magnetic ordering in dysprosium is a little more complex than originally thought. For crystal 1 it would appear that between 125° and 179^OK. the magnetic structure is a simple spiral, the magnetic moments confined to the basal plane. Below 125^OK. the moments cant, and between 90° and 125^OK. the magnetic structure is a conical spiral, the canting angle increasing with decreasing temperature. Below 90^OK. the metal becomes ferromagnetic with an easy cone of magnetization. At 0^OK. the cone angle is about 179°. For crystals 2 and 3 the structure between 90° and 179^OK. is a simple spiral. At 90^OK. the metal becomes ferromagnetic with an easy cone of magnetization.

A simple analysis would seem to indicate that the first order transition in dysprosium is controlled by the strong dependence of the exchange parameters with lattice dimensions rather than the hexagonal anisotropy. Although the calculated variation of c does not agree too well with the experimental estimates, the indication is that the approach is correct.

REFERENCES

†   Present address: Institute for Atomic Research, Ames, Iowa.

1.   D. R. Behrendt, S. Legvold and F. H. Spedding, 1958,
Phys. Rev., 109, 1544.

2.   T. T. Jew and S. Legvold, 1963, U.S.A.E.C. Report, ISP-867.

3.   J. M. Williams, 1965, Thesis - University of Manchester.

4.   H. Miwa and K. Yosida, 1961, Prog. Theo. Phys. (Japan),
26, 693.

5.   F. J. Darnell and E. P. Moore, 1963, J. Appl. Phys. 34, 1337.

6.   A. E. Clark, B. F. DeSavage and R. Bozorth, 1965, Phys. Rev.
138, 216.

7.   S. Legvold, J. Alstad and J. Rhyne, 1963, Phys. Rev. Letters,
10, 509.

CHEMICAL AND ELECTRON OPTICAL STUDIES OF SOLS, GELS, AND OXIDE MICROSPHERES PREPARED FROM RARE-EARTH HYDROXIDES [x]

C.J.Hardy,[xx] S.R.Buxton, and T.E.Willmarth

Oak Ridge National Laboratory, Oak Ridge, Tennessee

Abstract

Hydroxides of individual rare-earths, principally praseodymium, neodymium, and europium, were precipitated from nitrate solutions with ammonium hydroxide, washed with water, and aged at 25 and 80°C. to form sols containing about 0.5M metal hydroxide and a small amount of nitrate. Gel spheres of 100 to 800μ diameter were prepared by partial dehydration of droplets of sols suspended in 2-ethylhexanol. The structure of the precipitates, sols, and gels was examined by electron microscopy and electron diffraction.

The initial precipitates of praseodymium and neodymium hydroxides consisted of amorphous particles of 30 to 60A diameter. The washed precipitates changed over a period of 1 to 2 hours at 25°C into translucent sols which contained rod-shaped crystals of the tri-hydroxides loosely aggregated into bundles 600 to 1000A long and 50 to 100A wide. The hydroxides of europium and heavy rare earths formed similar sols of low viscosity and low pH (7) only after the precipitates had been aged for many hours at 25° or 1 to 2 hours at 80°C, and the aggregates of rods grew much larger (up to 3μ long). The amorphous particles appeared to aggregate into net-like sheets; these broke up into small rod-shaped crystals which aggregated into bundles and slowly increased in length. The bundles were oriented randomly in the gel spheres, but were packed in regular arrays in precipitates which had sedimented slowly.

Spheres of rare-earth oxides of 50 to 500μ diameter prepared by programmed heating of gel spheres to 900 to 1450°C had densities of 95 to 98% of the theoretical crystal densities, low surface areas and high crushing strength. The preparation, properties, and structure of europium oxide spheres was examined in detail because of their applications in the nuclear field. Electron micrographs of replicas of fractured, and polished and etched, surfaces of the europium oxide spheres showed small grains of 300 to 500A in the cubic oxide at 900°, and large grains of 5 to 10μ in the monoclinic oxide heated at 1450°C. The large grains contained highly ordered sub-units of 0.2 to 0.5μ, but these were probably polycrystalline because X-ray line-broadening indicated crystals of 500 to 750A.

Introduction

This paper discusses the preparation of rare-earth hydroxide sols and gels, and the characterization of the colloidal particles by chemical analysis, spectroscopy, electron microscopy, and electron diffraction measurements. The gels, in the form of microspheres, were calcined to dense oxides, and their structure examined. Rare-earth oxides in this form have potential applications in industry, and in particular in the nuclear field, eg. europium, samarium, and gadolinium oxides, in control rods and as burnable poisons in fuel elements.[1]

Experimental

Preparation of Precipitates, Sols, and Gels— Hydroxides of individual rare-earths, principally praseodymium, neodymium, and europium of 99.9% purity, were precipitated by adding 0.2M solutions of their nitrates to an excess of 8M ammonium hydroxide at 25°C. The precipitates were centrifuged, washed 5 to 6 times with CO_2-free water until the pH of the wash liquor was about 9, and then aged at 25 or 80°C until they formed sols with a pH of 6.5 to 7 (1 to 2 hours at 25° for the lower rare-earths, or at 80° for europium and higher rare-earths). The sols contained 0.4 to 0.6M metal hydroxide and a mole ratio of residual nitrate to metal varying from 0.06 for the higher rare-earths to 0.26 for the lower ones. Gel spheres of 100 to 800μ diameter were prepared from the initial sols, or from sols evaporated up to 3M metal hydroxide, by partially dehydrating droplets of sol suspended in an immiscible alcohol, 2-ethylhexanol, for about 30 minutes.[2]

Preparation of Oxide Spheres— The gel spheres were converted into oxide spheres by drying them in vacuum at 120°C for several hours, heating them at about 100°/hour to 500° in vacuum and holding them at that temperature for 3 hours to decompose the residual nitrate, and then heating them in vacuum or air at 100°/hour to 1000 to 1450°C to form dense oxide. The carbon content of the final oxides was low, eg. 0.002 to 0.005 wt%. Densities, surface areas, and crushing strengths were measured (for details see ref.(2)).

Optical and Electron Microscopy— Samples of the precipitates and sols were diluted with CO_2-free water and examined on Formvar coated copper grids in a Philips EM200 electron microscope within 10 minutes of taking the samples at selected aging times. Electron diffraction measurements were made on selected areas of about 1 square micron. Transmission electron micrographs were obtained of ultra-thin (200A) sections of gel spheres embedded in epoxy resin and cut with a LKB Ultratome using a glass knife. The external and internal structure of the oxide spheres was examined by (a) optical microscopy of as-received spheres, and of spheres polished flat with alumina and diamond abrasives in silicone oil instead of water to prevent hydration, and (b) electron microscopy of replicas of as-received surfaces, etched polished surfaces, and fractured surfaces (two-stage replicas, Faxfilm, Pt/Pd shadowed, carbon-coated).

Results and Discussion

Structure of Precipitates and Sols of Rare-Earth Hydroxides

The initial gelatinous precipitate of praseodymium hydroxide aged for 18 min. at 25°C consisted of particles of 30 to 60A diam., (Fig.1A), which electron diffraction patterns (Fig.2A) showed to be amorphous. When the precipitate was washed with water and aged for 80 min. (Figs.1B,2B) it contained some rod-shaped particles 300 to 600A long, and after aging for a further hour it became a watery translucent sol (pH 7, viscosity 2cp). The sol consisted almost entirely of rod-shaped crystals (Fig.1C) with a sharp electron diffraction pattern (Fig.2C), which corresponded to a hexagonal cell with dimensions a = 6.48A, c = 3.77A in agreement with the X-ray data for praseodymium trihydroxide [3]. The primary crystals were loosely aggregated into bundles of parallel rods 600 to 1000A long and 50 to 100A wide. The colloidal particles were found to be positively charged from measurements in a Tiselius electrophoresis instrument (by F.J.Smith).

The structure of the initial precipitates of neodymium and europium hydroxides was similar to that of praseodymium hydroxide. The neodymium hydroxide formed a fluid sol after about 2 hours at 25°C, and the sol contained particles of about the same shape and size as those described above. However, europium hydroxide had to be aged for many hours at 25°, or 1 to 2 hours at 80°C, before it formed a sol of low viscosity and low pH(<7), and the rod-shaped crystals grew to a much larger size (up to several microns). Samples of freshly precipitated europium hydroxide were therefore aged at 25°C in the mother liquor (8M NH_4OH-0.2M NH_4NO_3), and also in water after thorough washing, and electron micrographs were obtained at several times from 10 min. to a few days. Results are shown in Fig.3 for the initial precipitate, and for precipitates aged in water. Rod-shaped particles about 600A long and 30A wide were first seen after 7 hours aging, the remaining particles being agglomerated into net-like sheets. Large bundles of roughly parallel rods were seen in samples aged for 17 to 24 hours, the sizes being 1000 to 5000A long and 100 to 500A wide. The size did not increase appreciably up to 72 hours aging, at which time net-like sheets were still present. The electron diffraction patterns for samples aged up to about 9 hours contained very broad diffuse bands similar to those in Figs. 2A and B; at 11 hours the bands were narrower and sharper and definite crystallinity was indicated (patterns similar to Fig.2C). The rate of growth of the bundles of rod-shaped crystals aged in the mother liquor was slightly greater than that observed in water. Samples aged in the mother liquor for 5 weeks contained bundles of rods from 0.5 to 3µ long, and these sedimented under gravity. A single crystal electron diffraction pattern of spots in a roughly square array was obtained from a bundle of rods in this long-aged precipitate. The pattern appeared to be from crystals oriented normal to the 110 plane. A small amount of material in the form of thin uniform sheets was seen in samples aged in the mother liquor

PHOTO 83060

SCALE ⊢ = 600Å
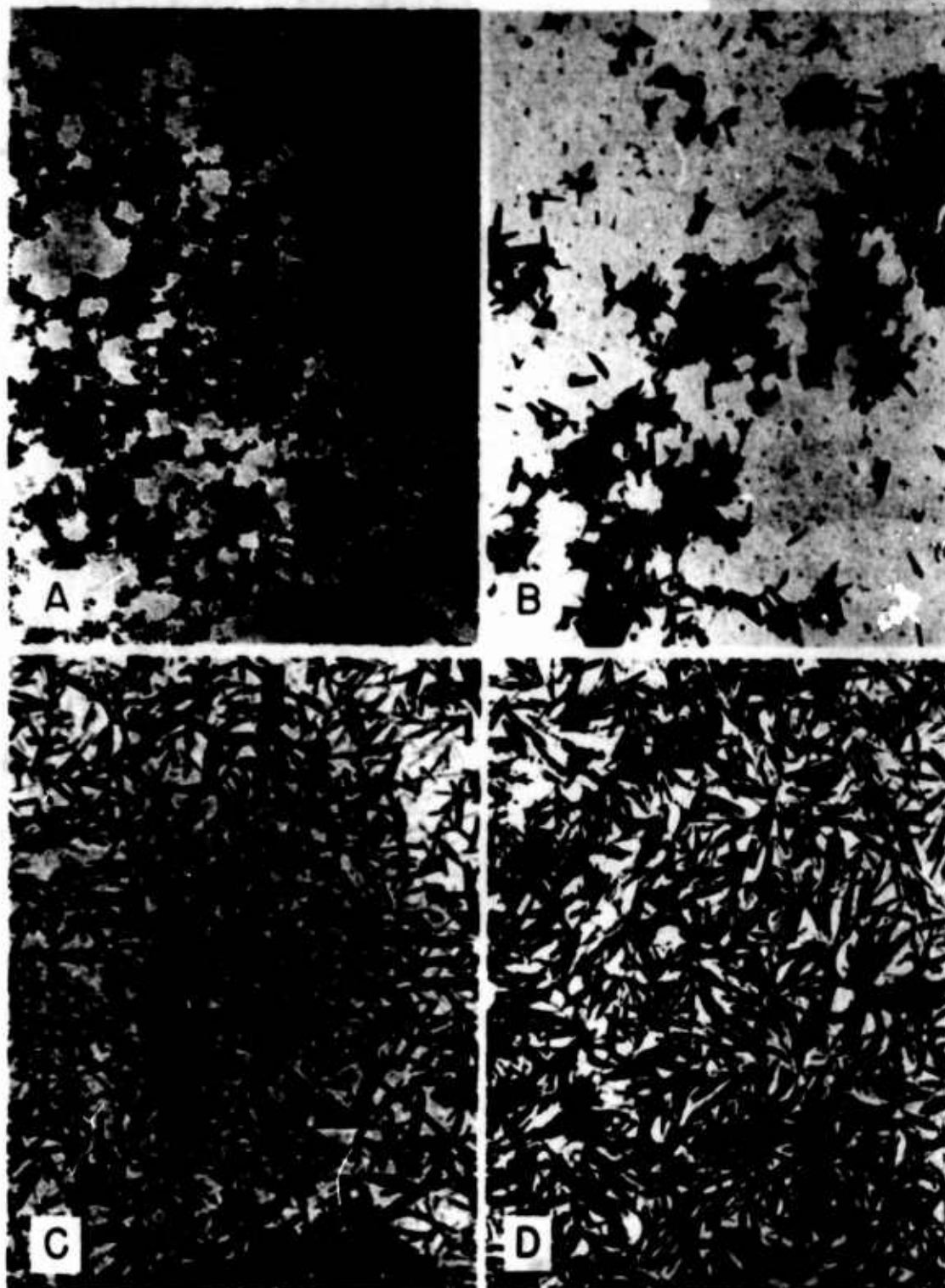
PHOTO 83062

PHOTO 83061

SCALE ⊢ = 600Å
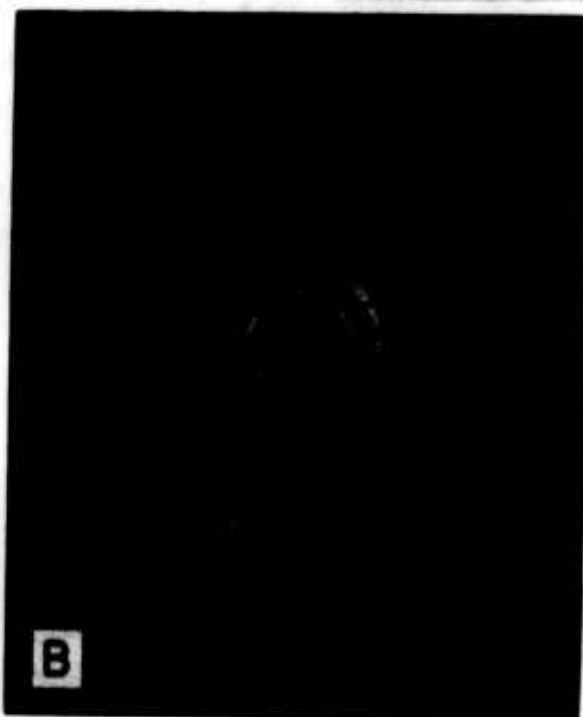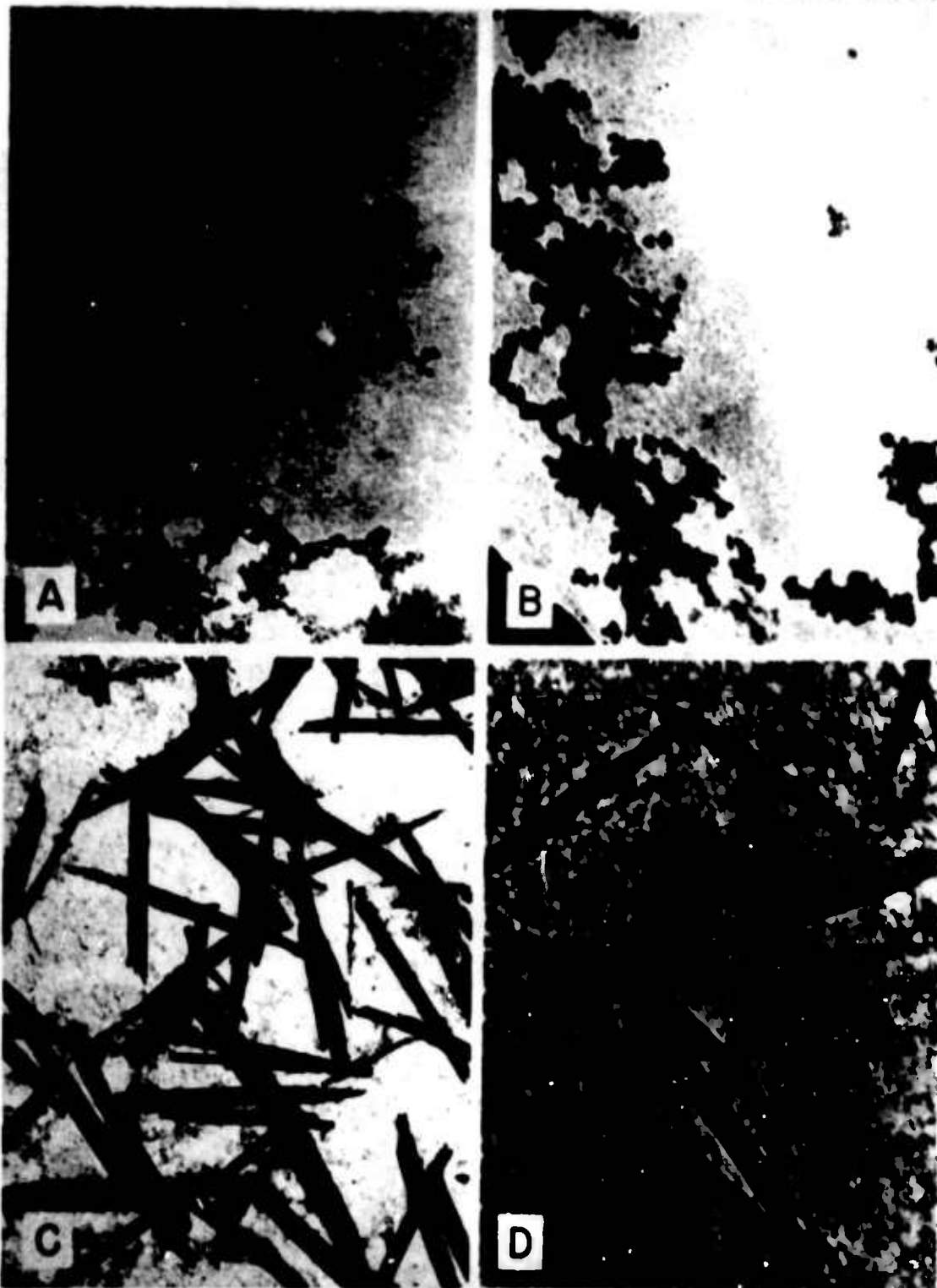
- 180 -

for 7 to 12 hours, compared with the bulk of the material which was in the form of net-like sheets. Some of the uniform sheets had clearly defined 120° angles between the edges. Hexagon-shaped particles about 600A long, and also single crystal diffraction patterns, have been reported recently [4] in neodymium hydroxide precipitates aged in water for 3 days.

The rod-shaped crystals showed many similarities to crystals of β-FeO.OH which were studied in detail by Watson and coworkers [5]. The crystals in the sols appeared to lie flat on the microscope grids and no information could be obtained on the dimensions of the bundles in the direction of the beam. Two other methods were therefore used to study the cross-section of the bundles, firstly the examination of thin sections cut through layers of sedimented particles, and secondly, examination of thin sections cut through gel spheres. In addition, several grids containing finely dispersed sol particles were examined at magnifications up to 658,000 in an attempt to resolve the structure of individual rods.

A layer of europium hydroxide particles which had sedimented to the bottom of the container over a period of a few weeks at 25°C was dehydrated and embedded in plastic in a similar way to that described by Watson [5]. Transmission electron micrographs through thin sections showed bundles of rods cut parallel and also at right-angles to the long axis. The length of the bundles was about 4000 to 5000A and the width showed only a narrow spread in size of 330 ± 50A. Some of the bundles had an approximately square cross-section, but nearly all had castellated edges similar to those observed in thin sections through europium hydroxide gel spheres (see next part and Fig.4). The packing of the bundles was not as uniform as the packing of crystals in layers of β-FeO.OH, eg. the checker-board pattern [5].

Many of the bundles of crystals in the washed and aged precipitates of europium hydroxide examined at high magnification (658,000) appeared to contain tubes and/or scrolls, each tube or rolled edge of a sheet having an outside diameter of about 60 to 70A, and an inside diameter of 20 to 25A. However, single dark lines of width about 20A were observed on micrographs of praseodymium hydroxide sols, in addition to groups of parallel lines (which looked like tubes), hence solid rods or very small tubes may coexist with the larger 60A tubes in these sols.

The following mechanism of growth of the bulk of the rod-shaped crystals and bundles is suggested as a result of the detailed examination of the electron micrographs taken at successive close intervals of time from 10 min. to 24 hours:
(a) the initial 30 to 60A amorphous aggregates form net-like sheets of which the individual strands break up into relatively short rods (400 to 500A long), or possibly tubes of small inside diameter; the net-like aggregates are probably three-dimensional in solution but appear to be sheets on the micrographs;
(b) the short rods crystallize, possibly by rejection of nitrate from within the central portions, the nitrate migrating to

surface sites or to a counterion layer;

(c) the rods increase in length to a greater extent than in diameter, probably by an "Ostwald Ripening" process by dissolution of amorphous material and re-precipitation on the ends of the rods which act as nuclei, or alternatively, by preferential aggregation of amorphous material on the ends of the rods; the slower rate of crystallization of the hydroxides of the higher rare-earths is in agreement qualitatively with the decreasing solubility of their hydroxides in water;

(d) the rods show a strong tendency to aggregate roughly parallel to each other to form the bundles, probably mainly by surface tension forces; this effect is more pronounced with the higher rare-earths.

Milligan has suggested [4] that the sheets in neodymium hydroxide precipitates roll up to form the rods, as has also been suggested for Halloysite [6] and alumina [7], but that it was not clear whether this occurred in solution or during the drying in the electron microscope. The latter view is in line with recent observations on Halloysite-type materials [8]. However, we think that the rods (or tubes) and bundles are present in the sols, because we observe some apparently thin flat sheets of europium hydroxide at intermediate aging times, and have not observed any rolling up of edges in the electron beam.

Structure of Gels of Rare-Earth Hydroxides

Transmission electron micrographs of thin (200A) sections cut through praseodymium and europium hydroxide gel spheres (Fig.4A and B respectively) showed that the bundles of crystals were oriented randomly. In Fig.4A several square cross-sections of width 30 to 150A are seen where the orientation of the bundles allowed them to be cut at 90° to the long axis. The large 140A square in the field has a mottled appearance due to several holes in it. The bundles are generally composed of parallel light and dark lines each about 20A wide, similar to the lines 30A wide seen on micrographs of β-FeO.OH [5]. It was not possible to decide conclusively whether the features represented solid rods, tubes, or thin sheets with rolled edges. The sections of europium hydroxide gel spheres showed (Fig. 4B) larger bundles 240 to 380A wide and up to 3000A long, and the cross-sections of the bundles had castellated edges with a repeat distance of 75 to 80A. These probably represent arrays of 4 x 4 or 3 x 3 units of rods or tubes.

Infrared spectroscopy of the gels showed the presence of hydroxyl groups and hydrogen-bonded water molecules and that the residual nitrate was coordinated to the metal ions, as in solid rare-earth nitrate hydrates [2], and was not present as nitrate ions.

Properties and Structures of Rare-Earth Oxide Spheres

Physical Properties — Spheres of rare-earth oxides of 50 to 500μ diameter prepared by heating gel spheres to 900 to 1500°C according to the crystal form required, had densities of 95 to 98% of the
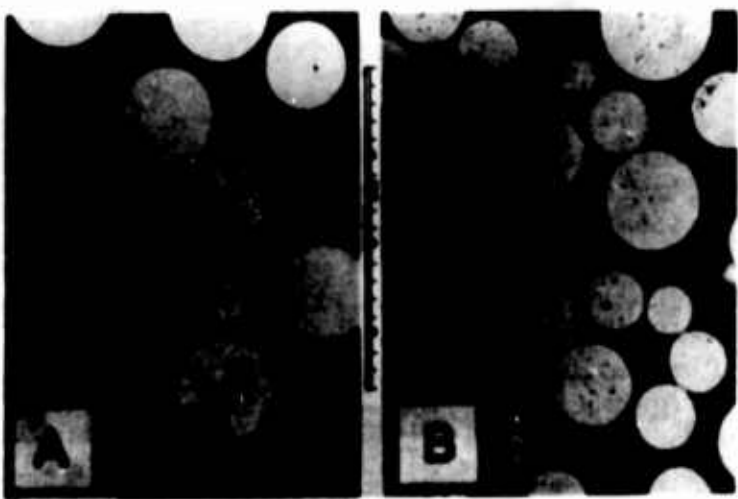
theoretical crystal densities, and surface areas of 0.01 to 0.1 m^2/g.
The crushing strength of the spheres ranged from 200g for 100μ to
2.5kg for 450μ diameter. Polished sections of 80 to 120μ spheres of
cubic Eu_2O_{11} are shown in Fig.5A and of monoclinic Eu_2O_3 in Fig.5B.
A large number of small closed pores were present in the Eu_2O_3 due
to the gel spheres being formed at too low (0.5M) a metal concen-
tration. Sols which were concentrated to about 2M metal and then
formed into gel spheres gave no significant porosity on calcination.

The preparation, properties, and structure of Eu_2O_3 spheres was
examined in detail because of their applications in the nuclear field
in control rods and as burnable poisons. The gel spheres were
heated to 900 to 1000°C to obtain cubic Eu_2O_3 (theoretical density
7.28g/cc, lattice dimension 10.87A [9]), and to 1450°C to obtain
monoclinic Eu_2O_3 (density 7.99g/cc, lattice dimensions a, 14.082A;
b, 3.604A; c, 8.778A; β, 100°00') which was considered to be the
more suitable form for fabrication into cermets. The cubic form is
slowly converted into the monoclinic form at 1050°, or in 2 hours
at 1400°C, and the change is not easily reversible [10].

The observation of a large difference in strength between
spheres of cubic Eu_2O_3 formed at 1000°C from gel spheres containing
amorphous particles (aged only a short time), and spheres of mono-
clinic Eu_2O_3 formed at 1450°C from gel spheres containing cryst-
alline particles led to a detailed study of the strength as a
function of the crystallinity of the gel and the temperature. The
general conclusions were that:
(a) the spheres of cubic oxide made by heating <u>amorphous</u> gel spheres
    to 1000°C were strongest (strength 600g for 150μ diameter, 94%
    dense); these had a glassy internal appearance and a slightly
    rough exterior surface;
(b) monoclinic oxide spheres made by heating the <u>amorphous</u> gel
    spheres to 1450°C were much weaker (229g);
(c) spheres of cubic oxide made at 1000°C from <u>crystalline</u> gel
    spheres had no appreciable strength (less than 50g), and many
    samples showed plastic deformation as opposed to the brittle
    fracture of spheres heated to a higher temperature, or made
    from amorphous gel spheres;
(d) the strength of monoclinic Eu_2O_3 spheres prepared at 1450°C
    from <u>crystalline</u> gel spheres was 190g, i.e. of the same order
    as that from <u>amorphous</u> gel spheres, hence the transformation of
    the cubic to the monoclinic structure is probably the main
    factor which causes the decreased strength above about 1000°C;
(e) spheres of cubic oxide calcined at 1000°C from freshly prepared
    amorphous gel spheres had the same strength as oxide spheres
    made from gel spheres aged 4 months at 25°C (which were expected
    to have crystallised). Electron microscopy of the aged gel spheres
    showed that the colloidal particles (300A long) were amorphous
    or only poorly crystalline compared to the large (7000A) crystals
    in gel spheres made from aged sols. The gel state therefore
    considerably hindered crystallisation compared to the sol state
    in which large crystals are formed in 24 hours at 25°C (Fig.3).
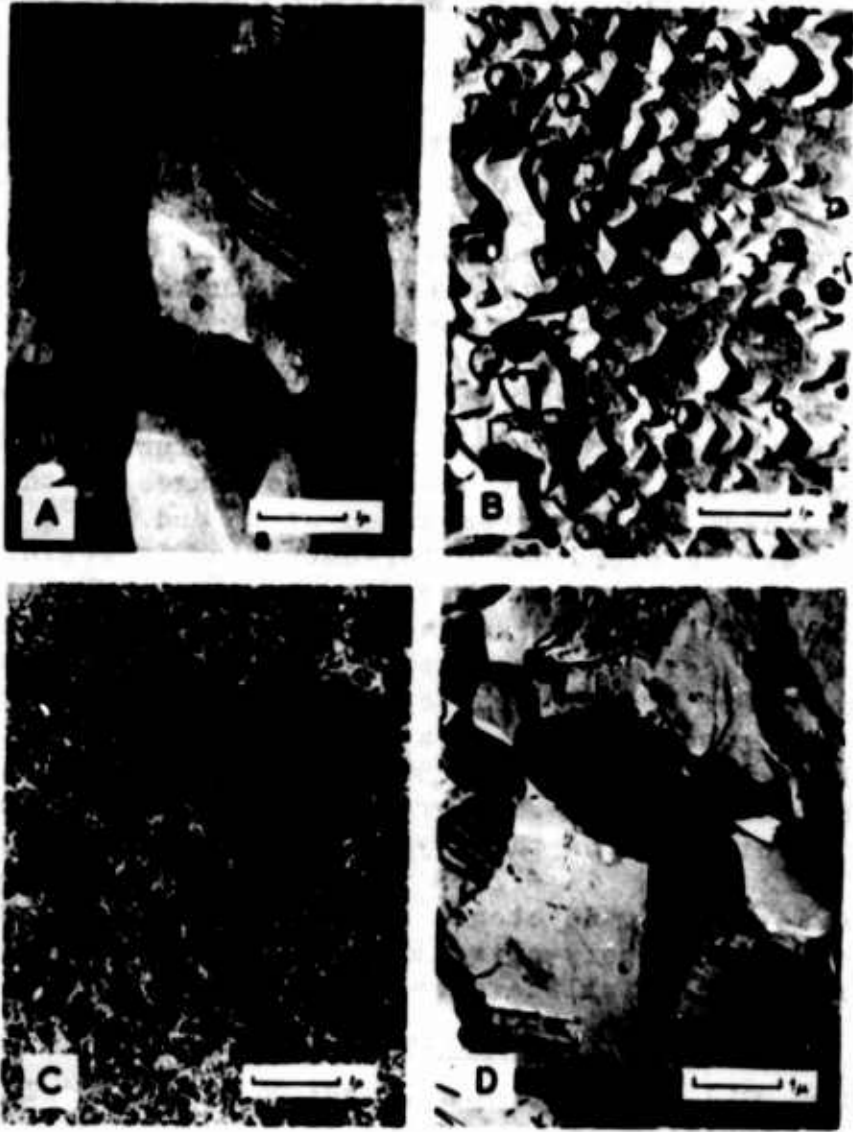
Structure of Europium Oxide Spheres — Electron micrographs of replicas of the external surface of monoclinic oxide spheres (1450°) showed grains of about 2 to 7µ width and irregular boundaries (Fig 6A). A pronounced series of steps was observed on the grains, the smallest step heights being about 200A. Electron micrographs of the polished internal surfaces of metallographic specimens (similar to those in Fig.4B) revealed no detailed structure. However, when the polished surfaces were etched for a few seconds in 8M nitric acid, replicas showed considerable detail:

(a) oriented arrays of crystals within each grain; one such array is shown in Fig.6B for a monoclinic oxide sphere (1450°C); adjacent grains showed different appearances due to different crystal faces being exposed and dissolved at different rates; the end-faces of the crystals in the grain in Fig.6B were 1000 to 3000A wide and the flat faces in adjacent grains were 2000 to 8000A wide;

(b) circular and elliptical closed pores about 2000A diameter.

Electron micrographs of the internal structure of spheres of europium hydroxide and oxide at the various stages in the calcination cycle were obtained. Gel spheres dried at 25 and 125°C in vacuum were sectioned with a microtome after embedding in resin, but those which were calcined at higher temperatures were too brittle for this method; replicas of fractured surfaces were therefore made. The micrographs of the gel spheres dried at 25 and 125°C were identical to that shown in Fig.4B; the fractographs of the cubic oxide heated at 900°C and the monoclinic oxide at 1450°C are shown in Fig.6C and D respectively. The size (300 to 500A) of the closely-packed small grains of cubic oxide in Fig.6C agrees with the X-ray line-broadening value of about 350A for the crystallite size. However, the large grains of 2 to 5µ in Fig.6D must contain sub-units of 0.2 to 0.5µ on the evidence of the etched surface in Fig.6B, and even these sub-units are probably poly-crystalline because X-ray results indicate a primary crystallite size of about 500A.

References

(1) S.R.Buxton, C.J.Hardy,and M.H.Lloyd, Paper to 3rd International Materials Symposium, Berkeley, Calif., June, 1966.
(2) C.J.Hardy, S.R.Buxton,and M.H.Lloyd, O.R.N.L.-4000 (1967).
(3) R.W.G.Wyckoff,"Crystal Structures", 2nd Edn., Interscience Publ., New York, 1963.
(4) W.O.Milligan and D.O.Dwight, J.Electron Micros.,14,264 (1965).
(5) J.H.Watson, R.R.Cardell, and W.Heller, J.Phys.Chem.66,1757 (1962)
(6) M.S.Taggart, W.O.Milligan, and H.P.Studer, Proc.3rd Natl.Conf. Clays and Clay Min., p.31, 1955; Natl. Acad. Sci.-N.R.C., Washington, D.C.
(7) P.W.Schmidt and W.O.Milligan, J.Electron Micros.,10,238(1961).
(8) E.W.Hope and J.A.Kittrick, Amer. Mineral.,49,859(1964).
(9) R.C.Rau,"Rare-Earth Research II",p.117, Proc.3rd Conf.Rare-Earth Res.,April,1963,Clearwater, Fla.,Ed.K.S.Vorres,Gordon and Breach, New York, 1964.
(10) C.E.Curtis and A.G.Tharp,J.Amer.Ceramic.Soc.,42,151(1959).

Structure of Lanthanum Dihydroxy Chloride

Forrest L. Carter
U. S Naval Research Laboratory, Washington, D. C.

ABSTRACT

Prepared hydrothermally $La(OH)_2Cl$ crystallizes in a mono-
clinic form with unit cell parameters of a = 6. 318 A, b = 3. 993 A,
c = 6. 931 A, and β = 113. 86°. The structure is non-centrosym-
metric and belongs to the $P2_1 - C_2^2$ space group. Lanthanum
has a coordination sphere of eight , of which two chlorines and
four oxygens form a distorted trigonal prism. The structure is
primarily a layer type with a structural backbone of lanthanum and
oxygen. Hydrogen bonds between the hydroxyl groups and chlorine
are responsible for the interlayer bonding.

Introduction

Crystalline yttrium dihydroxy chloride was recently[1] reported as a by-product of the hydrothermal growth of yttrium and rare earth ferrite-garnets. In this Laboratory lanthanum dihydroxy chloride was obtained[2] in an attempt to prepare lanthanum aluminate hydrothermally. The hydrothermal preparation of the dihydroxy chlorides of La, Nd, Sm, Gd, and Yb has since been accomplished and will be reported elsewhere[2] along with the unit cell parameters.

A complete structure determination of $La(OH)_2Cl$ is of particular interest for the following reasons:

1. The structure may be characteristic of the rare earth dihydroxy chlorides since those of Nd, Sm, Gd, and Yb appear to be isomorphous with $La(OH)_2Cl$.

2. R. F. Klevtsova[3] has determined the structure of $Y(OH)_2Cl$. A comparison of the orthorhombic structure of $Y(OH)_2Cl$ and the monoclinic structure of $La(OH)_2Cl$ is of some interest.

3. Compared to other crystalline rare earth compounds (like $LaOCl$, $LaCl_3$, etc.) the dihydroxy chloride structure should be comparatively free from internal strains and accordingly yield strain-free La-Cl and La-O bond distances.

4. The quality and intensity of the reflections are still good at $2\theta = 126°$ (MoK_α rad.). This permits reasonable resolution of the lighter atoms (H excluded).

Experimental Details

$La(OH)_2Cl$ occurs predominantly as coarse colorless needles when prepared hydrothermally at 500°C in a 15% NH_3Cl solution. A number of crystals were examined with a precession camera (MoK_α) but intensity data was collected from a rectangular prism

(≈ 0.5 mm long) on a Picker automatic four-circle diffractomer using a two-theta scan. Over 5000 reflections were collected of which half were independent. In addition 360 reflections having θ less than $26°$ were collected using balanced filters.

The unit cell parameters of monoclinic $La(OH)_2Cl$ at $24.5°C$ are

a = 6.318 ± 0.001A	β = 113.86 ± .03°
b = 3.993	vol = 159.88 A³
c = 6.931	

Systematic extinctions occur for the (o k o) reflections when k is odd. The corresponding space groups are $P2_1 - C_2^2$ or $P2_1/m - C_{2h}^2$. However statistical tests[4] using normalized structure factors (E_h) are summarized in Table I and clearly indicate that the correct space group is the non-centrosymmetric group $P2_1 - C_2^2$. Density considerations showed that only two formula molecules are in the unit cell.

Table I

Summary of Statistical Tests on $La(OH)_2Cl$

	Theoretical Values		Observed
	Centro.	Noncentro	
$\langle |E| \rangle$	0.798	0.886	0.892
$\langle |E^2-1| \rangle$	0.968	0.736	0.724
Distribution			
$|E| > 1$	32%	36.8 %	40.1%
$|E| > 2$	5	1.8	1.4
$|E| > 3$	0.3	0.01	0.0

Accordingly the structure was determined in a straightforward manner using a Harker section at $y = 0.5$ (Patterson) and the usual Fourier and least square techniques. In the current stage of refinement the R is .20 for all reflections with $\sin \theta / \lambda < 0.6$ but decreases rapidly with increase in $\sin \theta / \lambda < 0.9$.

In the $P2_1 - C_2^2$ group the origin may be arbitrarily taken to be anywhere along the unique b axis (i.e., the 2_1 screw axis) For descriptive purposes and for comparison with the $Y(OH)_2Cl$ structure we chose the origin such that $y = 0.25$ for La. If the structure was centered ($P2_1/m - C_{2h}^2$) then all atoms would be located on the mirror planes and have the general coordinates $(x, 1/4, z; \bar{x}, 3/4, z)$. The atomic coordinates given in Table II are not to be taken as final. We note that the current R factor is much less sensitive to the oxygen y coordinates than is indicated by the size of the least square shifts.

Table II

Atomic Coordinates for La(OH)$_2$Cl

	x	y	z
La	.1864	.2500	.3645
Cl	.7431	.2165	.9406
O$_1$	.5992	.2698	.4148
O$_2$	.0786	.2238	.6761

Crystal Structure

La(OH)$_2$Cl crystallizes in a layer structure where the somewhat pleated layers are parallel to the xy plane and are bonded together by hydrogen bonds of the type -O -H .... Cl. Consecutive metal atoms in the y direction are bridged by two oxygens at the distances 2.47 and 2.63 A (La-O$_1$), 2.49 and 2.61 A (La-O$_2$), and a chlorine at 2.98 and 3.09 A. If the structure were centered the lanthanum would be in a trigonal prism formed by four oxygens and two chlorines. Neighboring linear chains are related to the first by the twofold screw axis such that each metal atom is strongly bonded to two more oxygen atoms through the two larger rectangular faces of the trigonal prism. These oxygens are 2.49 and 2.51 A from the metal atom and (these oxygens) belong respectively to the trigonal prisms of the two neighboring chains of the same layer. If a reasonable position for the H atom is assumed the coordination about each oxygen is that of a distorted tetrahedron.

The above structure is in good agreement with the observed cleavage characteristics of the La(OH)$_2$Cl needles. It is difficult to cleave these needles perpendicular to their axis (b direction) without considerable damage. However with care it is possible to cleave the layers perpendicular to the x direction, thereby sepa-rating chains in the same layer, without obvious damage. Finally the layers may be separated with ease by cleaving parallel to the xy plane.

The orthorhombic structure of Y(OH)$_2$Cl and that of mono-clinic La(OH)$_2$Cl reported here are very closely related. Each are layer structures composed of nearly identical layers. However in Y(OH)$_2$Cl the unit cell contains two layers which are related by

twofold screw axis perpendicular to the layer; by contrast La(OH)$_2$Cl has a single layer per unit cell. Chains within the Y(OH)$_2$Cl layer are separated equal distances while in La(OH)$_2$Cl the chains are separated by similar but unequal distances. Of two possible space groups the authors R. F. Klevtsova and P. V. Klevtsov have indicated that Y(OH)$_2$Cl crystallizes in the centrosymmetric one, D_{2h}^{16} - Pbnm rather than C_{2v}^9 - Pbn2$_1$. This gives the yttrium atom the same coordination that lanthanum would have if it crystallized in the centrosymmetric structure P2$_1$/m - C_{2h}^2. However the structure and the statistical evidence (Table I) indicate the non-centrosymmetric group is correct for La(OH)$_2$Cl. If this distinction between the two structures is correct then we may be seeing a size effect of the larger lanthanum atom or possibly a slight disorder phenomena in the Y(OH)$_2$Cl crystal. At the meeting we anticipate reporting the final atomic parameters and a full statistical analysis of the collected data for the La(OH)$_2$Cl structure.

Finally we are happy to acknowledge kind assistance of D. Mitchell and S. Brenner of this Laboratory who gave technical aid in using the data reduction program of H. Norment and the least squares program of W. R. Busing, K. O. Martin, and H. A. Levy.

REFERENCES

1. P. V. Klevtsov, R. F. Klevtsova, and L. P. Sheina,
   Z. Strukt. Khim. 6, 469-71 (1965).

2. S. Levinson, F. L. Carter, and J. J. Rowe,
   (to be published).

3. R. F. Klevtsova, P. V. Klevtson, Dokl. Akad. Nauk SSSR 162,
   1049-52 (1965)

4. J. Karle and H. Hauptman, Acta Cryst. 9, 635 (1956);
   I. L. Karle, H. Hauptman, J. Karle and A. B. Wing,
   Acta Cryst. 11, 257 (1958).

Crystal Chemistry and Phase Equilibria

in The System Eu-Ti-O

Gregory J. McCarthy, William B. White and Rustum Roy

Materials Research Laboratory
Pennsylvania State University
University Park, Pennsylvania 16802

The Crystal Chemistry and Phase Equilibria of the ternary system Eu-Ti-O have been investigated in open and closed systems in the temperature range of 900 - 1500°C. The known bounding binary systems include the compounds Eu_2O_3 - Eu_3O_4 - EuO - Eu on the Europium-oxygen side and TiO_2 - the Ti_nO_{2n-1} homologous series - Ti_3O_5 - Ti_2O_3 - TiO - Ti_2O - Ti_3O - Ti on the Titanium-oxygen side. The join Eu_2O_3 - TiO_2 contains in addition to the known pyrochlore structure $Eu_2Ti_2O_7$, the monoclinic compound Eu_2TiO_5. On the joins Eu_2O_3 - Ti_2O_3 and EuO - TiO_2, the perovskite $EuTiO_3$ with divalent europium and tetravalent titanium is shown to have an extremely wide range of stability. The join EuO - TiO is apparently not binary and bulk compositions along this join dissociate into oxygen rich and oxygen poor phases. Particular attention has been placed on the highly reduced compounds in the metal-rich section of the diagram because of the possibility of finding compounds with unusual electrical properties.

Introduction

The system Eu-Ti-O is of interest because of the wide variety of

electrical, optical and magnetic properties of the compounds in the

bounding binary systems and the possibility of preparing ternary

phases with equally interesting properties. The Ti-O binary has

compounds varying from the insulating TiO_2 to the conducting TiO and

Ti. The Eu-O binary contains the ferromagnetic EuO, antiferromagnetic

Eu_3O_4 and paramagnetic Eu_2O_3. The stability fields of the known

ternary compounds $Eu_2Ti_2O_7$ and $EuTiO_3$ have not been established. The

origin of the ferromagnetic interaction in EuO is not yet settled, and some information could be derived from a study of the probable crystalline solutions between EuO and the isostructural TiO. Lastly, the metal rich region might provide phases with interesting and unusual electrical and magnetic properties.

Previous Investigations

The system Ti-O has been recently studied by Porter[1]. It includes the compounds TiO_2, Ti_nO_{2n-1} homologous series, Ti_3O_5, Ti_2O_3, TiO, Ti_2O, Ti_3O and Ti. Only the TiO_2 and Ti_nO_{2n-1} series were found to have equilibrium oxygen activities within the range of open system mixed gas atmosphere techniques. The highly reduced phases TiO, Ti_2O and Ti_3O must be prepared by closed system techniques.

The Eu_2O_3-TiO_2, Eu-O, and Eu-Ti binaries have not previously been systematically studied. In a study of EuO-Eu_2O_3 mixtures at 900°C, Bärnighausen[2] found only the Eu_3O_4 compound. Shafer[3] has shown that EuO has a limited stoichiometry with respect to Eu° and Eu^{3+} in crystalline solution, and Guerci and Shafer[4] found no compounds between Eu and EuO up to the liquidus surface. The latter authors proposed that EuO melts incongruently into some Eu_xO_y (not Eu_3O_4) phase + liquid. Brixner[5] prepared $Eu_2Ti_2O_7$ and found it to have a cubic pyrochlore structure. Brous and others[6], Shafer[3] and Holzapfel and Sieler[7] prepared $EuTiO_3$ and showed it to be a $A^{2+}B^{4+}O_3$ cubic perovskite.

Experimental

This system is an unusually difficult one to study because of the lack of a suitable container for many compositions of starting

materials over the required temperature range. No container was found for Eu metal because it readily attacks most metals and silica, because of its high vapor pressure in open systems or open vacuum experiments, and because of its affinity for the smallest traces of water and oxygen. Also high EuO compositions could not be reacted in silica due to the formation of divalent silicates. Evacuated silica capsules were utilized for mixtures near the Ti-O binary up to 1100°C. Welded noble metal capsules were used in the $EuO-Eu_2O_3-TiO-Ti_2O_3$ section of the diagram. Since in the rest of the diagram the starting materials attack noble metals, starting materials had to be reacted in purified inert atmospheres. All starting materials were pressed into pellets at 3000 psi.

The starting materials Eu, Eu_2O_3 and TiO_2 were 99.9% pure and the Ti metal was 99.2% pure.

Reactions of starting materials were carried out in globar and noble metal resistance furnaces open to controlled or inert atmospheres or in closed sealed containers. A microstrip furnace was utilized for high temperature, controlled atmosphere runs. Phase identification was carried out by microscopic and x ray diffraction techniques. Phase composition was determined by x-ray fluorescence, emission spectroscopy, and the electron microprobe. Oxygen content was measured in gravimetric oxidation of a single phase.

Results

Eu_2O_3-TiO_2 binary: This join was investigated up to 1500°C in air and under controlled oxygen activities. It contains the cubic pyrochlore, $Eu_2Ti_2O_7$ (a_o = 10.192 A°) and an equimolar phase, Eu_2TiO_5, whose x-ray reflections could be indexed on the monoclinic cell with a_o = 15.82 A°, b_o = 5.34 A°, c_o = 15.76 A° and β = 92.°29'. At 1400°C $Eu_2Ti_2O_7$ is the stable phase above oxygen activities of 10^{-11}. When P_{O_2} becomes less than 10^{-11}, $Eu_2Ti_2O_7$ reduces to $EuTiO_3$.

TiO_2-Ti compositions plus Eu: The EuO-TiO_2 join should, from crystal chemical data, be analogous to the SrO-TiO_2 and thus contain 2:1, 3:2, and 1:1 compounds. Only the 1:1 ($EuTiO_3$) compound was formed even though several different starting mixtures (EuO-TiO_2, EuO-$EuTiO_3$, Eu_3O_4-TiO etc.) and temperatures were tried.

The Magneli phases, Ti_nO_{2n-1}, accept only slight amounts of Eu. A typical phase assemblage at 5 mole % Eu_2O_3 is Magneli phase EuTiO_3.

The Eu_2O_3-Ti_2O_3 join was found to contain only the 1:1 compound, $EuTiO_3$.

The Ti-rich end of the ternary diagram is quite interesting because of the existance of a $(Eu,Ti)O_x$ crystalline solution having a moderately wide stability field. Hexagonal Ti metal takes up oxygen in an interstial crystalline solution which greatly affects the c_o parameter but leaves the a_o parameter relatively unchanged[8]. Thus x in $(Eu,Ti)O_x$ can be determined from 001 reflections (i.e. those which depend only on c_o) end the presence of Eu can be determined from hk0 reflections (those which depend only on a_o). Starting compositions

of $EuTiO_3$-Ti and Eu-Ti were studied at 900°C. Titanium metal accepts roughly 8 mole% $EuTiO_3$ and 30 mole% Eu. Runs in the EuO-TiO-Ti region showed $(Eu,Ti)O_x$ with x in the range 0 to approximately 0.5 to have a wide stability range. Increasing in Eu content appears to decrease the upper limit of x for the $(Eu,Ti)O_x$ stability field.

Eu_2O_3-EuO compositions plus Ti: Eu_2O_3 and EuO appear to accept little Ti while Eu_3O_4 accepts approximately 5 mole% Ti_2O_3 and TiO. Phase assemblages further into the ternary consist of $EuTiO_3$ plus one or two Eu oxides.

EuO-TiO: The EuO-TiO join is apparently not binary. Several starting mixtures whose bulk compositions lie on this join (EuO-TiO, Eu_3O_4-$TiO_{.8}$, $EuTiO_3$-Ti) gave products which lie in the oxygen rich and oxygen poor regions of the diagram.

$EuTiO_3$: $EuTiO_3$ is found to exist in two-phase and three-phase regions over a large portion of the diagram. It is found coexisting, within a few mole% of the Magneli phases, Eu_2O_3, Eu_3O_4, EuO, $(Eu,Ti)O_x$ and TiO.

References

1. Porter, Vernon, Ph.D. Dissertation, Pennsylvania State University (1965).

2. Barnighausen, H. J. Prakt. Chem. 34, 1 (1966).

3. Shafer, M. W. J. Appl. Phys. 36, 1145 (1965).

4. Guerci, C. F. and Shafer, M. W. J. Appl. Phys. 37, 1406 (1966).

5. Brixner, L. H. Inorganic Chemistry 3, 1065 (1964).

6. Brous, J., Fankuchen, I. and Banks, E.   Acta Cryst. $\underline{6}$, 67 (1953).

7. Holzapfel, A. and Sieler, J.   Zeit. für anorg. u. allgem. chem. $\underline{343}$, 174 (1966).

8. Bumps, E., Kessler, H. and Hansen, M.   Trans. Am. Soc. Metals $\underline{45}$, 1008 (1953).

Some Tensimetric Studies of the System $Ce_yTb_{1-y}O_x$

J. Kordis, E. I. DuPont de Nemours and Company, Experimental Station,
Wilmington, Delaware, and LeRoy Eyring, Department of Chemistry,
Arizona State University

ABSTRACT

The isobaric technique applied to a study of P, T, x relationships
has proved to be a powerful method of revealing the intricacies of the
complex phase relationships in the pure PrO_x and TbO_x systems. The sorting
out of this pattern of ordered intermediate phases of narrow ranges of
composition (homologous series), phases of wide composition range (non-
stoichiometric phases), "pseudo phase" formation which accompanies phase
reactions with symmetry reduction, and chemical hysteresis which is
generally observed in two phase regions, will advance our understanding
of the detailed nature of the solid state and the reactions which solids
undergo.

A study of the system $Ce_yTb_{1-y}O_x$ has been accomplished to reveal the
effect of cation substitution between analogous systems on their thermo-
dynamic behavior as revealed by tensimetric measurements. Mixed oxides
were prepared at intervals of 10 atom percent cerium and isobaric studies
made at oxygen pressures between 10^{-3} and one atmosphere. For one partic-
ular mixed oxide, $Ce_{0.2}Tb_{0.8}O_x$, isothermal studies (10^{-5} to one atmosphere)
were carried out as well.

To a first approximation there is no valency stabilization of the
TbO_x by the presence of CeO_x, however, a careful examination of the iso-
bars reveals the existence of a widely nonstoichiometic phase in the
mixed system which is observed in the pure PrO_x system but not in the
pure TbO_x studies reported at an earlier rare earth conference. In addi-
tion, apparent hysteresis and pseudo phase formation appear which are
characteristic of the behavior of the pure TbO_x and PrO_x systems. There
is a general "smearing out" of the isobars indicating less definite in-
termediate phases of narrow composition range and two-phase regions al-
though both are indicated in some instances.

Introduction

Cerium, praseodymium and terbium are the only lanthanides known to
exist in both the +3 and +4 oxidation states. The metal – oxygen systems
of these three elements are of considerable complexity due to the appear-
ance of a number of discrete intermediate phases in the composition in-
terval between dioxide and sesquioxide. Structurally, the intermediate
phases are closely related to the fluorite phase of the dioxide, from
which they are thought to be generated through the ordered abstraction

of oxygen[1,2]. In the case of the PrO_x[3,4] and TbO_x[5] systems it has been convincingly demonstrated that the compositions of all the phases present can be represented by a general formula, R_nO_{2n-2}; it seems likely that this also applies to the CeO_x system, although originally a different homologous series had been proposed for this system[12]. The present conceptions on the high temperature phase relationships in these systems derive almost exclusively from tensimetric studies[3-11].

With the individual oxide systems satisfactorily defined, the $(Ce,Tb)O_x$ system was chosen to extend the tensimetric studies to binary combinations of these oxides which would provide additional information essential to an understanding of the nature of the defect structure of these complex systems.

Experimental Part

Preparation of Mixed Ceria - Terbia

As starting materials $TbO_{1.5}$ (99.9+% purity) and ceric ammonium nitrate (99.98% purity) were used. The mixed oxides were carefully co-precipitated from an aqueous nitrate solution as the oxalates, followed by ignition in air to 900°C for 24 hours. Nine mixed oxide samples, at 10 atom percent intervals of the metallic constituents, were prepared.

Measurement of Oxygen Dissociation Pressures

The thermobalance technique employed was substantially the same as that used previously in the isobaric studies of PrO_x[4] and TbO_x[5]. Oxygen pressures were measured with a cathetometer levelled at a mercury filled precision bore U-tube manometer (internal diameter 20 mm). Sample temperatures were obtained with a Pt-Pt/10% Rh thermocouple located just below the sample container and enclosed within the silica reaction tube where the sample was suspended. The chart-recorded temperature was calibrated against a certified National Bureau of Standards Pt-Pt/10% Rh thermocouple.

The tensimetric studies, with one exception in the case of the $Ce_{0.2}Tb_{0.8}O_x$ mixed oxide, were confined to isobaric runs. With the aid of a temperature programmer the isobars were obtained as continuous curves. Linear heating and cooling rates of ~ 1.3°C/minute were employed.

Isothermal studies on the $Ce_{0.2}Tb_{0.8}O_x$ mixed oxide were carried out in the pressure range $\sim 1 - \sim 10^{-5}$ atmospheres. Pressures below ~ 1 mm Hg were maintained by Cu_2O/CuO mixtures.

Reference Reduction to the Sesquioxide Composition

The greatest difficulties were encountered in establishing the oxygen to total metal ratios, i.e., in assigning values to x in the mixed oxides

$Ce_yTb_{1-y}O_x$. A reference value of x was required in terms of which relative weight differences would yield all other values of x for a given mixed oxide. Clearly, the only choice to be made was between the dioxide, $Ce_yTb_{1-y}O_2$, and the sesquioxide, $Ce_yTb_{1-y}O_{1.5}$. Oxidation to dioxide was ruled out, because of the known difficulties in oxidizing terbia to TbO_2 with molecular oxygen, even at high pressures.

About five grams of the mixed oxide were placed in a platinum boat lined with 0.005" platinum foil, and the reduction carried out in dry hydrogen at about 1200°C for ten days. After completion of the reduction reaction only about one gram from the top of the sample, which was well separated from a reaction zone between platinum and mixed oxide, was skimm off for transfer to the thermobalance. The sample thus placed on the balance was evacuated at $\sim 10^{-4}$ mm Hg to 400 - 600°C before removal of adsorbed gases was complete. The weight at this point was assumed to represent the sesquioxide composition. In the case of the $Ce_{0.2}Tb_{0.8}O_x$ mixed oxide the reductions were carried out with three different samples for periods of four, seven, and fourteen days respectively at the usual temperature of ~ 1200°C. All three samples yielded the same value of x (in $Ce_{0.2}Tb_{0.8}O_x$) for the set of original isobars indicating the same initial composition. A complete isobaric run on a sample reduced for fourteen days was identical with that obtained with the sample used in the original isobaric studies at the same pressure (~ 710 mm Hg); thus the markedly different thermal history in the two cases had no apparent effect on the isobar obtained.

Results and Discussion

Oxygen Compositions of the Mixed Oxides and the Question of Valency Stabilization

In Table 1 the oxygen compositions of the mixed oxides oxidized in one atmosphere of oxygen are reproduced.

Table 1

Maximum Oxidation in One Atmosphere of Oxygen

y	x_1	x_2	x_3
0.100	1.833	1.831	1.836
0.200	1.853	1.856	1.854
0.300	1.871	1.869	1.873
0.400	1.890	1.890	1.891
0.500	1.907	1.915	1.909
0.600	1.928	1.932	1.927
0.700	---	1.955	1.945
0.800	---	1.972	1.963
0.900	---	1.992	1.982

x_1 from Hydrogen Reduction - Reference Composition: $Ce_yTb_{1-y}O_{1.5}$

x_2 from Vacuum Reductions - Reference Composition: $yCeO_2 \cdot (1-y)TbO_{1.5}$
$\equiv Ce_yTb_{1-y}O_{1.5} + 0.5y$

x_3 Assuming No Valence Stabilization: $yCeO_2 \cdot (1-y)TbO_{1.818}$
$\equiv Ce_yTb_{1-y}O_{1.818} + 0.182y$

The compositions are identical with those given by the initial vertical portions of the isobars shown in Figure 2. Vacuum degradation curves are shown in Figure 1. Curves for 99.9% pure terbia and ceria have been included for comparison. The intersection of the linearly extrapolated portions of the curves on either side of the sharp inflection at the highest temperatures was taken to be the composition $yCeO_2 \cdot (1-y)TbO_{1.5}$. It will be seen that the agreement between the data in the first two columns is quite good. The third column represents data based on the assumption that at maximum oxidation in one atmosphere of oxygen the terbium in the mixed oxides retains the same over-all oxidation state as it exhibits in pure terbia under similar conditions (i.e., at the composition $TbO_{1.818}$). Again, agreement of these data with those in the first two columns is satisfactory. These results strongly suggest that for mixed oxides with up to 60 mole percent ceria, in the oxygen composition field penetrated by the isobaric studies, the ceria is wholly present as the dioxide and there is no valency stabilization of terbium; i.e., the mixed oxides are resolv-

able into the components: $yCeO_2 \cdot (1-y)TbO_z$ $[z = (x - 2y)/(1 - y)]$. However, as the cerium content in the mixed oxides increases z becomes very sensitive to errors in x, so that there was no certainty that some valency stabilization had not occurred in the case of the mixed oxides with $y = 0.7$, 0.8 and 0.9, particularly as the discrepancies between the second and third column in Table 1 for these mixed oxides were somewhat larger than for the rest. A reference reduction experiment with $Th_{0.2}Tb_{0.8}O_x$ and $Th_{0.8}Tb_{0.2}O_x$ suggested, if the analogy is justified, that there is no valency stabilization of terbium in $Ce_yTb_{1-y}O_x$ even at the higher level of ceria content. Choice of thoria was governed by the fact that thorium exhibits only the +4 oxidation state under the conditions of these experiments. $Th_{0.2}Tb_{0.8}O_x$, after reduction to the reference composition $Th_{0.2}Tb_{0.8}O_{1.6}$ oxidized in one atmosphere of oxygen to $Th_{0.2}Tb_{0.8}O_{1.853}$ (compared with $Ce_{0.2}Tb_{0.8}O_{1.5} \rightarrow Ce_{0.2}Tb_{0.8}O_{1.853}$), while $Th_{0.8}Tb_{0.2}O_{1.9}$ oxidized to $Th_{0.8}Tb_{0.2}O_{1.964}$ (equivalent to $0.8ThO_2 \cdot 0.2TbO_{1.818}$). $Th_{0.2}Tb_{0.8}O_x$ and $Th_{0.8}Tb_{0.2}O_x$ had been derived from mixed oxalates and were, on reduction to $Th_yTb_{1-y}O_{1.5+0.5y}$ ($yThO_2 \cdot (1-y)TbO_{1.5}$), single phase (face-centered cubic) materials.

Isobaric Studies

The "one atmosphere" isobars (710 - 730 mm Hg) for all the mixed oxides (and 99.9% pure terbia) are shown collectively in Figure 2. The six selected isobars shown in Figure 3 are representative of the data obtained for $Ce_{0.2}Tb_{0.8}O_x$ and must serve to suggest the behavior at other compositions when considered together with those shown in Figure 2. The isobar represents a condensation of the data coming off the thermobalance recorder charts. Suitably spaced abstraction and plotting of a large number of points from these charts made a faithful construction of the isobars possible. The six representative isobars selected for reproduction have been exploded along the temperature axis for greater clarity. Pressures cited in the figures refer to their initial values at the low temperatures.

All these systems exhibit hysteresis effects. Hysteresis has also been observed in PrO_x(3,4), TbO_x(5), but not in the CeO_x system(6,8). Tentatively, the appearance of hysteresis in the PrO_x and TbO_x systems has been rationalized in terms of the existence of microdomain structures (microheterogeneity)(5,14,15). Similar consideration may, perhaps, equally well apply to the mixed oxides.

The $Ce_{0.2}Tb_{0.8}O_x$ isobars (Fig. 3) indicate a greater homogeneity range for the $Ce_{0.2}Tb_{0.8}O_{1.714 + \delta}$ phase as compared to the $Ce_{0.1}Tb_{0.9}O_{1.714 + \delta}$ phase. Also, the $Ce_{0.2}Tb_{0.8}O_{1.82 + \delta}$ phase is further expanded in comparison with the $Ce_{0.1}Tb_{0.9}O_{1.818 + \delta}$ phase. However, the isobaric curves on either side of $Ce_{0.2}Tb_{0.8}O_{1.714 + \delta}$, excluding the "pseudo-phase" to the left of it, are not so nearly horizontal which casts doubts on whether diphasic equilibria are still operative. The apparent hysteresis to the right of $Ce_{0.2}Tb_{0.8}O_{1.714 + \delta}$ is rather small, and disappears completely with the isobars obtained at the higher pressures. These trends are continued in systems of higher ceria content.

It has already been noted that two samples of $Ce_{0.2}Tb_{0.8}O_x$ of widely different thermal histories gave identical isobars at one particular, arbitrarily chosen, pressure of ~ 710 mm Hg. Another sample of $Ce_{0.2}Tb_{0.8}O_x$ was heated to a much higher temperature, ~ 1800°C, in a dynamic vacuum of ~ 10^{-6} mm Hg for three hours. Under these conditions of temperature and pressure, cationic mobility and reduction to the sesquioxide, respectively, are to be expected. However, if there was any tendency towards ordering on the grounds of the size differences of Ce^{3+} and Tb^{3+} ions, and because of the different crystal structures in which the two separate sesquioxide phases exist, it did not manifest itself at the lower temperatures since an isobaric run carried out at ~ 710 mm Hg was the same as those obtained with the two previous samples.

Isothermal Study of the $Ce_{0.2}Tb_{0.8}O_x$ System

The temperature programmed isobaric studies proved to be helpful in providing a fairly rapid scan of the whole $Ce_yTb_{1-y}O_x$ system; but, unfortunately, the experimental temperatures and, particularly, pressures were largely insufficient for deep penetration of the oxygen composition fields. Even where a satisfactory coverage of the oxygen compositions was possible, there remained the continued doubt concerning the attainment of "equilibrium" under the forced pace of temperature change at the rate of ~ 1.3°C/minute. In an isothermal study the sample weight could be followed to constancy over a prolonged period of time, while at the same time the pressure range could be conveniently extended to much lower limits. In any event, comparison of the isothermal and isobaric oxidation and reduction paths is of importance because of the presence of hysteresis.

The $Ce_{0.2}Tb_{0.8}O_x$ mixed oxide was selected on the basis of its greater similarity to the TbO_x system in comparison with mixed oxides of higher ceria content. One other consideration in its choice was the anticipation that the isothermal studies might demonstrate more conclusively the nature of the phase equilibria; i.e., monophasic or diphasic, in the region between ~ $Ce_{0.2}Tb_{0.8}O_{1.714}+\delta$ and $Ce_{0.2}Tb_{0.8}O_{1.82}+\delta$ than was the case with the isobaric runs (Fig. 3).

The results of the isothermal study in the pressure range ~ 1 mm - ~ 760 mm Hg are shown in Figure 4. The oxidation path always proceeded from the point where the sample had been first reduced in high vacuum. After incremental pressure increase to ~ 760 mm Hg, the pressure was then similarly reduced in small steps. Excepting at the two lowest temperatures, 457°C and 377°C, and here only at the lower pressures, weight constancy was attained rapidly after each pressure adjustment. The compression that low pressures suffer on a linear scale is responsible for what looks deceptively like a diphasic region in the 457°C and 377°C isotherms.

For fixed oxygen compositions (x), the isothermal and isobaric oxidation and reduction paths, respectively, give virtually identical pressure - temperature points in all instances, excepting the 1000°C isotherm where

oxidation at the higher pressures is less than would be expected from the isobaric runs. This situation is exactly analogous to what is observed in the pure TbO_x system(11).

The isotherms were extended to lower pressures for all the temperatures shown in Figure 4, except the 377°C isotherm, by the use of a Cu_2O/CuO buffer system. The results at low pressure are reasonably consistent with those at higher pressures in the region of overlap considering the hysteresis effects and the uncertainties in the free energy of the $Cu_2O + 1/2 \ O_2 = 2 \ CuO$ reaction(16).

The most significant features of these results are the indicated stability of $Ce_{0.2}Tb_{0.8}O_{1.714 \ + \ \delta}$ at temperatures between 800° and 400°C at pressures going down to 10^{-5} atmospheres including reversibility between 10^{-5} to 10^{-1} atmosphere oxygen pressure at 608°, and the absence of any horizontal regions that would indicate the presence of two phases. With respect to the latter point, X-ray analysis(13) of well-annealed samples (425°C for six weeks) at closely spaced composition (x) intervals gave also no indication of any diphasic regions between $Ce_{0.2}Tb_{0.8}O_{1.500}$ and $Ce_{0.2}Tb_{0.8}O_{1.853}$.

References

1. L. Eyring and B. Holmberg, "Nonstoichiometric Compounds," Advances in Chemistry Series No. 39 (American Chemical Society), 1963.

2. J. O. Sawyer, B. G. Hyde and L. Eyring, Bull. Soc. Chim. France, 1190 (1965).

3. J. M. Honig, A. F. Clifford and P. A. Faeth, Inorg. Chem. 2, 791 (1963).

4. B. G. Hyde, D. J. M. Bevan and L. Eyring, Phil. Trans. Roy. Soc. (London), Series A, 259, 583 (1966).

5. B. G. Hyde and L. Eyring, "On Phase Equilibria and Phase Reactions in TbO_x - O_2 and Related Systems," in Rare Earth Research III, Gordon and Breach, New York, 1965.

6. G. Brauer, K. A. Gingerich and U. Holtschmidt, J. Inorg. Nucl. Chem. 16, 77 (1960).

7. F. A. Kuznetsov, V. I. Belyi and T. N. Rezukhina, Dok. Akad. Nauk, S.S.S.R. 139, 1405 (1961).

8. D. J. M. Bevan and J. Kordis, J. Inorg. Nucl. Chem. 26, 1509 (1964).

9. E. D. Guth and L. Eyring, J. Am. Chem. Soc. 76, 5245 (1954).

10. R. E. Ferguson, E. D. Guth and L. Eyring, J. Am. Chem. Soc. 76, 3890 (1954).

11. J. Kordis and L. Eyring, unpublished work.

12. D. J. M. Bevan, J. Inorg. Nucl. Chem. 1, 49 (1955).

13. J. Kordis and L. Eyring, unpublished work.

14. P. A. Faeth and A. F. Clifford, J. Phys. Chem. 67, 1453 (1963).

15. B. G. Hyde, "Order, Stoichiometry and Reactivity of Metal Oxides," paper presented at the Gordon Conference on High Temperature Chemistry, July 1964.

16. O. Kubaschewski and E. Evans, Metallurgical Thermochemistry, Pergamon Press, New York, 1958.

Figure 1

Vacuum Degradation Curves for $Ce_yTb_{1-y}O_x$

Figure 2

Atmospheric Pressure Degradation Curves for $Ce_yTb_{1-y}O_x$

Figure 3

Selected Isobars for the $Ce_{0.2}Tb_{0.8}O_x-O_2$ System

Figure 4

An Isothermal Study on the $Ce_{0.2}Tb_{0.8}O_x-O_2$ System

$Ce_yTb_{1-y}O_x$

TEMPERATURE

$Ce_yTb_{1-y}O_x$

TEMPERATURE

PRESSURE, mm Hg

$Ce_{0.2}Tb_{0.8}O_x$

1000°C

500°C

392

215

107

420

100

420

1 600   1 700   1 800
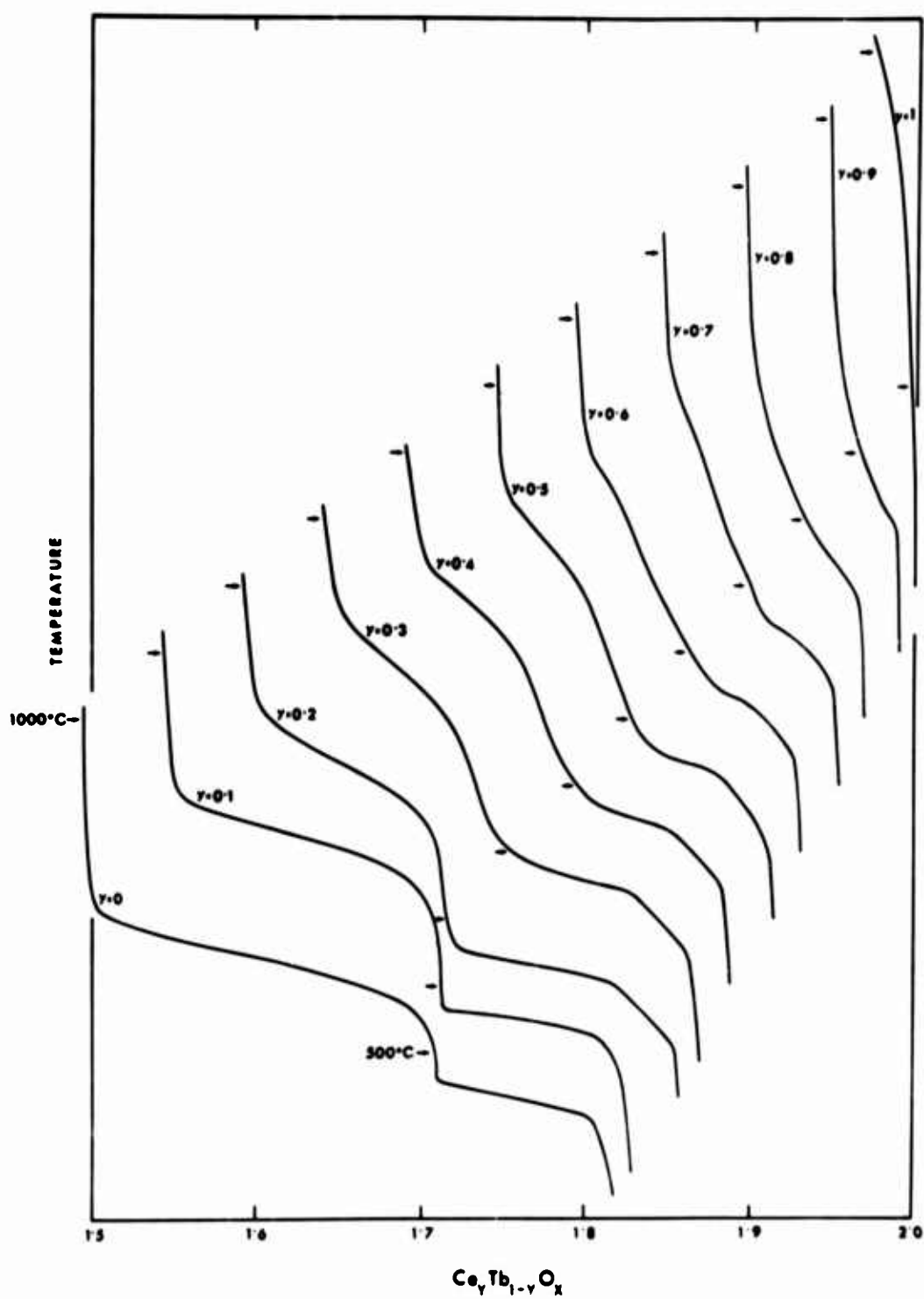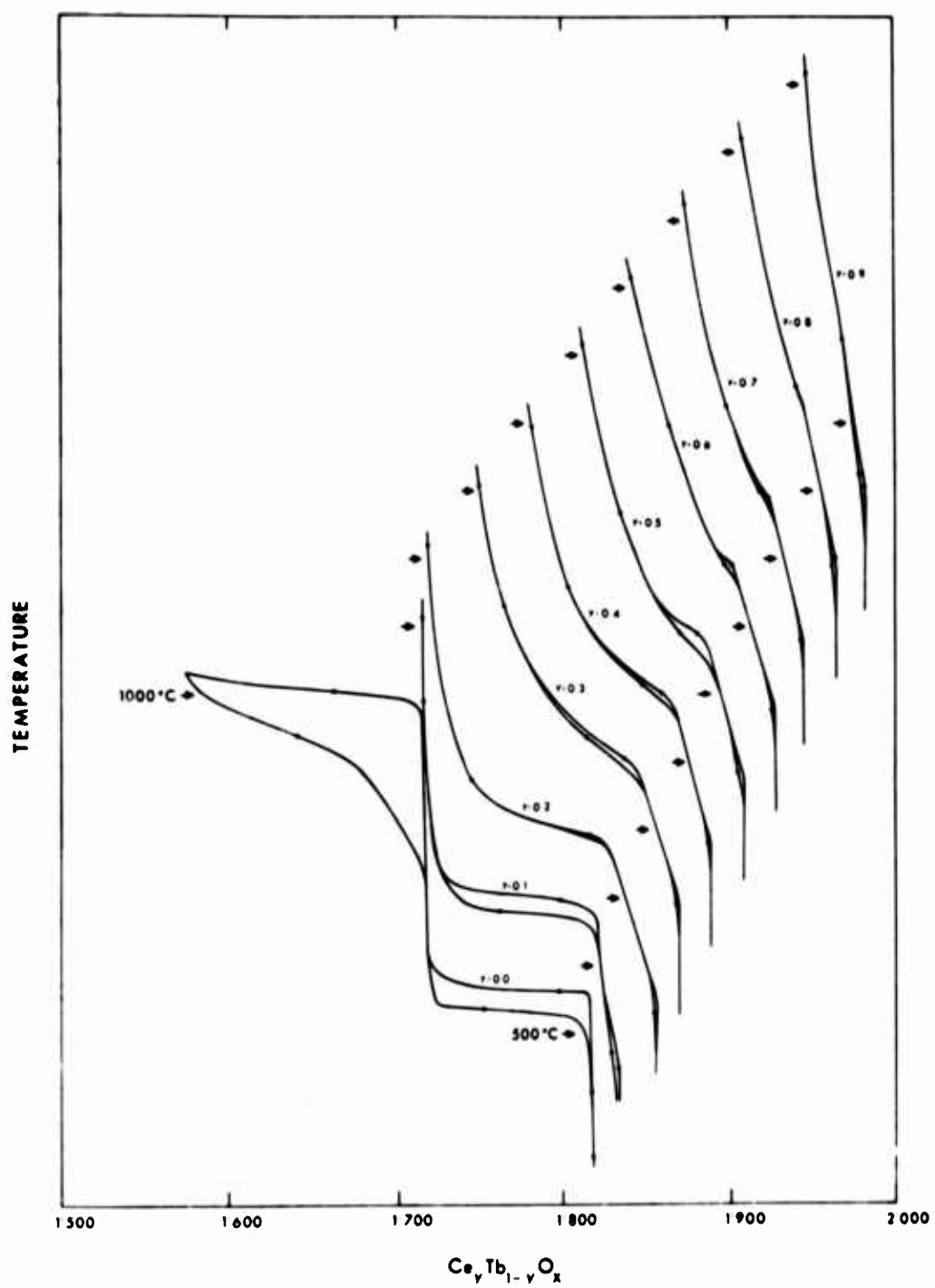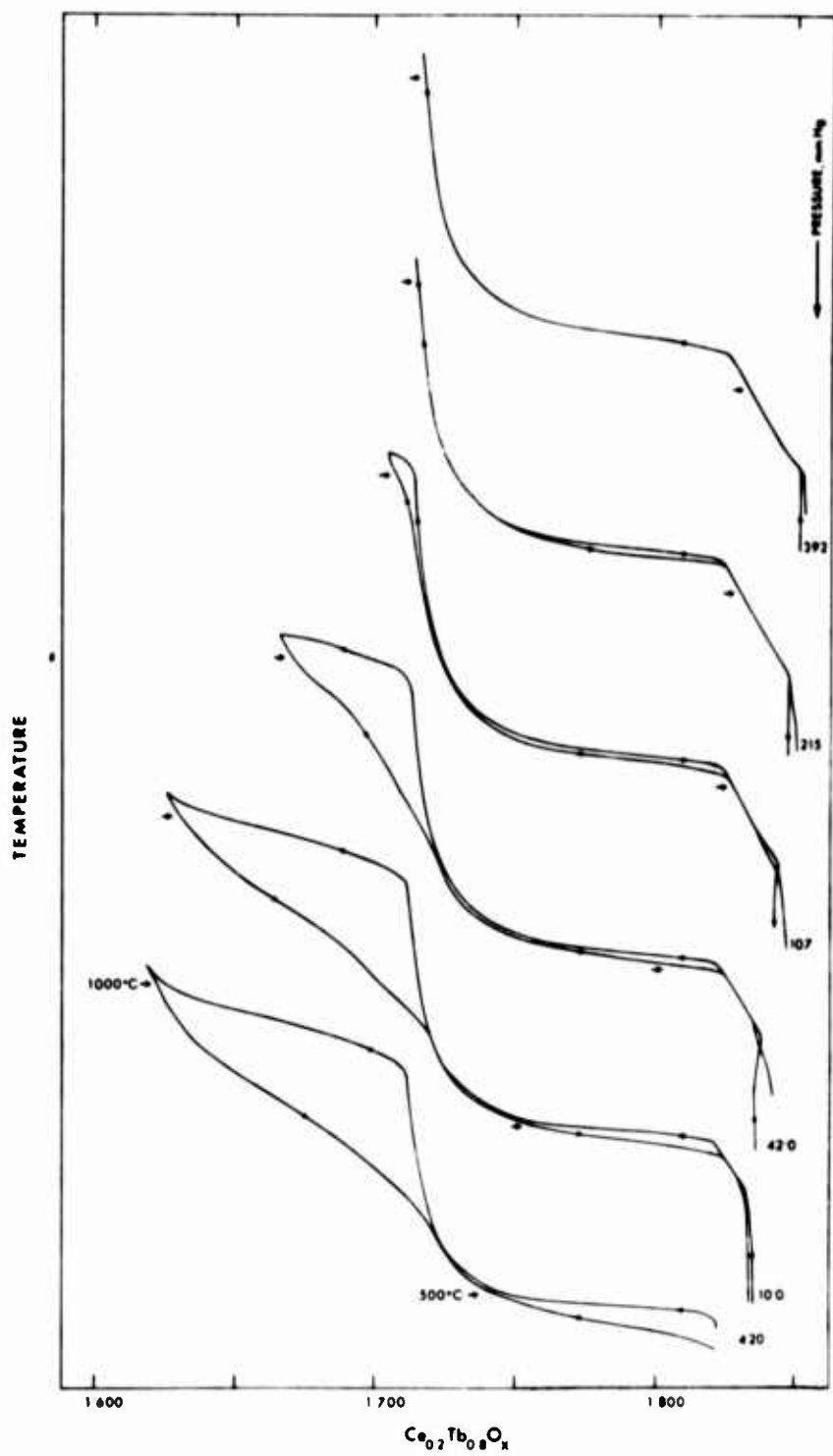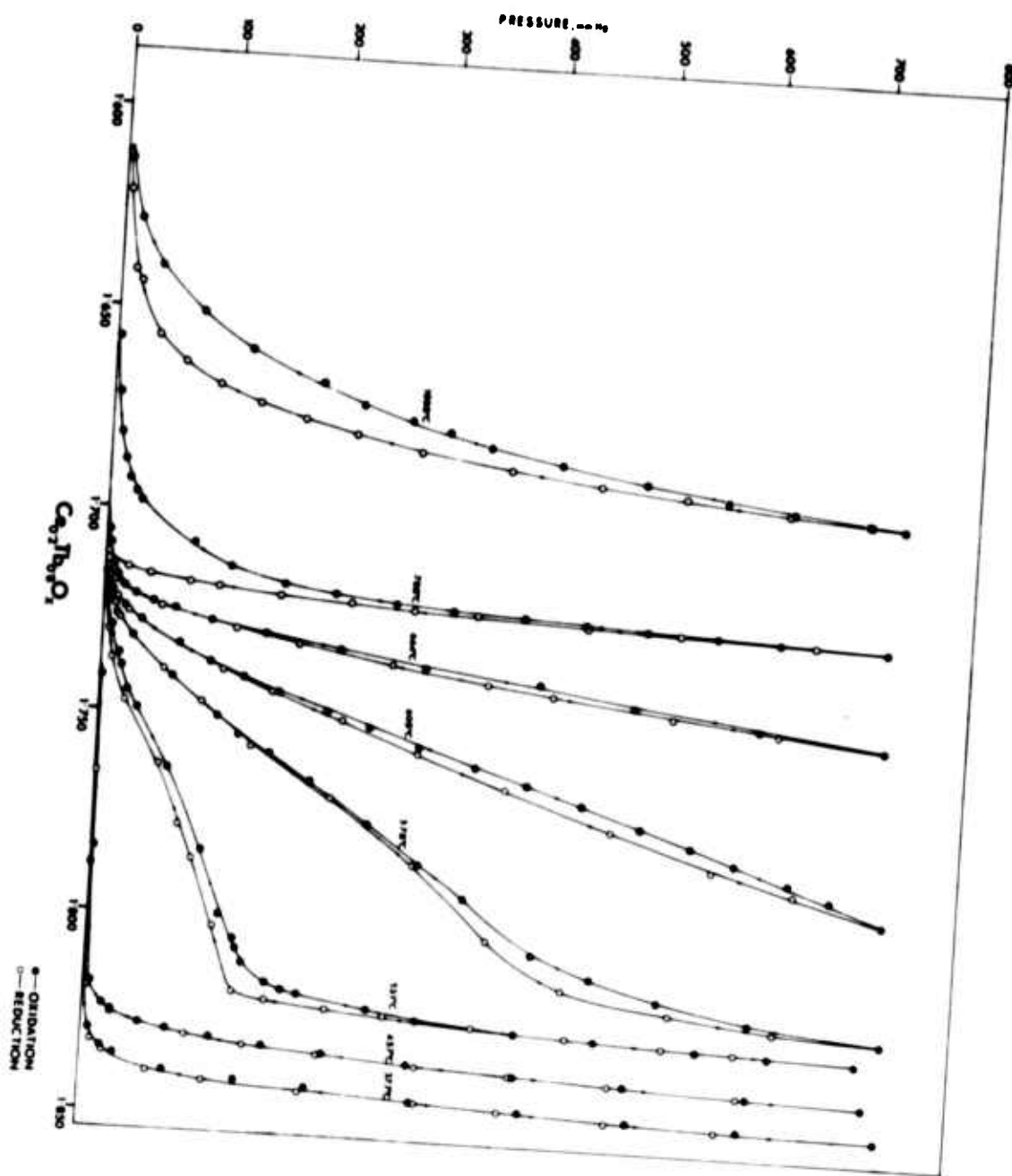
EQUILIBRIA, POINT DEFECT NATURE AND KINETICS IN THE

SYSTEMS OF RARE EARTHS AND DI- OR TETRAVALENT OXIDES*

by

Rustum Roy, A. M. Diness**, and T. L. Barry***

Materials Research Laboratory
The Pennsylvania State University
University Park, Pennsylvania

ABSTRACT

Detailed investigation by quenching, DTA, high temperature, x-ray and high-pressure water catalysis have been made on the systems $CaO-Yb_2O_3$, $CaO-Gd_2O_3$, $CaO-La_2O_3$, $ThO_2-Yb_2O_3$, $ThO_2-Gd_2O_3$, and $ThO_2-La_2O_3$. The results include the following:
1) New or revised equilibrium diagrams are presented for all the systems.
2) A most surprising feature is the large number of new compounds previously unreported. In the $CaO-Yb_2O_3$ system for example, there are four compounds -- all decomposing below 1800°C. In the $ThO_2-La_2O_3$ system, there are two previously unreported compounds.
3) The extent of crystalline solubility of the rare earths in CaO and ThO_2 does not follow the expected dependence on ionic radii or ionic field strength differences.
4) An anion vacancy model is confirmed for ThO_2(matrix)-Ln_2O_3(solute) solutions near 1900°C; a cation vacancy model for $CaO-Ln_2O_3$; and an interstitial anion model for the $Gd_2O_3-ThO_2$ - - an extensive new series of crystalline solutions with the C-type structure.
5) The kinetics of the solid state decomposition of $CaYb_2O_4 \rightarrow CaO + Yb_2O_3$ follows zero order kinetics. Interpretation of these and similar kinetic data to be discussed will be shown to be quite interesting.

The System $CaO-Yb_2O_3$

Four new crystalline phases were detected in the $CaO-Yb_2O_3$ system:[1] $Yb_2O_3:3CaO$, $Yb_2O_3:2CaO$, $Yb_2O_3:CaO$, and $2Yb_2O_3:CaO$. However, only the first three are stable under equilibrium conditions. The fourth phase, $2Yb_2O_3:CaO$, has been obtained only from the melt. Maximum crystalline solubility of Yb_2O_3 in CaO was determined to be slightly greater than 8 mole percent between 1850° and 2150°C, while no measurable solubility

of CaO in Yb_2O_3 was detected. All four compounds in this system dissociate into CaO plus Yb_2O_3 at temperatures below 1800°C. The entire system as summarized in Figure 1 is surely novel in oxide systems studied to date. Moreover, the compounds in this system provided examples for the study of decomposition kinetics of type $A_s \rightarrow B_s + C_s$

The System $CaO-Gd_2O_3$

A single compound $CaO:2Gd_2O_3$ exists in the system. This compound has the same stoichiometry as the metastable phase in the $CaO-Yb_2O_3$ system. Quenched melts of this 1:2, rare earth rich, composition yield x-ray patterns identical with the 1:2 compound prepared by subsolidus reaction, thus indicating the congruent melting nature of the compound. Specimens of this compound prepared at 1850°C and reheated below 1600°C show the subsolidus dissociation of the compound to a CaO crystalline solution plus B-type Gd_2O_3 in the temperature region 1600°C to 1150°C and to CaO crystalline solution and C-type Gd_2O_3 below 1150°C.

The crystalline solubility limit of Gd_2O_3 in the CaO lattice is slightly less than 6 mole percent between 1600 and 2100°C. A 2 mole percent CaO-98 mole percent Gd_2O_3 mixture reacted at 1850°C contained a substantial amount of a second phase, showing that the solubility, if any, of CaO in Gd_2O_3 is considerably less than 1 mole percent.

The System $CaO-La_2O_3$

Neither compound formation nor appreciable solubility of either end member in the other was observed. These results therefore agree with those of Rabenau[2], who studied the ternary system involving this binary with ZrO_2 at 1400°C. By using a method developed for calculating crystalline solubility limits, which is presented elsewhere[3], the solubility limit of La_2O_3 in the CaO lattice was determined to be 0.40 mole percent. No solubility of CaO in the rare earth oxide was detected.

The System $La_2O_3-ThO_2$

Two new crystalline phases were found in the $La_2O_3-ThO_2$ system[4] (Figure 2) under equilibrium conditions: $4La_2O_3:ThO_2$ and $2La_2O_3:ThO_2$. Both compounds exhibit interesting temperature stability minima. The 4:1 compound dissociates below 1000°C into La_2O_3 and ThO_2 crystalline solutions (cs). The 2:1 compound dissociates into $ThO_2(cs)$ and the 4:1 compound. Crystalline solubility of La_2O_3 in ThO_2 was determined to be approximately 35 mole percent at 1800°C and 39 mole percent at 1940°C (the eutectic temperature). Little, if any, crystalline solubility of ThO_2 in the A-type La_2O_3 was evidenced up to 1700°C. There results are in marked contrast to the few limited reports in the literature[5,6]. It is believed that these different firing procedures used favored metastable persistance of starting material structures and thus inhibited formation and identification of intermediate compounds in the systems. In addition, impurities present in earlier investigations might have interfered with the mixing and segregation processes
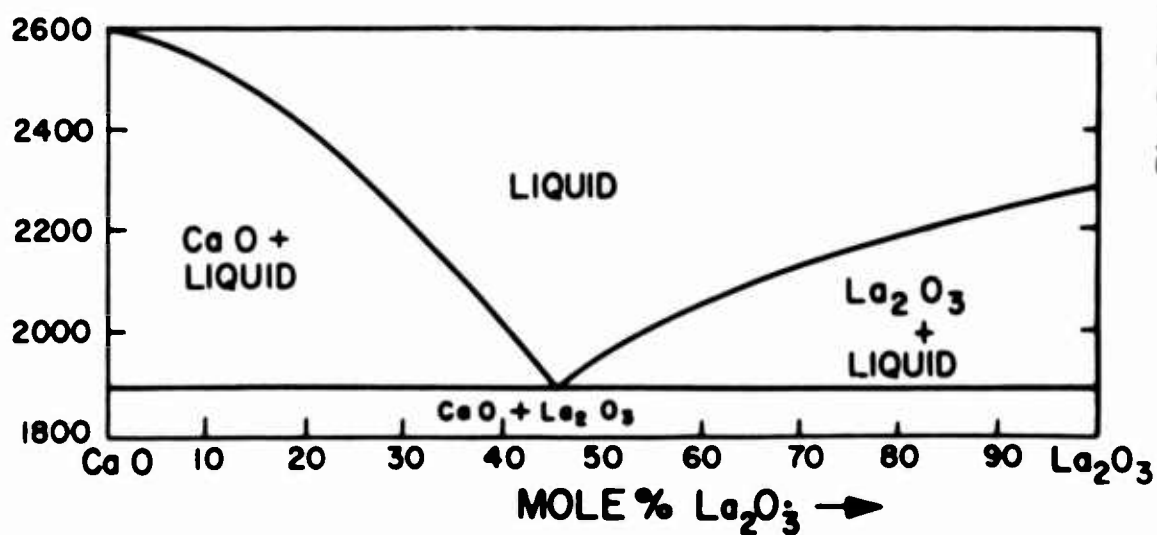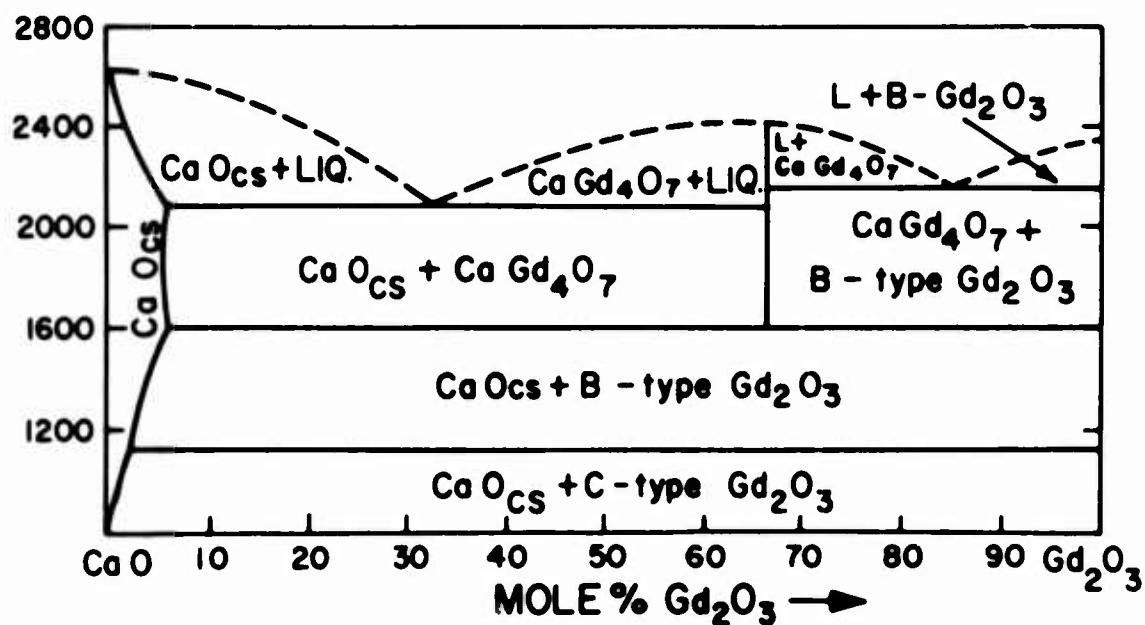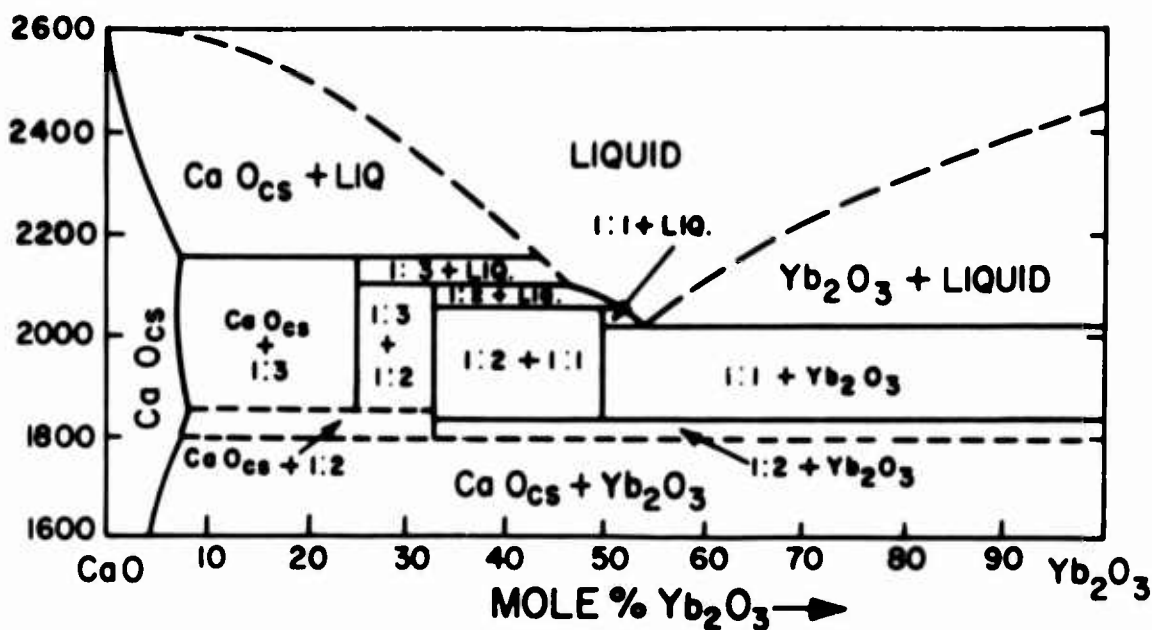
Fig.1 Phase Equilibria in the Systems CaO–La$_2$O$_3$, CaO–Gd$_2$O$_3$, CaO–Yb$_2$O$_3$
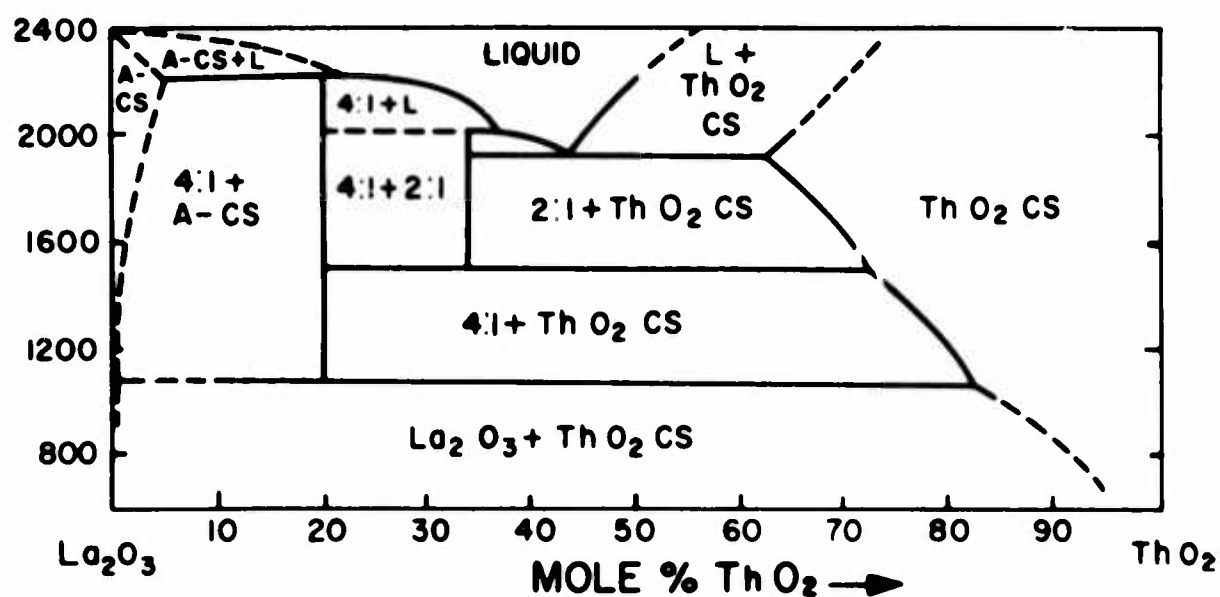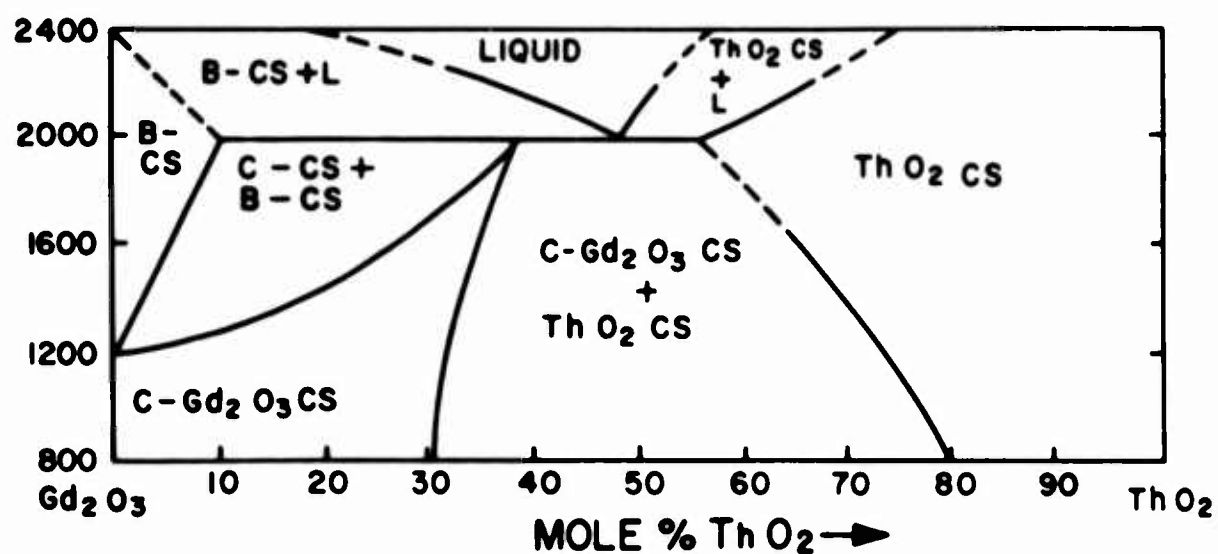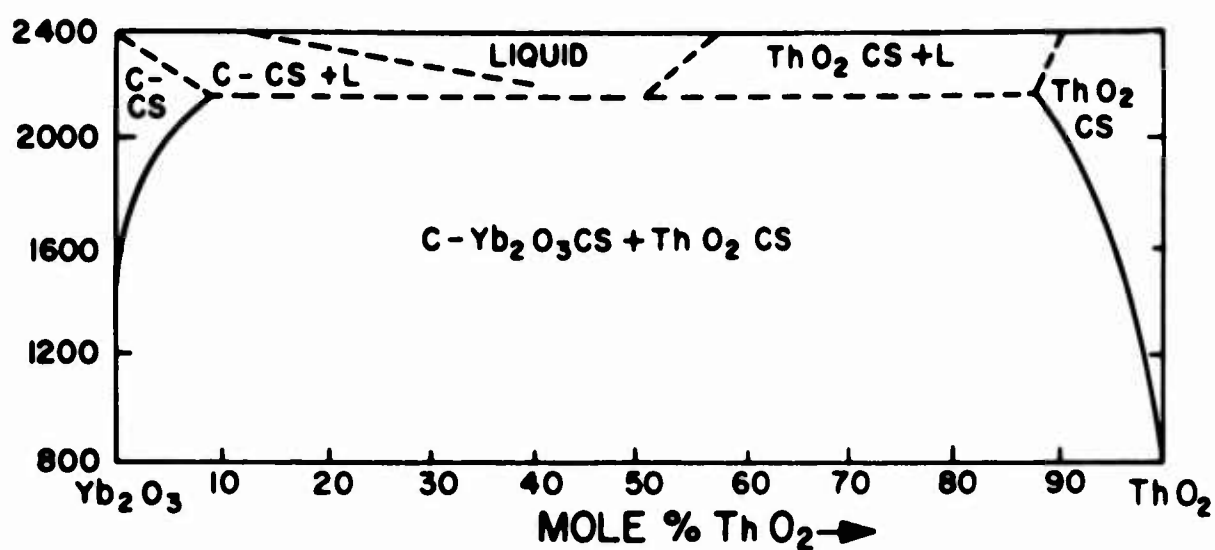
Fig.2 Phase Equilibria in the Systems $ThO_2-La_2O_3$, $ThO_2-Gd_2O_3$, $ThO_2-Yb_2O_3$

necessary for compound formation and subsequent phase segregation.
At the low temperature previously used, cationic mobility in these
materials is too low to be practically useful for reactions involving
cationic transport.

The System Gd_2O_3 -ThO_2

In the system Gd_2O_3-ThO_2, the fluorite crystalline solution field is
quite extensive. Approximately 19 mole percent Gd_2O_3 is dissolved in
ThO_2 at 800°C. This field widens to approximately 45 mole percent
Gd_2O_3 in ThO_2 at the eutectic temperature, 2000°$\pm$ 50°C. A new finding
is the extensive field of the C-type crystalline solution (greater
than 25 mole percent at 1800°C, 38 mole percent at 2000°C). The poly-
morphic C- to B-type Gd_2O_3 inversion temperature is raised substan-
tially by raising the ThO_2 content. The greatest cause of the dis-
crepancies between earlier work[5] and this investigation is most prob-
ably in the manner and extent of approach to equilibrium. The hydro-
thermal conditions superimposed upon the system aided greatly in re-
solving the subsolidus equilibria in the low temperature region of
the diagram.

The System Yb_2O_3-ThO_2

Yb_2O_3 is only moderately soluble in ThO_2 (10 mole percent at 1925°C).
Only small solubility of ThO_2 in the C-type Yb_2O_3 was noted (approx-
imately 3 mole percent ThO_2 at 1800°C). Good agreement exists with
earlier work[9] in comparing major features of phase equilibria involved.
No other features of note were detected in this system.

Extent of Crystalline Solubility

A summary of crystalline limits for rare earth sesquioxides in ThO_2
(fluorite field) is presented in Figure 3 as a function of (Gold-
schmidt) ionic radius. The curves and regions specified in this dia-
gram were included only to indicate trends in crystalline solubility.
Consideration of size alone would indicate a maximum solubility at
gadolinium with solubility dropping off when the ionic radius is
either increased or decreased from the value corresponding to this
element. A similar argument can be made for the set of systems CaO-
La_2O_3,CaO-Gd_2O_3,CaO-Yb_2O_3. It can be seen that crystalline solubility
predictions based upon size considerations alone (Ahrens or Goldschmidt)
are inadequate, even qualitatively, for such systems. An integrated
approach to the effect of various factors upon crystalline solubility
limits of a foreign ion in a host matrix has been attempted by use of
field strength considerations, which combine ionic size and charge
into one term. In oxide systems, differences in field strength values
of the order of $\pm$0.05 usually yield extensive or complete crystalline
solubility, while compound formation commonly occurs between cations
differing by approximately $\pm$0.30 in field strength. Thus, it might be
expected that if the difference in field strength decreases as one
compares members of the rare earth family with some common cation
(e.g., Ca^{2+} or Th^{4+}) the extent of crystalline solubility of the par-
ticular rare earth ions in CaO or ThO_2 would increase. However, of the
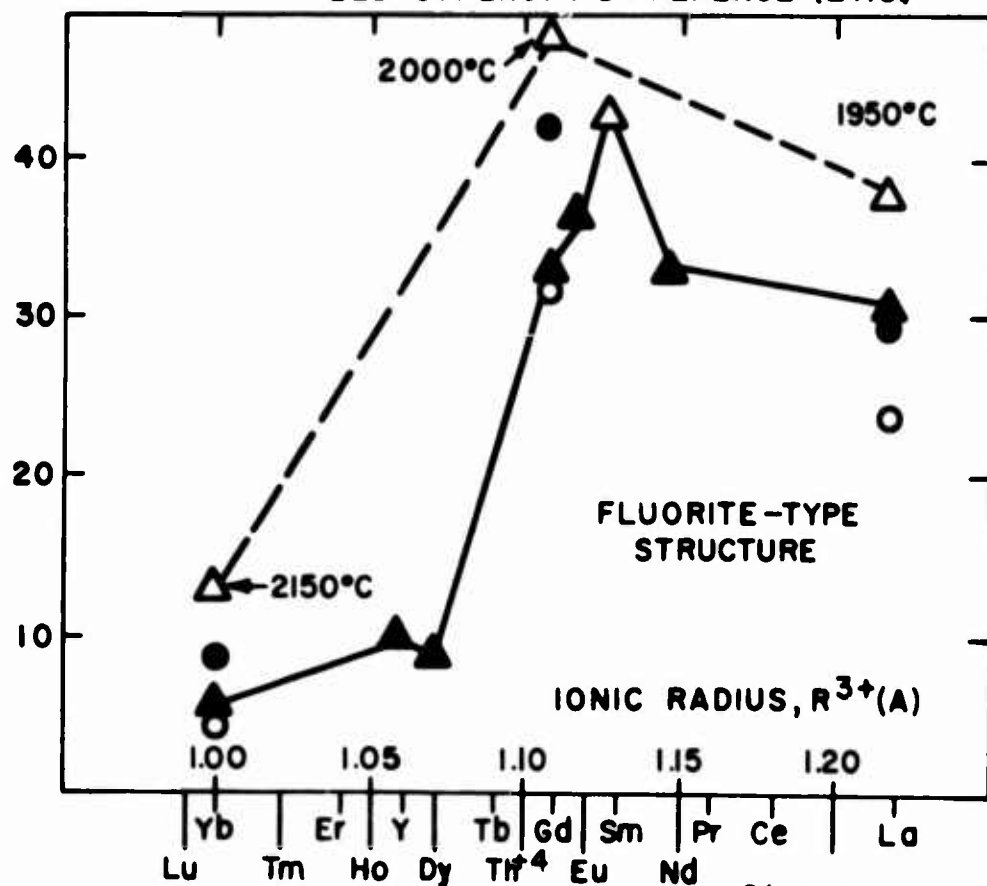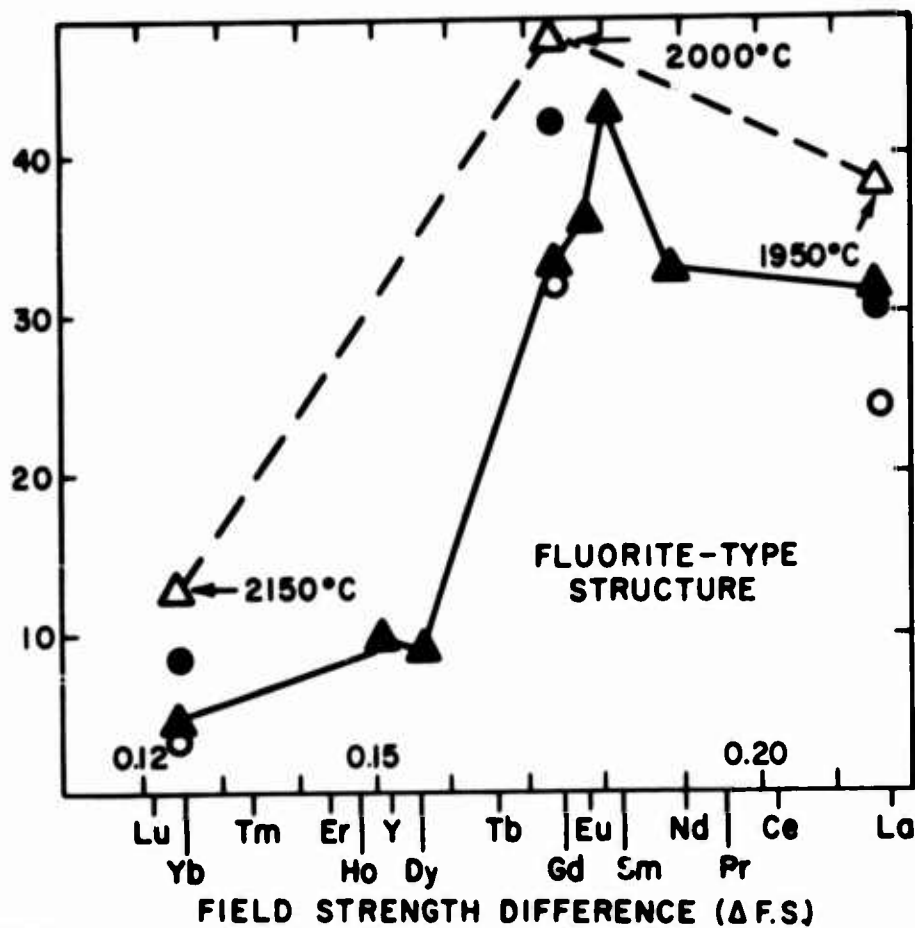
Fig. 3 Solubility limits, Ln^{3+} in ThO_2

three rare earth oxide-CaO systems studied in detail, this was not found to be true. In fact, the direct opposite of what was expected from this simple consideration was observed, using values of 0.99 Å, 1.14Å, 0.96Å, and 0.86Å, as radii for Ca^{2+}, La^{3+}, Gd^{3+}, and Yb^{3+}, respectively, in the systems $CaO-Ln_2O_3$. The differences in field strength are 0.115, 0.184, and 0.237, respectively. Thus, one would expect La_2O_3 to have the greatest solubility in CaO of the three rare earth oxides. The maximum solubility of La_2O_3 in CaO was determined to be 0.40 mole percent at 1850°C. The maximum solubilities of Gd_2O_3 and Yb_2O_3 in CaO at 1850°C were determined from plots of lattice constants of the crystalline solutions versus composition. The solubility of Gd_2O_3 in CaO is just slightly less than 6 mole percent while slightly more than 8 mole percent of Yb_2O_3 may be taken into the CaO lattice. The relative field strengths of the rare earth ions (Th^{4+} as basis of comparison, Figure 3) did not reach the 0.3 level. The La^{3+} - Th^{4+} set had the highest value, 0.23. On this basis, of any of the rare earth sesquioxide-ThO_2 systems, the La_2O_3 case would be most expected to show compound formation. However, in the prediction of crystalline solubilities the opposite to the results expected from field strength differences holds true; considerably greater extents of crystalline solution field of Ln_2O_3 in ThO_2 at a particular temperature are shown for Gd^{3+} (Δ F.S. = 0.19) and La^{3+} (Δ F.S. = 0.23) than for Yb^{3+} (ΔF.S. = 0.18). In reality, solubility reaches a maximum and then drops off as a function of Δ F.S. The failure of the field strength approach is one indication of the complexity in explaining phase equilibria and crystal chemical relations in these systems.

Characterization of Point Defects in Crystalline Solutions

Precise measurements of lattice parameters and densities were carried out using crystalline solutions in the systems Yb_2O_3-CaO, La_2O_3-, Gd_2O_3- and $Yb_2O_3-ThO_2$[4]. The lattice parameters were employed in calculating density values according to specific defect models. These values were, in turn, compared with the experimental values for density[12]. Thus, by this method, good agreement was found to exist between the experimental densities and (1) the cation vacancy model, in which Yb^{3+} substitutes for Ca^{2+} (NaCl structure), (Figure 4), (2) the anion vacancy model, in which Ln^{3+} substitutes for Th^{4+} (fluorite structure), and (3) the anion interstitial model, Th^{4+} substitutes for Gd^{3+} (C-type structure) (Figure 5). It must be kept in mind that the model situations considered are hypothesized as end-member or extreme models in an attempt to interpret experimental data. They represent only a few of many defect situations possible[13]. The hypothesis of interstitial oxygens in the C-type structure is a reasonable one in the light of previous findings in structurally similar fluorite crystalline solutions[14]. It is plausible to have anion interstitials in the C-type crystalline solutions since this structure is related to the fluorite structure by subtraction of one-quarter of the anions. This is in contrast to the NaCl field of the system $CaO-Yb_2O_3$ in which the anion interstitial model was less likely than the cation vacancy case (when Yb^{3+} is substituted for Ca^{2+} in the NaCl-type crystalline

Fig.4 Density vs. Composition for Defective
Crystalline Solutions of Yb_2O_3 in
CaO (NaCl Structure)

Fig.5 Density vs. Composition for
Defective Crystalline Solutions of
ThO_2 in Gd_2O_3(C-type Structure,1300C)
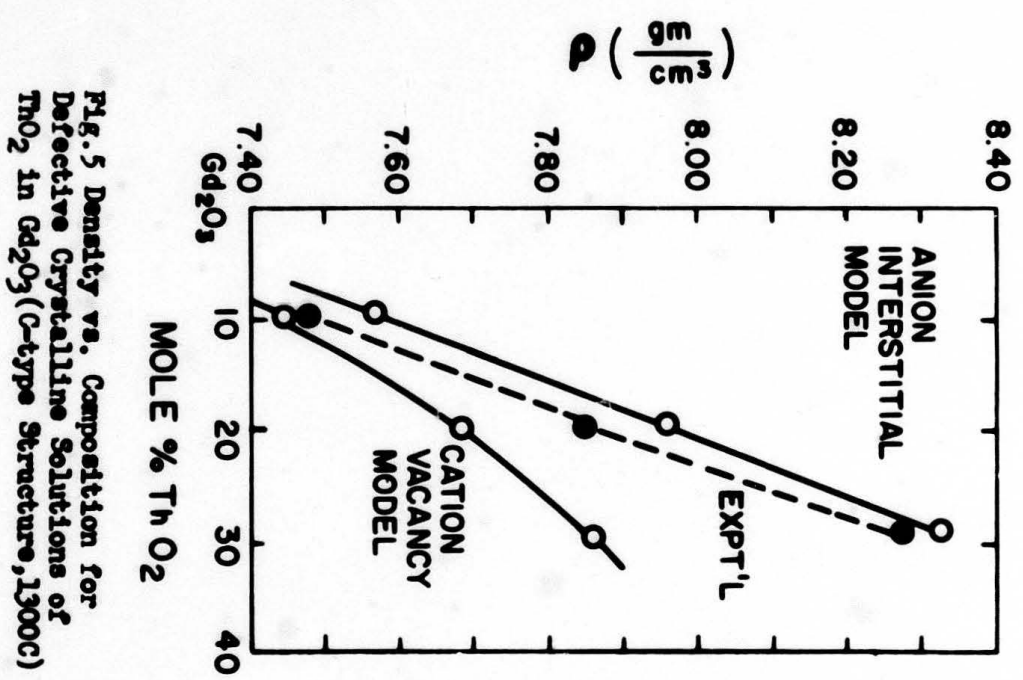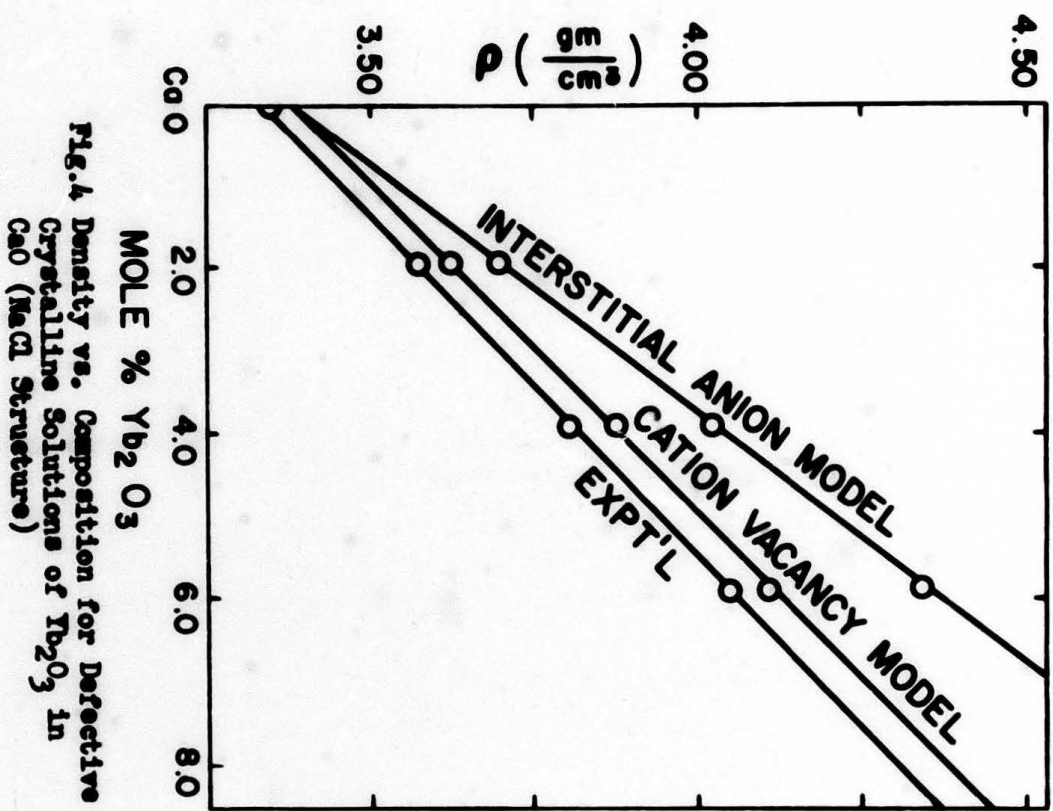
solutions). The cubic close-packed oxygen layers of the NaCl struc-
ture, with cations occupying octahedral holes, makes it necessary
to very greatly increase the lattice energy in order to stuff an
$O^=$ interstitially between those close packed layers. Neutron dif-
fraction studies strengthen the possibility of oxygen intersti-
tials in the large interstitial holes in such fluorite-like materials.[15]

Kinetics of Decomposition of $CaYb_2O_4$

The kinetics of decomposition of $CaYb_2O_4$[3] were studied employing quan-
titative analysis by x-ray diffraction methods employing a modified
method of "standard binary mixtures". This was required as the total
composition always remained constant with only the phase assemblage
changing. The linearity of the fraction reacted, or concentration
unreacted versus time curves obtained at various temperatures
(1000-1150°C) revealed that the decomposition proceeded according
to "zero order" kinetics. From a least squares refinement of the
data in Figure 6, the slopes of the curves (k, the specific
velocity constant) for the four temperatures were determined.
These values of k were used in turn for an Arrhenius plot (Figure 7)
to determine the activation energy. The activation energy obtained
for this process was 100 kilocalories per mole.

REFERENCES

1. T. L. Barry, V. S. Stubican, and R. Roy, J. Am. Cer. Soc., 49, 667 (1966)
2. A. Rabenau, Z. anorg. allgem. Chem., 288, 221(1956)
3. T. L. Barry, Ph.D. Thesis, The Pennsylvania State University, 1964
4. A. M. Diness, Ph.D. Thesis, The Pennsylvania State University, 1966
5. G. Brauer and H. Gradinger, Z. anorg. allg. Chem., 276, 209(1954)
6. F. Hurd and W. Dürrwächter, Z. anorg. allg. Chem., 265, 67(1951)
7. L. Eyring and B. Holmberg, in "Nonstoichiometric Compounds," (R. Ward, editor), pp. 46-57, American Chemical Society, Washington, 1963
8. A. M. Diness and R. Roy, to be submitted to J. Materials Science
9. K. Gingerich and G. Brauer, Z. anorg. all. Chem., 324, 48(1963)
10. A. Dietzel, Z. Elektrochem., 48, 9(1942)
11. T. L. Barry and R. Roy, to be published in the February issue of J. Am. Cer. Soc.
12. F. A. Kröger, "The Chemistry of Imperfect Crystals," p. 240, North-Holland Publishing Co., Amsterdam, 1964
13. W. vanGool, J. Phys. Chem. Solids, 27, 581(1966)
14. J. S. Anderson, D. N. Edington, L.E.J. Roberts and E. Wait, J. Chem. Soc., 1954, 3324; J.S. Anderson and J. Alberman, J. Chem. Soc., 1949, 303; F. Hurd and Niessen, Z. Elektrochem., 56, 972(1952)
15. B.T.M. Willis, Proc. Phys. Soc. (London), Ser A.274, 134(1963)
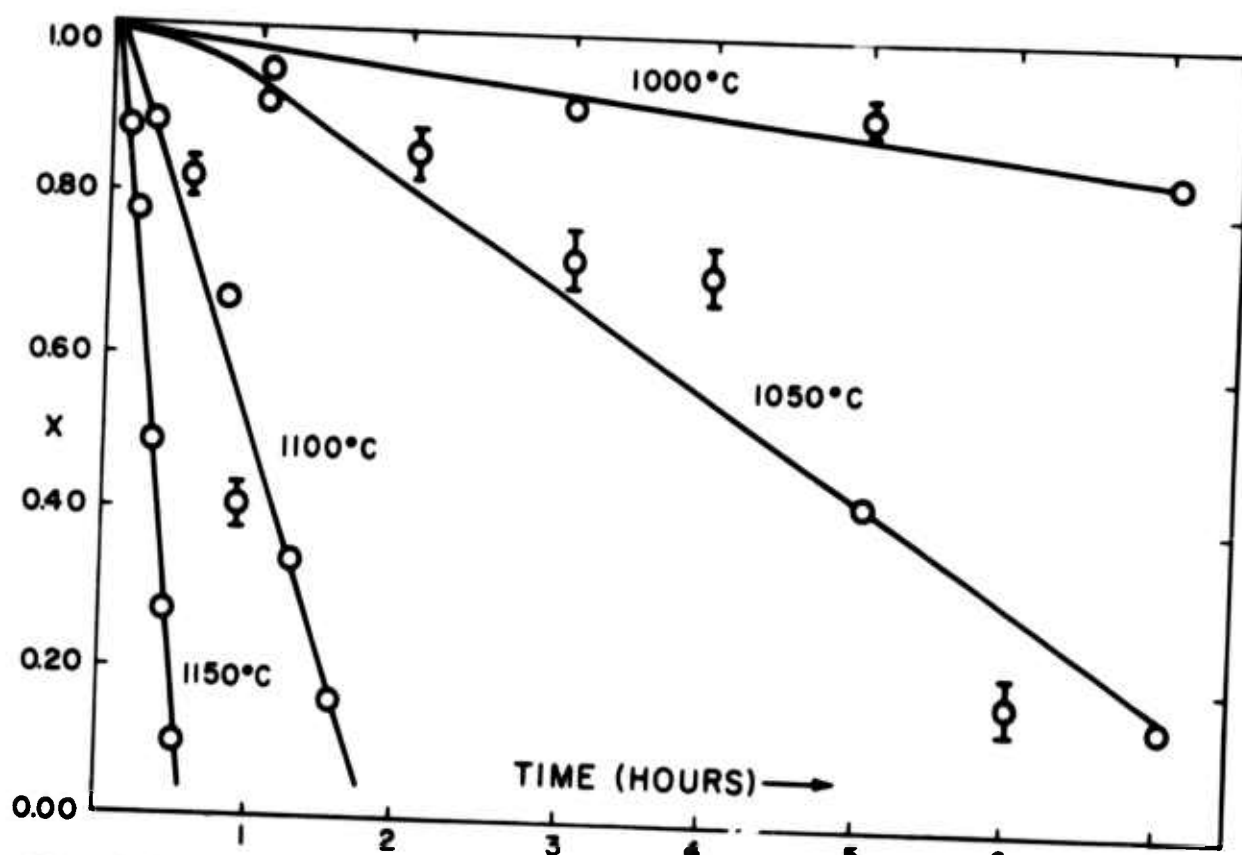
Fig. 6 Concentration Unreacted - Time Curves for $CaYb_2O_4$ at Various Temperatures
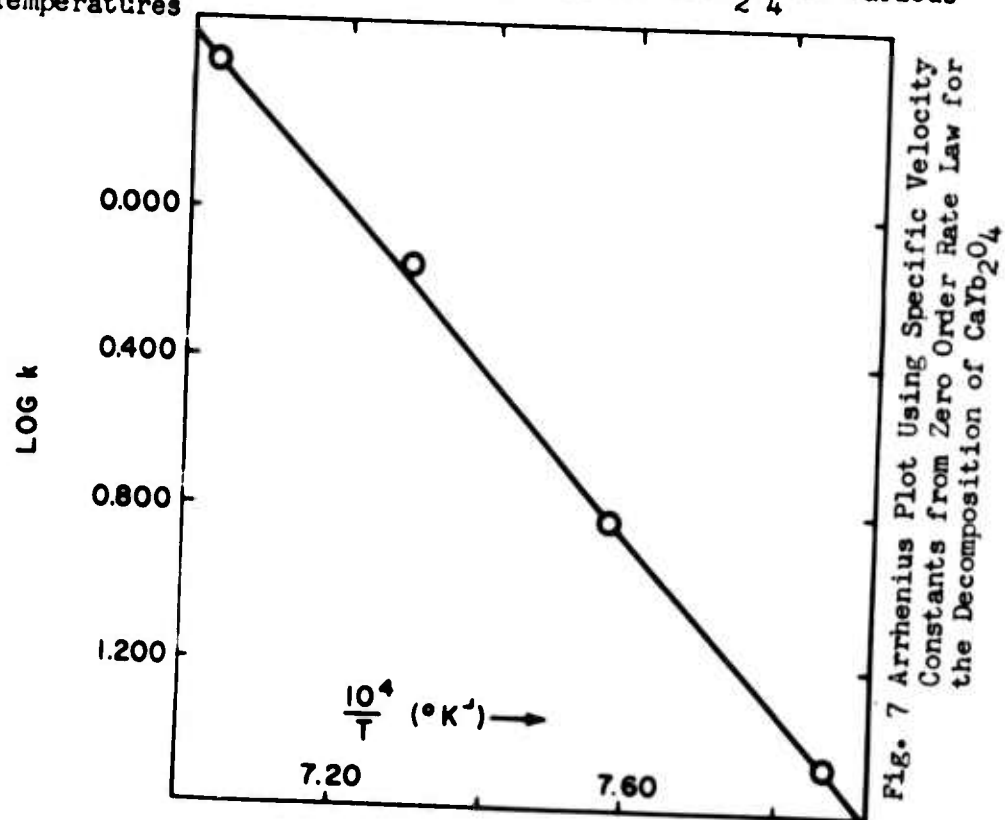
Fig. 7 Arrhenius Plot Using Specific Velocity Constants from Zero Order Rate Law for the Decomposition of $CaYb_2O_4$

Electrical Properties of Rare Earth Oxides and Related Systems

C.N.R. Rao, G.V. Chandrashekhar, P.N. Mehrotra and G.V. Subba Rao
Department of Chemistry, Indian Institute of Technology, Kanpur, India

The electrical conductivities of a number of rare earth sesquioxides
have been measured over a wide range of temperatures. All the sesquioxides show
a break in the conductivity curve around 550°C indicating a change in the
mechanism of conduction. Dependence of the conductivity on the oxygen partial
pressure as well as the thermoelectric power of the sesquioxides have been
investigated. Application of the polaron theory to these systems has been
discussed. The sesquioxides of lanthanum, praseodymium, neodymium and samarium
show breaks in the conductivity curves due to the C→A or C→B phase transformations.
Conductivity data on yttrium oxide does not show any break due to phase
transformation since this reversible transformation occurs over a wide range of
temperatures (350-950°C). Moisture has been found to reduce the temperature c
phase transformation as well as the activation energy for the conduction
process.

Electrical conductivities of non-stoichiometric oxides and the dioxides
of praseodymium and Terbium have been measured at various temperatures and the
activation energies reported. The dependence of the conductivity on oxygen
partial pressure has been examined for a few non-stoichiometric oxides.
Calculation of the Frohlich's coupling constant and the transition probability show
that the small polaron theory is applicable to these systems. The reflectance

spectra of praseodymium and terbium oxides have been determined as a function of the oxygen to metal ratio and minima have been found around a composition of $LnO_{1.75}$.

The crystal structures and electrical conductivities of $CeO_2-Nd_2O_3$ and $CeO_2-Y_2O_3$ systems have been investigated in order to compare their behaviour with those of the non-stoichiometric oxides of the corresponding compositions. The maxima in conductivity in these mixed oxide systems were found at ~ 30 mole present $LnO_{1.5}$ (Ln = Y or Nd) corresponding to the composition $Ce_9^{4+}Ln_4^{3+}O_{24}$. The crystal structures of all these mixed oxides could be interpreted in terms of a fluorite lattice with a B.C.C. super lattice.

Electrical conductivities of rare earth ferrites, manganites and chromites of the general formula $LnMO_3$ (M = Fe, Mn or Cr) have been studied. Ferroelectricity in a number of rare earth manganites and related compounds have also been examined.

—

CRYSTAL STRUCTURES OF SULFIDES Yb_3S_4 AND MnY_2S_4

-:-

(R. CHEVALIER, P. LARUELLE & J. FLAHAUT)

Crystallographic studies of the structures of the ytterbium sulfide Yb_3S_4 and the manganese ytterbium sulfide MnY_2S_4 were undertaken.

Yb_3S_4 is obtained by action of H_2S on Yb_2O_3 above 1 300° C. In fact, we observed an homogeneity range between $YbS_{1,47}$ and $YbS_{1,33}$ and the composition of the product is depending on the pression of H_2S and the temperature of the reaction. Crystals isolated after melting in H_2S atmosphere have the composition $YbS_{1,37}$ according to chemical, densimetric and magnetic determinations.

MnY_2S_4 is obtained by action of H_2S on the mixture of Mn_3O_4 and Y_2O_3 at about 1 300° C, or on the mixture of MnS and Y_2S_3. Twenty-eight compounds of this crystal type have been prepared with Mg, Fe, Cr, Ca and Yb^{II} instead of Mn, and with the heaviest rare earth elements.

Yb_3S_4 and MnY_2S_4 have very similar Debye-Scherrer diffractions patterns, and the two structures were thought to be closely related. In fact, preliminary examination of space groups on monocrystals by WEISSENBERG and BUERGER's precession methods show that their space groups were differents.

The ytterbium sulfide Yb_3S_4 is orthorhombic with a cell of dimensions :

a = 12,71 Å   b = 3,81 Å   c = 12,88 Å

and belongs to space group Pnma. Z = 4 molecules in a cell. MnY_2S_4, orthorhombic too, show a cell of similar dimensions :

a = 3,78 Å   b = 12,64 Å   c = 12,74 Å

but the systematic extinctions are characteristic of the space group Cmcm (or $Cmc2_1$, or C2cm, which is described as Ama2 in International Tables).

$*$
$*$ $*$

$...$

The structure of Yb_3S_4 was first investigated by PATTERSON projection along the shortest side of the cell. It cannot be interpreted with sufficient precision and the ytterbium atoms positions cannot be refined. Harker-sections at levels 0 and $\frac{1}{2}$ permit to find one rotation-peak, and the structure has been solved in this way. The earlier projections show clearly the metal atoms and after some adjustements, the sulphur atoms in positions compatible with the packing. Further refinement by BUSING and LEVY's least squares program leads to a reliability factor R less than 0,12, on 492 measured reflexions.

On two sites of rare earth atoms, where measured radii showed to be occupied by trivalent ytterbium, metal atoms fully occupy these sites. On the third rare earth metal site, where divalent ytterbium takes place, occupation is not complete and refinement showed an occupation coefficient near to 0,90. The deduced formula is therefore $Yb_{2,90}S_4$, or $YbS_{1,38}$, in good agreement with chemical studies which give a formula of $YbS_{1,37}$.

The trivalent ytterbium atoms exhibit six-fold coordination and the divalent one seven-fold coordination. The structure is similar of Eu_3O_4 (C. RAU, Acta Cryst. 20 - 716 - 1966) although rare earth atoms are in different locations because of great difference in oxygen and sulphur radii. Another difference comes from coordination of divalent atom which is of nine-fold type Eu_3O_4.

$*$
$*\ *$

The great difficulty of isolating a monocrystal of MnY_2S_4 and its poor quality permit to measure 192 reflexions only. The first hypothesis was built by locating metal atoms in positions analogous in projection with those found for Yb_3S_4 and compatible with symetry of Cmcm space group. With this hypothesis, projections gave a good aspect but factor R cannot be reduced under 0,24 value. Dif-

...

ference synthesis $(F_o - F_c)$ shows at this time a positive peak in manganese site
and it must be admitted that metals were in disorder on all their sites. That cor-
rection reduce R factor to 0,20 but at this stage, it was a streaking anomaly in
R factor of the successive layers (R = 0,16 for 0 kl reflexion, R = 0,22 for 1 kl,
R = 0,17 for 2 kl, R = 0,27 for 3 kl). Statistic tests on intensity values give
evidence that structure was not centrosymmetric and space groups $Cmc2_1$ and Ama2
were tried. The last one seemed to be more convenient, because it is compatible
with the same projection (R = 0,16 for 0 kl reflexion with fixed values of isotro-
pic thermal coefficients). In this structure, all metal atoms, manganese and yt-
trium seem to present a six-fold coordination.

THE RARE EARTH CHEMISTRY OF LASERS

P.N. Yocom
RCA Laboratories
Princeton, New Jersey

Abstract

A brief discussion of laser physics will be undertaken to show
that the important quantities for obtaining laser action are the
frequency of the transition, the fluorescent linewidth, the dipole
moment matrix element of the transition, and the cavity properties,
and how these quantities are interrelated. It will then be pointed out
how both di and trivalent lanthanide ions can provide the needed
properties under suitable conditions.

The subject of crystal lasers will be presented on the basis of
the charge on the ion replaced by the lanthanide ion. The properties
and preparation of divalent lanthanide ions will be presented as well
as the charge compensation of the trivalent ions in divalent sites.
Sensitization in crystalline hosts will be described and a short,
qualitative discussion of line broadening presented.

The glasses containing lanthanide ions that show laser action
will be described and the effects that a glass matrix have upon the
properties of the lanthanide ions discussed.

Finally short descriptions of the rare earth chelate systems that
show laser action will be given, along with mention of the inorganic,
non-aqueous, liquid laser system.

Introduction

Schawlow and Townes[1] first described the conditions for maser
action at optical frequencies in 1958. Then in 1960 Maiman[2] achieved
stimulated light emission from ruby ($Al_2O_3:Cr^{3+}$). Since that time
many laser systems have been demonstrated utilizing solids, liquids,
and gases. But from our point of view the interesting groups are the
optically pumped solids and liquids, an overwhelming number of which
are based on rare earth ions.

A laser consists of a resonant cavity containing an amplifying
medium; for solids the cavity is obtained by fabricating the material
into a Fabry-Perot configuration. For all of the materials we will
discuss, the amplifying medium is lanthanide ions in the excited state.

Let us quickly review the conditions needed for stimulated emission
in order to see why lanthanide ions are so useful in some classes of
lasers. Schawlow and Townes[1] gives for the excess number of atoms/cm^3
in the excited state, ΔN, needed to obtain laser action the following
relationship

$$\Delta N = \frac{3hc}{8\pi^2} \frac{\Delta \nu}{\nu} \frac{1}{\mu^2} \left(\left(\frac{1-R}{L} \right) + Q \right),$$

where ν is the frequency of the laser transition, $\Delta \nu$ is the fluorescent linewidth, μ is the dipole moment matrix element of the transition, L is the length of the cavity, R is the product of the reflectivities of the end mirrors, and Q combines all other losses such as scattering from the cavity.

For a discussion of the chemistry of rare earth lasers, the quantities of interest to us are $\Delta \nu$, ν, μ, and Q. For our purposes μ can be thought of as the allowedness of the transition under question and can be determined by absorption measurements. The quantity $\Delta \nu$ is one of the chief reasons lanthanide ions are so useful in lasers, for it can be reasonably small in a system that has a rather high concentration of active ions. As Kiss and Pressley[3] have pointed out, optically pumped solids and liquids are a good compromise for high cw power lasers, since they are dilute enough not to be limited by cooling problems as injection lasers (concentration 10^{22}/cc) or so dilute as to need large active volumes as in gas lasers (conc 10^{15} to 10^{17}). Also the number of frequencies which lanthanide ions can provide is large. The allowedness of the f-f transition is rather small but they are large enough to be useful for cw operation. The forbidden character of these transitions is actually helpful for energy storage and therefore Q switching and the generation of high peak powers. Snitzer[4] has observed that lanthanide doped glasses are more suitable for high energy pulsed operation and the lanthanide doped crystals are better for cw and high repetition rate use.

In many discussions of laser materials the quantity Q tends to be neglected probably because it is very difficult to control. However since it expresses the optical perfection of the laser, its refinement can make the difference between an excellent laser and just another one of many. At present the best optical perfection can probably be achieved in glass, but some crystals, e.g. calcium fluoride, can also be excellent. Most laser crystals are now made by pulling from the melt, by some form of the Bridgman technique, or by some form of the molten salt solution technique. The flame fusion technique has now been virtually abandoned for lasers because of the poor optical properties obtained. So far, the hydrothermal technique has not yet been exploited for lasers to any extent.

In generalizing on the techniques of crystal growth, it can be said that no one method, as yet, allows all the necessary conditions to be optimized. Pulled crystals and the Bridgman technique require a temperature gradient which introduces strain. The solution techniques require very little or no temperature gradients but nucleation is very difficult to control, and the solubility of the solvent ions in the crystal can lead to difficulties. Needless to say one must always try to achieve the highest possible purity of materials and use the ambient

atmosphere best suited to the system. Of course, one must always struggle with the "laws" of high temperature chemistry which say that everything reacts with everything and the higher the temperature the faster they react.

Table I

RARE EARTH IONS WHICH HAVE SHOWN LASER ACTION

Divalents	Transition	Ground State
Sm	$^5D_0 - ^7F_1$	$^7F_0$
Dy	$^5I_7 - ^5I_8$	$^5I_8$
Tm	$^2F_{5/2} - ^2F_{7/2}$	$^2F_{7/2}$
Trivalents		
Pr	$^3P_0 - ^3H_6$	$^3H_4$
	$^1G_4 - ^3H_4$	$^3H_4$
	$^4F_{3/2} - ^4I_{13/2}$	$^4I_{4/2}$
	$^4F_{3/2} - ^4I_{11/2}$	$^4I_{4/2}$
	$^4F_{3/2} - ^4I_{9/2}$	$^4I_{9/2}$
Eu	$^5D_0 - ^7F_2$	$^7F_0$
Ho	$^5S_2 - ^5I_8$	$^5I_8$
	$^5I_7 - ^5I_8$	$^5I_8$
Er	$^4I_{13/2} - ^4I_{15/2}$	$^4I_{15/2}$
Tm	$^3H_4 - ^3H_6$	$^3H_6$
Yb	$^2F_{5/2} - ^2F_{7/2}$	$^2F_{7/2}$

Table I is a list of those lanthanide ions which have indisputably shown laser action and the transition involved. All of these systems are four level lasers except divalent thulium which is three level. The disadvantage of a three level system is that over half the ions in the system must be in the excited state because the terminal level is the ground state. Many of these ions are four level only by virtue of the crystal field splitting of the ground state and thus can have a thermal population of the terminal state. In this case cooling is beneficial. Because of line broadening only trivalent neodymium, ytterbium, holmium, and erbium have shown laser action in glasses. Only trivalent neodymium in crystals has shown continuous laser action (cw operation) at room temperature; its terminal state is about 2000 wave numbers above the ground state.

One of the major disadvantages of trivalent lanthanide ions in lasers is that they have only weak absorptions in the f-f transitions

and the strong 4f to 5d transition is well up in the ultraviolet where none of the common light pumping sources have any output. This diffi-culty was the main reason for the development of the divalent lanthanide lasers. If a divalent lanthanide ion is in the 4f configuration, it is isoelectronic with the trivalent ion of the element of the next atomic number. However because of the lesser nuclear charge for the divalent ion, the energy separations between the electronic levels are decreased. This compression of the system brings the 4f-5d transition of the divalent ion into the visible where it can be coupled into with con-ventional pumping lamps.

Table II

SUMMARY OF LANTHANIDE LASER MATERIALS

Host Class	Specific Examples	Lanthanide Ions Showing Laser Action in this Class
Fluorite	CaF_2	Sm^{+2}, Dy^{+2}, Tm^{+2} Nd^{+3}, Ho^{+3}
Scheelite	$CaWO_4$	Pr^{+3}, Nd^{+3}, Ho^{+3}, Er^{+3}, Tm^{+3}
Fersmite	$Ca(NbO_3)_2$	Nd^{+3}, Er^{+3}
Tysonite	LaF_3	Pr^{+3}, Nd^{+3}
Garnet	$Y_3Al_5O_{12}$	Nd^{+3}, Ho^{+3}, Er^{+3}, Tm^{+3}, Yb^{+3}
C-type lanthanide	Y_2O_3	Eu^{+3}, Tm^{+3}
Oxides	Er_2O_3	
Glass	K-Ba-Si	Nd^{+3}, Yb^{+3}, Ho^{+3}, Er^{+3}
	La-Ba-Th-B	
	Na-Ca-Si	
	Li-Mg-Al-Si	
Chelates	tetrakis B-diketones	Eu^{+3}
Liquids	$SnCl_4$-$SeOCl_2$	Nd^{+3}
	$(CH_3)_2SO$	

Plan for Discussing the Systems

In discussing the various laser materials, the crystalline lasers will be dealt with first. This is a large group and will be broken down into the type of cations of which the host material is composed; that is, divalent and trivalent hosts. After discussing the crystal-line materials, the glasses will be treated followed by the chelates

and the recently developed liquid systems. Table II summarizes the various classes of rare earth lasers.

Crystalline Materials

Divalent Hosts

Some of the earliest lanthanide laser materials utilized hosts with divalent cations. In such hosts the trivalent lanthanides must be charge compensated in some manner. On the other hand, the lanthanides can exist in the divalent state in the alkaline earth halides.

Divalent Lanthanides

As mentioned earlier, the rationale for trying to make divalent lanthanides was that such an ion could be expected to have the broad, allowed, 4f to 5d transitions in the visible region and thus allow more efficient pumping than is possible with the narrow line, forbidden f-f transitions of the trivalent ions. Three divalent lanthanide ions have shown laser action, these are samarium, thulium, and dysprosium. The host most often used is calcium fluoride. As far as is known, all of the lanthanide ions can be obtained in the divalent state in all of the alkaline earth halides, however only divalent samarium, europium, dysprosium, holmium, erbium, and thulium show sharp line, f-f fluorescence, making them lasers or possible lasers. However, for our limited discussion only the chemistry of the three which have shown laser action will be dealt with.

The potential needed to reduce the trivalent ion to the divalent increases as one goes from samarium to thulium to dysprosium. By melting calcium fluoride with samarium trifluoride under hydrogen, sufficient divalent samarium is produced in the grown crystal to allow pulsed laser action to be observed. However, this technique is not sufficient to produce the necessary amounts of divalent thulium or dysprosium.

The more difficultly reducible lanthanides can be prepared from melts containing the trivalent ion by metallic reduction using lanthanide metal or alkaline earth metal, or by photoreduction of the melts.[5] The divalent ions can also be produced by subjecting crystals containing the trivalent ions to photoreduction by x-rays[6] or gamma rays, to metallic reduction by the alkaline earth metal which is also the host ion,[7] and by solid state electrolysis.[8,9] Because of the highly active nature of these divalent lanthanides, it has been found to be most practical to grow the crystal with the lanthanides in the trivalent state and then reduce them.

Studies of the alkaline earth fluorides have shown that trivalent lanthanide ions are quite soluble without added charge compensator.[10] By paramagnetic resonance Friedman and Low[11] have shown that the compensation is accomplished by an intersticial fluoride ion which can be located either adjacent to or some distance away from the trivalent ion, depending on the thermal history of the specimen.

The photoreduction of such trivalent containing crystals was first reported by Hayes and Twidell[6] and has since been extended by many workers. However these photoreduced lanthanide ions are not stable and revert to the trivalent state under the influence of light and/or heat.[12]

Stable divalent lanthanide ions may be produced by heating the crystal with the appropriate alkaline earth metal or by subjecting the crystal to solid state electrolysis at elevated temperatures. In both of the techniques producing stable divalents, it is postulated that the compensating, intersticial anion is removed from the crystal, allowing the reduction to proceed to completion. This is contrasted with the photoreduction technique in which only a small portion of the trivalent ions present can be reduced and an anionic, electron deficient species (a hole) remains in the crystal causing reoxidation if sufficient activation energy is supplied.

Trivalent Ions in Divalent Hosts

This group of materials is composed of essentially three classes: the fluorites (CaF_2), the scheelites ($CaWO_4$), and fersmite[13] ($Ca(NbO_3)_2$). Since trivalent ions are dissolved in these hosts, charge compensation is needed in all cases. The compensation in calcium fluoride materials has been previously mentioned.[11] Of this group the scheelites have been studied the most thoroughly and have produced the best lasers. As far as is known the calcium niobate chemistry[14] follows closely that of the sheelites. Some of the scheelites which have shown laser action are $CaWO_4$, $SrWO_4$, $CaMoO_4$, $SrMoO_4$, $PbMoO_4$ and $Na_{.5}Gd_{.5}WO_4$. Of these the neodymium doped $CaWO_4$ and $CaMoO_4$ have been run continuously at room temperature.

From a chemical point of view, $CaWO_4$ has been the most thoroughly studied of these materials, especially by Nassau[15-18] and coworkers. These studies have shown that charge compensation of the trivalent lanthanide can be accomplished by three different methods. If no second impurity is added with the lanthanide ions, compensation will occur through the formation of cation vacancies and clustering of the lanthanide ions. This process can be conceived of as the replacement of three divalent ions by two lanthanide ions and a vacancy. This method of compensation gives the lowest solubility values, the most complicated emission spectra, and the poorest laser characteristics.

The other methods of compensation involve the addition of a second impurity. By adding a monovalent ion such as sodium along with the lanthanide the compensation can be conceived of as replacing two calcium ions with one monovalent and one trivalent ion. The other method of compensation is accomplished by replacing the divalent anion by a tri- valent anion such as niobate (NbO_4^{-3}). Both of these compensation techniques give better laser results than vacancy compensation.

By replacing all of the divalent cation by monovalent and trivalent lanthanide ions, Peterson and Bridenbaugh[19] have obtained the material $Na_{0.5}Gd_{0.5-x}Nd_xWO_4$ which possess the scheelite structure and shows laser action. However, this material has neodymium linewidths 30 times larger than $CaWO_4$:Nd:Na thus rendering it a rather poor laser.

The subject of line broadening is a complex one and a theoretical understanding of all the broadening mechanisms is still incomplete. However from a chemical point of view, a few pertinent generalizations can be made. If a large number of non-equivalent sites exist for the emitting ion in a material, the linewidths are greatly broadened. The extreme example is probably found in glasses. Random occupation of a given crystallographic site by ions of differing charges gives a broadening effect as previously mentioned in connection with $Na_{.5}Gd_{.5-x}Nd_xWO_4$.

Besides the symmetry broadening effect, vibrational effects and strains can also cause line broadening. To avoid the vibrational broadening the material must be cooled or else a material must be chosen so that vibrational effects are small at the desired temperature of operation. Typically materials which operate continuously at room temperature have melting points above $1200^{\circ}C$.

Trivalent Ions in Trivalent Hosts

The main theme of our discussion of trivalent lanthanide ions to this point has been the means of charge compensating them in divalent sites. Obviously, the difficulties introduced by charge compensation are removed if no compensation is necessary. Most of the recent work with trivalent ions in crystalline hosts has been in hosts with trivalent sites, removing the necessity of compensation. The trivalent lanthanide laser hosts fall into three categories: tysonite (LaF_3), garnets ($Y_3Al_5O_{12}$), and c-type rare earth oxides (Y_2O_3). Since these systems show high solubility for lanthanide ions, the chemistry of substitution is very limited except to note that in most compound types two or three crystal types are found in going through the lanthanide series, thus giving some limit to isomorphous substitution. However, long before the solubility limit is reached luminescent quenching is observed.

An interesting aspect of trivalent host materials is that of sensitization. By this is meant, the incorporation of a second impurity into the system which acts as an absorber and then transfers its energy to the emitting lanthanide ion. The reason for this technique is, as mentioned previously in connection with the divalent lanthanides, the weak absorption characteristics of the trivalent ions. One of the best laser materials at the present time is yttrium aluminium garnet doped with neodymium, as it can be run (CW) at room temperature with a low threshold.[20] It has been found possible to sensitize this system with trivalent chromium[21] which has a broad absorption band in the green.

Another example of sensitization is the simultaneous transfer from ytterbium, thulium and erbium to holmium in yttrium aluminum garnet.[22] This transfer from one rare earth to another has been extended to making the host completely out of the sensitizing ion. An example of which is erbium oxide host doped with thulium.[23]

Glass Lasers

The lanthanide ions which have shown laser action in glass are trivalent neodymium, ytterbium, holmium, and erbium. Of these the most studied and most useful is neodymium. It has lased in almost all the basic glass systems such as the silicates, germinates, phosphates and borates; the main exception being the low expansion borosilicates. As mentioned previously, the lanthanide ion linewidths are greatly broadened in glass, a fact that makes glass lasers most suitable for high energy pulse work.

The glass lasers all emit in the infrared from about $.9\mu$ to 2μ. This circumstance is somewhat unfortunate because the glass constituents must be substantially free of such common transition elements as Ni, Co, Cu, Fe, and V all of which have absorptions in this region.

Sensitization is an important topic in glass lasers and a wide variety of sensitizing ions have been found[4]. However it must be born in mind that if an ion sensitizes in one glass matrix it will not necessarily do so in another matrix. With this restriction in mind, a few sensitizers for neodymium are UO_2^{2+}, Mn^{+2}, Ce^{+3}, Tb^{+3}, Eu^{+3}, and Cr^{+3}; for ytterbium Nd^{+3}, Ce^{+3}, and Cr^{+3}; for erbium Yb^{+3} and Mo^{+3}; and for holmium Yb^{+3}.

Of the solid lasers, glass is the easiest to fabricate in large or complex shapes with good optical perfection. A great limitation of glass is its low thermal conductivity which restricts high repetition rate uses.

Chelates

One of the main reasons chelates became interesting laser materials was the observation that energy absorbed in the chelate could be emitted by the rare earth ion[24]. At present only tetrakis, beta-diketone chelates of trivalent europium have shown laser action. Because of the high optical density of these materials in their pump bands they have been studied in dilute solution. In solution they show complex dissociation characteristics which has been discussed by Brecher, Samelson, and Lempicki[25].

These compounds in solution show fluorescent linewidths of about ten angstroms which is quite narrow for a rare earth ion in a fluid solution and indicates considerably symmetry stability for the tetrakis species.

In spite of this stability however, the particular cation used with the chelate can cause changes in the threshold for laser action[26], and also cause shifts in the laser frequency[27].

Another chemical effect on the laser action of europium chelates is the lowering of the threshold by deuterating the ligands. No effect on the emission spectrum or fluorescence life time is observed on deuteration inferring that the effect is one of energy transfer efficiency.

Neodymium Liquid Lasers

The aforementioned deuteration effect in europium chelates suggested to Heller and Lempicki[28,29] that high energy vibrations were in part responsible for lowering the efficiency of the chelate lasers. This analysis led to the development of a neodymium liquid laser system which contain no light atoms which produce high energy vibrations.

The most efficient of these systems is a solution of neodymium oxide in stannic chloride - selenium oxychloride. The neodymium fluorescent linewidth is rather large 160 Å but the efficiency of the system is reported to be about that of good $CaWO_4$:Nd. Apparently nothing is known, at present, about the exact nature of the neodymium species in this solution.

An organic system containing neodymium was recently reported by Heller[30]. It consists of the o-phenanthroline adduct of neodymium pentafluoropropionate dissolved in dimethyl sulfoxide. The composition of the adduct Heller reports as $Nd(CF_3CF_2COO)_3 \cdot C_{12}H_8N_2$. This system is not as efficient as the selenium oxychloride system and shows decomposition on standing.

References

1. A.L. Schawlow and C.J. Townes, Phys. Rev. 112, 1940 (1958).

2. T.H. Maiman, Nature 187, 493 (1960).

3. .J. Kiss and R.J. Pressley, Applied Optics 5, 1474 (1966).

4. L. Snitzer, Applied Optics, 5, 1487 (1966).

5. H.L. Pinch, J. Amer. Chem. Soc., 86, 3167 (1964).

6. W. Hayes and J.W. Twidell, J. Chem. Phys., 35, 1521 (1961).

7. Z.J. Kiss and P.N. Yocom, J. Chem. Phys., 41, 1511 (1964).

8. H. Guggenheim and J.V. Kane, Appl. Phys. Letters, 4, 172 (1964).

9. F.K. Fong, J. Chem. Phys., 41, 2291 (1964).

10. D.M. Roy and R. Roy, J. Clectrochem. Soc., 111, 421 (1964).

11. E. Friedman and W. Low, J. Chem. Phys. 33, 1275 (1960).

12. F.K. Fong, J. Chem. Phys. 41, 245 (1964).

13. D.H. Hess and H.J. Trumpour, Amer. Mineralogist, 44, 1 (1959).

14. A.A. Ballman, S.P.S. Porto and A. Yariv, J. Appl. Phys. 34, 3155 (1963).

15. K. Nassau and A.M. Brayer, J. Appl. Phys. 33, 3064 (1962).

16. K. Nassau and G.M. Loiacono, Phys. Chem. Solids 24, 1503 (1963).

17. H.J. Levinstein, G.M. Loiacono, and K. Nassau, J. Appl. Phys. 34, 3606 (1963).

18. K. Nassau, Phys. Chem. Solids 24, 1511 (1963).

19. G.E. Peterson and P.M. Bridenbaugh, Appl. Phys. Letters 4, 173 (1964).

20. J.E. Geusic, Marcos, and L.G. Van Uitert, Appl. Phys. Lett. 4, 182 (1964).

21. Z.J. Kiss and R.C. Duncan, Jr., Appl. Phys. Lett. 5, 200 (1964).

22. L.F. Johnson, J.E. Geusic, and L.G. Van Uitert, Appl. Phys. Lett. 8, 200 (1966).

23. M.B. Soffer and R.H. Hoskins, Appl. Phys. Lett. 6, 200 (1965).

24. S.I. Weissman, J. Chem. Phys. 10, 214 (1942).

25. C. Brecher, H. Samelson, A. Lempicki, J. Chem. Phys. 42, 1843 (1965).

26. E.P. Reidel and R.G. Charles, J. Appl. Phys. 36, 3954 (1965).

27. H. Samelson, V.A. Brophy, C. Brecher, A. Lempicki, J. Chem. Phys. 41, 3998 (1964).

28. A. Heller, Appl. Phys. Letters $\underline{9}$, 106 (1966).

29. A. Lempicki and A. Heller, Appl. Phys. Letters $\underline{9}$, 108 (1966).

30. A. Heller, J. Amer. Chem. Soc. $\underline{89}$, 167 (1967).

Eu^{+3} Fluorescence in Non-Rare Earth Oxide Hosts

Hans J. Borchardt
Central Research Department*
E. I. du Pont de Nemours and Company
Wilmington, Delaware

ABSTRACT

Attempts were made to dope a variety of non-rare earth oxides with Eu^{+3}. Of 19 oxides tried only ThO_2 gave a bright phosphor. Failure of the others is attributed to low Eu^{+3} solubility. $(ThO_2)_{.98}(EuF_3)_{.02}$ is a highly efficient phosphor with a quantum efficiency of ca. 0.64 under 2537 Å excitation. It is the first high efficiency Eu^{+3} phosphor not to contain a second rare earth ion and to have such a low optimum Eu^{+3} concentration.

INTRODUCTION

Europium-activated phosphors are of considerable current interest (1). The phenomenon of <u>efficient</u> europium fluorescence in certain oxide hosts was first reported in 1963 (2); numerous europium phosphors have been described since (3-13) and one of these has found commercial application (1,6).

Most of the europium phosphors reported to date are the ones where Eu^{+3} is in a rare earth-oxygen dominated host, i.e., compounds having the formula $(R_{1-x}Eu_x)_2O_3 \cdot A$ where $\underline{R}$ is Sc, Y, La, Gd, or Lu and $\underline{A}$ is nothing or another oxide. Attempts were made to introduce Eu^{+3} into a variety of non-rare earth oxides to determine whether efficient Eu^{+3} fluorescence occurs generally in non-rare earth oxygen dominated hosts as well. Most, if not all, stable, non-toxic, substantially colorless, binary oxides have been included in this study.

EXPERIMENTAL

Eu^{+3}-doped non-rare earth oxides were prepared by (1) direct reaction of the constituent oxides in air and (2) reaction of EuF_3 with an oxide in a sealed platinum tube under an external pressure of 30 atmospheres. The latter route was tried on the supposition that lower melting EuF_3 might be more reactive than Eu_2O_3. A closed system was employed to prevent loss of EuF_3 and/or F_2. Three sets of composites were prepared. The proportion of europium compounds in these were 2 mole percent EuF_3, 2 mole percent $EuO_{1.5}$ and 10 mole percent $EuO_{1.5}$, respectively. In the case of ThO_2, it was possible to co-precipitate oxalates and ignite these to the oxides. This procedure was followed to prepare $(ThO_2)_{.98}(EuO_{1.5})_{.02}$ and $(ThO_2)_{.90}(EuO_{1.5})_{.10}$.

The sources of the oxide starting materials are listed in Table I. EuF_3 was prepared by dissolving Eu_2O_3 in HNO_3, precipitating the fluoride with HF, centrifuging, drying, and finally heating for 1 hour at 650°C. Anal: F^- found: 26.7, theory: 27.3. The firing temperatures (Table II) differed depending upon the oxide. Reaction time in all cases was 4 hours.

After reaction, the products were examined under long (3650 Å) and short (2537 Å) wavelength ultraviolet hand lamps both at room and liquid nitrogen temperatures. The "brightness" of fluorescence with 2537 Å excitation is designated in Table II by the numbers 0 to 5. This is an arbitrary scale, previously employed (14), where 0 means no visually detectable fluorescence, 1 feeble emission, 5 emission comparable to that of commercial phosphors, and 2 through 4 corresponding intermediate intensities. For the brighter materials, quantum efficiencies were determined by procedures previously described (8). The brightnesses under 3660 A excitation are not given. In no case

was the material appreciably brighter under 3660 A than under 2537 A U.V. Debye-Sherrer x-ray powder diffraction patterns were determined for each product. The phases identified by the ASTM powder diffraction index are listed in Table II. The word "lines" in Table II indicates that lines in the x-ray pattern could not be attributed to either reactant. In all cases these "lines" were quite weak relative to those of the other phase present. Finally, the body colors of the products are also listed in Table II.

RESULTS

Perhaps the most striking result is that of all host materials tested, only ThO_2 yields a material with Eu^{+3} which fluoresces brightly at room temperature. To make these observations quantitative, the quantum efficiencies of the ThO_2 compositions, as well as those of the several next brightest materials, were measured. Results are given in Table III. These data confirm the qualitative observations but show much more clearly that the hosts other than ThO_2 did not provide media for efficient Eu^{+3} fluorescence.

Table II shows that cooling to 77°K does not result in a marked increase in the brightness of any materials except those in which ZrO_2 is the host. As noted in Table II, some white emission is seen in these cases. The ZrO_2 starting material itself fluoresces, emitting white light, and the intensity of this fluorescence increases on cooling (15). The ZrO_2 case can therefore be discounted for present purposes, although some unusual things seem to happen here (see footnote c to Table II).

Most of the products were found to be polyphase by x-ray diffraction. In these cases, it is likely that at least a portion of the Eu^{+3} did not enter the host. Taking into account the detection limit of a minor phase

with x-ray diffraction (often given as 5%) and the small
proportion of europium compound in the starting material
makes it likely that most of the europium did not enter
the host. In those cases where a single product phase was
observed either the europium entered the host or a second
phase was present in an amount below its detection limit
in the presence of the particular major phase.

DISCUSSION

The mechanism that has been postulated to account
for the efficient Eu^{+3} fluorescence in rare earth oxygen-
dominated hosts (8) would lead one to expect efficient Eu^{+3}
fluorescence in non-rare earth oxide hosts as well. Essen-
tially what is required is that Eu^{+3} be in an oxide so that
localized excitation via europium-oxygen charge transfer
states can occur (and/or excitation be transferred to Eu^{+3}
from the host) and that the concentration of Eu^{+3} be di-
luted with some "optically inert" ion. This optically
inert ion need not necessarily be one of the cited five
rare earth ions.* The alternative possibilities that may

---

* Sc, Y, La, Gd and Lu have no cation-oxygen transfer
states (no absorption seen in their U.V. diffuse reflec-
tance spectra, Fig. 6, Ref. 14) and, all but Gd, very
likely no free ion states (compare data on similar ions
in Ref. 16) at energies equal to or below the excitation
energy (2537 Å u.v.) hence these ions (Gd^{+3} excepted) can-
not interfere with absorption, much less emission. The
postulated mechanism argues that $Eu^{+3}-O^=$ absorbs so in-
tensely that it can compete effectively with other absorb-
ing entities so that the requirement of "optically inert"
reduces to one of not interfering with emission, i.e., no
states at or below the emission level of Eu^{+3}. The cations
used in this study have their first excited free ion states
in the range 8.0 to 198.5 ev (16) well outside of the range
of even the 2537 A excitation (4.88 e.v.). Absence of low
lying cation-oxygen charge transfer states is attested to
by the white body color of the oxides.

account for the present findings are

1. The postulated mechanism is wrong or
2. The solubility for Eu^{+3} is simply too low in most non-rare earth hosts or
3. Our preparative procedures were inadequate or
4. Some combination of 1, 2, and 3.

We would like to believe that conclusion 3 is unlikely and have two pieces of evidence to support this position: (1) two quite different preparative procedures were employed with substantially similar results, (2) the oxide route has been used successfully to form a wide variety of $(R_{1-x}Eu_x)_2O_3 \cdot A$ type phosphors (2,8,14) and there is no reason to believe that reaction rates should be much slower with the present materials.

The x-ray evidence strongly suggests that low solubility of Eu^{+3} in most non-rare earth oxide hosts is the reason for lack of fluorescence. The failure to observe intense fluorescence at 77°K is consistent with this. If intense fluorescence had been observed at low temperatures, one would have been compelled to conclude that the Eu^{+3} entered the host and that the fluorescence was quenched in some manner.

The finding that $(ThO_2)_{.98}(EuF_3)_{.02}$ fluoresces efficiently is particularly interesting because of the low Eu^{+3} concentration and the absence of a costly second rare earth component. The quantum efficiency compares favorably with the efficiency of the best europium phosphors reported to date (compare with quantum efficiencies in Table I, Ref. 7, Table I, Ref. 8, Fig. 1, Ref. 12, Table I, Ref. 13).

CONCLUSIONS

1. Eu^{+3} does not fluoresce efficiently in a wide variety of non-rare earth oxide hosts, in contrast to its behavior in rare earth oxygen dominated hosts. The prob-

able reason for this is insufficient solubility of Eu^{+3} in non-rare earth oxides.

2.   None of the findings conflict with the postulated (8) mechanisms of Eu^{+3} fluorescence in oxides.

3. $(ThO_2)_{.98}(EuF_3)_{.02}$ is a new highly efficient red phosphor which is, at the moment, unique because of low Eu^{+3} concentration and absence of costly second rare earth component.

REFERENCES

1. Anon., Chemical Week, Oct. 8, 1966, pp. 79-86.
2. H. J. Borchardt, J. Chem. Phys., $\underline{38}$, 1251 (1963).
3. N. C. Chang, J. Appl. Phys., $\underline{34}$, 3500-3504 (1963).
4. K. A. Wickersheim and R. A. Lefever, J. Electrochem. Soc., $\underline{111}$, 47-51 (1964).
5. R. C. Ropp, J. Electrochem. Soc., $\underline{111}$, 311-316 (1964).
6. A. K. Levine and F. C. Palilla, Appl. Phys. Letters, $\underline{5}$, 118-120 (1964).
7. A. Bril and W. L. Wanmaker, J. Electrochem. Soc., $\underline{111}$, 1363-1368 (1964).
8. H. J. Borchardt, J. Chem. Phys., $\underline{42}$, 3743-3745 (1965).
9. L. H. Brixner and E. Abramson, J. Electrochem. Soc., $\underline{112}$, 70-74 (1965).
10. L. H. Brixner, J. Electrochem. Soc., $\underline{112}$, 303-308 (1965).
11. L. H. Brixner, J. Electrochem. Soc., $\underline{112}$, 873 (1965).
12. A. Bril, W. L. Wanmaker and J. Broos, J. Chem. Phys., $\underline{43}$, 311 (1965).
13. G. Blasse and A. Bril, Solid State Communications, $\underline{4}$, 373-375 (1966).
14. H. J. Borchardt, J. Chem. Phys., $\underline{39}$, 504-511 (1963).
15. J. F. Sarver, J. Electrochem. Soc., $\underline{113}$, 124-128 (1966). This reference gives new results on ZrO_2 fluorescence.
16. C. E. Moore, "Atomic Energy Levels," NBS Circ. 467.

Table I

Source of Starting Materials

MgO	Baker and Adamson reagent magnesium carbonate heated 2 hrs. at 800°C.
CaO	Mallinckrodt $CaCO_3$ heated 2 hrs. at 800°C.
SrO	Baker and Adamson reagent $SrCO_3$ heated 4 hrs. at 1000°C.
TiO_2	J. T. Baker. Reagent.
ZrO_2	Fisher Scientific Purified.
HfO_2	Carborundum Co. "Hi Purity."
Nb_2O_5	Kawecki Chemicals Optical Grade.
Ta_2O_5	Kawecki Chemicals Optical Grade.
ZnO	Baker and Adamson. Reagent.
B_2O_3	J. T. Baker. Purified.
Al_2O_3	aker and Adamson reagent $Al(OH)_3$ heated 4 hrs. at 1000°C.
Ga_2O_3	A. D. MacKay. "99.999%."
In_2O_3	American Smelting and Refining Co.
SiO_2	Baker and Adamson reagent $SiO_2 \cdot XH_2O$ heated 4 hrs. at 1000°C.
GeO_2	Penn Rare Metals, Inc.
SnO_2	Baker and Adamson Reagent.
Sb_2O_3	Fisher Scientific. Reagent.
Bi_2O_3	Fisher Scientific. Reagent.
Eu_2O_3	Lindsay Chemical Division 99.9%.

Table II

Survey of Eu^{+3} Fluorescence in Oxide Hosts

Host	Firing T °C.	2% EuP3				2% EuO1.5				10% EuO1.5			
		Fluorescence 77°K	298°K	Body Color	Phases Present	Fluorescence 77°K	298°K	Body Color	Phases Present	Fluorescence 77°K	298°K	Body Color	Phases Present
MgO	1500	1	0	white	MgO + lines	3	1	white	MgO + lines	1	1	white	MgO + (a-Eu$_2$O$_3$)
CaO	1500	3	3	white	CaO + lines	4	4	white	CaO + lines	4	4	off-white	CaO + a-Eu$_2$O$_3$
SrO	1500	1	1	white	SrO	3	4	off-white	' Not SrO	4	4	off-white	' weak lines
TiO2	1200	0	0	tan	rutile	0	0	off-white	rutile	0	1	off-white	rutile
ZrO2	1500	5[a]	3[b]	white	monoclinic ZrO$_2$	5[c]	3[b]	off-white	monoclinic + tetragonal[d] ZrO$_2$	5	3[b]	white	monoclinic + tetragonal[d] ZrO$_2$
HfO2	1500	1	1	off-white	monoclinic HfO$_2$	2	1	off-white	monoclinic + tetragonal HfO$_2$	2	1	off-white	monoclinic + tetragonal HfO$_2$
ThO2	1500	5	5	white	ThO$_2$	5	5	white	ThO$_2$	5	5	white	ThO$_2$
Nb2O5	1200	0	0	black	' Not Nb$_2$O$_5$	1	1	white	Nb$_2$O$_5$	1	2	white	Nb$_2$O$_5$
Ta2O5	1200	0	0	pink-grey	Ta$_2$O$_5$ + lines	0	1	white	Ta$_2$O$_5$ + lines	2	2	white	Ta$_2$O$_5$ + lines
ZnO	1500	0	0	yellow	ZnO + EuP$_3$	0	0	yellow	ZnO	0	0	yellow	ZnO + a-Eu$_2$O$_3$
B2O3	700	2	2	white	B$_2$O$_3$ + EuP$_3$	2	2	white	' weak lines	3	2	white	' weak lines
Al2O3	1500	2	2	white	a-Al$_2$O$_3$ + lines	2	1	white	a-Al$_2$O$_3$ + lines	1	1	off-white	a-Al$_2$O$_3$ + lines
Ga2O3	1500	0	0	white	Ga$_2$O$_3$ + EuP$_3$	0	0	white	Ga$_2$O$_3$ + lines	0	0	white	Ga$_2$O$_3$ + lines
In2O3	700	0	0	yellow	In$_2$O$_3$	0	0	yellow	In$_2$O$_3$ + lines	0	0	yellow	In$_2$O$_3$ + lines
SiO2	1500	0	0	off-white	a-cristobalite + EuP$_3$	3	2	white	a-cristobalite	4	3	white	a-cristobalite + lines
GeO2	1000	0	0	white	tetrag. GeO$_2$ + EuP$_3$	3	2	white	hexagonal GeO$_2$	4	3	white	hexagonal GeO$_2$
SnO2	1000	0	0	white	SnO$_2$ + EuP$_3$	0	0	off-white	SnO$_2$	0	0	off-white	SnO$_2$ + lines
Sb2O3	700	0	0	off-white	ortho Sb$_2$O$_3$ + lines	0	0	white	Sb$_2$O$_4$ (cervantite)	0	0	off-white	Sb$_2$O$_4$ + cubic Eu$_2$O$_3$
Bi2O3	700	0	0	yellow	Bi$_2$O$_3$	0	0	yellow	Bi$_2$O$_3$	0	0	yellow	Bi$_2$O$_3$ + lines

a-white fluorescence of ZrO$_2$ - not Eu^{+3} fluorescence.
b-pink fluorescence. Probably white ZrO$_2$ + red Eu^{+3}.
c-on cooling from 298°K to 77°K color of fluorescence changes from pink to white to beige.
d-expanded ...

Table III

Material	Quantum Efficiency
$(ThO_2)_{.98}(EuF_3)_{.02}$	0.64
$(ThO_2)_{.98}(EuO_{1.5})_{.02}$	0.40
$(ThO_2)_{.90}(EuO_{1.5})_{.10}$	0.24
$(CaO)_{.90}(EuO_{1.5})_{.10}$	0.07
$(SrO)_{.90}(EuO_{1.5})_{.10}$	0.05
$(ZrO_2)_{.90}(EuO_{1.5})_{.10}$	0.04
$(SiO_2)_{.90}(EuO_{1.5})_{.10}$	0.04
$(GeO_2)_{.90}(EuO_{1.5})_{.10}$	0.04

Energy Transfer in Crystals Doubly Doped with Rare Earths
By L. Esterowitz, J. Bahler and J. Noonan
U.S. Army Night Vision Lab., Ft. Belvoir, Va.

ABSTRACT

It has been demonstrated in this laboratory that the infrared quantum counter (IRQC) fluorescence may be increased by using two species of rare earth impurity ions. In this work the effects on the energy cascade are studied as the sensitizer (Yb^{3+}) concentration is increased. In particular, level bypassing of the Ho^{3+} (activator), $^5F_5$, state is attributed to a resonant energy cross-relaxation process.

INTRODUCTION
(1)

It has been shown recently that the Ho^{3+} IRQC fluorescence

is increased by two orders of magnitude when a large concentration

of Yb^{3+} ions is added. This enhancement is due to the increase in

the infrared absorption, without adversly affecting the visible

fluorescence quantum efficiency. This is accomplished by using a

low activator concentration (avoiding concentration quenching) along

with a high sensitizer concentration. In this paper we investigate

the effects on the decay modes and energy transfer as the Yb^{3+} con-

centration is increased. The modes of energy cascade are important

considerations in determining optimum material parameters for both

IRQC's and lasers.

The many investigations of laser materials indicate that in

most cases the energy decay through an energy level system occurs

predominantly via a step-by-step cascade involving all intermediate

levels. There are numerous cases, however, where radiative transi-

tions occur which bypass levels. In this paper we will discuss level

skipping due to non-radiative processes.

EXPERIMENTAL

Single crystals of CaF_2 were used as the host lattice
with the following trivalent rare earth impurities: $1\%Ho^{3+}-1\%Yb^{3+}$,
$1\%Ho^{3+}-5\%Yb^{3+}$, and $1\%Ho^{3+}-10\%Yb^{3+}$. These rectangular samples
(7 x 7 x 15mm) were purchased from Optovac, Inc., buffed on all
six sides.

Absorption spectra (Fig. 1) of these crystals were run on
a Cary 14 recording spectrophotometer. Excitation spectra were run
with two Bausch & Lomb (f/4) monochrometers, one of which scanned
the excitation while the other monitored a desired fluorescent out-
put. The excitation pump source was a 1 Kw quartz-tungsten-iodine
lamp. The detectors used were either lead sulphide cells, S-1, S-11,
or S-20 photocathodes depending upon the output wavelength. The
spectral intensity distribution was normalized by calibrating the
pumps and monochrometers with an Eppley thermopile. The detectors
were calibrated for spectral response with a constant energy mono-
chrometer built by Bausch & Lomb under contract. From the above
spectra an energy level diagram (Fig. 2), showing the relevant levels
and transitions, was derived.

The experimental technique and apparatus for the IRQC have
been described in a previous paper.[2]

RESULTS AND DISCUSSION

The $^5I_6 \longrightarrow {}^5I_8$, 1.17$\mu$, Ho^{3+} transition was monitored while the excitation source was scanned from .35 to .675 microns. The excitation spectra, thus obtained, are shown in Fig. 3. In the $CaF_2:1\%Ho^{3+}-1\%Yb^{3+}$ sample the red (.64μ) pump is more efficient (Fig. 3a) than the green (.532μ) pump in exciting the $^5I_6 \longrightarrow {}^5I_8$ fluorescent transition. When the Yb^{3+} concentration is increased to 5%, we observe (Fig. 3b) that the green pump is more efficient than the red pump in populating the $^5I_6$ level. Finally when we reach a 10% Yb^{3+} concentration, the green excitation clearly dominates (Fig. 3c) the red. This suggests that many electrons initially in the $^5S_2$ state go directly to the $^5I_6$ state and bypass the Ho^{3+} fluorescence. As can be seen from Fig. 4, the efficiency of the green pump in populating the $^5F_5$ state (i.e. the initial state of the red fluorescence) decreases as the Yb^{3+} concentration increases.

SPACE FOR FIGURES 3 and 4

The above experiments strongly indicate that this level skipping or conversly the increase of the $^5S_2 \longrightarrow {}^5I_6$ transition probabil-ity is due to a cross-relaxation process invclving an exchange of energy between Ho^{3+} and Yb^{3+} ions (Fig. 5). As is shown in Fig. 1, the Yb^{3+} $^2F_{7/2} \longrightarrow {}^2F_{5/2}$ absorption band extends from .91 to .99 microns. The Ho^{3+} $^5S_2 \longrightarrow {}^5I_6$ transition occurs at .98 microns so

that there is an energy overlap between these two transitions. As the Yb^{3+} concentration increases, the cross-relaxation probability also increases due to the increase in Yb^{3+} ions and to the broadening of the Yb^{3+} absorption band. This broadening introduces a larger energy overlap for the Ho^{3+} and Yb^{3+} transitions. The resonant cross-relaxation process (Fig. 5) therefore depletes the Ho^{3+} $^5S_2$ and Yb^{3+} $^2F_{7/2}$ states to the profit of the Ho^{3+} $^5I_6$ and Yb^{3+} $^2F_{5/2}$ states. The energy residing in the Ho^{3+} $^5I_6$ state can be emitted as 1.17μ radiation corresponding to the $^5I_6 \longrightarrow {}^5I_8$ transition. The energy residing in the Yb^{3+} $^2F_{5/2}$ state may either decay to the ground state or transfer over (Fig. 5) to the Ho^{3+} $^5I_6$ level by a phonon assisted cross-relaxation process, the latter process contributing additional 1.17 radiation.

SPACE FOR FIGURE 5

Under U-V excitation the effect of adding Yb^{3+} is to decrease the green $^5S_2 \longrightarrow {}^5I_8$ output fluorescence due to the additional decay modes available for the energy residing in the $^5S_2$ state. Under broadband infrared excitation, however, due to the presence of the broad Yb^{3+} infrared absorption band, the green IRQC output fluorescence increases (1) (even though the internal fluorescence quantum efficiency of the $^5S_2$ state decreases) with increasing Yb^{3+} concentration. In contrast, the red $^5F_5 \longrightarrow {}^5I_8$ fluorescence

decreases both under   nd broadband infrared excitation as the Yb^{3+} concentration   ses. This result substantiates our conclusion that the presence of Yb^{3+} ions induces level bypassing of the $^5F_5$ state due to a resonant cross-relaxation process.

REFERENCES

[1] L. Esterowitz, J. Noonan, and J. Bahler (to be published in Appl. Phys. Letters).

[2] L. Esterowitz and J. Noonan, Appl. Phys. Letters, $\underline{7}$, 281 (1965).
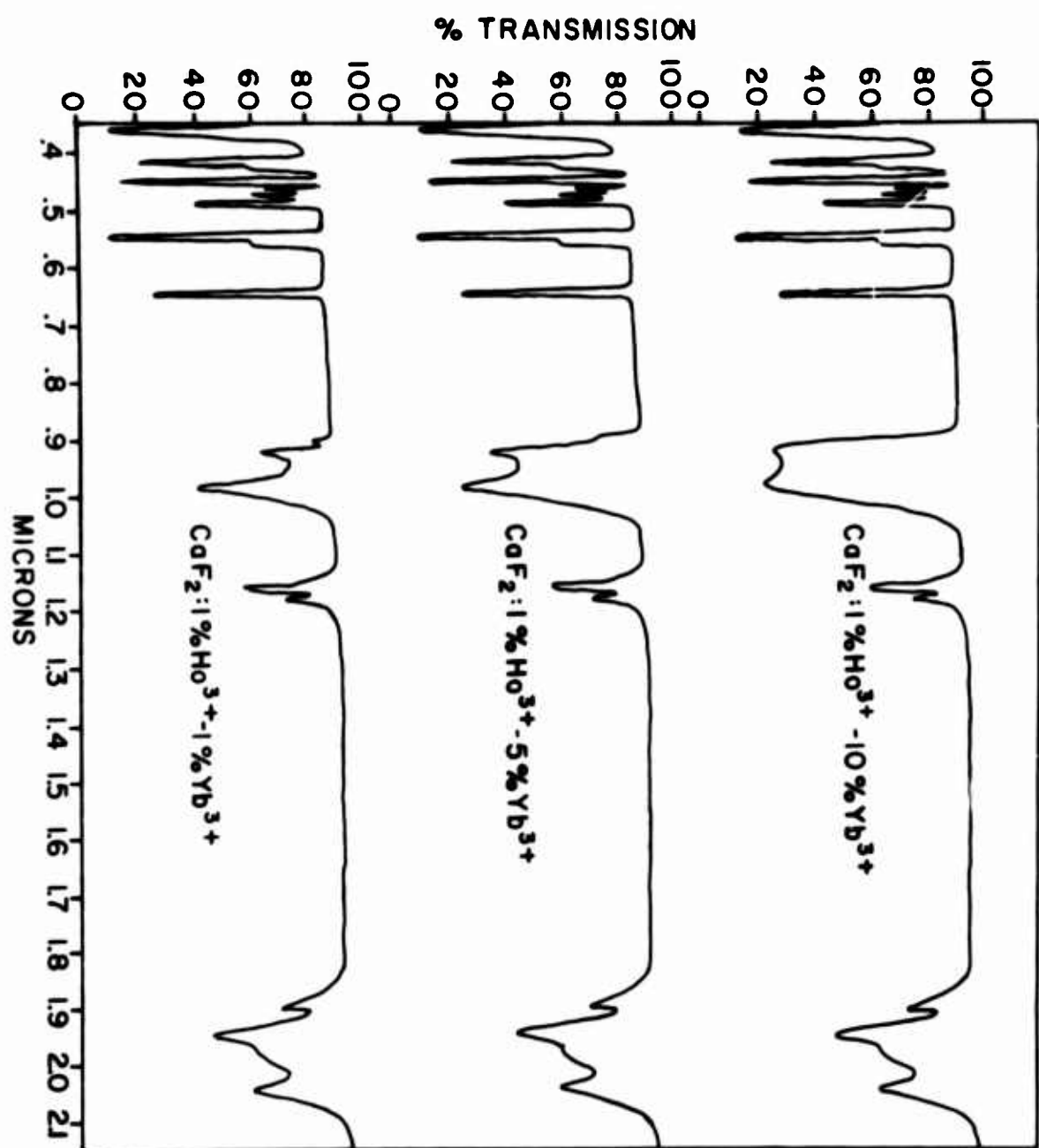
% TRANSMISSION

MICRONS

CaF$_2$:1%Ho^{3+}-10%Yb^{3+}

CaF$_2$:1%Ho^{3+}-5%Yb^{3+}

CaF$_2$:1%Ho^{3+}-1%Yb^{3+}

X10³ Cm⁻¹

Ho³⁺

32 —

28 —

24 —

20 —

16 —

12 —

8 —

4 —

$5G_{3,2}$

$3H_6$

$5G_5$

$3K_7$

$5G_4$

$5G_5$

$5F_1$

$3K_8$

$5F_{2,3}$

$5F_4$

$5S_2$

$5F_5$

$5I_5$

$5I_6$

$5I_7$

$5I_8$

.532

.64

.98

.88

1.12

1.9

.55μ

.65

1.17

WAVELENGTH - mμ

Ho^{3+}

Yb^{3+}

$^5S_2$

$^2F_{5/}$

$^5I_6$

1.17μ

$^5I_8$

$^2F_{7}$
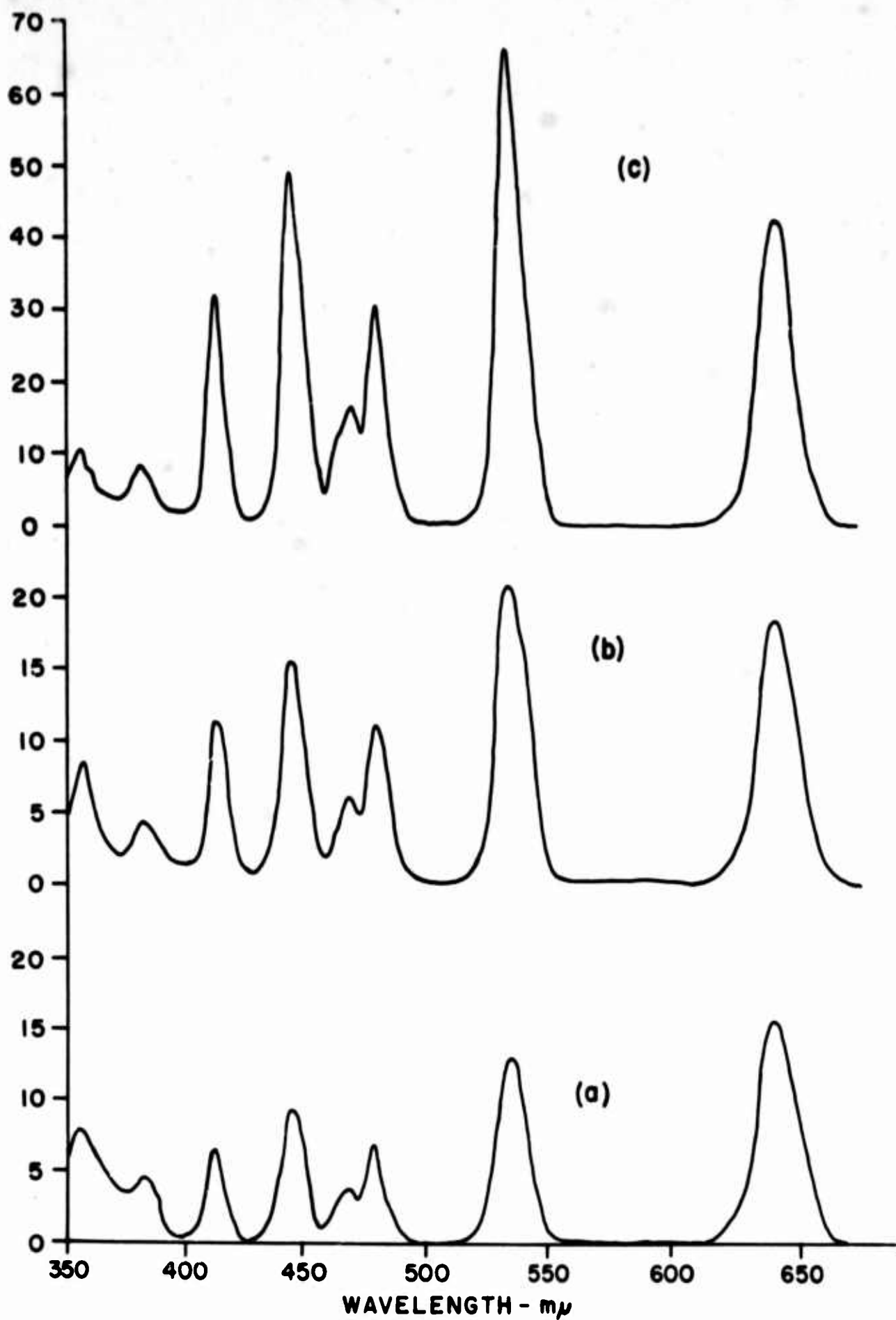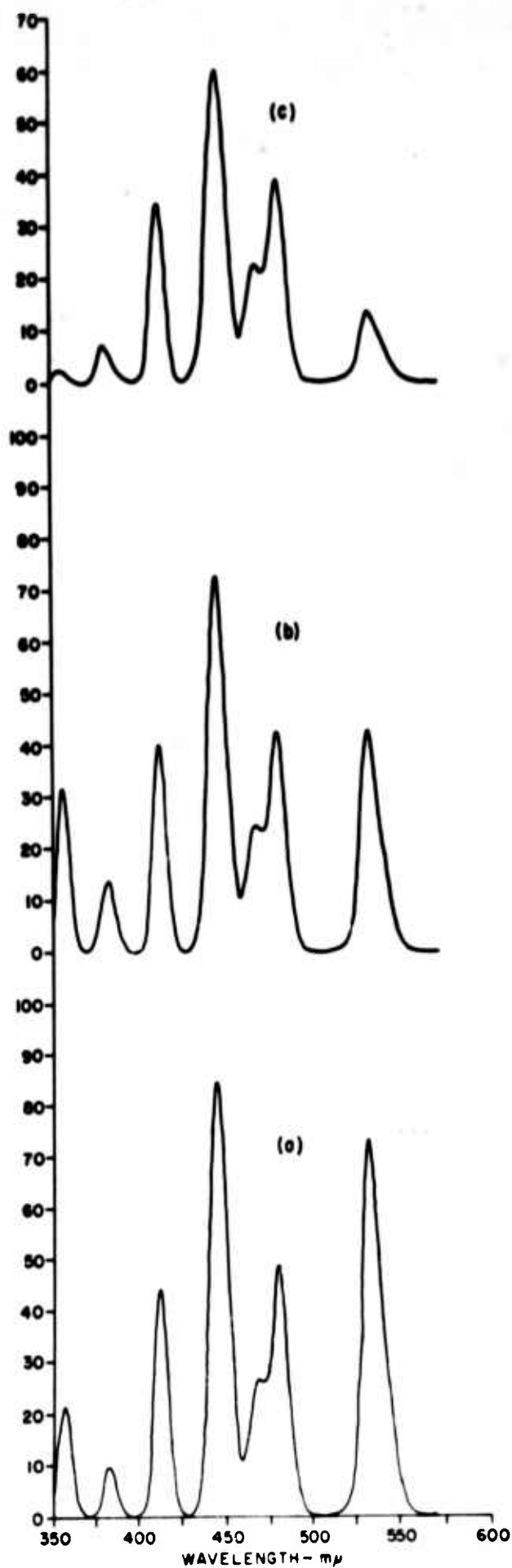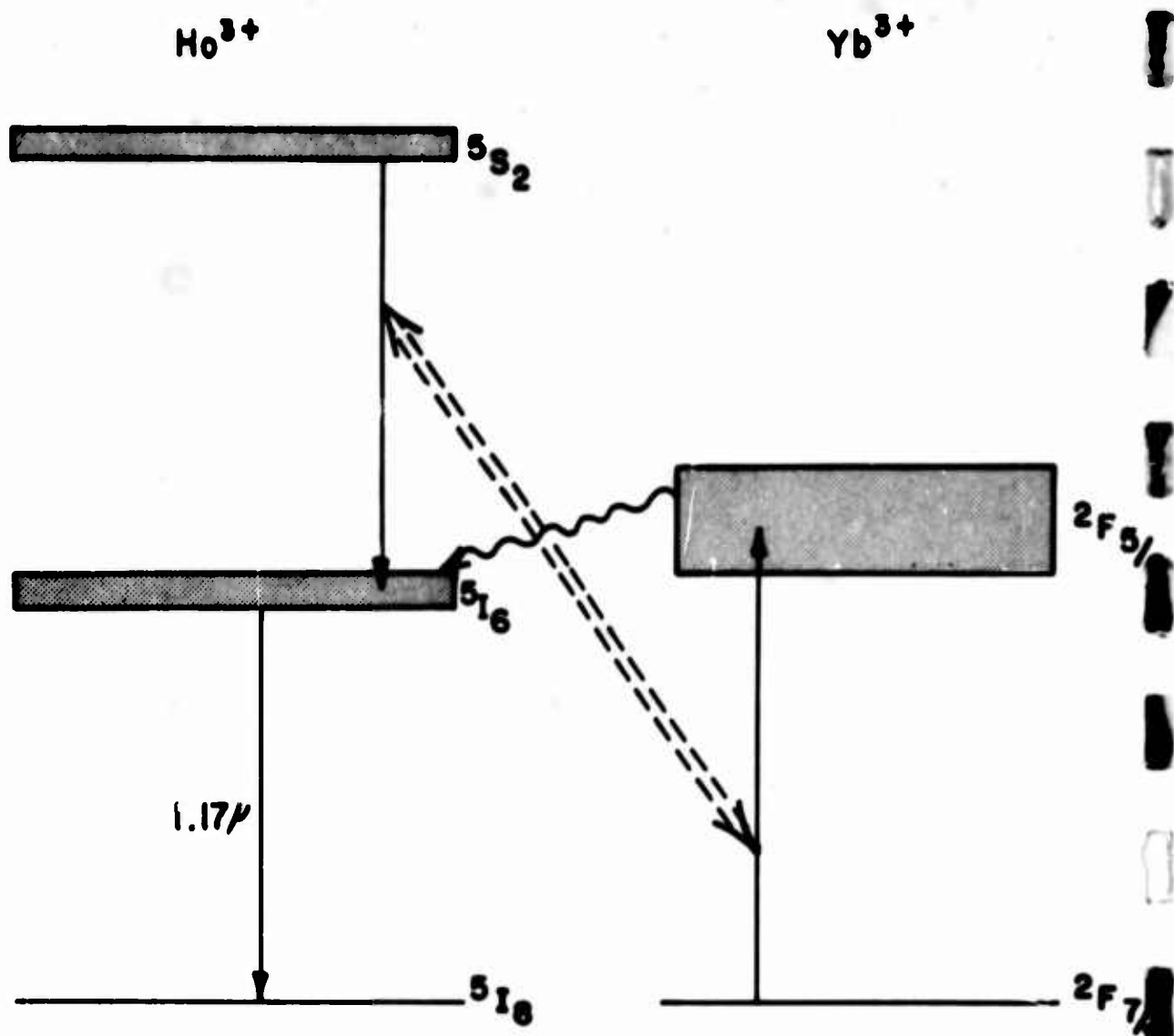
The Energy Levels of Tetravalent Dysprosium. Fluorescence and Absorption Spectra of Cesium Dysprosium(IV) Heptafluoride

Louis P. Varga, Oklahoma State University and
Larned B. Asprey, Los Alamos Scientific Laboratory
(work done at Los Alamos Scientific Laboratory)

ABSTRACT

When cesium salts of dysprosium containing 3:1 mole ratio cesium:dysprosium are reacted for several hours with fluorine gas at 200°-250°C and 50-60 psig, the white Dy(III) salt is converted to a bright orange material with an empirical formula approaching Cs_3DyF_7. Absorption and fluorescence spectra of fluorocarbon mulls of this material at liquid N_2 temperatures were taken using continuous recording spectrophotometers and the low lying f^n transitions were analyzed for evidence of the Dy(IV) species with the $4f^8$ configuration.

Since Dy(IV) is isoelectronic with Tb(III), comparison of the middle and near infrared absorption spectra of the orange fluorination product against that of some Tb(III) compounds and the parent Dy(III) compound allowed identification of all of the components of the ^7F ground state multiplet for Dy(IV). Less effective screening of the nuclear charge in tetravalent dysprosium resulted in a raising of the $4f$ energy levels compared with isoelectronic Tb(III), as expected. The approximate centers of the six levels above the $^7F_6$ ground state were found at 2000 cm^{-1}, 4120 cm^{-1}, 5480 cm^{-1}, 6560 cm^{-1}, 7250 cm^{-1} and 7460 cm^{-1} for J values 5, 4, 3, 2, 1, 0, respectively. These energies compare with the corresponding energy levels 2043 cm^{-1}, 3438 cm^{-1}, 4379 cm^{-1}, 5038 cm^{-1}, 5488 cm^{-1} and 5701 cm^{-1} for Tb(III) given by Thomas, Singh and Dieke.[1]

Excitation of fluorocarbon mulls of Cs_3DyF_7 at 4050 A° resulted in fluorescence at 5250 A° and a weaker line at 6300 A°. Assuming that the most intense fluorescence transition was $^5D_4 \rightarrow ^7F_5$, analogous to Tb(III), the $^5D_4$ level of Dy(IV) was placed near 21,000 cm^{-1}, some 600 cm^{-1} above the Tb(III) $^5D_4$ level.

An energy level diagram is presented comparing several unusual oxidation states of the lanthanides.

Considerable qualitative evidence has been found for a higher oxidation state of dysprosium.[2] Critical reviews of the data, however, have indicated possible alternate explanations for the observations other than the true existence of Dy(IV) with the f^8 configuration.[3] For instance, elevated temperature and pressure fluorination of the rubidium or cesium salts were required for any evidence of a higher oxidation state. The oxidizing power of the product, therefore, could be explained on the basis of elemental fluorine in the solid lattice. This followed from evidence for the existence of the addition compound CsF_3 in lower temperature fluorinations. Iodometric analyses for oxidizing power and weight gain determinations indicated no more than 75 to 80% conversion from Cs_3DyF_6 to Cs_3DyF_7.

Magnetic susceptibility measurements indicated that no more than half of the element in the oxidized compound could be Dy(IV). X-ray powder diffraction patterns showed no change in structure on fluorination of Cs_3DyF_6 indicating that the seventh fluorine did not distort the normal face-centered cubic lattice.

Previously published absorption data showed new absorption maxima for the Cs_3DyF_7 compound in fluorocarbon mulls at 25°C but there was an overabundance of lines which prevented a simple interpretation of the spectra.[3]

The extensive experimental and theoretical work of Dieke, Crosswhite and others[4] on crystal spectra of trivalent rare earth ions and on the third and fourth emission spectra of the rare earths has yielded invaluable information on the energy levels of divalent and trivalent lanthanides. Although the exact positions of the levels are a function of the ion environment, even for the shielded f orbitals, most absorption and fluorescence spectra of di- and trivalent lanthanides can be interpreted using these data. However, fifth spectra from arc and spark data have not been available to chemists interested in the higher oxidation states of the lanthanides.

Studies on all available oxidation states of the lanthanides have gained additional impetus in recent years due to the unique nature of the f^n transitions. A favorable combination of energy level spacings, energy level lifetimes and shielded orbitals result in sharp line fluorescence relatively independent of environment and laser action has been observed for most lanthanides.[5]

Because of shielding effects the lower effective nuclear charge of divalent lanthanides results in a scaling down of the energy levels. For Sm(II) the scaling factor is about 0.85 when compared with energy levels of the isoelectronic

Eu(III).[4b] Similar considerations then apply to Eu(II)
compared with Gd(III), etc. Thus several new transition
energies are made available for the construction of laser
materials.

Less effective screening of the nuclear charge in tetra-
valent lanthanides, conversely, results in a raising of the
$4f$ energy levels compared with the isoelectronic partner.
Thus Pr(IV) with the f^1 configuration has the single $^2F_{7/2}$
upper energy level similar to Ce(III) but with a higher
energy.[6] Likewise Tb(IV) would have similar but higher
levels than Gd(III), etc. The result is the further exten-
sion of the number of possible resonance fluorescence trans-
itions in the $4f$ shell.

These same considerations allow also a unique mechanism
for the identification and characterization of unusual oxi-
dation states of the lanthanides. In this study the orange
material resulting from the fluorination of cesium salts of
dysprosium containing 3:1 mole ratio cesium:dysprosium was
compared by middle and near infrared absorption spectro-
scopy and by visible fluorescence spectroscopy with the
corresponding energy level transitions of Tb(III) in order
to identify and characterize the levels of the isoelectronic
f^8 configuration of Dy(IV).

Experimental

Rare earths. - The purest available oxides were used and
no spectral evidence was found for significant impurity levels.
A sample of $Cs_3Dy(SO_4)_3$ which had been prepared in this lab-
oratory several years ago was found to be relatively stable
and non-hygroscopic.

Cs_3REF_6. - Rare earth oxides were dissolved in hydro-
chloric acid, fumed to near dryness, hydrofluoric acid added,
and the REF_3 precipitate centrifuged, washed with dilute
hydrofluoric acid, and dried in an oven. Three moles of high
purity CsF per mole of REF_3 were weighed in a dry box and the
two salts were ground in the dry box to an intimate mixture
with an equal volume of ammonium fluoride. This mixture was
placed in a platinum dish in a hood and heat was applied using
a Meker burner until fumes of NH_4F stopped coming off the
molten mass. The solid Cs_3REF_6 was ground to a powder in a
dry box, a capillary loaded for an X-ray powder pattern, and
the sample stored in polyethylene in a desiccator. Terbium,
dysprosium and holmium salts were prepared in this manner.

Anhydrous REF$_3$. - Water bands were noticed in the IR region using "wet prep" trifluoride salts prepared as above. Anhydrous trifluorides were prepared by subjecting the "wet prep" trifluorides to fluorine gas at 200° C and 50-60 psig for several hours. X-ray powder patterns indicated no oxidation of GdF$_3$, TbF$_3$ or DyF$_3$ in this procedure.

Cs$_3$REF$_7$. - When Cs$_3$TbF$_6$, Cs$_3$DyF$_6$ or Cs$_3$Dy(SO$_4$)$_3$ were fluorinated at 200-250° C and 50-60 psig. for periods ranging from 7 to 18 hours, oxidized products were obtained. In the case of terbium the product was white to gray and for dysprosium the usual product was bright orange. The fate of oxygen and sulfur in the case of fluorination of the sulfate salt was unknown. One of the best preparations of Cs$_3$DyF$_7$, the one on which the final spectra were obtained, involved three successive cycles of evacuation, elevated temperature and pressure fluorination, cooling, flushing with helium, reevacuation and opening the reactor for inspection after each cycle X-ray powder camera patterns were obtained on all products from the fluorinator. Fluorination of Cs$_3$HoF$_6$ yielded no change in color or chemical properties of the product.

The fluorination reactor. - The main features of this apparatus are described elsewhere.[3,7] However, the unit used in the present studies opened into a very efficient helium atmosphere dry box containing large trays of anhydrous magnesium perchlorate so that highly reactive products could be prepared for X-ray and spectral studies with minimum danger of moisture or air contamination.

Detection apparatus. - X-ray powder diffractive patterns were obtained using CuKα radiation with a Ni filter and a 114.6 mm powder camera. A Perkin-Elmer Model 521 IR spectrophotometer was used for the middle IR absorption studies and a Cary Model 14 spectrophotometer was used for the UV, visible and near IR absorption measurements and for all fluorescence measurements.

Sample preparation and mounts. - In spite of the helium atmosphere dry box the orange cesium dysprosium(IV) fluoride could not be extensively handled with the rubber gloves of the dry box without obvious bleaching. Rapid grinding of the material and subsequent operations such as dry loading of X-ray capillary tubes and sealing the capillary with Fluorolube oil (Hooker Chem. Corp.) or the preparation of dry mounts for spectral studies were occasionally successful. A surer method was immediate protection of the sample in the dry box with Fluorolube oil so that grinding and further sample preparation was carried out exclusively on the mull.

Fluorolube mulls of the Dy(IV) compound were pressed

between cesium bromide plates for spectral studies in the middle IR region. The plates could be removed from the dry box, mounted on a cold-finger, the cold cell evacuated and the sample brought to liquid nitrogen temperature without visual or spectral evidence for decomposition in the majority of attempts. All other compounds worked with were mulled with Fluorolube outside the glove box and successfully mounted on the cold finger without apparent decomposition or pick-up of moisture.

When absorbance measurements in the U.V., visible and near IR regions and all fluorescence measurements using the Cary 14 spectrophotometer were made, all samples were mounted on a Cary No. 1440650 liquid helium dewar. However, instead of liquid helium the central vessel was filled with liquid nitrogen in these studies. Again, in the case of Cs_3DyF_7, the Fluorolube mulls were pressed between crystal quartz or sapphire windows and mounted on the sample holder in the helium dry box. The prepared sample was rapidly fastened to the cold finger outside the dry box, the cold cell evacuated and the sample cooled. With care, other materials were mulled with Fluorolube and mounted outside the dry box.

Fluorescence excitation. - The excitation lamp was a Hanovia 150 w. compact xenon arc lamp operating on D. C. The arc was focused with an off-axis ellipsoidal mirror on the entrance slit of a Farrand f3.5 grating monochromator with a range 2200 to 7000 A°. The beam from the 10mμ bandwidth exit slit impinged on the sample through the quartz windows of the evacuated cold cell normal to the aperture of the Cary detector monochromator. The samples were mounted at an angle near 45° to the direction of the excitation beam so that fluorescence from the front surface of the solid sample entered the Cary optical system. The detector photomultiplier was mounted in the normal position as when the Cary fluorescence attachment was used.

Results of the Absorbance Studies

Terbium(III). - In Table I the observed absorption maxima for TbF_3 and Cs_3TbF_6 are compared with the energy levels for Tb(III) given by Dieke and Crosswhite.[4a] In the spectra of TbF_3 all of the ground state multiplets were observed except $^7F_6 \longrightarrow {}^7F_5$ at 2000 cm^{-1} corresponding to the lowest excited state. The observed transitions were all crystal field split. In the case of Cs_3TbF_6, Table I points up the important fact that this compound absorbed significantly nowhere in the IR or visible regions and showed only a gradual absorption toward the ultra violet.

Dysprosium(III). - Table I shows that both DyF_3 and Cs_3DyF_6 gave an abundance of lines for transitions from the $^6H_{15/2}$ ground state of Dy(III) to lines as far out as the $^6F_{5/2}$ state at 12,200 cm^{-1}. In the case of Cs_3DyF_6, however, an unexpected band centered at about 4200 cm^{-1} was apparent in the near IR spectrum as shown in Figure 1A and an unexpected pair of lines appeared at 1990 and 1830 cm^{-1} in the middle IR as indicated in Table I and in Figure 1B. The complete absence of absorption short of the ultraviolet in the case of Cs_3TbF_6 ruled out the possibility of impurity terbium in the dysprosium giving the $^7F_6 \longrightarrow {}^7F_5$ terbium(III) transition at 2000 cm^{-1} so the conclusion remained that the band at 4200 cm^{-1} and the pair of lines at 1990 and 1830 cm^{-1} were associated with dysprosium.

Dysprosium(IV). - The absorption lines observed for the orange Cs_3DyF_7 are listed in Table I. The presence of unoxidized Dy(III) was apparent by the group of lines at 7870, 9170, 11,100 and 12,340 cm^{-1}. However, six absorption maxima at longer wavelengths, also shown in Figure 1C and 1D, corresponded precisely in number and relative position to that expected for the components of the ^7F ground state multiplet of the $4f^8$ configuration isoelectronic with Tb(III) but with a higher nuclear charge. The approximate centers of the six levels above the $^7F_6$ ground state were found at 2000 cm^{-1}, 4120 cm^{-1}, 5480 cm^{-1}, 6560 cm^{-1}, 7250 cm^{-1} and 7460 cm^{-1} for J values 5, 4, 3, 2, 1, 0, respectively. These energies may be compared to the Tb(III) levels given in Table I and Figure 2.

Inspection of the Cs_3DyF_7 and Cs_3DyF_6 spectra indicated that the two absorption maxima of Cs_3DyF_6 at 1990 and 4200 cm^{-} corresponded very closely to two energy levels of Dy(IV). The f^n transition of Dy(III) closest in energy is at 3500 cm^{-1}. The possibility for there being a small amount of (IV) character in the dysprosium of Cs_3DyF_6 raises some interesting questions.

TABLE I. COMPARISON OF ABSORPTION SPECTRA

cm^{-1}

Terbium(III)				Orange "Cs₃DyF₇"			Dysprosium(III)			
$S'L'J'$ D&C[4] $^7F_6\rightarrow$		TbF₃	Cs₃TbF₆	$S'L'J'$ Dy(IV) $^7F_6\rightarrow$		Dy(III)	$S'L'J'$ D&C[4]		DyF₃	Cs₃DyF₆
$^7F_5$ 2043		no	no	$^7F_5$ 2000						1990
				(1824)						(1830)
$^7F_4$ 3438		3465†	no	$^7F_4$ 4120						4200b
							$^6H_{15/2}\rightarrow$			
							$^6H_{13/2}$ 3500		3550†	no
						5020				5030b
$^7F_3$ 4379		4500†	no	$^7F_3$ 5480						
$^7F_2$ 5038		5070†	no	$^7F_2$ 6560						
$^7F_1$ 5488		5520†	no	$^7F_1$ 7250						
$^7F_0$ 5701		5760†	no	$^7F_0$ 7460						
							$^6H_{11/2}$ 5800		5930†	no
				$^6H_{15/2}\rightarrow$						
				$^6H_{9/2}$		7870	$^6H_{9/2}$ 7600		7850†	7870b
				$^6H_{7/2}$		9170	$^6H_{7/2}$ 9000		9100†	9170b
							$^6H_{5/2}$ 10100		no	no
				$^6F_{7/2}$		11100	$^6F_{7/2}$ 10900		11000	11100
				$^6F_{5/2}$		12340	$^6F_{5/2}$ 12200		12360	12500
		2500A° cutoff		5000A° cutoff						

† most prominent line or the center of a bundle of crystal field split lines

no not observed

b broad

Cs₃DyF₆

A

B

Cs₃DyF₇

C

D
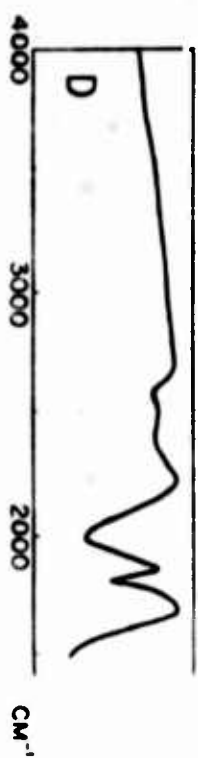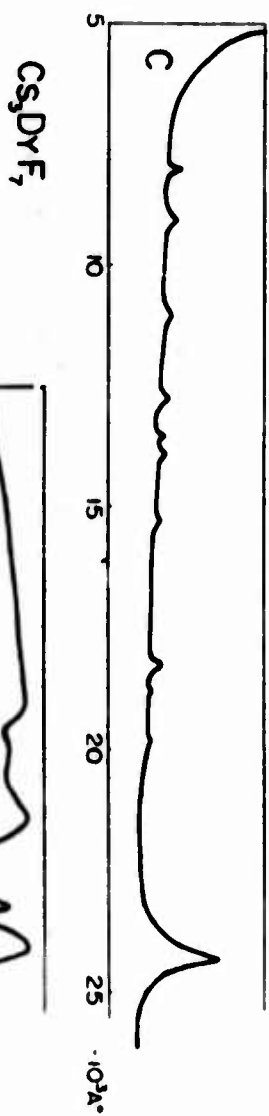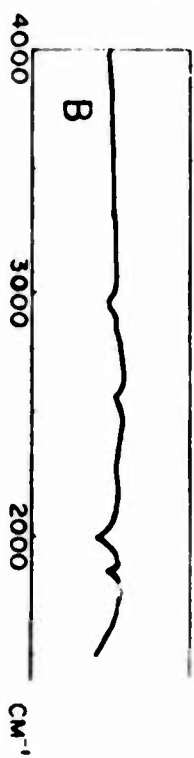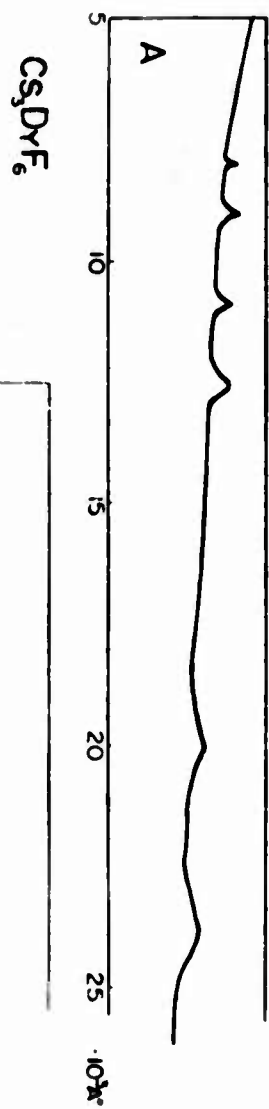
Results of the Fluorescence Studies

Terbium(III). - Efficient fluorescence of this ion takes place from the $^5D_4$ energy level to the ^7F ground state multiplet[4] and spectra have been reported for several compounds.[1] The most intense transition is $^5D_4 \longrightarrow {}^7F_5$ and this has been reported as a doublet in the SiO_2 lattice and in the $Tb(NO_3)_3$ $6H_2O$ crystal.[9]

Anhydrous TbF_3 gave no significant fluorescence in our experiments. On the other hand Cs_3TbF_6 yielded intense fluorescence in the region expected for the $^5D_4 \longrightarrow {}^7F_5$ transition when excited at 3800 A° and shorter wave lengths, an absorption region rich in lines for Tb(III) as indicated in Figure 2. The fluorescence transition $^5D_4 \longrightarrow {}^7F_5$ was easily resolved into 3 lines at 5405, 5495 and 5520 A° and weaker transitions for $^5D_4 \longrightarrow {}^7F_4$ at 5810 A° and $^5D_4 \longrightarrow {}^7F_6$ at 4860 A° also were observed.

Dysprosium(III). - In fluorescence studies on the compound Cs_3DyF_6 careful elimination of peaks due to xenon lines, second order diffraction effects and the fluorescence of quart left only one fluorescence line at 5670 A°. Comparisons with the work of Dieke and Singh[10] and Freeman and Crosby[11] indicated that this was the $^4F_{9/2} \longrightarrow {}^6H_{13/2}$ transition as shown in Figure 2.

Dysprosium(IV). - In studies on the fluorescence of the orange Cs_3DyF_7, two fluorescence transitions were observed. The most intense line was at 5250 A° and the other observed line was at 6300 A°. The assumption was made, analogous to Tb(III), that the most intense fluorescence transition was $^5D_4 \longrightarrow {}^7F_5$, placing the $^5D_4$ level near 21,000 cm^{-1} as indicated in Figure 2. Then the 6300 A° line probably corresponded to $^5D_4 \longrightarrow {}^7F_3$ of Dy(IV). Although the exact position of the $^5D_4$ level for Dy(IV) remains tentative, the experimental placement some 600 cm^{-1} above $^5D_4$ for Tb(III) is qualitatively correct.

Terbium(IV). - The first excited level for Tb(IV) was expected to be too high to see in absorption using a mull sample because of scattering problems in the ultraviolet. With excitation at 2550 A°, near the limit of our instrument, no fluorescence was seen at wavelengths greater than 3000 A° putting a lower limit of about 33,000 cm^{-1} for the first excited level. The placement of the level in Figure 2 was an estimate based on the above considerations and from comparison with the levels of isoelectronic Eu(II) and Gd(III).

Discussion

The spectral evidence for the existence of the Dy(IV) species with the f^8 electronic configuration appears adequate. The chemical species best describing the 3:1 cesium: dysprosium fluoride complex is Cs_3DyF_7, but further studies will be required to determine the yield of the Dy(IV) species and the Dy:F ratio in the crystal lattice as a function of preparative variables.

The energy levels for Dy(IV) shown in Figure 2 will remain tentative until the Cs_3DyF_7 structure is determined and questions such as the coordination number of the smaller Dy^{+4} ion and the symmetry of the system are known. Calculations on the energy levels of the free Dy^{+4} ion are in progress.

The appearance of the pair of lines at about 2000 and 4200 cm^{-1} in both Cs_3DyF_6 and Cs_3DyF_7 which was here assigned to the $^7F_6 \rightarrow {}^7F_5$ and $^7F_6 \rightarrow {}^7F_4$ transitions of Dy(IV) warrants further discussion. If, indeed, there is some Dy(IV) character in Cs_3DyF_6, then the nature of the electron acceptor and the mechanism for electron transfer must be defined. It is significant to recall that higher oxidation states of lanthanides in alkali metal fluoride salts are easier to obtain by fluorination the larger the ionic radius of the alkali metal and the higher the alkali metal:lanthanide ratio. It is probable that the looser structure due to the many large alkali metal ions is of some importance in allowing more fluoride ions to enter the structure. Yet it seems strange that these would be necessary criteria considering that 7 coordinate metal fluoride structures are known for tetravalent zirconium[12] and 7 and 8 coordinate structures are known for pentavalent niobium and tantalum[13] all of which undoubtedly have ionic radii smaller than Dy^{+4}. It is conceivable that some contribution to the stability of a higher oxidation state is found in the low potential required for electron exchange in compounds containing large alkali metals such as cesium. Reference to Dieke and Crosswhite[4a] on the relative energy requirements between $4f^n$, $4f^{n-1}\ 5d^1$ and $4f^{n-1}\ 6s^1$ transitions for the triply ionized lanthanides, however, indicate that excessive energy is demanded for promotion of the electron. The question concerning the similarity of the Cs_3DyF_6 and Cs_3DyF_7 spectra at 2000 cm^{-1} and 4200 cm^{-1} must go unresolved for the present.

Energy level diagram

$\cdot 10^3\ cm^{-1}$

40 — 38 — 36 — 34 — 32 — 30 — 28 — 26 — 24 — 22 — 20 — 18 — 16 — 14 — 12 — 10 — 8 — 6 — 4 — 2 — 0

$^6D_{9/2}$

^4f

$^6P_{7/2}$

$^5D_3$

$^5D_2$

$^5D_1$

$^5D_0$

$^8P_{7/2}$

$^6P_{7/2}$

$^5D_4$

$^5D_4$

$^5D_3$

$^7F_6$

$^7F_6$

$^7F_0$

$^4G_{11/2}$

$^4I_{15/2}$

$^4F_{9/2}$

$^6P_{7/2}$

$^7F_0$

$^3P_2$

$^1I_6$

$^1D_2$

$^1G_4$

$^3F_4$

$^3H_6$

$^4f^{13}-5d^1$

$^2F_{5/2}$	$^2F_{5/2}$	$^3H_4$	$^7F_0$	$^7F_0$	$^8S_{7/2}$	$^8S_{7/2}$	$^8S_{7/2}$	$^7F_6$	$^7F_6$	$^6H_{15/2}$	$^2F_{7/2}$	$^1S_0$
Ce⁺³	Pr⁺⁴	Pr⁺³	Sm⁺²	Eu⁺³	Eu⁺²	Gd⁺³	Tb⁺⁴	Tb⁺³	Dy⁺⁴	Dy⁺³	Yb⁺³	Yb⁺²
f^1	f^1	f^2	f^6	f^6	f^7	f^7	f^7	f^8	f^8	f^9	f^{13}	f^{14}

- 269 -

References

1. K. S. Thomas, S. Singh and G. H. Dieke, J. Chem. Phys., 38, 2180 (1963).

2. L. B. Asprey and B. B. Cunningham in "Progress in Inorganic Chemistry", F. A. Cotton, ed. Interscience, N. Y. (1960). Vol. II. pp. 267-302.

3. L. B. Asprey in "Rare Earth Research", E. V. Kleber, ed. Macmillan, N. Y. (1961), pp. 58-65.

4a. G. H. Dieke and H. M. Crosswhite, Appl. Optics., 2, 675 (1963); "Atomic Spectra", Chris Candler, Van Nostrand, N. J., 2nd ed. (1964). pp. 208-255.

 b. D. S. McClure in "Solid State Physics", Fred Seitz and David Turnbull, eds. Vol. 9, Academic Press, N. Y. (1959), pp. 453-476. See references cited.

5. A. Yariv and J. P. Gordon, Proc. IEEE, 51, 1-26 (1963).

6. L. B. Asprey, J. S. Coleman and M. J. Reisfeld, 152nd Meeting, A.C.S. New York, Sept. 12-16, 1966. Paper 52, Div. Inorg. Chem.

7. L. B. Asprey, J. Am. Chem. Soc., 76, 2019 (1954).

8. A. Heller and E. Wasserman, J. Chem. Phys. 42, 949 (1965)

9. W. F. Nelson, F. T. King and S. W. Barber in "Rare Earth Research II", K. S. Vorres, ed., Gordon and Breach, N. Y. (1964) pp. 573-582.

10. G. H. Dieke and S. Singh, J. Opt. Soc. Am. 46, 495 (1956)

11. J. J. Freeman and G. A. Crosby, J. Phys. Chem. 67, 2717 (1963).

12. G. C. Hampson and L. Pauling, J. Am. Chem. Soc., 60, 2702 (1938).

13. J. L. Hoard, J. Am. Chem. Soc., 61, 1252 (1939); J. L. Hoard, et. al., ibid, 76, 3820 (1954).

CATHODOLUMINESCENCE OF RARE EARTH-ACTIVATED YTTRIUM OXIDE*

R. A. Buchanan, K. A. Wickersheim, J. L. Weaver, L. E. Sobon
and E. E. Anderson

Lockheed Palo Alto Research Laboratory

Palo Alto, California

ABSTRACT

The current interest in rare earth-activated phosphors has stimulated us to undertake this general survey of the cathodoluminescent properties of rare earths in yttrium oxide. Y_2O_3:Eu and Gd_2O_3:Eu are phosphors whose cathodoluminescent properties have been previously reported. Their sharp line emission spectra, superior performance and chemical stability are some of the interesting characteristics of these materials. It seems worthwhile to investigate the relevant properties of the other rare earth activators in yttrium oxide. Those properties of special interest to be reported in this study are (1) optimum activator concentrations for electron excitation, (2) emission spectra from 2500 Å to 3 microns, (3) lifetimes of principal emission lines and (4) efficiencies.

The materials studied were in the form of powders which had been precipitated as oxalates and fired in air to form the phosphors. These phosphor powders were loaded into a demountable electron-gun vacuum system and excited with 9-kv electrons at beam current densities of about $2.5~\mu$ amp per cm^2. Survey spectra and lifetime studies were made using a 1/4-meter Jarrell-Ash monochromator system and photomultiplier detector. Lifetimes were measured using a pulsed electron beam and ordinary photomultiplier and oscilloscope techniques. Precise wavelength measurements and photometric measurements were taken with a Cary Model 14 used as a spectrometer with MPT and PbS detectors.

Several of the rare earths have most of their emission concentrated in a few closely spaced lines while others distribute their emission among several widely spaced groups of lines. Lifetimes of principal lines fall generally in the several hundred microsecond range and show a correlation with the energy gap from the emitting state to the next lowest state.

Introduction

Cathodoluminescence was first observed[1] independently by E. Becquerel and J. Plucker in 1858. Since then a steady stream of measurements has been reported on the cathodoluminescent properties of various materials. As early

as 1863 Crooks[2] studied the cathodoluminescence of rare earths and published several papers on their cathode-ray spectra (including[3] Eu in Y_2O_3) between 1879 and 1899.

In this short communication we cannot follow all such work to the present time. To our knowledge, no general survey of the cathodoluminescence of all the rare earths substituted individually into any single host lattice has been reported. Our interest will be limited to rare earth-activated Y_2O_3. A few recent publications dealing with the spectroscopic properties of selected rare earths in Y_2O_3 are listed in footnote 4.

The present study was motivated by an interest in materials having application in radiation and particle detection. In addition, it was anticipated that a general survey of rare earths in one host lattice might reveal some interesting and fundamental properties.

Though cubic in structure[5], yttrium oxide has a complex unit cell with two distinct types of rare earth sites differing in symmetry (C_2 versus S_6) and relative abundance (3 to 1). The inversely symmetric (S_6) site is presumed to contribute very little to the emission spectrum. A consideration of these sites and their symmetries will be essential to any detailed analysis of the spectrum but is unnecessary for the bulk of the observations to be presented in this paper.

Previous studies of rare earth luminescence have used ultraviolet excitation. Rare earths do not absorb uniformly in the ultraviolet and as a result excitation is nonuniform. The use of cathode rays has reduced the importance of nonuniformity of excitation in the observed emission characteristics.

Experimental Details

A 1/4-meter Jarrell-Ash monochromator and a Cary Model 14 RI spectrophotometer were used in this study. A special attachment consisting of a vacuum chamber containing a 10-position sample wheel and a standard 5UP Superior Electronics Corp. electron gun assembly was constructed for use on either the 1/4-meter Jarrell-Ash or the Cary instrument. The electron beam was controlled by an oscilloscope system. The details of this cathodoluminescence attachment will be presented in a separate communication.

The materials used in this study were prepared as fine powders by first dissolving the rare-earth and yttrium oxides in acid, then precipitating an oxalate and finally calcining the oxalate at about 1300°C.

After establishing a reproducible materials preparation procedure, we conducted a study of emission versus activator concentration for each rare earth. Five or six samples were prepared having activator concentration ranging from .01 to 10 mole percent. The spectrum of each sample was

surveyed on the 1/4-meter Jarrell-Ash monochromator system and the emission intensity was plotted as a function of activator concentration. The peak of the emission curve was accurate only to about plus or minus 20% of the stated value, but generally this curve was sufficiently flat that the intensity was not critically affected by errors in concentration of this magnitude. Generally, we chose the most intense line which we could observe with the R136 multiplier phototube for determining the optimum concentration.

Spectra of the samples having the optimum level of activation were taken with the Cary 14 RI. The spectral response of the Cary system was obtained using a calibrated tungsten iodine lamp[6]. The system's relative spectral response using the different detectors is shown in Fig. 4. Generally the system gain was adjusted to bring the strongest emission line to approximately full scale deflection for each spectrum.

Rise and decay times were measured for the total emission with the R136 and 7102 multiplier phototubes. In addition, the 1/4-meter Jarrell-Ash system was used to isolate the most intense lines for rise and decay time studies. Rise and decay times were measured by modulating the electron beam with a square wave and observing the emitted light wave form on an oscilloscope. The system response time was 8 μsec. and all reported values have been corrected for the system response.

The efficiency measurements were made using a black detector and observing the total luminescence of each phosphor under as nearly identical excitation conditions as possible. The Y_2O_3 phosphors and standard phosphors of known efficiency were mounted on the sample wheel. The radiation from each sample was collected by a toroidal mirror and focused on the detector. The detector signal was recorded as each of the samples in turn was excited by the electron beam. The phosphors of known efficiency ($CaWO_4$, $ZnO \cdot Zn$, $ZnCdS \cdot Ag$, $ZnS \cdot Ag$, $ZnSiO_4 \cdot Mn$, and $YVO_4 \cdot Eu$) gave detector signals which when plotted as a linear function of efficiency produced a reasonably straight line. The efficiency of the unknown phosphors was then determined from this graph. These efficiency results must be considered tentative. We plan to measure efficiencies by other techniques before accepting these results as final.

Results

The results are summarized in Table 1. Optimum activator concentration represents the mole percentage of activator necessary to give the most intense emission for the strongest emitting line of the spectrum. All subsequent measurements were made using that material from the concentration study whose composition was closest to optimum. The activator concentrations used for the life-time and spectral studies are listed on the spectra in Figs. 1 through 4.

Principal emission is the wavelength in nanometers of the strongest emission line or lines when the system spectral response is taken into account. In Pr, Er and Tm the visible and infrared emissions are roughly comparable in intensity, and both are listed. Gd, Eu and Dy have most of their emission in a few very closely spaced lines.

The efficiency considered here is the power efficiency, i.e., total watts emitted per watt of incident electron beam power (expressed in percent). The highest efficiency is found for Eu. Dy, Nd, Gd and Tb also have respectable efficiencies. It is significant to note that no rare earth yields an efficiency less than 1/7 that of Eu.

Rise and decay times of the most intense emission lines were measured individually with the Jarrell-Ash monochromator. Some correlation of decay time with energy gap between the emitting level and the nearest level below the emitting level is observed.

Spectra are presented in Figs. 1 through 4. The intensities of the emission peaks have not been corrected for the system spectral response which is shown in Fig. 4. In addition, the gain of the system has been adjusted for each spectrum such that the brightest line has a maximum deflection. The broad emission generally observed between 1000 and 3000 nm is due to electron-gun heater radiation which is incident on the phosphor and scattered diffusely into the spectrometer.

Discussion

It is widely accepted that only rare earths near the center of the series, i.e., Sm^{3+}, Eu^{3+}, Gd^{3+}, Tb^{3+} and Dy^{3+} fluoresce efficiently[7,8]. However, we observe that all rare earths in Y_2O_3 cathodoluminesce with a power efficiency which is constant to within a factor of about 7.

It is true, however, that the rare earths near the center of the series are the most intense visible and u.v. emitters while those toward the ends of the series are the most intense infrared emitters. This observation is consistent with the fact that the largest energy gaps occur for those ions nearest the center of the series.

The difficulties of infrared detection and the choice of host materials (usually containing waters of hydration) both contributed to a neglect by early workers of the significance of infrared emission and thus to the belief that the middle rare earths were the most efficient emitters.

The optimum activator concentrations vary remarkably from rare earth to rare earth. Though total efficiencies at the optimum concentration vary by only a factor of 7, the optimum concentrations themselves vary by well over two orders of magnitude. If one considers the efficiency per activator ion, the spectroscopic folk lore of the rare earths is altered drastically with certain ions long considered to be least efficient now coming out on top.

The principal emission listed in Table 1 has been indicated by a transition arrow for each rare earth in the energy level diagram shown in Fig. 5. An interesting correlation, as noted earlier, can be made between decay times and energy gap between emitting state and next lowest state. This has been plotted in Fig. 6. Gd, the center element of the rare earth series, has the largest

energy gap and the longest decay time. The next largest energy gap occurs for Tb which has the next longest decay time. This general correlation, with some scatter, is observed for the entire rare earth sequence. It is our feeling that the importance of phonon-assisted nonradiative relaxation and its strong dependence on the number of lattice phonons required to bridge the rare earth energy gap provide the explanation for this approximate correlation. However, in any attempt to formalize the correlation in terms of single ion relaxation we will have to consider intrinsic decay times (i.e., for low level activation) rather than the decay times at optimum concentration since the latter clearly reflect concentration quenching effects as well.

A practical consequence of the observation that all rare earths yield respectable cathodoluminescent efficiencies, is that almost all must be considered as practical activators in this system with their potential use being dependent largely on the wavelengths of emission desired.

References and Footnotes

(1) E. Newton Harvey, "A History of Luminescence" published by the American Philosophical Society, Philadelphia, 1957, page 410

(2) Ibid, page 413

(3) M. W. Crookes, Phil. Trans. Roy. Soc., 891, (1883), ibid, 691 (1885)

(4a) K. A. Wickersheim and R. A. Lefever, J. Electrochemical Soc. 111, 47 (1964)

(4b) R. C. Ropp, J. Electrochemical Soc. 111, 311 (1964)

(4c) N. C. Chang, J. Appl. Physics 34, 3500 (1963)

(4d) N. C. Chang and J. B. Gruber, J. Chem. Phys. 41, 3227 (1964)

(4e) A. Bril and C.O.J.C. de Laat, Electrochemical Technology 4, 21 (1966)

(4f) R. C. Ropp and E. E. Gritz, Electrochemical Technology 4, 24 (1966)

(4g) R. H. Hoskins and B. H. Soffer, Applied Physics Letters 4, 22 (1964)

(4h) J. B. Gruber, W. F. Krupke and J. M. Poindexter, J. Chem. Phys. 41, 3363 (1964)

(5) L. Pauling, Z. Krist. 75, 128 (1930)

(6) The Standard Lamp (Model L101), its calibration and power supply were obtained from Electro Optics Associates, Palo Alto, Calif.

(7) G. H. Dieke and L. A. Hall, J. Chem. Phys. 27, 465 (1957)

(8) Donald S. McClure, Solid State Physics, Vol. 9, (1959)

TABLE I - SUMMARY OF RESULTS

Activator	Pr	Nd	Sm	Eu	Gd	Tb	Dy	Ho	Er	Tm	Yb
Color	Pink	(IR)	Yellow	Red	(UV)	Green	White	Green	Green	Blue	(IR)
Optimum Conc. (%)	.03	0.5	0.2	4	3	0.3	0.2	1	1	0.8	2.5
Principal Emission (nm)	630/948	1080	608	611	316	544	572	549	564/1535	454/1935	977
Efficiency (%)	3.0	5.9	3.3	10.3	4.5	3.5	5.8	1.4	1.8	3.6	4.3
Rise/Decay Times-Total Emission (m sec.)	.08/.13	.20[a]/.40	.5/1.25	.50/1.1	.60/2.0	.7/1.4	.25/.4	.04/.07	.04/.07	.004/.006	.40[a]/.65
Rise/Decay Times-Principal Emission (m sec.)	.12[b]/.16	-/.26[c]	.6/1.2	.60/1.0	.70/2.0	.9/1.7	.15/.4	.06/.08	.05[b]/.07	.004[b]/.017	-

NOTES:

a. Total emission was measured with 7102 phototube. R136 phototube was used in all other measurements.

b. ...... to the principal emission in the visible spectrum.
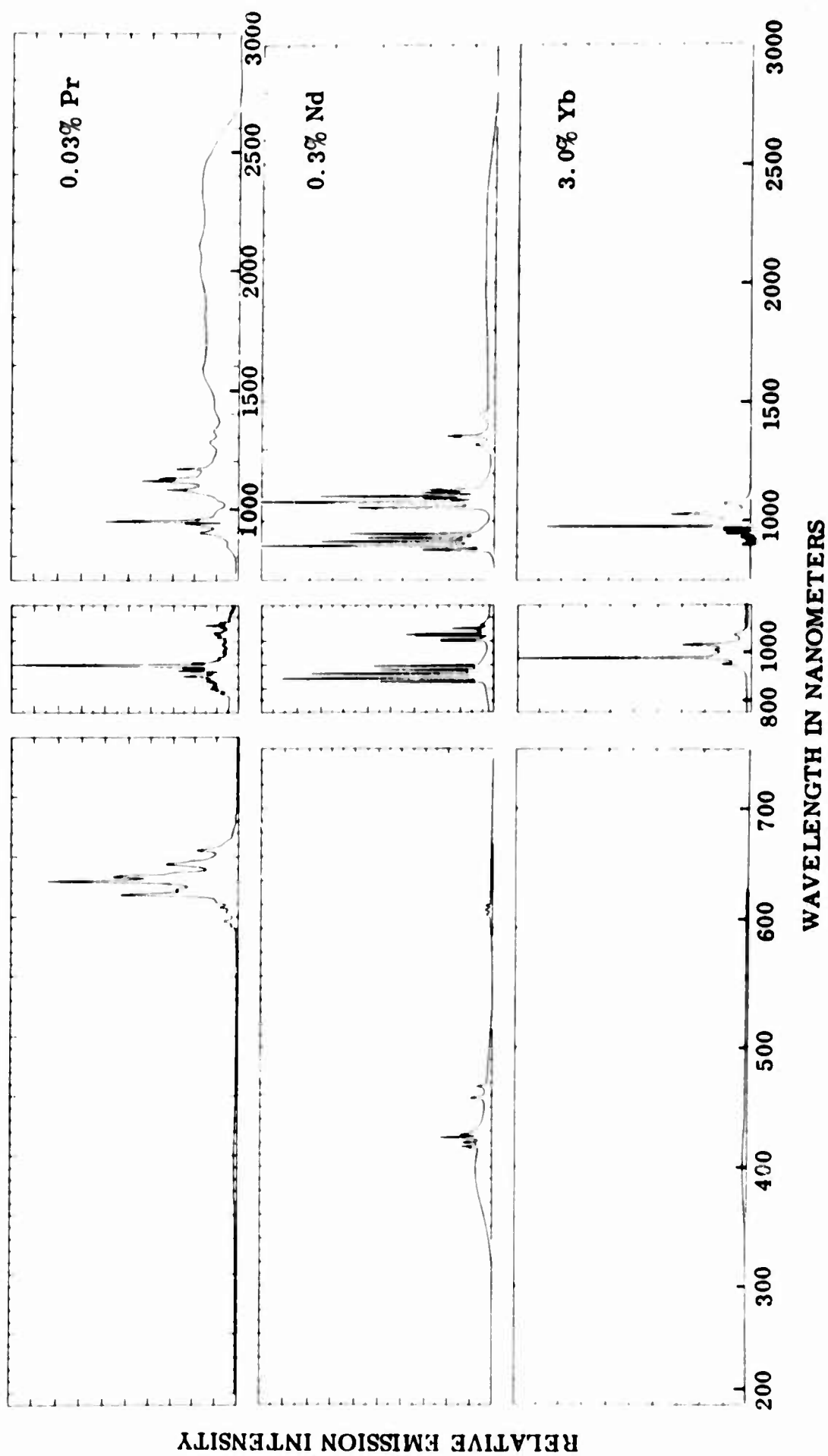
Figure 1

WAVELENGTH IN NANOMETERS

RELATIVE EMISSION INTENSITY

0.03% Pr

0.3% Nd

3.0% Yb

RELATIVE EMISSION INTENSITY

WAVELENGTH IN NANOMETERS

2% Gd

3% Eu

0.3% Sm

Figure 3

WAVELENGTH IN NANOMETERS

RELATIVE EMISSION INTENSITY

0.2% Tb

0.3% Dy

1% Ho

RELATIVE EMISSION INTENSITY

WAVELENGTH IN NANOMETERS

R 136

7102

PbS

Spectrophotometer
system response

3% Tm

1% Er
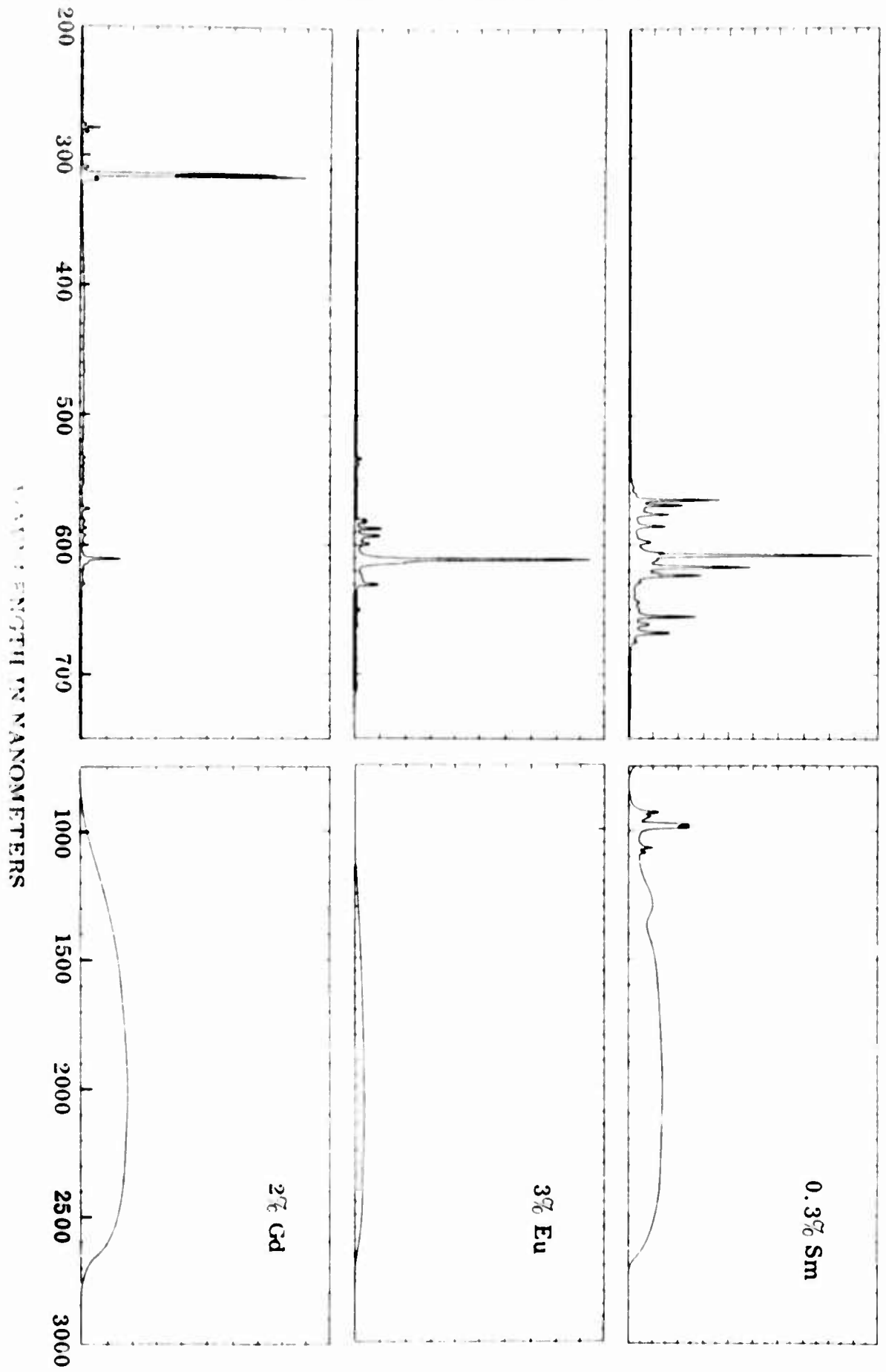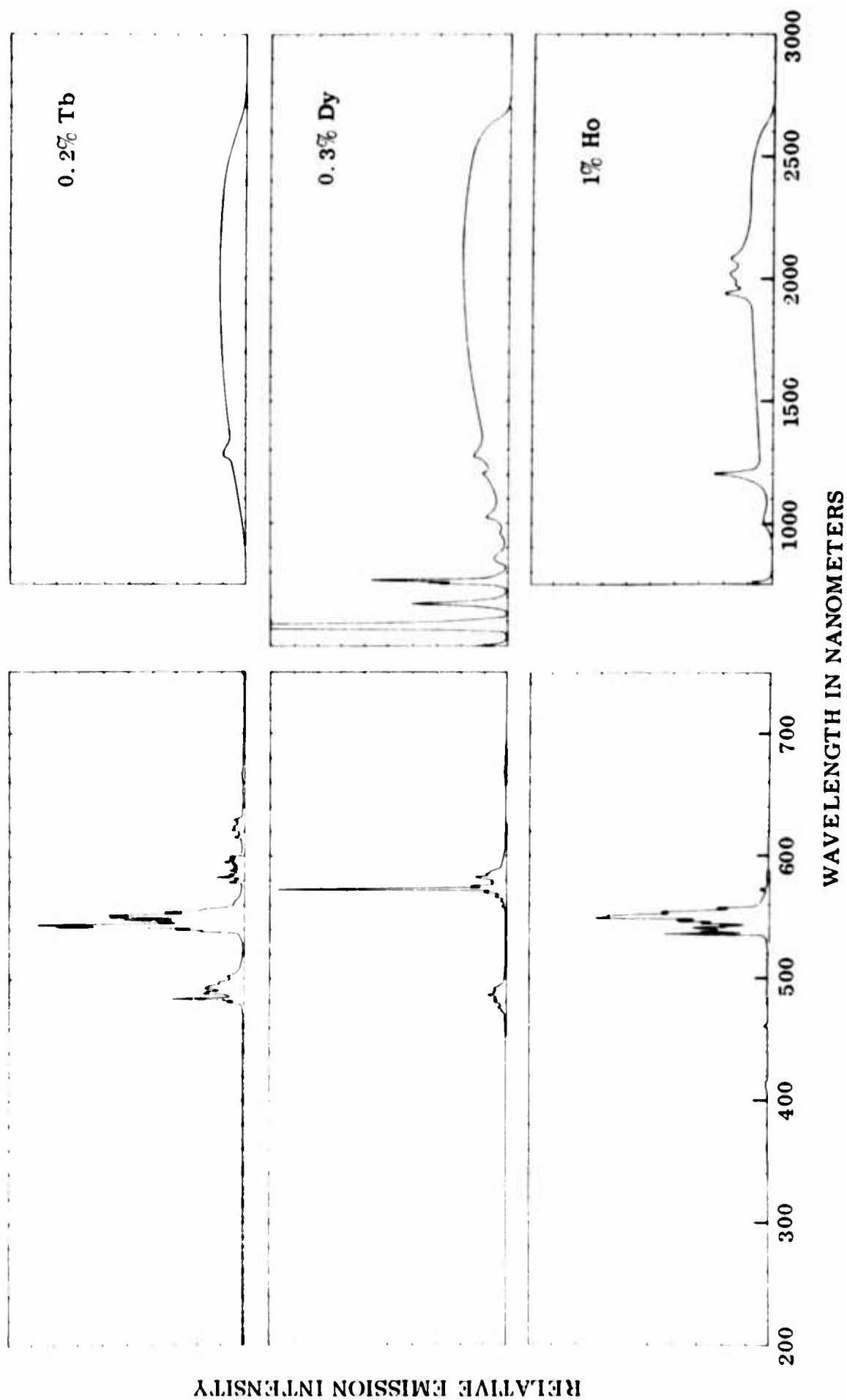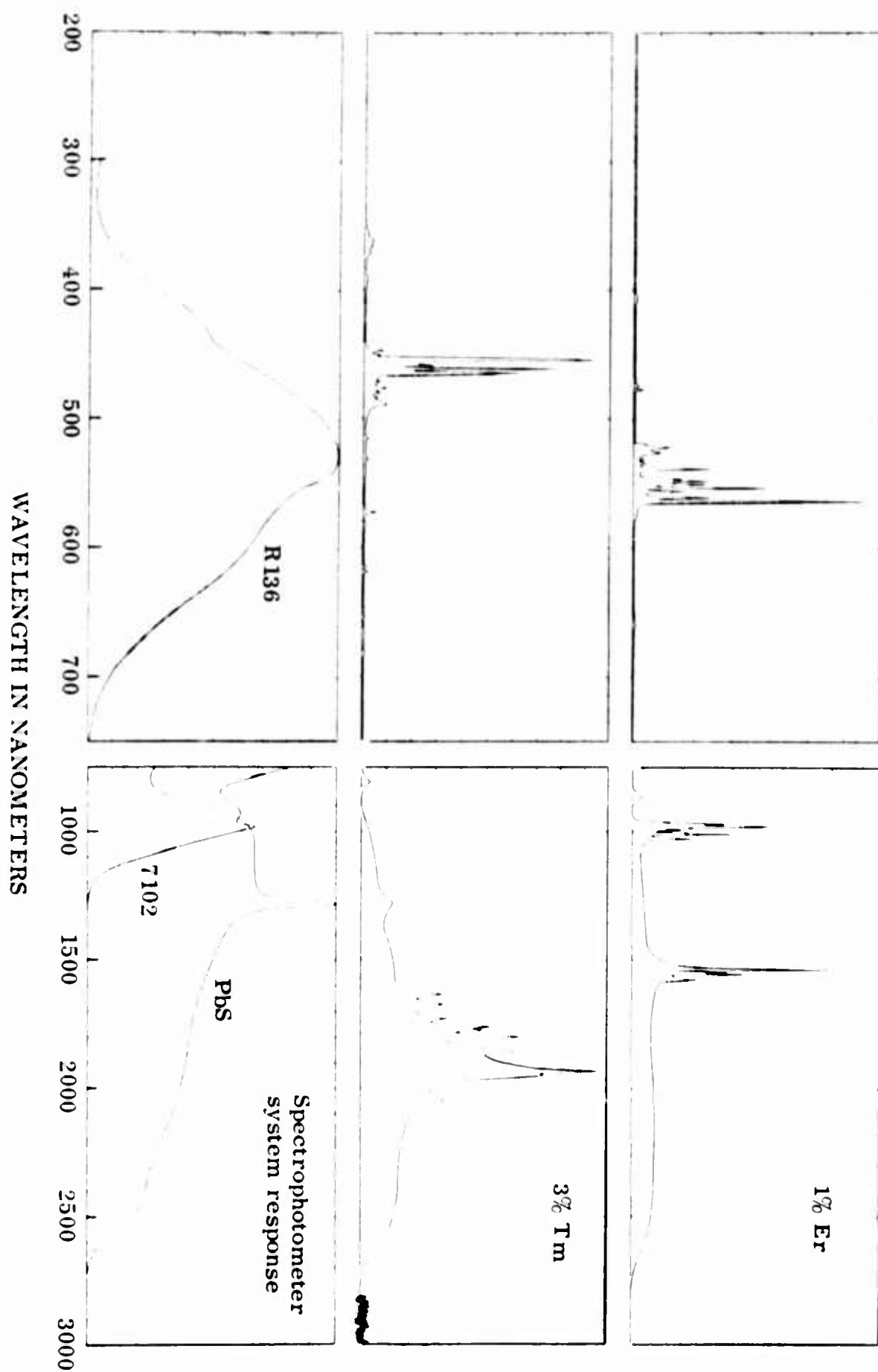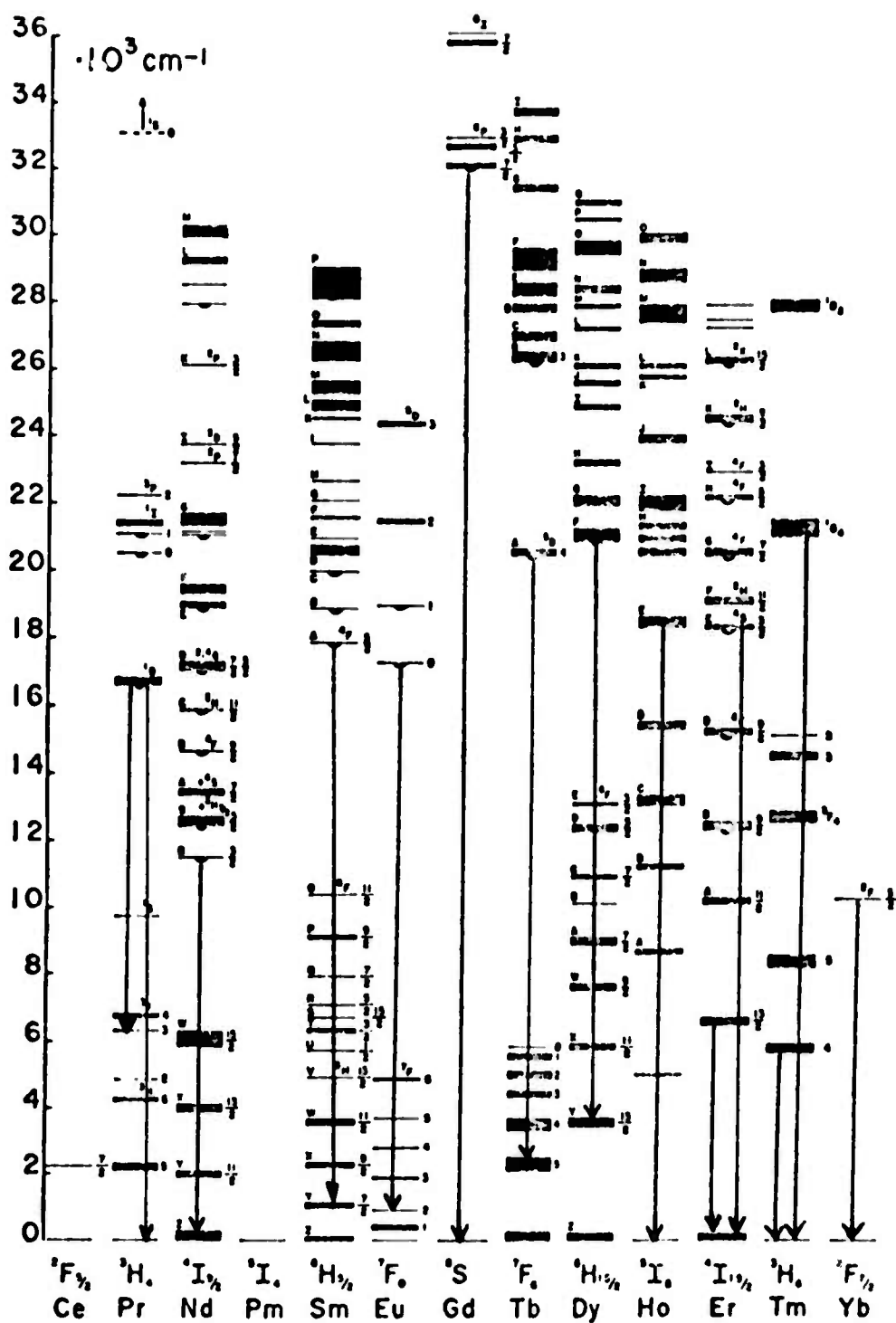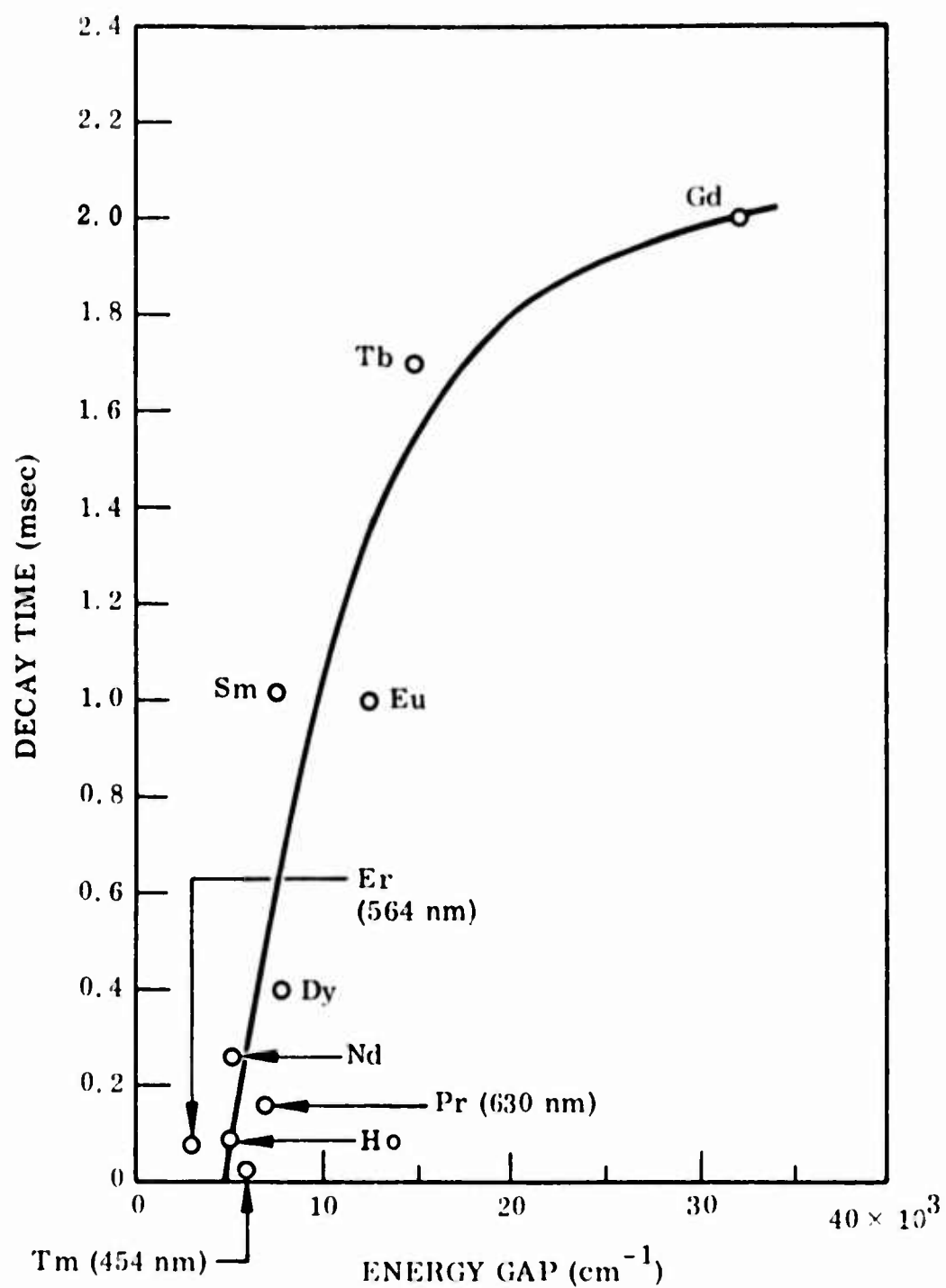
Figure 5

Figure 6

PREPARATION AND PROPERTIES

OF SOME FLUORESCENT RARE EARTH COMPOUNDS

Jean LORIERS

Centre National de la
Recherche Scientifique
92 - BELLEVUE
France

Rudolf HEINDL

Laboratoire Central
de Télécommunications
46 Avenue de Breteuil
PARIS   7°

ABSTRACT :

The authors describe the preparation and properties of some
fluorescent inorganic rare earth compounds derived from the ortho -
vanadates of general formula $Yt\ VO_4$ (Yt = Y , Gd, Lu or Sc) by balan-
ced cation-substitution.

Two series of compounds are described :
a) double and polycationic - orthovanadates with zircon structure.
b) $ABVO_4$-type compounds.

When doped with europium or other lanthanides, these compounds
have fluorescent properties similar to thoses observed with yttrium
orthovanadate as host material. The fluorescence spectra under U.V.
excitation have some interesting properties compared with those of
usual fluorescent orthovanadates.

The influence on intensity of emission lines is studied
with respect to changes in substitution elements and concentration
of doping lanthanide.

1 . INTRODUCTION

The interest in rare earth activated phosphors
has increased in the last few years, and, in particular,
attention has been drawn to the europium-activated yt-
trium or gadolinium orthovanadates (1), because of their
application as red emitting cathodoluminophors in color
television tubes (2), and as color correcting phosphors
in high-pressure mercury vapor lamps (3). These out-
standing properties have stimulated investigation of new
classes of rare earth-activated fluorescent compounds.
Both theoretical and technical preoccupations are invol-
ved in this search : First, the development of new

phosphors will give interesting precisions about the mecanism of rare earth ions fluorescence and the factors influencing them ; on the other hand, because the industrial importance of the europium-phosphors, the use of more common materials instead of the very expensive yttrium oxide for the phosphor preparation would be economically advantageous.

Moreover, the presence of oxidic-vanadium groups seem to be effective to enhace the Eu^{3+} fluorescence, specially under ultra-violet excitation : it has been shown (4)(5) that in the YVO_4 crystal-lattice, the $(VO_4)^{3-}$ radicals efficiently absorb the irradiating energy for subsequent transfert to the Eu^{3+} ions.

In the present work we report on two series of europium-activated orthovanadates related to YVO_4:Eu which contain little or no yttrium ; the compounds of the first serie all contain thorium paired with other ions, and were obtained by balanced yttrium-substitution in the YVO_4 tetragonal matrix, without modification of crystal structure ; the host-materials of the second serie are of $ABVO_4$ type, contain magnesium or alkaline-earth elements, and have different (lower) symetries.

2 . EXPERIMENTAL

2.1.Sample_preparation

The ingredients used for preparing the powdered luminophors were reagent-grade vanadium pentoxide or ammonium metavanadate, and oxides or carbonates of europium, rare earths, magnesium, alkaline-earths or alkaline elements. In some cases, the europium, thorium and alkaline-earth elements were first coprecipitated as oxalates before mixing with vanadium oxide. The required amounts of dry materials were thoroughly mixed, put in platinum-crucibles, and first fired in air at relatively low temperature (300-400°C), then re-mixed and re-fired at the final temperature (900-1100°C) for several hours.

2.2._X-ray_analysis and crystal structure.

A Philips PW 1051 diffractometer was used for crystal structure examination. The X-ray powder-diffraction patterns were taken at room temperature by Debye-Scherrer photographic method, using the CuK_α radiation. For the thorium containing compounds, the tetragonal zircon-like structure was identified by comparison with YVO_4 X-rays patterns ; thus the interplanar d-spacings could be easy indexed using the (hkl)-data given in the literature (6).

2.3. Fluorescence properties.

For optical examination, the powders were coated on flat plaques or packed in small rectangular quartz-tubs. Their fluorescence emission spectra were observed under ultraviolet exitation using a high pressure mercury vapor lamp, and photographied on a prism-spectrograph for subsequent densitometry. A recording fluorimeter was also used in some cases.

For comparative measures, the fluorescence spectrum was focused on the entrance slit of a mono-chromator, and the red and yellow luminous out-put was measured with a photomultiplier.

For temperature-dependance determination, the samples were put on an electrical heating plate and the fluorescence intensity measured with a photomultiplier.

3. RESULTS AND DISCUSSION

3. 1. Thorium containing vanadates with zircon structure

Recently, Schwartz (7) described the preparation and lattice-parameters of the thermally preparable orthovanadates $Me^{II}_{0,5} Th_{0,5} VO_4$, where Me^{II}= Cd, Ca and Sr, crystallising with the tetragonal zircon (or xenotine YPO_4) structure. We used these host-materials for preparing several europium-activared phosphors, and then extended the investigations to Zn-Th and Mg-Th double vanadates, and to Zr-compounds. In addition, we prepared the sodium-thorium phosphor : $Th_{2/3} Na_{1/3})_{1-\varepsilon} Eu_\varepsilon VO_4$ and some polycationic-paired thorium vanadates of general formula $(\Sigma Me)_{1-\varepsilon} Eu_\varepsilon VO_4$, where ΣM= a Na^I + b Me^{II} + C Y^{III} + d Th^{IV}, with a + b + c + d = 1, and a + 2b + 3c + 4d = 3 ; all these new compounds have the zircon structure, when Me^{II}= Ca, Sr, Zn or Cd.

During our work, Avella (8) communicated results on Th-Me^{II} and Zr-Me^{II} vanadate-phosphors ; so it is possible to compare some of their results with ours.

The possibility of synthetising double or polycationic orthovanadates isostructural with YVO_4 is governed by two main conditions :
a) the charge equilibrium will be respected, that is , the total valence charge of the cations associated to the $(VO_4)^{3-}$ anionic group must remain equal to 3 .

b) the size of the tetravalent and divalent cations must approximate that of the yttrium or rare earth ions (Y^{3+} has an ionic radius of 0,92 Å).

According to these rules, Avella reported that monophase products were obtained when Th^{4+}(ionic radius I,02 Å) is paired with Sr^{2+}(1,12 Å), Ca^{2+}(0,99Å) and $Cd(0,97Å)$, while with smaller cations such as Zn^{2+} (0,74Å) and Mg^{2+}(0,66Å), multiphase products resulted. However, we are able to prepare also pure Zn-Th and Mg-Th double vanadates, which are good luminophors when activated with europium.

The lattice parameters a and c of the tetragonal crystal lattice of these double vanadates, calculated from X-ray diffraction patterns, are given in Table 1, along with those of $Na_{1/3}Th_{2/3}VO_4$ and some typical polycationic vanadates. It can be seen that the lattice dimensions decrease with decreasing mean radius of the cations.

Spectral properties. All of the synthetised materials mentioned above are white or light tan in body colour; the most coloured are the Zn and Na-compounds. If unactivated, they present no notable luminescence under ultraviolet excitation at room temperature, but activated with 1 to 10 atoms percent of europium, they exhibit a strong red fluorescence. Activation with rare earths other than europium also gives fluorescence, specially with dysprosium and samarium. The emission spectra of six orthovanadates activated with Eu^{3+} (4 percent of the cations) are presented in Fig.1. All the spectra are identical, showing the lines corresponding to the $^5D_0 \longrightarrow {}^7F_{1,2,3,4}$ transitions, with marked predominance of the even $^5D_0 \longrightarrow {}^7F_2$ and $^5D_0 \longrightarrow {}^7F_4$ transitions (near 615-620 and 700 nanometers, respectively). The spectra of the Ca-Th and Sr-Th phosphors are quite similar to those given by Avella. However, we found that $Sr_{0,5}Th_{0,5}VO_4$:Eu was the best phosphor of the series we prepared, while $Ca_{0,5}Th_{0,5}VO_4$: Eu was a little less effective. Direct qualitative comparison of intensities between the phosphors can be made in Fig.1, by reference to the Sr-Th compound, which was taken as the standard. $Na_{0,33}Th_{0,66}VO_4$: Eu is also a very efficient phosphor, but it has a greyish or yellow body colour. Futhermore, it must be noted that in the polycationic vanadates,the introduction of yttrium seems to quench somewhat the fluorescence. Quantitative comparisons were also made, using the monochromator-photomultiplier assembly and taking a

Eu-activated yttrium vanadate (4%) as standard; the results are summarized in Table II; both the yellow $^5D_0 \to {}^7F_1$ emission (at 595nm) and red $^5D_0 \to {}^7F_2$ emission were measured, the slit aperture of the monochromator being 10/100 mm for yellow light and 15/100 mm for red light. One can see that Sr-Th and Na-Th vanadates are comparable in efficiency to the well known yttrium vanadate phosphor. For all these phosphors, as for the latter, the emission intensity first largely increases with europium content, then saturation effect appears at high concentrations. As shown for example in Fig.2, with the Sr-Th phosphors the maximum of efficiency is practically obtained about 6 - 7% Eu. When examined at increasing temperatures, the Ca-Th, and Na-Th compounds seem to have very stable luminosity (up to 300°C), while for the Zn phosphors the luminosity strongly decreases above 200°C with increasing temperature.

3. 2. ABVO₄-type orthovanadates

The purpose of our work in this field was to prepare new orthovanadates in which two cations (the one monovalent, the other bivalent) should be associated with the anionic trivalent $(VO_4)^{3-}$-group. Introduction of europium or of another activating rare earth necessitates that one of these two cations (designed by A) have a convenient size, i.e. its ionic radius must approximate that of Eu^{3+} (0,98Å). The following cations were selected in this scope : Na^+(0,97), Sr^{2+}(1,12), Ca^{2+}(0,99), Pb^{2+} (1,20), Cd^{2+}(0,97), Zn^{2+}(0,88). The B element can be choisen among any mono- or bivalent elements, that is, those mentioned above, and those having larger or smaller ions, such as K^+(1,33), Ba^{2+}(1,34), Li^+(0,68), Be^{2+}(0,35), Mg^{2+}(0,66).

Charge compensation, which is always needed in replacing the A^+ or A^{2+} cation by Eu^{3+}, can be achieved in different ways : a) valence compensation without cation compensation giving compounds of general formula $[AB]_{1-\varepsilon} Eu VO_4$ which present cation-vacancies; b) balanced substitutions of Na^+ by Eu^{3+} and V^{5+} by cations such as Ge^{4+}, Al^{3+}, Mg^{2+} resulting in completly compensated compounds (for example $Na_{1-\varepsilon}Eu_\varepsilon MgV_{1-\varepsilon}Al_\varepsilon O_4$) ; c) substitutions on B^{2+} giving $Na_{1+\varepsilon}Eu_\varepsilon B_{1-2\varepsilon}VO_4$-type compensated compounds, which seem to be less convenient with respect to ionic size.

Three series of vanadates were prepared, containing K, Na or Li as monovalent cation paired with the bivalent cations mentioned above. In the preparation of the phosphors, great care must be taken in firing the necessary ingredients, because the mixture often melts at low temperature before complete combination is achieved.

The X-ray diffraction photographs of all the new compounds obtained show several complicated patterns corresponding to unknown structures. The simpliest spectra are those of $CaKVO_4$, $SrKVO_4$, $CaNaVO_4$, while those of $Mg,SrVO_4$, $MgNaVO_4$, $CaLiVO_4$ seem to be quite similar, and present some analogy with the orthorhombic structure of Sr or Ca-scandates (AB_2O_4 type compounds) described by Carter and Feigelson (9). Additional works are in progress to elucidate this point.

Other compounds were prepared by substituting phosphor or arsenic for vanadium in the host compounds, as represented by the formula $ABV_{1-x}P_xO_4$ or $ABV_{1-x}As_xO_4$ (with $0 < x < 1$).

Spectral properties. Beryllium compounds, and Ba-Na or Pb-Na vanadates seem to be ineffective host lattices, while all the other compounds exhibit photoluminescence under ultraviolet excitation. Unactivated materials show generally some yellow matrix-emission, and the activation with Eu^{3+} results in moderate or strong orange to red fluorescence. The best results are obtained with the K-Mg and Na-Mg double vanadates , despite their greyish colour. The Sr-Li and Ca-Li compounds, which are white in colour, give also good phosphors ; activation of compounds containing two large cations (Sr-K,Sr-Na, Ca-K, Ca-Na, Cd-Na) produces moderate, but red emission. Complex phospho- or arseno-vanadates such as $NaMgV_{05}As_{05}O_4$ often offer better matrices than the simple vanadates for red-colour definition. $NaMgVO_4$:Eu was found to be the strongest phosphor of all the new double vanadates we prepared. Examined by the photomultiplier-method, it exhibits a total emission intensity about twice higher than that of the YVO_4:Eu standard with equal Eu-concentration. However, it has a very poor stability at increasing temperatures, and above 120°C, its emission becomes very feeble.

The emission spectrum of $NaMgVO_4$:Eu (presented in Fig.3) is of particular interest ; one can observe a drastic broadening of several emission lines, and a pronounced shift towards the short-wavelength side. This shift is marked enough to give the phosphor a dominant

orange fluorescence, despite the unusual intensity of the
red long wawelength line near 700nm. The emission lines
result mainly from the $5D_0 \rightarrow 7F_1$, $7F_2$ and $7F_4$ transitions,
while the $5D_0 \rightarrow 7F_0$ and $5D_0 \rightarrow 7F_3$ transitions are very
weak. All the observable transitions exhibit large split-
ting (the strong line at 630 nm being considered as a
$5D_0 \rightarrow 7F_2$ componant). Concerning the crystal structure,
one can say that the predominance of the magnetic dipole
transitions ($5D_0 \rightarrow 7F_{2,4}$) must be ascribed to the absence
of a center of symmetry, and the splitting of the lines
indicates a symmetry lower than cubic (10). The relati-
vely strong intensity of the magnetic dipole $5D_0 \rightarrow 7F_1$
transition,and the multiple diffuse vibronic transitions
located in the $5D_0 \rightarrow 7F_2$ transition range (between 615
and 630 nm) both contribute to the high fluorescence
of Eu^{3+} in $NaMgVO_4$. The efficiency of $Na\,Mg\,VO_4$: Eu
compared with YVO_4 : Eu is clearly visible in the inser-
ted photograph, which illustrate the differences bet-
ween the spectra of the two phorsphors.

4 . CONCLUSION

The comparative studies that we presented
on YVO_4, $(M^{II}\,Th^{IV})_{\frac{1}{2}}\,VO4$ and $Na\,Mg\,VO4$ europium-acti-
vated phorsphors illustrated the influence of crystal
symmetry on the fluorescence of the rare -earth ions
in mineral compounds : crystal field distorsion induced
by substitution of optically inactive cations in the
host-matrix produces only moderate alteration of the
emission spectra,while change in crystal structure can
result in drastic modifications in the spectral repar-
tition of the radiative transitions. Therefore it is
evident that various Eu-activated vanadates can offer
interesting properties for definite applications. The
thorium-containing vanadates, for example, may replace
the more expensive yttrium or gadolinium compounds in
color television tubes or Hg-vapor lamps ; $Na\,Mg\,VO_4$:
Eu, on the other hand,seems to be a good luminophor
suitable for utilisation in fluorescent tubes. One can
expect that several other new rare-earth phorsphors
will be discovered in the next futur.

5 . REFERENCES

1 A. BRIL, W.L. WANMAKER & BROSS, J. Chem. Phys. 43,
311 (1965)

2 A.K. LEVINE & F.C. PALILLA, Appl. Phys. Letters 5,
118, (1904)

3 F.C. PALILLA & A.K. LEVINE, Science (submitted to
Science 3.22.66)

4 F.C. PALILLA A.K. LEVINE & M. RINKEVICS, J. Electro-
chem Soc. 112, 776 (1965)

5 J. LORIERS, J.P. DENIS à J.P. BRIFFAUT, C.R. Ac. Sc.
262, 496 (1966)

6 W.O. MILLIGAN, L. WATT & H.H. RACHFORD, J. Phys. Ch
Chem. 53, 227 (1949)

7 H. SCHWARZ, Z. anorg. Albg. Chem. 334, 261 (1965)

8 F.J. AVELLA, J. Electrochem. Soc. 113, 855 (1966)

9 J.R. CARTER & R.S. FEIGELSON, J. Amer. Ceram. Soc.
47, 141 (1964)

10 G. BLASSE, A. BRIL & W.C. NIEUWPOORT, J. Phys. Chem.
Solids 27, 1587 (1966)

$Y VO_4 : Eu(4\%)$

$Mg Na VO_4 : Eu (4\%)$
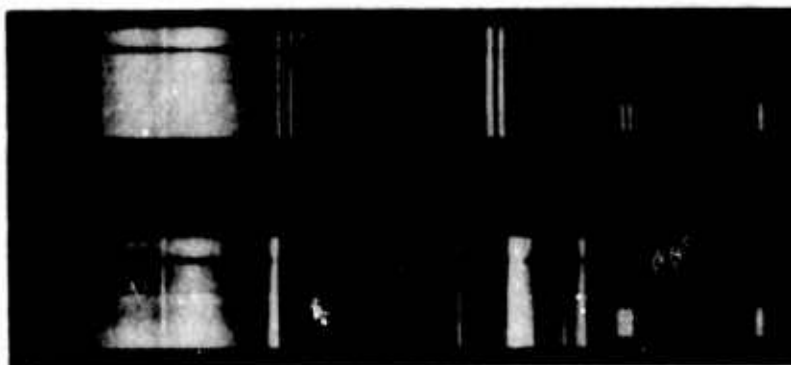
Comparison of the Eu^{2+} emission spectra in the YVO_4
and Na Mg VO_4 host lattices.

TABLE I . Lattice parameters of some typical vanadates
in relation to the mean radii of cations.

Compound	a (Å)	c(Å)	mean radius
$Mg_{0.5}Th_{0.5}VO_4$	7,16	6,45	0,840
$Ca_{0.5}Th_{0.5}VO_4$	7,26	6,445	1,005
$Sr_{0.5}Th_{0.5}VO_4$	7,39	6,50	1,070
$Na_{2/3}Th_{2/3}VO_4$	7,23	6,43	0,995
$Sr_{1/3}Y_{1/3}Th_{1/3}VO_4$	7,26	6,45	1,020
$Na_{0.2}Sr_{0.2}Th_{0.6}VO_4$	7,28	6,46	1,050
$Na_{0.2}Ca_{0.2}Y_{0.5}Th_{0.3}VO_4$	7,19	6,42	0,962

TABLE II . Relative luminosity of various vanadate phos-
phors (Eu concentration 4percent)compared with YVO_4:Eu

Eu-phosphor host-lattice	total orange $5D_0 \rightarrow 7F_1$ emission	total red $5D_0 \rightarrow 7F_2$ emission
$Y V O_4$	40	100
$(Sr_{0.5}Th_{0.5})VO_4$	28	85
$(Ca_{0.5}Th_{0.5})VO_4$	26	78
$(Mg_{0.5}Th_{0.5})VO_4$	24	64
$(Na_{0.33}Th_{0.66})VO_4$	29	88
$(Sr_{0.4}Y_{0.2}Th_{0.4})VO_4$	19	58
$(Sr_{0.33}Y_{0.33}Th_{0.33})VO_4$	12	22
$(Na_{0.2}Ca_{0.2}Th_{0.6})VO_4$	18	48
$(Na_{0.2}Y_{0.4}Th_{0.4})VO_4$	16	33
$(Na_{0.1}Ca_{0.2}Y_{0.5}Th_{0.3})VO_4$	14	35
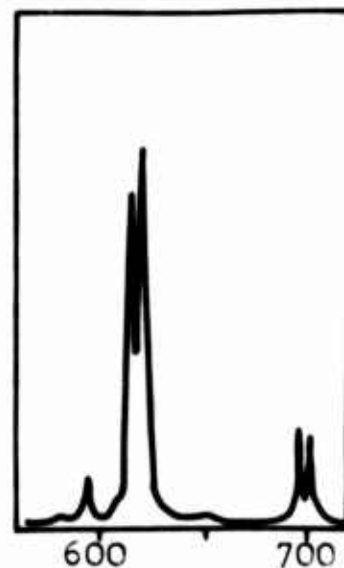
Fig.1 : Emission spectra of Eu-activated orthovanadates
containing thorium paired with various cations.
(Eu concentration : 4 percent in all phosphors).
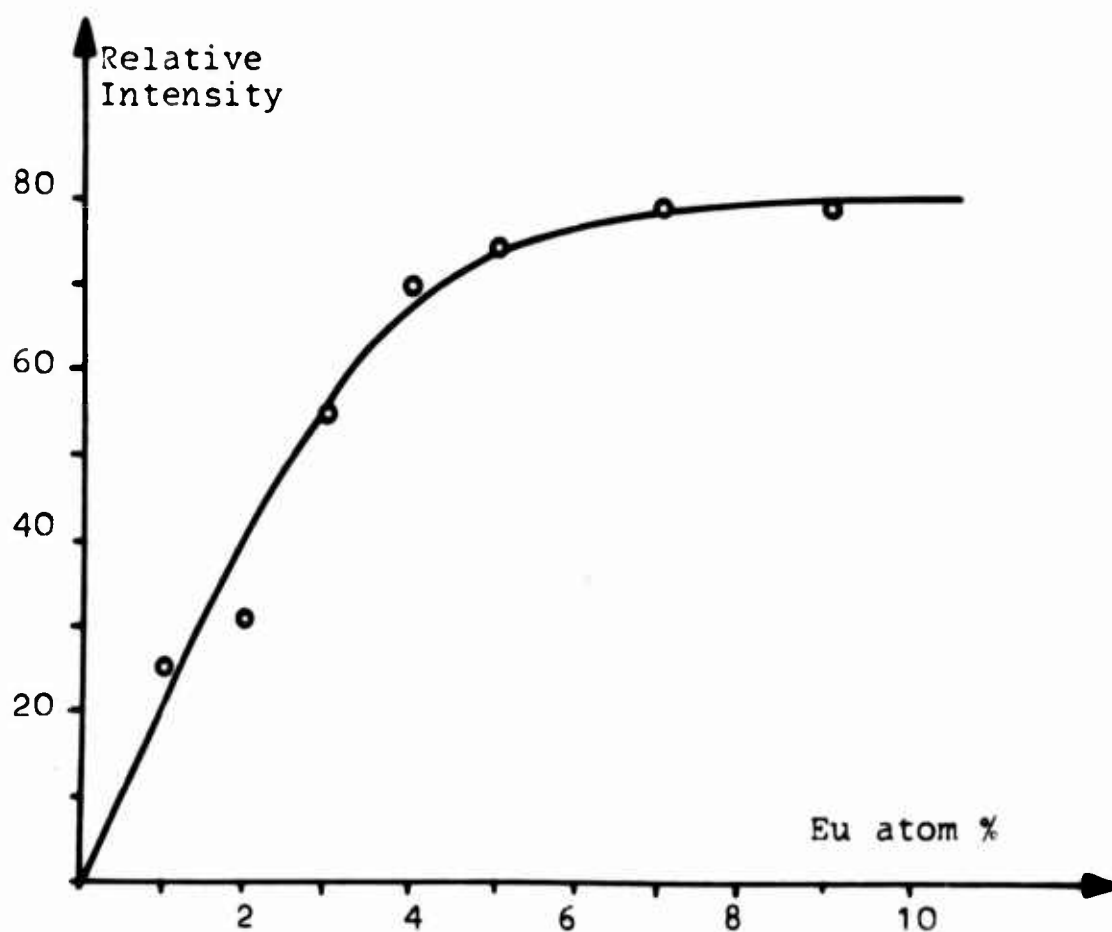
Fig.2 : Variation in fluorescence intensity of Sr–Th
double vanadate versus Europium concentration.

Fig. 3 Emission spectrum of NaMgVO4: Eu under ultraviolet excitation.
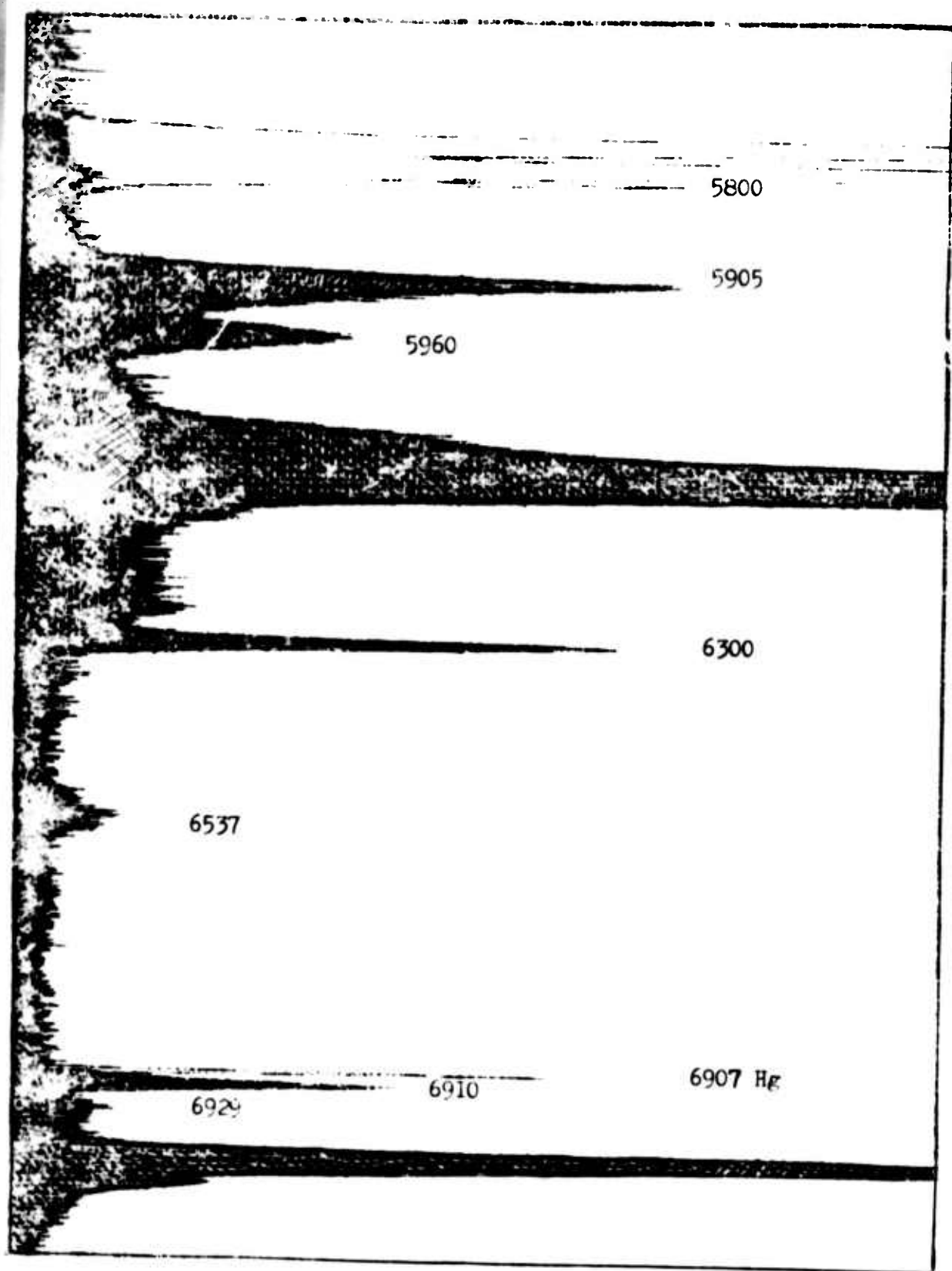
MAGNETIC PROPERTIES AND MAGNETIC STRUCTURES OF THE TCo$_3$
INTERMETALLIC COMPOUNDS, WHERE T IS A RARE EARTH METAL OR YTTRIUM

R. LEMAIRE, R. PAUTHENET, J. SCHWEIZER, I. SILVERA
Laboratoire d'Electrostatique et de Physique du Métal - GRENOBLE -
Centre d'Etudes Nucléaires - GRENOBLE - France

We have measured the magnetization of the rare earth-cobalt compounds TCo$_3$ at fixed temperatures between 2 and 1000° K in magnetic fields which varied up to 29,000 Oe. The curves of the thermal variation of the spontaneous magnetization show the ferrimagnetic character of certain of these substances notably in the case of compounds with T = Dy, Ho, Er, Tm, for which compensation points have been observed. The Curie temperatures lie in the range from 300° K to 612° K; they increase rapidly with the value of the spin moment of the associated rare earth element.

The study of the magnetic structures by neutron diffraction has shown that the coupling of the spins of the rare earth atoms with those of the cobalt atoms is antiparallel. This coupling results in a ferrimagnetic behavior of the magnetization in compounds with rare earth metals of the second series (J = L + S) and a ferromagnetic character in compounds with rare earth metals of the first series (J = L - S).

The intrinsic magnetic moment of the cobalt varies from one compound to another. It is at a minimum in YCo$_3$ with a value near 0.5 μ_B. Its maximum value is found in GdCo$_3$ at 1.6 μ_B. The electronic configuration of the cobalt is greatly modified by the effect of the conduction electrons of the rare earth or yttrium atoms and by the magnetic interactions due to these atoms.

The Magnetic Structure of $Fe_5Tb_3O_{12}$ at $4.2^{\circ}K$

F. TCHEOU, A. DELAPALME (C.E.N.-G.)

and E. F. BERTAUT (C.E.N.-G. AND C.N.R.S.) Grenoble, France.

The magnetic structure of $Fe_5Tb_3O_{12}$ at $4.2^{\circ}K$ is colinear in the ferrimagnetic iron sublattice but is non-colinear in the moments of Tb. There are Tb moments of 8.5 ± 0.3 μ_B on a cone whose axis is a [111] direction, and whose angular opening is 30°. The non-colinear component S' of the Tb moment is in the (111) plane. There are six sublattices to consider: C_1, C_2, C_3, C'_1, C'_2 and C'_3. The spin component S', on $C_1[\pm (\frac{1}{8} 0 \frac{1}{4}), + (\frac{1}{2} \frac{1}{2} \frac{1}{2})$, is antiparallel to the component S' on $C'_1[\pm (\frac{3}{8} 0 \frac{3}{8}), + (\frac{1}{2} \frac{1}{2} \frac{1}{2})]$. The spins on C_2, C_3 and C'_2, C'_3 can be deduced from C_1 and C'_1 by rotations of 120° and 240°, respectively.

The results of the effect of a magnetic field and of the change of temperature will be reported.

Neutron Scattering from Paramagnetic Terbium

J.W. Cable[*], M.F. Collins and A.D.B. Woods[†]

Atomic Energy Research Establishment
Harwell, Berks., England

Abstract

The energy distribution of neutrons scattered from
a single crystal of terbium at about $660°K$ ($T_N = 230°K$)
was studied as a function of momentum transfer (Q). The
measurements were carried out using both the twin rotor
time-of-flight spectrometer and the triple axis spectrometer
at Harwell. The distributions were approximately Gaussian
in shape with an additional tail which is believed not to be
connected with the paramagnetic scattering but more likely
with multiple or phonon scattering. The second moments of
the energy distribution, as determined from fitted Gaussian
curves, yield exchange interactions which are consistent
with those deduced from the spin wave dispersion curves in
the ferromagnetic state as measured by Møller and Houmann.
The distributions contain a large Q independent component
which arises from the anisotropy energy. Typical values of
$(< \hbar^2 \omega^2 >)^{1/2}$ near zone boundaries are ~ 3.2 meV.

[*] Visitor from Oak Ridge National Laboratory, now
returned.
[†] Visitor from Atomic Energy of Canada Limited, now
returned.

The notion that inelastic neutron scattering could be used to study exchange interactions in magnetic systems came from Van Vleck[1] who pointed out that the exchange interactions would give rise to an energy broadening of an otherwise elastic peak in the scattered neutron distribution. The first experiments showing this effect were carried out by Brockhouse[2] who demonstrated that such broadening was observable in materials with sufficiently large exchange interactions. De Gennes[3] gave the first complete treatment of the effect of the exchange interactions on the second moment, $< h^2 \omega^2 >$, of the energy distribution and pointed out its dependence on the momentum transfer, $\hbar Q$. This Q dependence was demonstrated for MnF_2 by Cribier and Jacrot[4] and a number of measurements on various other materials has been made[5-7].

The present investigation was carried out on a single crystal of terbium with the object of studying the energy distribution of scattered neutrons in the [001] and [110] crystallographic directions. It was hoped that the analysis of the Q dependence of the second moment of the energy distribution would yield information on the exchange and anisotropy interactions in the paramagnetic state. The measurements reveal surprisingly little dependence on Q indicating that anisotropy plays an important role in a

description of the scattering.

<center>THEORY</center>

The Hamiltonian is taken to be[8]

$$H = - \sum_{\vec{i},\vec{\rho}} J_{\vec{\rho}} \; \vec{J}_{\vec{i}} \cdot \vec{J}_{\vec{i}+\vec{\rho}} + \sum_{i} A(J_i^z)^2$$

where the first term gives the Heisenberg exchange interaction and the
second the anisotropy due to the crystal field. Higher terms in the
description of the anisotropy energy are an order of magnitude, or more,
less than the leading term[9] as given above and will not be considered.

No solution has yet been found for the neutron scattering function
$S(\vec{Q},\omega)$ from a Heisenberg paramagnet even at limitingly high temperatures.
The scattering from a paramagnet with a Hamiltonian just containing the
second term in the equation above can be solved, giving:

$$S(\vec{Q},\omega) = \frac{1}{3} NJ(J + 1)(1 - \hat{Q}_z^2)\delta(\hbar\omega)$$

$$+ \frac{N(1 + \hat{Q}_z^2)}{2(2J + 1)} \sum_{m=-J}^{J} [J(J + 1) - m^2 + m]\delta(\hbar\omega + 2Am - A)$$

where $\hat{Q}_z$ is the z direction cosine of the scattering vector $\vec{Q}$. The scatter
ing consists of a set of δ functions.

In terbium the exchange and anisotropy energies are of the same
order of magnitude so that it might be expected

that the existence of these δ functions in the scattering is completely smeared out. This indeed corresponds to what is observed experimentally. Even near $Q = 0$ these levels are expected to have some exchange broadening.[10]

Moments of the energy distribution of the scattering may be calculated exactly as pointed out by De Gennes.[3] The second moment of the scattering is given by

$$< h^2 \omega^2 > = \frac{8}{3} J(J + 1) \sum_{\rho} J_{\rho}^2 (1 - \cos \vec{Q}.\vec{\rho}) +$$

$$\frac{A^2}{10} (1 + \hat{Q}_z^2) [4 J(J + 1) - 3)$$

Consideration of the fourth moment shows that the scattering is likely to be approximately Gaussian in form except near reciprocal lattice points.

EXPERIMENT

Energy distributions have been measured in the a and c ([110] and [001]) directions using both the twin rotor time-of-flight spectrometer[11] at the Pluto reactor and the triple axis spectrometer[12] at the Dido reactor at AERE. With the triple axis spectrometer distributions were measured in the constant momentum transfer (constant - $\vec{Q}$) mode of operation.[13]

The measurements were carried out using a single

crystal of terbium 0.3 cm in diameter and 5 cm long. The crystal had a mosaic spread of about three degrees. The temperature of the crystal was about $660°K$ ($\pm$ $10°K$). This temperature was chosen so that the results would not be affected by any short range order considerations. Experiments showed that the short range order had practically disappeared at this temperature.

Figures 1 and 2 show typical scattered neutron distributions observed with each instrument. The time-of-flight measurements in particular show evidence of a high energy tail. We believe that this is not paramagnetic single scattering but is contributed to by a variety of effects such as multiple scattering and magnetovibrational scattering. No neutron groups corresponding to well defined phonons were observed.

Distributions obtained from the empty furnace at the same temperature were subtracted from the results. The resolution function and the contribution of the incoherent nuclear scattering ($\sigma_{inc} \approx 7$ barns) were determined from measurements of the scattering from vanadium.

In addition to these measurements some distributions were obtained from terbium powder using the triple axis crystal spectrometer at the Oak Ridge National Laboratory and are in good agreement with the average single crystal results.

AECL Ref # A-3344-F

Counts (with background subtracted) vs Energy transfer milli eV.

AECL Ref # A-3344-G

Energy transfer milli eV.

High energy tail

Elastic components

Gaussian component

Counts (with background subtracted) vs Time of flight μ sec.
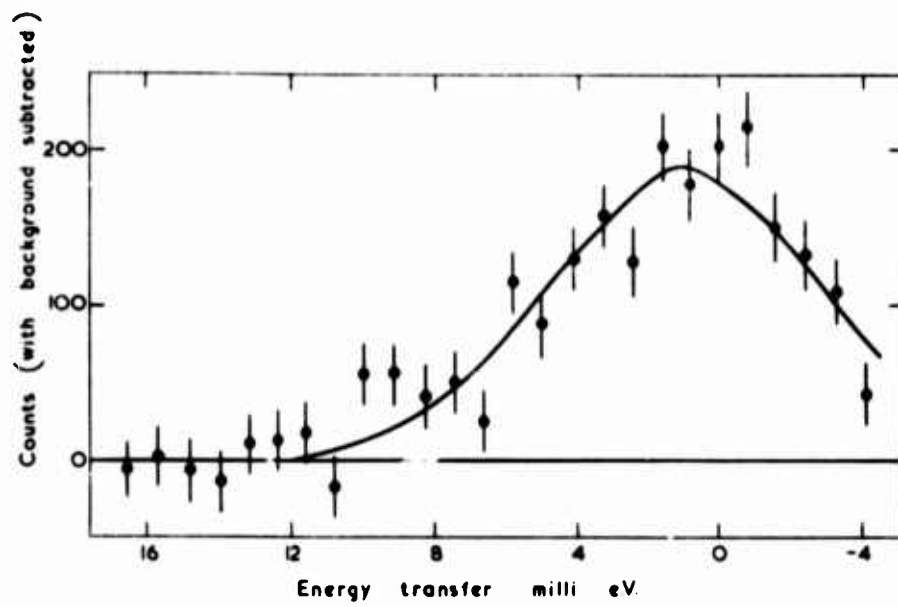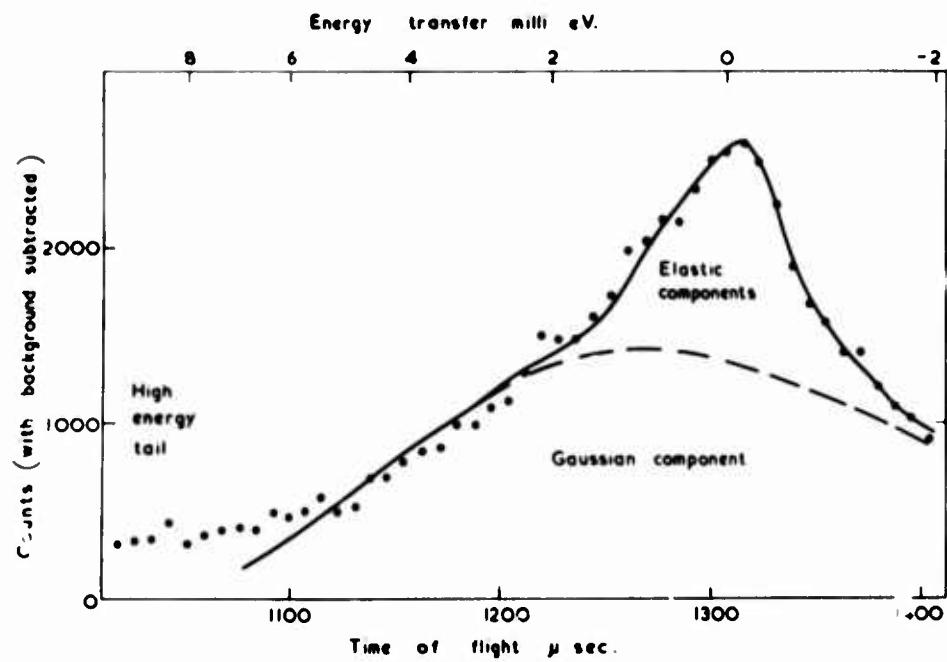
ANALYSIS

The analysis was carried out using the time-of-flight data for which the statistical accuracy was higher. The triple axis measurements were used mainly as a check on these. The following assumptions were made:

1) The paramagnetic scattering was Gaussian in shape.

2) The high energy tails, which represented gross distortions from a Gaussian were not due to the paramagnetic scattering.

3) The value of Q was constant in the time-of-flight data. (In view of the apparent weak dependence on Q this does not appear to be too bad an assumption.)

The observed distributions were fitted by a least squares method to a Gaussian scattering function (converted to time-of-flight units) and an elastic peak. Second moments were extracted from the widths of the Gaussian functions.

Figure 3 shows $< \hbar^2 \omega^2 >$ for both the a and c directions as deduced from these measurements. The solid lines show the predicted widths on the basis of exchange energies derived from the data of Møller and Houmann[14] and an anisotropy coefficient as determined by the low-temperature magnetization data of Rhyne and Clark.[9] Nearest-neighbour exchange energies only have been taken because paramagnetic scattering widths depend on sums over squares of exchange energies whilst spin-wave energies depend on sums over the exchange energies themselves; thus para-

magnetic scattering is much less sensitive to small inter-
actions to distant neighbours than are spin-wave spectra.
The agreement between the calculated curves and our results
is quite good. In particular the width due to the aniso-
tropy is much better described by the low temperature torque
measurements than by the high temperature susceptibility
measurements[15] by about a factor of two.

A.E.C.L. Ref. # A-3344-E
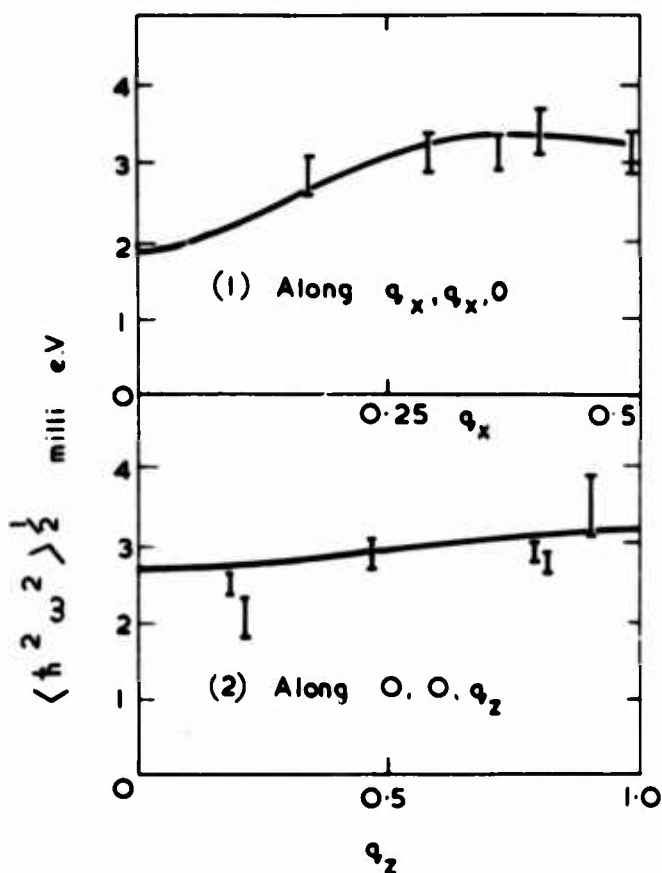
CONCLUSIONS

The paramagnetic scattering from single crystal terbium has been measured at 660°K in both the a and c directions. The results are consistent with exchange and anisotropy constants derived from spin wave and torque measurements carried out at low temperatures.

ACKNOWLEDGEMENTS

REFERENCES

1) J.H. Van Vleck, Phys. Rev. 55, 924 (1939).

2) B.N. Brockhouse, Phys. Rev. 99, 601 (1955).

3) P.G. De Gennes, J. Phys. Chem. Solids 4, 223 (1958).

4) D. Cribier and B. Jacrot, in "Inelastic Scattering of Neutrons in Solids and Liquids", (IAEA, Vienna, 1963) Vol. II, p. 309.

5) B.N. Brockhouse and P.K. Iyengar, Bull. Am. Phys. Soc. 3, 195 (1958).

6) K.U. Deniz, G. Venkataraman, N.S. Satyamurthy, B.A. Dasannacharya, and P.K. Iyengar, in "Proc. Int. Conf. on Magnetism" (The Institute of Physics and The Physical Society, London, 1964), p. 322.

7) M.F. Collins and R. Nathans, J. Appl. Phys. 36, 1092, (1965); also M.F. Collins, Proc. Phys. Soc. (London) 86, 973 (1965).

8) R.J. Elliott in "Magnetism", edited by G.T. Rado and H. Suhl (Academic Press Inc., New York, 1963), Vol. 11A, Chap. 7.

9) J.J. Rhyne and A.E. Clark, J. Appl. Phys. (in press).

10) D. St. James, Thesis, Paris (1962).

11) R.F. Dyer and G.G.E. Low in "Inelastic Scattering of Neutrons in Solids and Liquids" (IAEA, Vienna, 1961) p. 179.

12) D.H. Saunderson, C. Duffil and R.I. Sharp, AERE-R 4895 (1965).

13) B.N. Brockhouse in "Inelastic Scattering of Neutrons in Solids and Liquids" (IAEA, Vienna, 1961) p. 113.

14) H.B. Moller and J.C.G. Houmann, Phys. Rev. Letters 16, 737 (1966).

15) D.E. Hegland, S. Legvold and F.H. Spedding, Phys. Rev. 131, 158 (1963).

Magnon Dispersion Relation in Rare Earth Metals
from Inelastic Neutron Scattering

H. Bjerrum Møller
AEK h earch Establishment Risø, Roskilde, Denmark

and

J. C. Gylden Houmann and A. R. Mackintosh
Technical University, Copenhagen, Denmark

The magnon dispersion relation in Tb and a Tb-10% Ho
alloy have been studied over a wide temperature range by in-
elastic neutron scattering. The experiments were carried
out at the DR3 reactor, using both constant $\bar{q}$ and constant
E methods.

In pure Tb, the dispersion curves at 90°K, in the
ferromagnetic phase have a finite energy at $\bar{q} = 0$, due to
magnetic anisotropy, followed by a quadratic rise at low $\bar{q}$
and have a pronounced kink in the c-direction[1]. The dis-
persion relations have a symmetry consistent with the spin
space group[2]. The results have been analysed in terms of
$J(0) - J(\bar{q})$ where the Fourier transformed exchange para-
meter $J(\bar{q})$ is defined so that

$$J(\bar{q}) = \sum_{\bar{R}_m} J(\bar{R}_m) e^{i\bar{q}\bar{R}_m}$$

For the c-direction of pure Tb, $J(\bar{q})$ is rather flat
at low $\bar{q}$ and has a kink which reflects that in the disper-
sion curve. As the temperature is increased, $J(\bar{q})$ scales
approximately with the ordered moment, in agreement with the
theory based on the random phase approximation[3]. In addi-
tion it develops a shallow maximum at low $\bar{q}$, which reflects
the tendency towards spiral ordering.

When 10% Ho is added to Tb, this tendency towards spiral ordering is considerably enhanced and the spiral structure is stable over a greater temperature range. In addition $J(\bar{q})$ in the ferromagnetic phase is flatter at low $\bar{q}$ than in pure Tb and has a more pronounced kink. The magnon dispersion relations have also been measured in the c-direction in the spiral phase at 200°K. The magnon energies increase linearly from zero at low $\bar{q}$, as expected. The $J(\bar{q})$ determined from these measurements has a pronounced maximum at low $\bar{q}$, and the kink is developed to a point at which a clear maximum also occurs at higher $\bar{q}$[4].

In all cases $J(\bar{q})$ may be decomposed into a smoothly varying function, which has the sinusoidal form appropriate to a nearest neighbor Heisenberg interaction, plus peaks centered approximately at $\bar{Q}$ and $|\bar{\tau} + \bar{Q}|$ where $\bar{Q}$ is the wavevector of the spiral order and $\bar{\tau}$ is the (002) reciprocal lattice vector. These peaks may be ascribed to transitions between parallel electron and hole sheets of the Fermi surface, which are believed to determine $\bar{Q}$ in the periodically ordered phases of the heavy rare earth metals[5]. The peaks decrease discontinuously at the spiral-ferromagnetic transition, due to the splitting of the energy bands of different spin in the ferromagnetic phase.

We have also observed a strong coupling between magnons and transverse phonons propagating in the c-direction which leads to mixed excitations and a splitting apart of the dispersion curves. Since this interaction is not observed in pure Tb and measurements at different temperatures show that it is greatest for intermediate $\bar{q}$ values, it may be associated with the large spin deviations occurring at the Ho sites in resonant magnon modes.

References

1. H. Bjerrum Møller and J.C. Gylden Houmann
    Phys. Rev. Letters 16, 737 (1966)

2. W. Brinkman and R. J. Elliott
    Proc. Roy. Soc. (to be published)

3. F. Keffer and R. Loudon
    J. Appl. Phys. 32, 25 (1961)

4. H. Bjerrum Møller, J. C. Gylden Houmann and
        A. R. Mackintosh
        (to be published)

5. R. W. Williams, T. L. Loucks and A. R. Mackintosh
    Phys. Rev. Letters 16, 168 (1966)

MAGNETIC BEHAVIOR OF TRIVALENT TERBIUM IN SEVERAL COMPOUNDS HAVING THE PEROVSKITE STRUCTURE

J. Sivardiere, J. Mareschal, S. Quezel-Ambrunaz,
G. F. de Vries

CEN-G, Chemin des Martyrs, Grenoble, France

and

E. F. Bertaut

CEN-G and C.N.R.S., Chemin des Martyrs, Grenoble, France

The compounds $ATbO_3$ (A = Cr, Fe, Al, Co, Ga, Mn) having the deformed perovskite structure have been studied by neutron diffraction. The A sublattice, if A is a magnetic ion, orders at high temperatures ($T<T_{N1}$) according to a mode G; for $T<T_{N2}$, the sublattice of Tb orders on being coupled with A and for $T<T_{N3}$ independently of A; this last named ordering is only observed as A is not magnetic. It is due to a great extent to dipole interactions. The Néel temperatures have been determined, and the magnetic behavior of Tb studied for $T<T_{N3}$ and $T_{N2}<T<T_{N3}$.

HIGH-TEMPERATURE NEUTRON DIFFRACTION STUDY OF LaC_2 and YC_2

by

A. L. Bowman, N. H. Krikorian, G. P. Arnold, T. C. Wallace
N. G. Nereson

Los Alamos Scientific Laboratory
University of California
Los Alamos, New Mexico
87544

ABSTRACT

The dicarbides of lanthanum and yttrium have been examined by high-temperature neutron- and X-ray-diffraction and by thermal analysis. A tetragonal to cubic transformation has been observed at $1060°$ for LaC_2 and at $1320°$ for YC_2. The lattice parameters of LaC_2 are a = 4.00, c = 6.58A at $900°$ and a = 6.02A at $1150°$. The parameters of YC_2 are a = 3.74, c = 6.20A at $1100°$ and a = 5.66A at $1400°$.

The structure of the tetragonal phases was found to be the C11a calcium carbide-type, in agreement with previous room temperature results. The structure of the cubic phases is the B1 sodium chloride-type with C_2 groups, similar to the structure of KCN. Both phases are isomorphous with the corresponding uranium dicarbide phases.

INTRODUCTION

The existence of the rare earth dicarbides (including yttrium) is well established. The crystal structures of LaC_2, CeC_2, TbC_2, YC_2, YbC_2 and LuC_2 have been described from room temperature neutron diffraction studies (Atoji, 1961) as the C11a calcium carbide structure: tetragonal, space group $I4/mmm$, with metal atoms in $(0,0,0)$ and carbon atoms in $(0,0,z)$, $z \sim 0.40$.

A systematic investigation of these dicarbides by thermal analysis, X-ray diffraction and high-temperature neutron diffraction has shown that they transform to cubic phases at high temperatures. Possible exceptions are YbC_2 and EuC_2. The existence of EuC_2 could not be confirmed. In addition, the tetragonal structure of LuC_2 could not be obtained, except through the addition of erbium as an impurity. The details of the neutron diffraction experiments are described in this paper. The remainder of this work has been described previously (Krikorian et al., 1967).

EXPERIMENTAL

Samples of lanthanum dicarbide and yttrium dicarbide were prepared from the high-purity elements by arc-melting and pulverizing. The compositions by chemical analysis were $LaC_{2.0}$ with < 500 ppm oxygen and free carbon, and $YC_{1.8}O_{0.1}$ with 3 w/o free carbon. The samples were examined by high-temperature neutron diffraction (M. Bowman et al., 1966) in graphite holders under an atmosphere of flowing helium. The diffraction data were obtained from $2\theta = 25$ to $70°$ at a wave-length of 1.3926A, and were corrected by subtracting a blank run on the graphite sample holder. The corrected patterns are shown in Figs. 1 and 2. Additional scans were taken at $2\theta = 25 - 30°$ for LaC_2 and at $2\theta = 27 - 32°$ for YC_2 in order to determine the transition temperatures. Observed intensities were determined by least-squares analysis of the diffraction data

(Bowman et al., 1965), and were fitted to trial structures by least-squares solution of the equation (Bacon, 1962)

$$I = K \frac{\exp(-\mu t \sec \theta)}{\sin^2 2\theta} \exp(-2B \frac{\sin^2 \theta}{\lambda^2})jF^2. \qquad (1)$$

Scattering amplitudes of 0.78 for yttrium (Paton and Marlen, 1965), 0.83 for lanthanum and 0.661 for carbon (all x 10^{-12} cm) were used.

RESULTS AND DISCUSSION

A tetragonal to cubic transition was observed at 1060° for LaC_2 and at 1345° for YC_2, in excellent agreement with the values of 1060° and 1320° determined by thermal analysis. The latter values should be considered more accurate, due to the difficulty of temperature measurement in the neutron diffraction experiments.

The structures of the tetragonal phases were found to be the C11a type, in agreement with the previous room-temperature results. The LaC_2 pattern at 900°C gave K = 0.24 ± 0.01, B = 3.1 ± 0.6, z = 0.404 ± 0.002, R = 0.08, where $R = \Sigma w|I_o - I_c|/\Sigma wI_o$. Lattice parameters were a_o = 4.000, c_o = 6.58, giving a C-C distance of 1.26 ± 0.03A. A correction for thermal motion by the equation (Busing and Levy, 1964)

$$d^* = d + 0.0253 (B/d) \qquad (2)$$

gave d^* = 1.32. This correction is an extreme one. The true value probably lies between d and d^* as extremes. The YC_2 pattern at 1100° gave K = 0.47 ± 0.02, B = 3.7 ± 0.3, z = 0.391 ± 0.001, R = 0.04. With lattice parameters a_o = 3.737, c_o = 6.196, the C-C distance is 1.35 ± 0.02A, or 1.44A with thermal correction.

The structures of the cubic phases were found to be the KCN-type, isomorphous with cubic uranium dicarbide (A. Bowman et al., 1966). This structure is face-centered, space group Fm3m, with metal atoms in $(\frac{1}{2},\frac{1}{2},\frac{1}{2})$ and C_2 groups with centers at (0,0,0) ran-

domly oriented along [1 1 1] directions. Intensities were calculated
on the basis of one-fourth of a carbon atom in (x,x,x). The C_2 groups
may also be described by a free rotator model. There seems to be no
significant difference between the two models. The LaC_2 pattern at
$1100°$ gave $K = 0.06 \pm 0.01$, $B = 5.6 \pm 2.0$, $x = 0.061 \pm 0.012$, $R = 0.02$.
With $a_o = 6.022$, $d_{C-C} = 1.27 \pm 0.06A$ and $d* = 1.38A$. The YC_2 pattern
at $1400°$ gave $K = 0.10 \pm 0.01$, $B = 5.2 \pm 1.2$, $x = 0.074 \pm 0.007$, $R = 0.09$. With $a_o = 5.66A$, $d_{C-C} = 1.45 \pm 0.04A$ and $d* = 1.52A$.

The observed C-C distances in LaC_2 of $1.26 - 1.38A$ are in
reasonable agreement with the room temperature value of $1.30A$ (Atoji,
1961). The values of $1.35 - 1.52A$ observed for YC_2 are much larger
than the room temperature value of $1.275A$. Rather than attach any
significance to this difference, we would prefer to attribute it to
the large amount of oxygen in the sample. We hope to confirm this
with additional experiments carried out under high vacuum.

REFERENCES

ATOJI, M. (1961) J. Chem. Phys. 35, 1950.

BACON, G. E. (1962) Neutron Diffraction. Oxford: Clarendon Press.

BOWMAN, A. L., WALLACE, T. C., YARNELL, J. L., WENZEL, R. G., and
    STORMS, E. K. (1965) Acta Cryst. 19, 6.

BOWMAN, A. L., ARNOLD, G. P., WITTEMAN, W. G., WALLACE, T. C., and
    NERESON, N. G. (1966) Acta Cryst. 21, 670.

BOWMAN, M. G., HULL, D. E., WITTEMAN, W. G., ARNOLD, G. P., and
    BOWMAN, A. L. (1966) Rev. Sci. Instr. 37, 1543.

BUSING, W. R. and LEVY, H. A. (1964) Acta Cryst. 17, 142.

KRIKORIAN, N. H., WALLACE, T. C. and BOWMAN, M. G. (1967). Proceedings
    of the Colloque International Sur les Derives Semimetallique du
    Centre National de la Recherche Scientifique et Universite de
    Paris (Orsay).

PATON, M. G. and MARLEN, E. N. (1965) Acta Cryst. 19, 679.

TABLE 1

NEUTRON DIFFRACTION DATA

$LaC_2(t)$				$YC_2(t)$			
d	h k l	I_o	I_c	d	h k l	I_o	I_c
2.83	1 1 0	56.0	55.7	3.10	0 0 2	18.2	16.5
2.15	1 1 2	24.0	21.1	2.64	1 1 0	93.2	93.2
2.00	2 0 0	20.5	24.2	2.01	1 1 2	19.8	22.8
1.92	1 0 3	13.4	12.5	1.87	2 0 0	40.1	38.5
1.73	2 1 1	0.0	0.9	1.81	1 0 3	30.1	31.5
1.71	2 0 2	7.9	11.5	1.61	2 1 1	1.6	1.3
1.64	0 0 4	0.0	0.0	1.60	2 0 2	15.5	12.1
1.42	1 1 4	0.0	0.1	1.55	0 0 4	0.0	0.5
1.41	2 2 0	12.5	9.4	1.34	1 1 4	0.0	1.2
1.39	2 1 3	9.4	10.0	1.32	2 2 0	13.2	13.5
1.31	3 0 1	7.9	5.5	1.30	2 1 3	23.2	22.7
1.30	2 2 2						
1.27	2 0 4						
1.26	3 1 0	24.5	25.7				
1.25	1 0 5						

$LaC_2(c)$				$YC_2(c)$			
d	h k l	I_o	I_c	d	h k l	I_o	I_c
3.01	2 0 0	55.1	55.1	2.83	2 0 0	68.0	68.0
2.13	2 2 0	30.8	30.8	2.00	2 2 0	35.3	33.2
1.82	3 1 1	0.0	2.3	1.70	3 1 1	5.3	9.4
1.78	2 2 2	7.3	8.1	1.63	2 2 2	6.4	8.3
1.50	4 0 0	5.3	1.5	1.41	4 0 0	0.0	0.5
1.38	3 3 1	5.6	2.3	1.30	3 3 1	8.1	5.1
1.34	4 2 0	2.7	3.8	1.26	4 2 0	5.2	2.5
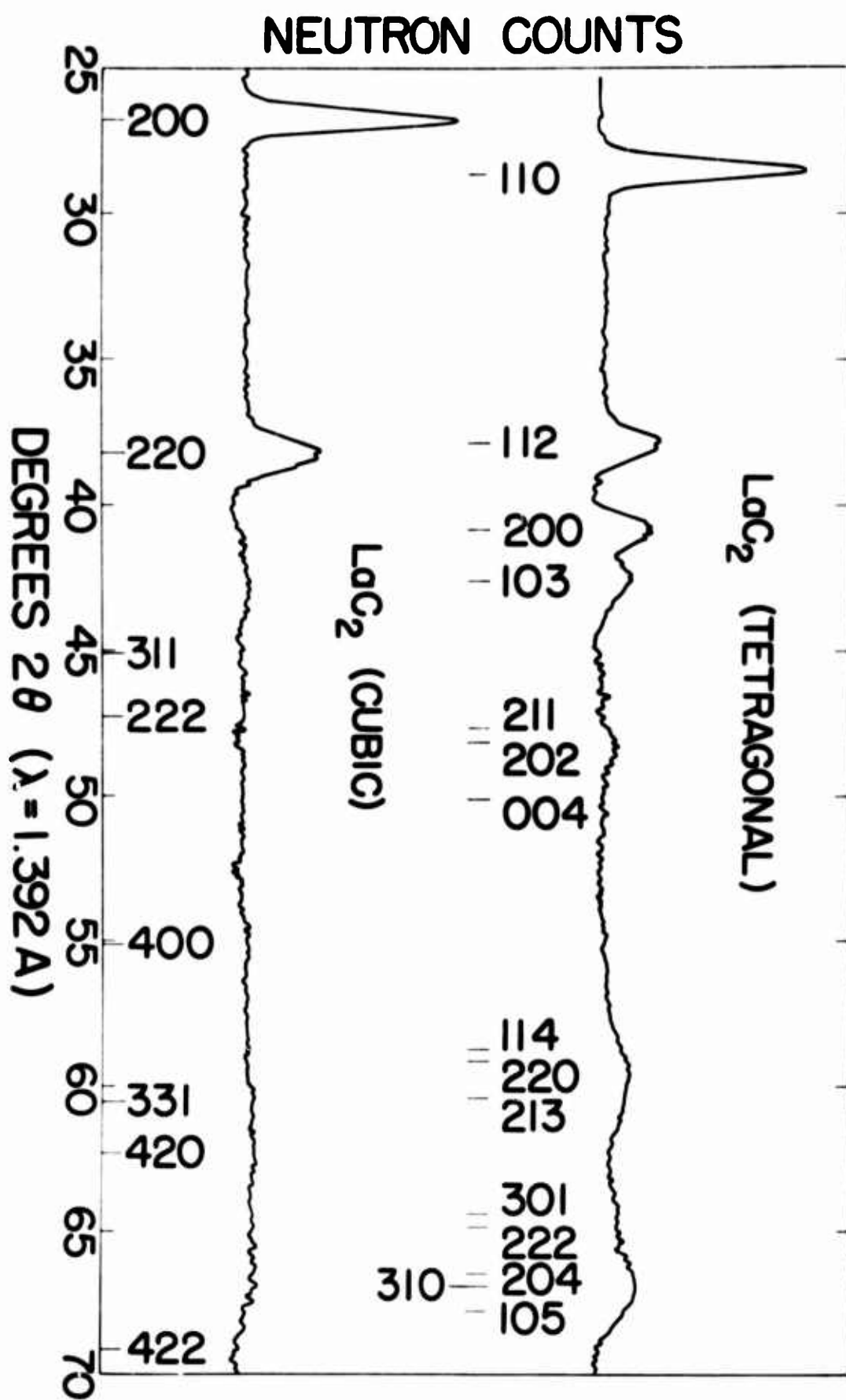
Fig. 1. Neutron diffraction patterns of LaC₂

NEUTRON COUNTS

DEGREES 2θ (λ = 1.392 A)

LaC₂ (TETRAGONAL)

LaC₂ (CUBIC)

Fig. 2. Neutron diffraction patterns of YC₂
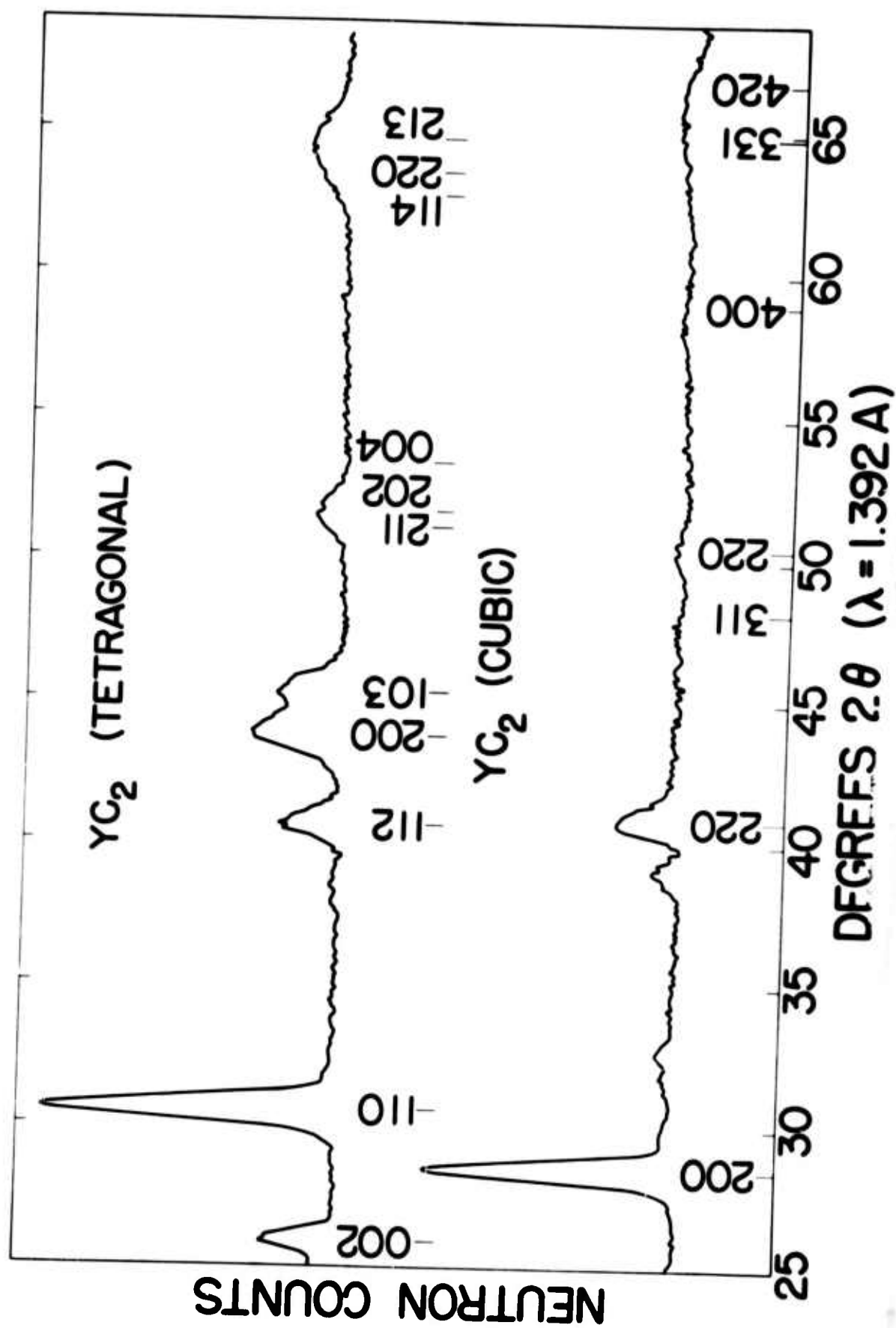
CURRENT PROBLEMS AND STUDIES IN THE COORDINATION
CHEMISTRY OF THE RARE EARTH-METAL IONS

Therald Moeller

Noyes Chemical Laboratory, University of Illinois,

Urbana, Illinois

ABSTRACT

The currently interesting problems to be considered
include the structure of and bonding within the complex
species, the thermodynamic stabilities of the complex
species in solution, those properties that arise from f
configurations, and the applications that depend upon spe-
cific properties of individual complexes. Structural
studies, although still infrequent and limited in number,
support the view that coordination number six and octa-
hedral geometry are the exception rather than the rule.
Higher coordination and spatial arrays that are uncommon
among complexes derived from the d-transition-metals are
important. Although the bonding between cation and ligand
is, by general agreement, primarily electrostatic in nature,
small but significant covalent contributions are indicated
by spectral and other studies. Ligand field stabilization,
however, is minimal. The puzzling irregularities in the
thermodynamic stabilities (i.e., formation constants, free
energy changes) of complexes with particular ligands as the
ion Ln^{3+} is varied appear to result from combinations of
various factors. More exacting evaluation of entropy and
enthalpy contributions, considerations of permitted geom-
etry as functions of ligand and cation size, and an in-
creasing awareness of the significance of the hydration
sphere of the cation in aqueous solution afford new ap-
proaches to this problem. Detailed evaluations of environ-
mental effects upon absorption spectra now provide us with
a better understanding both of the properties of $4f$ elec-
trons and their chance of participating in bonding.
Particularly exciting is the process of energy transfer
through an excited chelating ligand to an appropriate rare
earth-metal ion, with the consequent emission of coherent
radiation.

INTRODUCTION

Few areas in the chemistry of the rare earth-elements
have developed as rapidly as that of coordination chemis-
try (1). Although developments even as late as the middle
1950's were small in number, a non-encyclopedic review
covering the literature only through 1962 contained in an
excess of five hundred references (2), and a detailed sum-
mary restricted to the general area under current dis-
cussion cited nearly three hundred references for the
period 1963-1965, inclusive (3). Although the utility of
certain complex species in effecting improved separations
and the intriguing alterations produced in certain proper-
ties due to $\underline{f}$ electrons have prompted some of this activity,
much of it reflects rather the overall expansion character-
istic of inorganic chemistry and the desire to extend the
significant advances made in $\underline{d}$ transition-metal chemistry
to other areas.

Extensions of observations on the coordination chemis-
try of the $\underline{d}$ transition-metal ions to the rare earth-metal
ions, however desirable they may appear to be, are defini-
tely limited. Complexation of a rare earth ion (most com-
monly Ln^{3+}) yields species of substantial thermodynamic
stabilities only with a limited number of ligands; affects
the magnetic, color, and light absorption properties of that
ion only to a limited degree; produces products that exhibit
only a limited extent of covalency; and does not often lead
to isomeric products or to products the substitution re-
actions of which proceed slowly enough to be readily moni-
tored. Both the ground-state electronic configurations of
the rare earth-metal ions and the radial extensions of the
$4\underline{f}$ orbitals characteristic of these configurations are of
importance in accounting for these differences in proper-
ties. Shielding of the $4\underline{f}$ orbitals is sufficient to limit

seriously the participation of electrons in the.. in bonding. Indeed, except quite generally for their absorption spectra and paramagnetism, the complexes of the $Ln^{...}$ ions compare better with those of the alkaline earth-meta. ions than with those of the $\underline{d}$ transition-metal ions. On the other hand, the availability of the $4\underline{f}$ orbitals does allow unique internal energy transfer processes in certain complexes that allow the emission of coherent radiation.

Problems of the greatest current interest in the area of coordination chemistry are concerned with behaviors of ligands, structure and bonding, thermodynamic stability and trends therein, effects of complexation on the properties of $\underline{f}$ electrons, and applications.

LIGANDS

Many of the more recently reported studies have involved ligands of the same structural types as those investigated earlier (2). The polyaminopolycarboxylic acids, hydroxycarboxylic acids, and 1,3-diketones are cases in point. Other currently interesting ligands include simple anions and species that are purely nitrogen donors.

Coordination by simple anions (e.g., SCN^-, NO_3^-, Cl^-) in aqueous solution is largely limited to ion-pair association, or lack of disruption of the inner hydration sphere of the cation (4). The fluoride ion is exceptional in bonding by displacing water molecules from the primary hydration sphere (5). The ions $[LnCl_4]^-$, $[LnCl_5]^{2-}$, and $[LnCl_6]^{3-}$ have all been distinguished in melts (3), but the most convincing evidence for the existence of anionic halo complexes is the isolation of the salts $[(C_6H_5)_3PH]_3^+[LnX_6]^{3-}$ (X = Cl, Br, I) (6). The nitrate ion can be bonded either mono- or bidentately, depending upon the species in question (7,8).

Early failures to isolate species based upon neutral ligands in which the only donor atoms are nitrogen atoms probably reflect the use of aqueous media and the consequent precipitation of hydrous oxides or hydroxides. More recently, both 1,10-phenanthroline and dipyridyl derivatives have been synthesized (3,8), and experiments in our own laboratory and under anhydrous conditions have yielded the ethylenediamine compounds $Ln(en)_{3,4}(NO_3)_3$. Simultaneous bonding through oxygen and nitrogen atoms is common, e.g., in the polyaminepolycarboxylic acid and 8-quinolinol chelates.

Among the most striking of recent observations are volatility without decomposition (9,10) and laser behavior (11), both with specific types of 1,3-diketone complexes.

STRUCTURE AND BONDING

Although the ions $[LnX_6]^{3-}$ in the triphenylphosphonium salts appear, from absorption spectral studies, to exemplify 6-coordination in nearly perfect octahedral geometry (6), 6-coordination, although seemingly indicated by numerous compound compositions and thus tacitly assumed for many years, is apparently the exception rather than the rule. Square anti-prismatic geometries involving 8-coordination by oxygen atoms are characteristic of crystals of the compounds $[Ce(CH_3COCHCOCH_3)_4]$ (12) and $[Y(CH_3COCHCOCH_3)_3(H_2O)_3]$ (13). Coordination number 8 is also exemplified by the ion $[Eu(H_2O)_6Cl_2]^+$ in crystals of the salt $EuCl_3 \cdot 6H_2O$, but coordination number 10 characterizes the unit $[Pr(H_2O)_4(NO_3)_3]$ containing bidentate nitrate ions (3). The $[Ln(H_2O)_9]^{3+}$, $[La(EDTA)(H_2O)_3]^-$, and $[Tb(EDTA)(H_2O)_3]^-$ ions illustrate 9-coordination, and the acid $[HLa(EDTA)(H_2O)_4]$ 10-coordination (1-3,14). The EDTA species have quasi-$\underline{D}_{2d}$ dodecahedral geometries, with the

four carboxylate oxygen atoms and the two nitrogen atoms of the ethylenediaminetetraacetate group and an oxygen atom from one water molecule defining seven of the eight coordination positions (14). The mean of the other water molecules defines the other position. A similar dodeca-hedral geometry characterizes the 8-coordinate ions $[Eu(RCOCHCOR)_4]^-$ (15). The ion $[Ce(NO_3)_6]^{2-}$ in aqueous solution exemplifies bidentate nitrate ions and 12-coordination with an icosahedral geometry of oxygen atoms about the central Ce^{4+} ion (7).

Although substantially complete electrostatic bonding in the complexes of these elements has been assumed in terms of spectral, magnetic, and thermodynamic data, it must be admitted that quantitative evidences are lacking. Uses of absorption spectra and magnetic data are limited since the electrons responsible for these phenomena are in 4f orbitals that are well shielded from any ligand effects. Participation of the 4f electrons in covalent bonding seems unlikely. So also does participation of higher-energy orbitals (e.g., 5d, 6s), although the latter cannot be excluded solely on the basis of absorption spectral effects. A well-defined nephelauxetic effect (16) and variations in absorption spectra upon complexation (17) argue for small but significant covalent contributions. So also do the results of an investigation of environmental effects on f-f transitions for a series of neodymium(III) complexes in aqueous solution, which show consistency with inner- and outer-sphere interactions by the ligands (18).

THERMODYNAMIC STABILITY

Thermodynamic stability of a complex species is measured by the free-energy change (ΔG) that occurs during its formation from its components. Both the enthalpy

($\Delta\underline{H}$) and entropy ($\Delta\underline{S}$) ·es characteristic of the re-
action are reflected .e free-energy change and may be
significant in determining its magnitude. The free-energy
change is, of course, directly related to the thermodynam-
ic formation constant ($\underline{K}$) of the species in question. Al-
though concentration-based formation constants are readily
measurable and have been determined for many species
(2,3,19), often at constant ionic strength, few truly
thermodynamic data are available for the standard state of
infinite dilution. Enthalpy changes have been most com-
monly determined in terms of the temperature dependence of
formation-constant values. Relatively few calorimetrical-
ly determined values are available (1-3), but the need for
such values is readily apparent since enthalpy changes on
complexation of the rare earth-metal ions are commonly
rather small.

Thermodynamic data indicate that for a given ligand
a cation of this type gives a generally less stable complex
than a comparably charged $\underline{d}$ transition-metal ion. Exact
comparisons among the rare earth-metal ions themselves are
restricted by the limited number of ligands for which data
for the entire series are available. Predictions, in terms
of a general scheme of electrostatic bonding, that stabili-
ty should increase as the crystal radius of the cation Ln^{3+}
decreases (i.e., with increasing nuclear charge) for a
given ligand are in general agreement with observation for
the lighter cations ($La^{3+}-Sm^{3+}$ or Eu^{3+}), but not neces-
sarily for the heavier cations ($Eu^{3+}-Lu^{3+}$) and the Y^{3+}
ion. Significant observations include general discontin-
uity in stability in the vicinity of the Gd^{3+} ion, several
types of variation in stability among complexes of the
heavier cations, and the appearance of the Y^{3+} ion
(crystal radius that of the $Dy^{3+}-Ho^{3+}$ ion) with either the

lighter or the heavier cations, depending upon the ligand being studied (2).

No completely adequate explanation for these observations has yet been offered. Those that have been proposed can be classified broadly as thermodynamic and structural. Among the polyaminepolycarboxylate complexes, the entropy change is more significant in determining thermodynamic stability than the enthalpy change (20-22). Trends in entropy change vary from ligand to ligand, however, and values for a given ligand show little regularity as the cation is changed. Early conclusions (20) that for the EDTA chelates the break in stability at the Gd^{3+} ion reflects change in the number of coordination sites in the ligand ion have not been substantiated. Structural studies in the EDTA series (14) suggest that change in the coordination number of the central Ln^{3+} ion may occur in the general Gd^{3+}-ion region, thus affecting stability variations. An increasing body of evidence supports the view that stability is determined by the extent to which the primary hydration sphere of the Ln^{3+} ion is altered in the complexation process (4,5,23,24). If this sphere is unaltered (outer sphere complexes), complexation is favored by enthalpy change and opposed by entropy change; if this sphere is altered (inner sphere complexes), complexation is opposed by enthalpy change and favored by entropy change. The chelates are of the second type. Observed variation is thus a reflection of the relative magnitudes of these effects and the changing size of the hydration sphere as the Ln^{3+} ion is changed. Elimination of the complicating effects of changes in hydration number of the ions Ln^{3+} by reaction of the crystalline ethyl sulfates with diglycolate and dipicolinate ions has given a monotonic change in enthalpy of formation with atomic number and

some evidences of slight ligand-field stabilization. Ligand- or crystal-field contribution is always small (ca. 1 kcal./mole) and probably insignificant in determining overall stability.

EFFECTS ON f ELECTRONS

Electrons in the 4f orbitals determine the magnetic and light absorption and emission properties. Inasmuch as these electrons are effectively shielded, their properties cannot be altered as extensively as are those of the d electrons in the transition-metal ions. Data on the effects of complexation on magnetic properties are too fragmentary to permit the drawing of positive conclusions (25). Alteration in the symmetries of ions by the fields imposed by complexing ligands do displace and alter the intensities of the hypersensitive bands in the absorption spectra, as mentioned above, but the changes observed are small when compared with those noted for the d transition metals and not subject to the same interpretation.

The most significant effect of this type is in terms of fluorescence spectra and laser behavior (11), as based upon Weissman's original observation (26) that certain europium(III) chelates, either as crystals or in benzene solution, fluoresce via a mechanism involving the broad absorption of radiant energy by the aromatic groups in the ligands and the reemission of a portion of this energy as narrow and highly characteristic spectral lines. It has been shown subsequently that initial absorption of energy gives a vibrational level in the first excited singlet state (S). This process is followed by deactivation through internal conversion to lower levels with the release of energy as molecular fluorescence or phosphorescence. Not the least significant pattern may involve successively an internal conversion to a triplet state,

a radiationless transition to a lower-lying Ln^{3+} ion state, and a radiative transition to a still lower-lying ionic state (27). The last of these processes gives line-like, coherent radiation and is responsible for the laser effect. Chelates of the ions Sm^{3+}, Eu^{3+}, Tb^{3+}, and Dy^{3+}, in particular those of the type $[Ln(RCOCHCOR')_4]^-$, where either R or R' or both are aromatic, are especially effective.

APPLICATIONS

Improvement in fractional separations in terms of the varying stabilities of complex species is a highly practical application. Other applications are in analytical procedures and possibly in amorphous transparent or liquid lasers.

REFERENCES

(1) T. Moeller, Werner Centennial, Volume 60, Advances in Chemistry Series. American Chemical Society, Washington, D. C. (1967).

(2) T. Moeller, D. F. Martin, L. C. Thompson, R. Ferrús, G. R. Feistel, and W. J. Randall, Chem. Rev., 65, 1 (1965).

(3) T. Moeller, E. R. Birnbaum, J. H. Forsberg, and R. B. Gayhart, Progress in the Science and Technology of the Rare Earths (L. Eyring, Ed.), Vol. 3. Pergamon Press, New York, N. Y. (1968).

(4) G. R. Choppin and P. J. Unrein, J. Inorg. Nucl. Chem., 25, 387 (1963); G. R. Choppin and J. Ketels, ibid., 27, 1335 (1965); G. R. Choppin and W. F. Straznik, Inorg. Chem., 4, 1250 (1965).

(5) J. B. Walker and G. R. Choppin, Chemistry of the Lanthanide and Actinide Elements, Volume 61, Advances in Chemistry Series. American Chemical Society, Washington, D. C. (1967).

(6) J. L. Ryan and Chr. Klixbüll Jørgensen, J. Phys. Chem., 70, 2845 (1966).

(7) R. D. Larsen and G. H. Brown, J. Phys. Chem., 68, 3060 (1964).

(8) F. A. Hart and F. P. Laming, J. Inorg. Nucl. Chem., 26, 579 (1964); 27, 1605, 1825 (1965).

(9) K. J. Eisentraut and R. E. Sievers, J. Am. Chem. Soc., 87, 5254 (1965).

(10) S. J. Lippard, J. Am. Chem. Soc., 88, 4300 (1966).

(11) A. Lempicki, H. Samelson, and C. Brecher, Appl. Opt., Suppl. No. 2, 205 (1965).

(12) B. Matkovic and D. Grdenic, Acta Cryst., 16, 456 (1963).

(13) J. A. Cunningham, D. E. Sands, and W. F. Wagner, Paper presented at Southeastern Regional Meeting of the American Chemical Society, Louisville, Ky., October, 1966.

(14) B. Lee, M. D. Lind, and J. L. Hoard, Abstracts 152nd National Meeting of the American Chemical Society, New York, N. Y., September, 1966.

(15) C. Brecher, A. Lempicki, and H. Samelson, J. Chem. Phys., 41, 279 (1964).

(16) Chr. Klixbüll Jørgensen, Fifth Rare Earth Research Conference, Ames, Iowa (1965).

(17) L. I. Katzin and M. L. Barnett, J. Phys. Chem., 68, 3779 (1964).

(18) G. R. Choppin, D. E. Henrie, and K. Buijs, Inorg. Chem., 5, 1743 (1966).

(19) L. G. Sillén and A. E. Martell, Stability Constants of Metal Ion Complexes, Special Publication 17,

The Chemical Society, London (1965).

(20) R. H. Betts and O. F. Dahlinger, _Can. J. Chem._, 37, 91 (1959).

(21) T. Moeller and R. Ferrús, _J. Inorg. Nucl. Chem._, 20, 261 (1961); _Inorg. Chem._, 1, 49 (1962).

(22) P. L. E. de la Praudiere and L. A. K. Staveley, _J. Inorg. Nucl. Chem._, 26, 1713 (1964).

(23) I. Grenthe, _Acta Chem. Scand._, 17, 2487 (1963); 18, 283, 293 (1964).

(24) L. A. K. Staveley, D. R. Markham, and M. R. Jones, _Nature_, 211, 1172 (1966).

(25) T. Moeller and E. P. Horwitz, _J. Inorg. Nucl. Chem._, 12, 49 (1959).

(26) S. I. Weissman, _J. Chem. Phys._, 10, 214 (1942).

(27) R. E. Whan and G. A. Crosby, _J. Mol. Spect._, 8, 315 (1962).

OM_4 Tetrahedron Linkages

An Important Feature in Rare Earth Oxide and Oxysalt Structures

PAUL E. CARO

Institute for Atomic Research and Department of Chemistry
Iowa State University, Ames, Iowa 50010

Abstract

Rare earth oxides and oxysalt structures are considered with respect to the coordination of the oxygen atom. Metallic atoms are found to be in tetrahedral positions around the oxygen atom, and all known structures can be described as tridimensional or bidimensional packing of OM_4 tetrahedra joined together by sharing of edges. In $A-M_2O_3$, $B-M_2O_3$ structures and the oxysalts the packed tetrahedra appear as an infinite polymeric complex cation $(MO)_x^{x+}$. Possible implications for the structure of non-stoichiometric oxides are discussed. Optical studies show that the rare-earth atoms in oxides are to some extent covalently bonded, and it is suggested that the oxygen atoms are involved in a directional bonding, possibly of a sp^3 type.

The three crystalline forms of the trivalent rare earth oxides M_2O_3, A-hexagonal, B-monoclinic and C-cubic, the fluorite structures of the tetravalent rare-earth oxides MO_2, the fluorite-related structures of non-stoichiometric oxides MO_x (M=Ce, Pr, Tb) and the various known structures of rare-earth oxysalts $(MO)_xX_y$, where X is an anionic atom or group, have a common character: the presence of oxygen atoms surrounded tetrahedrally by four rare earth atoms. A- and B-M_2O_3 also contain oxygen atoms with a higher coordination number. Coordination of four for oxygen occurs only for the above group of oxide structures (mainly lanthanide and actinide oxides) and also for such oxides as ZnO (würtzite group) and Cu_2O (cuprite group). A coordination of four also exists for the corundum group structure, but in that case the metallic atoms do not form a regular tetrahedron around the oxygen atom.

Prior to the examination of the individual structures, we shall discuss the conditions imposed on the size of the atoms involved by the particular arrangement they have. As will be shown later the structures are characterized by the fact that the OM_4 tetrahedra are linked together by sharing of edges. Besides its four metallic neighbors an oxygen atom has six oxygen neighbors symmetric to itself with respect to the edges of the imaginary tetrahedron made by the four metallic

atoms. This situation implies definite geometrical relations between the size of the atoms. Definition of the radii of individual atoms or ions is subject to some controversy. L. Pauling (1) and J.C. Slater (2) for instance, have chosen different series of values. Use of a given series depends on some assumptions on the nature of the bonding of the atom involved. It is possible, however, to avoid speculating on the atomic radii by taking into account only the distance between atoms in a crystal which does not change whatever model is used. In our case the size of the tetrahedron is defined by the O-M distances; if the O-M distance is fixed, the O-O distance is fixed too, in the present geometry (O-M = $\frac{\sqrt{3}}{2}$ O-O). The conventional (Pauling) radius for the

oxide ion is 1.38 Å. If the oxide ions are in contact, O-O = 2.76 Å and the corresponding O-M is 2.40 Å (i.e. for a cation of radius 1.02 Å). We do not have to consider the case where O-O is greater than 2.76 Å (oxygens not in contact) because the largest tetrahedral O-M distance in the structures studied is precisely 2.40 Å (in A-La$_2$O$_3$). If we assume that the O-O distance can be somewhat smaller than the sum of conventional ionic radii it is possible to accommodate smaller cations. A review of oxide crystal structures shows that O-O distances may be as low as 2.50 Å (α - Al$_2$O$_3$: 2.49 Å, α - Fe$_2$O$_3$: 2.55 Å, (Fe, Mn)$_2$O$_3$(bixbyite, C-form rare earth oxide type): 2.51 Å) (3). Assuming 2.50 Å as the smallest possible distance of approach of oxide ions, we find that the smallest O-M distance is 2.15 Å. The range of O-M distances possible for the arrangement is thus from 2.40 Å to 2.15 Å; hence conventional cationic radii from 1.02 Å to 0.77 Å can be accommodated.

Templeton and Dauben (4) have determined the radii of rare earth M^{3+} ions from the O-M distances in C-form rare earth oxides, using Pauling's 1.38 Å value for the oxide ion. They found radii extending from about 1.06 Å (La, extrapolated, there is no C-M$_2$O$_3$) to 0.848 Å (Lu). As would be expected, the rare-earth elements have precisely the right range of ionic radii for building crystalline edifices involving a tetrahedral coordination around the oxygen, with linkage of the tetrahedra through the edges. Ce^{4+} and Pr^{4+}, form oxides with O-M = 2.41 Å and 2.32 Å respectively, so they are in the range too.

This imperative size condition is fulfilled by 3+ and 4+ rare earth ions and also by Tl^{3+} (0.95 Å), Th^{4+} (0.99 Å) and other actinide elements; Zr^{4+} is at the limit of the range (0.80 Å) and the existence of a fluorite structure for ZrO$_2$ is disputed (5). For structures in which OM$_4$ tetrahedra are not linked by their edges but by their corners (ZnO, Cu$_2$O) such a restriction does not hold (Cu$^+$ = 0.96 Å and Zn^{2+} = 0.74 Å.)

I. The Fluorite type structure

This structure is classical but we shall recall it in detail because it is our basis for the discussion of the other structures.

On a plane perpendicular to the [111] direction of the cubic unit cell oxygen atoms project in positions labeled ABC as in the classical

cubic close packing of spheres. Each sheet of oxygen atoms is in a (111) plane and the order of success ion of the planes down [111] is ABC, ABC etc.... Each oxygen atom is at the center of a tetrahedron made by four rare-earth atoms. With respect to the orientation of the tetrahedra, the order of succession of the oxygen planes is ABC, A'B'C', ABC, A'B'C'..., since the tetrahedra corresponding to the oxygen atoms in A and A' do not have the same orientation (see fig. 1.)

In fig. 1 and 3, the tetrahedra are cut by a plane passing through one edge and the middle of the opposite edge (plane of paper). This contour is outlined. Conventional (Pauling) ionic radii have been used.

Each oxygen atom has six oxygen neighbors at its contact, none of which belong to the plane of the atom considered (this is a difference with respect to the cubic closest packing of spheres for which each sphere has twelve like neighbors). For an atom B, three of the neighbors are in layer A and three in C to give a trigonal antiprism or an octahedron viewed down the S_6 axis.

The metallic atoms project also in positions ABC but with twice the oxygen planes repeat distances. Between each plane of metallic atoms there are two planes of oxygen atoms. The order of succession of metal and oxygen planes along the [111] direction is: A oxygen, B oxygen, A metal, C oxygen, A' oxygen, C metal, B' oxygen, C' oxygen, B metal, A oxygen, B oxygen... The corresponding stoichiometry is MO_2 .

With respect to the tetrahedra arrangement it is easy to see that each tetrahedron shares its six edges with the tetrahedra centered on the six oxygen neighbors. Each corner, that is to say each metallic atom, is common to eight tetrahedra. For a metallic atom in a sheet A (metal), for instance, there are 8 oxygen neighbors at the corners of a cube: 1 in A, 3 in B, 3 in C, 1 in A'.

The fluorite structure can thus be described as a tridimensional packing of OM_4 tetrahedra sharing their edges.

We intend to show that the rare earth oxides structures can be described as packing of OM_4 tetrahedra basically related to the one in fluorite. The subject is ordinarily treated in terms of cation coordination (17) which is very irregular and yields a complicated picture. If the tetrahedra corresponding to the anion coordination are abstracted a much more simple pattern emerges.

II. The $C-M_2O_3$ structure

This is a fairly complicated structure which is ordinarily described as a fluorite one with one quarter of the anions missing. Positions of the oxygen vacancies are shown in fig. 4, which is a projection of oxygen positions on a plane (111). If there were no vacancies the projection

would be the one for fluorite. Characteristic triangular clusters of vacancies are outlined for planes ABC (not for A'B'C'). If we consider the remaining atoms, we see that each oxygen has only four like neighbors instead of six in the fluorite structure. (For instance, atom A_{60} has two missing neighbors C'_{52} and C'_{61}). It is equivalent to say that each tetrahedron shares only four edges with other tetrahedra. Each metallic corner is common to six tetrahedra (hence the formula M_2O_3), but the disposition of the six oxygen atoms around a metal ion is not regular; there is a configuration where the missing atoms are on the diagonal of the cube in fluorite and one where they are across a face diagonal. This structure is also a tridimensional edifice of OM_4 tetrahedra, but each of them has only four edges in common with other tetrahedra. This loose packing is perhaps responsible for the slight inequalities observed in the O-M distances; for Y_2O_3 they vary between 2.25 Å and 2.35 Å. (6)

III. The A-M_2O_3 and the oxysalts structure

The structure of A-M_2O_3 has been determined by L. Pauling (7) and by W. C. Koehler and E. O. Wollan (8). It is represented in a view perpendicular to the c hexagonal axis along (100) on fig. 3(a). The character of that structure is that the metallic atom, La for instance, (A-form exists for La, Pr, Nd) has four close oxygen neighbors at 2.40 Å, and three remote at about 2.70 Å. The structure shows that the close oxygen atoms are within tetrahedra of metallic atoms, and that the remote oxygen atoms have 6 octahedral metallic neighbors. The structure can be described as made of sheets of OM_4 tetrahedra linked by their edges with the remote oxygen atoms between the sheets.

An interesting point is that these remote oxygen atoms can be replaced by other atoms, for instance by sulfur to give the oxy-sulfides $(MO)_2S$, (9), or even by groups such as CO_3^{2-} to give the very stable, hexagonal, "basic" carbonates $(MO)_2(CO_3)$ (10). Other oxysalts have structures in which basically the same sheets of connected tetrahedra are found but with a different arrangement within the sheets. This is the case for the oxychloride MOCl structures or for the molybdates Ln_2MoO_6 (i. e. $(LnO)_2MoO_4$ (11) (12).

In A-M_2O_3 each sheet is formed by tetrahedra sharing three of their edges, each corner being common to four tetrahedra. In MOCl each sheet is formed by tetrahedra sharing four of their edges, each corner being again common to four tetrahedra. In the first case each plane array of points M or O in the succession M-O-O-M in the sheet has the two dimensional symmetry p 3ml; in the second case they have the two dimensional symmetry p 4m. The arrangement of tetrahedra is represented in perspective in fig. 2. The relation between the two arrangements is similar to the relation between the disposition of SZn_4 tetrahedra in the two forms of Zn sulfide: zinc blende (MOCl) and würtzite (A-M_2O_3), but in the case of ZnS, the tetrahedra share

corners in a tridimensional structure (13). Both types of sheets can be deduced easily from the packing of tetrahedra in the fluorite structure.

The composition of the sheets is $(MO)_n^{n+}$, and considering the large number of rare earth oxy-compounds with general formula $(MO)_x X_y$, they must be considered as a kind of complex cation $(MO)_n^{n+}$, forming its own salts (14). A more descriptive formulation for $A-M_2O_3$ would consequently be $(MO)_2O$.

A. Müller-Buschbaum and H.G. v. Schnering (15) have recently examined anew the structure of $A-M_2O_3$, and found that it is best described assuming a "micro-twinning" produced by the combination of what would be two sheets in our model plus a sheet reversed with respect to the $\underline{c}$ axis. It is not impossible that real monocrystals of the $A-M_2O_3$ structure could be subject to disorder in the $(LnO)_n^{n+}$ sheets themselves or in the order of the sheets along the $\underline{c}$ axis.

IV. The B-M_2O_3 structures

The B-M_2O_3 structure was determined by D. T. Cromer (16) with Sm_2O_3. It has a monoclinic symmetry that is not basically different from the A-form. The structure is represented in fig. 3 (b) down the short b monoclinic axis, with the contour of the unit cell outlined. The a axis is along the long side of the unit cell. A comparison with the drawing for $A-M_2O_3$ shows immediately the analogy between the two structures. They are made of the same kind of $(MO)_n^{n+}$ sheets, but along what was the $\underline{c}$ axis in the hexagonal structure the succession of the sheets is not regular. This comes from the fact that the oxygen atoms between the sheets are not as far from the rare-earth atoms, and are in distorted octahedral and square pyramidal sites. A samarium atom has four oxygen neighbors within tetrahedra at 2.31 Å (±0.10) and three others between the sheets at 2.54 Å (±0.10) (2) and 2.86 Å (±0.20) (1). A very slight displacement is involved with respect to $A-M_2O_3$, but it is enough to break the hexagonal symmetry. Experimental positions of atoms given by Cromer are very close to the ones we get in the drawing fig. 3 (b) made simply by bringing the sheets in the A-form a little closer to the interlayer oxygen atoms.

V. The MO_x non-stoichiometric systems

Non-stoichiometric oxides occur for those rare earth elements which have a degree of oxidation +3 and +4, i.e. Ce, Pr, Tb. There are numerous definite compounds between x=1.5 and x=2.0 which correspond to the general formula MnO_{2n-2}. The structures are known to be basically related to the fluorite type, but have not been determined (for lack of monocrystals) except for the compound M_7O_{12} (x=1.714) (17). Projections of the vacancies in the fluorite net of M_7O_{12} are shown in fig. 5. The rhomboedral unit cell is outlined. All of the remaining oxygen atoms have one missing neighbor. The structure is

again built of OM_4 tetrahedra, here sharing five of their edges with other tetrahedra. The metallic atoms at the corners have either six oxygen neighbors, as for instance the metallic atom in A_{50}, or seven as the metallic atom in A_{51}. For each six-coordinated metallic atom, there are six which are seven-coordinated. The overall formula is consequently M_7O_{12}.

M_7O_{12} can be described otherwise as a fluorite structure in which all the oxygen planes have $1/7$ of the atoms missing. We find that there is another structure for which the remaining oxygen atoms have one missing neighbor, hence, also made of tetrahedra sharing five of their edges, but corresponding to fluorite oxygen planes which have $1/6$ of their atoms missing. This structure is very complicated and positions of vacancies in a plane repeat only after 36 oxygen planes along [111]. In M_7O_{12} they repeat after three planes. The stoichiometry is M_6O_{10} and corresponds to an unknown member of the family M_nO_{2n-2}. This is not surprising owing to the greater simplicity of the equivalent structure M_7O_{12}.

We have seen previously the importance of the sheets $(MO)_n$ in the structures of the rare earth oxides. It was natural to try to fit them into the pattern of the non-stoichiometric oxides. We find that all the discrete compositions known can be accounted for in terms of $(MO)_n$ sheets linked together by OM_4 tetrahedra, (i.e.: a tridimensional edifice of OM_4 tetrahedra). The linking tetrahedra corresponds to fluorite oxygen planes with either $1/6$ or $1/5$ of the atoms missing. No satisfactory result is obtained if these oxygen planes have $1/7$ of their atoms missing. The most interesting scheme is for the compound Pr_6O_{11} ($n=12$ in M_nO_{2n-2}). There is an equal number of oxygen planes with $1/6$ vacancies and of complete planes. $(MO)_n$ sheets are thus linked together by two oxygen planes with vacancies. Pr_9O_{16} would correspond to $(MO)_n$ sheets joined by a succession O-O-M-O-O ($2/3$ of the oxygen planes in fluorite with $1/6$ vacancies); $Pr_{10}O_{18}$, to $(MO)_n$ sheets joined by two oxygen planes with $1/5$ of vacancies; $Pr_{11}O_{20}$, to $(MO)_n$ sheets joined by one oxygen plane with $1/6$ vacancies and one with $1/5$.

Of course, it is impossible to verify this hypothesis at this time, but such a layer-type structure with vacancies only in some planes, satisfies some of the characteristics of the systems. For one thing, contrary to the prediction of the empirical formula M_nO_{2n-2}, there is no known compound between Pr_6O_{11} and PrO_2. In our scheme Pr_6O_{11} is the last compound possible in which $(MO)_n$ sheets are not in contact; $(MO)_n$ sheets in contact means the formation of a true fluorite unit, hence a biphasic domain between Pr_6O_{11} and PrO_2, as observed. Moreover, it is difficult to determine a unit cell more precisely than the pseudo-fluorite observed with the powder patterns. Hindrance in vacancy ordering is generally considered responsible for the lack of superstructures. The disposition of vacancies in our connecting planes is probably the same from sheet to sheet but that does

not mean necessarily that a stacking order occurs for vacancies along [111]. If not, it could be impossible to define an exact unit cell. In fact all these products need a very long annealing time before showing sharp lines on their fluorite type X-Ray pattern. Some of them show additional lines and in the case of Pr_9O_{16}, they have been interpreted (22) on the basis of a hexagonal unit cell with a $\underline{c}$ value corresponding to the length implied in our hypothesis for the repetition unit along [111] for that compound.

Occurrence of different ions, e.g. Pr^{3+} and Pr^{4+}, which are supposed to be distributed at random on the metallic positions, should not disturb too much the tetrahedra geometry because $O^{2-}-Pr^{3+} = 2.393\,\text{Å}$ (in $C-Pr_2O_3$) and $O^{2-}-Pr^{4+} = 2.336\,\text{Å}$ (in PrO_2), so that the tetrahedra will have nearly equal size. However, if another rare-earth atom such as terbium is introduced in the system [$O^{2-}-Tb^{3+} = 2.30\,\text{Å}$, and $O^{2-}-Tb^{4+} = 2.22\,\text{Å}$], it is likely that connection of tetrahedra could be hampered by size effects. This is perhaps the reason for the disappearance of the M_7O_{12} phase (M=Pr, Tb) in mixed Pr-Tb oxides. (18).

VI. Conclusion

The dominant fact in rare earth oxides seems to be the tetrahedral coordination of the oxygen atom. These structures are far more regular with respect to the anion coordination than they are with respect to the cation coordination. Directional bonding could be involved, for instance through sp^3 hybridization on the oxygen atom. It has been known for some time that the optical spectra of rare earth M^{3+} ions in oxides and oxysalts show a definite shift toward the red with respect to the free ion (nephelauxetic effect). This has been interpreted by C.K. Jorgensen and collab. (19)(20)(21) as an indication of some extent of covalent bonding of the rare earth ion. The fact that the oxides and oxysalts structures can be described as tri or bi-dimensional edifices of OM_4 tetrahedra suggests that they could be regarded as inorganic polymolecular complexes.

Bibliography

(1) L. Pauling, The Nature of the Chemical Bond 3rd Ed. Cornell University Press (1960).
(2) J.C. Slater, J. Chem. Phys., 41, 3199 (1964).
(3) R.W.G. Wyckoff, "Crystal Structures", Vol. II, Interscience New York (1960).
(4) D.H. Templeton, C.H. Dauben, J. Am. Chem. Soc., 76, 5237 (1954).
(5) D.K. Smith, H.W. Newkirk, Acta Cryst. 18, 983 (1965).

(6) M. G. Paton, E. N. Maslen, Acta Cryst. 19 , 307 (1965).
(7) L. Pauling, Z. Krystallogr. 69 . 415 (1928).
(8) W. C. Koehler and E. O. Wollan, Acta Cryst. 6 , 741 (1953).
(9) W. H. Zachariasen, Acta Cryst. 2 , 60 (1949).
(10) P. Caro, J. Sawyer, Papers 7, 8 in "The Solid State Chemistry of
     Rare Earth Oxides", COO. 1109-22, LeRoy Eyring, editor, Ari-
     zona State University (1966)).
(11) A. F. Wells, "Structural Inorganic Chemistry", 3rd Ed., Oxford,
     1962, p. 391.
(12) G. Blasse, J. Inorg. Nucl. Chem. 28 , 1488 (1966).
(13) A. F. Wells, Ref. (11), p. 53.
(14) P. Caro, Comptes Rendus Acad. Sciences Paris, 262 , 992 (1966).
(15) H. Müller-Buschbaum, H. G. V. Schnering, Z. Anorg. Allg. Chem.
     340 , 232 (1965).
(16) D. T. Cromer, J. Phys. Chem. 61 , 753 (1957).
(17) L. Eyring, B. Holmberg, "Non-Stoichiometric Compounds", Ad-
     vances in Chemistry Series 39, 46 (1963).
(18) J. Kordis, Paper 2 in Ref. (10).
(19) C. K. Jorgensen, R. Pappalardo E. Rittershaus, Z. für Natursfors.h.
     19A , 424 (1964) and 20A , 54 (1965).
(20) C. K. Jorgensen, R. Pappalardo, J. Flahaut J. de Chimie Physique
     444 (1965).
(21) S. P. Sinha, Spectrochimica Acta 22 , 57 (1966).
(22) L. Eyring, N. C. Baenziger, J. App. Phys. Supp. 33 , no 1. 428
     (1962).

Fig. 1.

(view perpendicular to [111])

FLUORITE STRUCTURE
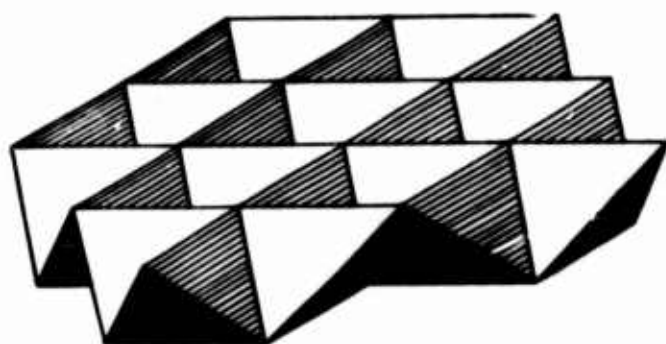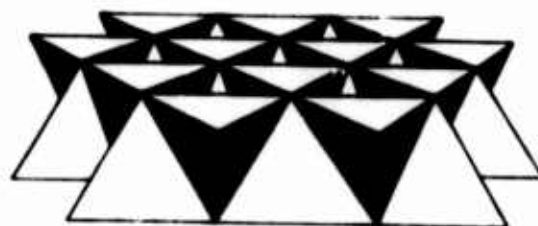
$(MO)_n^{n+}$ sheets in MOCl $(MO)_n^{n+}$ sheets in A-M_2O_3

Fig. 2.

C AXIS HEXAGONAL

IDEAL. Ln₂O₃ A-FORM

Fig. 3a.

IDEALIZED Ln₂O₃ B FORM
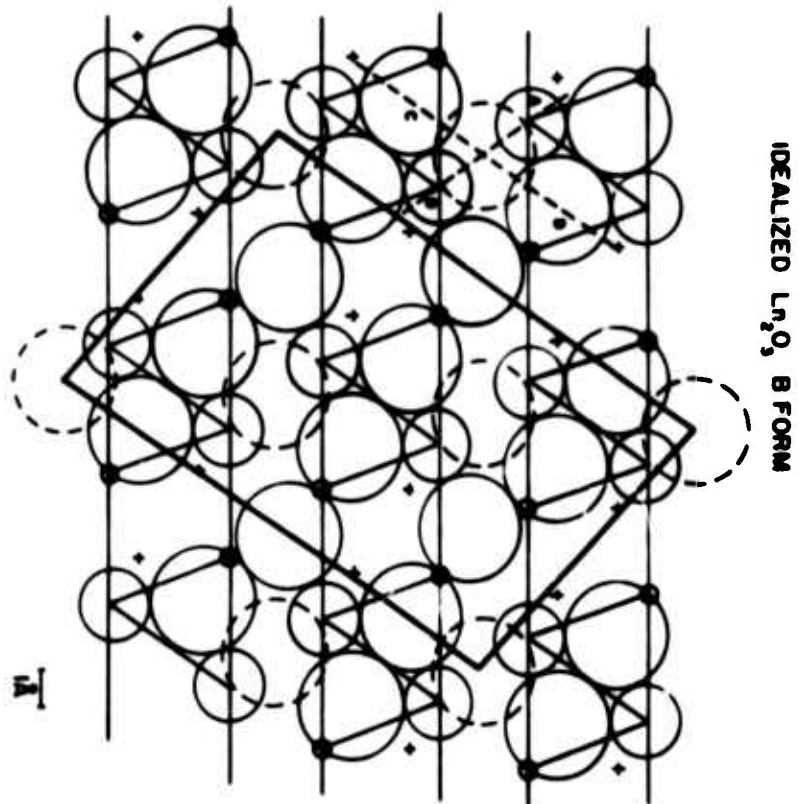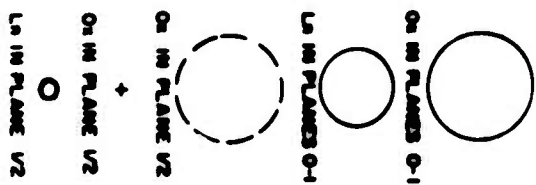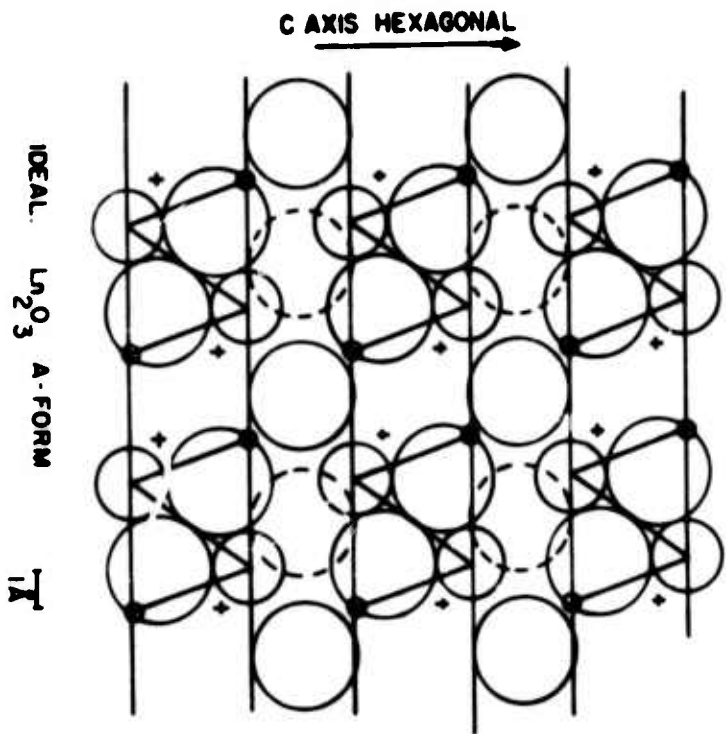
Fig. 3b.

Ln$_2$O$_3$ C - FORM
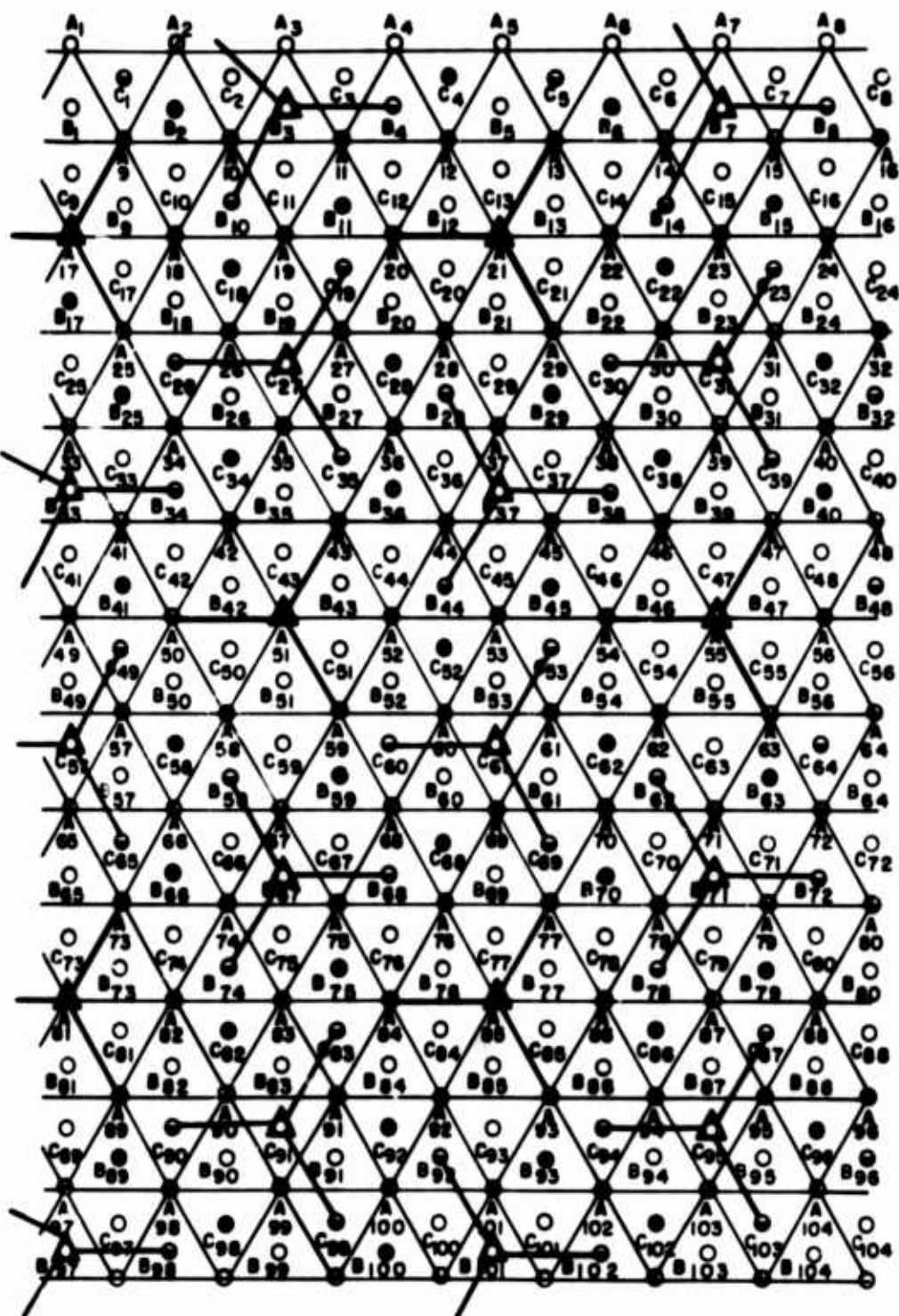
● MISSING IN A'B'C' ⊙ MISSING IN A B C △ MISSING IN ABC, &
A' B'C'

Fig. 4. Projections of vacancies in C-M$_2$O$_3$ on a plane (111)

Erratum: B$_{17}$ is an o point.
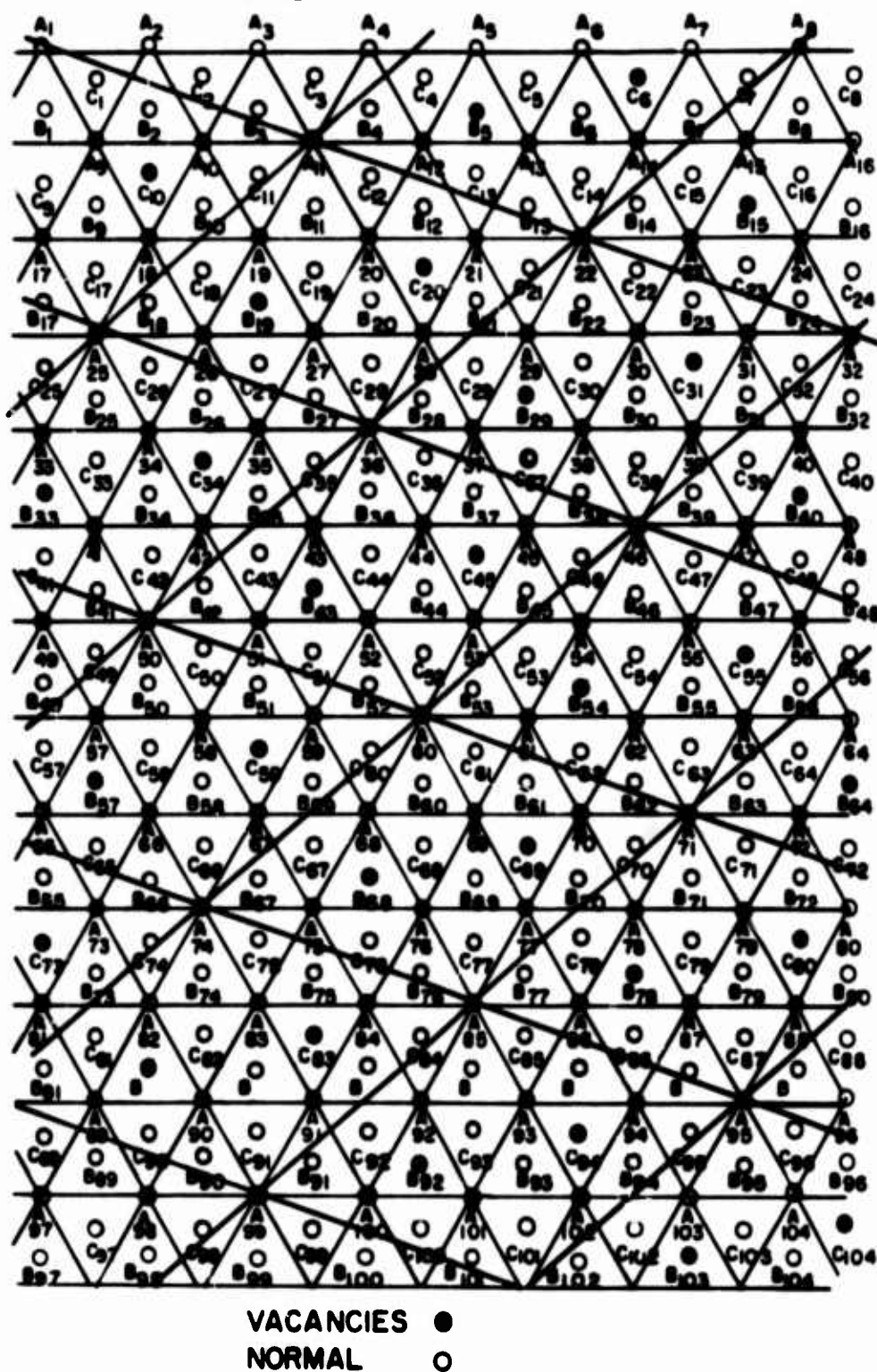
Fig. 5. Projections of vacancies in M_7O_{12} on a plane (111)

Liquid-Liquid Extraction Discrimination Among Rare Earths[*]

D. F. Peppard and G. W. Mason

Abstract

In the application of liquid-liquid extraction techniques
to the large scale processing of rare earths, a prime considera-
tion is the single-stage discrimination among the lanthanide (III)
constituents of the feed. This discrimination is best shown, in
an over-all fashion, by a log K vs. Z plot. In such a plot, a
straight line passing through all 15 points corresponds to a
constant separation factor, r, between any two adjacent members.
Such a straight line plot is seldom encountered, the more usual
log K vs. Z plot indicating much more promising separations
possibilities in one Z range than in another. In some instances,
the data are best correlated by use of two curves, one for the
odd-Z elements and the other for the even-Z. The possibilities
for separating a given odd-Z (or even-Z) element from its two
adjoining members may thus be widely different, perhaps promising
for the (Z-1) neighbor but unpromising for the (Z+1) member.

The principal factors determining the shape of the log K vs.
Z curve in systems involving acidic extractants are: (1) Forma-
tion of non-extractable M(III) complexes in the aqueous phase;
(2) Extraction of mixed species, that is, entities containing

---

both the anionic form of the acidic extractant and anions of
the mineral acid employed; (3) Variation in structure of the
acidic extractant; (4) Variation of extractant dependency of
K with Z; (5) Change in the nature of the diluent employed,
for example, the diluent determining the state of aggregation
of the extractant.

Possible applications of each of these factors to improved
rare earth separations will be discussed.

AUGMENTING THE SEPARATION OF GADOLINIUM AND EUROPIUM AND EUROPIUM AND SAMARIUM MIXTURES IN ION EXCHANGE ELUTIONS WITH EDTA[1]

J. E. POWELL AND H. R. BURKHOLDER

Institute for Atomic Research and Department of Chemistry
Iowa State University, Ames, Iowa 50010

ABSTRACT

Scrutiny of thermodynamic data and proposed models for the hydrated ethylenediaminetetraacetato chelates of the rare earths has suggested a rather obvious means of improving displacement chromatographic separations of Gd-Eu and Eu-Sm mixtures on cation exchange columns. Increasing the operating temperature from 25 to 92°C was found to effect an increase in the Gd-Eu separation factor from a skimpy 1.1 to a robust 1.47±.07 and the Eu-Sm separation factor from 1.4 to 1.8, presumably by destroying a degree of internal hydrogen bonding which occurs to a varying extent in the case of the less constrained lighter rare earth EDTA chelates at room temperature. Apparently this type of internal hydrogen bonding is not possible in the case of the smaller heavier rare earth EDTA chelates (Gd through Lu). This interesting and important effect has been correlated with a similar trend noted in the stability behavior of terbium, dysprosium and holmium β-hydroxyethylethylenediaminetriacetates with increased temperature.

INTRODUCTION

The major difficulty encountered in resolving mixtures of europium and gadolinium by ion exchange has been the small magnitude of the separation factor afforded by difference in stabilities of europium and gadolinium chelates[2,3]. (See upper curve in Fig. 1.) When EDTA is employed as the eluant at 25°C, for example, $\alpha_{Eu}^{Gd} = K_{Gd\ Ch}/K_{Eu\ Ch} \simeq 1.1$[3]; and it is necessary to elute a band of sorbed Eu-Gd mixture approximately 10 times its length down an ion exchange system to attain the steady state. At this point the inherent overlap between 99.9% pure, 99.9% pure, etc., Gd and Eu products is $L = 6h/\log \alpha_{Eu}^{Gd}$, $L = 8h/\log \alpha_{Eu}^{Gd}$, etc., where h is the height equivalent to a theoretical plate (usually 1 cm or more)[2,3]. Obviously the length of the sorbed

band must exceed L if any "pure" product is to be had. The purpose of this work is first to examine the theories regarding chelate stabilities in order to decide whether or not it is feasible to improve the Gd-Eu and Eu-Sm separation factors, and then to perform confirmatory experiments.

It has been suggested by some on the basis of stability constant data[4] that the ligand in ethylenediamine-N, N, N', N'-tetraacetato complexes of the trivalent rare earths behaves hexadentately in combining with the lighter rare earth cations but only pentadentately when bonding to the heavier, but smaller, rare earth cations and to yttrium. Others[5] have speculated that the EDTA anion is pentadentate in its chelates with the lighter rare earth cations but only tetradentate in its association with the heavier lanthanons. These arguments were advanced to account for the non-monotonic behavior of $\Delta F°$, $\Delta H°$ and $\Delta S°$ for the reaction $R(OH_2)_n^{3+} + Ch^{4-} \rightarrow [R(OH_2)_{n-m}Ch]^- + mH_2O$ across the rare earth series.[6] (See Fig. 2.) Both of these views have been nullified by recent precision X-ray diffraction data.[7]

From lanthanum through terbium (at least) the $[Ln(OH_2)_3Ch]^-$ anion is the dominant species in crystalline salts having the stoichiometry $MLnCh \cdot 8H_2O$, where M is ammonium, sodium or potassium, Ln is a rare earth and Ch designates EDTA. This nine-coordinated configuration is believed to persist on through lutetium. The lanthanum and terbium compounds have been found to be completely isostructural so that the anomaly occurring between Sm and Gd can no longer be attributed to a change in the basic dentate character of the EDTA anion or to a change in the coordination number of the chelated rare earth ion. It is possible, however, that part of the over-all bond energy of the lighter rare earth chelates is derived in a more subtle manner through a type of internal bonding in which the four uncomplexed carboxyl oxygen atoms augment the negativity of the electron donating oxygen atoms of the three adjacent coordinated water molecules. It is not implied that quasi-chelate rings form directly from carboxyl oxygen atoms to hydrogen atoms of the coordinately bound water molecules but circuitously through other water molecules located just outside the primary

coordination sphere. Such an effect would impart a dentate character to the EDTA anion nominally greater than six in the case of the larger rare earth cations. Decreasing radius might produce such a strain that the quasi-chelate structure would gradually diminish and perhaps fail to exist at all with Ln^{3+} cations having radii less than about 0.93Å. A regular decrease in stability with increased radius is consistent with an unvarying bonding mode, and the stability would be expected to continue decreasing along the dashed extension of the straight line through the Lu-Gd data in Fig. 1 if the Ln-EDTA bond strength were not enhanced in some way from samarium through lanthanum.

An even greater anomaly, of the type observed near the middle of the rare-earth EDTA chelate stability sequence, occurs in the case of β-hydroxyethylethylenediaminetriacetato (HEDTA) chelates, but the transition occurring is more drastic, being manifested from neodymium through holmium rather than reaching completion at gadolinium. (See lower curves of Fig. 1.) The stability defect in the case of the heavier rare earth chelate species is much more obvious with HEDTA than with EDTA. Log $K_{Ln(EDTA)}$-log $K_{Ln(HEDTA)}$ from Ln = La to Ln = Pm is remarkably constant and less than one log unit. This constant small depression of the log $K_{Ln(HEDTA)}$ values relative to log $K_{Ln(EDTA)}$ reflects the difference in bonding potential of the CH_2CH_2OH and CH_2COO groups; plus, of course, any related difference in hydrogen bonding. It would not be amiss then to suggest that HEDTA, as well as EDTA, behaves hexadentately in coupling to the lighter rare earths. From Nd through Gd, in both cases, one can envision a progressive rupture of hydrogen bonds between carboxyl oxygen atoms and water molecules. The rapid divergence of the stability curves from Gd through Ho heralds a marked deviation in the bonding characters of HEDTA and EDTA. While increased nuclear charge draws both nitrogen atoms and four carboxyl oxygen atoms of EDTA ever closer, the effect on HEDTA is to pull the two nitrogen atoms and three carboxyl oxygen atoms closer in such a way that a strain results which tends to prevent the hydroxyl oxygen atom from freely occupying a coordination site. Probably a water molecule enters the equatorial site in an increasing percentage of cases, and the change in denate

character is gradual rather than abrupt. One would judge then that the straight line through the (Lu-Gd) EDTA data and its dashed extension represents the stability curve for an uncomplicated $[Ln(OH_2)_3(EDTA)]^-$ anion in which EDTA is hexadentate and, likewise, that the straight line through the (Lu-Ho) HEDTA data represents the stability curve for a simple $[Ln(OH_2)_4(HEDTA)]$ anion in which HEDTA is pentadentate.

The models suggested then for EDTA chelate formation are: (1) at least enneahydrated rare earth cations initially in all cases, since X-ray diffraction studies indicate 9 moles of water in coordination sites about the cations in lanthanum, praseodymium, erbium, and yttrium ethylsulfates[8, 9]; (2) a nine-coordinated chelate species $[Ln(OH_2)_3Ch]^-$ from lanthanum through neodymium (perhaps promethium) in which a number of hydrogen bonds form between uncoordinated carboxyl oxygen atoms and coordinated water molecules, and tend to enhance the chelate stability above that expected to be due to a simple hexadentate attachment; (3) a gradual change in the number of existing hydrogen bonds, due to strains introduced as Ln decreases in radius from Sm to Eu to Gd, accompanied by progressive reduction in the nominal dentate character of the ligand anion to a minimum value of six; (4) an uncomplicated nine-coordinated chelate species $[Ln(OH_2)_3Ch]^-$ with Ln = Tb, Dy, Ho, Er, Tm, Yb, Lu, and Y, which receives no stability contribution at all from hydrogen bonding.

Now it is immediately apparent that, if something were done to cause Eu^{3+}, Sm^{3+}, etc., to form lesser hydrogen bonded chelate species, the stability constants of the EDTA chelates of these lanthanons would drop to values represented by the extension of a straight line through the Lu-Gd data in Fig. 1. The formation reaction would become less exothermic and the entropy would increase (Fig. 2). It is also apparent that a rise in temperature would accomplish this end since temperature elevation would tend to increase the entropy of the system by destroying the tenuous hydrogen bonded structure between the uncoordinated carboxyl oxygen atoms and the coordinated water molecules.

One way to test the above hypothesis is, of course, to determine painstakingly the temperature dependence of individual Ln-EDTA

stability constants; but a simpler test can be made by taking advantage of the fact that the minimum number of band displacements required to resolve a mixture by displacement chromatrography depends solely on the mole fraction of the component which elutes first in the original mixture and the separation factor[2,3], that is

$$\nu = \frac{1 + (\alpha - 1) N_o}{(\alpha - 1)} .$$ (1)

Another convenient means of ascertaining the separation factor at 92°C is to prepare an excess of a known mixture of two dilute pure rare earth EDTA solutions, heat it, and pass it slowly through a section of H^+-form resin bed maintained at 92°C until the composition of the effluent solution coincides with that of the feed solution. Then the rare earth mixture is stripped from the resin bed to determine the molar ratio of the components sorbed.

$$\alpha_B^A = \frac{\text{ratio of A to B in solution}}{\text{ratio of A to B in resin bed}}$$ (2)

Actually when the value of $\alpha - 1 = \epsilon$ is small, it is more precise in view of analytical considerations to compute ϵ directly[10] instead of α. This is possible from material balance data obtained from such an experiment since

$$\epsilon = \frac{\Delta n}{X_o Q(1 - X_o - \Delta n/Q)}$$ (3)

Δn is the total number of moles of component B missing from a series of weighed rare earth oxide samples derived from individual fractions of the effluent solution collected prior to achieving equilibrium (i. e., sorbed on the resin bed in excess of what would have resulted had no separation of components occurred), X_o is the original mole fraction of B in the aqueous solution, and Q is the total capacity of the resin bed (total number of moles of rare earth mixture sorbed).

EXPERIMENTAL

The experimental setup consisted of a number of identical ion exchange columns constructed of standard, 2-in. i. d., flanged PYREX pipe, 5 ft. long, fitted with Teflon resin-bed supports and gaskets, and Plexiglas end closures (reinforced externally by steel plates). The columns were interconnected when it was so desired by means of 8-mm

PYREX tubing and Beckman Teflon fittings. Each column unit was mounted on a rack in a steam heated, thermostated, 10 x 10 x 8 ft., insulated room and filled to a height of 45 in. with 40-50 mesh spheres of Do.ex 50-X8 cation-exchange resin in the H^+-cycle.

In the first experiment, the columns were backwashed with deaerated distilled water, and two columns of the set were charged with an excess of dilute (Eu-Gd) chloride solution applied by back flow to obtain a uniform band of sorbed Eu-Gd mixture. The excess chlorides were removed by further backwashing with de-aerated distilled water, and the rare earth saturated resin beds were allowed to settle.

In the second experiment, two columns were saturated with an excess of (Sm-Eu) chloride mixture and the excess rare earths were removed as described above.

In both cases, the charged columns were connected in series and the sorbed band of binary rare earth mixture (two columns in length) was eluted down a series of additional resin beds at a flow rate of 65 ml/min with 1.01 M ammonium EDTA at pH 8.32 (originally made up at 25°C), with the enclosure temperature maintained at 92°C. The ammonium EDTA solution was heated to 90°C before entering the 92°C enclosure and fed through a column containing moist ammonium-form resin beads and air. The top of the resin bed in this column was maintained slightly above ambient temperature by means of an external heating tape. A venting system at the top of the first column of the experimental series allowed air bubbles issuing from the de-aerator to be discharged from the system. The eluant was forced through the system by a pump located outside the heat shield, and the eluate was discharged from the system at a point higher than the top of the last column to ensure that further degassing would not occur in the experimental columns due to a pressure drop. The Gd-Eu and Eu-Sm bands moved down the resin bed system at a rate of about 19 in. per day in both experiments and analytical profiles of the developing chromatograms were obtained by periodically analyzing small portions of solution as the bands passed between adjacent columns of the system, i.e., a complete profile of each developing chromatogram was obtained approximately every half band length of travel. In this way it was possible to estimate the minimum displacement distances required to achieve steady state conditions to about a fifth of a band length (steady state is approached at a constant rate and achieved when the constant composition plateau of a developing chromatogram disappears).

The separation factors α_{Eu}^{Gd} and α_{Sm}^{Eu} were calculated by means of eqn. (1) and are given in Table 1. The theoretical plate height, in each case, was calculated from a plot of the log of the ratio of the two components involved as a function of the distance from the front of the chromatogram after steady state conditions were achieved through the relationship

$$h = \Delta L \cdot \log \alpha_B^A / \Delta r. \qquad (4)$$

TABLE 1.

SEPARATION FACTORS AND PLATE HEIGHTS CALCULATED FROM THE ELUTION OF Gd-Eu AND Eu-Sm MIXTURES WITH EDTA AT 92°C.

Mixture	N_o	ν	$\alpha - 1$	α_B^A	h
A - B					(cm)
Gd-Eu	0.610	3.04±.2	0.41±.04	1.4±.05	0.7±.1
Eu-Sm	0.396	1.85±.2	0.68±.10	1.7±.1	0.7±.1

The values of α_B^A and ϵ were also evaluated by the alternate method outlined briefly above.

TABLE 2.

SEPARATION FACTOR DATA OBTAINED AT 92°C IN THE PRESENCE OF EDTA BY AN ALTERNATE PROCEDURE.

Mixture	α_B^A	ϵ	$1 + \epsilon$	α_B^A(ave.)
A - B				
Gd-Eu	1.53	0.478	1.478	1.5
Eu-Sm	1.77	.82	1.82	1.8

It is of interest that the latter values are a bit higher than those observed in the elution experiments. It is likely that complete equilibrium was not achieved at the flow rate used in the elution experiments. If such were the case, the transport rate would be affected, a greater than the minimum number of band displacements would be required, and $\alpha - 1$ and α calculated would be low. The figures reported for α_{Eu}^{Gd} and α_{Sm}^{Eu} in Table 1, therefore, probably represent minimum rather than true values.

CONCLUSIONS

The observed separation factors in these systems represent a substantial improvement over those reported previously for elution with EDTA at room temperature (α_{Eu}^{Gd} = 1.1 and α_{Sm}^{Eu} = 1.4)[2]. From this fact it may be inferred that the models proposed herein are substantially correct. Although the factors were smaller than projected purely on the basis of an extension of the straight line plot through the Lu-Gd

data[11] of the upper curve of Fig. 1, they are sufficiently large that elu-
tion with EDTA above 90°C becomes competitive with other techniques
for isolating pure europium from its concentrates. Additional benefits
stemming from the application of heat are: (1) substantial improvement
in theoretical plate height, allowing faster flow rates to be used; and
(2) increased solubility of the H_4Ch species of EDTA, allowing H^+ re-
taining ion to be used in place of Cu^{+2} or Zn^{+2}, so that recycling of
both eluting agent and water becomes economically attractive.

Similar enhancement of separation factors through temperature
elevation should occur in the cases of Ho-Dy and Dy-Tb pairs when
HEDTA rather than EDTA is the eluant, but it is by no means clear
what will occur with pairs of elements from Gd through Nd in the more
complex HEDTA system. That the HEDTA Ho-Dy and Dy-Tb separa-
tion factors do actually improve with elevated temperature is obvious
from data published by Moeller and Ferrús.[12] (See Fig. 3.) One can
only conclude from the observed trend over a 25° temperature range
that continued elevation of temperature would depress log K_{Ln}(HEDTA)
still further in the cases of terbium, dysprosium and holmium, yet not
much affect the stabilities of the erbium, thulium and ytterbium chelates.
Consequently, the Tb-Ho chelate stabilities would finally drop to levels
corresponding to points lying on an extension of a straight line through
the Er-Yb data.

REFERENCES

1. Work was performed in the Ames Laboratory of the U. S. Atomic Energy Commission.

2. J. E. Powell and F. H. Spedding, Chem. Eng. Progress Symposium Series, No. 24, 55 (1959) 101.

3. J. E. Powell, "The Separation of Rare Earths by Ion Exchange," in Progress in the Science and Technology of the Rare Earths, edited by L. Eyring, Pergamon Press, Oxford (1964) p. 62.

4. E. J. Wheelwright, F. H. Spedding and G. Schwarzenbach, J. Am. Chem. Soc., 75 (1953) 4196.

5. R. H. Betts and O. F. Dahlinger, Canad. J. Chem., 37 (1959) 91.

6. J. L. Mackey, J. E. Powell and F. H. Spedding, J. Am. Chem. Soc., 84 (1962) 2047.

7. J. L. Hoard, Byungkook Lee and M. D. Lind, J. Am. Chem. Soc., 87 (1965) 1612; Byungkook Lee, thesis, Cornell University, Ithaca, N. Y. (1966).

8. E. B. Hunt, R. E. Rundle, and A. J. Stosick, Acta Cryst., 7 (1954) 106.

9. D. R. Fitzwater and R. E. Rundle, Z. Krist., 112 (1959) 362.

10. F. H. Spedding, J. E. Powell, and H. J. Svec, J. Am. Chem. Soc., 77 (1955) 6125.

11. J. L. Mackey, M. A. Hiller, and J. E. Powell, J. Phys. Chem., 66 (1962) 311.

12. T. Moeller and R. Ferrús, J. Inorg. Nucl. Chem., 20 (1962) 261.
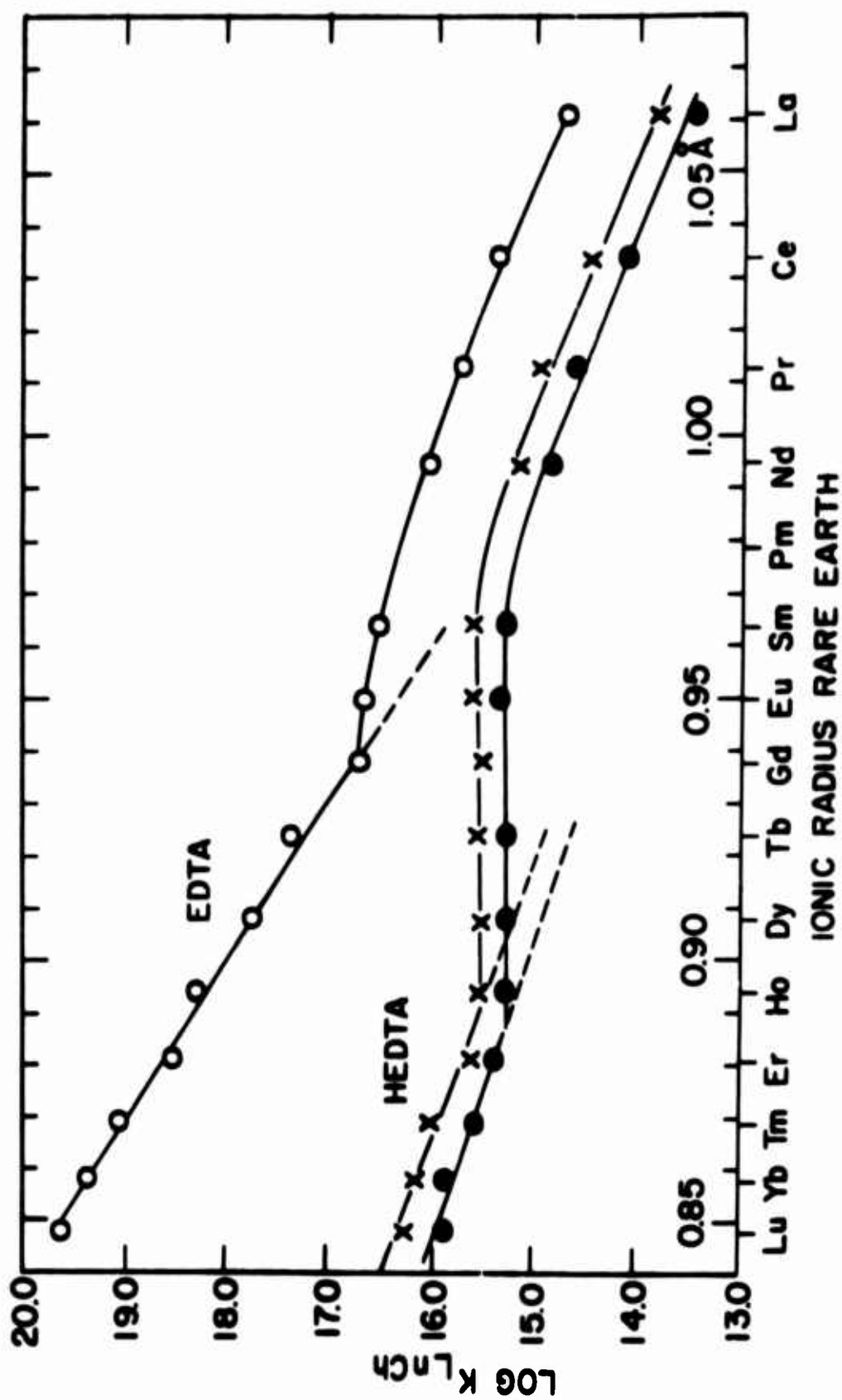
Fig. 1. Stabilities of rare earth EDTA and HEDTA chelates as a function of cationic radius: o , Wheelwright, Spedding and Schwarzenbach[4]; ✕, Mackey, Hiller and Powell[1]; ●, Moeller and Ferrus[12].
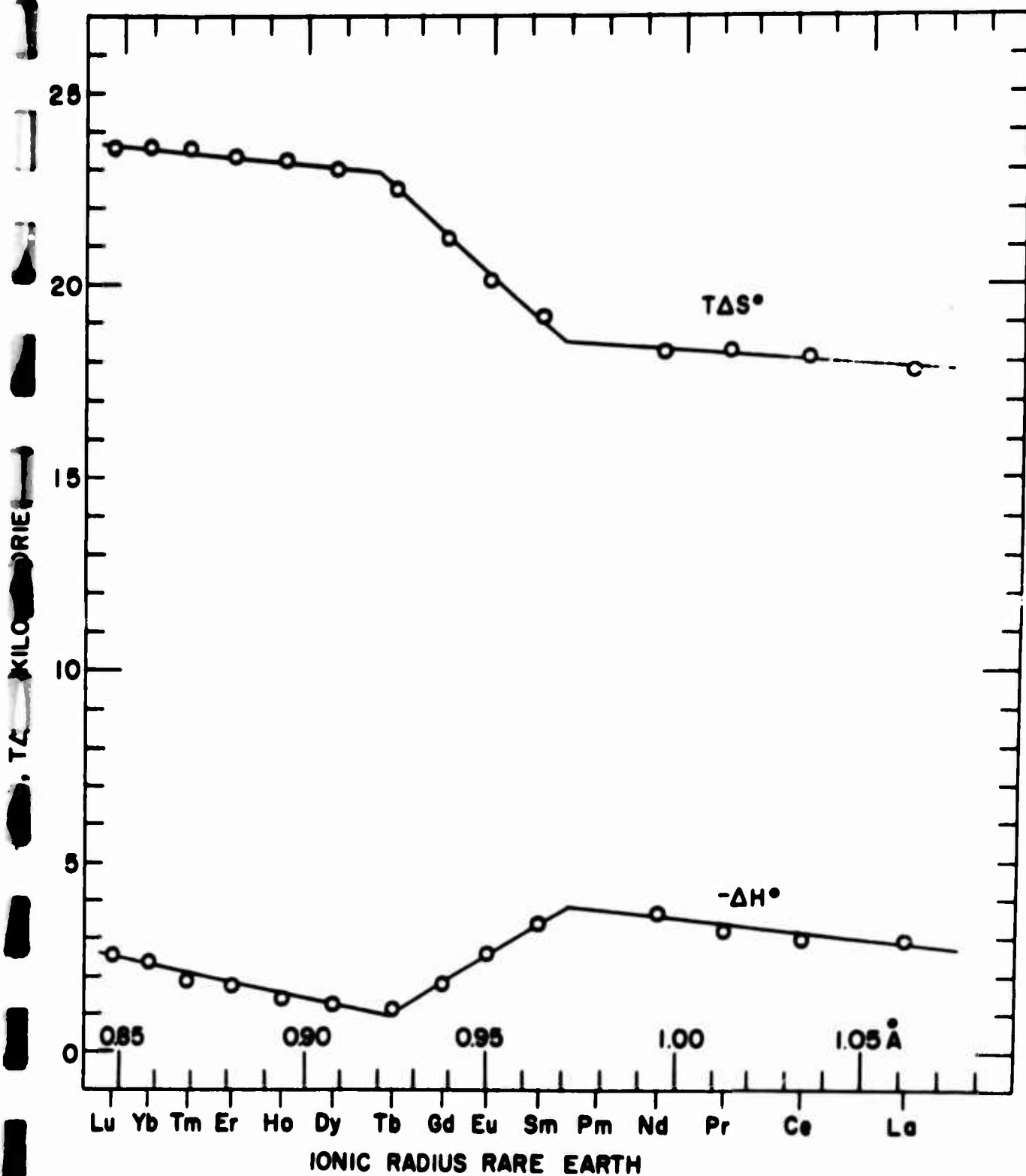
Fig. 2. Enthalpy and entropy contributions to $R\,T\,\ln K_{Ln(EDTA)}$ $(-\Delta F^\circ)$ as a function of cationic radius.
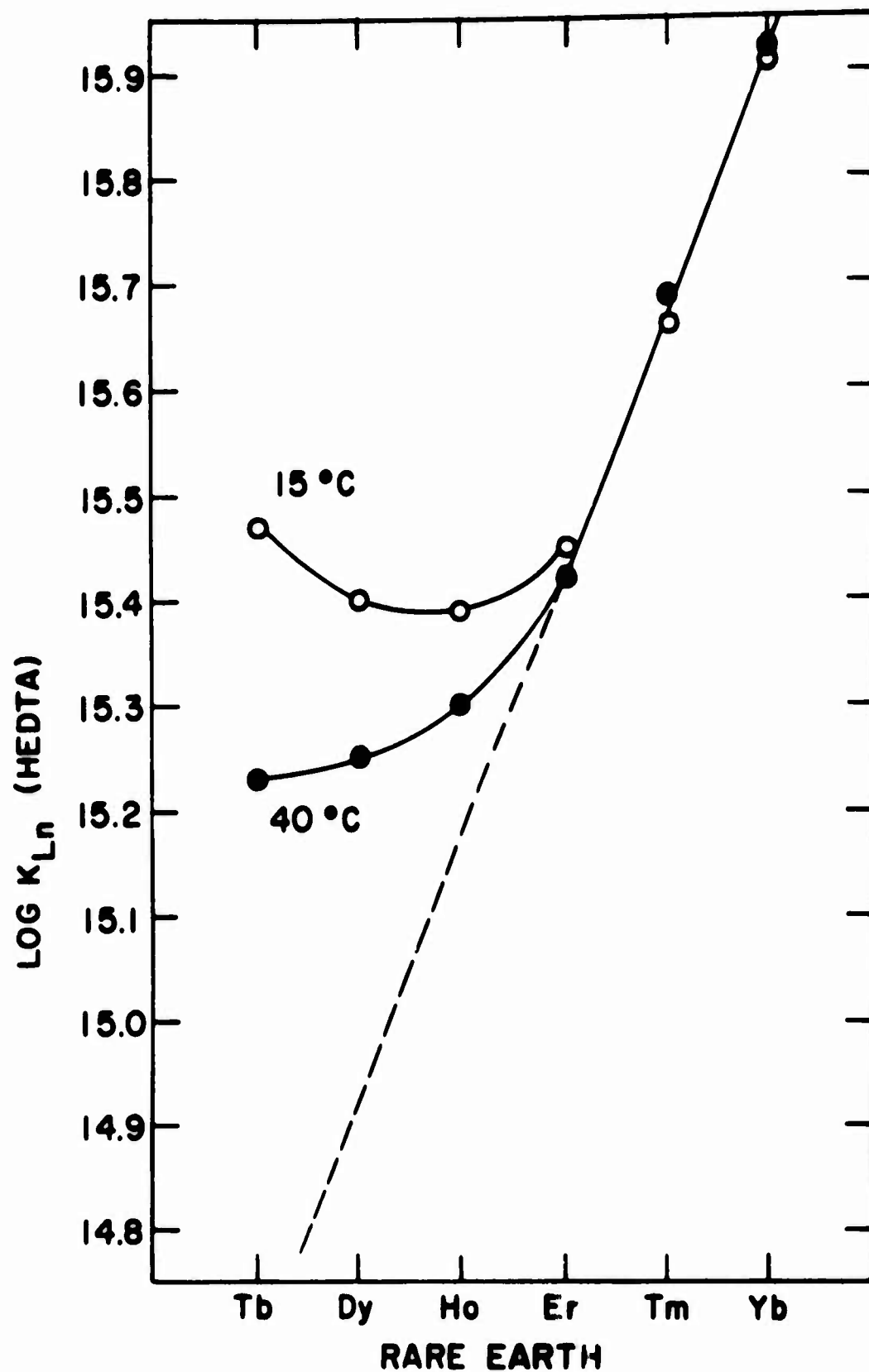
Fig. 3.   The effect of increased temperature on the Tb-Yb HEDTA stability constants.

A Study of Some Geometrical and Mechanical Effects

on the Extraction of Europium by Lithium Amalgam

from Aqueous Lithium Citrate Electrolytes

by

John B. Goddard,[*] John M. Campbell[†] and E. I. Onstott

ABSTRACT

The amount of Eu extracted into lithium amalgam from aqueous
lithium citrate electrolytes was enhanced when the phases were
separated by dumping the amalgam and electrolyte from the reaction
vessel into a second vessel containing a chloroform layer to con-
strain the electrolyte phase. As much as 39% of the Eu in the electro-
lyte was extracted in a time interval estimated to be less than one
second using this phase separation procedure. If the phases were
separated by a second technique by adding the chloroform layer to
the reaction vessel, other conditions remaining the same, the amount
of Eu removed in this short time interval was reduced to 3.5%. The
amount of Eu extracted by this faster mechanism was found to increase
with the amount of amalgam used whereas the steady-state rate was
inversely dependent on this parameter. Surface area of the amalgam
exposed to the electrolyte affected the steady-state extraction rate
in the expected manner with the rate being proportional to surface
area, but a change in the surface area of the amalgam exposed to the
electrolyte did not significantly affect the extraction of Eu by the
faster mechanism when the amount of amalgam was kept constant.

[*]Present address, Department of Chemistry, Northwestern University,
Evanston, Illinois

[†]Present address, Department of Chemistry, University of Alberta,
Edmonton, Canada

INTRODUCTION

A prior study of the extraction of Eu by lithium amalgam showed that an appreciable fraction of the Eu in the lithium citrate electrolytes was extracted at rates much higher than the steady-state rates[1]. The enhanced rates were found to be related to the method of contacting the phases. In this paper we report the results of further studies of the effects of geometry and manipulative techniques on the extraction rates.

EXPERIMENTAL

The Eu was followed with Eu 152-154 tracer, made by neutron irradiation of 99.9% oxide in the Los Alamos reactor facilities. Scintillation counting of liquid samples in polyethylene test tubes was done with a Baird-Atomic 530 spectrometer.

Electrolytes were made up to a fixed composition of 0.1M $EuCl_3$ in 0.7M lithium citrate. Eu Cl_3 was made by dissolving the oxide (99.9% purity, purchased from American Potash and Chemical Co.) in HCl. Lithium citrate stock solution was prepared from lithium carbonate and citric acid. The pH of the electrolyte was adjusted to a predetermined value with LiOH or HCl so that the pH after extraction was about 6, but not greater than 7. The pH change on extraction with 25 ml of electrolyte was about 0.5 unit, but with 5 ml of electrolyte, the pH change was as great as 1.5 units.

Saturated lithium amalgam was prepared by electrolysis of saturated LiOH at a current density of 0.08 amp/cm^2. One hundred ml of mercury were placed in a cylindrical vessel with a 5mm bore drain cock. An insulated platinum wire contacted the cathode, and carbon anodes were used. Electrolysis of about 200 ml of LiOH electrolyte containing surplus crystals of LiOH H$_2$O was allowed to proceed for about an hour when a solid phase started to appear.

The saturated amalgam was drained, sometimes through cotton gauze, and stored under mineral oil until used. Composition of the amalgam was determined by first reacting the amalgam with a known amount of 1M HCl, then adding excess 0.1M NaOH, then titrating the excess NaOH with standardized 0.1M HCl. Saturated liquid amalgam was used in extraction experiments only after separation from solid amalgam by draining through a stopcock or draining through cotton gauze. The average lithium content of saturated amalgam at 22°C was 0.044% by weight.

The vessels used for extractions were polyethylene centrifuge tubes or polythylene graduates or glass beakers or glass separatory cylinders. An extraction was started by placing the amalgam in the bottom of the reaction vessel, then adding the electrolyte simultaneously with starting a timer. Two different procedures were used to quench the reaction. The first, which was also used in the previous study,[1] consisted of dumping as rapidly as possible the contents of the reaction vessel through a layer of chloroform which constrained the electrolyte and allowed the amalgam phase to fall to the bottom of the quench beaker. After separation, the amalgam was then washed with several hundred ml of distilled water to insure removal of adsorbed electrolyte. In the second quench procedure, the extraction was done in a separatory cylinder, but the chloroform was added to the same vessel and the amalgam then drained off. In no case was the extraction vessel deliverately agitated, but the dumping motion in the first quenching procedure obviously caused severe agitation of the phases. The Eu extracted was stripped with warm HCl and determined by counting.

RESULTS

The results obtained by the two different quench procedures are shown in Fig. 1. When the phases are separated by dumping, the amount of Eu extracted is higher, but the steady-state extraction rates, as
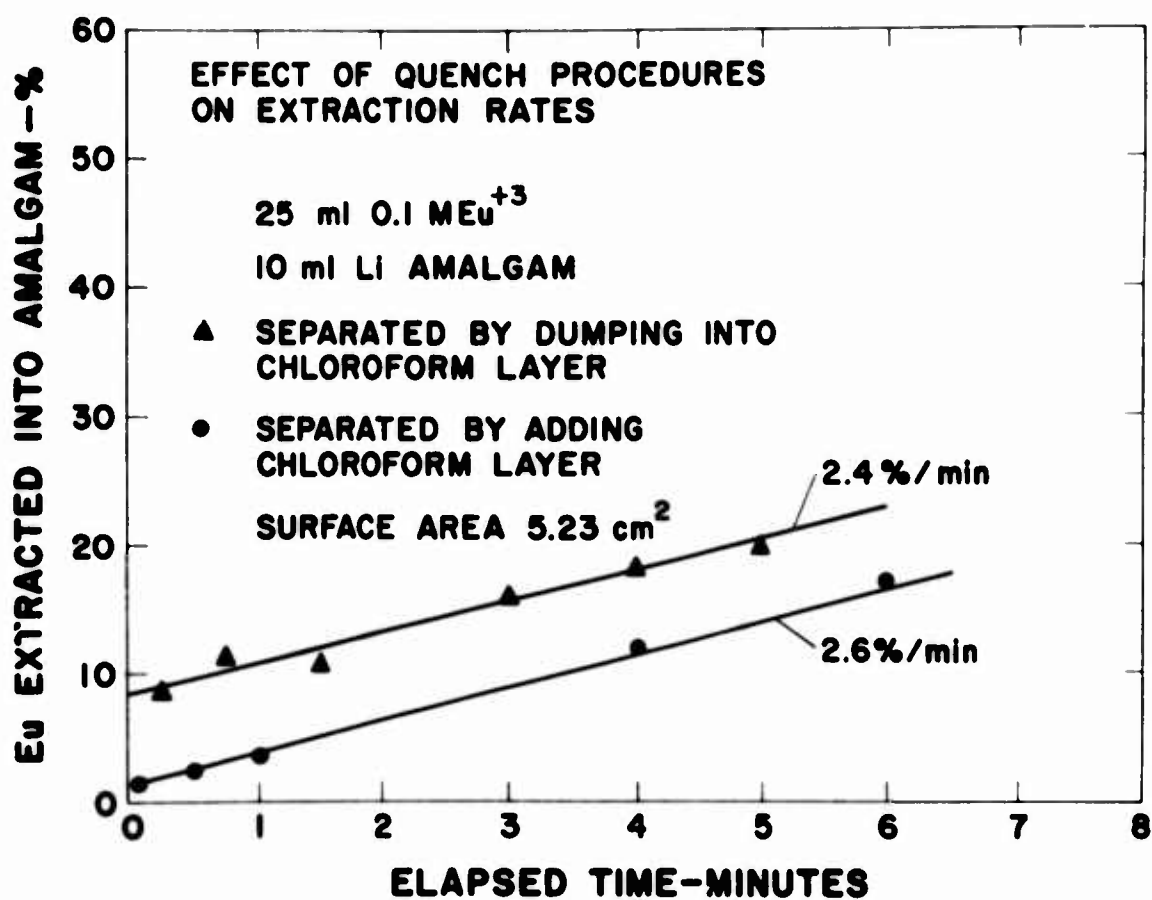
FIGURE 1

represented by the line slopes, are about the same. The relative amount of Eu extracted from the electrolyte can be increased by decreasing the amount of electrolyte and increasing the amount of amalgam as shown in Fig. 2. Again the steady-state rates of extraction of Eu are about the same for the two quench procedures.

Experiments were done in which the amount of amalgam was kept constant, but the surface area exposed to the electrolytes during steady-state extraction was varied by varying the cylindrical cross-section of the extraction vessels. In these experiments the reactions were quenched by the dumping procedure. The data in Fig. 3 show that the steady-state extraction rates depend on the interface surface area, but the amount of Eu extracted by the faster mechanism is not changed significantly.

Another set of experiments were done to find the effect of changing the amount of amalgam while keeping the surface area exposed to the electrolyte fixed. Data for these experiments are plotted in Fig. 4 and Fig. 5. The relative amount of Eu extracted by the faster mechanism, as represented by the intercepts, increased as the amount of amalgam was increased. With large amounts of amalgam the steady-state extraction rates were about the same, but with a very small amount of amalgam the steady-state rates were higher.

DISCUSSION OF RESULTS

Previous work showed that more Eu was extracted when the amalgam was allowed to fall through the electrolyte than when the electrolyte was added to the amalgam.[1] The plots in Fig. 1 and Fig. 2 show definitely that the dumping procedure increased the amount of Eu extracted. The enhanced Eu extraction on dumping is probably due to at least two effects: first, the severe agitation of the phases just prior to separation by the chloroform layer, and second, the probable increase in surface area of the amalgam exposed to the electrolyte during the time of free fall just prior to the separation

EFFECT OF QUENCH PROCEDURES ON EXTRACTION RATES

5 ml 0.1 M Eu^{+3}

60 ml Li AMALGAM

SURFACE AREA 5.23 cm^2

▲ SEPARATED BY DUMPING

● SEPARATED BY ADDING CHLOROFORM LAYER

EFFECT OF INTERFACE AREA ON EXTRACTION RATES

25 ml 0.1 M Eu^{+3}

10 ml Li AMALGAM

SEPARATED BY DUMPING
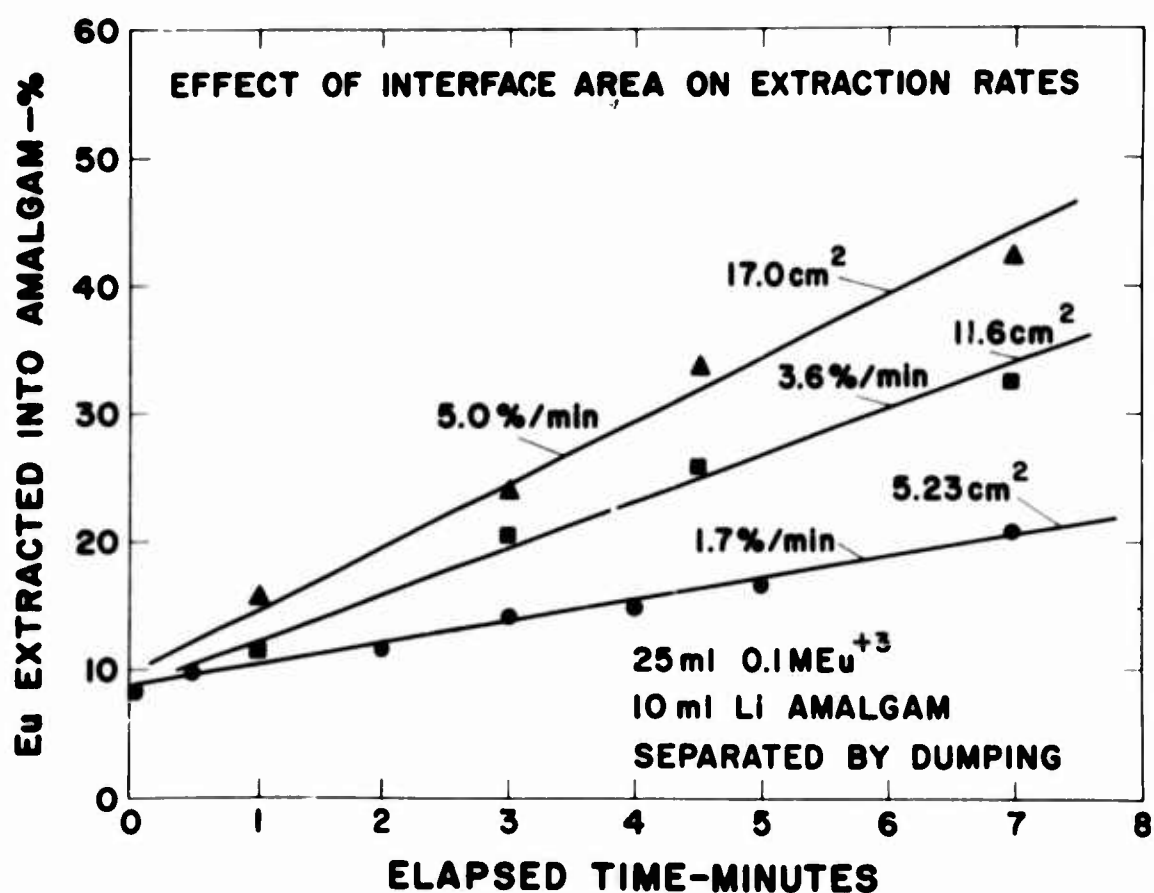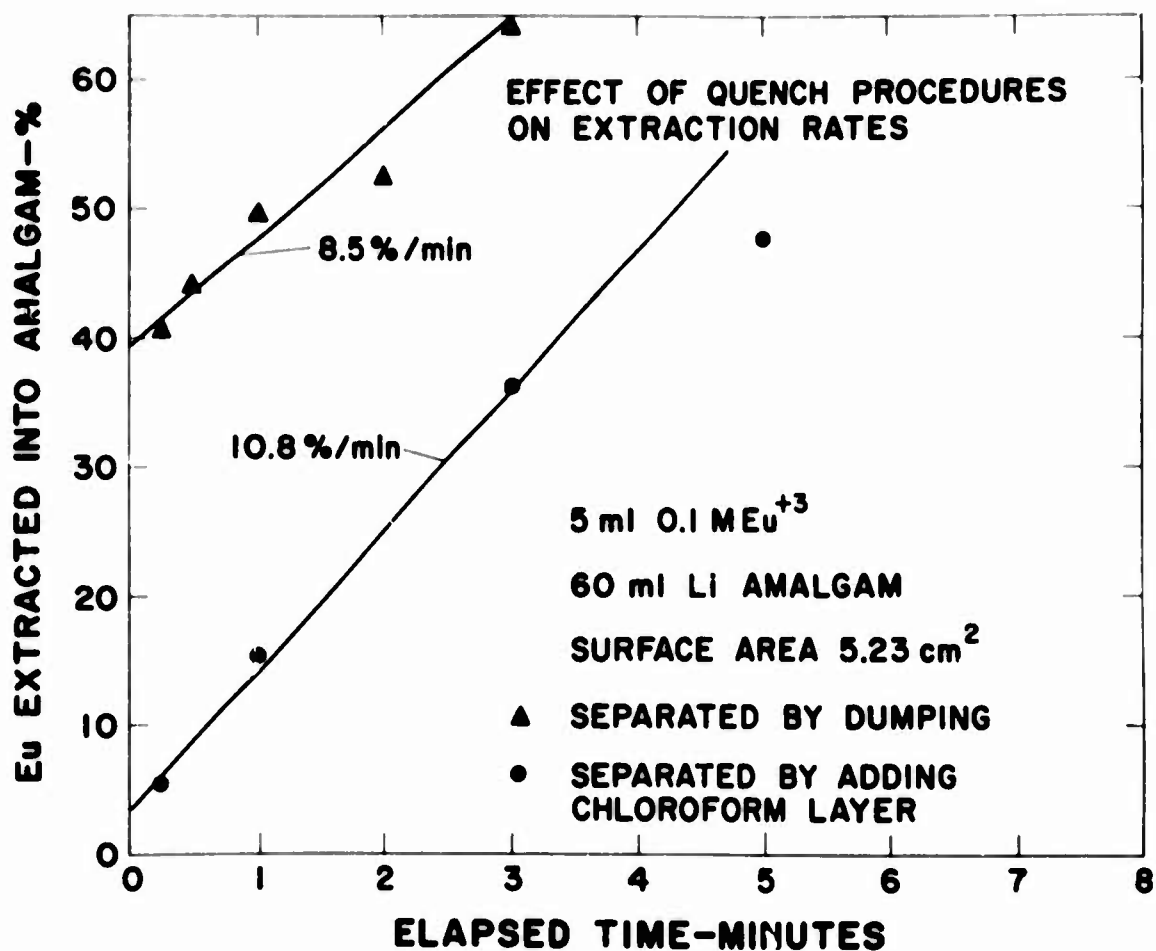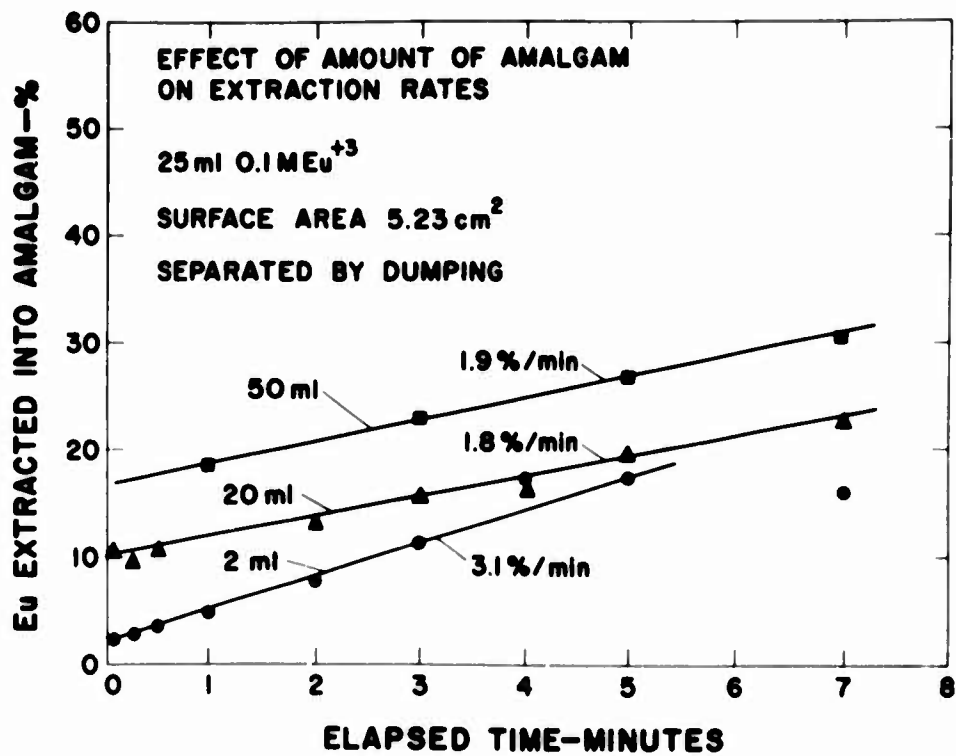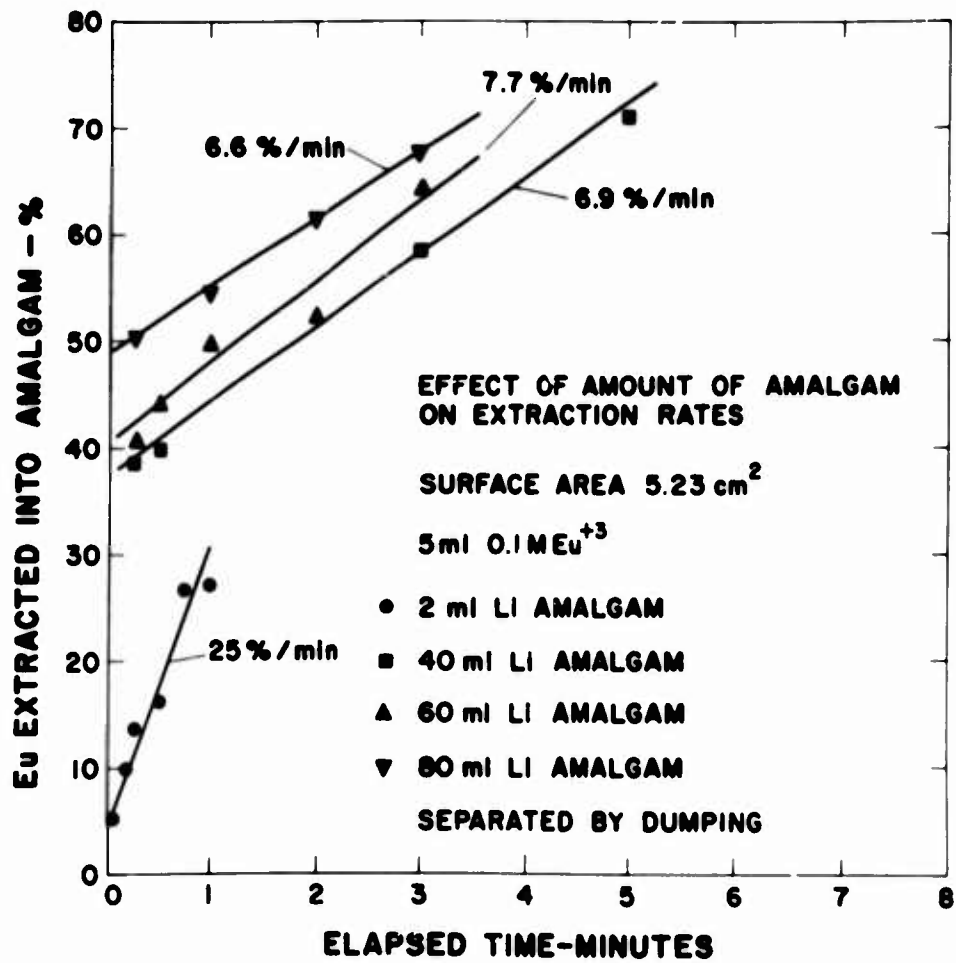
FIGURE 4

FIGURE 5

of phases. What was interpreted to be an initial fast extraction of Eu^1 actually can be more reasonably be interpreted to be a fast extraction during the final separation step. However, a small enhanced extraction of Eu on contact of the phases has not been ruled out.

Fig. 3 and Fig. 4 show that the amount of Eu extracted by the faster mechanism depends much more on the gross amount of amalgam than on the surface area of the interface between the phases. The dependence on the gross amount of amalgam is probably related to the surface area of the amalgam during the separation process.

Fig. 4 and Fig. 5 show that the steady-state rate of extraction of Eu is higher when a small amount of amalgam is used. This effect can be explained also in terms of increased surface area. When a small amount of amalgam is used, the extraction vessel below the electrolyte level is completely wet by the electrolyte including the bottom of the vessel beneath the amalgam. Thus the surface area exposed to the electrolyte can be as much as three times larger.

Steady-state extraction rates of Eu varied according to the surface area of the interface between the amalgam and the electrolyte as shown by the plots in Fig. 3. The rate constants are (top to bottom), 0.29, 0.31, and 0.33 percent per min-cm^2. Such behavior is expected for diffusion controlled processes.

If a rapid separation of europium from other rare earths is desired, then a severe agitation of the amalgam and electrolyte will be beneficial. If a systematic study of mass transfer phenomena is desired, then any undue agitation of the phases either on contacting the phases or on separating them should be avoided as much as possible to eliminate spurious extraction at the outset of the reaction or at its termination.

REFERENCE

[1]Proceedings of the Fifth Rare Earth Research Conference, Iowa State University, Ames, Iowa, Book Three, p. 119, Aug. 1965.

ION-EXCHANGE PURIFICATION OF PROMETHIUM
AND THE PREPARATION OF Pm_2O_3

by

E. J. Wheelwright

ABSTRACT

Optimum conditions for the purification of the individual light rare earth elements by ion-exchange elution have been determined for the eluting agents EDTA, HEDTA and DTPA. These conditions apply directly to the isolation of macro quantities of pure Pm from the fission product rare earths.

A modified DTPA elution process is shown to be optimum. The substitution of Zn^{+2} for H^+ as the "barrier" ion permits an increase in the eluant concentration from 0.025 to 0.050 $\underline{M}$ DTPA; resulting in a 50% reduction of both the time cycle and the volume of waste generated. When 8% cross-linked resin is used and the resin beds maintained at 60 - 70°C, the absorbed rare earth band can be advanced down the resin at rates up to 18 cm/hr without significant loss of separation efficiency.

In order to supply the Pm^{147} needed for the AEC's isotopic heat source research and development program and for prototype heat source fabrication during the interim period before the Isochem Fission Product Conversion and Encapsulation Plant goes on stream in late 1968, an ion-exchange facility has been installed in one of the shielded cells of Battelle-Northwest Laboratories' High Level Radio-chemistry Facility. Included are seven 9-foot high ion-exchange columns ranging from 8 inches down to 1 inch I.D. The 8-inch column is stainless steel and the others are glass. Each column is water-jacketed for controlled-temperature operation. Included also in the facility are associated tanks, valves and

instrumentation. The instrumentation includes two particularly useful units --
an in-cell gamma spectrometer which can monitor both individual samples and in-
line streams and an automated optical spectrometer for in-line monitoring. The
sensing units of both instruments are in the shielded cell and the instrumentation
is in the operating gallery. The plumbing arrangement is such that one or more
of the columns can be connected together in series by the use of flexible poly-
ethylene tubing jumpers, with the in-line instrumentation sensing units interposed
between the columns or on the effluent line of the final column in the series.

To date, eleven production runs (each requiring 7 to 8 days of continuous
operation) have been completed and 1×10^6 curies (1080 grams) of Pm^{147} have been
purified. The chemical purity of the product is 98 to 99%. Decontamination
factors from Eu^{154} (the only detected non-Pm radiochemical impurity) exceeded 10^5.
The technology developed and plans for expansion of capacity will be presented.

All of the purified Pm has been converted to Pm_2O_3 by a process involving
oxalate precipitation, filtration and calcination in oxygen at 1100°C. Since the
purified promethium is essentially free of high-energy beta or gamma radiation, a
shielded glove box facility with 0.030" thick leaded gloves was utilized for these
operations. By using localized shielding around bulk amounts of Pm and carefully
designed process manipulations, personal exposure rates have been maintained
at less than half the permissible rate.

The Preparation of Thorium Dicarbonate, Uranyl Carbonate

and the Sesquicarbonates of La, Ce, Pr, Tb and Y

from the Corresponding Anhydrous Acetates*

E. L. Head

University of California

Los Alamos Scientific Laboratory

Los Alamos, New Mexico 87544

Two methods for the preparation of the rare earth sesquicarbonates
have been described at previous rare earth conferences.

This paper represents a continuation of those studies and
describes a method for the preparation of La, Ce, Pr, Tb, and Y sesqui-
carbonates; thorium dicarbonate; and uranyl carbonate from their
respective anhydrous acetates. Methods are described for the prepara-
tion of the various anhydrous acetates used. Typical analytical data
for the compounds prepared and thermal decomposition diagrams for the
thorium dicarbonate and uranyl carbonate are given.

The method consistently produced carbonate product yields of
about 75 to 80% for the sesquicarbonates, 90 to 95% for thorium dicar-
bonate, and 90 to 93% for uranyl carbonate. Use of the hydrated
acetate salt in the case of La, Ce, and Pr produced carbonates which
were much more difficult to filter and in yields of less than 50%.

Introduction

Because of the difficulties associated with their preparation, knowledge of the physical properties of the carbonates as a class of compounds has lagged behind that now available for many other classes of "common" salts. The neutral or near-neutral region in aqueous solution chemistry constitutes one of the more difficult areas of study. Whereas most acid salts are prepared in pH ranges where hydrolysis problems are not incurred, the carbonates are formed in the pH range of about 4 to 5.5, the area in which hydrolysis problems begin to arise.

Two general methods for the preparation of the rare earth sesqui-carbonates have been described at previous rare earth conferences. One method (1,2) involved the hot hydrolysis of trichloroacetic acid solutions of the various rare earths under a pressure of CO_2 gas. The preparation and thermal decomposition diagrams of rare earth carbonate products prepared by this method were described at the Third and Fourth Rare Earth Conferences. The conditions of this reaction are determined largely by the irreversible decomposition of the trichloroacetate ion in the temperature region of $60°$ to $80°C$. A second method (3) was developed which permitted preparation of the carbonates by exposing an aqueous solution of the hydrated rare earth acetate salt to CO_2 gas under pressure. This method produced the carbonates at room temperature, but the application of heat reduced the reaction time and increased the particle size and yield of the product. The unexplained randomness in the magnitude of the carbonate yields obtained with this method led to further investigation of the rare earth carbonate-acetate system.

This paper describes a modified procedure whereby the various carbonates were prepared from their corresponding anhydrous acetates. The study was extended to include the actinides* Th and U.

---

* Reported in part at the Southwestern Regional ACS Meeting, December, 1966.

Preparation of Compounds

Anhydrous Acetates - The Th, uranyl, La, Ce, and Pr acetates were prepared from commerically available hydrated nitrates of 99.9% purity and the Tb and Y acetates from saturated chloride solutions obtained by dissolving $TbO_{1.81}$ and Y_2O_3 in concentrated HCl. The thorium and uranyl acetates were prepared by refluxing the nitrates in a 50% acetic acid-acetic anhydride mixture for 3 hours and the remaining acetates by refluxing the respective starting materials in acetic anhydride for 4 hours. All preparations were carried out under flowing N_2 gas. Finally the reaction mixture was cooled to 25°C and filtered under argon on a sintered glass disc. Acetone and ether were used as wash media. The anhydrous acetates were stored in a vacuum desiccator which contained anhydrous $Mg(ClO_4)_2$.

Carbonates - The initial concentration of the acetate salt used in the preparation of all of the carbonate compounds represented in the accompanying table was about 0.06 M; the reaction time, 2 hours; the temperature, 45° to 60°C (92°C in the case of Tb and Y); and the CO_2 pressure, 900 PSIG. The Th compound was prepared during a reaction period of 10 hours at 30°C and at a CO_2 pressure of 900 PSIG.

The general procedure for preparing the carbonates was as follows: A glass beaker containing the acetate-water mixture (the salt was not immediately soluble) was sealed in a pressure reactor (1) which was then filled with CO_2 gas to the desired pressure. Admission of the CO_2 was begun within about 3 minutes after the water was added to the sample. The reactor was heated to the operating temperature in 15 minutes and there maintained for the desired period. The reaction was terminated by cooling the reaction mixture to 25°C, releasing the pressure, and recovering the carbonate product by filtration on a sintered glass disc. The product was washed with acetone and ether and left exposed to air for at least 4 hours before placing in a closed bottle. Uranyl carbonate was prepared in an analogous manner except that 95% ethanol was used as the reaction medium because when water was used the particle size of the product was very small, the filtration

time was greatly extended, and the yield was reduced to about half of that obtained with 95% ethanol.

Analyses

Both the acetate salts and the carbonate products were analyzed for C and H by conventional oxygen combustion analyses. The sample was ignited to 1000°C and the solid combustion product weighed as the lanthanon sesquioxide, ThO_2, or U_3O_8 except Ce, Pr, and Tb which were weighed as CeO_2, $PrO_{1.83}$, and $TbO_{1.81}$, respectively.

In addition to the combustion analysis the carbonate products from La and U were decomposed with acid and the evolved CO_2 measured. The difference between this value and the total CO_2, as determined by combustion analysis, was assumed to be due to acetate as $La(OAc)_3 \cdot 2 H_2O$ and $UO_2(OAc)_2 \cdot 2 H_2O$, respectively.

Results

The anhydrous acetates discussed above possessed molar ratios of acetate to positive ion as follows: La, 2.92; Ce, 3.03; Pr, 3.00; Tb, 3.00; Y, 2.99; Th, 3.95; and uranyl (UO_2^{+2}), 1.99.

Data relating to the carbonate products prepared from the above acetates by the method described are given in the accompanying table. The Molar Ratios of CO_2 and H_2O to lanthanon sesquioxide (Ln_2O_3), thorium dioxide (ThO_2), and uranyl ion (UO_2^{+2}), respectively, were obtained from the oxygen combustion data. The Per Cent Composition value was obtained by the addition of the weight percentages of the three observed combustion products, i.e., CO_2, H_2O, and oxide (Ln_2O_3, ThO_2, or U_3O_8 depending upon the particular carbonate compound; the observed weights for CeO_2, $PrO_{1.83}$, and $TbO_{1.81}$ were converted to their equivalent weight of sesquioxide.) The amount by which this value exceeds 100.0% in the case of thorium and the lanthanons and 98.4% in the case of uranium is an indication of the amount of organic material (e.g., acetate) present in the product. The uranium value of 98.4% is the result of the net oxygen loss incurred by the decomposition of uranyl carbonate to form U_3O_8. The Per Cent Yield value is based upon

the ratio of the oxide equivalents contained in the final carbonate product and the original acetate sample.

An indication of the effect of acetate contamination on the analyses can be obtained from the results of acid hydrolysis. For example, a lanthanum carbonate product with the ratios CO_2/La_2O_3 = 3.16 and H_2O/La_2O_3 = 7.67 and a Per Cent Total = 101.0 was dissolved in acid and the evolved CO_2 measured. The difference in the amounts of CO_2 found by combustion and by hydrolysis was attributed to $La(C_2H_3O_2)_3 \cdot 2 H_2O$. The remaining CO_2 was attributed to lanthanum carbonate which then had the formula $La_2(CO_3)_{2.96}(OH)_{0.04} \cdot 7.45 H_2O$. Similar treatment of a uranyl carbonate product with the corresponding values of 0.99, 0.50, and 98.8% indicated that the remaining uranyl carbonate had the formula $UO_2(CO_3)_{0.95}(OH)_{0.10} \cdot 0.43 H_2O$.

Table I

Carbonates Prepared from Anhydrous Acetates

Sample	Molar Ratios		% Total (Oxide+CO₂+H₂O)	% Yield
	CO_2/Oxide	H_2O/Oxide		
La	3.12	7.58	101.0	74
Ce	3.10	7.99	100.8	84
Pr	3.14	8.09	100.5	77
Tb	3.16	2.87	100.9	74
Y	3.15	2.68	102.0	78
Th	1.99	3.60	100.1	91
U	0.94	0.75	99.0	92

Thermal decomposition diagrams for thorium dicarbonate and uranyl carbonate are shown in Figures 1 and 2, respectively. The thermal decompositions were carried out on an Ainsworth Vacuum Recording Balance at a heating rate of 36°/hour and under the various conditions of vacuum, 550 mm of O_2 pressure (absolute) and 550 mm of CO_2 pressure (absolute). The curves for decomposition in CO_2 and O_2 are the result of first removing the hydration water in vacuum with subsequent decomposition occurring in the designated atmosphere. In Figure 2 the curve

time was greatly extended, and the yield was reduced to about half of that obtained with 95% ethanol.

Analyses

Both the acetate salts and the carbonate products were analyzed for C and H by conventional oxygen combustion analyses. The sample was ignited to 1000°C and the solid combustion product weighed as the lanthanon sesquioxide, ThO_2, or U_3O_8 except Ce, Pr, and Tb which were weighed as CeO_2, $PrO_{1.83}$, and $TbO_{1.81}$, respectively.

In addition to the combustion analysis the carbonate products from La and U were decomposed with acid and the evolved CO_2 measured. The difference between this value and the total CO_2, as determined by combustion analysis, was assumed to be due to acetate as $La(OAc)_3 \cdot 2H_2O$ and $UO_2(OAc)_2 \cdot 2H_2O$, respectively.

Results

The anhydrous acetates discussed above possessed molar ratios of acetate to positive ion as follows: La, 2.92; Ce, 3.03; Pr, 3.00; Tb, 3.00; Y, 2.99; Th, 3.95; and uranyl (UO_2^{+2}), 1.99.

Data relating to the carbonate products prepared from the above acetates by the method described are given in the accompanying table. The Molar Ratios of CO_2 and H_2O to lanthanon sesquioxide (Ln_2O_3), thorium dioxide (ThO_2), and uranyl ion (UO_2^{+2}), respectively, were obtained from the oxygen combustion data. The Per Cent Composition value was obtained by the addition of the weight percentages of the three observed combustion products, i.e., CO_2, H_2O, and oxide (Ln_2O_3, ThO_2, or U_3O_8 depending upon the particular carbonate compound; the observed weights for CeO_2, $PrO_{1.83}$, and $TbO_{1.81}$ were converted to their equivalent weight of sesquioxide.) The amount by which this value exceeds 100.0% in the case of thorium and the lanthanons and 98.4% in the case of uranium is an indication of the amount of organic material (e.g., acetate) present in the product. The uranium value of 98.4% is the result of the net oxygen loss incurred by the decomposition of uranyl carbonate to form U_3O_8. The Per Cent Yield value is based upon

the ratio of the oxide equivalents contained in the final carbonate product and the original acetate sample.

An indication of the effect of acetate contamination on the analyses can be obtained from the results of acid hydrolysis. For example, a lanthanum carbonate product with the ratios $CO_2/La_2O_3 = 3.16$ and $H_2O/La_2O_3 = 7.67$ and a Per Cent Total $= 101.0$ was dissolved in acid and the evolved CO_2 measured. The difference in the amounts of CO_2 found by combustion and by hydrolysis was attributed to $La(C_2H_3O_2)_3 \cdot 2\ H_2O$. The remaining CO_2 was attributed to lanthanum carbonate which then had the formula $La_2(CO_3)_{2.98}(OH)_{0.04} \cdot 7.45\ H_2O$. Similar treatment of a uranyl carbonate product with the corresponding values of 0.99, 0.50, and 98.8% indicated that the remaining uranyl carbonate had the formula $UO_2(CO_3)_{0.95}(OH)_{0.10} \cdot 0.43\ H_2O$.

Table I
Carbonates Prepared from Anhydrous Acetates

Sample	Molar Ratios		% Total (Oxide+CO_2+H_2O)	% Yield
	CO_2/Oxide	H_2O/Oxide		
La	3.12	7.58	101.0	74
Ce	3.10	7.99	100.8	84
Pr	3.14	8.09	100.5	77
Tb	3.16	2.87	100.9	74
Y	3.15	2.68	102.0	78
Th	1.99	3.60	100.1	91
U	0.94	0.75	99.0	92

Thermal decomposition diagrams for thorium dicarbonate and uranyl carbonate are shown in Figures 1 and 2, respectively. The thermal decompositions were carried out on an Ainsworth Vacuum Recording Balance at a heating rate of 36°/hour and under the various conditions of vacuum, 550 mm of O_2 pressure (absolute) and 550 mm of CO_2 pressure (absolute). The curves for decomposition in CO_2 and O_2 are the result of first removing the hydration water in vacuum with subsequent decomposition occurring in the designated atmosphere. In Figure 2 the curve

represented by erect triangles was obtained with a carbonate product in which the water of hydration and about one half of the total CO_2 was removed in vacuum with subsequent decomposition in O_2. Also in Figure 2 the curve represented by x's is shown for comparison purposes and represents the decomposition of commercial γ-UO_3 in O_2 after first removing the hydration water in vacuum.

Discussion

References to various methods which have been employed to prepare the rare earth carbonates have been cited in previous papers (1-4). The preparation of the normal carbonate of thorium does not appear to have been reported previously although Ryabchikov and coworkers (5) have proposed that $Th(CO_3)_2 \cdot n\, H_2O$ is precipitated during the high frequency titration of thorium nitrate solution with ammonium carbonate but that it is hydrolyzed immediately to a basic thorium carbonate. Previously reported methods of preparing uranyl carbonate have consisted mainly of (a) treating aqueous suspensions of UO_3 with CO_2 at either atmospheric or higher pressures (6-8), (b) heating an ethanol solution of uranyl nitrate under CO_2 pressure (7), or (c) air oxidation of U(IV) oxycarbonate (9).

The method of carbonate preparation described in this paper has proven to be general in nature and produces high yield products with relatively low contamination. Use of the anhydrous acetate has resulted in reproducibly increased yields of the order of 75% to 100% in some cases over those obtained formerly with the hydrated acetate salts. Although use of water for washing the freshly prepared uranyl carbonate products caused dissolution and loss of virtually all of the product, the other carbonate products exhibited no appreciable hydrolysis after stirring in water for 30 minutes.

The anhydrous acetates of Th and uranyl exhibited no weight change after exposure to laboratory air overnight. The other acetates were not tested in this manner.

The curves in Figures 1 and 2 show that the presence of CO_2 has

little or no effect upon the thermal decomposition of either thorium carbonate or uranyl carbonate. Oxygen has a noticeable effect on the thermal decomposition of uranyl carbonate. This effect is being investigated. The plateau which occurs in uranyl carbonate at about 600° in oxygen corresponds to an O/U ratio of 2.9. Additional information is necessary to interpret the curves more fully.

Acknowledgment

The author expresses his appreciation for the helpful suggestions of C. E. Holley, Jr.

References

1. E. L. Head and C. E. Holley, Jr., Rare Earth Research II, p. 51. Gordon and Breach, New York, 1964.

2. E. L. Head and C. E. Holley, Jr., Rare Earth Research III, p. 707. Gordon and Breach, New York, 1965.

3. E. L. Head, Inorg. Nucl. Chem. Letters 2, 33 (1966).

4. Sr. M. Clarus Strouth, "Thermal Decomposition of Yttrium, Scandium, and Heavy Lanthanon Oxalates and Carbonates," Thesis, Michigan State University, 1962, Univ. Microfilm (Ann Arbor, Mich.), Order No. 62-3192.

5. D. I. Ryabchikov, M. P. Volynets, V. A. Zarinskii, and V. I. Ivanov, Zhur. Analit. Khim. (English translation) 18, 307 (1963).

6. Eugene Staritzky and Don T. Cromer, Anal. Chem. 28, 1211 (1956).

7. I. I. Chernyaev, V. A. Golovna, and G. V. Ellert, Zhur. Neorg. Khim. (English translation) 1, 2726 (1956).

8. M. Bachelet, E. Cheylan, M. Douis, and J. C. Goulette, Bull. Soc. Chim. France 1956, 441.

9. Balaram Sahoo and D. Patnaik, Nature 185, 683 (1960).
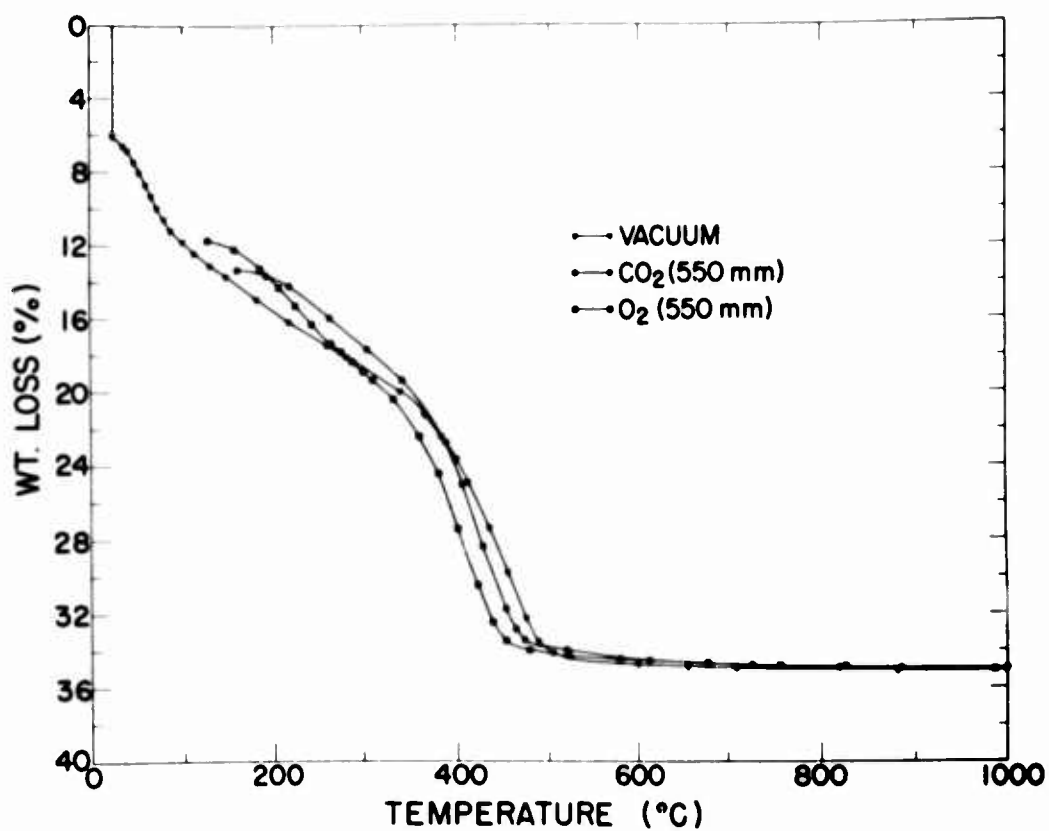
Th $(CO_3)_2 \cdot 3.2\,H_2O$ - THERMAL DECOMPOSITION DIAGRAM
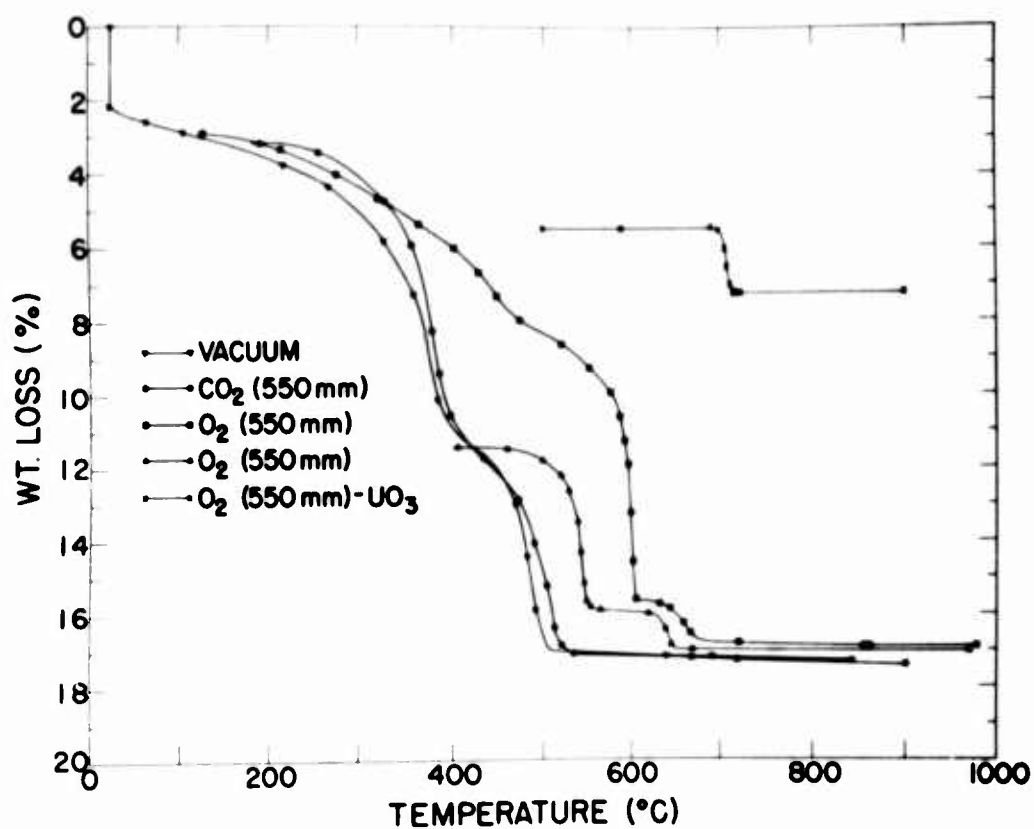
$UO_2\,CO_3 \cdot 0.7\,H_2O$ - THERMAL DECOMPOSITION DIAGRAM

PREPARATION, CHARACTERIZATION, AND SOME THERMODYNAMIC PROPERTIES OF LANTHANUM-OXIDE-CARBIDE, $La_2O_2C_2$

A. Duane Butherus and Harry A. Eick

Department of Chemistry, Michigan State University,
East Lansing, Michigan 48823

ABSTRACT

A lanthanum-oxide-carbide of the general formula $La_2O_2C_2$ has been prepared by the reaction of molten lanthanum metal with carbon monoxide, by the reaction of lanthanum metal with the sesquioxide and carbon, by the reaction of lanthanum dicarbide with the sesquioxide and carbon, and by the reaction of sesquioxide with graphite. All reactions were carried out in a carbon monoxide atmosphere. Some of the preparations which were zone refined by slow passage of an arc over an approximately 7 cm long sample produced a crystalline phase which both x-ray powder diffraction and micrographic analysis indicated to be monophasic. Analysis of this specimen for total carbon, free carbon, and metal indicated the composition mentioned previously. Vapor phase chromatographic analysis of the acid hydrolysis product indicates the principal species to be acetylene. A carbon monoxide equilibration study undertaken on the reaction,

$$La_2O_3(s) + 3 C(s) = La_2O_2C_2(s) + CO(g)$$

in a closed constant volume system produced the following data:

$$\Delta H_{298}^{\circ} = 82.16 \pm 2.0 \text{ kcal/gfw}$$

$$\Delta S_{298}^{\circ} = 36.67 \pm 3.5 \text{ e.u.}$$

By combining these values with the appropriate thermodynamic data, a heat of formation of -313.6 ± 3.0 kcal/gfw is calculated for this phase.

A third law heat calculated with tabulated free energy functions for the sesquioxide, graphite, and carbon monoxide, and estimated for the oxide-carbide species is in agreement with the values cited above. The stability of this phase will be compared to that of an analogous neodymium species.

INTRODUCTION

Although the existence of oxycarbide phases has been known for some time 1-5), the first study involving an inner transition metal appeared only recently (6) when a phase of the composition $Nd_2O_2C_2$ and some of its properties were reported. The preparation and thermo-chemical investigation of an apparently isostructural lanthanum analogue of this oxycarbide is reported below.

EXPERIMENTAL

Preparation: Sample preparations were undertaken using one of the arc melting techniques developed for the preparation of the analogous neodymium phase (6). The starting materials consisted of 99.9% pure calcined sesquioxide (Research Chemicals, Phoenix, Ariz.), 99% pure lanthanum metal (Research Chemicals), and previously outgassed graphite powder (Fisher Scientific, Detroit, Mich.). Samples in the mole ratio indicated by equation (1) were arc melted under a one atmosphere pressure of carbon monoxide (99.5% minimum purity) using a graphite electrode.

$$La(s) + La_2O_3(s) + 3 C(s) \rightarrow 3/2 La_2O_2C_2(s) \tag{1}$$

Equilibrium Pressure Studies: After the fused oxycarbide button had been pulverized in a helium-filled glove box, it was placed in a graphite crucible outgassed previously by heating it at temperatures up to 1900°C under a vacuum of 1×10^{-6} torr. The crucible was inserted into an induction generator current concentrator, and the entire concentrator assembly was placed in a glass envelope which formed a closed evacuable chamber whose volume was approximately to 2.65 liters.

The system was evacuated immediately to minimize hydrolysis. Subsequently, the crucible was heated to approximately 1000° under vacuum to effect a final outgas. The reaction chamber was isolated from the pumping system, and C.P. carbon monoxide (Matheson, 99.5% minimum purity) was bled into the system until the pressure, as measured by a Wallace and Tiernan absolute pressure manometer, was approximately 30 torr. The temperature of the crucible was then elevated until the carbon monoxide pressure began to decrease, indicating absorption of the carbon monoxide by the oxycarbide. (This absorption usually occurred at about 1350°.) The temperature was controlled at this value using a Latronics Corporation, two-color optical pyrometer to control the induction furnace via a Model 90 Leeds and Northrup automatic controller.

When the carbon monoxide pressure had stabilized at a constant, minimum value, the cavity temperature of the crucible was determined by sighting into it through a pinhole with a Leeds and Northrup disappearing filament type optical pyrometer which had been calibrated at the National Bureau of Standards. The carbon monoxide pressure was measured with a U-shaped absolute pressure mercury manometer. The difference in height between the legs of the manometer was measured with a Gaertner Scientific Company model M-908 cathetometer. Carbon monoxide was then pumped from the system to lower the pressure by 2-5 torr, and the system was allowed to re-equilibrate at the same temperature.

If the pressure increased to within 0.3 torr of the value observed previously at this temperature, the pressure was considered to be the equilibrium value, assuming the total pressure measured was identical

with the partial pressure of carbon monoxide.

Additional data were collected by an analogous procedure: an arbitrary amount of carbon monoxide was either added or pumped off, the temperature was either increased or decreased by some arbitrary increment, and the pressure subsequently either increased or decreased to a constant value. Equilibrium conditions were then verified by either adding or removing carbon monoxide so that the equilibrium value was approached from both above and below.

Analysis: In each equilibration experiment, a gas sample was removed from the system at the completion of the series and analyzed mass spectrometrically to confirm that only carbon monoxide was present.

Weighed samples of the oxycarbide, pulverized previously by grinding thoroughly a number of arc melted ingots in a helium-filled glove box, were hydrolyzed in 1 $\underline{N}$ HCl, digested for 4 hours on a hot plate, and filtered through a filter crucible. The quantity of free carbon was determined from the weight change of the dried filter crucibles. (The crucibles were then re-ignited in a muffle furnace to confirm the weight loss data.) Lanthanum was precipitated as the oxalate and determined gravimetrically. Another portion of the pulverized sample was weighed into a quartz boat and burned in a stream of dry oxygen in a tube furnace. The carbon monoxide so produced was oxidized by cupric oxide to carbon dioxide; any water produced was absorbed by a drying column and the carbon dioxide absorbed in a tared ascarite-filled tube. The mass of carbon dioxide absorbed was considered a measure of the total carbon content in the specimen. Bound carbon was

assumed to be the difference between total carbon and free carbon content, and the oxygen content was determined by difference. Four samples were analyzed gravimetrically for lanthanum and three samples were analyzed for bound carbon.

X-Ray Powder Diffraction and Infrared Analysis: Samples of various compositions were checked both micrographically and by x-ray powder diffraction using copper $K\alpha$ radiation ($\lambda\alpha_\mu = 1.5418\text{Å}$). Both a 114.59 mm Debye-Scherrer powder camera and a Siemens diffractometer were used. Some of the lines were indexed tentatively on the basis of a monoclinic unit cell, employing parameters obtained from poor quality Weissenberg photographs taken of a single crystal fragment.

An infrared spectrum was obtained on a Unican SD 200 spectrometer using the KBr pellet technique.

RESULTS

Equilibration Studies: Three series of equilibrations were performed using individually prepared samples. A graph of the log p_{co} versus $1/T$ for reaction (2) is illustrated in Figure 1.

$$La_2O_2C_2(s) + CO(g) = La_2O_3(s) + 3\,C(s) \qquad (2)$$
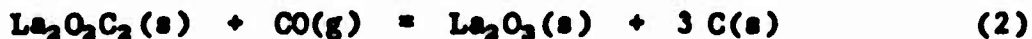
A linear least squares analysis of the data give the following results for the enthalpy and entropy (together with their standard deviations) for equation (2) at a mean temperature of 1809°:

$$\Delta H^\circ_{1809} = 79.6 \pm 1.0 \text{ kcal/gfw}$$

$$\Delta S^\circ_{1809} = 36.6 \pm 3.5 \text{ e.u.}$$

Correcting these values to 298°, using the ΔC_p approximation developed previously for $Nd_2O_2C_2$ (6), gives:

$$\Delta H_{298}^\circ = 82.2 \pm 1.9 \text{ kcal/gfw}$$
$$\Delta S_{298}^\circ = 37.7 \pm 3.6 \text{ e.u.}$$

The larger errors reported here reflect estimated uncertainties in the heat capacity of the oxycarbide species and reported errors in the heat capacities of the other components. A third law treatment of the data, using free energy functions approximated in a manner similar to that reported for $Nd_2O_2C_2$ (6), resulted in the following value of the enthalpy:

$$\Delta H_{298}^\circ = 80.89 \pm 0.71 \text{ kcal/gfw}.$$

The error reported above represents the standard deviation of the values and not the actual error in the heat. The agreement between second and third law values is considered to be acceptable.

Assuming that the second law value of the heat is more correct, $\Delta G_{298}^\circ = 70.9 \pm 2.9$ kcal/gfw. By combining these data with the heats and free energies of formation of $La_2O_3(s)$ (7,8) and $CO(g)$ (9), the heat and free energy of formation of $La_2O_2C_2$ are calculated to be:

$$\Delta H_f^\circ = -320.0 \pm 2.0 \text{ kcal/gfw}$$
$$\Delta G_f^\circ = -315.6 \pm 2.9 \text{ kcal/gfw},$$

at 298°K.

Analysis: A mass spectrometric analysis of the gas liberated during one equilibration study indicated the following: CO - 97.60%; H_2 - 1.02%; O_2 - 1.38%. Thus, the pressures measured are apparently within 2% of the actual carbon monoxide pressure.

The results of the chemical analyses are: La, $83.4 \pm 0.6\%$; C, $7.5 \pm 0.9\%$; and O (difference), $9.1 \pm 0.7\%$. The errors reported represent the standard deviation of the individual measurements. Calculated percentages for $La_2O_2C_2$ are: La = 83.22%, C = 7.19%, and O = 9.59%.

X-Ray Diffraction: Table I lists the principal interplanar d-values of this phase and their relative intensities. The presence of the three solid phases -- La_2O_3, $La_2O_2C_2$, and C -- in the equilibrium mixture was confirmed by x-ray powder diffraction analysis. (Three different phases were also observed micrographically.)

Infrared Analysis: The infrared spectrum showed no peaks in either the carbonyl region, 2000 cm^{-1}, or in the acetalyde region, 2200 cm^{-1}. One faint peak was observed in the 700 cm^{-1} region -- possibly a C-H rocking mode of acetylene which is present in small traces as a decomposition product.

DISCUSSION

A comparison of the heats observed in this reaction with those observed for $Nd_2O_2C_2$ is of interest.

For reaction (3),

$$M_2O_2C_2(s) + CO(g) = M_2O_3(s) + 3 C(s) \qquad (3)$$
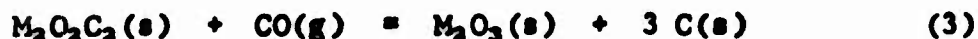
ΔH°_{298} changes from 82.2 ± 1.9 kcal/gfw for M = lanthanum to 75.9 ± 3.0 kcal/gfw for M = neodymium. Similarly, the heat of formation of the oxide-carbide at 298° varies from -329.8 ± 3.0 for neodymium, to -320.0 ± 2.0, indicating that the stability of this phase varies in a

manner similar to that exhibited by the sesquioxide, since Nd_2O_3 is only slightly more stable than La_2O_3. This behavior is consistent with an ionic species, and substantiates further our belief that the phase is ionic in nature.

The presence of the bond in the IR which is assignable to acetylene indicates that this lanthanum species hydrolyzes to acetylene just as its analogue, the neodymium member, did, and it seems probable that the acetylenic unit is substituted for an oxide ion in the sesquioxide structure. The failure to obtain satisfactory single crystals has precluded a detailed single crystal analysis.

An attempt to prepare the samarium analogue of this phase met with failure, resulting instead in a phase which exhibited a different x-ray diffraction pattern. This behavior makes a direct comparison with the lanthanide sesquioxide possible (though tenuous) in that only for these lighter members is the hexagonal A-type structure stable.

The precision of these measurements is greater than that obtained on the neodymium analogue -- probably as a result of refined experimental technique and not as a result of a better behaved system.

REFERENCES

1. C. B. Alcock, H. A. Eick, B. G. Rauh, and R. J. Thorn, in <u>Nuclear</u> <u>Metallurgy</u>, p. 257, Vol. X, J. T. Waber, P. Chiotti, W. N. Miner, Ed. Edwards Bros., Ann Arbor, Michigan, 1964.

2. R. F. Stopps, J. V. Hamme, J. Am. Ceram. Soc., <u>47</u>, 59 (1964).

3. P. Chiotti, W. C. Robinson, and M. Kanno, J. Less Common Metals, <u>10</u>, 273 (1966).

4. G. V. Samsonov, T. Ya. Kosolapova, M. D. Lyutaya, and G. N. Makavenko, Redkozem. Elementy. Akad. Nauk. SSR, Inst. Geokhim. Analit. Kim., <u>8</u>, (1963).

5. J. M. Leitnaker and T. G. Godfrey, J. Chem. and Eng. Data, <u>11</u>, 392 (1966).

6. A. Duane Butherus, Ralph B. Leonard, Gerald L. Buchel, H. A. Eick, Inorg. Chem., <u>5</u>, 1567 (1966).

7. K. K. Kelly and E. O. King, Bull. 592, Bureau of Mines, U.S. Government Printing Office, Washington (1961).

8. E. Huber and C. E. Holley, J. Am. Chem. Soc., <u>75</u>, 3594 (1953).

9. F. D. Rossini, et al., Ed., U. S. National Bureau of Standards Circular 500, Series I, U.S. Government Printing Office, Washington, D. C., p. 99 (1952).

TABLE I

d-Values of $Nd_2O_2C_2$

Intensity	d, Å	Intensity	d, Å	Intensity	d, Å
m	7.30	vw	1.992	vw	1.455
vvw	5.16	vvw	1.962	vvw	1.403
m	3.65	vvw	1.908	vw	1.378
mw	3.53	vvw	1.834	vvw	1.362
vw	3.479	s	1.748	w	1.286
vw	3.356	w	1.705	w	1.258
vvs	3.172	vw	1.669	vw	1.233
s	3.042	vw	1.651	mw	1.209
ms	2.958	vw	1.638	vvw	1.156
vw	2.613	vw	1.620	vw	1.184
vw	2.446	vw	1.594	mw	1.089
vw	2.412	vw	1.577	vvw	1.066
w	2.269	vw	1.533	vvw	1.014
w	2.025	vw	1.491	w	0.859
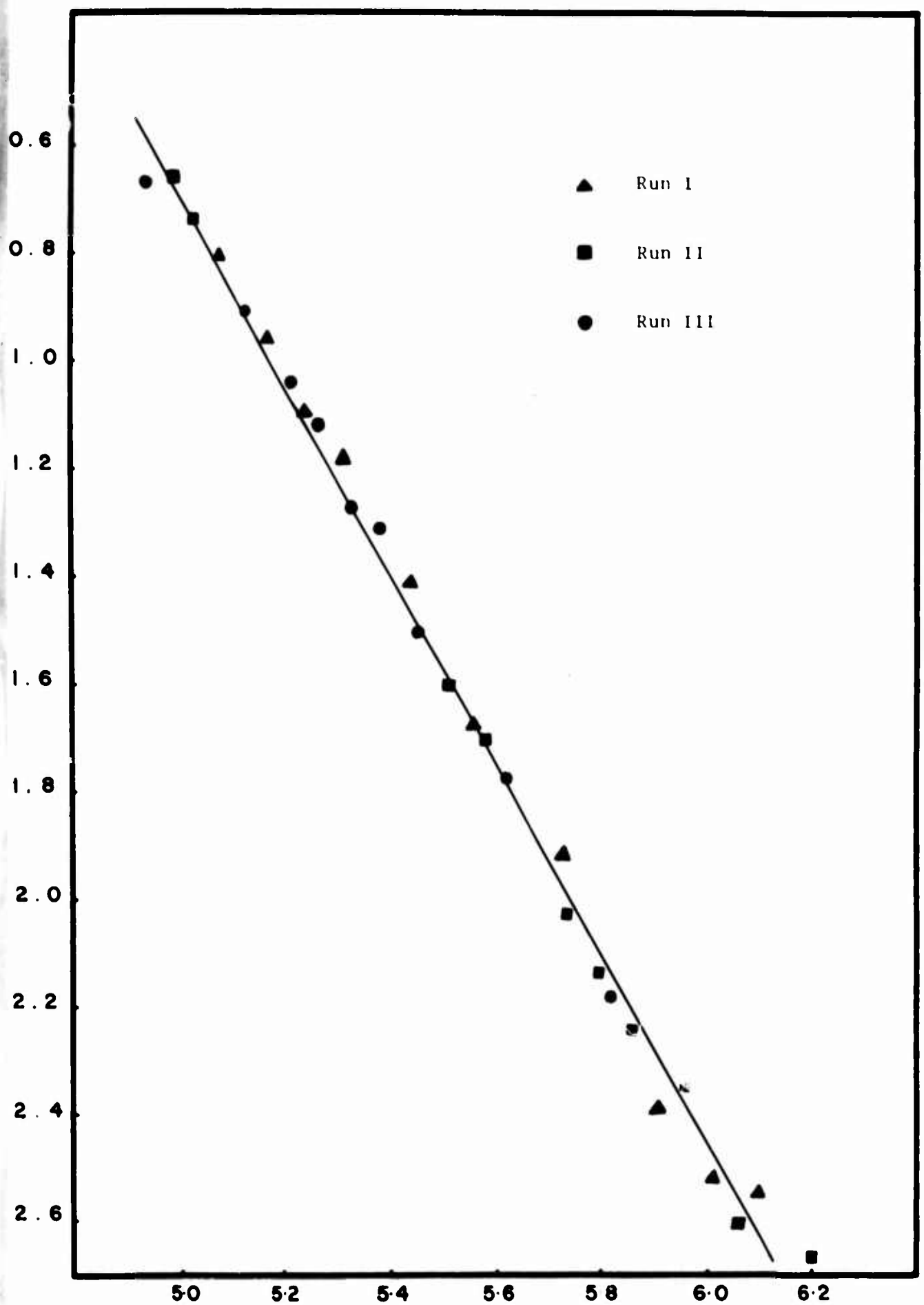
Figure 1. Plot of Log P_{co} vs. $1/T \times 10^4$

PRECIPITATION of RARE EARTH OXIDES from MOLTEN SALTS

Georg Brauer

University of Freiburg-im-Breisgau, Germany

ABSTRACT

Rare earth oxides or oxide nitrates have been preci-
pitated from anhydrous rare earth nitrates dissolved in
molten mixtures of alkali nitrates by self-decomposition
at 400°C. La and Nd form oxide nitrates under these condi-
tions. Ce, Pr, and Tb are precipitated as higher oxides
CeO_2, $PrO_{1.83}$, and $TbO_{1.80}$ respectively. The other rare
earths are precipitated as sesquioxides with the B-type
structure (Sm, Eu, Gd) or with the C-type structure (Dy
through Lu). Thus, the B-type modifications of Sm_2O_3,
Eu_2O_3, and Gd_2O_3 must be the really stable phases at 400°C.
A new version of the phase stability diagram of the A-,
B-, and C-type polymorphs of the rare earth sesquioxides
has been proposed.

INTRODUCTION

Pyrolytic decomposition of hydroxides, nitrates, oxa-
lates, carbonates, sulfates etc. is the generally used
and best known method to prepare rare earth oxides. These
reactions have to be performed at elevated temperatures
ranging from 400° to 1200°C. Always, if the decomposition
of the salt can be completed below 400° to 700°C, the for-
mation of the cubic C-type modification of the trivalent

oxides is observed, regardless of the existence of other modifications (A-type, B-type) of these oxides. In the cases of La_2O_3 through Eu_2O_3, transformations from the C-type structure of the initially prepared oxide to the A-type or to the B-type modifications occur on heating to an appropriate higher temperature. However, none of these transformations C-to-A or C-to-B of the oxides La_2O_3 through Eu_2O_3 have been found to be reversible by simple heat treatment (hydrothermal experiments disregarded); and in the case of Gd_2O_3 the statement of reversibility is to be regarded with scepticism. Hence, we believe the transformations of La_2O_3 through Gd_2O_3 to be monotropic. The C-type forms must be considered as metastable, generated beyond true thermodynamic equilibrium by a hindered or topotactic solid-to-solid reaction. The so-called transformation temperatures ($C \rightarrow A$, $C \rightarrow B$) are only those temperature ranges where the lattice particles become mobile.

If this is true one should try to find other experimental conditions at lower temperatures where the formation of the real stable oxide modification is less hampered. With this aim, we investigated the precipitation of rare earth oxides from fluid salt mixtures with low melting points such as alkali nitrates.

EXPERIMENTAL RESULTS

From a sodium+potassium+rare earth nitrate melt, the rare earths are easily precipitated by self-decomposition of the nitrates [1])[2]). The reaction sequence is probably: $NO_3^- \rightleftarrows NO_2^+ + O^{2-}$; $3\ O^{2-} + Ln^{3+} \rightarrow Ln_2O_3$; $NO_2^+ + NO_3^- \rightarrow 2NO_2$, as suggested by DUKE[3]). With a slowly increasing temperature, the precipitation generally commences at about 380°C and is completed towards 420°C. We have isolated precipitates of rare earth compounds from the cooled and solidified melt by using dimethyl-sulfoxide as solvent for the alkali nitrates. Water was carefully excluded in the solvent and in the atmosphere while handling the isolated compounds. The precipitates have been found to be the oxide nitrates (formula $LnONO_3$) in the cases of La and Nd, and to be the oxides in the cases of Ce, Pr, and Sm through Lu.

We identified the structure of the melt-precipitated sesquioxides as <u>B-type</u> in the cases of Sm_2O_3, Eu_2O_3, and Gd_2O_3 and as <u>C-type</u> in the cases of Dy_2O_3 through Lu_2O_3. Cerium, praseodymium and terbium, as to be expected, form oxides with a higher valency: CeO_2, $PrO_{1.83}$, and $TbO_{1.80}$.

DISCUSSION

It is not surprising that Ce, Pr and Tb are precipitated as higher oxides from the nitrate melt at 400°C. Some rather qualitative estimations can be made as to the activity of free oxygen in the melt: This activity must be higher than that corresponding to $\frac{1}{5}$ atm pressure of molecular oxygen, since terbium reaches to an oxidation state of $TbO_{1.80}$; and the activity must be lower

than that corresponding to 10 atm of oxygen since praseo-dymium does not exceed an oxidation state of $PrO_{1.83}$. Molecular oxygen and molten alkali nitrate are connected by the equilibrium $NaNO_3 \rightleftharpoons NaNO_2 + \frac{1}{2}O_2$ as shown by CASES-CASANOVA[4].

The remarkable result of the described experiments is the formation of B-type Sm_2O_3, Eu_2O_3, and Gd_2O_3 at as low a temperature as $400°C$ instead of the expected C-types. Even the addition of small amounts of the corresponding C-type modification as a seed did not alter the preference of the B-type formation. From these observations one has to conclude that the B-form of these oxides is the really stable modification even at low temperatures. We therefore propose to change the till now accepted phase stability diagram of the polymorphs of the rare earth sesquioxides as shown in Fig. 1: The $B \rightleftharpoons C$ equilibrium curve should steeply drop between Gd_2O_3 and Tb_2O_3.

REFERENCES

[1]) J.K.MARSH, J.Chem.Soc. (London) 1946, 17.

[2]) F.WEIGEL, K.PÜTZL, Chem.Ber. 96, 188 (1963).

[3]) F.R.DUKE, J.Chem.Education 39, 57 (1962).

[4]) J.CASES-CASANOVA, Bull.Soc.chim.France 1959, 429.

FIGURE CAPTION

Fig. 1. Phase stability diagram of the rare earth ses-
quioxides. Areas of the structure types A, B, C.
○ designates C-form oxide precipitated at 400°C from
the melt; ● designates B-form oxide precipitated at
400°C; ☐ designates oxide nitrate precipitated; ■ desig-
nates A-form oxide precipitated. The till now accepted
borders of the phase areas are given by dashed lines.
The new proposed C$\rightleftharpoons$B transformation equilibrium is
given by a solid line.
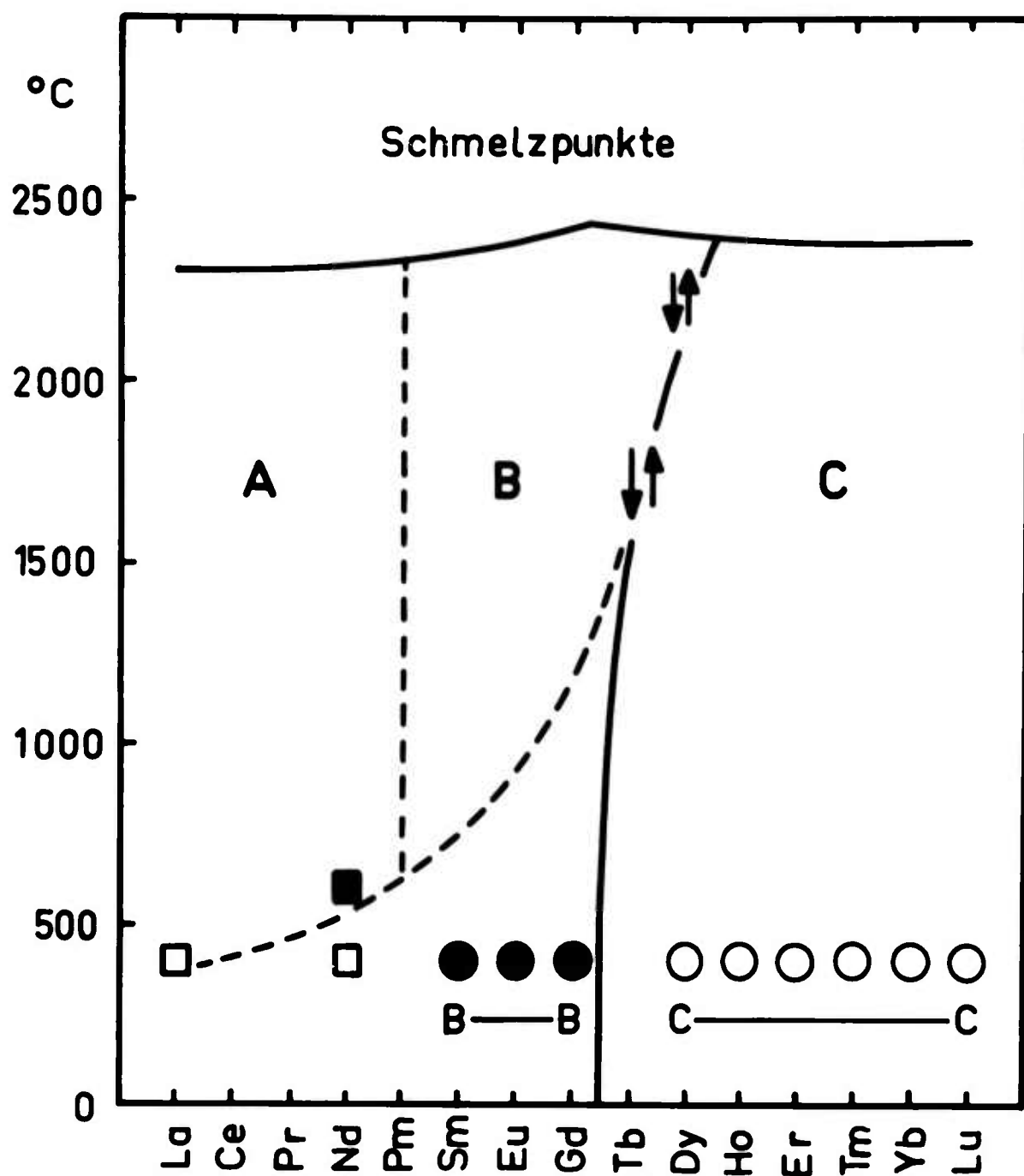
TITLE: THE DIVALENT STATE IN LANTHANIDES

AUTHOR: C. G. KIRKPATRICK

ABSTRACT:

The lanthanide elements (atomic numbers 58-71) have long been considered a stable trivalent species, except for ytterbium, europium and sometimes samarium. It is now apparent that this belief rested largely on the use of aqueous solvents in which the studies were conducted. The advent of optical maser phenomena involving the rare earths, and subsequent investigations in crystalline and glassy media, have made the trivalent question a good deal less clear.

Drs. F. Fong and M. Hiller of the NAA Science Center, and this author, proposed a model for divalent laser materials. The model proposed postulated that (1) the ease of reduction of rare earth impurities is dependent on the third ionization potential of the impurity, (2) the reduction technique must raise the fermi level above the level of the divalent ion, and (3) the temperature of crystal growth must be low enough that trapped electrons can remain on divalent sites.

A series of growth attempts have been made with KCl and Sm, Eu, Yb, Tm and Dy as impurities. Rare earth metals, graphite crucibles and hydrogen under pressure have been used as reductants. The postulate was not confirmed.

An extensive literature survey has failed to reveal any irregularities in the trend of first, second, or third ionization potentials in the series which might account for the observed differences in reducibility. J. D. Corbett et al, in a recent article, discusses a related problem and proposes the heats of sublimation of the metals as a criteria for reduction. A new model is proposed which is compatible with available data.

' ALKOXY AND ACYLOXY DERIVATIVES OF LANTHANONS '
By
R.C.Mehrotra, J.M.Batwara, S.N.Misra, T.N.Misra
and U.D.Tripathi
Chemical Laboratories, University of Rajasthan,
Jaipur(India).

The preparation and properties of alcoholates,
$MCl_3.3ROH$ (where M is La, Ce, Pr, Nd, Gd, Er or Yb and
R is Me, Et, Pr^i or Bu) have been described. The tri-
isopropanolates serve as convenient starting materials
for the synthesis of tri-isopropoxides, $M(OPr^i)_3$, by
refluxing their solutions in isopropanol-benzene
mixture with stoichiometric quantities of sodium
isopropoxide. The isopropoxides can in some cases be
purified by crystallisation and volatilisation and
undergo alcoholysis reactions by which other alkoxide
derivatives can be prepared. All these alkoxides are
found to be soluble in common organic solvents except
the methoxides, which can, therefore, be synthesized
by the alternative lithium methoxide method also.

The reactions of these alkoxides particularly of
isopropoxides have been studied in benzene medium with
acetyl chloride, acetyl bromide, phenols, glycols,
β-diketones and β-ketoesters. A wide variety of
metallo-organic compounds including anhydrous
β-diketonates of lanthanons have been synthesized for
the first time.

The acyloxy derivatives, $M(OOCR)_3$ (where M is La,
Ce, Pr and Nd and R is $C_{11}H_{23}$, $C_{15}H_{31}$, $C_{17}H_{35}$) have been
synthesized by treating their chlorides or nitrates with
appropriate sodium soap solutions in water. The
precipitated tri-acylates can be crystallized from
benzene in which they depict monomeric behaviour. The
tri-acyloxides as well as chloride acyloxide derivatives
have been synthesized by the reactions between lanthanon
chlorides and carboxylic acids in benzene solution.
Preliminary thermogravimetric studies of lanthanon
soaps have also been carried out.

Although considerable interest has been shown in the chemistry of alkoxides[1] and acyloxides[2] of transition elements during the last decade, only a few scattered references are available on similar derivatives of inner transition elements[3-10]. A renewed interest has arisen in recent years[11-12] in the metallo-organic derivatives of lanthanons due to their potential applications as laser materials.

ALKOXY DERIVATIVES OF LANTHANONS:

In view of the above, a comprehensive study[13-16] of the preparation and properties of lanthanon alkoxides has been undertaken in these laboratories for the last few years and it has been further shown that these alkoxides serve as very useful starting materials for the preparation of a wide variety of organic derivatives of lanthanons.

The chief characteristics of lanthanon elements, largely determined by their highly electropositive character and by the size of the Ln^{+3} ions, are reflected in the chemistry of their alkoxides also. Compared to other transition metal alkoxides, these have now been found to be much less volatile, and coupled with their general non-crystallisibility from suitable solvents, this presents serious difficulties in the final purification of the products. For the preparation of the alkoxides of these electropositive elements, the obvious method of the reaction of the metals with alcohols (reported successfully in a recent publication by Mazdiyasni[7], et al) was attempted a number of times but was not pursued as the products could not be purified to a sufficient degree. The following two methods for the preparation of soluble isopropoxides and insoluble

methoxides have been found to be of general applicability.
Soluble Alkoxides: The alcoholates $LnCl_3.3ROH$, prepared
by the direct action of anhydrous chlorides with alcohols
serve as convenient starting materials. The isopropoxides
of a number of lanthanons (La, Pr, Nd, Gd, Er and Yb)
have been prepared in quantitative yields by adding to a
solution of the corresponding tris-isopropanolate in
isopropanol, a stoichiometric quantity of sodium
isopropoxide,

$$LnCl_3.3Pr^iOH + 3Na(OPr^i) \xrightarrow{\text{Benzene}} Ln(OPr^i)_3 + 3NaCl\downarrow + 3Pr^iOH$$
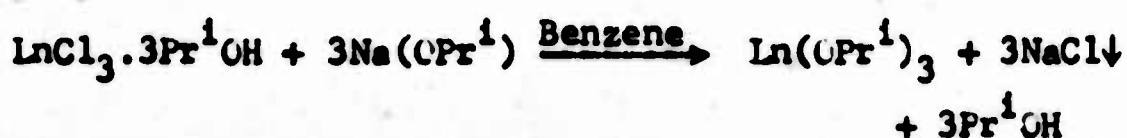
Repeated experiments have shown that for the separation
of easily filtrable granular sodium chloride, it is
essential that sodium isopropoxide in isopropanol and
benzene solution is added to the lanthanon chloride
isopropanolate and not, in the reverse direction. The
isopropoxides can in some cases be purified by crystalli-
sation or sublimation (Table I).

Alcohol interchange technique has been employed
for the synthesis of a large number of higher alkoxides
of lanthanons via simple metathetic reactions of the type:

$$Ln(OPr^i)_3 + 3ROH \longrightarrow Ln(OR)_3 + 3Pr^iOH\uparrow$$

(where R is Bu, Bu^{sec}, Bu^{tert}, Am^n, Am^{iso}, Am^{sec}.
and Am^{tert}).
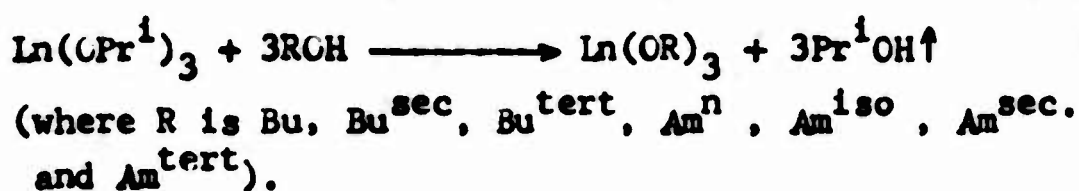
The isopropanol liberated during the course of the
reaction is fractionated out azeotropically with benzene.
With increasing ramification in the alcohols employed,
the alcoholysis reactions tended to become less facile
and the relative ease of reaction can be represented by:
primary secondary tertiary. A few typical results are
summarised in Table II.

Insoluble Alkoxides: The method suggested by Bradley[3] for the synthesis of lanthanum methoxide:

$$LaCl_3 + 3LiOMe \xrightarrow{\text{Methanol}} La(OMe)_3\downarrow + 3LiCl$$
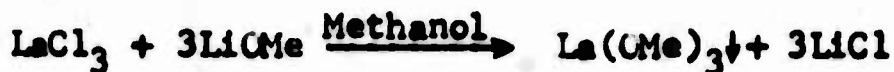
was employed for the preparation of methoxides of higher lanthanons also. However, in view of their insoluble character, the methoxides do not appears to interchange the methoxy groups readily with higher alkoxy and other organic ligands. The isopropoxides have, therefore, been generally employed for the synthesis of other metallo-organic derivatives. Even the methoxides can be precipitated readily by treating the isopropoxides with excess methanol.

Another group of insoluble derivatives of a similar nature synthesised during the course of this work are the phenoxides which can be readily isolated by stoichiometric reactions of the following type:

$$Ln(OPr^i)_3 + x\ C_6H_5OH \xrightarrow{\text{Benzene}} Ln(OPr^i)_{3-x}(OC_6H_5)_x + x\ Pr^iOH$$
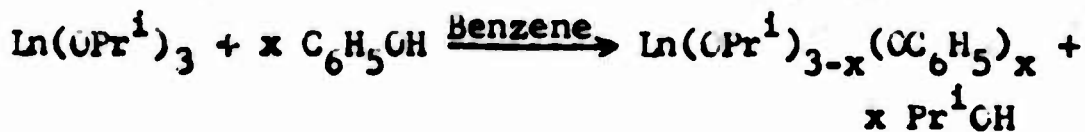
(where x = 1,2 or 3)

Reactions of Lanthanon Isopropoxides:

(i) With Acetyl Halides: The isopropoxides have been found to react exothermally with stoichiometric quantities of acetyl chloride and bromide in benzene with the formation of the corresponding halide derivatives[13-16]:

$$Ln(OPr^i)_3 + n\ CH_3COX \longrightarrow Ln(OPr^i)_{3-n}X_n.m\ CH_3COOPr^i + (n-m)CH_3COOPr^i.$$
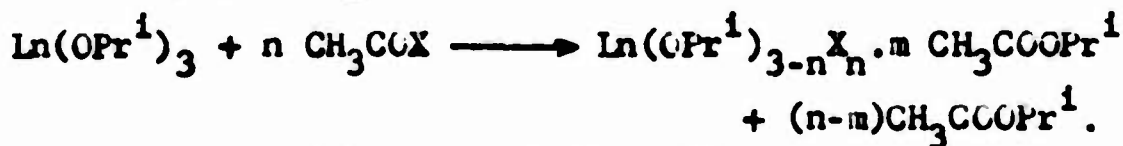
(where n = 1,2 or 3)

The halide alkoxides show an increasing tendency to add molecules of isopropyl acetates as the substitution proceeds further.

(ii) **With Glycols:** By the reactions of lanthanon isopropoxides with stoichiometric quantities of various glycols[13-14](e.g., ethylene glycol, propylene glycol, 1 methyl trimethylene glycol, 1,2 dimethyl ethylene glycol, tetramethylene glycol, pentamethylene glycol, hexylene glycol and pinacol), the following three types of derivatives have been isolated:
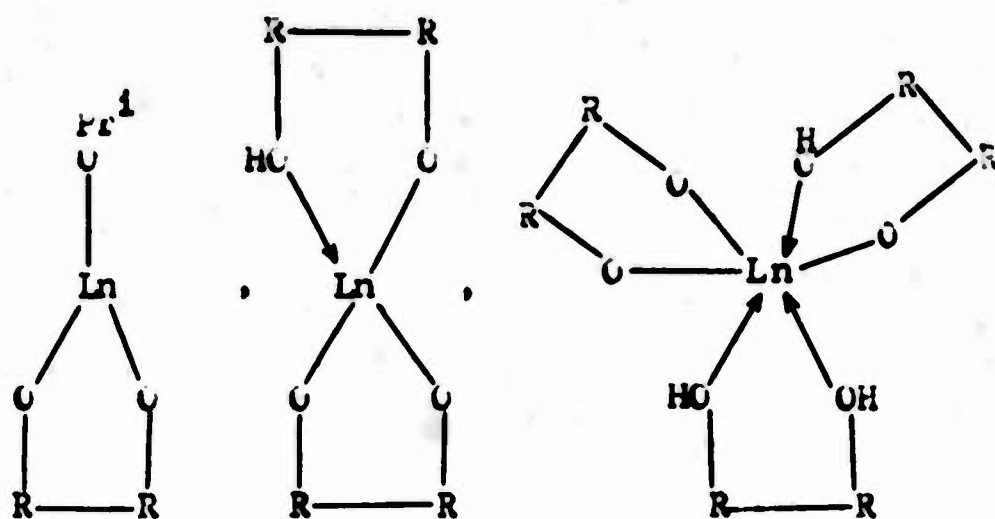
Most of these derivatives are in soluble in organic solvents, but some glycols (e.g., pinacol and hexylene glycol) tend to give soluble products.

(iii) With β-diketones and β-ketoesters: The reactions of lanthanon isopropoxides with various β-diketones[13-16] (e.g., acetylacetone, benzoyl acetone, and dibenzoyl methane) and β-ketoesters(e.g., methyl acetoacetate and ethyl acetoacetate) have been found to yield the corresponding derivatives as represented by the following general equation:

$$Ln(OPr^i)_3 + x \ R.CO.CH_2CO.R' \longrightarrow$$
$$Ln(OPr^i)_{3-x}(R.CO.CH.COR')_x + x \ Pr^iOH$$
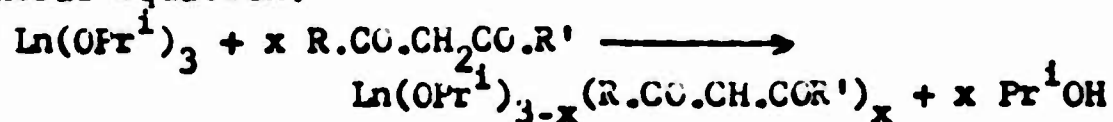
(where x = 1,2 or 3 and R = CH_3, C_6H_5, OCH_3, or OC_2H_5 and R' = CH_3 or C_6H_5).

The β-ketoester products have been reported for the first time and for the β-diketonate derivatives, these straightforward synthetic methods assume special importance in view of long standing controversies regarding the synthesis of the tris-products in the anhydrous state[17-18](Tables III & IV).

ACYLOXY DERIVATIVES OF LANTHANONS:

In view of the highly electropositive character of the lanthanons, their soaps Ln(OOCR)$_3$, (where R is $C_{11}H_{23}$, $C_{15}H_{31}$, $C_{17}H_{35}$) can be readily synthesized by treating their nitrates or chlorides with sodium carboxylate solutions in water:

$$MX_3 + 3NaCOOR \longrightarrow M(OOCR)_3 + NaX$$

The tri-acyloxides are readily precipitated in aqueous solution and can be further purified by recrystallisation from benzene.

The chloride acyloxide derivatives could not be synthesized in aqueous solutions even through the reactantes were taken in different ratios. These derivatives, including acetates can, however, be easily synthesised by simple metathetic reactions of the type:

$$MCl_3 + x\ RCOOH \longrightarrow MCl_{3-x}(RCOO)_x + x\ HCl$$

A study of the thermogravimetric properties of the acyloxy derivatives of lanthanons shown that they are stable upto 300°C, beyond which they decomposed slowly according to the following equation:

$$RCOO-Ln{\overset{\displaystyle OOCR}{\underset{\displaystyle OOCR}{\big<}}} \longrightarrow 1/2Ln_2O_3 + 3/2CO_2 + 3/2\ {\overset{\displaystyle R}{\underset{\displaystyle R}{\big>}}}C=O$$
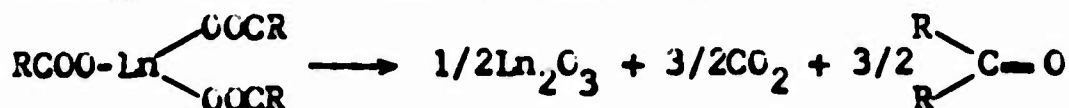
Evolution of carbon dioxide appears to be completed at about 350°C, after which there is a rapid loss of weight at a specific temperature which is characteristic for each ketone.

The properties of triacyloxides of lanthanons show marked differences from the corresponding aluminium acyloxides[19] which have been studied extensively in recent years. Although both are monomeric in boiling benzene, the latter are highly susceptible to hydrolysis and gel readily. On the contrary, lanthanon derivatives appear to be so resistant to hydrolysis that they can be prepared from aqueous solution and the viscosities of their hydrocarbon solutions to be unaffected by the addition of water.

ACKNOWLEDGEMENT:

REFERENCES:

1. Bradley, D.C., Prog. Inorg. Chem., 2, 303, 1960 ;
   Mehrotra, R.C. et al, Raj. Univ. Studies, 1965 ;
   Mehrotra, R.C. Presidential Address, Chemistry
   Section, Indian Science Congress, 1967 (and about
   200 references therein).

2. Mehrotra, R.C., J.Friedlich Schiller Univ., Jena,
   14, 171, 1965 VIth International Symposium on
   Lubricants and Lubrication Technology, Jena, 1964.

3. Bradley, D.C. and M.M.Faktor, Chem. & Ind., 1332,
   1958.

4. Sinha, R.P.N., Science & Culture, 25, 494, 1960.

5. Misra, S.N., T.N.Misra, R.N.Kapoor, and R.C.Mehrotra,
   Chem. & Ind., 120. 1963.

6. Sankhla, B.S., S.N.Misra and R.N.Kapoor, ibid., 382, 1965.

7. Mazdiyasni, K.S., C.T.Lynch and J.S.Smith, Inorg. Chem., 5, 342, 1966.

8. Batwara, J.M., U.D.Tripathi, R.K.Mehrotra and R.C. Mehrotra, Chem. & Ind., 1379, 1966.

9. Misra, S.N., T.N.Misra and R.C.Mehrotra, J. Inorg. Nucl. Chem., 25, 195, 1963.

10. Misra, S.N., T.N.Misra and R.C.Mehrotra, J. Inorg. Nucl. Chem., 25, 201, 1963 ; J. Ind. Chem. Soc., 43, 61, 1966.

11. Lempicki, A., and H.Samelson, Lasers Vol. I, Ed. A.K.Levine, Marcel Dekker (N.Y.), 1966, p. 181.

12. Crossby, G.A., Molecular Crystals 1, 37, 1966.

13. Misra, T.N., Ph.D. Thesis, University of Rajasthan, 1963.

14. Misra, S.N., Ph.D. Thesis, University of Rajasthan, 1964.

15. Batwara, J.M., U.D.Tripathi and R.C.Mehrotra, J. Chem. Soc. (in press).

16. Batwara, J.M., U.D.Tripathi and R.C.Mehrotra, (unpublished results).

17. Moeller, T., et al, Chem. Rev., 65, 1, 1965.

18. Pope, G.W., J.F.Steinbach and W.F.Wagner, J. Inorg. Nucl., 20, 304, 1961.

19. Mehrotra, R.C., Nature, 172, 74, 1953 ; Pande, K.C. and R.C.Mehrotra, J. Inorg. Nucl. Chem., 2, 60, 1956; 4, 128, 1957 ; Mehrotra, R.C. and A.K.Rai, J. Ind. Chem. Soc., 39,1, 1962; 40, 359, 1963.

TABLE I
Isopropoxides of Lanthanons

Isopropo-xides.	Colour	Purification sublimation/ °C/0.01 mm or crystalli-sation.	Analysis			
			% Metal		% OPr^i	
			Found	Calc.	Found	Calc.
La(OPr^i)$_3$	White	250-280	43.7	43.9	55.8	56.1
Pr(OPr^i)$_3$	Green	Crystallised	44.4	44.2	55.4	55.8
Nd(OPr^i)$_3$	Reddish-violet	230-250	44.8	44.9	55.2	55.1
Gd(OPr^i)$_3$	Light yellow	200-210	47.0	47.0	52.9	53.0
Er(OPr^i)$_3$	Pink	180-190	48.5	48.5	51.2	51.5
Yb(OPr^i)$_3$	White	Crystallised	49.2	49.4	50.6	50.6

Table II

Products of alcohol interchange reaction of Ln(OPr^i)$_3$, as exemplified by gadolinium

Alkoxide	Nature	Analysis	
		% Metal	
		Found	Calc.
Gd(OMe)$_3$	White powder insoluble in benzene	62.7	62.8
Gd(OEt)$_3$	White powder sparingly soluble in benzene	53.5	53.8
Gd(OBu^n)	Golden yellow coloured powder soluble in organic solvents	42.0	41.8
Gd(OBu^s)$_3$	Yellow powder soluble in organic solvents	42.8	41.8
Gd(OBu^t)$_3$	-do-	42.3	41.8
Gd(OAm^n)$_3$	-do-	39.1	38.5
Gd(OAm^t)$_3$	-do-	39.5	38.5

TABLE III

Reactions between lanthanon isopropoxides (e.g., $Gd(OPr^i)_3$) with β-diketones (e.g., benzoylacetone)

S.No.	Reactants (g)	Molar ratio	Product & nature	Molecular complexity	%Metal Found	%Metal Calc.	Azeotrope Found	Azeotrope Calc.
1.	$Gd(OPr^i)_3$ 2.37 Bzac* 1.32 benzene 70	1:1	$Gd(OPr^i)_2(Bzac)$ Yellow foamy solid	3.07	35.84	36.04	.47	.48
2.	$Gd(OPr^i)_3$ 2.15 Bzac 2.08 benzene 65	1:2	$Gd(OPr^i)(Bzac)_2$ Yellow foamy solid	2.95	29.22	29.18	.74	.77
3.	$Gd(OPr^i)_3$ 1.88 Bzac 2.74 benzene 74	1:3	Golden yellow solid, hygroscopic $Gd(Bzac)_3$	1.67	24.4	24.5	1.00	1.01

* Bzac = Benzoyl acetone.

TABLE IV

Reactions between Lanthanon isopropoxides (e.g., $Gd(OPr^i)_3$) with β-ketoesters (e.g., ethylacetoacetate) and alcohol interchange reactions of the products

S.No.	Reactants (g)	Molar ratio	Products and nature	Molecular complexity	Analysis %Metal Found	%Metal Calc.	Azeotrope(g) Found	Azeotrope(g) Calc.
1.	$Gd(OPr^i)_3$ 2.0 * eaa 0.76 Benzene 55	1:1	$Gd(OPr^i)_2(eaa)$ Yellow solid	3.00	39.08	38.88	.357	.359
2.	$Gd(OPr^i)_3$ 1.47 eaa 1.14 Benzene 52	1:2	$Gd(OPr^i)(eaa)_2$ Yellow solid	3.09	33.78	32.99	.537	.530
3.	$Gd(OPr^i)_3$ 1.29 eaa 1.52 Benzene 48	1:3	$Gd(eaa)_3$ Yellow Microcrystalline solid	2.07	29.05	28.86	.688	.700
4.	$Gd(OPr^i)_2-$ .718 (eaa) Bu^{t}OH 4.7 Benzene 54	1: excess	$Gd(OBu^t)_2(eaa)$ Yellow solid	2.97	36.68	36.36	.180	.186
5.	$Gd(OPr^i)-$ 1.0 (eaa)$_2$ Bu^{t}OH 5.0 Benzene 51	1: excess	$Gd(OBu^t)(eaa)_2$ Yellow solid	2.98	32.63	32.28	.148	.148

* eaa = ethyl acetoacetate

PROBLEMS AND PROGRESS IN METALLURGY OF THE RARE EARTHS

Karl Gschneidner, Jr.
Department of Metallurgy and
Institute for Atomic Research
Iowa State University
Ames, Iowa   50010

The problems in the metallurgy of the rare earths have been divided into three basic areas: chemical, physical and mechanical. The first of these three is the most important since the rate of progress in the chemical area effects much of the work being carried out in the latter two fields.

The most difficult problem today, as it has been for many years, and as it will be in the foreseeable future is the preparation of "high purity" metals. Each time another nine is achieved, there is an ever-ready demand for further lowering of the impurity content. In addition to this recurring problem, concurrent problems are the differences in the behavior of the individual rare earths which requires a variety of procedures for preparing the individual metals, and the need for continuous improvement of analytical techniques.

Primarily because of the lack of purity, most of the rare-earth phase diagrams determined before 1945 are incorrect. Of the 1160 possible rare-earth binary alloys systems, only a few per cent of these have been well established. This points out the need for accurate knowledge of the phase relationships, which are especially needed for studies of the physical properties of intermetallic compounds and solid solution alloys. A systematic study, not only of the phase relationships, but of many of the physical properties is underway and these results should add much to our understanding of the alloying behaviors of these metals.

The paucity of investigations on the mechanical properties of these metals is unfortunate. Although the results from a few measurements of the ultimate

tensile and yield strengths, elongation and hardness are available, these were undoubtedly made on low purity (~ 99%) metals. Essentially no information is available on the modes of plastic deformation; slip systems; point (vacancies and solutes), line (dislocations) and clustered defects; stacking fault energies; work and precipitation hardening; fracture; creep; fatigue; and workability of the rare earths. With the availability of higher purity rare-earth metals, this area of research will begin to bear fruit and may yield valuable insight to the theory of the plastic behavior of metals.

The crystal structure sequence of the rare-earth metals, and their polymorphic transformations have been studied for many years. But as our range for observing these is extended by either temperature, pressure, composition (or by any two or all three variables) and as new research techniques are applied, we will have a better knowledge of the nature of the forces interacting between atoms, and we will know a great deal more about the transformation mechanisms.

SELF-IRRADIATION EFFECTS IN A CERIUM ALLOY
CONTAINING 15 AT. % PLUTONIUM*

R. O. Elliott, W. N. Miner and F. W. Clinard, Jr.

University of California, Los Alamos Scientific Laboratory,
Los Alamos, New Mexico

ABSTRACT

Four samples of an α-phase cerium alloy (85 at. % Ce-15 at. %
Pu) were stored at 20°K for 1076 hr. The plutonium used in making
the samples was variably enriched with Pu^{238} isotope to provide
four different levels of irradiation. Accumulation of lattice
damage due to the alpha activity of plutonium was followed by
periodically measuring the electrical resistivities of the samples
during storage at low temperature. Annealing of damage was then
followed from 20° to 350°K, by the isochronal method. Results are
discussed in terms of the nature of the lattice damage.

Background. Between room temperature and 0°K cerium can exist in three allotropic forms, α, β and γ. The γ-form (fcc with a_o = 5.16A) and the β-form (double hcp) exist at room temperature. On cooling, γ transforms electronically, at roughly 110°K, to the more dense α-form (fcc with a_o = 4.85A). On heating, the reverse transformation, $\alpha \rightarrow \gamma$, takes place with considerable hysteresis at about 170°K.

The relative amounts of these phases can be altered by small amounts of alloy additions[1,2] or impurities,[3] by heat treatment[3] and by deformation.[4] Some β is formed in γ cerium cooled to low temperature, and under repeated cycling the proportion of β retained at room temperature increases.[3] This tendency to form β during thermal cycling is enhanced by the addition of 2 at. % of any of the lanthanides.[2] On the other hand, the addition of plutonium suppresses the formation of β so that with the proper alloy content and heat treatment β will not be formed during low temperature cycling. Plutonium additions extend the range of α-phase stability in cerium-rich alloys by raising both the $\gamma \rightarrow \alpha$ and $\alpha \rightarrow \gamma$ transformation temperatures.[1]

Plutonium, and alloys containing plutonium, are continually irradiated by the alpha activity, and at low temperatures detectable radiation damage may be produced. A summary of Vineyard's[5] picture of this self-damage in plutonium is as follows. The common plutonium isotopes (except Pu^{241}) decay by emitting alpha particles having energies between 5 and 5.5 MeV. The main isotope of plutonium is Pu^{239}. It has a half-life of 24,360 yr, 9×10^{-13} of the atoms present decaying each second by alpha-particle emission with energy about 5.15 MeV. The residual U^{235} nucleus recoils with an energy of about 87 KeV, and must be taken into account when damage effects are computed. The absorption of the energy of these decay products by the lattice is responsible for self heating in plutonium and in alloys containing plutonium.

The alpha activity has little or no effect on the physical properties of plutonium at room temperature, but at low temperatures some of the defects produced in the lattice remain and very

substantially affect properties such as electrical resistivity,[6,7] stored energy[8] and thermal expansion.[9] Vineyard estimates that an alpha particle travels about 6 μ in α-phase plutonium before coming to rest, probably as an interstitial helium atom. The recoil nucleus travels a much shorter distance, perhaps only 60Å, before coming to rest and lodges presumably as either an interstitial or substitutional impurity. Both particles make numerous secondary displacements while slowing down. The formation of large clusters and the production of phase transformation due to "spike" effects are also possible. His calculations predict that roughly 2000 interstitial-vacancy pairs are created per disintegration. There is an estimated 1% concentration of interstitial-vacancy pairs accumulated in Pu^{239} when it is stored for 1500 hr at low temperature.

Calculations for α-cerium containing 15 at. % plutonium show a similar picture of the damage process, except that the range of alpha particles is 8 to 9 μ and the range of the recoil nucleus is about 90Å. The length of time required to produce 1% interstitial-vacancy pairs in the alloy depends on the isotopic content of plutonium, being about 10,000 hr when the solute is Pu^{239}. The present work represents the first time to our knowledge that radiation damage studies have been made in the rare earths.

Samples and Procedure. Four samples were used in the investigation. All contained 85 at. % cerium and 15 at. % plutonium, but their Pu^{238} content provided four different levels of alpha activity. Pu^{238} has a much shorter half-life than does Pu^{239}; it decays about 280 times faster than Pu^{239}. Consequently increasing the proportion of Pu^{238} at the expense of Pu^{239} in an alloy containing plutonium will increase the alpha activity but leave the plutonium content of the alloy unchanged. Table 1 lists the isotopic compositions of the four samples and their self heats, as calculated from the known self heats of the isotopes.

The cerium was electrowon metal furnished by the U. S. Bureau of Mines, Reno, Nevada. Spectrochemical analyses showed that it contained the following impurities, in ppm (by weight): 500 Mo, 300 Fe, 100 Mg, 100 Al, 50 Cu, 30 Si and 20 Li, and chemical analysis revealed the presence of 320 C and 120 O_2. Any other impurities present were below the detectable limits for the methods used. The electrorefined Pu^{239}

Table 1. Self heats (in mW/gm of sample) and plutonium
isotopic analyses (in at.%) of 4 samples of a
cerium alloy containing 85 at.% Ce - 15.% Pu.

Sample No.	Self heat	Pu^{238}	Pu^{239}	Pu^{240}	Pu^{241}
1	1.56	0.13	14.07	0.76	0.05
2	2.71	0.26	13.95	0.76	0.05
3	4.84	0.52	13.71	0.74	0.05
4	11.36	1.29	12.99	0.70	0.04

contained 69 (ppm) W, 36 Am, 35 C, 30 Fe, 10 H, 4 N, 2 Ni and between
10 and 80 O_2. The 85 per cent enriched Pu^{238} stock that was mixed with
the Pu^{239} to provide the different levels of alpha activity was not
analyzed to identify specific impurities, but is known to have been
less pure than the Pu^{239}. However, the Pu^{238} stock was used in such
small proportions, ranging from 0.13 to 1.29 a/o, that it could hardly
have caused any serious degradation of the overall purities of the
specimens.*

The alloy components for each specimen were arc melted together,
and the resulting button was inverted and remelted 7 to 9 times to
insure its homogeneity. After the final melting, an elongated ingot
was arc cast in a depression in the water-cooled copper hearth of the
arc furnace. The ingot was then rolled at room temperature to form a
square cross-sectional rod (0.290 in. by 0.290 in.), which was machined
to form a cylindrical specimen 1/4 in. dia by 1 in. long.

Plutonium is soluble in α-cerium up to about 37 at.% at 592°C.
The equilibrium solubility decreases rapidly with decreasing temper-
ature.[10] Single-phase γ alloys containing 15 at. % plutonium can be
retained at room temperature and below by being quenched rapidly from
600°C into cold water. Therefore, after being machined the samples
were wrapped in tantalum foil, sealed in an argon atmosphere within
silica capsules, held at 600°C for 17 hr and then quenched in cold

---

* The overall impurity level of the alloy samples is higher than
that normally encountered in radiation damage studies. The metal
stocks used, however, were of the highest purity obtainable.

water. The density of the samples, 7.81 g/cm^3, indicated that they were indeed mostly γ phase, this value falling exactly on the density-vs-composition curve that has been established by X-ray data for γ-phase cerium-plutonium alloys.[10]

The four samples were loaded into the apparatus and quenched from room temperature to 20°K, where they were stored for 1076 hr to allow accumulation of measurable amounts of lattice defects. Resistivity measurements were made periodically at the storage temperature to follow the accumulation of defects. Annealing of the defects was then accomplished by the isochronal method, the specimens being heated rapidly to the first (lowest) annealing temperature, held there for 30 minutes, and then quenched back to the 20°K reference temperature where the resistivities were again measured to determine the amount of any annealing that had taken place. This procedure was followed in subsequent heatings to successively higher annealing temperatures, interrupted by cooling back to 20°K for the resistivity measurements. During the 30-min anneals the temperature was held constant to ± 0.5°K.

After the annealing runs had been completed, resistivity-vs-temperature data were obtained between ~ 2°K and room temperature, while the specimens were being heated at the rate of 1/2°K/min, to reveal whether any β cerium had been formed during the numerous quenchings to 20°K and whether any massive precipitation of δ plutonium had occurred. The absence of any evidence for the magnetic ordering of β in the vicinity of 12°K indicated that no β had formed,[4] and the lack of any lowering of the $\alpha \rightarrow \gamma$ cerium transformation temperature suggested that little, if any, precipitation of δ plutonium had taken place.

Details of the temperature and resistivity measuring systems have been reported elsewhere.[11] The accuracy of the temperature measurement was estimated to be ± 0.5°K, and the overall sensitivity of the resistivity apparatus was such that changes as small as 0.01 $\mu\Omega$-cm were detectable.

Accumulation of Damage. Accumulation of self-irradiation damage occurred in all four samples during storage at 20°K and is shown in

Figure 1* as increases in resistivity with time. These increases reflect the formation of interstitial-vacancy pairs (Frenkel pairs), produced in the lattice by the alpha particles and recoil uranium nuclei resulting from the radioactive disintegration of plutonium. The fraction of the plutonium atoms that disintegrates per second depends on the isotopic content of the plutonium (see Table 1), being 5.37×10^{-13} for Sample 1. The initial rate of resistivity rise of this sample amounted to 1.08×10^{-3} μ Ω-cm per hour or 3.0×10^{-7} μ Ω-cm per second. Thus, assuming that 2000 atoms are displaced per alpha-disintegration, the resistivity rise per 1% Frenkel pairs is indicated to be

$$\frac{3.0 \times 10^{-7} \ (\mu \ \Omega\text{-cm/sec})}{5.37 \times 10^{-13} \ (\text{dis./sec}) \ 2000 \ (\text{F pairs/dis.})} \times \frac{1}{100} \cong 2.8 \ \mu \ \Omega\text{-cm}$$

This approximate value was also obtained by such an analysis of the other three samples.

The above value is very substantially lower than that predicted by Walker's rule.[12] This rule is based on the empirical observation that 1% of F pairs in a given metal causes an increase in the residual resistivity about equal to the resistivity change that occurs between 0°K and room temperature in the same metal. It has been roughly verified for a number of common metals. If Walker's rule is applicable, then 1% of F pairs would be expected to raise the low-temperature resistivity of our alloy by ~ 15 μ Ω-cm and would suggest the production of about 400 F pairs per disintegration that would contribute to the resistivity.

The nature of heavy charged-particle damage[13] leads one to expect highly localized damage, including the formation of large clusters of defects and also possible spontaneous recombination of close interstitial-

---

* The curves shown in Figure 1 have been corrected to take account of the dimensional changes that occurred in the samples when γ transformed to α, but no corrections were made for the smaller changes due to thermal expansion. The curves represent computer best fits of the data, with standard deviations of ± 0.066, ± 0.054, ± 0.060 and ± 0.077 μ Ω-cm for Samples 1, 2, 3 and 4, respectively.

vacancy pairs. Although 2000 atoms may have been displaced per
disintegration, only about 400 appear to have been retained as
interstitials in the lattice. Presumably the others are at traps
or sinks and do not contribute much to resistivity. Thus, this
model explains qualitatively why the initial rates of rise were much
lower than anticipated.

It can be seen in Figure 1 that the rate of resistivity rise
decreased with time. The effect was most pronounced in Sample 4, which
had the greatest alpha activity. This negative curvature may be
attributed to increased clustering and recombination of interstitial-
vacancy pairs as the defect concentration increased. An additional
mechanism might be the annealing of damaged regions by thermal spikes.
Vineyard estimates that 10^4 atoms would be involved in spike effects
for every disintegration in plutonium. Since 4 atoms in 10^{12} dis-
integrate each second in Sample 4, every atom should be involved once
in a thermal spike within about a year. Therefore, at least 10% of
the atoms could have been annealed in this sample during storage for
1076 hr.

The initial slopes of the damage curves, as seen in Figure 2, are
a linear function of the self-heats of the samples. In contrast to
this, a non-linear damage rate is predicted by Neely and Sosin[14] when
interstitials, created during irradiation, are trapped by intrinsic
defects such as impurities. According to their model, the added
resistivity is proportional to the square-root of the integrated
electron flux. In the present samples one might reasonably infer
that no significant trapping of interstitials by plutonium impurity
atoms occurred or that if trapping did occur the ability of trapped
interstitials to influence the resistivity was unimpaired. (One in
seven atoms is plutonium, a smaller atom than cerium, and thus might be
expected to be a trap for interstitials.)

Annealing. The isochronal annealing of radiation damage was rather
similar in all four samples, with the exception of the region from
250° to 350°K. Therefore, we have chosen to show in Figure 3 the
complete isochronal annealing curve for Sample 4 and only the region
above 250°K for the other samples. The annealing behaviors were

considerably different above 255°K and will be discussed below. There appear to be four minor stages or sub-stages of annealing, at 65°, 82°, 120° and 200°K, and one major stage in the 255° - 280°K region, as may be seen in the figure. The 255° - 280°K stage is partially obscured by the onset of the α → γ transformation.

The annealing can also be viewed as taking place continuously throughout the range from 30° to 25°K, but proceeding faster in the two regions near 80° and 250°K. The absence of discrete steps in the annealing behavior is consistent with the complex nature of the damage discussed earlier. About 60% of the resistivity had been recovered at 250°K. Interstitials typically have lower migration energies than do vacancies, and therefore it is believed that most of this 60% recovery is associated with annealing of interstitials. It is likely that a significant number of vacancies remained in the lattice at the α → γ transformation temperature.

The isochronal data above the α → γ transformation temperature are shown in Figure 3 for all four samples. It is seen that above 255°K the fraction of resistivity remaining at 20°K first rose and then fell with increasing annealing temperature. Similar resistivity effects are known to occur when supersaturated solid solution alloys undergo a precipitation-hardening reaction.[15] If such an explanation is applied here, the implication is that the precipitation of δ-phase plutonium alloy[10] is not disturbed by thermal cycles through the α ⇌ γ transformation, which were inherent in the experiment. The question remains of whether such a possible precipitation effect is associated with radiation damage or whether it is solely a thermal effect. This aspect of the present results is under investigation.

REFERENCES

1. K. A. Gschneidner, Jr., R. O. Elliott and R. R. McDonald, J. Phys. Chem. Solids 23, 1191 (1962).

2. F. W. Clinard, Jr., to be published in J. Appl. Phys.

3. R. O. Elliott and W. N. Miner, to be published in Trans. A.I.M.E.

4. M. K. Wilkinson, H. R. Child, C. J. McHargue, W. C. Koehler and E. O. Wollan, Phys. Rev. 122, 1409 (1961).

5. G. H. Vineyard, private communication (1961).

6. D. A. Wigley, Ph. D. thesis, University of Oxford (1964).

7. R. O. Elliott and C. E. Olsen, in Studies in Radiation Effects: Part I. Physical and Chemical, edited by G. J. Dienes, to be published by Gordon and Breach, New York.

8. J. C. Taylor, R. G. Loasby, D. J. Dean and P. F. Linford, 3rd Intl. Confr. on Plutonium, London (1965); proceedings to be published.

9. R. Lallement and P. Solente, 3rd Intl. Confr. on Plutonium, London (1965); proceedings to be published.

10. F. H. Ellinger, C. C. Land, K. A. Johnson and V. O. Struebing, Trans. A.I.M.E. 236, 1577 (1966).

11. F. W. Clinard, R. O. Elliott and W. N. Miner, Phys. Stat. Sol. 11, 595 (1965).

12. P. G. Lucasson and R. M. Walker, Phys. Rev. 127, 1130 (1962).

13. A. C. Damask and G. J. Dienes, Point Defects in Metals, Chpt. 1, Gordon and Breach, New York (1963).

14. H. H. Neely and A. Sosin, Phys. Rev. 152, 623 (1966).

15. D. S. Billington and J. H. Crawford, Jr., Radiation Damage in Solids, p. 187, Princeton University Press, Princeton, N. J. (1961).
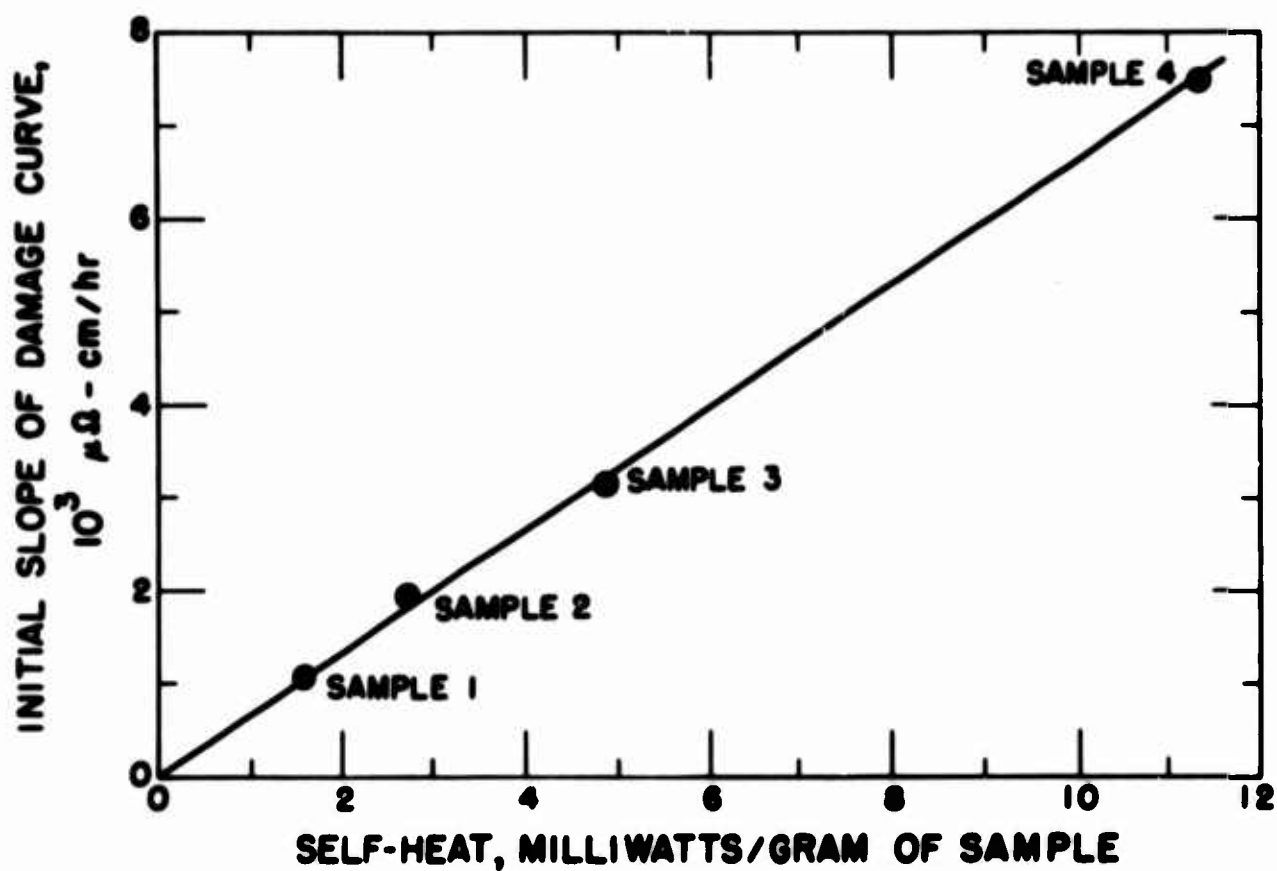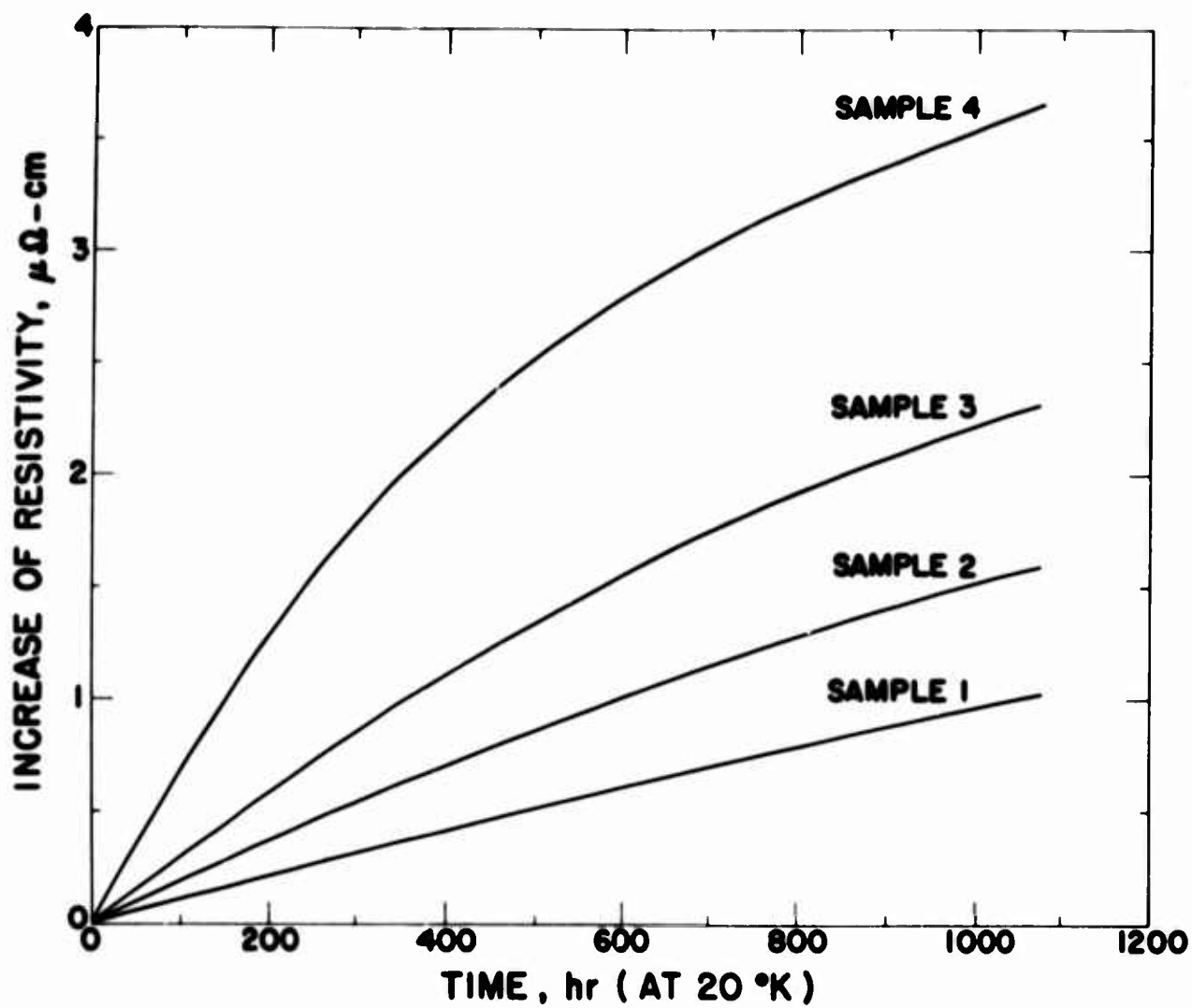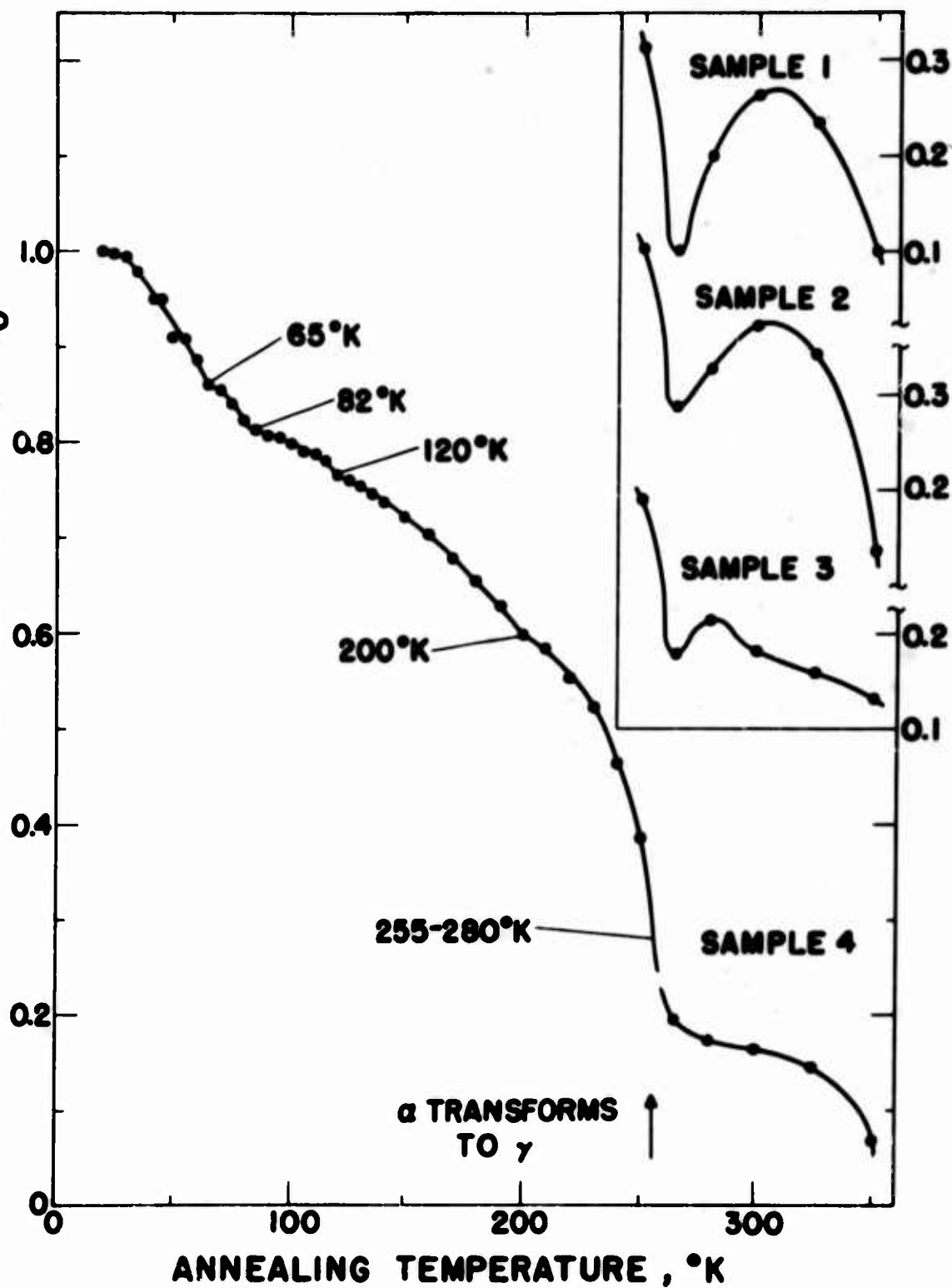
A METALLOGRAPHIC STUDY OF THE ALLOTROPIC PHASE TRANSFORMATIONS IN CERIUM*

C. C. Koch and C. J. McHargue
Metals and Ceramics Division
Oak Ridge National Laboratory
Oak Ridge, Tennessee

ABSTRACT

Some aspects of the phase transformations in cerium were studied by using metallography. The percent dhcp formed by athermal transformation vs temperature as determined by X-ray diffraction has been confirmed by quantitative metallography. The influence of plastic deformation on the transformation has been studied by deforming cerium specimens at temperatures above and below M_s. Metallography definitely indicates that deformation promotes the fcc $\rightarrow$ dhcp reaction. A M_d temperature has been determined. It appears that a tensile component of deformation is necessary for the fcc $\rightarrow$ dhcp transformation which may explain the conflicting evidence of the effect of deformation on this transformation. The influence of deformation on subsequent athermal transformation and reversion has been studied.

The morphology of the fcc $\rightleftarrows$ dhcp transformation has been examined and lattice relationships have been inferred.

INTRODUCTION

The allotropic phase transformations which occur in cerium near
and below room temperature have been the subject of several investi-
gations in the past decade. Limited X-ray evidence as well as
anomalies in physical properties suggested the existence of three
possible crystal structures in the temperature range 4.2°K to room
temperature (1,2). By a detailed X-ray study, McHargue and Yakel (3)
confirmed the existence of these structures, catalogued the tempera-
ture range over which each was found, and observed the transforma-
tions to be very sensitive to prior metallurgical history. The
crystal structure of an annealed cerium specimen at room temperature
is fcc. At $263 \pm 10^{\circ}$K the fcc phase begins to transform to a double
hexagonal close-packed phase (dhcp) which is isomorphous to the ABAC
stacked structure of lanthanum, praeseodymium, and neodymium. At
lower temperatures (95°K $\rightarrow 40^{\circ}$K), first the fcc, then the dhcp phase
transforms to a collapsed fcc phase (fcc') thereby undergoing a
16.5% volume decrease. The transformation temperatures in cerium
are summarized in Table 1. (3). A subsequent neutron diffraction

Table 1. Transformation temperatures in cerium

Transformation	Start ($^{\circ}$K)	Finish ($^{\circ}$K)
fcc → hcp*	263 ± 10	**
hcp → fcc	373 ± 5	420 ± 5
fcc → fcc'	96 ± 5	near 4.2
fcc' → fcc	160 ± 10	195 ± 15
hcp → fcc'	between 40 and 77	**
fcc' → hcp	125 ± 5	200 ± 10

*Specimens annealed at 625°K.

**Reaction never observed to go to completion.

study (4) essentially confirmed the above results. However, there was a conflict regarding the influence of plastic deformation on the fcc → dhcp transformation. The X-ray results indicated deformation stabilized the fcc phase while neutron diffraction evidence showed deformation promotes the fcc → dhcp transformation. Another X-ray investigation (5) claimed that large amounts of plastic deformation promote the transformation to dhcp and increase its percentage formed on subsequent low-temperature treatments. Recently, Rashid and Altstetter (6) studied the transformations in cerium by dilatometric, resistometric, X-ray diffraction, and metallographic techniques. Their work confirmed the sequence of phases formed and gave additional evidence on the influence of cycling and the morphology of the transformations. They also found that deformation induces the fcc → dhcp transformation.

Most of the investigations of the phase transformations in cerium to date have been by X-ray diffraction or more "indirect" physical property measurements. Rashid and Altstetter have observed surface relief markings due to the fcc → dhcp and fcc → fcc' transformations. However, no extensive study of these transformations, by optical or electron microscopy, has been reported. This is probably due to the difficulties involved in the metallographic preparation of cerium. The chief problems to the metallographer are the preparation of a strain-free surface and the protection of this surface from oxidation during further preparation and examination. Recently a metallographic technique has been developed for cerium (7) using chemical polishing and anodizing which clearly reveals the structure, protects it from the atmosphere, and helps identify the phases present. This work was initiated, therefore, to use metallography to study the phase transformations in cerium, with special emphasis on the controversial influence of plastic deformation on the fcc $\rightleftarrows$ dhcp transformation.

EXPERIMENTAL

Cerium ingots of 99.9+ purity were obtained from Johnson and Matthey and Company, Ltd. These ingots were remelted in degassed Ta crucibles in a dynamic vacuum of 10^{-7} mm Hg. Cylindrical specimens approximately 0.250 in. in diameter by 0.080 in. high were cut from the above ingot. All specimens were wrapped in tantalum foil and heated for 1 hr at 773°K in a dynamic vacuum no worse than 5×10^{-6} mm Hg. This treatment produced the fcc structure which is stable at room temperature. For cooling below room temperature, specimens were immersed in solid CO_2 - acetone solutions (298° to 195°K) or liquid nitrogen. Heated silicone oil was used at temperatures up to 473°K for short periods. Deformation was carried out by compressing the cerium cylinders approximately 40% in a hydraulic press. Polished aluminum dies were used, and for deformation temperatures greater than 20°C the specimen and dies were immersed in heated silicone oil. Tests conducted below 298°K involved precooling the dies, and immersion of the assembly in the appropriate coolant. The temperature was measured with a thermocouple placed against the specimen.

Metallographic preparation of all specimens was carried out by a chemical polishing and anodizing technique, the details of which are described elsewhere (7). The thickness and therefore the interference color of the anodic films was found to be a function only of crystal structure for a given voltage in the electrolytic cell. All our specimens were anodized at 22 ± 2 volts. These conditions produced a blue anodic film on the fcc crystals and a yellow or tan film on dhcp regions. A point counting technique described by Hilliard (8) was used to obtain the volume percent of the two phases present in a given sample. A number of the metallographic specimens were placed in a Norelco diffractometer for X-ray diffraction analysis. The thin anodic oxide film served to protect the specimens for these studies and did not interfere with the results; no oxide lines were detected.

RESULTS AND DISCUSSIONS

Athermal Transformation fcc ⇄ dhcp

Since the low-temperature allotropic transformations in cerium have many of the characteristics of a martensitic transformation, for the purposes of this paper the terminology of martensite will be applied. Therefore, the temperature at which fcc → dhcp starts ($263 \pm 10^{\circ}$) will be termed M_s, and dhcp → fcc (373 ± 5) will be called A_s, etc.

The athermal fcc → dhcp transformation was studied by cooling previously annealed specimens (773°K anneal) to various temperatures and observing the transformation at room temperature. This was feasible since A_s is well above room temperature ($373 \pm 5^{\circ}$K). The percent fcc phase was determined by quantitative metallography and is plotted against temperature in Fig. 1 along with the X-ray results of McHargue and Yakel (3). Considering the scatter inherent due to variation in purity, strain, and grain size from specimen to specimen the agreement is excellent. This experiment served the dual purpose of verifying the earlier X-ray results and justifying the use of the metallographic

ORNL DWG 67-1420

Percent fcc vs Temperature (°K)
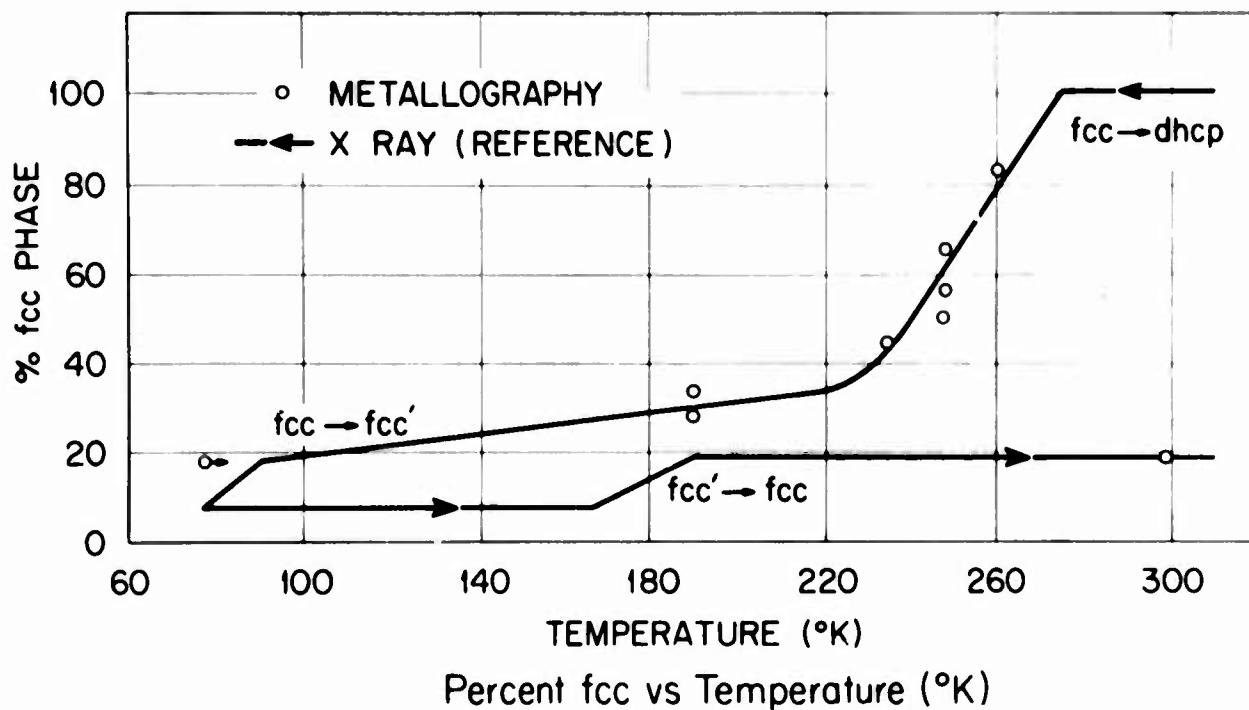
technique. An example of the microstructure of cerium athermally trans-
formed at 195°K is presented in Fig. 2. The dark (blue) areas are fcc
while the lighter (yellow) regions are dhcp.

Fig. 2. Cerium athermally transformed
at 195°K. Magnification 500 X.

The dhcp → fcc reversion temperature range (373 - 420°K) was also
confirmed metallographically.

Influence of Deformation

The influence of plastic deformation on the stability of the fcc
structure above M_s was examined by compressing specimens approximately
40% at temperatures from room temperature to 473°K. Deformation at
room temperature was found to promote the fcc → dhcp transformation.
Transformation was observed throughout the specimen cross section but
was most prevalent away from the center. The microstructure of cerium
deformed at room temperature is shown in Fig. 3. The light regions are
the dhcp transformation product. X-ray diffractometer traces indicated
only broad increases in intensity at angles where the dhcp lines are
expected. This is consistent with the work of Dillamore et al. (5) who
could resolve dhcp lines only after deformations by rolling of 70% or
greater. Therefore it seems the metallographic technique is more sensi-
tive than X-ray diffraction for observation of the strain-induced
transformation.
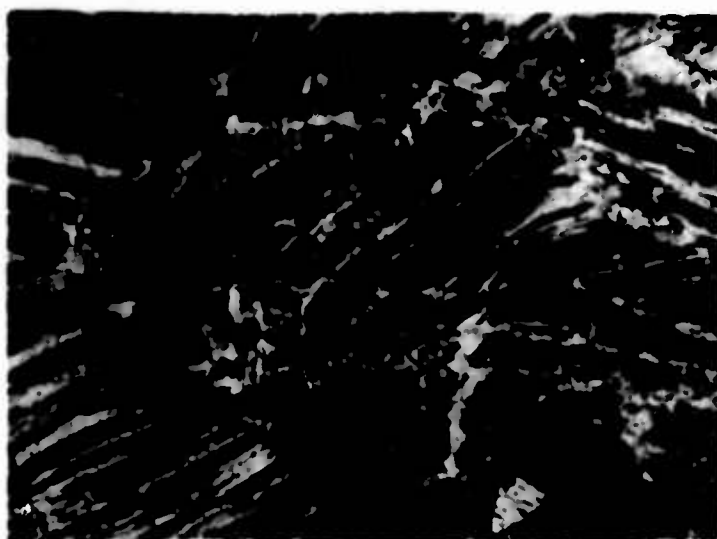
Fig. 3. Cerium plastically deformed
at 298°K. Magnification 1000 X.

A constant (~ 40%) amount of deformation was maintained for the
various temperatures of deformation. As the temperature was increased,
progressively less transformation product was observed, until in a
specimen deformed at 468°K only small amounts of dhcp phase were present
in a few grains. Corresponding to the smaller percentages of dhcp
formed at higher temperatures, this transformation product became more
localized toward the edge of the specimen. At temperatures greater than
323°K the center of the specimen was completely free from dhcp phase.
This is illustrated in the photomicrographs of Figs. 4(a) and 4(b). In
Fig. 4(a) the microstructure is that of the edge of a specimen deformed
at 338°K showing the deformation-induced dhcp phase. No transformation
is evident in Fig. 4(b), a micrograph from the center of the same speci-
men. It was also observed that the amount of dhcp phase varied markedly
with grain orientation. Since plastic compression introduces macro-
scopic tensile stresses near the edge of a cylindrical specimen, it would
appear that such stresses are necessary to produce the transformation to
dhcp at the higher temperatures. The ease of transformation is also
dependent on orientation.

The influence of deformation above M_s on subsequent athermal trans-
formation by cooling below M_s was also investigated. Athermal transforma-
tion occurred only at the very center of deformed specimens, that is in

- 422 -
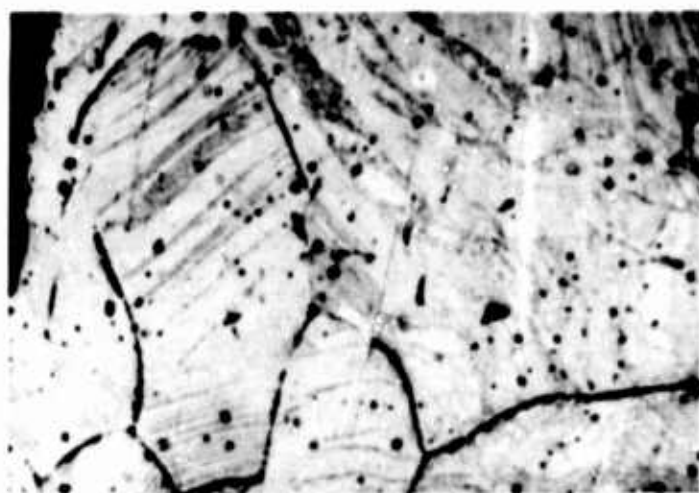
Fig. 4(a). Cerium deformed at 338°K -
edge of specimen. Magnification 160 X.
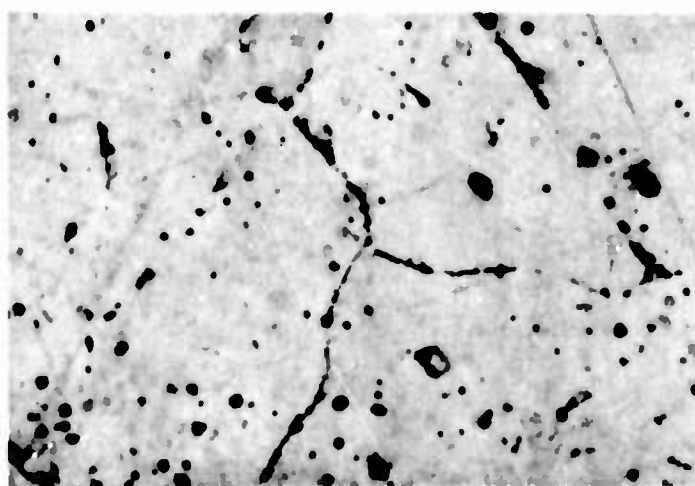
Fig. 4(b). Cerium deformed at 338°K -
center of specimen. Magnification
160 X.

the region where no deformation dhcp was formed. The photomicrograph of
Fig. 5 illustrates this, showing the center of a specimen athermally
transformed at 195°K after deformation at 368°K. Therefore, as in many
martensitic reactions (9), deformation above M_s stabilizes the parent
(fcc) phase in cerium.

In addition, the effect of plastic deformation below M_s on the
phase transformations in cerium was studied. A specimen was deformed
at 195°K. Stress-state was again seen to be of great importance. The
center of the specimen contained the approximate amount dhcp expected
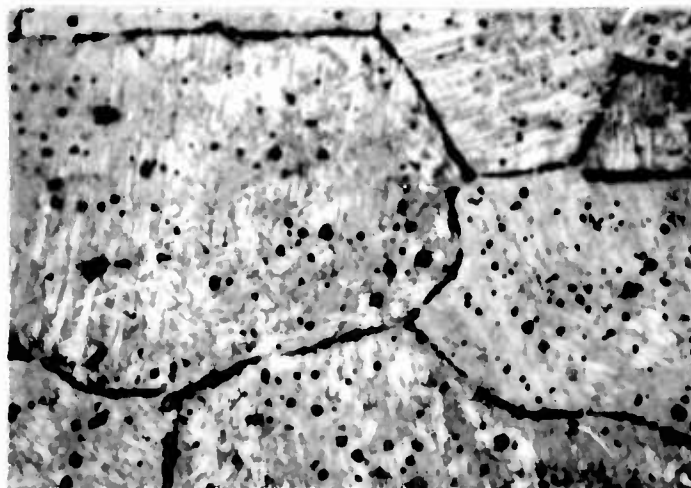
Fig. 5. Cerium athermally transformed at
195°K after deformation at 338°K -
center of specimen. Magnification 160 X.

from athermal transformation at 195°K (270%) while the edges contained
about half this amount (~ 40%). It appeared that tensile deformation
induced the dhcp → fcc transformation; exactly the opposite behavior
produced above M_s. This remarkable result was also observed by
McHargue and Yakel (3). In their X-ray studies, deformation by roll-
ing at 199°K decreased the amount of dhcp phase from 48 to 23%.

The deformation martensite in cerium differs from other systems
in that M_d is higher than A_s or A_f. Small amounts of dhcp were pro-
duced by deformation as high as 468°K while A_f is only 420 ± 5°K.
Previous dilatometry (6) on cerium indicated deformation at 298°K
raised the A_s temperature to 463°K, consistent with our work.
Apparently the deformation-induced dhcp phase is more stable than the
dhcp formed athermally upon cooling. A summary of the influence of
deformation on the phase transformations in cerium is given in Table 2.

Morphology of the Athermal Transformations

The morphology of the dhcp transformation product in cerium (e.g.
Fig. 2) is very similar to that of hcp formed from the fcc → hcp
reaction in cobalt. Microstructures of transformed polycrystalline
cobalt (10) look almost identical to those of cerium. The martensitic
transformation in cobalt is a particularly simple one, with a coherent

Table 2. Influence of deformation on the fcc $\rightleftarrows$ dhcp transformation

Deformation Temperature	Resulting Transformation
195°K	At edge, dhcp $\rightarrow$ fcc
298°K	fcc $\rightarrow$ dhcp throughout, > % at edge
318°K	fcc $\rightarrow$ dhcp " " "
338°K	fcc $\rightarrow$ dhcp only at edge
368°K	fcc $\rightarrow$ dhcp " "
378°K	fcc $\rightarrow$ dhcp " "
418°K	fcc $\rightarrow$ dhcp " "
468°K	fcc $\rightarrow$ dhcp few grains near edge

interface between the fcc and hcp phases, and an orientation relationship such that the plane in common across the coherent interface is the {111} of the fcc structure and the (0001) plane of the hcp structure. Metallography of cerium lends support to the belief that the fcc $\rightarrow$ dhcp is probably also a coherent martensitic transformation as in cobalt. Besides the similarity in microstructures between cerium and cobalt, a semiquantitative study of the morphology in cerium also infers this. Angles between traces of intersecting transformation product were measured on athermally transformed cerium. A distribution plot of these angles gave the maximum frequency of occurrence between 64 to 72 degrees. This is consistent with the angle between {111} planes of 70.5 degrees.

The morphology of the reverse dhcp $\rightarrow$ fcc transformation was briefly examined. Figure 6 is a photomicrograph of a cerium specimen partially transformed to dhcp at 195°K, then heated to 383°K for partial reversion of the dhcp areas. It is evident that the fcc phase so formed does not have a regular crystallographic appearance of the coherent martensitic transformation. It is possible that the reversion product is a massive-type interface-controlled reaction, with an incoherent interface. That the reversion transformation has some isothermal component (3,6) might support this view.

Fig. 6. Cerium athermally transformed at
195°K then partial reversion at 383°K.
Magnification 1000 X.

SUMMARY

1. A quantitative metallographic study has confirmed X-ray data on the athermal fcc → dhcp transformation in cerium.

2. Tensile deformation above M_s induces deformation dhcp and stabilizes the remaining fcc to subsequent athermal transformation. Strictly compressive deformation (above 323°K) does not influence the transformation.

3. The M_d for the fcc → dhcp transformation lies above both A_s and A_f for the reverse reaction.

4. The morphology of the fcc → dhcp transformation in cerium is similar to the morphology of the coherent martensitic transformation in cobalt. The reverse transformation, however, appears to have an incoherent interface.

REFERENCES

1. F. Trombe and M. Föex, C. R. Acad. Sci. Paris 223, 949 (1946).

2. A. F. Schuch and J. H. Sturdivant, J. Chem. Phys. 18, 145 (1950).

3. C. J. McHargue and H. L. Yakel, Acta Met. 8, 637 (1960).

4. M. K. Wilkinson, H. R. Child, C. J. McHargue, W. C. Koehler, and E. O. Wollan, Phys. Rev. 122, 1409 (1961).

5. I. Dillamore, I. R. Harris, and R. E. Smallman, Acta Met. 12, 155-58 (1964).

6. M. S. Rashid and C. J. Altstetter, Trans. Met. Soc. AIME 236, 1649 (1966).

7. C. C. Koch and M. L. Picklesimer, Trans. Met. Soc. AIME, accepted for publication.

8. J. E. Hilliard and J. W. Cahn, Trans. Met. Soc. AIME 221, 344 (1961).

9. J. W. Christian, The Theory of Transformations in Metals and Alloys, Pergamon Press, 1965.

10. H. Bibring, F. Sebilleau, and C. Buckle, J. Inst. Metals 87, 71 (1958-59).

THE YTTRIUM-LEAD ALLOY SYSTEM[*]

O. N. Carlson, F. A. Schmidt and D. E. Diesburg

Institute for Atomic Research and Department of Metallurgy

Iowa State University, Ames, Iowa

ABSTRACT

The yttrium-lead alloy system was investigated by thermal analysis, microscopic and X-ray methods. An inverse peritectic reaction occurs on the yttrium-rich end of the system and there is a eutectic at 14 at. % Pb and 1240°C between yttrium and the compound, Y_5Pb_3, which melts congruently at 1760°C. The lead-rich side of the system consists of a series of peritectic reactions associated with three additional compounds. From X-ray diffraction data and microscopic evidence, the compositions of these compounds were determined to be Y_5Pb_4, YPb_2 and YPb_3. Horizontals corresponding to the decomposition temperatures of these compounds occur at 1650, 945 and 740°C, respectively.

This study of the yttrium-lead system was undertaken to determine the phase relationships existing and to propose a phase diagram. A knowledge of these relationships can then be used to determine if any of the alloys present in the system have a potential use in nuclear design.

Two compounds of yttrium and lead have been reported in the literature. Jeitschko and Parthé (1) prepared a compound which they identified as Y_5Pb_3 having a $D8_8$ structure. The compound YPb_3 has been reported by Kuzma, et al., (2) to have a cubic structure of the Cu_3Au type. Although these are the only compounds reported, several compounds of different stoichiometry exist between yttrium and other Group IVA elements. For example, yttrium is known to form a disilicide and digermanide (3-5). A monosilicide and monogermanide have also been reported for yttrium and other rare earth metals as have the existence of the Y_5Si_4 and Y_5Ge_4 compounds (6-10).

Consideration of size and electrochemical factors as criteria for predicting the alloying behavior of metals indicate that compound formation should occur in the yttrium-lead system (11). Although the atomic size of these two metals is well within the 15% limit usually required for extensive solid solubility, the large difference in electro-negativities indicates preferential compound formation.

EXPERIMENTAL PROCEDURE

Materials

The lead used in this investigation was obtained from the Cominco Products Company and was of 99.99% purity. It was used in the as-received condition in the preparation of the yttrium-lead alloys. The yttrium metal was prepared by the authors using the magnesium intermediate alloy process (12). This material was of 99.9+% purity and contained 500 ppm oxygen, 20 ppm nitrogen, 125 ppm iron and 80 ppm carbon as major impurities.

Alloy Preparation

The alloy specimens were prepared by arc-melting the yttrium sponge and lead together under purified argon in conventional arc-melting equipment employing a tungsten electrode and a water-cooled copper crucible. The 30-g specimens were homogenized by remelt-ing several times, inverting the sample between melts. Most of the alloys, especially those containing more than 30 at. % Pb, were found to be reactive in air. For this reason care was taken throughout this investigation to minimize handling of specimens in the atmosphere. Although yttrium melts below the boiling point of lead (1725°C), some weight loss was encountered during melting; therefore, chemical analyses for both yttrium and lead were made on each alloy after thermal analysis.

Thermal Analysis

A 20-g portion of each alloy was placed in a tantalum crucible which was welded closed in vacuo. Differential cooling curves were

run on the alloys by inserting a thermocouple into a well in the top of the sealed crucible. This crucible, together with one containing a columbium reference specimen, was placed in a National Research Corporation 2940 tungsten resistance furnace. A matched W/W-26% Re thermocouple was used for those analyses above 1500°C while a Pt/Pt-13% Rh thermocouple was used for the lower temperature range. Both types of thermocouples were shielded by high purity alumina insulators. The specimen temperature and the temperature differential were plotted simultaneously on a Leeds and Northrup X - X recording potentiometer. A cooling rate of between 10 and 20°C per minute was maintained.

Heat Treatment and Microscopic Examination of Alloys

Because of the reactivity of yttrium at elevated temperature all annealing treatments were made in vacuo. Samples were quenched by heating in an inert gas atmosphere to the desired temperature, holding for 4 hr, and then dropping them into a brine solution.

Specimens were prepared for microscopic examination by grinding on silicon carbide papers through 600-grit size. They were then electropolished and etched in a 6% perchloric acid-methanol solution which had been chilled to -70°C (13). Those samples which were reactive with air were quickly placed in a beaker of absolute ethanol chilled to -70°C. This beaker had a sight-glass fused in the bottom so that the specimen could be photographed while protected from moisture by the absolute alcohol.

EXPERIMENTAL RESULTS

The results of the thermal analysis and microscopic data obtained from thirty-one alloys are summarized in the proposed phase diagram in Fig. 1. Thermal analysis was used to determine the location of the horizontal associated with the inverse peritectic, eutectic and peritectic reactions. The stoichiometry of the various compounds was confirmed by chemical analysis and by microscopic and X-ray evidence.
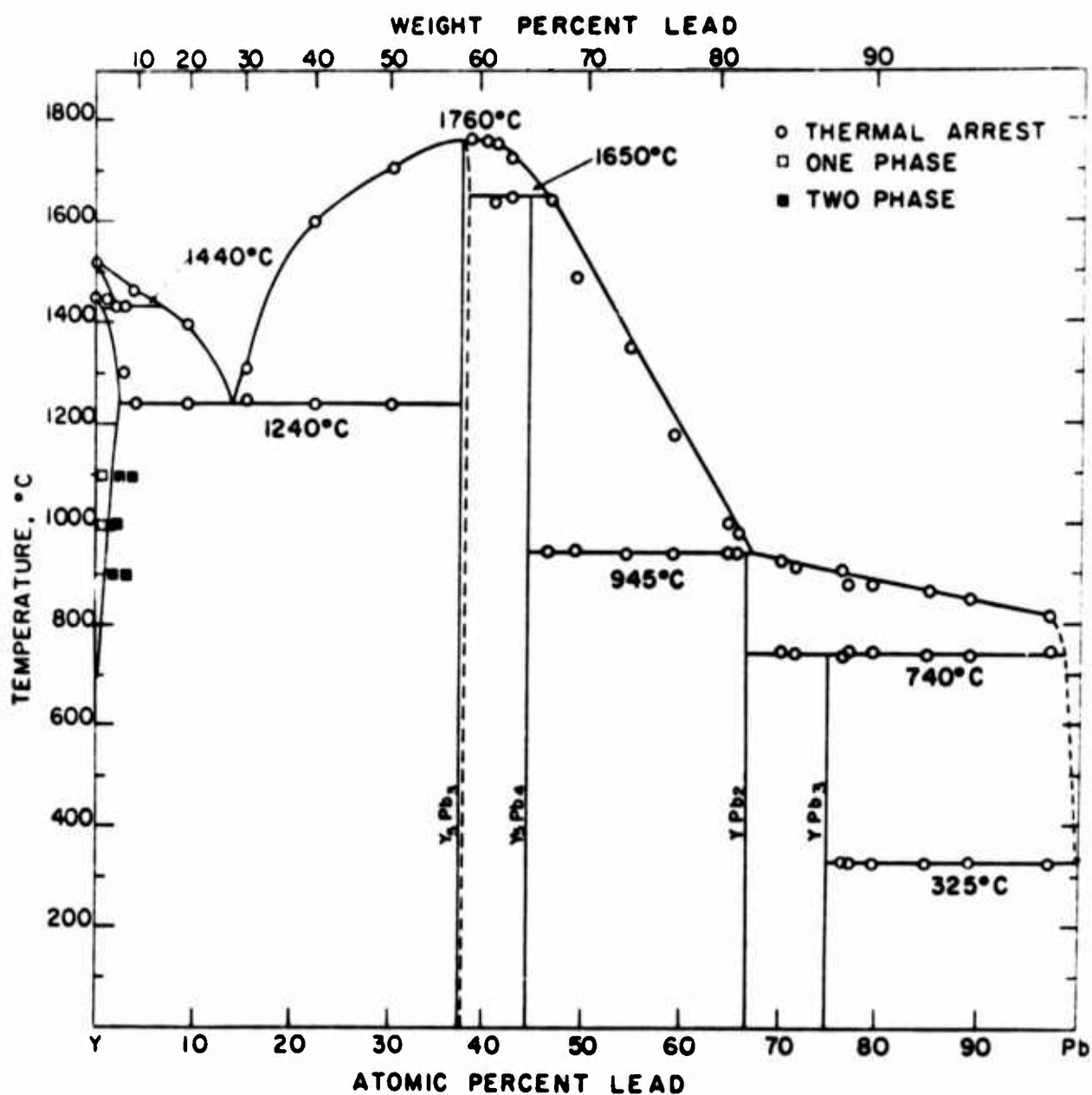
Fig. 1. Proposed yttrium-lead phase diagram and plot of experimental data.

Inverse Peritectic and Eutectic Reactions

An inverse peritectic reaction occurs in the yttrium-rich end of the system at approximately 1400°C and 2 at.% Pb. The evidence for this reaction was obtained from heating and cooling curves that showed a decrease of approximately 25°C in the alpha to beta transformation of pure yttrium.

A eutectic reaction occurs at 14 at.% Pb and 1240°C as determined from the results of thermal analysis. The composition is based primarily upon microscopic evidence as is seen from the structure of a 16 at.% Pb alloy (see Fig. 2) which contains a small amount of primary Y_5Pb_3 in a eutectic matrix.

Intermediate Phases

Four intermetallic compounds were identified in the yttrium-lead system as having the following formulae: Y_5Pb_3, Y_5Pb_4, YPb_2 and YPb_3. The Y_5Pb_3 compound melts congruently while the other three compounds undergo peritectic decomposition reactions.

The first compound encountered was Y_5Pb_3 which has been reported to have hexagonal symmetry with $a_o = 8.971$ and $c_o = 6.614$ Å (1).
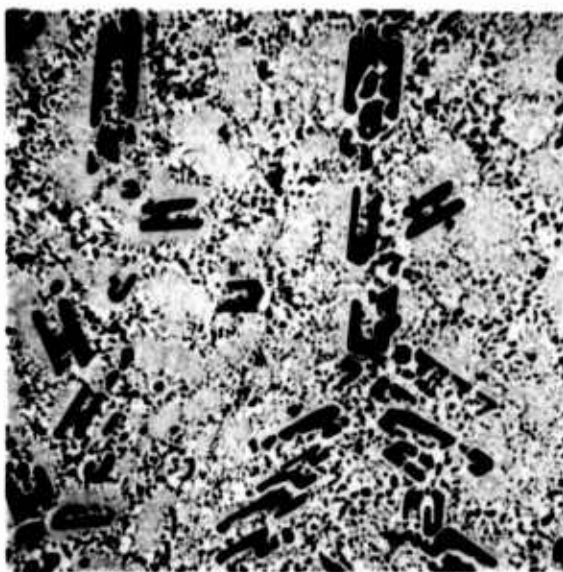
Fig. 2. Y-16 at.% Pb alloy. Primary Y_5Pb_3 (large dark areas) surrounded by eutectic. Electropolished in chilled 6% HCl)$_4$ - CH_3OH solution. X250.

An alloy close to this stoichiometry also was prepared during this investigation and its melting point determined as 1760°C. From an X-ray diffraction pattern of an alloy, containing 38 at. % Pb, $\sin^2\theta$ values were obtained that were found to compare very closely to the values of Jeitschko and Parthé (1). A photomicrograph of this alloy is presented in Fig. 3. Evidence for a limited degree of solid solubility in Y_5Pb_3 is a small but measurable difference between the lattice parameters of the compound in the 35.0 and 42.8 at. % Pb alloys.

Another compound which is formed peritectically at 1650°C occurrs in the vicinity of 44.4 at. % Pb corresponding to the composition of Y_5Pb_4. A 44.0 at. % Pb alloy has a microstructure that is almost entirely one phase as seen in Fig. 4. Powder patterns of several alloys containing between 44.0 and 46.6 at. % Pb were indexed on the basis of an orthorhombic cell with a = 7.994 (± .005), b = 15.10 (± .01) and c = 8.241 (± .005)Å. The x, y and z atom positional parameters determined by Smith, Johnson and Tharp for Sm_5Ge_4, space group $Pnma-D_{2h}^{16}$ (14) are shown in Table I. These parameters were used to compute the $\sin^2\theta$ values and intensities of Table II establishing the structure of Y_5Pb_4 as isotypic with Sm_5Ge_4.

Continuing across the system, another compound was found near the stoichiometric composition of YPb_2. A peritectic horizontal associated with this compound was observed from the thermal data at 945°C. A 65.0 at. % Pb alloy lies in close proximity to a one phase region as is seen from the photomicrograph of Fig. 5. Diffraction data from powder patterns of several alloys in the composition range of 59.0 to 71.5 at. % Pb were indexed on the basis of an orthorhombic cell of the $ZrSi_2$ type with a = 4.550 (± .004), b = 16.46 (± .01) and c = 4.450 (± .004)Å. The $Cmcm-D_{2h}^{17}$ space group and the atom positional parameters determined by Iandelli for the compound $ErSn_2$ were used to generate $\sin^2\theta$ and intensity data for the intermetallic compound YPb_2 (15). These parameters were $y_Y = 0.10$, $y_{Pb} = 0.75$ and $y'_{Pb} = 0.43$. The excellent agreement between the observed and calculated values for $\sin^2\theta$ seen from Table III is taken as evidence for the occurrence of YPb_2.

Table I. Positional Parameters Used to Calculate the Intensity of the Y_5Pb_4 Reflections. Parameters Obtained by Smith, Johnson and Tharp (14).

Atom	Wyckoff notation and number of positions		x	y	z
Y (I)	8	d	.1205	.1157	.3388
Y (II)	8	d	-0.253	.1004	-.1781
Y (III)	4	c	.2880	.2500	.0024
Pb (I)	4	c	-.0868	.2500	.1115
Pb (II)	4	c	.1761	.2500	-.3667
Pb (III)	8	d	.2206	-.0499	-.5688

Table II. Comparison Between the Calculated and Observed $\sin^2\theta$ and Intensity Data for the Y_5Pb_4 Orthorhombic Structure with Space Group Pnma - D_{2h}^{16} (Cu Radiation)

Average values from 44.0 and 46.6 at.% Pb in Y			Calculated $\sin^2\theta$ and intensities	
I_o	$\sin^2\theta_o$	h k l	$\sin^2\theta_c$	I_c
W	.0201	1 1 1	.0207	47
W	.0285	1 2 1	.0285	99
W broad	.0345	0 0 2	.0350	172
W M	.0364	2 0 0	.0372	181
S	.0403	1 3 1	.0415	790
M	.0422	0 4 0	.0417	200
MW	.0438	1 0 2	.0443	63
M	.0460	0 2 2	.0454	86
M	.0472	{1 1 2 / 2 2 0}	{.0469 / .0476}	{45 / 70}
MS	.0558	2 2 1	.0564	292
VS	.0679	1 3 2	.0678	1000
S	.0695	2 3 1	.0694	437
S	.0720	2 0 2	.0722	459
W broad	.0744	2 1 2	.0748	84
M	.0765	0 4 2	.0767	303
M broad	.0802	2 4 0	.0789	274
MW broad	.0817	{0 1 3 / 2 2 2}	{.0814 / .0826}	{37 / 220}
M	.0836	1 5 1	.0832	265
MW	.0858	1 4 2	.0860	152
S	.0882	{2 4 1 / 1 0 3}	{.0876 / .0881}	{518 / 27}
S	.0909	1 1 3	.0907	585

Table III. Comparison between the observed and calculated $\sin^2\theta$ and intensity data for YPb_2 with $ZrSi_2$(C49) structure type (Cu radiation).

Average values for reflections common to 59.0, 64.4, 65.6 and 71.5 at. % Pb in Y.			Values calculated on the basis of a=4.550Å, b = 16.46Å and c=4.450Å.	
I_o	$\sin^2\theta_o$	h k l	$\sin^2\theta_c$	I_c
VW broad	.0315	1 1 0	.0309	78
W	.0353	0 4 0	.0351	23
W broad	.0409	0 2 1	.0388	24
VW	.0455	1 3 0	.0485	25
MW	.0644	0 4 1	.0651	57
S	.0736		lead	---
VS broad	.0793	{1 3 1	.0785	1000
		{0 6 0	.0790	217
MS broad	.0980		lead	---
VW	.1078	0 6 1	.1090	31
M	.1149	2 0 0	.1148	153
M broad	.1200	0 0 2	.1200	143
W	.1353	1 7 0	.1362	30
VW	.1495	1 1 2	.1509	21
VW	.1535	2 2 1	.1536	8
VVW	.1551	0 4 2	.1551	7
W	.1666	1 7 1	.1662	25
W	.1796	2 4 1	.1799	28
S lead	.1956	2 6 0	.1938	116
S	.1983	0 6 2	.1990	111
VW	.2048	1 9 0	.2064	23
VW	.2265	2 6 1	.2238	20
S	.2336	2 0 2	.2349	102
S	.2368	1 9 1	.2364	134
VW	.2474	0,10,1	.2494	14
W	.2561	1 7 2	.2562	22
S	.2679		lead	---
MW	.2921		lead	
W	.3068	0 4 3	.3052	6
MW	.3082	3 3 1	.3081	125
S broad	.3175	{2 6 2	.3138	106
		{1 3 3	.3185	118
VW	.3471	0,12,1	.3459	14
VW	.3909		lead	---
VW	.4297	{1,13,1	.4294	17
		{2,12,0	.4307	19
VW	.4596	4 0 0	.4593	18
W lead	.4612	2,12,1	.4607	19
VW	.4741	1 9 3	.4765	46
W	.4842		lead	---
W	.4862	3 7 2	.4859	9

The existence of YPb_3, which was reported by Kuzma, et al., was confirmed by this investigation (2). This compound has a cubic structure of the Cu_3Au type with $a_o = 4.814Å$. A photomicrograph of an alloy containing 76 at. % Pb lying close to the compound composition is shown in Fig. 6.

DISCUSSION

The limits of primary solid solubility of lead in yttrium were estimated from the microscopic examination of quenched alloys. As can be seen from the data plotted on Fig. 1, the maximum solubility in yttrium at the eutectic temperature is approximately 2 at. % Pb. This decreases to less than 1 at. % at 900°C.

The horizontal at the lead end of the diagram, which occurs at 325°C, is believed to be associated with a eutectic reaction. No effort was made to determine the solubility of yttrium in lead.

Additional values for $\sin^2\theta$, which are consistent with the extinction rules for the space groups, were generated for the orthorhombic structures of Y_5Pb_4 and YPb_2. The calculated intensities associated with these values are very weak and their corresponding reflections were not observed on the X-ray diffraction patterns.

Several similarities may be noted between the yttrium-lead system and those of yttrium with the other Group IVA elements. Yttrium is reported to form Y_5X_3 and YX_2 or Y_3X_5 compounds with silicon, germanium and tin (1, 8, 10, 15) while the analog of YPb_3 has not been observed. The compound corresponding to Y_5X_4 is also present in the silicon and germanium systems (8, 10), however, this compound has not yet been reported between yttrium and tin. Silicon and germanium also form a YX compound (7, 9) but the monostannide has not been observed nor was YPb found in this investigation.

All of the yttrium-lead compounds are reactive to air and care must be exercised to prevent their decomposition. The high melting point observed for the Y_5Pb_3 compound is certainly a unique feature of the system and further study of this compound would be interesting and perhaps useful.
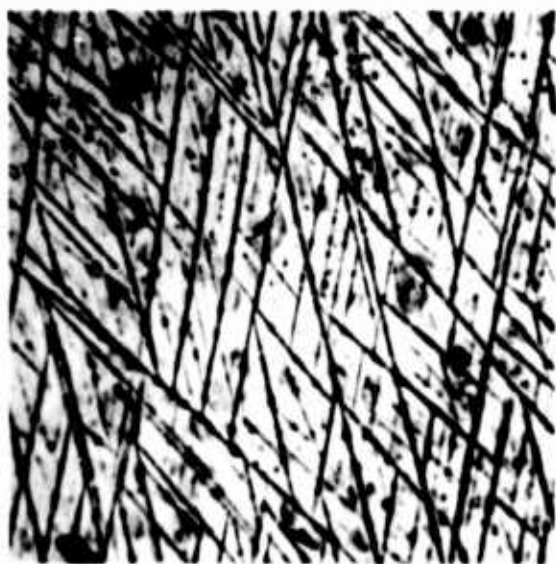
Fig. 3. Y-38.0 at. % Pb alloy. Slow cooled from 1825°C. Y_5Pb_3 matrix. Electropolished in 6% $HClO_4$ - CH_3OH. X250.
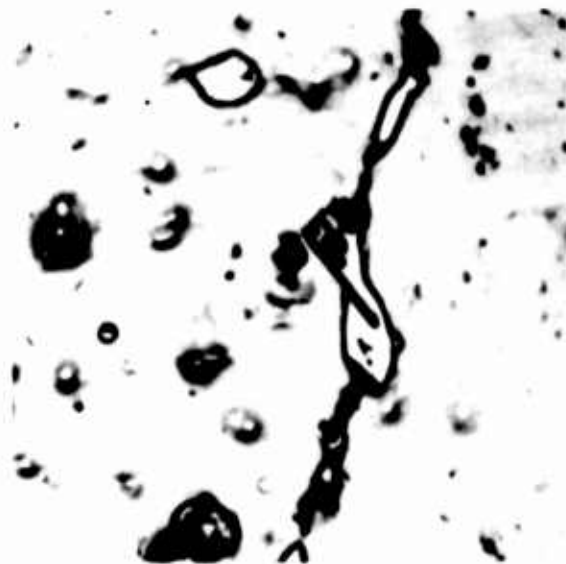
Fig. 4. Y-44.0 at. % Pb alloy. Annealed for 4 hr at 1600°C and 24 hr at 900°C. Y_5Pb_4 matrix plus second phase. Electropolished 6% $HClO_4$-CH_3OH. X150.

Fig. 5. Y-65.0 at. % Pb alloy. Annealed 4 hr at 900°C and 24 hr at 700°C. YPb_2 matrix plus small amounts of Y_5Pb_4. Electropolished in 6% $HClO_4$-CH_3OH. X250.
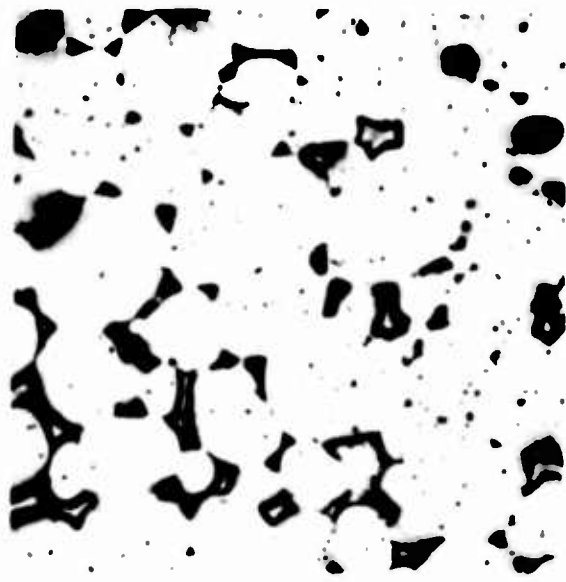
Fig. 6. Y-76.0 at. % Pb alloy. Annealed 4 hr at 700°C. YPb_3 matrix plus lead. Electropolished in 6% $HClO_4$-CH_3OH. X250.

SUMMARY

1. An yttrium-lead phase diagram is proposed which consists of an inverse peritectic reaction, a eutectic reaction and four intermetallic compounds.

2. The existence of the compounds Y_5Pb_3 and YPb_3 were confirmed. Y_5Pb_3 has hexagonal symmetry and melts congruently at 1760°C. YPb_3 is cubic and forms peritectically at 740°C.

3. Two new compounds, Y_5Pb_4 and YPb_2, were identified and indexed on the basis of orthorhombic cells. They are formed as the result of peritectic reactions at 1650 and 945°C respectively.

4. The maximum solid solubility of lead in yttrium is estimated at 2 at. % lead at 1240°C. No effort was made to determine the yttrium solid solubility in lead.

REFERENCES

1. W. Jeitschko and E. Parthé, "Stannides and Plumbides of Sc, Y, La and Ce with $D8_8$ Structure," Acta Cryst., 19 (1965) 275.

2. Y. B. Kuzma, R. V. Skolozdra and V. Ya Markiv, "Crystal Structure of Compounds RPb_3 in System Rare Earth Metal-Lead," Dopovidi Akad. Nauk Ukr. RSR, 8 (1964) 1070.

3. J. A. Perri, I. Bender and B. Post, "Rare Earth Metal Disilicides," J. Phys. Chem., 63 (1959) 616.

4. I. P. Mayer, E. Banks and B. Post, "Rare Earth Disilicides," J. Phys. Chem., 66 (1962) 693.

5. O. Schob and E. Parthé, "Digermanides of Scandium and Yttrium, " Monatsh. Chem., 95 (1964) 1466.

6. A. G. Tharp, G. S. Smith and Q. Johnson, "Structure of the Rare Earth Germanides at or Near Equiatomic Proportions, " Acta Cryst., 20 (1966) 583.

7. E. Parthé, "The Crystal Structure of YSi and $Hf_5Ge_3(C)$", Acta Cryst., 12 (1959) 559.

8. C. E. Lundin, "A Survey of the Heavy Rare Earth Silicides, " Rare Earth Research, E. V. Kleber, Ed., 1963, p. 306. The Macmillian Company, New York.

9. O. Schob and E. Parthé, "AB Compounds with Sc, Y and Rare Earth Metals, " Acta Cryst., 19 (1965) 214.

10. G. S. Smith, A. G. Tharp and Q. Johnson, "Crystallographic Data on New Rare Earth - Germanium and Silicon Compounds, " Nature, 210 (1966) 1148.

11. W. Hume-Rothery and G. V. Raynor, Structure of Metals and Alloys, 3rd edition, 1954. Institute of Metals, London.

12. O. N. Carlson, J. A. Haefling, F. A. Schmidt and F. H. Spedding, "Preparation and Refining of Yttrium Metal by Y-Mg Alloy Process, " J. Electrochem. Soc., 107 (1960) 540.

13. E. N. Hopkins, D. T. Peterson and H. H. Baker, "A Universal Electropolishing Method, " U.S. A. E. C. Report, ORNL-TM-1161 (1966).

14. G. S. Smith, Q. Johnson and A. G. Tharp, "Crystal Structure of Sm_5Ge_4, " submitted to Acta Cryst.

15. A. Iandelli, "On the Behaviour of Tetra-and Divalent Rare Earths in Metallic Compounds, " Instituto di Chemica Fisica, Universitá di Genova, Genova, Italy.

YTTERBIUM-LEAD AND EUROPIUM-LEAD SYSTEMS[1]

O. D. McMasters
Assistant Metallurgist

Institute for Atomic Research
Ames, Iowa

ABSTRACT

Differential thermal, metallographic and X-ray parametric methods
were used to establish the ytterbium-and europium-lead phase diagrams.
The terminal solid solubilities, eutectic points, liquidus curves and
horizontal reaction temperatures of these systems were determined.
The intermetallic compounds Yb_2Pb, $YbPb$, $YbPb_3$, Eu_2Pb, $EuPb$ and
$EuPb_3$ melt congruently. Both $YbPb$ and $EuPb$ compounds exhibit a
polymorphic transformation. Compounds Yb_5Pb_3 and Eu_5Pb_3 form
a peritectic reaction. Lattice parameter values and crystal structure
data are given for most of these compounds. The valency characteristics
of the rare-earth component in these alloys are discussed. The
crystal chemistry of these compounds are compared to those of the
alkaline-earth and trivalent rare-earth compounds.

INTRODUCTION

Determination of the ytterbium-lead and europium-lead phase

diagrams is a part of a systematic study of the rare-earth-lead alloy

systems. Valence characteristics, intermetallic compound formation,

crystal structures and physical property data are to be considered in

the comparative analysis of these alloys. Similar information for the

divalent alkaline-earth-lead systems will be included in the systematic

study. Such investigations should yield a better understanding of

alloy formation.

EXPERIMENTAL PROCEDURES

Materials. The lead used in this investigation was obtained from

Cominco Products, Inc. and was specified to be 99.99% pure. The

ytterbium and europium were prepared at the Ames Laboratory by

the lanthanum reduction of the oxide followed by a distillation of the

metal.   These metals were analyzed to be better than 99. 9% pure.

Alloy Preparation.   Alloys were prepared by melting appropriate amounts of the materials in tantalum crucibles which had been sealed under inert gas atmospheres.   Homogenization was achieved by re-melting the alloys with the crucibles in an inverted position and repeating the process.   All specimens obtained from the alloy samples were prepared in a dry-argon filled glove box because of their rapid reaction with air and moisture.

Thermal Analysis.   Differential thermal analysis methods were used to determine the liquidus curves and reaction horizontals of the systems.   In order to conserve both ytterbium and europium, the composition was changed by adding lead to master alloys and resealing the thermal analysis crucibles.   The thermal arrests were recorded on an X-Y recorder and measured potentiometrically.

X-ray and Metallographic Methods.   Slice specimens for metallography and powder specimens for X-ray diffraction were obtained from rod-shaped samples which had been prepared in sealed 0. 625 cm diam tantalum crucibles.   The specimens were heat treated in sealed tantalum crucibles and the X-ray powder specimens were sealed in 0. 3 mm diam glass capilaries.   Both copper and chromium radiation were used to obtain the powder patterns of these alloys.

Most of the metallographic specimens were electropolished in a 6% perchloric acid-methanol solution which was maintained at -70°C[1]. Photomicrographs were taken through a sight-glass in the bottom of a beaker which contained absolute ethanol chilled to -70°C.

RESULTS AND DISCUSSION

The ytterbium-lead and europium-lead phase diagrams shown in Figures 1 and 2 respectively, summarize the results of this investigation. The differential thermal analyses data are plotted and the eutectic compositions which were determined by metallographic methods are shown in these figures. X-ray diffraction methods were used to investigate the terminal solid solubilities and the intermetallic compounds of these systems.

Terminal Solid Solubilities. The lattice parameter of ytterbium ($a_O = 5.486 \pm .001 \mathring{A}$) and of europium ($a_O = 4.588 \pm .001 \mathring{A}$) did not change for the Yb-rich and Eu-rich powder specimens which had been heat treated at and quenched from 700°C. From these error limits and assuming Vegard's law is followed it is concluded that the solid solubility of lead in ytterbium and europium is less than 0.2 and 0.3 at.% respectively. Lead additions lower the 792°C transformation temperature of ytterbium about 5°C. Associated with this effect is an inverted peritectic reaction.

The 327°C melting point of lead was raised about 2°C by ytterbium additions and about 1°C by europium additions. A peritectic reaction occurs in each case. The solid solubility of ytterbium and europium in lead was found to be less than 0.15 and 0.10 at.%, respectively, by the X-ray diffraction method described above.

Intermetallic Compounds. X-ray powder diffraction methods were used to establish the crystal structures and lattice parameters of most of the compounds of these systems.

Yb$_2$Pb and Eu$_2$Pb (33.3 at.% Pb). The rare-earth richest compounds
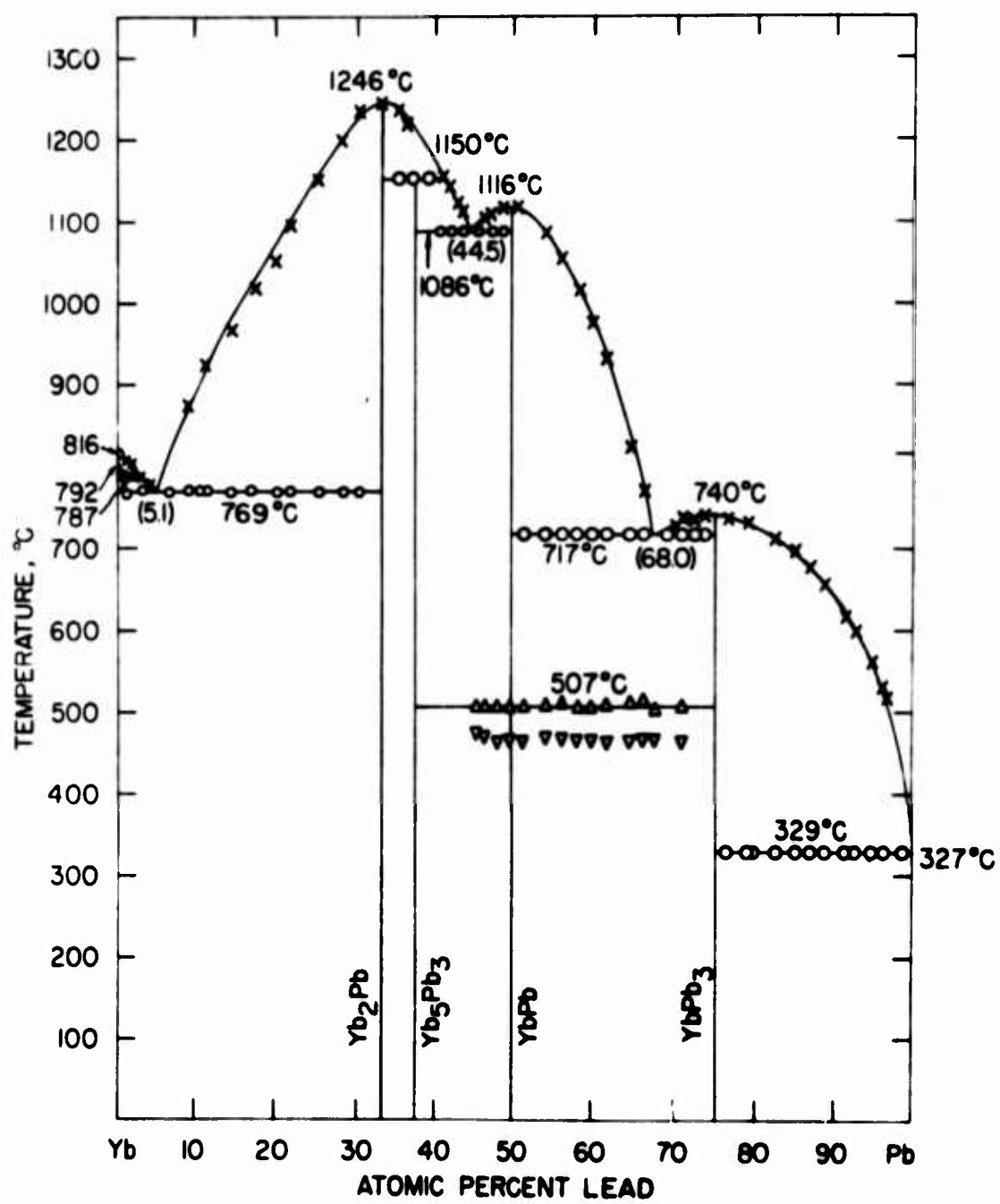
Fig. 1. Ytterbium-Lead Phase Diagram
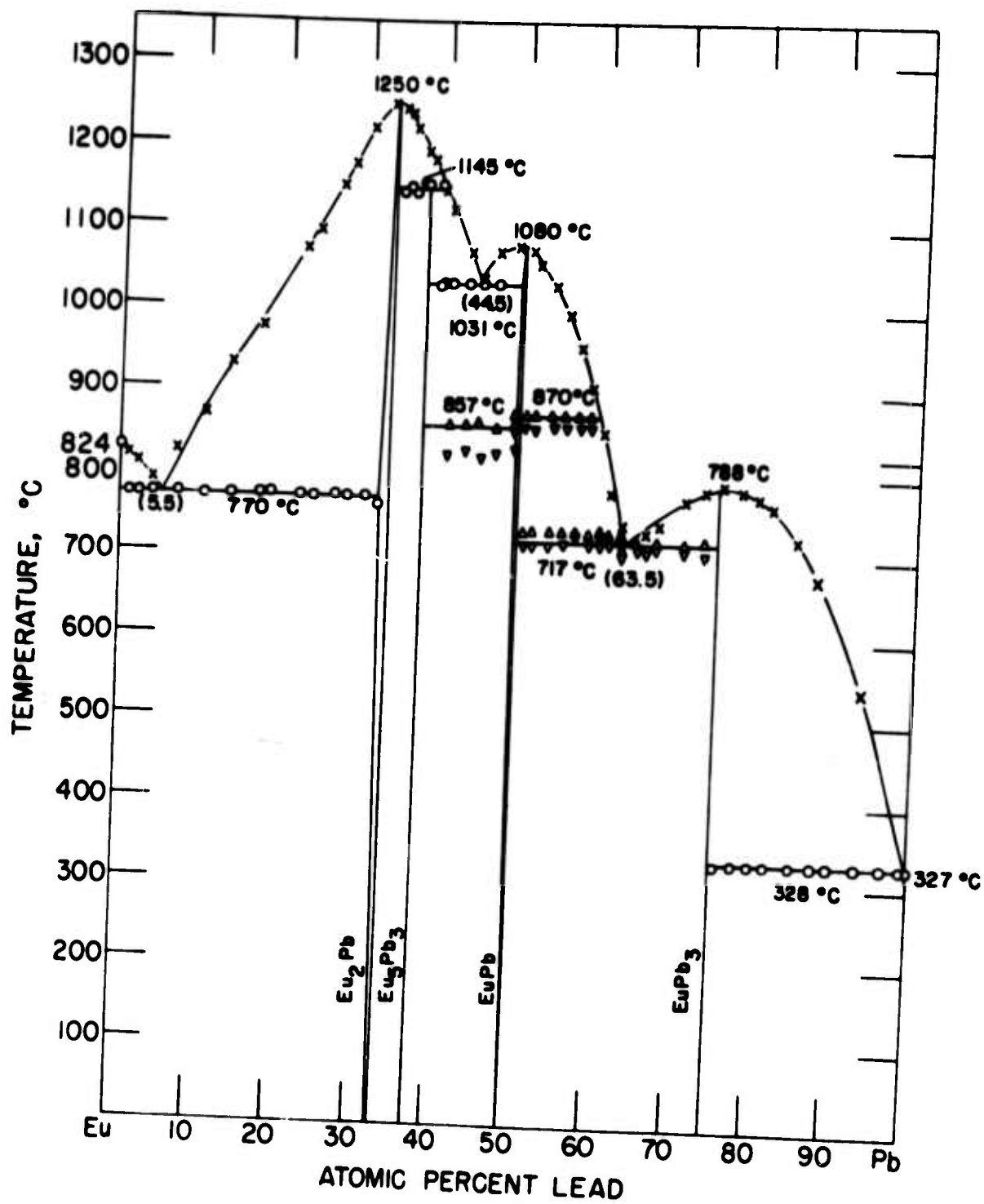
Fig. 2. Europium-Lead Phase Diagram

of these systems crystallize in the $PbCl_2$ ($\underline{C}$ 23) type structure with the space group being $Pnma$-D_{2h}^{16}. The crystallographic data for this structure were generated on the basis of the $\underline{x}$ and $\underline{z}$ positional parameters reported for Ca_2Ge[3] through the use of a computer program written by Jeitschko and Parthé.[4] The best agreement between experimental and observed $\sin^2\theta$ and intensity data (copper radiation) was established for these cells and their orthorhombic lattice parameters are:

Yb_2Pb - $\underline{a}_o$ = 7.478 ± .005Å, $\underline{b}_o$ = 5.225 ± .002Å, $\underline{c}_o$ = 9.549 ± .004Å and
Eu_2Pb - $\underline{a}$ = 7.87 ± .01Å, $\underline{b}$ = 5.40 ± .01Å, $\underline{c}$ = 10.03 ± .01Å.

The extrapolated parameters for Yb_2Pb were obtained through the use of the Vogel-Kempter[5] computer program and are based on chromium radiation back-reflection data. The Nelson-Riley function was used in this extrapolation.

Yb_2Pb and Eu_2Pb melt congruently at 1246 ± 3°C and 1250 ± 3°C respectively.

$\underline{Yb_5Pb_3}$ and $\underline{Eu_5Pb_3}$ (37.5 at. % pb). Procedures similar to those described above were used to show that Yb_5Pb_3 crystallizes in the hexagonal Mn_5Si_3 ($\underline{D}8_8$) type structure. The space group is $P6_3/mcm$-D_{6h}^3 and the lattice constants are $\underline{a}_o$ = 9.325 ± .003Å and $\underline{c}_o$ = 6.929± .003Å. These parameters and the atomic positional parameters[6] $\underline{x}_{Yb}$ = 0.232 and $\underline{x}_{Pb}$ = 0.605 yielded the calculated $\sin^2\theta$ and intensity data in good agreement with the observed reflection data.

The powder patterns for Eu_5Pb_3 could not be indexed as having either the $\underline{D}8_8$ structure or the closely related tetragonal $\underline{D}8_m$ type structure. Most of the reflections could be accounted for by a primitive tetragonal cell with $\underline{a}$ = 13.14 and $\underline{c}$ = 10.41Å, but the actual structure

of the compound was not resolved in this investigation.

Both Yb_5Pb_3 and Eu_5Pb_3 form by peritectic reactions at 1150 ± 2°C and 1145 ± 3°C respectively.

YbPb and EuPb (50. at. %Pb). These two compounds melt congruently at 1116 ± 2°C and 1081 ± 2°C respectively. Both YbPb and EuPb exhibit a polymorphic transformation but the crystal structures of the two forms could not be established on the basis of powder pattern data in either case. YbPb transforms at 507 ± 3°C upon heating. The average value of the transformation temperature upon cooling at a rate of 5°C/min is 466 ± 5°C. The temperature of the transformation of EuPb on heating of the Eu-rich alloys is 857 ± 3°C and for the Pb-rich alloys is 870 ± 3°C. The respective cooling curve arrests occurred at 825 ± 3°C and 858 ± 3°C. This temperature difference suggests that EuPb exists over a range of compositions and this is indicated in Fig. 2.

$YbPb_3$ and $EuPb_3$ (75 at. %Pb). The lead richest compounds of these systems melt congruently at 740 ± 2°C and 788 ± 2°C respectively. Both crystallize in the cubic $AuCu_3(\underline{L1}_2)$ type structure and their lattice parameters have been reported.[7, 8] The lattice parameters were determined to be $\underline{a}_o$ = 4.8628 ± .0008Å for $YbPb_3$ and $\underline{a}_o$ = 4.915± .001Å for $EuPb_3$ and these are in good agreement with the previously published results. No solid solution field was indicated in either of these determinations.

CONCLUSIONS

Both ytterbium and europium, which are divalent metals, appear to remain divalent when alloyed with lead. Evidence in favor of this conclusion is summarized here. Lattice parameter values for the trivalent rare-earth RPb_3 compounds vary linearly when plotted against the rare-earth trivalent ionic radius, but the parameters of $YbPb_3$ and $EuPb_3$ are much larger than those of their trivalent lanthanide neighbors. A similar deviation is noted in the case of the lattice parameter data for Yb_5Pb_3. Compounds of stoichiometry R_2Pb apparently do not form in the trivalent rare-earth-lead systems.[9] Yb_2Pb and Eu_2Pb crystallize in the isotypic Ca_2Pb structure.[10] From magnetic susceptibility measurements on some of the alloys near the compound stoichiometries of these lead systems, Iandelli[11] has shown that both ytterbium and europium in these alloys are essentially divalent.

Ytterbium- and europium-lead alloys could be used at relatively high temperatures in the form of intermetallic compounds which are suitably protected from air and moisture.

REFERENCES

1. "Ytterbium-Lead System," (IS-1461) Accepted for publication in
   Trans. Met. Soc. AIME (1967).

   "Europium-Lead System," (IS-1505) Submitted for publication in
   J. Less-Common Metals (1967).

2. E. N. Hopkins, D. T. Peterson and H. H. Baker, "A Universal
   Electropolishing Method," US. A. E. C. Report, ORNL-TM-1161
   (1966).

3. W. B. Pearson, A Handbook of Lattice Spacings and Structures of
   Metals and Alloys, Pergamon Press, Inc., New York, 1958.

4. W. Jeitschko and E. Parthe, "A Fortran IV Program for the
   Intensity Calculation of Powder Patterns," Univ. of Penn.,
   Laboratory for Research on the Structure of Matter, ca. 1965.

5. R. E. Vogel and C. P. Kempter, Acta Cryst., 1961, vol. 14,
   p. 1130.

6. W. Jeitschko and E. Parthe, "D8$_8$ Phases of the Rare Earth
   Elements with Tin and Lead," Submitted to Acta. Cryst., 1966.

7. V. B. Kuzma, R. V. Skolozdra and V. Va. Markiv, Dopovidi
   Akad. Nauk Ukr. SSR, 1964, p. 1070.

8. A. Palenzona, J. Less-Common Metals, 1966, vol. 10, p. 290.

9. Current work in progress at The Ames Laboratory.

10. P. Eckerlin, E. Leicht and E. Wölfel, Z. anorg. Chem., 1961,
    Vol. 307, p. 145.

11. A. Iandelli, "On the Behavior of Tetra-and Divalent Rare Earths
    in Metallic Compounds," Final Technical Report, European
    Research Office, United States Army, Apr., 1966. (to be published)

SYNTHESIS AND IDENTIFICATION OF INTERMETALLIC

COMPOUNDS IN THE Fe-Ho SYSTEM*

T. J. O'Keefe, G. J. Roe, and W. J. James

Departments of Metallurgical Engineering and Chemistry
University of Missouri at Rolla

Abstract

The intermediate phases in the iron-holmium system were investigated by means of X-ray diffraction, electron microprobe analysis, and metallographic techniques. The phases which were either definitely or tentatively identified were $HoFe_2$, $HoFe_3$, Ho_6Fe_{23}, $HoFe_5$, and Ho_2Fe_{17}.

The lattice parameters were determined by the Straumanis technique using Fe $K\alpha$ radiation. Work in progress is also discussed.

Discussion

The purpose of this study was to investigate the intermediate phases in the holmium-iron system and to determine the procedures required to produce small quantities of these compounds as single phases. These materials were to be used in neutron diffraction studies of their magnetic structures.

Melts of iron-holmium alloys with 25.78% (wt.) to 83.09% holmium were made by induction heating. Various homogenizing treatments were made and all of the resulting structures were examined by standard X-ray diffraction and metallographic techniques.

The lattice parameters of the phases which have been tentatively identified are

---

*Contribution #23 from the Graduate Center for Materials Research.

Phase	Lattice Parameters (A°)			
$HoFe_2$	a = 7.30			Cubic
$HoFe_3$	a = 5.08	c = 24.45		Hexagonal
Ho_6Fe_{23}	a = 12.04			Cubic
$HoFe_5$	a = 4.86	c = 4.10		Hexagonal
Ho_2Fe_{17}	a = 8.46	c = 8.28		Hexagonal

Problems have also been encountered in obtaining a pure, homogeneous, single phase of most of the compounds identified. The rate of cooling, within the limits available, did not seem to greatly affect the as-cast structure. Homogenization treatments of the $HoFe_2$, with traces of phases present, at 1000°C was not sufficient to produce a one phase structure. Only by extended times at temperatures near the solidus (approximately 1320°C) was there any evidence of elimination of the second phase. A similar treatment was used for the $HoFe_3$, but this phase seemed to have a lower melting point than the $HoFe_2$.

The $HoFe_5$ and Ho_6Fe_{23} have not been produced as a single phase or even approaching a single phase. Ho_2Fe_{17} has also been produced as a single phase. A single phase was assumed when no extraneous lines were present on the X-ray films. In some cases there appeared to be additional phases present when examined metallographically, but these were not evident upon subsequent X-ray analysis.

Further work is now being conducted in an attempt
to verify the existence of the reported compounds, or to
clarify the region between $HoFe_3$ and Fe.

Diffusion couples have been prepared using pure iron
and pure holmium and one consisting of $HoFe_2$ and Ho_2Fe_{17}.
The Ho-Fe couple was held at 850°C for three weeks and
the $HoFe_2$-Ho_2Fe_{17} couple at 1000°C for 4 weeks. The sam-
ples were then examined by metallographic and microprobe
analysis. It is also hoped that the phase diagram can be
obtained in the near future by using differential thermal
analysis techniques.

THE CERIUM-IRON AND CERIUM-NICKEL BINARY SYSTEMS

By: J. M. Gebhart, III, D. E. Etter and P. A. Tucker

Monsanto Research Corporation*
Mound Laboratory, Miamisburg, Ohio

ABSTRACT

The phase equilibria in the cerium-iron and cerium-nickel binary systems were investigated by differential thermal analysis, thermal analysis, metallography and x-ray diffraction, and a phase diagram was developed for each binary system. Both of the systems have been reported in the literature;[1,2] however, the present work shows considerable disagreement with the earlier diagrams in the liquidus temperatures as well as the temperatures and compositions of the binary invariant points. Many of these discrepancies are probably the result of differences in purity of the cerium metal used in the studies. The current studies were conducted with cerium which melted at 804°C and had a reported purity of 99.9%.

The cerium-iron binary system contains two intermetallic compounds which both melt incongruently. The compound $CeFe_2$ melts incongruently at 920°C forming $CeFe_7$ and liquid of 44 at. % Ce; $CeFe_7$ melts incongruently at 1065°C forming γFe and liquid of 36 at. % Ce. A eutectic between γCe and $CeFe_2$ occurs at 86 at. % Ce and a temperature of 593°C. Both $CeFe_2$ and $CeFe_7$ exhibit a small, but undefined, range of homogeneity. No appreciable solid solubility of Fe in γCe or Ce in αFe was observed. The $\gamma Ce \rightleftarrows \delta Ce$ transformation was observed at 715°C, 5°C lower than in the pure Ce, suggesting a slight solubility of Fe in δCe.

An unexplained thermal arrest at 605°C was observed, just 12°C above the eutectic isotherm, in alloys from 15 to 67 at. % Fe. The reaction was observed by DTA only during cooling, and its magnitude increased with increasing Fe content. Efforts to investigate the possible existence of an additional undefined compound in the system were negative. The possibility that the 605°C thermal arrest represented an allotropic transformation of $CeFe_2$ was discounted by the absence of the reaction in alloys containing greater than 67 at. % Fe. A similar unexplained thermal arrest in Ce-Mn alloys was reported by Thamer[3] who conducted differential

congruently at 505°C. A eutectic occurs on the cerium-rich side of the compound at 78 at. % Ce and a temperature of 477°C, and another eutectic occurs on the nickel-rich side at 67 at. % Ce and a temperature of 495°C. The phase designated here as Ce_5Ni_2 appears to be the same compound identified by Roof, Larson, and Cromer[4] as Ce_7Ni_3. This hexagonal compound was designated Ce_5Ni_2 because a maximum melting point was found to occur at 28.6 at. % Ni and because metallographic examination of this composition revealed only a single phase. Metallographic and differential thermal analysis of the 30 at. % Ni composition indicated the presence of a second phase, CeNi, which occurred as one constituent of the 495°C eutectic. The compound CeNi melts congruently at 680°C. A eutectic occurs on the nickel-rich side of the compound at 45 at. % Ce and a temperature of 655°C. The f.c.c. compound, $CeNi_2$, melts incongruently at 830°C forming $CeNi_3$ and liquid of 38 at. % Ce; $CeNi_3$ melts incongruently at 960°C forming Ce_2Ni_7 and liquid of 31 at. % Ce. Ce_2Ni_7 melts incongruently at 1065°C forming a solid phase richer in nickel content and liquid of 28 at. % Ce. The highest melting compound, $CeNi_5$, melts congruently at 1325°C. A eutectic between $CeNi_5$ and Ni occurs at 9 at. % Ce and a temperature of 1205°C.

thermal analysis on alloys contained in tantalum. The un-explained thermal arrest in this work was observed when the alloys were analyzed in either tantalum or molybdenum containers. Examination of the alloys by metallography and electron microprobe x-ray analysis to correlate the re-action with possible container attack proved inconclusive.

In the metallographic investigation of cerium-rich alloys, an anisotropic cerium phase was observed in slow-cooled alloys. Analysis of these alloys by x-ray diffraction indicated f.c.c. γCe and $CeFe_2$ plus additional lines which could not be attributed to these phases. Consideration was given to the possibility that βCe had been stabilized by Fe. However, DTA and dilatometric analysis failed to indicate a transformation regardless of the heat treatment of the alloy. It was finally demonstrated that the undefined phase resulted from very brief exposure of the alloys to atmospheric gases, although the x-ray results did not cor-relate with any previously defined stoichiometric cerium oxide phase.

The cerium-nickel binary system contains six intermetallic compounds; three melt congruently, and three melt incon-gruently. The most cerium-rich compound, Ce_5Ni_2, melts

One portion of the cerium-nickel system remains unresolved and is still under investigation. Sharp and reproducible thermal arrests, indicating isothermal reactions at 1080°, 1095°, and 1120°C, are observed for alloys between the compounds Ce_2Ni_7 and $CeNi_5$. This evidence suggests additional unreported binary compounds which melt incongruently.

REFERENCES

1. M. Hansen (ed.), Constitution of Binary Alloys, New York, McGraw-Hill, Inc., 1958, p. 451.

2. Ibid., p. 458.

3. B. J. Thamer, J. Less Common Metals, 7 (1964) 341-346.

4. R. B. Roof, Jr., A. C. Larson, and D. T. Cromer, Acta Cryst., 14, 1084 (1961).

Studies of the Samarium-Gadolinium System

A. S. Yamamoto and C. E. Lundin

Denver Research Institute
University of Denver, Denver, Colorado

ABSTRACT

Phase relations in the Sm-Gd alloy system were established by col-
lective analysis of various data. These data were obtained from micro-
scopic examination, X-ray diffraction analysis, thermal analysis,
density and microhardness measurements as well as Knudsen-effusion
experiments. Thermodynamic activities of samarium in the hexagonal
close-packed phase in the temperature range from 1073 to 1373°K were
calculated from the vapor-pressure data obtained in the Knudsen effu-
sion studies. A plot of activities versus mole fraction shows a nega-
tive deviation from ideality, or a tendency for unlike atom attraction.
The phase equilibria exhibit complete miscibility both in liquid and
solid. The characteristics of the two component metals are very
similar, thus favoring the formation of such continuous solutions.
Both metals are close-packed hexagonal, but differ in crystallographic
stacking sequence from samarium-like (ABABCBCACA....) to gadolinium-
like (ABAB....) which is reflected in the alloy system by a gradual
transition from the samarium structure to the gadolinium structure.

I. INTRODUCTION

The properties of intra-rare-earth alloys are of considerable
theoretical interest because of the insight they bring to alloying
behavior, in general, and solid solution theory, in particular. One
has a much greater degree of freedom to control the parameters which
affect alloy behavior by employing the appropriate rare-earth elements
than with any other element in the periodic table.

The option to select rare-earth components from 15 elements allows
one to construct a wide variety of binary systems. The systematic and
well-behaved properties of the rare-earth metals even further enhance
this feature of selectivity. In such a way, the alloying of samarium

with gadolinium represents an attempt to determine the effect of a subtle difference in crystal structure between these two elements on the various properties of their solid solutions. Samarium and gadolinium are almost identical in every other respect. Any deviation in the characteristics of this system from an ideal system, such as the Pr-Nd system,[1,2] can be attributable to the different crystal structures of the components. The Pr-Nd system was studied earlier by these authors as the first in a series of binary systems on the hypothesis that the system would show thermodynamically ideal behavior. The elements were chosen, because they are nearly identical in every respect. On evaluating the experimental evidence, the system was confirmed to be ideal. The only significant difference between the Pr-Nd system and the Sm-Gd system is that in the former the components are invariant in property comparison, and in the latter, there exists one variable, namely, crystal structure. The work described herein demonstrates the effect this one variable has on the character of the solid solutions of the system.

II. EXPERIMENTAL

The samarium and gadolinium metals were purchased from the Ames Laboratory, Iowa State University and were of select purity. The chemical analyses were reported to include no more than 0.1 w/o total in impurities in both metals. The alloys were prepared by standard arc melting techniques. Since the vapor pressure of samarium is rather high, some loss of samarium was expected in the melting. To assess this loss, chemical analyses of the alloys were conducted by X-ray spectrographic analysis. A tungsten-target, X-ray spectrographic tube with associated Norelco X-ray equipment was operated at 40 kv and 35 ma to obtain the characteristic GdL_β and SmL_β emission. A lithium-fluoride analyzing crystal was used to separate the emitted wavelengths and a sealed proportional counter coupled with a pulse-height discriminator was employed for detection. Standard alloy samples were prepared at 10 atomic percent intervals by dissolving a known amount (0.5g) of each in nitric acid, evaporating to dryness, and triplicate samples were diluted to a known volume (10 ml) with dilute nitric acid. The

intensity data obtained were formulated into an equation by a least-squares treatment which represents a linear relationship between the atomic percent Gd and fractional X-ray intensity of that metal in the series of alloys. The analyzed atomic percent values had a confidence limit of ± 0.29. The unknown samples were treated in triplicate similarly. The table below presents the alloys and their actual analyzed compositions.

Intended Gd, At.%	Analyzed Gd, At.%
10	9.63
20	19.89
30	30.42
40	40.47
50	51.45
60	62.81
70	72.87
80	82.60
90	92.01

Compositions of a few additional alloys were calculated based on the weight-loss data recorded in arc-melting each alloy.

The Knudsen-effusion apparatus employed on this study was described previously.[1] The alloy was contained in a tantalum crucible which was completely enclosed by welding. The diameter of the knife-edged orifice for these studies varied from 3.672×10^{-2} to 5.921×10^{-2} cm. One exception to the previous procedures used during the effusion studies was the measurement of the effused vapor. Rather than capture and analyze the condensate collected on a cold target above the effusion orifice, the weight loss of the crucible before and after effusion was determined. The loss was attributed solely to samarium metal, since the vapor pressure of the gadolinium was at least four orders of magnitude less than that of the samarium. To verify this assumption, condensate was collected from several Gd-rich alloys. There was negligible response at the gadolinium, L_β position on an X-ray spectroscopic analysis of each condensate.

X-ray diffraction analysis of powders of the alloys was obtained with a 114.6 mm Debye-Scherrer camera employing nickel-filtered, CuK_α radiation. The powders were -325 mesh, prepared in an inert atmosphere

dry box, wrapped in tantalum foil, sealed in evacuated quartz capsules, and stress relieved at 350°C for 24 hr. Lattice parameters were calculated by Cohn's least-squares method, and the errors by the Jette-Fotte techniques.

Thermal analysis of each alloy was conducted employing the Knudsen-effusion apparatus. Since a calibrated tungsten/tungsten-25% rhenium thermocouple is inserted into a well provided in the effusion crucible for monitoring the temperature during an effusion run, the same arrangement is used to conduct thermal analysis in an independent run. The error in the measurement is estimated to be less than ± 5°C.

The displacement method was used to determine the room-temperature densities of samarium, gadolinium, and their alloys. The medium used was monobromobenzene which was calibrated for variations in room temperature. Weighing was done on an analytical balance having an accuracy of ± 0.2 mg.

Metallography was accomplished by grinding with succeedingly finer SiC papers (240, 400, and 600 grit) with a medium of Deobase* and paraffin, and the polishing and etching were done simultaneously by electrolytic technique. The solution consisted of 100 cc of methanol and 50 cc of NHO_3 held in a container in an ice bath. The voltage was 12 v and the specimen area about 16 mm^2. Immersion times were of the order of 10 sec.

III. RESULTS AND DISCUSSION

Several experimental parameters were examined in the study of alloy behavior in the Sm-Gd binary system. Determination of thermo-dynamic activities of the components in the Sm-Gd alloys was the principal experiment. The other data obtained in corroboration with the activities were lattice parameters, atomic volumes, thermal analysis data, room-temperature densities, microhardness and metallographic analysis.

---

* High-purity kerosene

The vapor pressures of each alloy were measured in the temperature range from 1070 to as high as 1424°K. The alloy phase at these temperatures throughout the system generally consisted of the hexagonal close-packed modification. At the samarium-rich end, however, some of the data points were in the high-temperature, body-centered-cubic phase (or β-phase). The vapor-pressure data for the alloys were treated by a least-squares method. These data, in turn, were used to calculate the activities in the hexagonal close-packed phase at a temperature level of 1173°K. Since the vapor pressure of gadolinium was negligible compared to that of samarium, the vapor losses were all samarium. Calculation of the activities of samarium is accomplished using the following equation:

$$a_{Sm} = \frac{P_{Sm}}{P_{Sm}^O}$$

where P_{Sm}^O is the vapor pressure of the pure samarium (assuming the vapor is a perfect gas). The vapor-pressure data of pure samarium were reported previously in the temperature range of 1033-1173°K as follows:[3]

$$\log P(\text{mm Hg}) = - \frac{11,900 \pm 300}{T} + 9.71 \pm 0.24$$

In addition, the activity of gadolinium was derived from the activity of samarium by integration of the Gibbs-Duhem equation. The activities are plotted versus mole fraction gadolinium in Figure 1, in which a negative deviation from Raoult's law is observed. The negative deviation implies a tendency for unlike atoms to attract one another, or compound-formation tendency. The curve at no place levels off as a plateau, which is refutation of the presence of a two-phase region. Therefore, a complete solid solution exists at 1173°K in the hexagonal close-packed phase. Apparently, the difference in crystal structure between samarium and gadolinium is not sufficient to cause a two-phase miscibility gap. The crystal structure difference is subtle; both components are hexagonal close packed, but with different stacking sequences. The stacking-sequence difference is not sufficient to interrupt the solid solubility, and it changes gradually from one pure component to

the other across the alloy system. However, the deviation from ideality indicates that in the solid solution a short-range ordering and association of samarium and gadolinium atoms are occurring.

The lattice parameters as well as atomic volumes (calculated from the X-ray densities) for the Sm-Gd alloys are plotted as a function of atomic percent of gadolinium in Figure 2. As one can observe, there is a negative deviation of atomic volume from ideality up to nearly 50 atomic percent Gd. Thus, there is a volume change on mixing. The c/a ratio shows that the room-temperature solid solution retains the characteristics of samarium metal in the Sm-rich region and of gadolinium in the Gd-rich region. The transition from one type of stacking sequence to the other occurs at about 40 atomic percent Gd. In the case of the c_O value for the samarium structures, the original c_O parameter is divided by 4.5 to facilitate a comparison with the parameter of gadolinium, which has the ABAB stacking sequence. The lattice parameters are shown to vary from samarium to gadolinium without an abrupt change but with obvious deviations from the linear relationship between the two component metals. No breaks in continuity of the parameters are further evidence of complete solid solubility in the alloy system.

The X-ray diffraction data of samarium and gadolinium determined in this investigation and found in the literature are compared below:

		This Study	Literature[4]
Sm	a_O, Å	3.632 ± 0.025	3.626 ± 0.005
	c_O, Å	26.29 ± 0.12	26.18 ± 0.06
	c/a	7.239	7.220
	ρ_{X-ray}, g/cm³	7.478	7.537
Gd	a_O, Å	3.6338 ± 0.0029	3.634 ± 0.003
	c_O, Å	5.7833 ± 0.0077	5.781 ± 0.005
	c/a	1.592	1.591
	ρ_{X-ray}, g/cm³	7.896	7.898

Thermal analysis was conducted on each alloy as well as the component metals. The data obtained for samarium and gadolinium are compared below with the literature values which have been compiled by Gschneidner:

		This Study	Literature[4]
Sm	Melting Temp., °C	1073 ± 5	1073 ± 1
	Transition Temp., °C	911 ± 5	924 ± 7
Gd	Melting Temp., °C	1314 ± 5	1312 ± 2
	Transition Temp., °C	1240 ± 5	1260 ± 2

Figure 3 shows the final plot of liquidus, solidus, and transformation temperatures for the Sm-Gd alloy system. The general trend observed in both narrow fields of Liquid + β and β + α is reasonable indeed. The thermal analysis data reveal no evidence of a two-phase field. The system has been shown to exhibit complete solid solubility in the room-temperature and high-temperature phases as with other experimental parameters, i.e. thermodynamic activities, lattice parameters and atomic volumes. There is no previous investigation regarding the phase equilibria of this alloy system found in the literature.

Room-temperature density data for the Sm-Gd alloys show that the density increases linearly with increasing amounts of gadolinium up to nearly 50 atomic percent Gd and then changes rather gradually to the density of pure gadolinium. No abrupt transition is seen here again to suggest the existence of a two-phase field in the system.

Microhardness of the as-arc-melted Sm-Gd alloys was determined as a function of atomic percent of gadolinium. The trend observed is typical for a complete solid solution alloy system. A maximum in hardness is located at approximately 60 atomic percent Gd.

A discernible microstructural change appears to occur around 40 atomic percent Gd. The samarium or samarium-rich alloy structure is replaced by the structure representative of gadolinium. No two-phase structure was observed in a series of the Sm-Gd binary alloys examined in this study. The observation also supports the findings from other experimental parameters which have been described earlier.

REFERENCES

1. C. E. Lundin, A. S. Yamamoto and J. F. Nachman, "Studies of Solution Ideality in the Praseodymium-Neodymium System," Acta Met., 13 (1965) 149-154.

2. C. E. Lundin and M. J. Pool, "Heats of Mixing in Praseodymium-Neodymium Solid Solutions," J. Less-Common Metals, 9 (1965) 48-53.

3. A. S. Yamamoto, C. E. Lundin and J. F. Nachman, "Vapor Pressures of Samarium and Gadolinium," Proceedings of the Fourth Conference on Rare Earth Research, 22-25 April 1964, Phoenix, Arizona, Gordon and Breach Science Publishers, New York, 1965, p. 203-214.

4. Karl A. Gschneidner, "Application of Vacuum Metallurgy in the Purification of Rare-Earth Metals," presented at the Eighth Annual Conference on Vacuum Metallurgy, New York, N. Y., 21-23 June 1965.
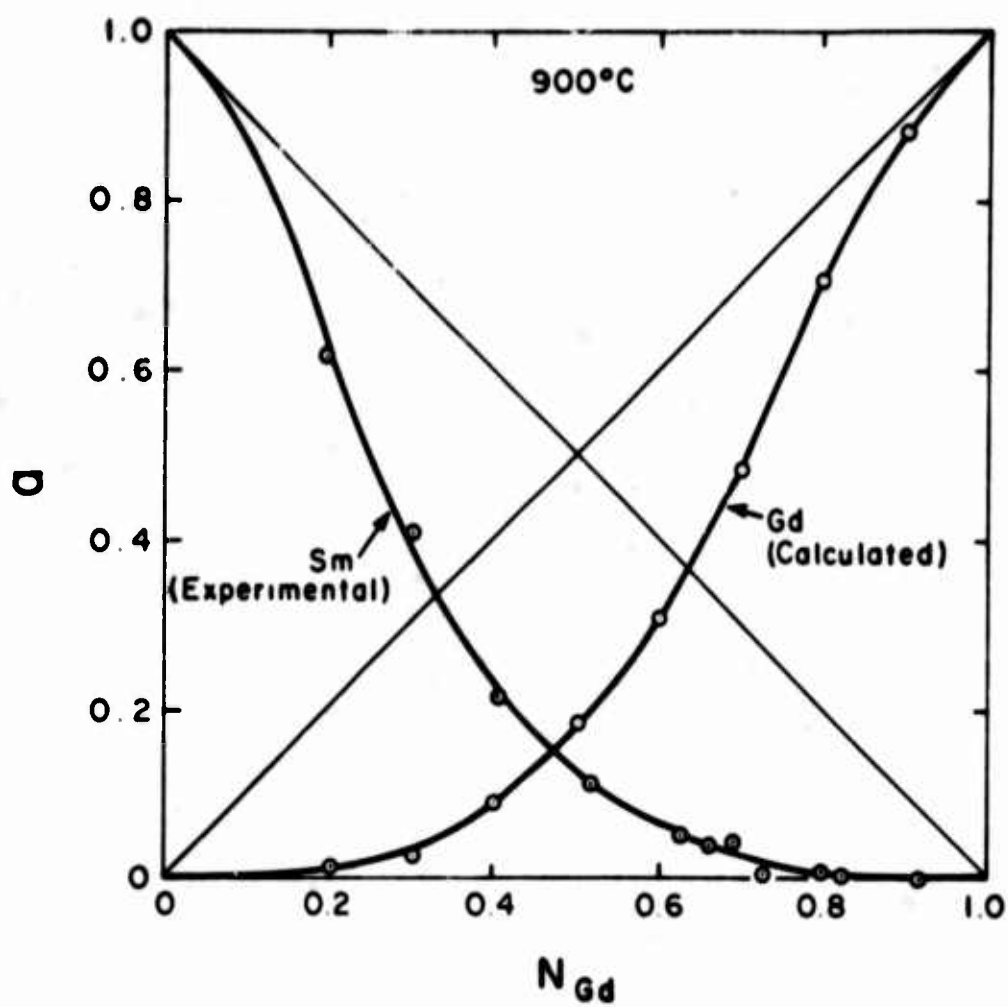
Figure 1. Activities of Samarium and Gadolinium in Sm-Gd Alloys at 900°C
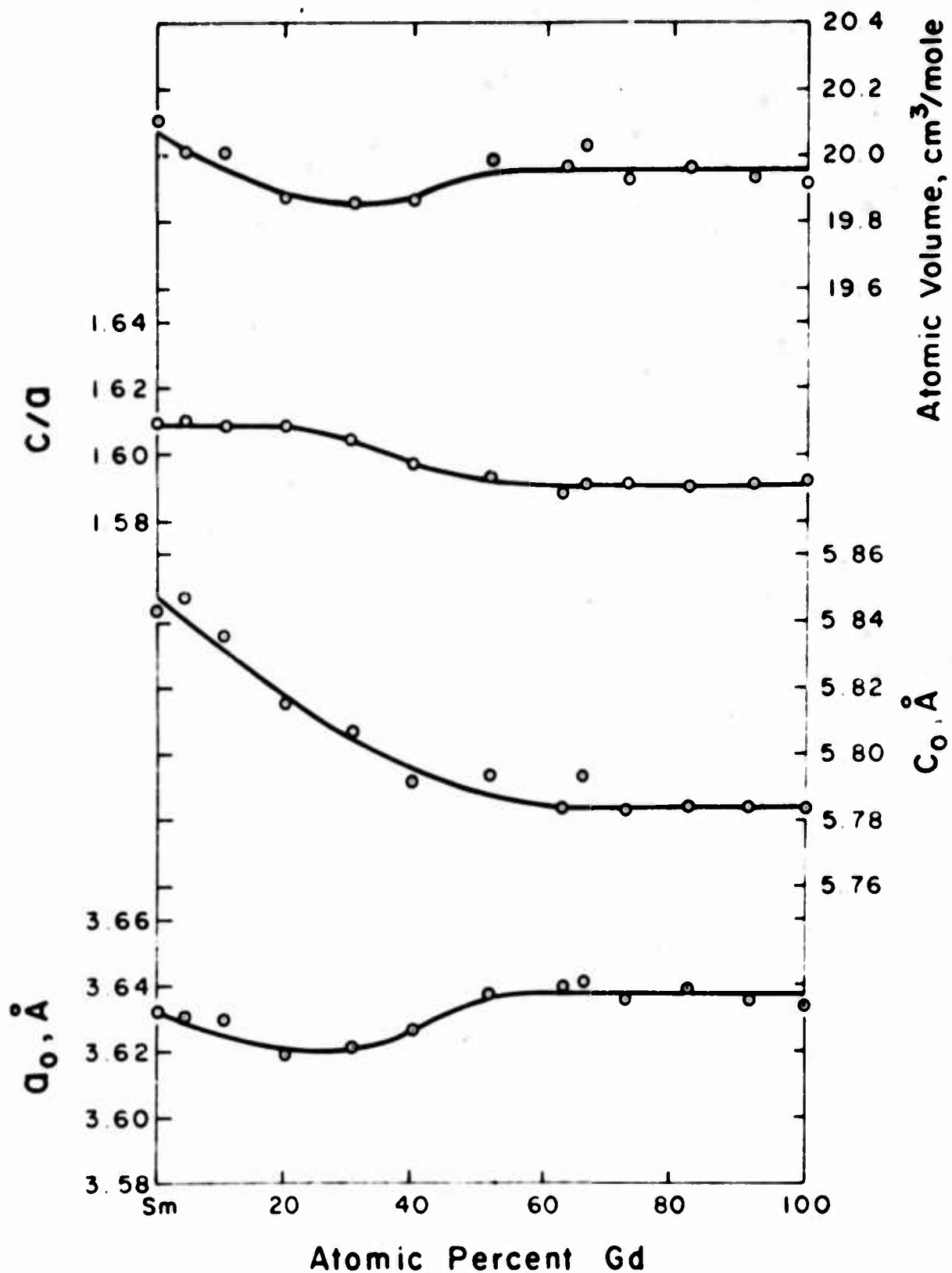
Figure 2. Plot of Lattice Parameters and Atomic Volumes vs. Composition for the Sm-Gd Alloy System
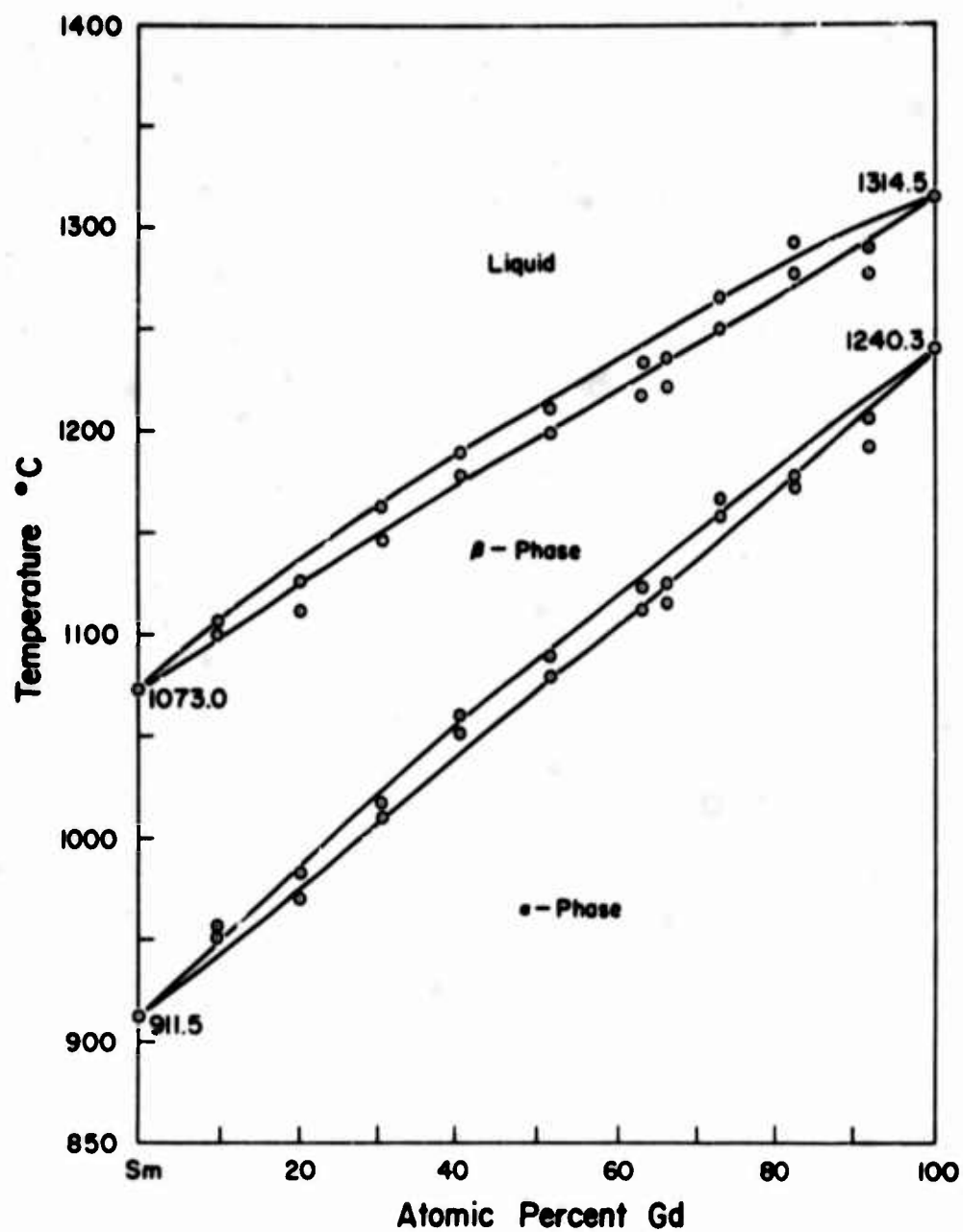
Figure 3. Phase Diagram of the Sm-Gd Binary System

THE ALLOYS OF SAMARIUM WITH GADOLINIUM AND CERIUM

E. M. Savitsky, V. F. Terehova, R. S. Torchinova

A. A. Baikov Metallurgical Institute of the Academy of
Sciences of the USSR, Moscow, USSR

Abstract

The Sm-Ce, Sm-Gd binary systems have been investigated
by means of microstructural, X-ray and thermal analysis.

The hardness and magnetic susceptibility vs temperature
curves were built in the temperature range $-183 + 25^{O}C$.

In the Sm-Gd system a complete solid solubility of high
temperature b.c.c. modifications of samarium and gadolinium
and a wide series of solid solutions between low temperature
h.c.p. modification of gadolinium and rhombohedrical of samar-
ium have been found. The two phase region existed between
59-75 w/o Gd. No intermetallic compounds were found in this
system.

In the Sm-Ce system b.c.c. solid solutions between high
temperature modifications were found to form over the full
range of concentrations. The solid solubility of γ-Ce (f.c.c.
in Sm was rather small. There was two phase region in the con
centration range 0.5-15.6 w/o Sm between f.c.c modification
of cerium and hexagonal solid solution which formed on the
basis of h.c.p. β-Ce and Sm. In the concentration range of
15.6-70 w/o Sm the existence of the wide region of hexagonal
solid solutions was established. The solid solubility of

cerium in samarium is probably less than 10 w/o. The Ce-Sm alloys with samarium content >70 w/o appeared to be the two-phase mixture of hexagonal and rhombohedrical structures.

Magnetic susceptibility of Ce-Sm alloys was measured in the temperature range -183 + 25°C. The paramagnetic suscepti-bility vs temperature curves showed linear character in wide temperature interval. The paramagnetic susceptibility values as a function of cerium content varied from 8.5 x 10^{-6} to 17.7 x 10^{-6} e.m.e./mole.

Effect of the s-f Exchange in Dilute Alloys

Kei Yosida

Institute for Solid State Physics, University of Tokyo

It has been well established that the s-f exchange
interaction between the conduction electrons and the
localized spin of 4f-electrons plays a decisive role in
the magnetic and electrical properties of rare earth
metals and alloys.   The s-f exchange interaction has a
remarkable effect particularly in dilute alloys of rare
earth in non-magnetic metals. Since Kondo has succeeded in
explaining the resistivity minimum in dilute alloys of Mn
and Fe in noble metals the effect of the s-f or s-d exchange
on the electrical resistivity of dilute alloys has been
investigated in detail by Suhl, Abrikosov, Nagaoka and
many others. In this paper, these investigations are
reviewed in connection with dilute alloys of rare earths
and recent experiments on this anomalous effect are also
briefly mentioned.

The s-f exchange interaction between the conduction
electrons and a localized spin can simply be described as

$$V_{ex} = - \frac{1}{2N} \Sigma J(k-k')e^{i(k'-k)R} \left\{ (a^*_{k'\uparrow}a_{k\uparrow} - a^*_{k'\downarrow}a_{k\downarrow})S_z \right.$$

$$\left. + a^*_{k'\downarrow}a_{k\uparrow}S_+ + a^*_{k'\uparrow}a_{k\downarrow}S_- \right\} \quad , \qquad (1)$$

where $a^*_{k\uparrow}$ and $a_{k\uparrow}$ denote the creation and annihilation oper-
ators for the conduction electron with wave vector k and
up spin. S_z and $S_\pm$ are the three components of the local-
ized spin. N represents the total number of lattice points
and R the position of the localized spin.

The origin of the exchange integral $J(k,k')$ is not so
simple as has been supposed in earlier days and its k-depen-
dence is also complicated depending on the wave-function of

the conduction electrons and the state of the localized spin, but the main part of J would depend only on $|k-k'|$. The conventional assumption of constant J which corresponds to taking only an s-part has been useful in discussing the qualitative nature of the s-f exchange interaction and this assumption will also be adopted in the following discussion.

In rare earths the state of the 4f-electrons is specified by the vector sum of the spin S and the orbital angular momentum L. Therefore, spin S in Eq. (1) is replaced by $(g-1)J$ where g is the Landé g factor and $g-1$ is negative or positive according to the less-than half-filled or the more-than half-filled shell. Or alternatively if S is regarded as the total angular momentum J, the effective exchange integral J_{eff} can be expressed as

$$J_{eff} = (g - 1)J. \tag{2}$$

Therefore, as is well-known, J_{eff} becomes negative or positive according as 4f-shells are less-than half-filled or more-than half-filled.

In rare earth metals, particularly for lighter elements the crystalline field is often greater than s-f exchange. In such a case, the Hamiltonian (1) must be projected to the lowest manifold, then in general the effective exchange becomes anisotropic and for the cubic crystals the effective exchange will change its magnitude. For example, in cubic cerium the lowest energy level is doublet and in this sub-

space $J = -\frac{5}{3} S$ where S is the effective spin with a magnitude of one-half. Thus, the effective exchange integral can be written as $J_{eff} = -\frac{5}{3}(g - 1)J$. Therefore, for this case J_{eff} becomes positive, changing its sign again as far as the lowest subspace is concerned. However, the upper energy-level cannot be neglected in actual cases, so that the situations become complicated in rare earths except gadolinium.

Under a simplified assumption of a constant J, Kondo[1] calculated the transition rate for an incident electron in state k to other states by the impurity spin up to the third order in J, namely the second Born approximation and obtained the following expression:

$$T_k = \frac{\pi}{\hbar} S(S+1)\left(\frac{J}{2N}\right)^2 \rho(\varepsilon_k)\left(1 + \frac{J}{N} \Sigma_q \frac{2f_q - 1}{\varepsilon_q - \varepsilon_k}\right), \quad (3)$$

where $\rho(\varepsilon)$ denotes the state density per spin and f_q represents the Fermi distribution function. The second term of this expression arises from non-commutativity between the spin components, namely a dynamical character of the localized spin as pointed out by Kondo and it has a logarithmic singularity as

$$\frac{J}{N} \Sigma_q \frac{2f_q - 1}{\varepsilon_q - \varepsilon_k} \sim \frac{J\rho}{N}\log\frac{|\varepsilon|}{D} \quad . \quad (4)$$

The resistivity can be obtained from Eq. (3) as

$$R = R_o(1 + 2 \frac{\rho J}{N}\log \frac{kT}{D}), \tag{5}$$

where R_o is a usual Born term and proportional to J^2 and $S(S+1)$ and the square state-density with its width of 2D is assumed. The second term is so-called Kondo anomalous term and $J<0$ it gives rise to the resistivity minimum of Cu-Mn alloys combined with the lattice contribution.

The logarithmic behavior of the resistivity has been observed also in La- and Y-rare earth dilute alloys by Sugawara[2] although some of them have a ferromagnetic effective J. In the rare-earth alloys, the exchange integral J is much smaller than that of CuMn alloys but the state density is much higher than Cu. Therefore, the logarithmic behavior begins to appear at about 10^oK. However, this phenomenon becomes somewhat complicated because of the crystalline field effect except for Gd. The anomalous resistivity for the anisotropic exchange has been calculated by Miwa and Nagaoka[3].

Since the Kondo term diverges as temperature goes to zero, higher terms become important at low temperatures. Many investigations[4-8] have been done for this purpose, By collecting the most divergent terms, Abrikosov[4] obtained the expression

$$R = R_o \frac{1}{(1 - \frac{\rho J}{N}\log \frac{kT}{D})^2 + C}, \tag{6}$$

where C is a constant proportional to J^2 and $S(S+1)$. A similar
and more complete expression has been derived by Suhl[5] who
used the Chew-Low method which is non-perturbative and
he has shown that this expression cannot be used for lower
temperature than $T_K = D \exp(N/\rho J)$ because the scattering
amplitude becomes non-analytic in the physical plane for
the antiferromagnetic coupling $(J < 0)$. On the other hand,
Nagaoka[6] found an approximate solution which holds for
$T \ll T_K$. This solution gives the resistivity which continues
to increase down to the absolute zero at which it reaches a
constant value which is independent of J and S. Suhl and
Wong[7] also obtained a similar behavior for resistivity by
an analytic continuation of the high temperature expression
towards the lower temperature side. The important point
in Suhl-Wong theory, the resistivity is quite continuous
at $T = T_K$ and T_K gives only a temperature scale for the
Kondo anomaly.

In order to see what happens in the impurity spin in
connection with the Kondo effect, it is necessary to calcul-
ate other quantities than resistivity. The spin polariza-
tion connected with the impurity spin was obtained by
Yosida and Okiji[9] with the use of the simple perturbation
method. According to their calculations, the magnitude of
the localized spin $< S >$ decreases with lowering temperature
as

$$\frac{\langle S \rangle}{S} = 1 + \frac{1}{2} \frac{\rho J}{N} \frac{\frac{\rho J}{N} \log \frac{kT}{D}}{1 - \frac{\rho J}{N} \log \frac{kT}{D}} . \tag{7}$$

This expression was obtained by collecting the most divergent terms of the perturbation series in J. The spin polarization of the conduction electrons induced by the localized spin is at the same time given by

$$\sigma = \frac{\rho J}{2N} \langle S \rangle . \tag{8}$$

For ferromagnetic exchange $J > 0$, $\langle S \rangle$ gradually decreases towards $S(1 - \rho J/2N)$ as temperature is lowered and the total spin $\langle S \rangle + \sigma$ becomes equal to the original value of S at the absolute zero of temperature. This is consistent with the fact that the s-f exchange interaction conserves the total spin. On the other hand, for antiferromagnetic exchange $J < 0$, the magnitude of the localized spin decreases more rapidly and becomes minus infinity at T_K, namely the perturbation series becomes divergent at this temperature in coincidence with the appearance of a pole in the scattering amplitude. Therefore, the expression (7) for $\langle S \rangle$ is useless at low temperatures. The magnetic susceptibility can be derived from the above two expressions for the spin polarization as

$$\chi = \frac{g^2 \mu_B^2 S(S+1)}{3kT} (1 + \frac{1}{2} \frac{\rho J}{N} \frac{1}{1 - \frac{\rho J}{N} \log \frac{kT}{D}}). \tag{9}$$

This expression was also derived directly by Miwa, Scalapino and Giovannini, Paulson and Schrieffer[10].

According to rare earth experiments[11], the induced polarization of hexagonal La by Gd impurity is about 0.5 μ_B and from this value $\rho J/2N$ is estimated as 0.07. This value seems to be larger than that evaluated from the anomalous resistivity by Sugawara[2]. This suggests that the conduction electrons responsible for the magnetic susceptibility are different from those for the resistivity. The induced polarization of Gd in Y is even greater than the above value, namely 2 μ_B. Therefore, we must consider the deformation of the 4f-shell as proposed by Bonnerot, Caroli and Coqblin[12]. Sugawara[2] observed a remarkable resistivity minimum in Y-Ce dilute alloys. This is consistent with negative J_{eff} for Ce in Y, but a large residual resistivity found in this case also shows a possibility that the 4f-shell is considerably deformed from the free ion state.

The behavior of the localized spin described by Eq. (7) suggests that at the absolute zero the localized moment is quenched, namely the ground state of the present system is in a singlet state in which the expectation value of S vanishes. Standing on this point of view, we consider the following singlet state[13]:

$$\psi_0 = \Sigma_k \Gamma_k (a^*_{k\downarrow}\alpha - a^*_{k\uparrow}\beta)\psi_v, \tag{10}$$

where α and β are, respectively, the up-spin and down-spin eigenfunction for the localized spin whose magnitude is assumed to be one-half and ψ_v represents the wave function

- 477 -

of the Fermi sea. ψ_o represents a singlet state in which an electron excited above the Fermi sea is antiferromagnetically coupled with the localized spin. This singlet state is the simplest one among other singlet states. If we introduce the s-f exchange interaction (1) into this state, the Fermi sphere will be deformed by the electron and hole excitations. The perturbation method applied to the starting wave-function of Eq. (10) gives the following energy eigenvalue:

$$E = E_o + \widetilde{E} . \tag{11}$$

E_o is the perturbed energy of the normal state with spin degeneracy which can be expressed by a power series in J and $\widetilde{E}$ is determined by the following equation:

$$1 = 3x + 3x^3 + 6x^4 + 18x^5 + 54x^6 + \ldots$$

$$x = \frac{\rho J}{4N} \log \frac{|\widetilde{E}|}{D} > 0 . \tag{12}$$

For this equation only the most divergent terms are retained. The power series given by (12) with respect to x is convergent if x is smaller than about 1/3 because the ratio of neighboring two terms in this power series is 2x, 3x and 3x, respectively. Within this radius of convergence Eq. (12) has its positive root, namely the zero-th approximation gives a root of $x_o = 1/3$ and the first approximation a root of $x_1 = 0.305$ and as one goes to higher approximation this positive

root decreases gradually and it is expected that x_∞ tends to 1/4. Thus, the ground singlet state energy is lower than the normal energy by

$$\widetilde{E} = - D\exp(N/\rho J).$$ (13)

This energy can be interpreted as a binding energy of a singlet bound state although this bound state has a many-body character and not a one-electron state. For $J > 0$, we can calculate the energy of the triplet state in a similar way and we obtain the equation corresponding to Eq. (12). However, for this case we cannot obtain any root within the radius of convergence. Therefore, it is plausible that no bound state appears for a triplet state.

The effect of a magnetic field on the singlet ground state obtained above is difficult to treat generally, but the suscep-tibility for a weak field can be calculated and obtained as[14]

$$\chi = \frac{\mu_B^2}{|\widetilde{E}|} \sim \frac{\mu_B^2}{kT_K} .$$ (14)

This result holds in any stage of approximation if the root of Eq. (12) is taken for $\widetilde{E}$ and therefore, it is correct as far as the present model is concerned. Thus, it is expected that the susceptibility increases as temperature decreases and tends to a constant value given by Eq. (14), saturating at low temperatures. This tendency of the susceptibility was also obtained by Dworin[15], but his low temperature value

- 479 -

is different from ours.   The transition rate for an incident
electron calculated on the present model becomes independent
of J.   This seems to imply that the present model is not
incompatible with Suhl and Nagaoka theories although Suhl's
equation for determining the scattering amplitude would not
allow the singlet state.   Recently, Hamann[16] has succeeded
in solving Nagaoka's integral equation for the double time
Green's function and obtained the result that the zero-temp-
erature susceptibility becomes infinity.   This result is
certainly inconsistent to our result, but since we have not
yet succeeded in extending our theory to finite temperature,
the problem of clarifying the relation of the present model
to other scattering theories must be left to future investi-
gations and in particular experimental investigations are
demanded to settle the present problem.

References

1. J. Kondo, Prog. Theor. Phys. 32, 37(1964).
2. T. Sugawara, J. Phys. Soc. (Japan)20, 2252(1965), ibid.
    21, 725(1966).
3. H. Miwa and Y. Nagaoka, Physics Letters, 22, 394(1966).
4. A. A. Abrikosov, Physics, 2, 5(1965).
5. H. Suhl, Phys. Rev. 138, A515(1965), Physics, 2,39(1965),
    Phys. Rev. 141, 483(1966).
6. Y. Nagaoka, Phys. Rev. 133, A1112(1965), Prog. Theor. Phys.
    37, 13(1966).
7.   H. Suhl and D. Wong, Physics, to be published.
8. S. Doniach, Phys. Rev. 144, 382(1965).

9. K. Yosida and A. Okiji, Prog. Theor. Phys. 34, 505(1965).
10. H. Miwa, Prog. Theor. Phys. 34, 1040(1965).
   D. J. Scalapino, Phys. Rev. Letters, 16, 937(1966).
   B. Giovannini, R. Paulson and J. R. Schrieffer, Phys. Letters, 23, 517(1966).
11. D. K. Finnemore, D. C. Hopkins and P. E. Palmer, Phys. Rev. Letters, 15, 891(1965). W. E. Gardner and H. Williams, Proceedings of the 10-th International Conference on Low Temperature Physics, Moscow(1966).
12. J. Bonnerot, B. Caroli and B. Coqblin, Proceedings of the Conference on Low Temperature Calorimetry, Helsinki(1966).
13. K. Yosida, Phys. Rev. 147,223(1966), Prog. Theor. Phys. 36, 875(1966), A. Okiji, Prog. Theor. Phys. 36, 712(1966), J. Kondo, Phys. Rev. to be published.
14. H. Ishii, to be published.
15. L. Dworin, Phys. Rev. Letters, 16, 1042(1966).
16. D. R. Hamann, to be published.

Band Structure, Fermi Surface and Physical Properties
of the Rare-Earth Metals
A. J. Freeman, National Magnet Laboratory*,
Massachusetts Institute of Technology, Cambridge, Massachusetts

A review is given of our present understanding of some of the electric,
magnetic and optical properties of the rare-earth metals based on recent
ab initio energy band calculations.

I. Introduction

The heavy rare-earths form a class of metals distinguished by a number of

unusual magnetic and other properties. In sharp contrast with the case of other

metal groups little has been known, until very recently, either theoretically or

experimentally about the band structure and Fermi surface of these metals.

This situation led to the development of a body of theoretical work based on a

simple free-electron model which has had some notable successes in explaining

several of the observed magnetic properties (including their antiferromagnetic

ordering properties and temperature dependences) and the striking resistivity

anomaly associated with the onset of magnetic ordering.

In this talk, we describe the current understanding of some of the electric,

magnetic and optical properties of the rare-earth metals which has been de-

rived from detailed ab initio energy band calculations of their electronic struc-

ture and Fermi surfaces. These calculations have shown that the free-electron

model is completely inappropriate for the rare-earths and cast doubt upon the

interpretation of any physical property which is based on this model.

II. Calculations and Results

Accurate energy band calculations were made using the non-relativistic APW method for the hcp metals La, Gd, Tm and Lu and the bcc metal Eu. A number of different crystal potentials were constructed, based on different assumed atomic configurations, as a superposition of atomic potentials made up from free atom Hartree-Fock and Hartree-Fock-Slater wave functions. For example, for Gd (for which we have done the most extensive sets of calculations) we have used atomic charge densities obtained by using the calculational procedure of Herman and Skillman applied to the atomic configurations $4f^7 5d^1 6s^2$, $4f^7 5d^2 6s^1$, $4f^7 5d^3 6s^0$, and $4f^8 5d^0 6s^2$ and the Hartree-Fock atomic charge density for the Gd configuration $4f^7 5d^1 6s^2$. The effect of different exchange potentials was also investigated by performing calculations using the standard Slater $\rho^{1/3}$ approximation and $2/3 \, \rho^{1/3}$ as suggested recently by Kohn and Sham and earlier by Gaspar. As expected, the differences in the potentials occur in the outer regions of the atom since we have varied the configuration of the outer electrons only. All of these potentials gave qualitatively the same energy band results with a maximum variation in the relative energies of the conduction band states of about 0.5 eV.

The energy bands, density of states and Fermi surfaces of the hcp metals we have investigated are found to be (remarkably) similar and differ from each other only in details. As will be shown, the conduction bands are not all represented by the free electron model but instead are of mixed s-d character and strongly resemble the energy bands of transition metals. These d bands, which originate from the atomic 5d states, contribute a high density of states in the vicinity of the Fermi energy. The total width of the d bands is about 0.5

Rydbergs (6 eV). This width is nearly the same as that obtained by Wood for the 3d-bands in iron. The Fermi energy is found to lie at a peak in the density of states. (The Fermi energy, for three electrons per atom, is $E_F = 0.25$ measured from the bottom of the band as compared with a value of 0.54 ry for the free electron model.) At the Fermi energy, the calculated density of states is large, $N(E_F) = 1.8$ electrons per atom per eV compared with the free electron value of 0.6 eV^{-1}. This is due to the fact that the electron bands in the vicinity of the Fermi surface are of mixed s-d character and are consequently much flatter than would be expected from a free electron model.

As can be seen by inspecting free ion wave functions, the 4f electrons are tightly bound to the atom and do not overlap neighboring atoms appreciably. Consequently in the band model, the 4f electrons form a very narrow band. For example, for Gd the calculations yield a 4f band with a width of about 0.05 eV located approximately 11 eV below the bottom of the 5d - 6s bands. This separation, however, is very sensitive to the potential used in the calculations and is consequently unreliable. Furthermore, the energy band picture for the 4f states essentially neglects the intra-atomic coulomb and exchange energies of these electrons which amounts in Gd to several electron volts. For this reason, the 4f electrons cannot be treated as band electrons but must be considered as localized and so do not fit within the band picture at all.

The electronic properties of the rare-earth metals are determined largely by the shape, form, and topology of their Fermi surface. The complete Fermi surface for holes in Gd and Th will be presented. Close similarity between the two was obtained. The Fermi surface, which permits open orbits both along the c-axis of the crystal and in the plane perpendicular to this axis has much

structure and a number of unusual and interesting features, such that it would be very interesting to study the de Haas-van Alphen, Schubnikov-de Haas and cyclotron resonance phenomena in these materials. (Unfortunately, the purity of the rare-earth metals is not at present sufficiently high to allow one to make these measurements.) Since the qualitative features of the Fermi surface are found not to change with the different potentials used, we feel that these qualitative features are reliable. This Fermi surface is found to bear no resemblance at all to the Fermi surface of the free electron model. It should be recognized that with the inclusion of relativistic effects, an energy gap, representing itself as a discontinuity in the Fermi surface will occur in the ALH plane.

Recently, Loucks and associates have done relativistic APW calculations for some of the rare-earth metals. This now allows us to ascertain the effects of including relativistic terms in the calculations. A comparison, to be discussed, shows remarkable close agreement between the non-relativistic and relativistic calculations; for example, the Fermi surfaces agree within the accuracy of the computations.

Eu, which is bcc, is quite different from the metals just discussed, not only in its crystallographic structure but also in some of its observed properties. Because of the uncertainty introduced by the interpretation of the magnetization measurements by Bozorth and Van Vleck as to the appropriate configuration to assign to the 4f electrons, we have done calculations for both the divalent ($4f^7 6s^2$) and trivalent ($4f^6 5d^1 6s^2$) configurations. As with the hcp metals just discussed, the calculated bands differ markedly from the free-electron model, because the bands originating from the 5d and 6s atomic

states overlap and are strongly mixed. The bands show a close resemblance to those of the bcc transition metals like V, Cr and Fe. By comparing the calculated specific heat with experiment, we infer that the divalent configuration is appropriate but not the trivalent.

III. Comparison with Experiment

Unlike the case several years ago, when we obtained our first result, there now exist a number of different experiments with which to compare our calculated results. In the talk, we will discuss in some detail:

a) specific heat, magnetization and photo-emission data

b) resistivity and positron annihilation experiments

c) optical measurements.

We can compare the data of a) with our computed density of states, b) with our Fermi surface and c) with the band structure itself. We find that there is good qualitative agreement between theory and experiment in all cases. Even the resistivity anomalies at the antiferromagnetic ordering temperature, mentioned in the Introduction as being an outstanding success of the free electron model, are reproduced by our computed d bands and Fermi surface.

IV. Acknowledgements

The work discussed here was carried out in collaboration with J. O. Dimmock, Lincoln Laboratories, M.I.T. and R. E. Watson, Brookhaven National Laboratory. The help of Mrs. Anna Furdyna with the computations and the determination of the Fermi surfaces is deeply appreciated. I am grateful to T. L. Loucks, University of Iowa, for preprints prior to publication.

POSITRON ANNIHILATION IN RARE EARTH SINGLE CRYSTALS.

R. W. Williams

Department of Physics, Iowa State University, U. S. A.

and

A. R. Mackintosh

Technical University, Lyngby, Denmark

Abstract

We have measured the angular correlation of the photons emitted when positrons annihilate with electrons in single crystals of the rare earth metals Y, Gd, Tb, Dy, Ho and Er and also in single crystals of certain alloys. A comparison of the results for Y with the calculations of Loucks shows that the independent-particle model gives a good approximation to the angular distribution, although correlation effects probably smear out some of the details. The angular distributions in the c-direction in the paramagnetic phases show a rapid drop at low angles followed by a hump, and these features are associated with rather flat electron and hole regions of Fermi surface normal to the c-axis. There is a strong correlation between the size of the hump and the ability of the magnetic metals to form a periodic magnetic structure. In the spiral phase of Ho, the hump is much reduced, indicating that the flat electron and hole surfaces are substantially modified by the magnetic ordering. The implications of these results on the relation between the conduction electrons and the magnetic order in rare earth metals are discussed.

The experiments described in this paper were undertaken in order to test the single-particle theory of positron annihilation, and to use this technique to study the electronic structure of the hcp rare earth metals. Because of the relatively low purity of available samples, it is difficult to apply the conventional techniques of Fermi surface determination to the rare earths. In addition, the magnetic ordering at low temperatures severely restricts the number of methods which may be used to study the electronic structure in the paramagnetic phase, and it is this which is of primary interest in understanding the relationship between the conduction electrons and the magnetic structures.

The angular correlation of the photons emitted by annihilating electron-positron pairs was measured by a conventional two-slit technique[2] in the rare earth metals Y, Gd, Dy, Tb, Ho and Er, and in a 50% Ho-Er alloy. Band structure calculations[3,4] indicate that the Fermi surfaces of the rare earths are highly anisotropic and this anisotropy was apparent in the angular distribution of the photons. For directions in the basal plane, the distribution was close to the parabola corresponding to three free electrons per atom, but for the c-direction, the number of coincidences dropped rapidly at low angles and then formed a hump at higher angles, as shown in Fig. 1.

To test the validity of the independent particle model of positron annihilation, a detailed calculation of the angular distribution in the c-direction was made by Loucks[5]. In this model the number of coincidences at an angle θ is proportional to

$$N(\theta = \frac{\hbar p_z}{mc}) = \int\int_{-\infty}^{\infty} dp_x \, dp_y \, \sum_{\underline{k}} \Gamma(\underline{p},\underline{k}) \qquad (1)$$

where the sum is over all occupied states and

$$\Gamma(\underline{p},\underline{k}) = |\int \psi_{\underline{k}}(\underline{r}) \, \psi_+(\underline{r}) \, e^{-i\underline{p}\cdot\underline{r}} \, d\underline{r}|^2$$

$$= B_{\underline{g}}(\underline{p},\underline{k}) \, \delta(\underline{p}-\underline{k}+\underline{g}) \qquad (2)$$

The energy eigenvalues for the electrons and the Fermi
surface were calculated by the APW method, while the eigen-
functions $\psi_{\underline{k}}(\underline{r})$ were expanded as a linear combination of
APW's. The ground-state positron wavefunction $\psi_+(\underline{r})$ was
obtained from a numerical solution of the Schrödinger
equation. The theoretical results, shown in Fig. 1, re-
produce the rapid drop at low angles and the hump observed
in the experiments, but both of these features are more
pronounced than observed in practice. An examination of
the theoretical results reveals that the rapid drop is
due to a rapid reduction in the number of occupied states
in a section through the Brillouin zone as k_z is increased,
while this feature, together with a precipitous drop in
$\Gamma(\underline{p},\underline{k})$ as p goes beyond the zone boundary also accounts
for the hump. If we write formally

$$N(p_z) = A(p_z)F(p_z)$$

where $A(p_z)$ is the number of occupied states in a section of the zone, and is periodic with the period of the reciprocal lattice, then $F(p_z)$ is approximately constant if p_z is within the zone and drops rapidly beyond it. This reflects the exclusion of the positron wavefunction from the ion core by the Coulomb repulsion and the consequent attenuation of terms with g different from zero in (2).

We conclude therefore that the independent particle model provides a good first approximation to the theory of electron-positron annihilation in metals and that the rapid drop in coincidences with angle reflects the rapid change in occupation of states, which is a consequence of the rather flat electron and hole sheets normal to the c-axis. The difference between the calculated and experimental angular distributions may be due to errors in $\Gamma(\underline{p},\underline{k})$ caused by inadequate wavefunctions, but it seems more likely to be predominantly a consequence of the broadening of the electron and positron states by the Coulomb interaction.

The c-axis distributions in Dy, Ho, Er and the 50% Ho-Er alloy are all qualitatively very similar to that in Y, with a rapid fall at low angles followed by a pronounced hump. These metals all form periodic magnetic structures over a wide temperature range. On the other hand in Gd, as shown in Fig. 2, and in Tb, this structure is much reduced, although the distributions are still quite different from the free electron model.Tb forms a spiral structure over a temperature range of only ten degrees while Gd is ferromagnetic below its ordering temperature. When Y is added to Gd, however, a spiral structure

rapidly results. There is therefore a perfect correlation between the appearance of a hump in the angular distribution and the formation of periodic magnetic structures.

It is well known that antiferromagnetism in metals is stabilized by the exchange coupling of electron and hole surfaces which run parallel to each other over a large area[6] and that the separation of these surfaces determines the wavevector of the magnetic ordering. There is abundant evidence that in Cr alloys[7], for instance, this mechanism determines the stable structure and we have earlier suggested[8] that it is also operative in the rare earth metals. There is not necessarily any correlation between the occurrence of electron and hole surfaces of constant separation in the c-direction and surfaces which are flat and normal to the c-direction, but our results show that such a correlation does exist in the hcp rare earths. This aspect of the results will be clarified by a further study of the band structure calculations[4].

References.

1.   S. DeBenedetti, C. E. Cowan, W. R. Konneker
        and H. Primakoff, Phys. Rev. 77, 205 (1960).

2.   D. R. Gustafson, A. R. Mackintosh and D. J.
        Zaffarano, Phys. Rev. 130, 1455 (1963).

3.   A. J. Freeman, J. O. Dimmock and R. E. Watson,
        Phys. Rev. Letters 16, 94 (1966).

4.   S. C. Keeton and T. L. Loucks (to be published).

5.   T. L. Loucks, Phys. Rev. 144, 504 (1966).

6.   W. M. Lomer, Proc. Phys. Soc. 80, 489 (1962).

7.   W. C. Koehler, R. M. Moon, A. L. Trego and
        A. R. Mackintosh, Phys. Rev. 151, 405 (1966).

8.   R. W. Williams, T. L. Loucks and A. R. Mack-
        intosh, Phys. Rev. Letters 16, 168 (1966).

Figure Captions.

Fig. 1.   The observed and calculated photon coincidence
          distributions in a c-axis Y crystal. The free
          electron parabola is also shown. The calcula-
          tions have been corrected for experimental
          resolution.

Fig. 2.   Comparison between coincidence distributions
          for c-axis Ho and Gd crystals.
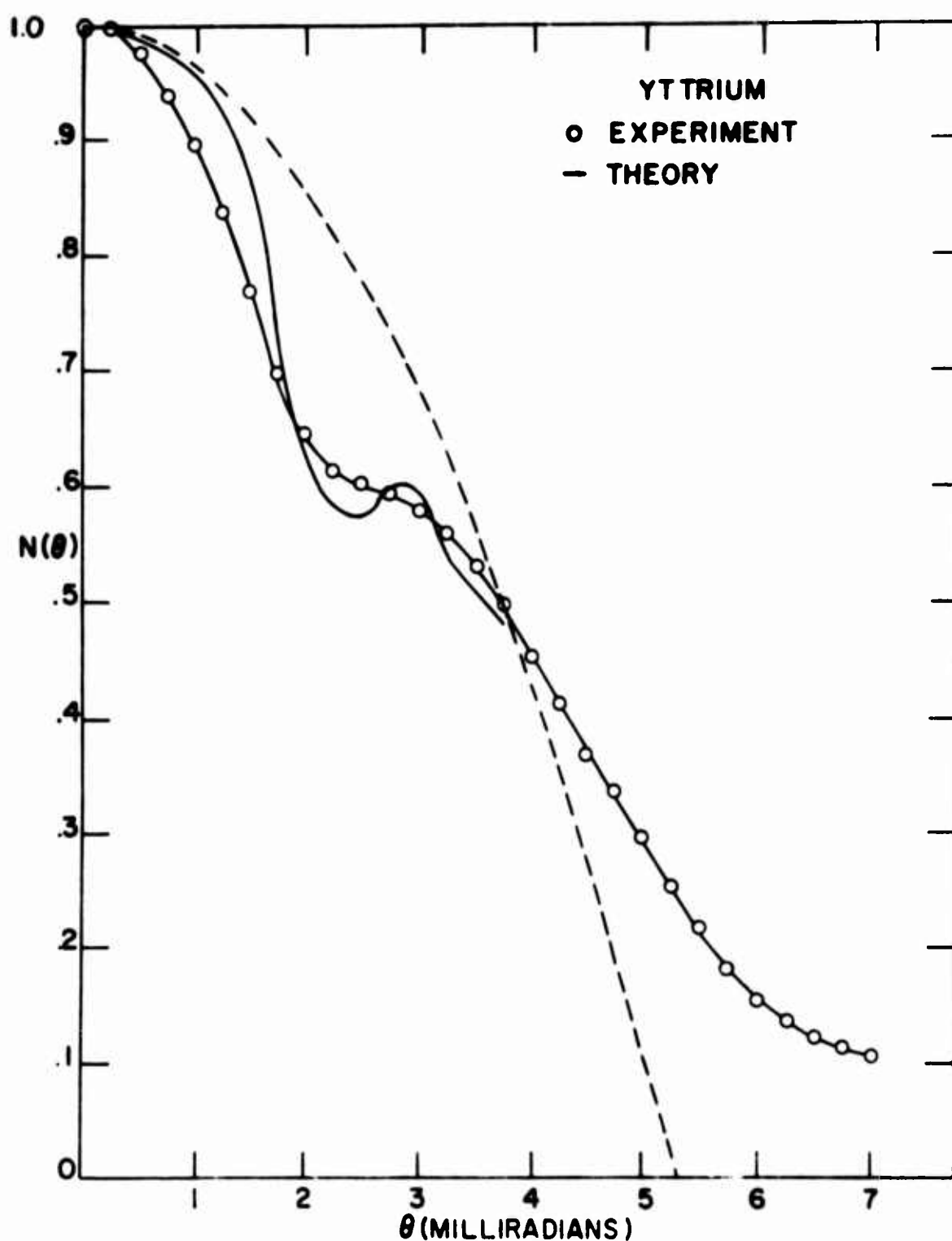
Fig. 1. The observed and calculated photon coincidence distributions in a c-axis Y crystal. The free electron parabola is also shown. The calculations have been corrected for experimental resolution.
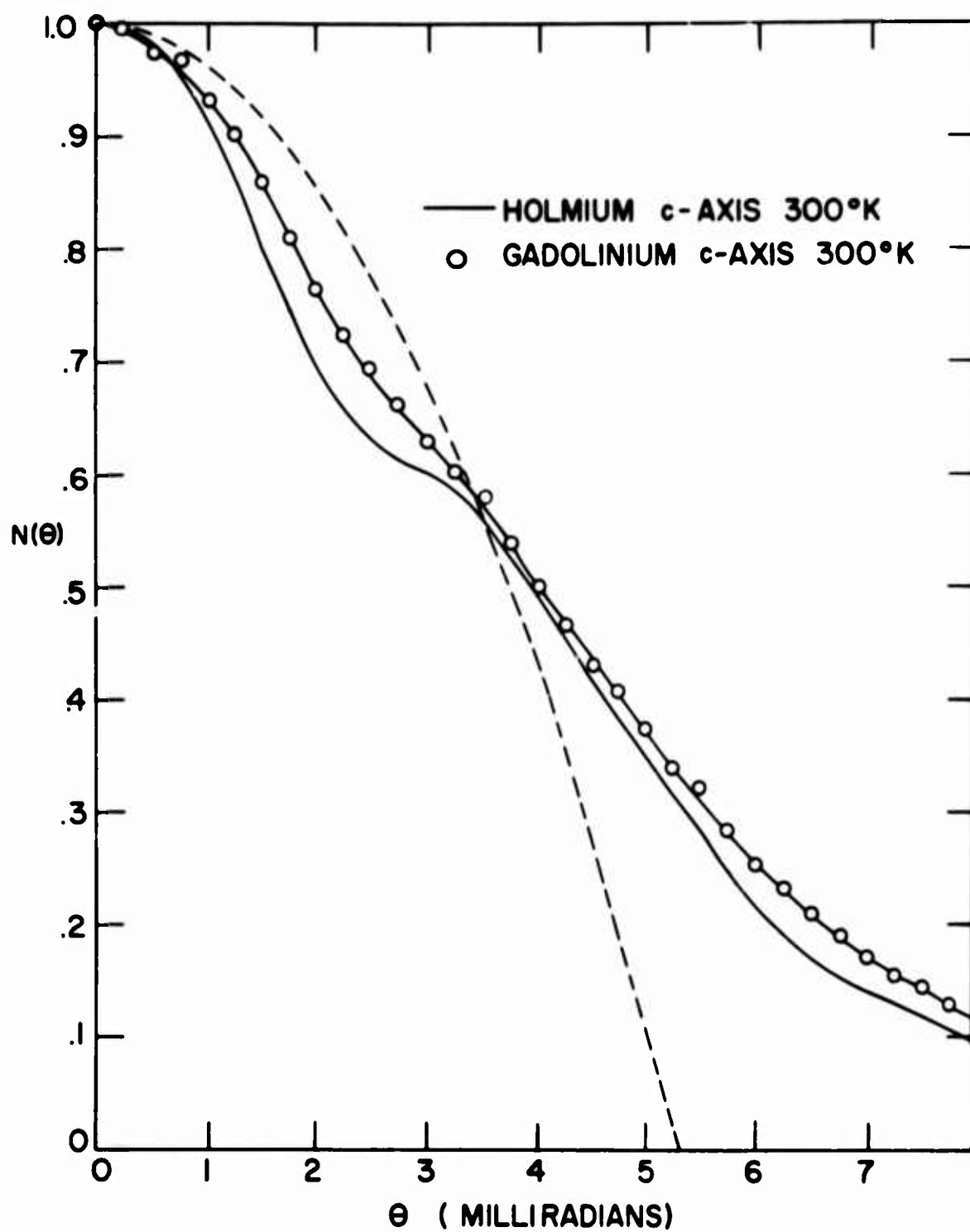
Fig. 2. Comparison between coincidence distributions for c-axis Ho and Gd crystals.

Hyperfine Interaction in Rare Earth Metals and Compounds[*]

G. Brunhart

Brookhaven National Laboratory, Upton, New York

Abstract

The possible origins of the effective magnetic hyperfine fields
at the nuclei of the rare earth elements have stimulated considerable
theoretical and experimental interest. The group of the rare earth
elements is formed by filling the 4f electron shell and it is the effect
of these 4f electrons that plays the major role in the interpretation
of the effective magnetic fields. Although several contributions to the
effective field must be considered, in general the magnetic field pro-
duced by the 4f electrons dominates. Kondo has calculated the 4f con-
tribution for several rare earth elements and predicts very large hyper-
fine fields, in some cases as much as several thousand kilo-oersted.
Exceptions are Gd^{3+} and Eu^{2+}, which have a half-filled 4f shell and
whose angular momentum is zero. In these two cases the dominant contri-
bution comes from exchange polarization, i.e. the interaction of the core
electrons with unpaired outer electrons. In the case of metallic solids
there is also the possibility that the polarization of the conduction
electrons might cause significant contribution. Watson and Freeman have
made extensive studies of such contributions to the effective field.
The nuclear polarization that often can be quite easily achieved in rare
earth elements is directly dependent on the effective magnetic field and
can be measured using polarized neutrons as a probe. Measurements have
been made on a series of rare earths, from Sm through Tm, using polarized
neutrons and polarized targets, and values for the magnitude and sign of
the hyperfine constants and effective fields have been obtained.

Many experiments investigating the structure and energy levels of
nuclei make use of nuclear polarization. In the study of the neutron
resonance structure, e.g., which is done in transmission measurements,
the use of polarized targets and polarized neutrons will yield additional
information about the spin of compound states that are responsible for

---

the resonances. As the attainment of nuclear polarization involves the interaction of the nucleus with magnetic fields one can use such experiments with polarized nuclei and polarized neutrons to study the magnetic properties of materials and to measure the magnitude and sign of the magnetic fields acting at the nucleus.

Nuclear polarization can be achieved in nuclei with non-zero magnetic dipole moment, i.e., non-zero nuclear spin through the action of a magnetic field. The magnetic moment μ of the nucleus couples with the applied field H removing the $(2I+1)$-fold degeneracy of the ground state. By lowering the absolute temperature T and making the field H large the energy spacing between the $(2I+1)$ levels can be made large enough in order to favor the population of the lowest level over the others. The nuclear magnetic dipole moments are relatively small so that the force μH with which the magnetic field H acts on the nucleus is also small. In order to obtain any appreciable polarization the quantity $(\mu H)/(kT)$ must be made as large as possible which shows the need for very low temperatures T and large magnetic fields H. The largest fields available in the laboratory without unreasonable effort used to be about 20 kilo-gauss. Such fields will produce at best a nuclear polarization of the order of one percent. Superconducting magnets today will allow a further decrease in the temperature T as well as a significant increase in the applied field H which should add a factor of 10 in the obtainable nuclear polarization.

It was realized, however, that in some cases extremely large magnetic fields exist at the nucleus due to the peculiarities of the electron configuration of these atoms. The largest such fields are found in the rare earth elements. Only small external fields are necessary to polarize the large internal fields because of the much larger atomic magnetic dipole moments.

The electron configuration for some of the rare earth ions occurring in various paramagnetic salts are summarized in Table I. To a first approximation these ions differ only in the number of 4f electrons.

TABLE I

Z	Ion	K	L		M			N				O		State
		1s	2s	2p	3s	3p	3d	4s	4p	4d	4f	5s	5p	
62	Sm^{3+}	2	2	6	2	6	10	2	6	10	5	2	6	$^6H_{5/2}$
63	Eu^{3+}	2	2	6	2	6	10	2	6	10	6	2	6	$^7F_0$
64	Gd^{3+}, Eu^{2+}	2	2	6	2	6	10	2	6	10	7	2	6	$^8S_{7/2}$
65	Tb^{3+}	2	2	6	2	6	10	2	6	10	8	2	6	$^7F_6$
66	Dy^{3+}	2	2	6	2	6	10	2	6	10	9	2	6	$^6H_{15/}$
67	Ho^{3+}	2	2	6	2	6	10	2	6	10	10	2	6	$^5I_8$
68	Er^{3+}	2	2	6	2	6	10	2	6	10	11	2	6	$^4I_{15/}$
69	Tm^{3+}	2	2	6	2	6	10	2	6	10	12	2	6	$^3H_6$

Otherwise they are identical as far as their electron shells are concerned. All shells and subshells are filled except the 4f shell. One would expect that only the unpaired 4f electrons contribute to the magnetic properties of the ions. As we will see later this is not quite true since other subtle effects must be taken into account. Furthermore, since the 4f electrons are deep inside the ions, shielded by the completed 5s and 5p subshells, the magnetic properties of the 4f electrons depend very little on the crystalline environment.

To be sure a simple model such as the shell model is not expected to give rigorous results particularly with regard to the effective field at the nucleus, i.e. the field which produces hyperfine splitting. A careful study must be made to account for all possible contributions to the hyperfine field. Exact calculations, however, are very difficult

as the electron wave functions can only be approximated. Kondo[1] has made calculations of the effective magnetic field for a series of rare earths considering only the contribution of the 4f electrons which is indeed the dominating part of the field. The calculated fields are several thousand kilo-oersted. Such strong fields due to the hyperfine interaction with the nucleus lead to large nuclear polarizations which have been observed.

Two exceptions to the pattern are of special interest. In Gd^{3+} and Eu^{2+} the 4f shell is half-filled and the resulting angular momentum is zero and consequently the large field is absent. These two ions then afford the opportunity to study the other more subtle contributions to the effective field. Such contributions should show definite dependence on the surroundings of the ion. Allowing the radial wave functions for electrons differing only in their spin orientation, i.e. in m_s, to be slightly different (the unrestricted Hartree-Fock wave function) one finds that these electrons become "unpaired" and that they have a non-zero electron density at $r = 0$.[2] In this way different shells will interact. Via the Fermi contact term the core s electrons will contribute to the effective magnetic field and this contribution is considered to be the source of negative effective fields that have been observed in ferromagnetics.[3] On the other hand an interaction of inner shells with the conduction electrons will lead to a polarization of these electrons which gives a positive contribution to the effective field.

It is clear that a study of the effective fields and their hyperfine interactions will give an important insight into the atomic structure and electron charge distribution of the elements. The rare earths are very important in such a study because the fields involved are very large and as a result the measurements can more easily be performed. The measurements that will be reported here are part of the work of a group at Brookhaven National Laboratory with which I am associated, the individual contributions being cited in the references. The experimental interest of our group is primarily concerned with neutron physics,

however, work with the rare earth elements has touched on some of the interesting magnetic features. More work of this type is planned.

Briefly the experimental procedure is as follows: The target is cooled by adiabatic demagnetization to about 50 millidegrees K in an external magnetic field of 17 kilogauss. A neutron beam from the Brookhaven Graphite Reactor is energy-selected and polarized by Bragg reflection off a magnetized cobalt-iron crystal. The neutron spin can be rotated by a magnetic spiral arrangement to be either parallel or antiparallel to the spin of the target nuclei. The transmission of the polarized target is measured for both the parallel and anti-parallel interaction. A convenient quantity, the transmission effect $\langle \mathcal{E} \rangle$, may be defined,

$$\langle \mathcal{E} \rangle = \frac{T_p - T_a}{T_p + T_a} = \frac{C_p - C_a}{C_p + C_a} \tag{1}$$

where T is the sample transmission and C is the counting rate of the transmitted beam, p and a, respectively, refer to the parallel and anti-parallel interaction of the target and neutron spin. $\langle \mathcal{E} \rangle$ is a function of the nuclear polarization f_N and, in a simplified way, is given by[4]

$$\langle \mathcal{E} \rangle \approx -f_n^0 \tanh(N \sigma t \rho f_N). \tag{2}$$

In the equation, N is the density of the target nuclei, t the target thickness, σ the total cross section, and f_n^0 the incident neutron beam polarization. ρ is a weighting factor which has the two possible values $I/(I+1)$ or -1 depending on the compound nucleus spin J which for s-wave interactions is either $I+\frac{1}{2}$ or $I-\frac{1}{2}$, respectively. Exact equations for $\langle \mathcal{E} \rangle$, including Doppler broadening and instrument resolution, are given

in the literature.[5] The nuclear polarization f_N is given by a
Brillouin function[4]

$$f_N = B_I(\beta) = \frac{2I+1}{2I}\coth(\frac{2I+1}{2}\beta - \frac{1}{2I}\coth(\frac{\beta}{2}), \tag{3}$$

where $\beta = A/(2kT)$, A being the magnetic hyperfine constant and kT being
the Boltzmann constant and absolute temperature. The hyperfine constant
is related to the effective field through the relation

$$\beta = \frac{A}{2kT} = \frac{\mu H_{eff}}{IkT} \qquad \text{or} \qquad H_{eff} = \frac{AI}{2\mu} \tag{4}$$

where μ is the nuclear magnetic dipole moment. It is customary to give
$\frac{A}{k}$ as hyperfine constant. It is then, in principle, possible to measure
the magnitude as well as the sign of H_{eff} by determining the magnitude
and sign of $\langle\ell\rangle$. However, it is necessary that the sign of μ, the
nuclear magnetic moment, is known and in general the sign of H_{eff} cannot
be determined in the experiment but must be known also. In many cases,
however, where at least two neutron resonances with opposite spins are
available the weighting factor ρ, i.e. J the compound spin, can be
determined uniquely without the knowledge of the sign of H_{eff}.[5,6] In
these cases then the sign of H_{eff} is a definite result of the experi-
ment.

The following summarizes some of the results of our work as they
pertain to the hyperfine fields in rare earths.

Samarium.[7]

Data were taken on samples of Sm-metal, Sm-ethyl sulphate, and
Sm-Mg nitrate. Practically no polarization was found in the metal in
agreement with the suggestion that Sm is antiferromagnetic below
$14.8°K.$[8] Large negative polarizations were found in the salts

(f_N = -0.15 at T ~ $0.1°$K) but no attempt was made to determine an accurate value for the hyperfine constant and H_{eff}. Assuming that μ is negative for Sm H_{eff} is positive.

Europium.[9]

The experiment was undertaken with the purpose of determining the sign of the effective field acting on the europium nucleus in the Eu^{2+} ion. This ion has a half-filled 4f shell and there is speculation of conduction electron effects. The field H_{eff} was found negative in samples of EuS as well as Eu metal.

Gadolinium.[5]

Measurements were made on Gd metal. The hyperfine constants were found to be $\frac{A}{k}$ = (8.0±0.8)x10^{-40} K for Gd^{155}. Assuming that the nuclear magnetic moment of Gd^{157} is μ = -0.33 nm H_{eff} is found to be H_{eff} = -(348±34) kilo-oersted.

Gadolinium is an example where the compound spins could be determined absolutely, i.e. without the knowledge of the signs of μ and H_{eff}. Figure 1 shows the measured values of $\langle \mathcal{E} \rangle$ as function of energy and calculated curves assuming various possible combinations of spin values for the contributing resonances. Clearly only one calculated curve will fit the experiment. The negative sign given for H_{eff}, therefore, depends only on the assumed sign for the nuclear magnetic moment.

Terbium.[6]

Due to the large magnetic anisotropy in Tb metal no special effort was made to determine the magnetic hyperfine constant and the effective field. However, large polarizations were obtained, f_N = 0.133 at T = $0.25°$K. The spin determinations were done absolutely and since the magnetic moment for Tb^{159} is known to be positive a positive H_{eff} follows from our measurements.

Dysprosium.[10]

The data were taken with a Dy metal sample. The analysis is as yet incomplete but since the spin determination can be done absolutely our results combined with the known sign of the magnetic moment will
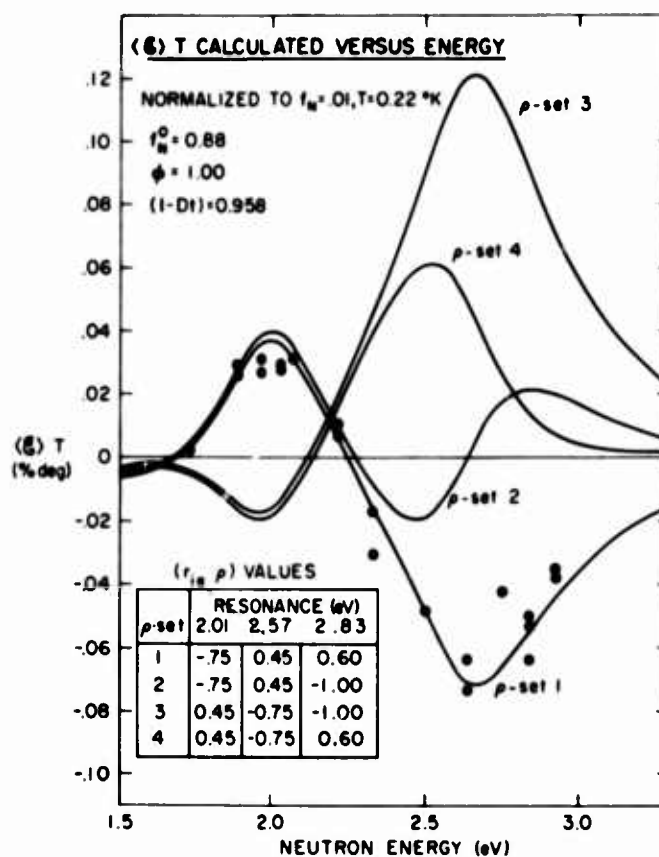
Fig. 1.   Experimental and calculated values of $\langle\varepsilon\rangle T$ as function
of neutron energy. The effect $\langle\varepsilon\rangle$ is calculated for
four possible spin combinations. Only set 1 shows
agreement with the data points.

confirm the positive sign of H_{eff}. The value for the hyperfine constant in Dy^{163} has been found to be $\frac{A}{k} = 0.122 \pm 0.01^\circ K$. Assuming the value for the magnetic moment to be $\mu = 0.51$ nm the effective field has the value $H_{eff} = 8.16 \times 10^6$ oersted.

Holmium.[4,11]

Measurements were made with samples of Ho ethyl sulphate, Ho metal (polycrystalline), and a Ho single crystal. In the latter the nuclear polarization reached practically 100%, Fig. 2. The data obtained with the single crystal were good enough to include the electric quadrupole interaction in the fitting. The respective hyperfine constants are $\frac{A}{k} = 0.610 \pm 0.005^\circ K$ and $\frac{P}{k}$ $0.002 \pm 0.001^\circ K$. Taking the nuclear magnetic moment to be $\mu = 3.29$ nm the effective field is calculated to be $H_{eff} = (8.80 \pm 0.46) \times 10^6$ oersted.
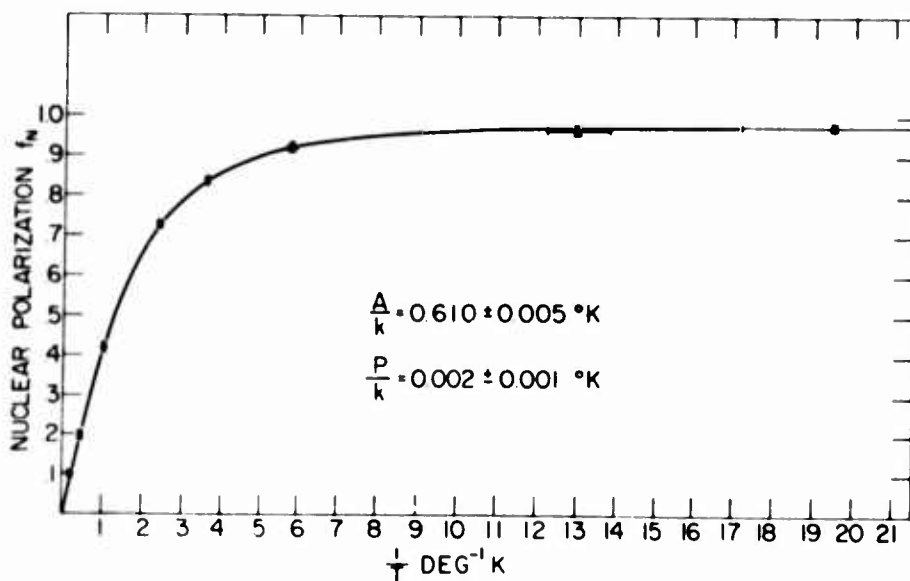
Fig. 2. Measured nuclear polarization as function of the inverse
absolute temperature. Curve is fitted polarization
function.

Erbium.[10]

Erbium has two closely spaced low energy resonances and again an absolute spin determination was possible. Data were taken on samples of Er ethyl sulphate and Er metal. The magnetic hyperfine constant was found to be $\frac{A}{k} = 0.078^\circ$ K. It is hoped that more recent data will also yield a value for $\frac{P}{k}$. Assuming a magnetic moment of $\mu = -0.48$ nm the effective field value is $H_{eff} = 7.75 \times 10^6$ oersted. The sign of the field is positive.

Thulium.[12]

Polarizations of about 10% could be obtained at $T = 0.05^\circ$ K in a sample of thulium metal. The hyperfine constant was found to be $\frac{A}{k} = 0.206 \pm 0.030^\circ$ K. The nuclear magnetic moment was taken to be $\mu = -0.229$ nm. With this value of μ the effective field was calculated to be $H_{eff} = (6.14 \pm 0.80) \times 10^6$ oersted.

In the course of our spin determination series we have also worked with rare earth alloys. The objective here was to induce a polarization in materials that do not show any hyperfine interaction. An alloy[13] of 92.2% holmium and 7.8% indium was tried very successfully and since the spin of 1.456 eV In^{115} resonance was already known, the measurement of the transmission effect for pure In allowed the determination of the sign of the induced field at the nucleus. The hyperfine constant for indium was determined to be $\frac{A}{k} = -0.013 \pm 0.002^\circ$ K which corresponds to an effective field of $H_{eff} = -130$ kilo-oersted. This negative field could be contributed to the polarization of the core s-electrons in indium but at present it is not possible to distinguish between several interactions which could individually or collectively produce this effective field.

A similar investigation was undertaken with an alloy of Ho-Sm and it was found that a large positive field was induced in samarium.

During a series of special measurements with separated isotopes of Gd^{155} and Gd^{157} to determine the spins of the two low energy resonances measurements were made on Gd_2O_3, $GdCl_3$, and $Gd_2(SO_4)_3$. These compounds

are now undergoing further investigation.

The described nuclear polarization method has been found very useful in measuring hyperfine fields and in some instances in determining the absolute sign of the effective fields at the nucleus. Although the original purpose of the experiment is quite a different one it is planned to continue the investigation in effective fields and hyperfine interactions especially in rare earth alloys and compounds.

It should be mentioned that similar experiments have been done with 3d elements, in particular alloys of iron.

REFERENCES

1. J. Kondo, J. Phys. Soc. Japan 16, 1690 (1961).
2. R. E. Watson and A. J. Freeman, Phys. Rev. 123, 2027 (1961);
   Phys Rev. Letters 6, 277 (1961); 6, 388 (E) (1961);
   Phys. Rev. 127, 2058 (1962).
3. S. S. Hanna et al, Phys. Rev. Letters 4, 513 (1960).
4. H. Postma et al, Phys. Rev. 126, 979 (1962).
5. F. J. Shore et al, Phys. Rev. 138, B1361 (1965).
6. H. Postma, F. J. Shore, and C. A. Reynolds, Physica 30, 713 (1964).
7. H. Marshak et al, Phys. Rev. 128, 1287 (1962).
8. J. M. Lock, Proc. Phys. Soc. (London) B70, 566 (1957).
9. L. Passell, V. L. Sailor, and R. I. Schermer, Phys. Rev. 135, A1767 (1964).
10. G. Brunhart et al, Bull. Am. Phys. Soc. 7, 305 (1962).
11. G. Brunhart, H. Postma, and V. L. Sailor, Phys. Rev. 137, B1484 (1965).
12. R. A. Al-Kital et al, Nuclear Phys. A91, 644 (1967).
13. V. L. Sailor, Phys. Rev. 127, 1124 (1962).

Temperature Dependence of the Hyperfine Field in Rare Earth-Gold Compounds[*]

B. D. Dunlap, A. E. Dwight, G. M. Kalvius, and C. W. Kimball[†]

Argonne National Laboratory, Argonne, Illinois

Ordered binary alloys of gold with various rare earths (Yb, Tm, Er, Ho) have been investigated by observing the Mössbauer hyperfine fields in Er^{166}, Tm^{169}, Yb^{171}, and Au^{197} nuclei. In these compounds the Au spectra are asymmetric doublets which are roughly independent of temperature. In some cases the rare-earth Mössbauer spectra show magnetic splittings and evidence of electronic relaxation effects.

Ordered binary alloys of Cu, Ag, and Au with rare-earth materials having the Cs-Cl structure have been investigated by means of resistivity measurements,[1] susceptibility measurements,[2-4] and neutron diffraction.[5] These methods in general indicate the appearance of magnetic ordering at some temperature; however, the different methods are not always in agreement with one another.

In a previous paper[6] we have used the isomer shift of Au^{197} for an investigation of charge transfer in ordered rare-earth alloys. This work is now expanded with the combined use of the Mössbauer resonances of the rare-earth and the gold nuclei in the temperature range between 4.2°K and 300°K. Mössbauer resonances have been observed

in Er^{166}, Tm^{169}, Yb^{171}, and Au^{197}. The results for these systems are summarized below.

Erbium. Below 10°K the erbium spectrum of Er^{166} in ErAu corresponds to a magnetic splitting having nearly the free-ion field acting at the nucleus. This spectrum contains five equally spaced lines having equal intensities, as is appropriate for the $2^+ \rightarrow 0^+$ transition in Er^{166}. As the temperature is increased one sees an enhancement of the central line followed by a collapse of the hyperfine pattern into a broad single line. Such behavior is characteristic of situations in which the electronic relaxation time is comparable with the nuclear Larmor frequency ($\simeq 10^{-8}$ sec).

Susceptibility measurements on ErCu,[2] ErAg,[3] and ErAu,[4] as well as neutron diffraction measurements on ErAg [5] show that the magnetic moment of the Er ion is temperature dependent. This dependence is attributed to crystal field effects. These same effects will contribute to the detailed shape of the observed relaxation spectra taken as a function of temperature in a way similar, for example, to that discussed by Nowick and Wickman for $ErFeO_3$.[7]

Thulium. At room temperature the hyperfine spectrum of Tm^{169} in TmAu consists of a single line, which is about

1.5 times broader than the narrowest line width available from our source. As the temperature is lowered, the resonance broadens slowly. At 78°K the line is about three times natural width, but no well-resolved structure is seen. At 4.2°K the spectrum is widely split.

Ytterbium. Yb^{171} in YbAu shows a single unsplit line at 4.2°K.

Gold. At 4.2°K an asymmetrical doublet is observed for Au^{197} in HoAu, ErAu, TmAu, and YbAu. In all these alloys the doublet splitting has approximately the same value ($\sim$2 mm/sec), except for the case of YbAu where the splitting is somewhat smaller. As the temperature is increased, the pattern becomes more symmetrical; however, the separation of the lines is practically independent of temperature between 4.2°K and 78°K.

References

[*]Based on work performed under the auspices of the U. S. Atomic Energy Commission.

[†]Present address: Northern Illinois University, DeKalb, Illinois.

[1]C. C. Chao, "A Study of CsCl-Type Intermediate Phases Involving Rare Earth Elements," AEC, Res. and Dev. Rpt. No. 36, Contract No. AT(04-3)-221 (1965).

[2] R. E. Walline and W. E. Wallace, J. Chem. Phys. $\underset{\sim}{41}$, 3285 (1965).

[3] R. E. Walline and W. E. Wallace, J. Chem. Phys. $\underset{\sim}{42}$, 604 (1965).

[4] F. Kissell and W. E. Wallace, J. Less Common Metals $\underset{\sim}{11}$, 417 (1966).

[5] J. W. Cable, W. C. Koehler, and E. O. Wollan, Bull. Am. Phys. Soc. $\underset{\sim}{9}$, 213 (1964).

[6] C. W. Kimball, G. M. Kalvius, and M. V. Nevitt, Bull. Am. Phys. Soc. $\underset{\sim}{11}$, 267 (1966).

[7] I. Nowick and H. H. Wickman, Phys. Rev. Letters $\underset{\sim}{17}$, 949 (1966).

MAGNETOSTRICTION IN DILUTE RARE EARTH IRON GARNETS

A. E. Clark, J. J. Rhyne, and E. R. Callen

U. S. Naval Ordnance Laboratory
White Oak, Silver Spring, Maryland

ABSTRACT

The conventional single-ion theory of magnetoelastic coupling has successfully accounted for the temperature dependence of the huge magnetostriction observed in the heavy rare earth metals. It has also accounted for the temperature dependences in YIG and the high temperature behavior of the magnetostriction of Dy, Ho, and Er iron garnets. In this paper we have extended these measurements to low temperatures on GdIG and on a series of partially substituted $Dy_x Y_{1-x} IG$ single crystals. We show that: (1) the magnetostriction is linear in Dy concentration, establishing a single-ion source, and (2) conventional statistical theory, which ignored crystal field effects, can be preserved for some magnetostrictive modes, but must be modified for others.

INTRODUCTION

Callen and Shtrikman[1] have shown that for molecular field theory, spin wave theory, and various decouplings of Green function theory, the reduced single-ion density matrix has the simple form:

$$\rho_m = exp[X(T,H) m] \Big/ tr \ exp[X(T,H) m] . \qquad (1)$$

Here X is an arbitrary theory-dependent function of temperature and field, and $m(= \vec{S} . \alpha)$ is the component of the individual ionic spin operator along the axis of quantization. These authors then show that for all such theories the magnetostriction (and the anisotropy) takes the same form, independent of X(T,H). Specifically, for large S:

$$\lambda(T, H) = \lambda_0 \ \hat{I}_{\ell+\frac{1}{2}} \left\{ \mathcal{L}^{-1}[m(T, H)] \right\} , \qquad (2)$$

where $I_{\ell+\frac{1}{2}}$ is a normalized hyperbolic Bessel function of degree $\ell+\frac{1}{2}$, $\mathcal{L}^{-1}(m)$ is the inverse Langevin function of the reduced moment m, and λ_0 is a constant equal to the magnetostriction at

T = 0. The entire temperature and field dependence of the magnetostriction is thus completely specified in terms of the magnetic moment. There are no adjustable parameters. This expression has accounted for the temperature dependences of the magnetostriction in the heavy rare earth elements and the high temperature dependences in DyIG, HoIG, and ErIG.[2]

In the rare earth garnets, the crystal field is sufficiently strong that the energy levels are not eigenstates of S_z as in Eq. 1. However, Eq. 2 follows even when only a much weaker form of Eq. 1 applies. That is, when J_z states are approximate eigenstates, so that:

$$\langle J_\ell^n \rangle_i \; \cong \; \langle J_\ell \rangle_i^n \tag{3a}$$

and the energy of these equi-spaced levels takes the form:

$$\varepsilon_i \; \cong \; C \langle J_\ell \rangle_i \; , \tag{3b}$$

the quantum analog of Eq. 2 will still approximately hold. It is in this more general sense that the theory can be applied to the appropriate magnetostrictive modes of the rare earth garnets.

In order to apply the single-ion theory to the rare earth garnets, it is assumed that the magnetoelastic energy is composed of a sum of terms, one for each magnetic sublattice:[3]

$$\mathcal{H}_{me} = \sum_n \mathcal{H}_{me}(n) \; . \tag{4}$$

In the rare earth garnets there are three magnetic sublattices: ferric ions on the 24d (tetrahedral) sites, ferric ions on the 16a (octahedral) sites, and rare earth +3 ions occupying the 24c (dodecahedral) sites. A strong negative interaction exists between the ferric ions on the a and d sites which accounts for the ferrimagnetism in YIG, and a much weaker ferrimagnetic interaction occurs between the ions on the c and d sites. The magnetoelastic Hamiltonian for each magnetic sublattice in terms of single-ion angular momentum operators has the following general form:[3]

$$\mathcal{H}_{me}(n) = -\sum_{\mu,\ell} B^{\mu,\ell}(n) \sum_i \varepsilon_i^\mu K_i^{\mu,\ell}(J_n) \; , \tag{5}$$

where the $B^{\mu,\ell}(n)$ are temperature independent magnetoelastic coupling coefficients, ϵ_i^μ the elastic strain components, and $K_i^{\mu,\ell}(J_n)$ the symmetry polynomials of degree ℓ in the angular momentum operators of the n'th sublattice. (The strains ϵ_i^μ, and the operators $K_i^{\mu,\ell}$, transform according to the cubic symmetry group and are labeled by the irreducible representation μ and by the basis function i of the μ'th representation. Actually, the strains and spin operators describing the individual sites are lower than cubic, but in summing over the sites in the cubic unit cell, only the projections on cubic basis functions remain.) The expression for the magnetostriction is found by calculating the free energy to first order in the magnetoelastic coupling coefficients and minimizing it with respect to the strains. In this way,

$$\lambda = \lambda^{\gamma,2}\left[\tfrac{1}{2}(\alpha_x^2-\alpha_y^2)(\beta_x^2-\beta_y^2) + \tfrac{1}{2}(\alpha_z^2-\tfrac{1}{3})(\beta_z^2-\tfrac{1}{3})\right]$$
$$+ \lambda^{\epsilon,2}\left[\alpha_x\alpha_y\,\beta_x\beta_y + \alpha_y\alpha_z\,\beta_y\beta_z + \alpha_z\alpha_x\,\beta_z\beta_x\right] + \lambda^{\gamma,4}\cdots\cdots . \tag{6}$$

The α"s and β's denote the direction cosines of the magnetization and the measurement direction respectively. The γ magnetostriction mode represents a change in the length of the crystal along its principle axes without a change in the angle between them. The ϵ mode entails an angle change between the crystal $[100]$ axes but not their length change. When conditions (3) are satisfied, the magnetostriction constants of Eq. 6, in terms of the magnetoelastic coupling coefficients of the individual magnetic sublattices, are:

$$\lambda^{\gamma,2} = \tfrac{3}{2}\lambda_{100} = [1/2(C_{11}-C_{12})]\sum_{n=1}^{J} B^{\gamma,2}(n)\,\hat{I}_{5/2}[\mathcal{L}^{-1}(m_n)]$$

and

$$\lambda^{\epsilon,2} = \tfrac{3}{2}\lambda_{111} = (1/4\,C_{44})\sum_{n=1}^{J} B^{\epsilon,2}(n)\,\hat{I}_{5/2}[\mathcal{L}^{-1}(m_n)]. \tag{7}$$

Here m_n is the reduced magnetization of the n'th sublattice.

The temperature dependence of each magnetostriction constant of the rare earth iron garnets is thus specified by 3 magnetoelastic coupling coefficients plus the temperature dependence of the sublattice moments. Our observed linear dependence of magnetostriction on concentration justifies the assumption that the magnetoelastic coupling coefficients of the two iron sublattices are the same in the substituted garnets as in YIG. Furthermore, the observed temperature depencences of the iron sublattices do not differ appreciably from those of YIG.[4] Hence the entire temperature (and field) dependence of the magnetostriction of the rare earth garnets differs from that of YIG only through the magnetostriction coupling of the rare earth ion B_R, and the temperature (and field) dependence of the rare earth sublattice moment, m_R. The magnetostriction constants then simplify to:

$$\lambda^{\gamma,2} = \lambda_{YIG} + \frac{B_R^{\gamma,2}}{2(C_{11}-C_{12})} \; \hat{I}_{5/2}\left[\mathcal{L}^{-1}(m_R)\right]$$

and

$$\lambda^{\epsilon,2} = \lambda_{YIG} + \frac{B_R^{\epsilon,2}}{4\,C_{44}} \; \hat{I}_{5/2}\left[\mathcal{L}^{-1}(m_R)\right] \; . \tag{8}$$

EXPERIMENT

The two magnetostriction constants, $\lambda^{\gamma,2}$ and $\lambda^{\epsilon,2}$, were measured on single crystals of gadolinium iron garnet and on single crystals of dysprosium-yttrium iron garnet, $Dy_{3x}Y_{3(1-x)}Fe_5O_{12}$ from $4.2^{\circ}K$ to $300^{\circ}K$. A temperature-controlled cryostat provided temperature regulation to better than $0.1^{\circ}K$. The single crystal samples of GdIG were grown by J. R. Cunningham of N.O.L. and those of DyYIG for x = .005, .01, .05, and .10 were grown by L. E. Sobon and generously forwarded to us by K. A. Wickersheim and R. L. Comstock of Lockheed Palo Alto Research Laboratories. Small (100) platelets about 4 mm on a

side were sliced from the crystals and special low
magnetoresistive strain gages (Kyowa K-19-1 or Gulton
KN-3-A1) were affixed parallel to the [001] direction
(for $\lambda^{\gamma,2}$ strains) and the [011] direction (for $\lambda^{\epsilon,2}$ strains).
Standard strain gage methods were used to measure sample
magnetostriction as a function of field intensity and
direction. Thermal and magnetoresistive compensation was
achieved by mounting a dummy gage in the same thermal and
magnetic environment as the sample gage and electrically
connecting the gages in adjacent arms of a Wheatstone bridge.
With these precautions the enormous low temperature pseudo-
strains which normally arise from the magnetoresistance of
strain gages were reduced to less than 1×10^{-6} at 77°K and
about 2×10^{-6} at 4°K.

Table I. Magnetostriction of YIG and GdIG

T	YIG[a]		GdIG	
	$\lambda^{\gamma,2} \times 10^6$	$\lambda^{\epsilon,2} \times 10^6$	$\lambda^{\gamma,2} \times 10^6$	$\lambda^{\epsilon,2} \times 10^6$
4.2°	-1.0	-8	11.2±2.0	-6.2±2.0
77°	-1.0	-7.8	6.7±0.05	-7.0±1.0
296°	-2.1	-4.3	0.25±0.05	-4.4±0.2

(a) A. Clark, B. DeSavage, W. Coleman, E. Callen, and
H. Callen, J. Appl. Phys. **34**, 1296 (1963).

Values of $\lambda^{\gamma,2}$ and $\lambda^{\epsilon,2}$ for GdIG are presented in
Table I and compared to those of YIG. Since the ground
state of the Gd^{+3} ion has zero orbital angular momentum
(L = 0), its contribution to the magnetic anisotropy and
magnetostriction is expected to be very small. Subtracting
the magnetostriction of YIG from GdIG we find the contribution
of the Gd^{+3} ion to be 12×10^{-6} and 1.8×10^{-6} for the γ

and ε modes respectively. From the pressure dependence of
the EPR spectrum of GdIG, Phillips and White[5] calculated
the Gd^{+3} contributions to be 6.3×10^{-6} and 2.5×10^{-6},
in good agreement with the   atic magnetostriction results.

On the other hand (and consistent with the large magneto-
striction observed in the heavy rare earth metals), when rare
earth ions with a degenerate ground state are substituted
for yttrium in the garnet they dominate the magnetoelastic
energy. These large magnetoelastic energies are illustrated
in Table II.

Table II. Magnetoelastic Coupling Coefficients

	Ion	$B^{\gamma,2}(cm^{-1})$	$B^{\epsilon,2}(cm^{-1})$
Garnet	Dy^{+3}	-830	-1090
	Gd^{+3}	15	5.5
Element	Dy^{+3}	1400^a	1600^a
	Gd^{+3}	17^b	11^b

(a) A. Clark, B. DeSavage, and R. Bozorth, Phys. Rev.
    138, A216 (1965)
(b) J. Alstad and S. Legvold, J. Appl. Phys. 35, 1752
    (1964)

Here: $B^{\gamma,2} = \lambda^{\gamma,2}/2(C_{11}-C_{12})$ and $B^{\epsilon,2} = \lambda^{\epsilon,2}/4C_{44}$, where
the elastic moduli C_{11}, C_{12}, and C_{44} of the garnets were
taken equal to those of YIG. Although the garnets have
overall cubic symmetry and the metals are hexagonal close
packed, there are only two possible (lowest order) shearing
strain modes in both, which can be labeled by γ and ε.
Although the magnetostriction in the rare earth iron garnets
is substantially smaller than that of the elements, it is
observed that the magnetoelastic energy/ion is the same order
of magnitude. This is because the metals are softer and have
a higher density of rare earth ions.

The effect of diluting the concentration of rare earth ions in the garnet is shown for DyIG in Figs. 1 and 2. The data points are found by subtracting the magnetostriction of YIG from the total magnetostriction of the substituted garnet and multiplying the result of 100/(% of sites substituted). The magnetostriction is directly proportional to the number of rare earth ions and hence the magnetoelastic energy is truly single ion in origin. (A few low concentration points fall away from the curve. Because of the small difference between the magnetostriction of YIG and of samples with very low rare earth concentration, there is a large uncertainty in these data points.) On the basis of this proportionality, one expects the magnetocrystalline anisotropy to also scale linearly with rare earth concentration. Pearson[7] has observed that for Dy, Ho, Er, and Yb iron garnets, the anisotropy energy is indeed proportional to concentration. However, for TbIG it changes sign. An investigation of the magnetostriction of YIG doped with small quantities of Tb should prove valuable in identifying the source of this non-linear behavior.

The theoretical single-ion expression of Eq. 2 for the temperature dependence of the magnetostriction is compared to the experimental results in Figs. 1 and 2. The sublattice moments were calculated from the moment measurements of Harrison et al[8] on DyIG and YIG. For $\lambda^{\epsilon,2}$, the agreement with the data is remarkable except at the very lowest temperatures. The only adjustable parameter is the $T = 0$ value of the magnetostriction (1.22×10^{-3}). On the other hand, examination of the γ magnetostriction mode (Fig. 2) shows that there is little resemblance between the conventional theory and experiment. Two incidental causes for the difference are possible: (1) non-saturation of the magnetostriction when the moment is along the magnetically hard direction, and (2) the appearance of higher order magnetostriction coefficients (eg. $\ell = 4$ coefficients in Eq. 3)

at low temperatures. To examine the first possibility,
measurements were made in fields up to 110 kOe at the high
field facility of the Naval Research Laboratory. These
fields are much larger than the anisotropy fields in DyIG
for $T > 50°K$. It is clear from Fig. 3 that the samples were
already saturated in fields of 10 kOe at $97.7°K$ and above
40 kOe at $50.8°K$. Higher order coefficients have an angular
dependence of $\sin^2 2\theta$ where θ is the angle between the measure-
ment direction and the moment direction. A plot of $\lambda^{\gamma,2}$ vs
θ is shown in Fig. 4. No significant $\sin^2 2\theta$ term is
detectable as low as $50.8°K$. Hence we conclude that the
temperature dependence of the ϵ and γ modes are substantially
different, and while conditions (3) presumably are satisfied
for the ϵ strain, they apparently are not for the γ strain.

Wickersheim[9] has shown from a detailed spectroscopic
investigation of YbIG that the ground state exchange splitting
is strongly dependent upon moment direction. For example,
he shows that as the moment is rotated from [100] to [110], the
splitting of one of the rare earth sites increases by as much
as a factor of three. The spectrum of DyIG is far more complex
than that of YbIG and is not completely understood. However,
Hüfner and Schmidt[10] have determined the four lowest levels
of the $6_{H_{15/2}}$ ground state multiplet for Dy^{+3} for the moment
parallel to [111]. The levels are nearly equally spaced (for
both inequivalent rare earth sites) with a splitting of $\sim$
30 cm^{-1}. Therefore, condition (3) may be satisfied for $\lambda^{\epsilon,2}$.
The energy levels have not been measured for the moment parallel
to [100]. In view of our magnetostriction results, it appears
likely that the splittings are substantially altered into an
uneven array. This angular dependence of the energy level
scheme will result in a dependence of moment with field
direction. This has not yet been observed. It should be
pointed out that the sublattice moments used to calculate
$\hat{I}_{5/2}$ were those for m parallel to the easy direction [111].

If the dependence of the moment with temperature is substantially altered with rotation to [100], the theoretical curve of Fig. 2 may also be significantly altered.

The high magnetic field magnetostriction measurements clearly illustrate the paramagnetic nature of the Dy^{+3} ion in the exchange field of the iron sublattices. In the substituted garnet $Dy_xY_{1-x}IG$ with $x < .25$, the effective field of the iron at the rare earth site is antiparallel to the applied field at all temperatures. (For $x > .25$, it is antiparallel only above the compensation point.) In Fig. 3, we show the magnetostriction coefficient, $\lambda^{Y,2}$, as the field approaches the effective field of the iron. At all temperatures, the magnetostriction decreases sharply as the external field is applied. As the field approaches 120 kOe, there is a noticeable deviation from the normal linear dependence of the magnetostriction on field as expected for a paramagnet far from saturation. At an external field equal and opposite to the effective field of the iron sublattice at the rare earth site, the magnetostriction of the paramagentic rare earth ion should drop to zero. In the absence of a crystal field the approach should be parabolic. This is indicated by the dotted line in the figure. For illustration we have estimated the effective field from molecular field theory. According to the theory, the magnetostriction is given by $\hat{I}_{5/2}[\mu|H_m-H|/kT]$, where H_m is the effective molecular field and H is the applied field. Although the theory does not predict the correct dependence of $\lambda^{Y,2}$ with temperature, the fit to the field dependence of the magnetostriction appears satisfactory. At $50.8^{\circ}K$, the value of H_m according to the molecular field theory is 138 kOe. With slightly larger magnetic fields it would be possible experimentally to obtain H_m as a function of temperature for the heavy rare earth garnets.

1. H. Callen and S. Shtrikman, Solid State Commun. $\underline{3}$, 5 (1965)

2. A. Clark, B. DeSavage, N. Tsuya and S. Kawakami, J. Appl. Phys. $\underline{37}$, 1324 (1966)

3. E. Callen, A. Clark, B. DeSavage, W. Coleman, and H. Callen, Phys. Rev. $\underline{130}$, 1735 (1963)

4. E. Boyd, V. Moruzzi, and J. Smart, J. Appl. Phys. $\underline{34}$, 3049 (1963)

5. T. Phillips and R. White, 12th Conf. on Mag. and Mag. Materials, Washington, D. C. (1966)

6. A. Clark, B. DeSavage and R. Bozorth, Phys. Rev. $\underline{138}$, A216 (1965)

7. R. Pearson, Mullard Research Laboratories Report 407 (1961) R. Pearson and R. Cooper, J. Phys. Soc. (Japan) $\underline{17}$ Suppl. B-I (1962)

8. F. Harrison, J. Thompson, and K. Tweedale, Proc. Inter. Conf. on Magnetism, Nottingham (1964) F. Harrison, J. Thompson, and G. Lang, J. Appl. Phys. $\underline{36}$, 1014 (1965)

9. K. Wickersheim, Phys. Rev. $\underline{122}$, 1376 (1961)

10. S. Hüfner and H. Schmidt, Phys. kondens. Materie $\underline{4}$, 262 (1965)
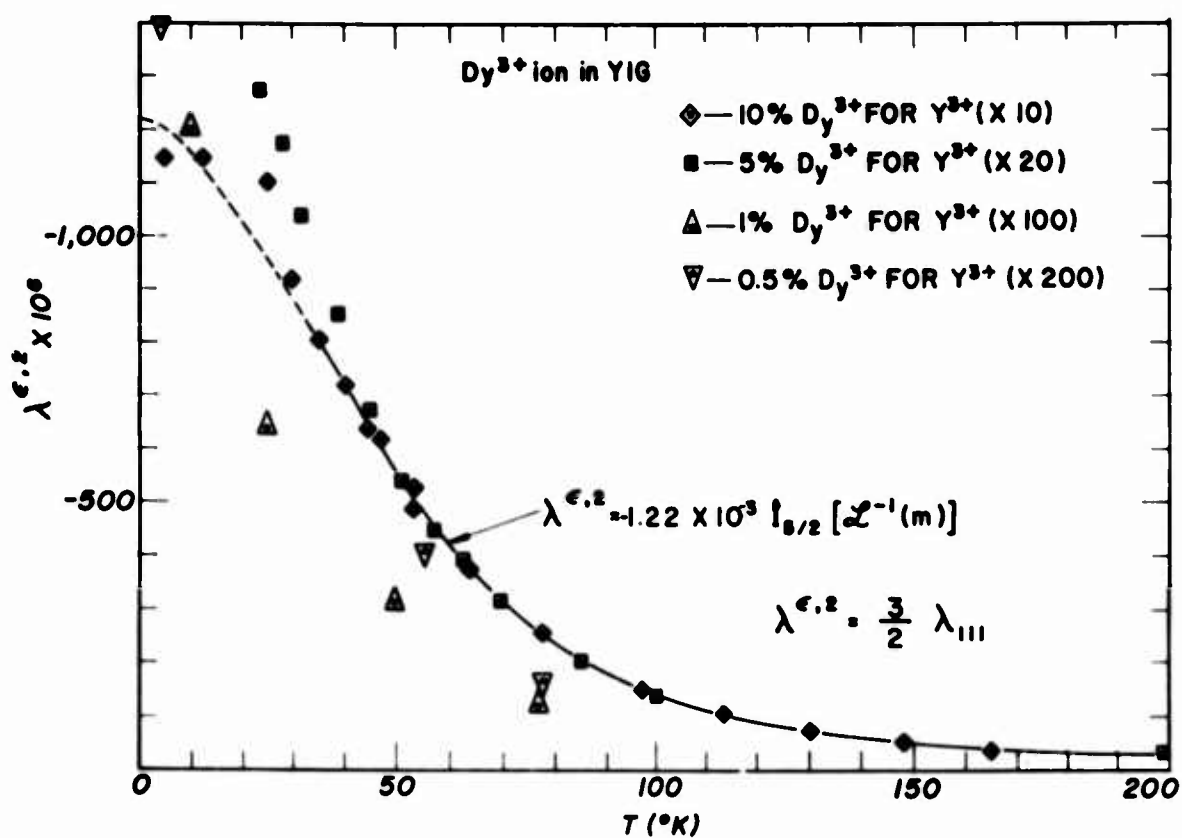
Fig. 1. The temperature dependence of $\lambda^{\epsilon,2}$ of Dy^{+3} in DyIG.
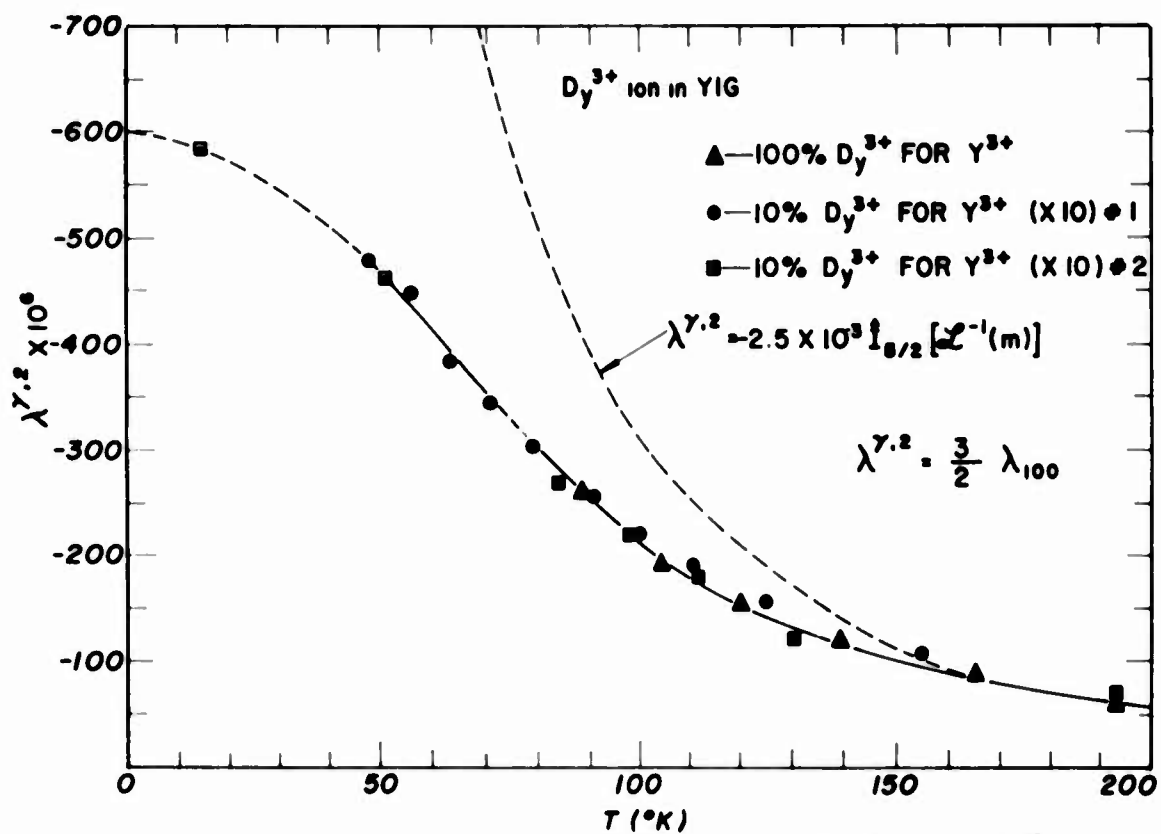
Fig. 2. The temperature dependence of $\lambda^{\gamma,2}$ of Dy^{+3} in DyIG.
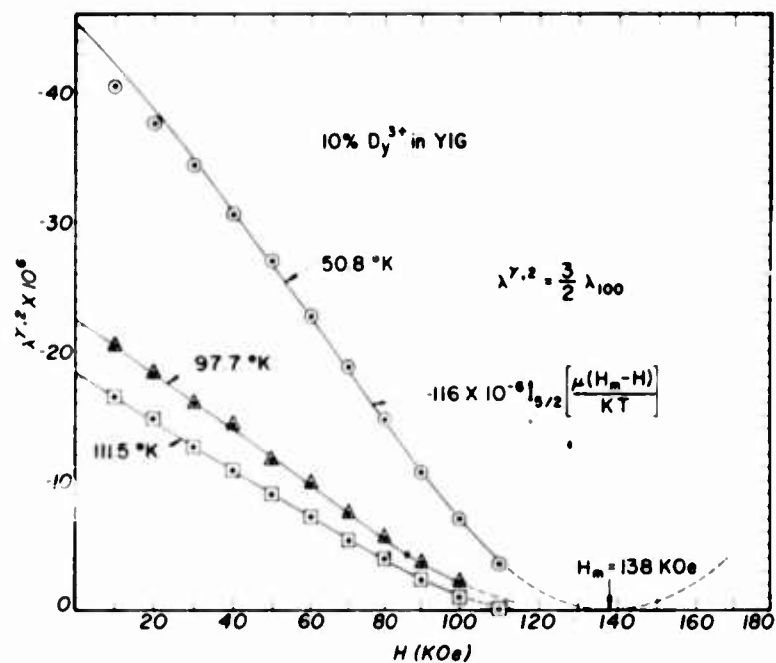
Fig. 3. High field dependence of the magnetostriction in DyIG.
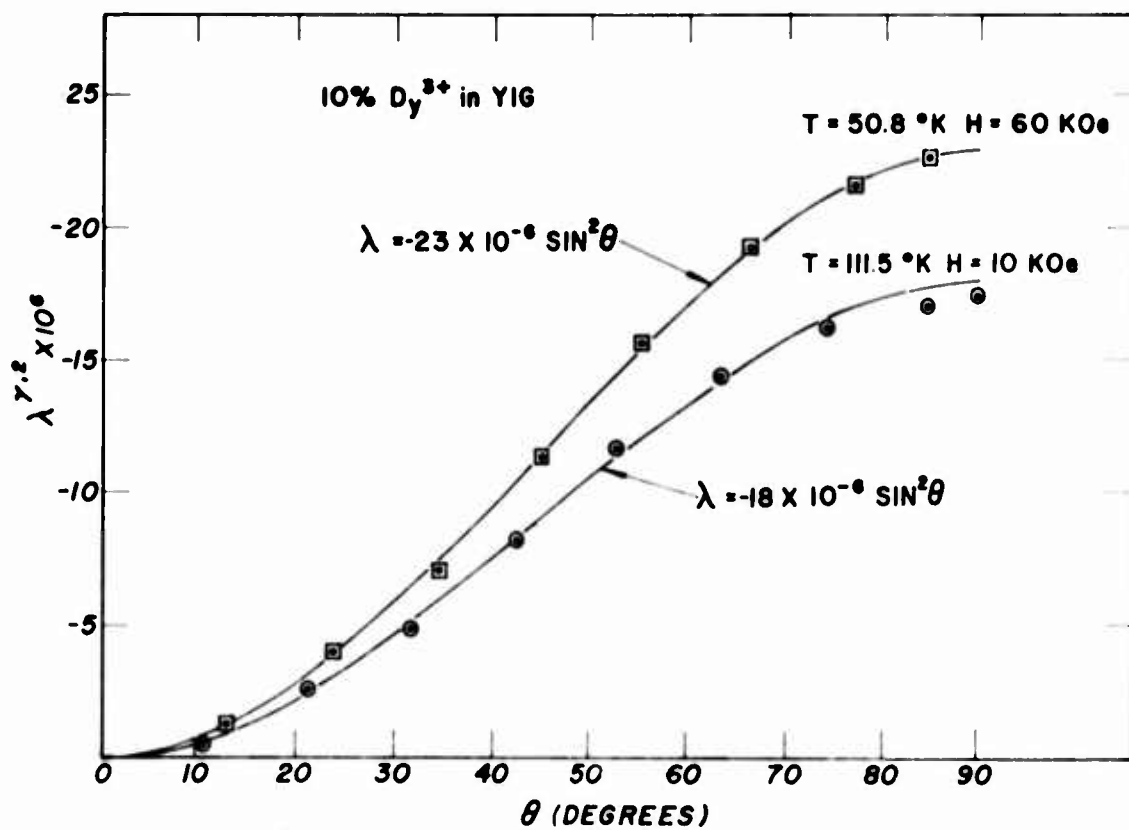
Fig. 4. $\lambda^{Y,2}$ as a function of the angle between the measurement direction and the moment direction.

Elastic Moduli of Gd Metal

by

E. S. Fisher and D. Dever
Metallurgy Division
Argonne National Laboratory
Argonne, Illinois, U.S.A.

Abstract

The elastic moduli of Gd single crystals have been measured over the temperature range of 4° to 923°K. The results indicate that some degree of magnetic ordering exists between T_c and 330°K. A sharp transition is indicated at 286°K for compressional modes and 289°K for shear modes. It is suggested that a change in direction of the magnetic moments occurs abruptly at 218°K. The Debye Θ calculated from the 4°K data is 181.5°K. This, together with the Debye Θ calculated for Er (Θ = 191°K) suggests that the Debye Θ of the trivalent rare earth metals are linearly related to the atomic weights. The anisotropy ratio, $A = c_{44}/c_{66}$, increases with temperature in the paramagnetic phase as expected for h.c.p. metals that transform to the b.c.c. structure at high temperatures.

Introduction

The elastic moduli of single crystals are extremely sensitive to small changes in the factors contributing to the interatomic binding energy. For this reason the absolute values are generally extremely difficult to derive from theory. The number of contributing factors increases when magnetic ordering occurs and the theoretical problem

becomes even more complex. Nevertheless, the changes in the elastic moduli due to the added contributions now become of interest in detecting transformations, establishing transformation temperatures and observing the anisotropic effects of exchange forces. The temperature dependence of the elastic moduli in Gd should then reflect the short range order effects in paramagnetic Gd predicted by Darnell and Cloud[1] and the effects of the changes in the direction of the magnetic moments between 200° and 240°K.[2] The values of the elastic moduli at 4°K permit the evaluation of the Debye Θ, or the lattice contribution to low temperature specific heat. The latter is particularly important for resolving the magnetic contribution to the total heat capacity of a ferromagnet.[3]

The elastic moduli of the paramagnetic phases of the heavy rare earths are also of interest because of the temperature induced structural phase changes that have been reported to occur at high temperatures.[4] We have noted that the basic criterion for the occurrence of the h.c.p. $\rightleftarrows$ b.c.c. phase transformation in other h.c.p. metals is that the shear modulus anisotropy ratio, $A = c_{44}/c_{66}$, has a positive temperature dependence and is greater than unity at high temperatures.[5] We presume that the high temperature structures of the rare earths are b.c.c. and therefore expect A for the paramagnetic phases to have the characteristics noted above. Our measurements of Dy and Er single crystals have in fact turned out as expected;[6] A is very near unity at T_N and increases with temperature.

Experimental

The technique and apparatus that were used for measuring the changes in elastic moduli with temperature are described in several publications.[7] This measuring technique does not require large path lengths but does require 2 flat and parallel faces that are normal to the direction of wave propagation. Three single crystals of Gd were used for this study, each with approximately 2 mm dimensions between parallel faces and 3 to 4 mm in lateral dimensions. Crystal A was oriented for wave propagation along a direction $90°$ to the "c" axis, from which the c_{11} modulus was obtained from the velocity of compressional waves and the c_{44} and c_{66} moduli are obtained from shear waves polarized approximately $0°$ and $90°$ to the "c" axis, respectively. Since $c_{66} = (c_{11}-c_{12})/2$ for hexagonal symmetry we obtained 3 of the 5 independent moduli from Crystal A. Crystal B was oriented for wave propagation $45°$ to the "c" axis, from which we obtained c_{13} from either the quasi-longitudinal wave (Q.L.) or the quasi-shear wave (Q.S.). The other shear mode was pure shear (P.S.) and permits a cross-check on the c_{44} and c_{66} moduli determined from Crystal A. Crystal C, with faces parallel to the basal planes, permitted evaluation of c_{33} from the compressional wave and a second independent evaluation of c_{44} from the one and only shear mode.

The purity of our crystals has not been determined. The crystals were made by heating a 1/4" diameter rod at $1150°C$ for approximately 3 weeks while enclosed in a tantalum envelope and outer quartz capsule with a partial pressure of purified argon gas. The rod was a casting

purchased from the Lunex Corp. and was prepared from fairly pure sponge. Metallographic examination of the crystals showed some dispersed large inclusions, that are presumed to be tantalum compounds that entered during the casting process. The same type of inclusions were observed in the Dy and Er crystals prepared from similar stock. In Dy the inclusion concentration was considerably greater and the errors in internal consistency, or cross-check deviations, were in the order of 1%. In Gd and Er these deviations were less than 0.5% and we presume that the absolute values of the elastic moduli are not significantly different from those in more pure crystals. This presumption is based on the fact that a second set of Dy crystals, prepared from arc melted sponge, was free of inclusions. The cross-check deviations in this set were less than 0.3% but the absolute values of the moduli were reduced by only 0.3% of the previous measurements.

Results

The values of the stiffness moduli at several temperatures are given in Table I and the curves obtained from plotting the data are given in Figures 1, 2 and 3. It can be seen in Figure 1 that the effect of the paramagnetic $\rightleftarrows$ ferromagnetic transition is quite pronounced for c_{33} (compressional wave along the "c" axis) but produces only a change in slope for c_{11} and the shear moduli, c_{44} and c_{66}. c_{33} has a maximum in the paramagnetic phase at 330°K and the slope inversion occurs at 286 ± 0.5°K. It appears that c_{11} does not have any anomalous temperature dependence in the paramagnetic phase; c_{11} changes slope abruptly at 289°K and is essentially constant between 289° and 286°K,
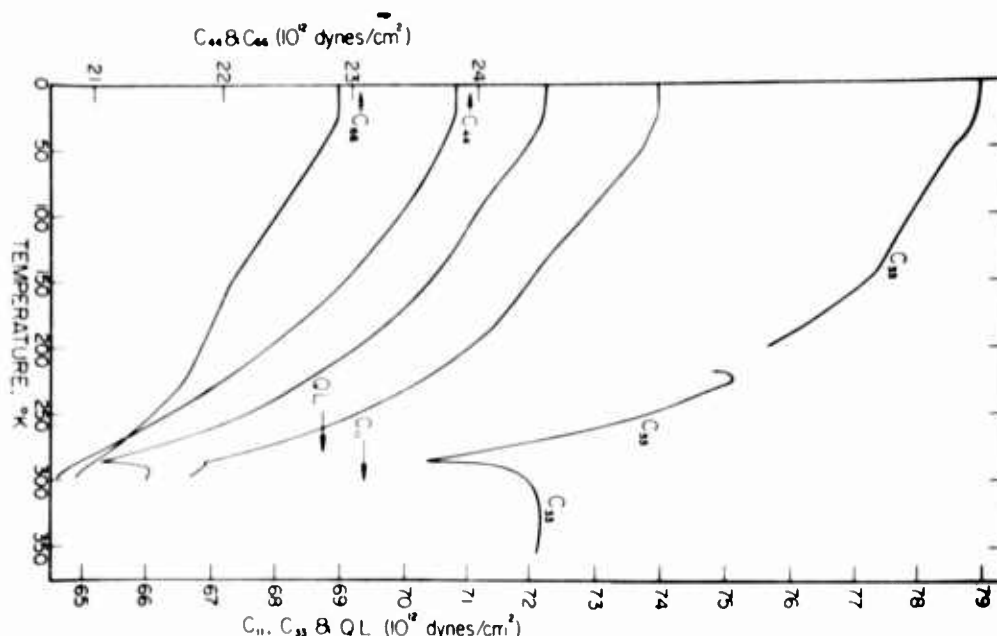
Fig. 1. Variation of elastic stiffness moduli with temperature
of Gd single crystals (4° to 355°K).

at which point the slope again changes abruptly. The effects on the
shear moduli are best shown in Figure 2; in both cases there is an
abrupt enhancement of the temperature dependence on cooling below 289°K.
c_{13}, which is computed from the Q.L. data as well as c_{33}, c_{11} and c_{44},
also shows a slope inversion at 286°K.

At temperatures below T_c there are some unusual bends in the
curves but, with exception for c_{33}, there are no sharp changes in slope
that are characteristic of a phase transition. The c_{33} anomaly has the
following characteristics: the curvature at 225°K could be described as
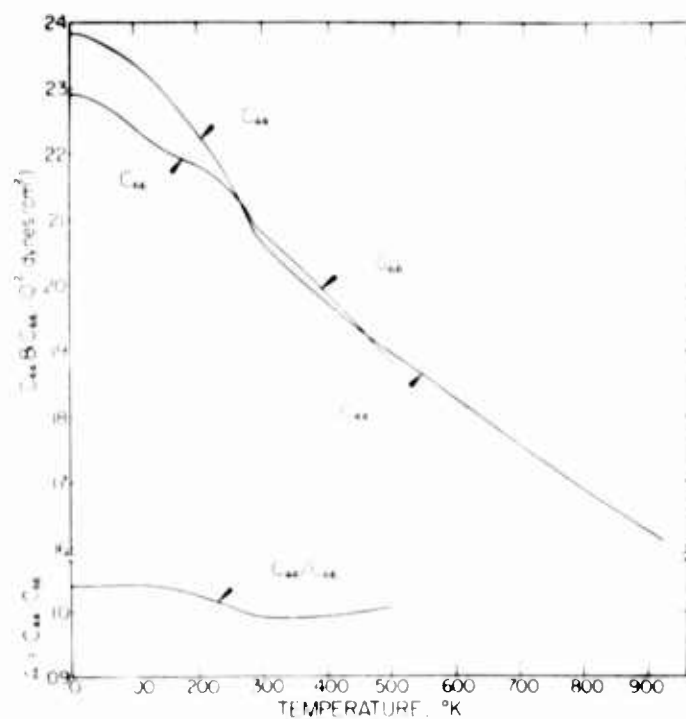
Fig. 2. Variation of principal shear moduli and shear anisotropy ratio, A = c_{44}/c_{66}, (4° to 923°K for c_{44} and 4° to 500°K for c_{66}).
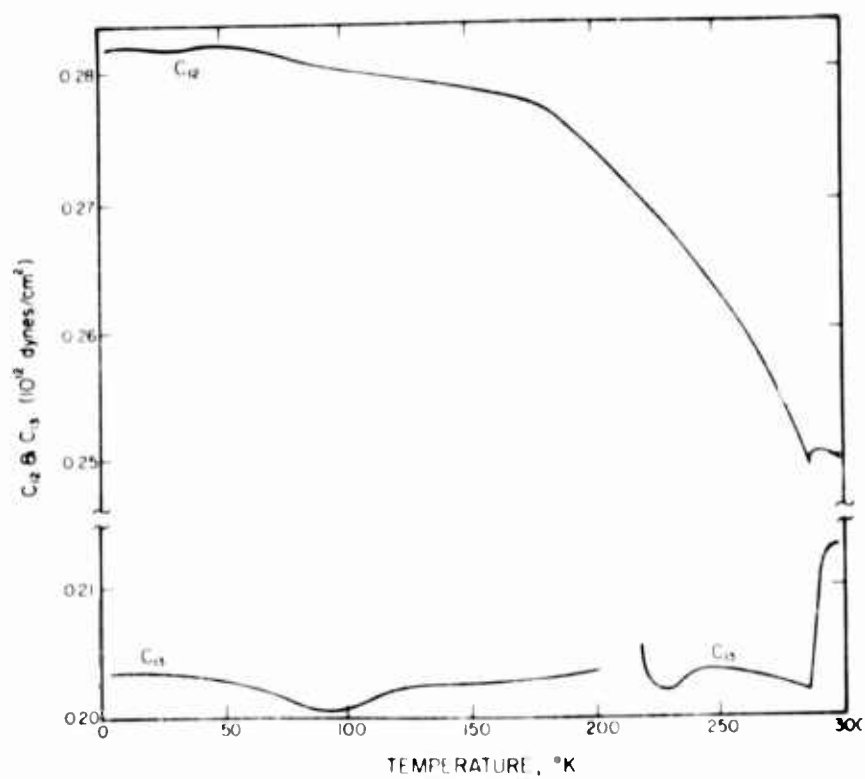
Fig. 3. Variation of cross coupling moduli, c_{12} and c_{13}, with temperature of Gd single crystals (4° to 298°K).
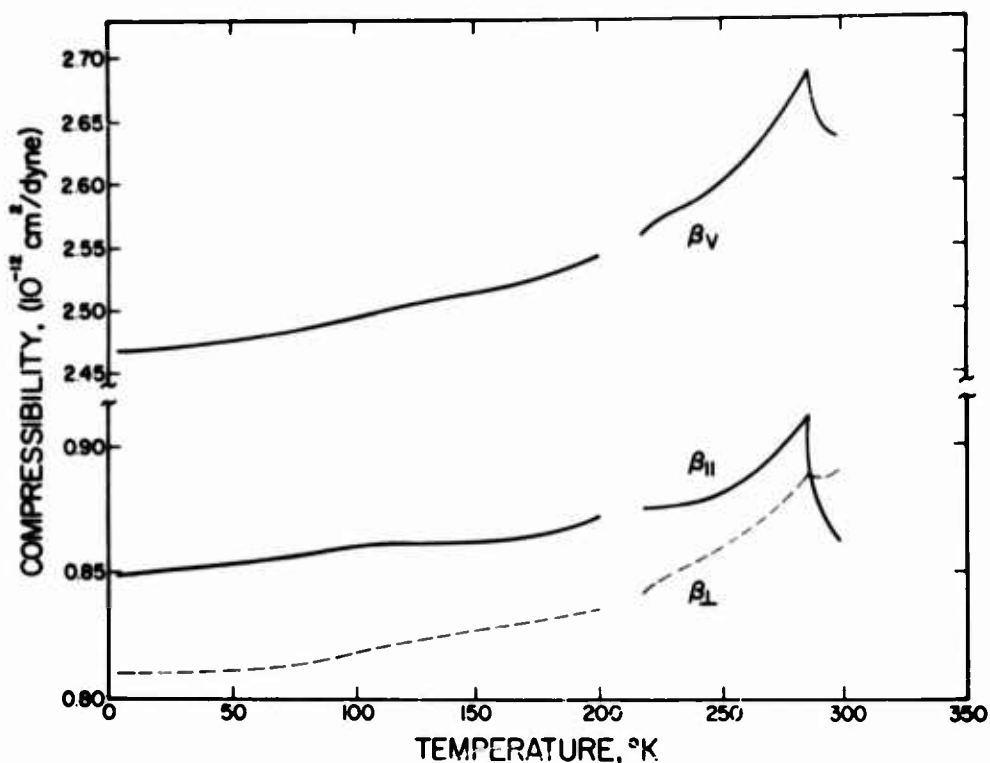
Fig. 4. Variation of linear and volume compressibilities of Gd single
crystals with temperature (4° to 298°K, $\beta_{||}$ and $\beta_{\perp}$ are linear
compressibilities for 0° and 90° to "c" axis, respectively).

almost a sharp peak, (2) below 218°K the acoustic attenuation becomes

so large that no measurements could be made between 218° and 200° ±

0.5°K, (3) an extrapolation of the curve obtained below 200°K indicates

that 218°K is another point of slope inversion. The c_{13} anomaly appears

λ shaped. The c_{66} curve also seems to undergo a relatively large slope

change near 220°K; the other moduli, however, show no indication of any

sort of anomaly in this range of temperature.

The computed linear and volume compressibilities at several tem-

peratures are listed in Table II and the curves are shown in Figure 4.

The compressibility parallel to the "c" axis, $\beta_{||}$, shows a characteris-

tic λ shape at 286°K. $\beta_{\perp}$, shown as the dashed line, shows only a slight

peak at 286°K. The shape of the volume compressibility curve.

$\beta_V = \beta_{||} + 2\beta_\perp$, is dominated by $\beta_{||}$. The calculations are necessarily interrupted between $200°$ and $218°K$ because of the lack of c_{33} data. It appears that sharp slope changes may occur between these temperatures, with a slight λ point for $\beta_{||}$ and an inverted λ for $\beta_\perp$. There would then be almost no effect on β_V.

The measurements above room temperatures were made only to investigate the temperature dependence of $A = c_{44}/c_{66}$. The A vs. temperature curve is shown in Figure 2. At T_c, $A < 1$ but increases with temperature and becomes greater than 1 at $460°K$.

Discussion

Correlation with Dy and Er: The effects of magnetic ordering on the elastic moduli of Gd are similar in several respects to the effects observed in Dy and Er.[6]

a) In all 3 metals the c_{33} curve undergoes a very sharp inversion at the ordering temperature and is affected anomalously over a wide range of temperatures in the paramagnetic phase. It appears that some degree of magnetic ordering exists up to $330°K$ in Gd.

b) The T_N or T_c indicated by the different modes of deformation are not always the same.

c) The transformations are not accompanied by a large acoustic attenuation; changes in the directions of aligned moments do however involve attenuation that may be associated with the ΔE effect. The abrupt anomaly in c_{33} at $218°K$ apparently reflects an abrupt shift in direction of the moments.[2]

<u>Debye Θ</u>: Because of the magnetic contribution to the low temperature heat capacities the conventional method of deducing the Debye Θ from C_p/T vs. T^2 plots cannot be applied without ambiguity because the magnetic heat capacity may also have close to a T^3 dependence.[3] From the point of view of determining the deviation from T^3 it is quite important that the 0°K Debye Θ be determined independently, especially in Gd. The Debye Θ computed from our 4.2°K data by Anderson's[8] velocity averaging procedure is 181.5°K. This value is considerably above the value obtained by Jelinek et al.[9] (Θ_c = 153.7°K). It does, however, fit reasonably well with the assumption that the Debye Θ is a linear function of atomic weight between La and Lu.[10] This latter assumption gives Debye Θ = 176°K. It is quite far removed from the assumption that all of the trivalent rare earths have the same Debye Θ as Lu, 210°K.

As further evidence that the interpolation between La and Lu gives a reasonably accurate Debye Θ, that for Er is computed to be 191°K from the 4.2° elastic moduli. The interpolated Debye Θ for Er is 195°K.

<u>Relationship to other h.c.p. metals</u>: The temperature dependence of the anisotropy ratio, A = c_{44}/c_{66}, in the paramagnetic phase agrees with that predicted from the fact that Gd does have a structural transformation at high temperatures (1535°K).

Acknowledgement

Table I. Elastic Moduli of Gd a† ͏ ͏ral Temperatures
(units of 10^{12} dynes/ ͏ ͏lues apply to
density of 7.888 gm/cc,

T, °K	c_{11}	c_{33}	c_{12}	c_{13}	c_{44}	$c_{66} = \left(\dfrac{c_{11}-c_{12}}{2}\right)$
4	0.7400	0.7901	0.2822	0.2034	0.2382	0.2289
50	0.7374	0.7862	0.2822	0.2028	0.2369	0.2275
100	0.7287	0.7792	0.2805	0.2008	0.2337	0.2241
150	0.7202	0.7723	0.2790	0.2026	0.2293	0.2206
200	0.7105	0.7569	0.2740	0.2035	0.2235	0.2182
218	0.7050	0.7481	0.2703	0.2052	0.2209	0.2173
225	0.7025	0.7514	0.2689	0.2020	0.2197	0.2168
250	0.6922	0.7387	0.2632	0.2034	0.2158	0.2145
286	0.6690	0.7036	0.2494	0.2018	0.2088	0.2100
289	0.6691	0.7150	0.2504	0.2100	0.2080	0.2094
298	0.6667	0.7191	0.2499	0.2132	0.2069	0.2084
330		0.7217			0.2037	0.2055
355		0.7211			0.2013	0.2032
400					0.1973	0.1989
500					0.1900	0.1884
923					0.1610	

Table II. Linear and Volume Compressibilities of Gd at Several Temperatures (units of $10^{-12} cm^2/dyne$)

T, °K	$\beta_{||}$	$\beta_{\perp}$	β_V
4	0.849	0.809	2.468
50	0.854	0.811	2.475
100	0.861	0.820	2.500
150	0.862	0.826	2.514
200	0.872	0.836	2.544
218	0.875	0.841	2.558
225	0.875	0.847	2.570
250	0.880	0.859	2.599
286	0.911	0.888	2.688
289	0.878	0.887	2.653
298	0.862	0.890	2.643

References

1. F. J. Darnell and W. H. Cloud, J. Appl. Phys. $\underline{35}$, 935 (1964).

2. C. D. Graham, Jr., J. Phys. Soc. Japan $\underline{17}$, 1310 (1962).

3. O. V. Lounasmaa and L. J. Sundstrom, Phys. Rev. $\underline{150}$, 399 (1966).

4. F. H. Spedding, J. J. Hanak and A. H. Danne, J. Less-Common Metals, $\underline{3}$, 110 (1961).

5. E. S. Fisher and D. Dever, Trans. AIME $\underline{239}$, 48 (1967).

6. E. S. Fisher, Presented at Conference on Rare Earths, Durham, England September 1966.

7. E. S. Fisher and C. J. Renken, Phys. Rev. $\underline{135}$, 482 (1964).

8. O. L. Anderson, J. Phys. Chem. Solids $\underline{24}$, 909 (1963).

9. F. J. Jelinek et al., Phys. Rev. $\underline{149}$, 489 (1966).

10. O. V. Lounasmaa, Phys. Rev. $\underline{133}$, A222 (1964).

The Heat Capacity of Scandium from 1 to 23°K*

Howard E. Flotow and Darrell W. Osborne

Argonne National Laboratory, Argonne, Illinois 60439

The heat capacity of a well-characterized, polycrystalline
scandium sample was measured from 0.9 to 23°K. The results are in
reasonable agreement with previous measurements below 4°K, except
that a small anomalous addendum to the heat capacity was detected.
This anomaly follows a T^{-2} dependence down to 2.9°K. rises to a
maximum of about 1.3 mJ deg^{-1} (g at. Sc)$^{-1}$ near 1.2°K, and has an
associated entropy of 3.2 mJ deg^{-1} (g at. Sc)$^{-1}$. It is believed to
be due to small concentrations of magnetic impurities found in the
sample. An evaluation of the results from 2.9 to 8.4°K gave
γ = 10.66 ± 0.10 mJ deg^{-2} (g at.)$^{-1}$ and θ = 359.5 ± 4.2°K.   A
table of smoothed heat capacities and thermodynamic functions for
scandium at selected temperatures between 5 and 298.15°K is presented.

INTRODUCTION

The heat capacity of scandium has been determined by Montgomery
and Pells[1] between 1.7 and 4°K. They evaluated the electronic and
lattice parameters to be γ = 11.3 ± 0.1 mJ deg^{-2} (g at.)$^{-1}$ and
θ = 470 ± 80°K, respectively. Lynam, Scurlock, and Wray[2] have
measured the heat capacity of the same scandium specimen between
0.5 and 3°K and report γ = 10.9 ± 0.1 mJ deg^{-2} (g at.)$^{-1}$ and
θ = 344 ± 25°K. The latter authors also measured a second specimen
of scandium in another apparatus from 0.15 to 0.5°K and obtained
anomalous results which could not be interpreted satisfactorily.[2]
Heat capacity data for scandium in the temperature range 51 to 298°K
have been reported by Weller and Kelley.[3]

In this paper we report the heat capacity of a well-characterized
sample of scandium from 1 to 23°K. Below 5°K a small anomaly was
found which is probably due to impurities. However, it was possible
to obtain a reliable value for γ and to obtain a much better estimate

---

of the lattice heat capacity and Debye θ from the new data above 3°K. Some thermodynamic properties of scandium at selected temperatures between 5 and 298.15°K have been calculated from the present heat capacity data at the lower temperatures and from the data given by Weller and Kelley[3] at the higher temperatures.

EXPERIMENTAL

The scandium metal was a polycrystalline vacuum-distilled sample which was obtained from Johnson, Matthey and Company. The oxygen content was determined to be 630 ± 30 parts per million by the inert-gas fusion technique. The results of a spectrographic analysis gave the following results in parts per million: Ag, < 100; Al, 20; As, < 1000; B, < 10; Ba, < 1; Be, < 1; Bi, < 100; Ca, < 20; Cd, < 10; Ce, 100; Co, < 10; Cr, 20; Cs, < 10; Cu, 20; Dy, < 5; Er, < 5; Eu, < 5; Fe, 100; Ga, < 2; Gd, 100; Ho, < 5; K, 100; La, 100; Li, < 1; Mn, < 5; Mo, < 100; Na, 10; Nd, < 20; Ni, 10; Pb, < 10; Pr, < 20; Rb, < 10; Sb, < 100; Si, 10; Sm, < 10; Sn, < 100; Sr, < 1; Ta, 60; Tb, < 5; Ti, < 100; Tm, < 10; V, < 10; Y, 10; Zn, < 20; Zr, < 100. The above values are accurate to about a factor of 2. By neutron activation analysis the following rare earth impurities were found in parts per million: La, 50; Ce, 47; Nd, 6; Gd, 65; Eu, < 0.3; Tb, 0.9; Ho, 0.1; Tm, $\leqslant 2$; Yb, $\leqslant 3.5$; Lu, 6.7. These values are reliable to $\pm 25\%$. Finally, the iron content was determined by chemical analysis to be 167 ± 5 parts per million.

The heat capacity measurements were made by the isothermal method with an apparatus which has been described in an earlier publication.[4] That publication gives the details of the measuring techniques, of the calibrated platinum-encapsulated germanium resistor used to measure the temperatures, and of the calorimeter design (See Fig. 4 of reference 4).

The scandium crystals were broken into pieces 1 to 4 mm on an edge and then pressed in a die at 1 kbar pressure to form a specimen which fits inside the calorimeter. The technique is similar to one

used in this laboratory to prepare powdered samples for calorimetric measurements,[5] except that in this case a copper capsule was not used. After pressing, each of two specimens prepared as described above was cleaned of surface contamination by light filing with a new Swiss file, and they were then annealed at 700°C for 1 hour in an evacuated quartz tube at a pressure of 1×10^{-6} mm Hg. The two specimens were put into the calorimeter, which was soldered shut in vacuo.[5] Thermal contact between the scandium and the calorimeter was achieved by Apiezon T grease between the contacting surfaces[4,5] so that no helium exchange gas was required for any of the measurements. The mass of the scandium sample was 14.535 g in vacuo.

RESULTS

The experimental heat capacity data are presented in order of ascending temperature in Table I. The temperature rise for each run is approximately 10% of the average temperature. These values have been corrected for the finite temperature increments but have not been corrected for impurities in the sample. The heat capacity of the empty calorimeter and of the Apiezon T grease[6] were determined in separate experiments. The estimated probable error in the heat capacities is ± 0.2%. This error estimate is based in part on the calibration of the germanium thermometer[4] and on the heat capacity data obtained for pure copper[4] with this apparatus.

DISCUSSION

The results below $9°K$ are plotted as C_p/T vs. T^2 in Fig. 1, where the circles represent the experimental heat capacities and the squares, through which a straight line is drawn, represent the experimental heat capacities less a correction for impurities estimated in the following manner. The magnetic, electronic, and crystalline properties of scandium metal do not indicate that an anomalous contribution to the heat capacity is to be expected within the temperature range of this experiment. Accordingly we have analyzed the data with the assumption that the heat capacity of pure scandium can be represented

Table I: Experimental Heat Capacity Results for Scandium. At. wt. = 44.956. Units are °K, mJ, and g at.

$\bar{T}$	c_p	$\bar{T}$	c_p	$\bar{T}$	c_p
0.899	10.80	2.439	27.72	7.952	106.0
0.997	11.91	2.523	28.65	8.312	112.7
1.001	11.96	2.686	30.47	8.803	122.8
1.099	13.05	2.781	31.53	9.100	129.0
1.105	13.11	2.965	33.62	9.719	142.9
1.207	14.22	3.063	34.73	9.976	148.8
1.212	14.28	3.265	37.04	10.52	162.3
1.328	15.55	3.372	38.28	10.94	173.0
1.328	15.54	3.580	40.73	11.57	190.2
1.415	16.43	3.704	42.21	11.96	201.8
1.462	16.99	3.921	44.85	12.74	226.6
1.463	16.95	4.071	46.73	13.13	240.1
1.466	17.04	4.304	49.63	14.00	272.7
1.561	18.01	4.512	52.33	14.37	287.7
1.615	18.66	4.724	55.14	15.12	320.5
1.618	18.63	4.740	55.32	15.34	330.8
1.619	18.69	4.929	57.95	16.50	389.8
1.730	19.87	5.196	61.54	16.88	411.6
1.783	20.44	5.381	64.23	16.94	414.9
1.783	20.49	5.726	69.12	18.02	481.1
1.786	20.53	5.918	72.05	18.59	520.6
1.925	22.02	6.301	77.83	19.75	607.2
1.982	22.60	6.525	81.45	20.48	668.9
2.097	23.89	6.918	87.71	21.69	781.3
2.203	25.11	7.200	92.64	22.62	880.1
2.277	25.87	7.587	99.28		
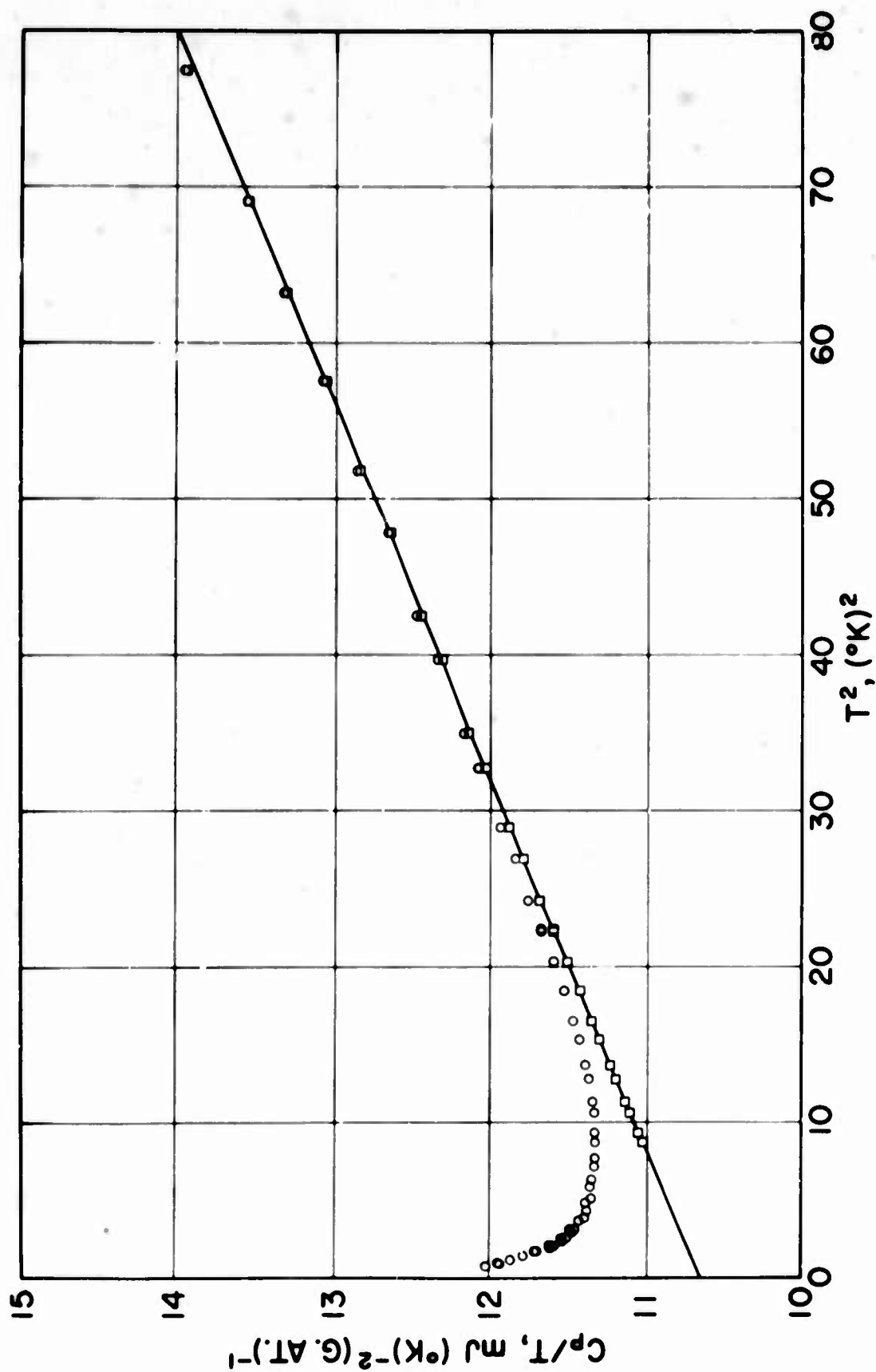
FIG. 1. Heat capacity of scandium, plotted as C_P/T vs. T^2. O: (Observed c_P)/T; □: (Observed c_P − 8.0 x T^{-2})/T.

by an electronic term proportional to T and a lattice term proportional to T^3 at temperatures which are not too high, and that the excess heat capacity due to the impurities can be represented by a term proportional to T^{-2} at temperatures which are not too low.

It was found that the experimental data between 2.9 and 8.4° K can be fitted with the equation

$$C_p = 10.66 \, T + 0.04182 \, T^3 + 8.0 \, T^{-2} \text{ mJ deg}^{-1} \text{ (g at. Sc)}^{-1} \qquad (1)$$

with a standard deviation of 0.055%. Above 8.4°K the experimental C_p points lie increasingly above equation (1) because powers of T higher than 3 are needed to represent the lattice heat capacity at higher temperatures. From 2.9 to 8.4°K the excess heat capacity due to impurities, calculated from equation (2),

$$C_{excess} = C_p - 10.66 \, T - 0.04182 \, T^3 \text{ mJ deg}^{-1} \text{ (g at. Sc)}^{-1} , \qquad (2)$$

is represented by the term $8.0 \, T^{-2}$. Below 2.9°K the excess heat capacity calculated from equation (2) grossly deviates from a T^{-2} dependence and seems to reach a maximum of 1.3 mJ deg^{-1} (g at. Sc)$^{-1}$ near 1.2°K. This of course is the behavior expected if C_{excess} is due to the impurities and is a Schottky function or a sum of Schottky functions. The excess entropy due to the impurities was evaluated from a graphical integration of a plot of C_{excess}/T vs. T from 0 to 3°K and an integration of $8.0 \, T^{-2} dT$ at higher temperatures. The estimated excess entropies in mJ deg^{-1} (g at. Sc)$^{-1}$ are 1.4 from 0 to 0.9°K, 1.4 from 0.9 to 3.0°K, and 0.4 from 3°K to ∞, for a total of 3.2 ± 0.8.

Estimated Effect of Impurities. Although neither theoretical nor experimental information allows a quantitative calculation of the excess heat capacity at the lowest temperatures, an examination of possible effects from known impurity concentrations may be helpful to suggest the course of future investigations.

The largest impurity is 630 parts per million of oxygen. Microscopic examination of the scandium crystals revealed a white deposit, which one can reasonably assume to be mainly Sc_2O_3. If all of the

oxygen impurity is present as Sc_2O_3, about 0.12 at. % of the scandium would be in the form of the oxide. The heat capacity of Sc_2O_3 has not been measured below $50°K$, but no anomaly is expected at low temperatures. The correction for this impurity is probably small (< 0.2%) and has therefore been neglected.

Rare earth impurities probably give rise to Schottky anomalies in the heat capacity, with an associated entropy of $k \ln (2J + 1)$ per atom, where k is Boltzmann's constant and J is the degeneracy of the ground level of the free ion, assumed to be M^{+2} for europium and ytterbium and M^{+3} for all the other rare earths. Thus, Phillips and Matthias[7] have measured the heat capacity of $La_{0.993}Gd_{0.007}$ and have concluded that the entropy associated with the gadolinium is within experimental error equal to the expected value, namely 0.007 R ln8 per mole of alloy. The calculated excess entropy for the present sample is 0.21 mJ deg^{-1} (g at. Sc)$^{-1}$ due to 47 ppm cerium, 0.32 due to 65 ppm gadolinium, 0.12 due to 20 ppm praseodymium (the limit of detection of this element), and 0.16 due to all the other rare earths, a total of 0.81 ± 0.2 mJ deg^{-1} (g at. Sc)$^{-1}$.

Thus, there is a discrepancy of 2.4 ± 1.0 mJ deg^{-1} (g at. Sc)$^{-1}$ between the observed excess entropy, 3.2 ± 0.8, and the calculated entropy due to the rare earth impurities, 0.81 ± 0.2 mJ deg^{-1} (g at. Sc)$^{-1}$. The only other known impurity in the sample which could possibly account for this discrepancy is the 167 ppm of iron. However, the effect of dilute solid solutions of iron in scandium is uncertain, because the theory does not give an unambiguous answer and the available experimental results are conflicting. Clogston et al.[8] have reported that the solution of 1 at. % iron in scandium greatly increases the magnetic susceptibility at low temperatures and that this observation suggests a large localized moment in the alloy. On the other hand, Blum and Freeman[9] have reported that Mössbauer experiments on 1% Fe^{57} in scandium over the range 1.5 to $300°K$ have shown no localized moments. If the discrepancy of 2.4 ± 1.0 mJ deg^{-1}

$(g at. Sc)^{-1}$ is attributed solely to the 167 ppm Fe, the value of J for iron calculated from equation (3) is 3.8, corresponding to a localized magnetic moment of 7.6 Bohr magnetons per iron atom if g = 2, with a factor of 3 uncertainty. It is apparent that more definitive experiments on the quantitative effects of low/concentrations of rare earths, iron, and other magnetic materials must await much purer scandium metal than is presently available.

γ and θ_0 Scandium. The present work indicates that up to 8.4°K the heat capacity of pure scandium is given by the first two terms on the right-hand side of equation (1). The coefficient γ in the familiar expression for the contribution of the conduction electrons to the heat capacity (γT) is therefore 10.66 ± 0.10 mJ deg^{-2} (g at.)$^{-1}$. The Debye θ near 0°K, designated as θ_0, is obtained from the co-efficient of the second term, A_2, by means of the relation $\theta_0 = (12R\pi^4/5)^{1/3} A_2^{-1/3}$, and is found to be 359.5 ± 4.2°K. The uncertainties indicated were estimated by considering the effect of the impurity correction. A least squares fit of the uncorrected C_p data from 4.5 to 8.4°K with only linear and cubic terms gives $\gamma = 10.76$ mJ deg^{-2} (g at.)$^{-1}$ and $A_2 = 0.04041$ mJ deg^{-4} (g at.)$^{-1}$, or $\theta_0 = 363.7$°K.

Table II presents a comparison of the values of γ and θ_0 obtained in the present work with those obtained calorimetrically by Montgomery and Pells[1] and by Lynam et al.[2] using the same specimen as Montgomery and Pells. It can be seen that the present results agree within the sum of the estimated experimental errors with those of Lynam et al. but not with those of Montgomery and Pells. Also given in Table II is the value of θ_0 obtained by Fisher and Dever[10] from measurements of the elastic moduli at low temperatures. The agreement is seen to be quite satisfactory, suggesting that adequate correction has been made for the effect of impurities in the present calorimetric data.

A plot of the Debye θ for scandium as a function of temperature is shown in Fig. 2. The circles are values which were calculated from our data above 2.9°K by subtracting the first and last terms of equation (1) (i.e., the contributions of the conduction electrons and of the impurities, respectively) from the observed C_p and fitting each residual with a Debye heat capacity function. The dotted lines below 10°K show the variation of θ caused by a ± 0.5% change in the value of C_p. The squares were obtained from the data of Weller and Kelley[3] after subtraction of 10.66 T mJ deg^{-1} (g at.)$^{-1}$. No C_p-C_v correction was made because no values for the thermal expansion of scandium are available. However, it is likely that the C_p-C_v correction will have a negligible effect on the values of θ below 20°K. Above 20°K the θ's calculated in this manner may differ appreciably from the actual θ's, but the plot is useful for estimating the heat capacity in the region 23 to 51°K where there are no experimental data.

Table II. Comparison of Reported Values of γ and θ_0 for Scandium. Units are mJ deg^{-2} (g at.)$^{-1}$ for γ and °K for θ_0.

Authors	γ	θ_0
Montgomery and Pells[a]	11.3 ± 0.1	470 ± 80
Lynam et al.[b]	10.9 ± 0.1	344 ± 25
Present work	10.66 ± 0.10	359.5 ± 4.2 K
Fisher and Dever[c]	----	360 ± 2

[a]Reference 1.

[b]Reference 2, specimen I.

[c]Reference 10.
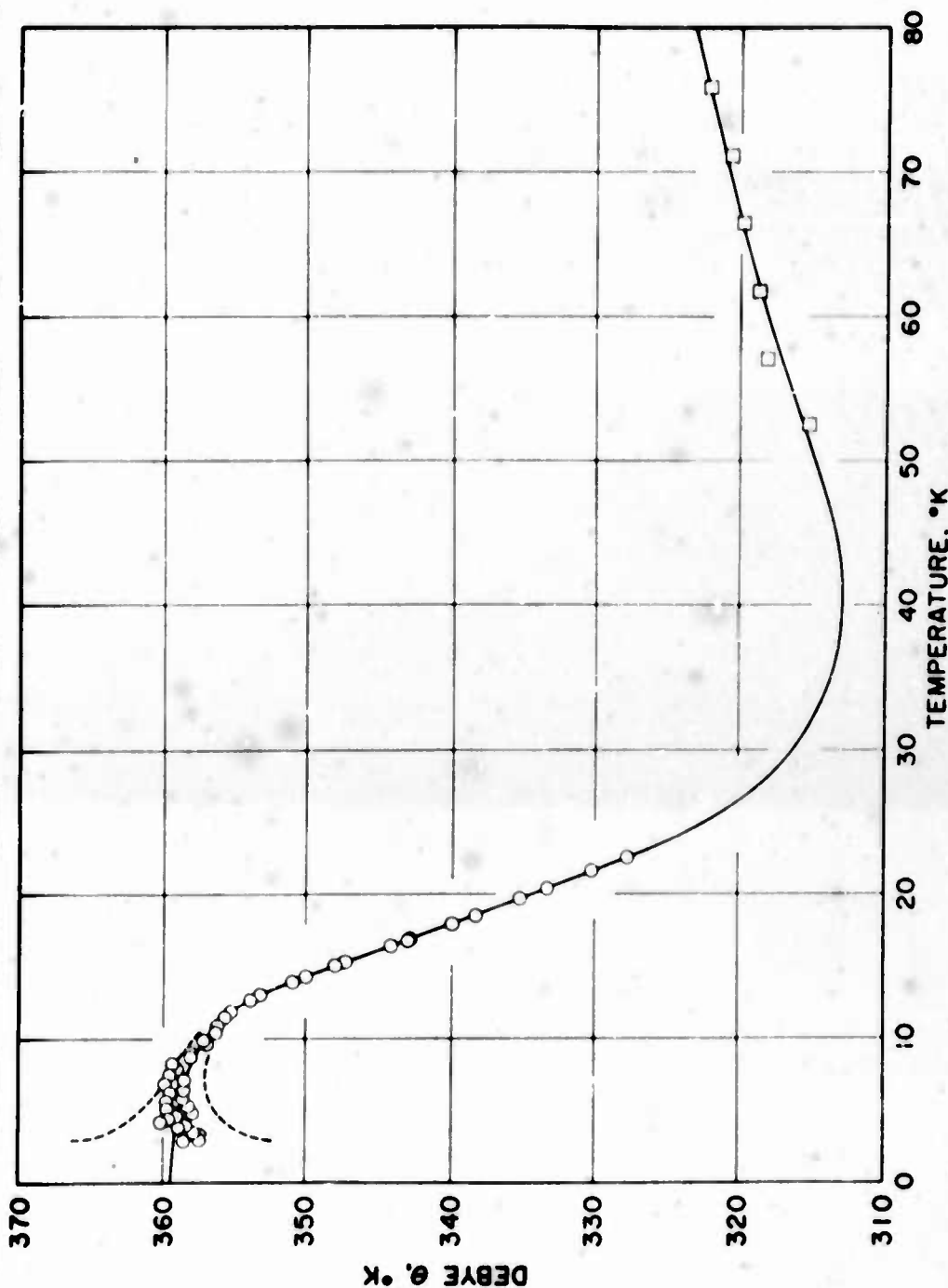
FIG. 2. Debye θ's for scandium. No correction was made for $(C_P - C_V)$. All the C_P data were corrected for the contribution of the conduction electrons by subtracting $10.66 \times T$ mJ deg^{-1} (g at.)$^{-1}$. O: Present data, corrected also for impurities by subtracting $8.0 \times T^{-2}$ mJ deg^{-1} (g at.)$^{-1}$ from the observed C_P; □: data of Weller and Kelley. The dashed lines show the effect of $\pm\frac{1}{2}\%$ change in C_P.

THERMODYNAMIC FUNCTIONS

The heat capacity C_p, entropy $S°$, enthalpy function $(H° - H_0°)/T$ and Gibbs energy function $(G° - H_0°)/T$ are given at selected temperatures between 5 and $298.15°$K in Table III. Entries up to $25°$K were calculated from the present C_p data less the correction $8.0\ T^{-2}$ mJ $\deg^{-1}$ (g at.)$^{-1}$ for impurities. Between 25 and $50°$K values of C_p were calculated at intervals of $2.5°$K from the graphical values of θ (Fig. 2), plus the electronic heat capacity, γT. Above $50°$K the experimental data of Weller and Kelley[3] were used. The calculations were performed by using a computer to fit the heat capacity points to

Table III. Some Thermodynamic Properties of Scandium at Selected
Temperatures. Units are J, $°$K, and g at.

T	C_p	$S°$	$(H° - H_0°)/T$	$-(G° - H_0°)/T$
5	0.0585	0.0551	0.0280	0.0271
10	0.1492	0.1206	0.0638	0.0568
15	0.3151	0.2090	0.1170	0.0920
20	0.6286	0.3380	0.2017	0.1363
25	1.168	0.5315	0.3368	0.1947
50	6.54	2.819	1.974	0.845
100	16.44	10.74	6.99	3.75
150	21.10	18.40	11.01	7.39
200	23.40	24.83	13.86	10.97
250	24.65	30.19	15.90	14.29
298.15	25.58	34.61	17.39	17.22
	±0.08	±0.10	±0.05	±0.05

two polynomials, one for $T < 45°K$ (standard deviation 0.090%) and the other for $T \geq 45°K$ (standard deviation 0.150%). The tabulated values of C_p between 50 and 298.15°K differ by less than the estimated experimental error of 0.3% from those given by Weller and Kelley. They reported a value for $S°$ at 298.15°K of 34.31 ± 0.25 J deg^{-1} (g at.)$^{-1}$, which is based upon heat capacities above 51°K. The smaller uncertainty assigned to our tabulated value, ± 0.10, reflects a smaller estimated error in the entropy at 51° K.

ACKNOWLEDGMENTS

REFERENCES

1. H. Montgomery and G. P. Pells, Proc. Phys. Soc. 78, 622 (1961).
2. P. Lynam, R. G. Scurlock, and E. M. Wray, in Proc. 9th International Conference on Low Temperature Physics, J. G. Daunt, D. O. Edwards, F. J. Milford, and M. Yaqub, eds., Plenum Press, New York (1965), Part B, pp. 905-907.
3. W. W. Weller and K. K. Kelley, U.S. Bureau of Mines, Report of Investigations, No. 5984 (1962).
4. D. W. Osborne, H. E. Flotow, and F. Schreiner, Rev. Sci. Instr., in press.
5. H. E. Flotow and D. W. Osborne, Rev. Sci. Instr. 37, 1414 (1966).
6. E. F. Westrum, Jr., C. Chou, D. W. Osborne, and H. E. Flotow, Cryogenics, in press.
7. N. E. Phillips and B. T. Matthias, Phys. Rev. 121, 105 (1961).
8. A. M. Clogston, B. T. Matthias, M. Peter, H. J. Williams, E. Corenzwit, and R. C. Sherwood, Phys. Rev. 125, 541 (1962).
9. N. Blum and A. J. Freeman, Rev. Mod. Phys. 36, 406 (1964); N. Blum, National Magnet Laboratory Report, No. NML-64-2 (1964).
10. E. Fisher and D. Dever, private communication.

Crystal Field Heat Capacities of $PrNi_2$ and PrBi[*]

by

M. Dixon, M. Aoyagi, R. S. Craig and W. E. Wallace

Department of Chemistry, University of Pittsburgh, Pittsburgh, Pa.
15213

ABSTRACT

Heat capacities of $PrNi_2$, $CeNi_2$, PrBi and LaBi have been measured from 1.5°K to 300°K. The first two compounds are cubic Laves phases while the latter two have the NaCl structure.

One of the objectives of this investigation was to evaluate the crystal field heat capacity of $PrNi_2$. The heat capacity of $CeNi_2$ was measured in order to obtain an estimate of the vibrational contribution, the difference in heat capacity between $CeNi_2$ and $PrNi_2$ being taken as the crystal field heat capacity of the latter. The excess heat capacity of $PrNi_2$ is observed as a broad maximum at about 12°K. The excess heat capacity below 30°K is considerably larger than is expected from the crystal field contribution.

The heat capacity of $CeNi_2$ exhibits an anomaly in the liquid helium temperature range. It is suggested that the anomaly results from a small population of trivalent Ce ions which begin to order at about 2.5°K.

The crystal field heat capacity of PrBi was found by taking the difference in heat capacity between PrBi and LaBi. The crystal field heat capacity thus found appears as a somewhat broader anomaly than is predicted from the limiting susceptibility. The measurements on PrBi show some other interesting features. The data on elemental Pr obtained by Lounasmaa when plotted as C/T versus T^2 show a kink in the curve at about 3.5°K and a minimum at about 1.5°K. These two effects also show up in the PrBi data, the kink in the C/T versus T^2 curve appearing at about 3.6°K and the minimum at about 2°K. It is suggested that the anomalous effects in both Pr and PrBi are due to a small population of quadrivalent Pr ions which order at low temperatures.

I. INTRODUCTION

For some time experiments have been underway at the University

of Pittsburgh to investigate the effect of the crystal field on the

heat capacities of intermetallic compounds involving lanthanides. The

splitting of the energy levels produced by the crystal field is

expected, in certain instances, to give rise to a Schottky type anomaly in the heat capacity. The magnitude of the expected crystal field heat capacity had been calculated for several compounds from magnetic data obtained in our laboratory. The calculations were based upon methods developed by Penney and Schlapp[1] and extended by Schumacher and Hollingsworth.[2] The work described here was undertaken to provide experimental data with which the predicted crystal field heat capacities could be compared.

II. Measurements on PrBi

PrBi occurs in the rocksalt structure. The susceptibility of this substance was measured in our laboratory by Dr. Tsuchida, who found that it behaved as a Van Vleck paramagnet at low temperatures.[3] Using the limiting susceptibility, Wallace and Tsuchida estimated the overall splitting to be 199°K which gave an excellent representation of the susceptibility-temperature data.

Heat capacity measurements have been completed on PrBi. In order to obtain the crystal field heat capacity the vibrational heat capacity must be subtracted from the measured total. LaBi was selected as a non-magnetic substance, similar in structure to PrBi, whose vibrational heat capacity is expected to approximate that of PrBi. Heat capacity measurements on LaBi have accordingly been carried out. The difference between the heat capacity of PrBi and LaBi, taken to be the crystal field heat capacity, is plotted in Fig. 1. The dashed curve is the crystal field heat capacity computed using a value for the over-all splitting of 199°K obtained from the limiting magnetic susceptibility. Terms higher than 4th order and exchange effects were neglected

in the calculations. It is noted that there is only approximate
agreement in the temperature at which the maximum occurs in the two
curves. There is obviously an excess heat capacity both above and be-
low the temperature of the maximum which is not accounted for in the
calculations.

In addition to the comparison of the measured and computed
crystal field heat capacities, the work on PrBi reveals some interesting
characteristics. The data on elemental Pr obtained by Lounasmaa[4]
plotted as C/T versus T^2 show a minimum at about $1.5°K$ and a kink
in the curve at about $3.5°K$. Measurements on elemental Pr by Dr.
Dixon in our laboratory confirm the existence of the kink at $3.5°K$,
though our measurements did not extend to low enough temperatures to
show the minimum at $1.5°K$. Measurements on PrBi show both a kink at
about $3.5°K$ and a minimum at about $2°K$. Data for elemental Pr and
PrBi are both shown in Fig. 2. The factors responsible for these
anomalies are certainly not yet clear, though some suggestions will be
presented later.

III. Measurements on PrNi$_2$

PrNi$_2$ is a cubic Laves phase. Magnetic measurements on this
compound by Drs. Farrell[5] and Kissell in our laboratory indicate that
it may also become a Van Vleck paramagnet in the liquid helium tempera-
ture range. However, analysis is quite complex in this case since
the exchange and crystal field interactions are probably of comparable
magnitude. Heat capacity measurements have been made in an effort to
clarify matters. CeNi$_2$ is used to give an estimate of the vibrational
heat capacity, the difference in heat capacity between the Pr and Ce

compounds being taken as the crystal field heat capacity. This is
shown in Fig. 3. The observed crystal field heat capacity can be
accounted for roughly by an overall splitting of $47°K$. The observed
agreement may be fortuitous, since a simple splitting pattern, neglec-
ting sixth order contributions and the effect of exchange, has been
used.

A number of interesting and unusual effects have been turned
up in this study. (1) When the overall splitting is adjusted so that
the calculated value fits the maximum in the crystal field heat capacity
curve, an excess heat capacity is observed below $3°K$. (2) The heat
capacity of $PrNi_2$ between 2 and $4°K$ is quite large compared with its
component elements. (Fig. 4.) (3) The C/T versus T^2 curve for $PrNi_2$
is anomalous. (Fig. 5.) (4) $CeNi_2$, which is taken as having only vi-
brational heat capacity, shows an anomaly below $2.5°K$. (Fig. 6.) This
last effect is quite surprising since there can be no hyperfine contri-
bution for Ce. (5) The heat capacity of $PrNi_2$ in the temperature range
below about $25°K$ depends to an appreciable extent upon the thermal
history of the sample. The data shown in Fig. 3 were taken after the
initial cooling from room temperature. Subsequent data taken after
the sample had warmed to room temperature and again cooled showed a
somewhat broader and flatter maximum. Warming to $77°K$ also produced
a detectable shift in the curve, though not as great as was produced
by warming to room temperature. The behavior was reminiscent of the
effect observed in the heat capacity of elemental Ce by Parkinson,
Simon and Spedding.[7]

The similarity of the C/T vs T^2 plots for PrBi and elemental Pr suggest at once that the corresponding anomalies are closely related. The origin of the anomalies in Pr has been the subject of some speculation. This element is generally assumed to resist magnetic ordering at low temperatures and to become instead a Van Vleck paramagnet. In common with most of the other rare earths, Pr has what has been regarded as a nuclear contribution, C_N, revealed as a rise in heat capacity below 1.5°K (Fig. 2). Bleaney[6] has drawn attention to the puzzling nature of C_N for Pr. The magnetic contribution to C_N vanishes for a Van Vleck paramagnet and the quadrupole interaction is too small to account for the observed rise in heat capacity below 1.5°K. Lounasmaa raised, and simultaneously decided against, the possibility that C_N may not be of nuclear origin but may instead originate with impurities or with a higher valence state (+4) for Pr. In view of the appearance of similar anomalies in PrBi and CeNi$_2$ it may be profitable to reconsider the latter possibility.

The low temperature upturns observed in PrBi and CeNi$_2$ cannot be of nuclear origin. The magnetic and heat capacity data clearly indicate that PrBi is a Van Vleck paramagnet. In view of this and of its cubic symmetry (which excludes a quadrupole interaction) the upturn cannot be of nuclear origin. The same conclusion is reached as regards the anomaly in CeNi$_2$, since the Ce isotopes are without magnetic and quadrupole moments. The results for CeNi$_2$ are interpreted in terms of a small population of Ce^{+3} which is ordering chemically and/or magnetically below 2°K in a matrix of non-magnetic Ce^{+4} ions. The idea

of a mixture of valence states in Ce is not new. Parkinson, Simon and Spedding postulated such a situation in their discussion of thermal hysteresis in elemental Ce.[7]

The anomalies in PrBi and Pr are interpreted in an analogous fashion with the presumption that a small fraction of the ions are in the +4 state. It is suggested that the anomaly at 3.5°K is due to magnetic ordering of Pr^{+4} ions and that the upturn below 2°K is due to chemical ordering. While the reverse might also be postulated, the above suggestion is preferred in light of some very recent experiments performed at our Institution by Dr. R. A. Butera.[8] He finds a ferromagnetic component in elemental Pr, involving roughly 1% of the Pr ions, with a Curie temperature of roughly 2.8°K.

References

1. W. G. Penney and R. Schlapp, Phys. Rev. 41, 194 (1932).

2. D. P. Schumacher and C. A. Hollingsworth, J. Phys. Chem. Solids 27, 749 (1966).

3. T. Tsuchida and W. E. Wallace, J. Chem. Phys. 43, 2084 (1965).

4. O. V. Lounasmaa, Phys. Rev. 133, A211 (1964).

5. J. Farrell and W. E. Wallace, Inorg. Chem. 5, 105 (1966).

6. B. Bleaney, Proc. Roy. Soc. A276, 39 (1963).

7. D. H. Parkinson, F. E. Simon and F. H. Spedding, Proc. Roy. Soc. A207, 137 (1951).

8. R. A. Butera, to appear.

Heat Capacity (joules g.atom⁻¹deg.⁻¹)

$C_{PrBi} - C_{LaBi}$

Calculated from susceptibility

T(°K.)
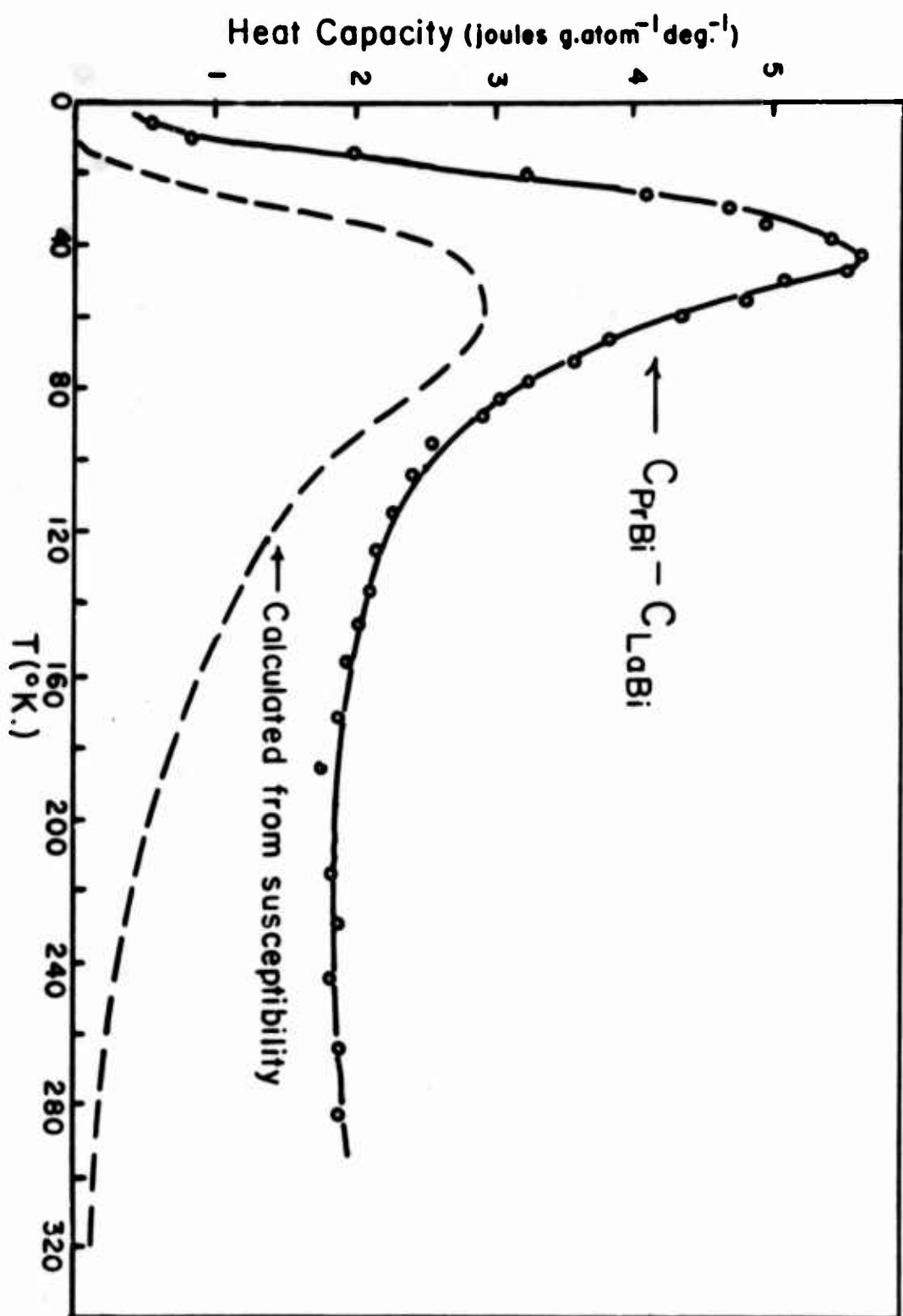
Fig.1. Comparison between measured and calculated crystal field heat capacities. The measured value is regarded as the difference between the heat capacities of PrBi and LaBi.
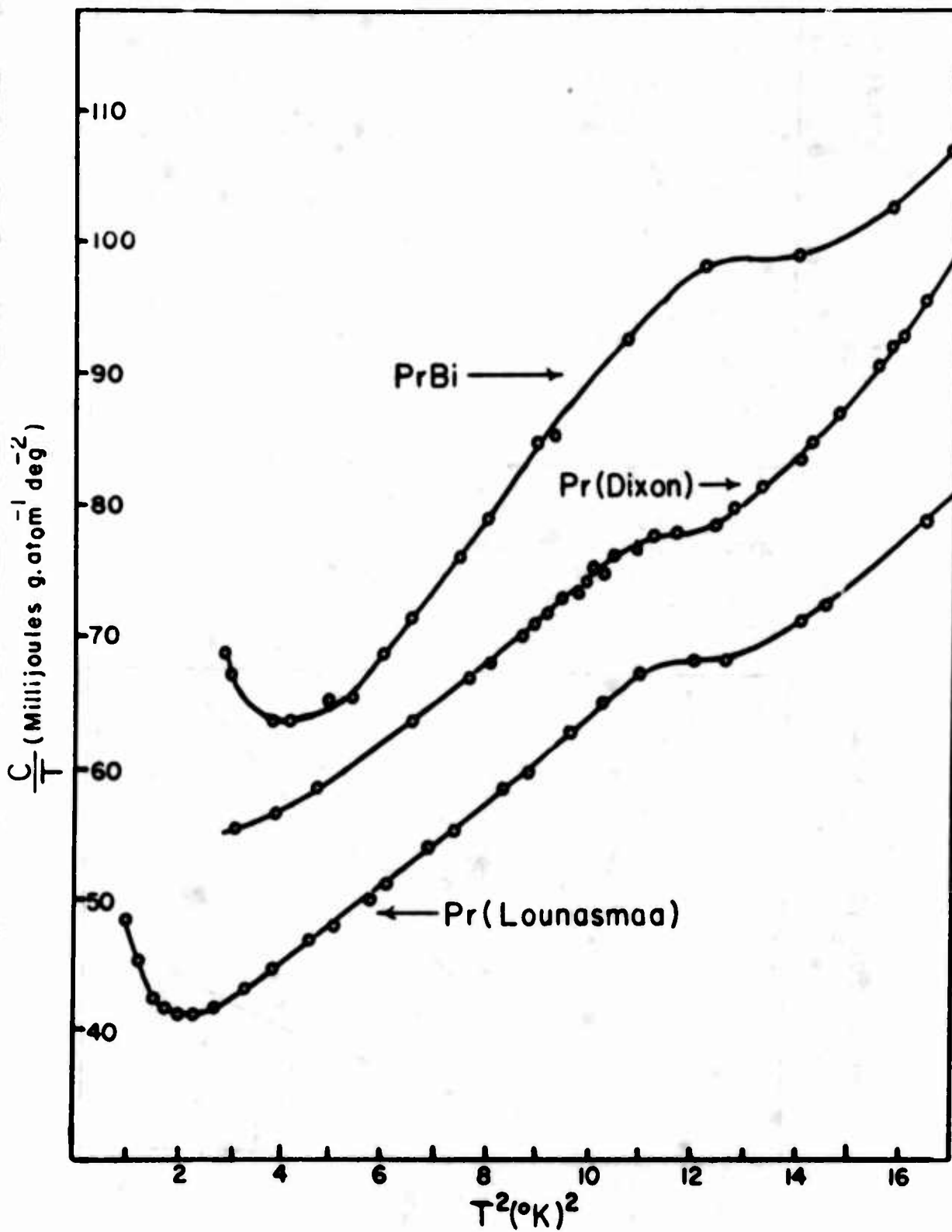
Fig. 2. C/T versus T^2 plots for PrBi and Pr.
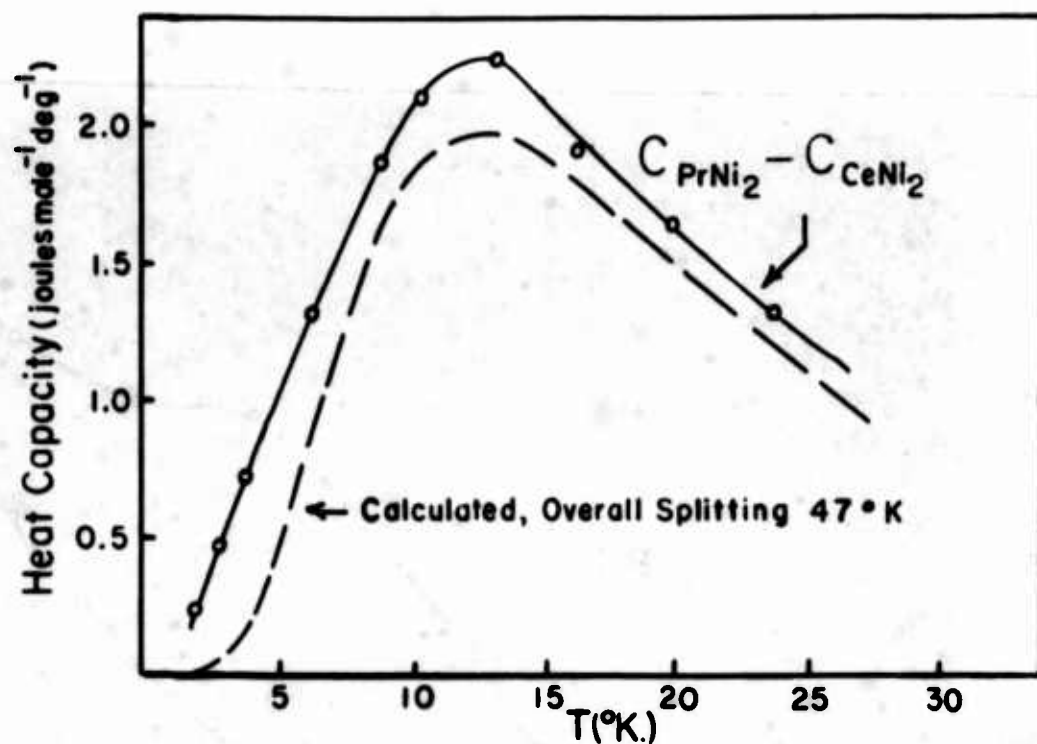
Fig.3. Comparison between measured and calculated crystal field heat capacities. The measured value is taken as the difference between the heat capacities of $PrNi_2$ and $CeNi_2$.
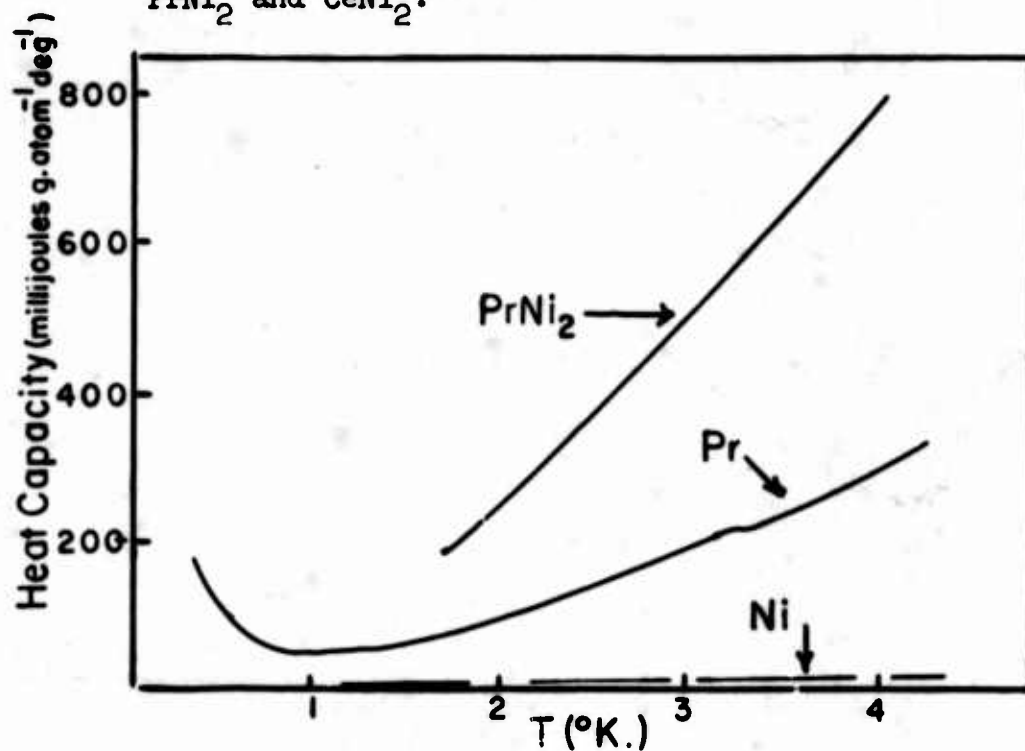
Fig. 4. Heat capacities of $PrNi_2$, Pr, and Ni plotted versus temperature.
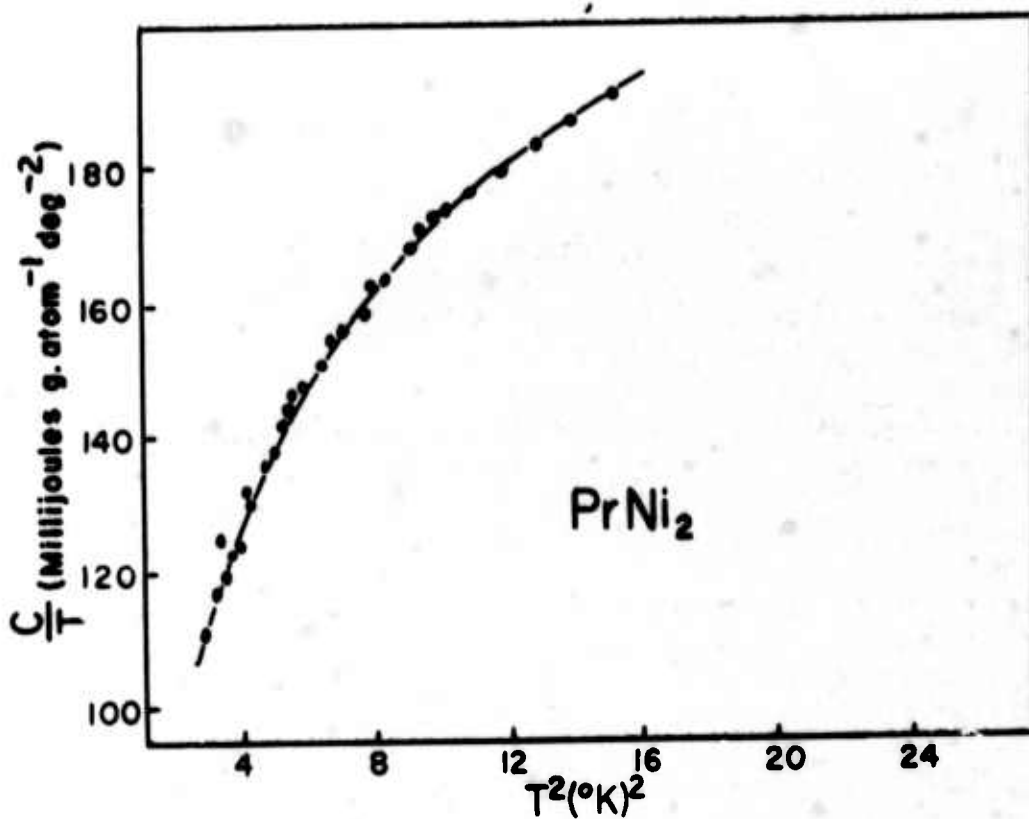
Fig. 5. C/T plot for PrNi$_2$.
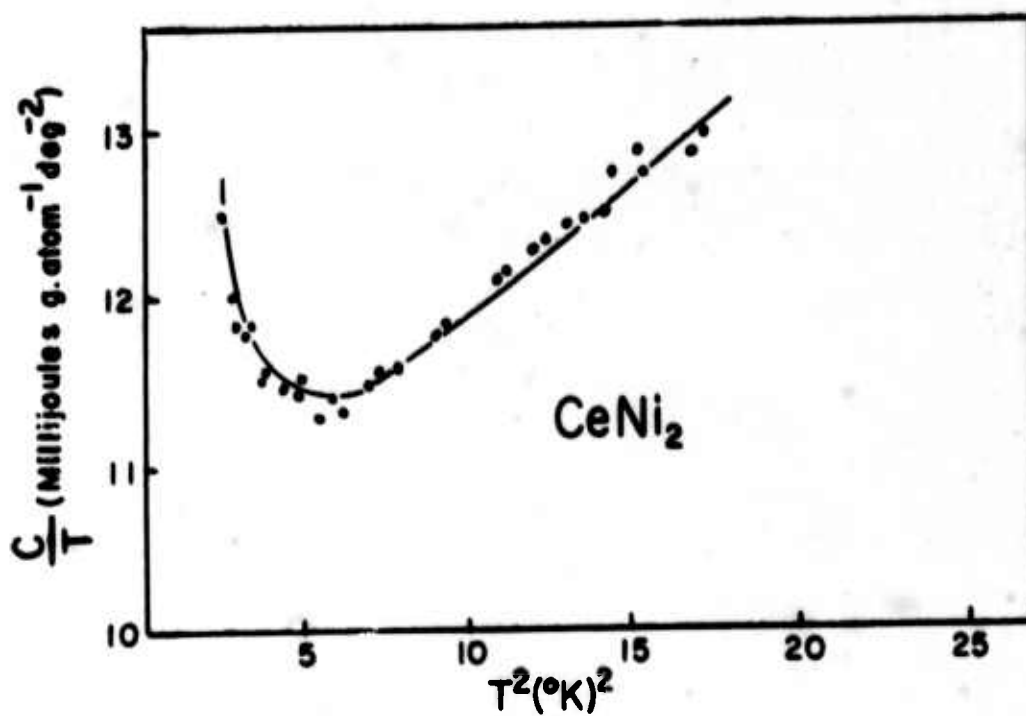
Fig. 6. C/T plot for CeNi$_2$.

ON THE EXISTENCE OF AN ANTIFERROMAGNETIC

PHASE IN RFe_7 COMPOUNDS

by

H. Weik, E. Susedik and M. Turner

Physics Department

University of Cincinnati, Ohio

Results of previous neutron diffraction studies on peritectic compounds of Pr and Nd with Fe of the type RFe_7 suggested the existence of an antiferromagnetic phase beyond the magnetically measured Curie temperatures. In order to prove or disprove this supposition, measurements of the specific heat and electric resistivity were performed with an arc-melted and homogenized Nd-Fe sample of the same composition and treatment as used in the neutron diffraction studies.

The specific heat measurements, performed between room temperature and 110°C, exhibit a relative maximum at 56°C, in agreement with the magnetically determined Curie temperature of 53°C, and show with increased sample temperature a farther increase, indicating a ferromagnetic-antiferromagnetic transition. Measurements of the electric resistivity are in agreement with this and seem to indicate a Neel temperature at about 300°C.

The results are supporting newer magnetic measurements of other RFe_7 compounds in which signs of antiferromagnetism had been found.

A few years ago a group in Dayton, Ohio, working on rare earth - iron and cobalt compounds, produced and investigated compounds of the type RFe_7, particularly $NdFe_7$ and $PrFe_7$.[1] Curie-temperatures were found to be 53° and 7^OC, respectively.

Following these magnetic and X-ray studies, we investigated both substances in a short study in Switzerland by means of thermal neutrons.[2] We found that there was no magnetic disorder at temperatures beyond the magnetically determined Curie-temperatures. The conclusion: there might be a second magnetic phase, i.e. the substances might be anti-ferromagnetic following the ferromagnetic phases. In the neutron diffraction diagrams, weak additional peaks in the high-temp. curves were found, indicating the existence of a magnetic unit cell that is different from the chemical cell.

Since time was limited for the neutron experiments, we were searching for a confirmation of a disprove of the supposition of an antiferromagnetic phase by performing specific heat and electric resistivity measurements.

Specific heat measurements

The specific heat of a substance is that amount of thermal energy that is necessary to increase the temperature of the substance by one degree Kelvin.

In a paramagnetic substance, that has no phase transformations, the specific heat - temp. curve is a smooth curve, that levels off at temperatures in the range of the Debye-temp. A phase transformation shows off as a peak in the curve, since evidently an extra amount of thermal energy is necessary to produce the transformation.

This holds for both kinds of transformations, the phase transformation of the first kind - the crystallographic phase changes - as well as of the second kind, to which magnetic phase changes belong (which occur without latent heat and volume change, as known). -- We cannot go into details here, for instance the differences in the type of peak for the two different types of transformations.

The occurrence of maxima in the specific heat curve thus offers an excellent tool to investigate magnetic ordering processes, and the best procedure would be to perform measurements over the whole temperature range in question, i.e. between say $0^{\circ}C$ and at least $400^{\circ}C$ for the case of $NdFe_7$, onto which our measurements were concentrated.

Since this wide range offers some inconvenience, we tried another way: we investigated - with great accuracy - the environment of the specific heat peak of the ferromagnetic transition at $53^{\circ}C$, particularly the temp. range following the peak. This leads to conclusive results for the following reasons:

Contrary to the case of a paramagnetic substance, where the heat supplied to the sample increases almost entirely the vibrational energy of the lattice and thus practically is temp. independent, - in a substance that exhibits magnetic ordering, part of the internal energy is magnetic in nature and thus temp.-dependent. This means, the specific heat - temp. curve increases with temperature, exhibits peaks at the individual magnetic transitions, and emerges into a part that has almost zero slope, which corresponds to the paramagnetic phase.

Fig. 1 shows a typical example :[3] the pertinent characteristics of the curve is : lower peak, indicating the ferromagnetic-antiferromagnetic transition, rapid rise (in a relatively short temperature interval), characteristic for an intermediate antiferromagnetic phase, and a second, absolute maximum at the antiferromagnetic to paramagnetic transition.

Experimental procedure: The experiments were carried out in the temp. range 20 to 110°C. The sample was arc-melted from the constituents Nd and Fe to form a compound of 12.5 at.% Nd and 87.5 at.% Fe. After machining to a cylinder (mass about 5 grams), the sample was annealed in an inert atmosphere for about 24 hours at 1000°C to form a single phase alloy.

The specific heat was measured using standard techniques (Fig. 2): heating the sample by adding thermal

energy (heating for 30 seconds with 0.15 amps) and measuring the temp. increase. This was done by using a thermistor as one arm of a wheatstone bridge and recording the temp. change with a chart recorder. After correcting for thermal losses, the specific heat can be calculated from the equation,

$$\Delta Q = cm\Delta T$$

where ΔQ is the heat input, producing the temperature difference ΔT, m is the mass of the sample and c the specific heat.

The <u>results</u> are shown in Fig. 3. The numbers given on the ordinate are relative numbers, since the mass m in the equation was the mass of the sample plus the mass of the heater and the heater binding. The mass of the sample was not large enough to permit one to neglect the mass of the heater and binding in the calculation.

The different runs are indicated by different symbols. Even though none of the runs covers the entire temp. interval (due to the length of time needed for one individual run), the points of the individual runs agree fairly well and exhibit the behavior that could be expected from the assumption of an antiferromagnetic phase above about 55°C, which temperature corresponds to the magnetically measured Curie temperature above.

It appears that there is a small additional
relative maximum between 80 and 90°C; but the scatter-
ing of the data in this temperature range is rather
wide to say anything definitely. However, the steep
rise of the curve at temperatures higher than 90°C is
very pronounced and seems to be clear evidence of the
existence of a second magnetic phase in addition to the
low-temp. ferromagnetic phase.

Electric Resistivity Measurements

After having obtained some confirmation that an
antiferromagnetic phase might really exist, an attempt
was made to determine the Neel temperature of the
substance. For this, it was decided to use the electric
resistivity as a probe.

One can assume that the total resistivity of the
sample consists of three contributions

$$\rho(T) = \rho_o + \rho_{ph}(T) + \rho_s(T) ,$$

where ρ_o is the residual resistivity due to impurities,
$\rho_{ph}(T)$ is due to electron-phonon scattering, and $\rho_s(T)$ is
due to the electron-spin interaction. According to van
Peski-Tinbergen and Dekker,[4] the spin-disorder resistiv-
ity for paramagnetic substances is temperature independent.
Therefore, a plot of the total resistivity versus
temperature should exhibit a sharp change in slope near

the Neel temperature, since in the magnetically ordered state, the resistivity is temperature dependent and roughly proportional to T^2. Beyond the Neel temperature, the only contribution is the electron-phonon interaction which is about linear with the temperature. Fig. 4 shows an example taken from pure terbium.[5] Thus, even though our substance is a compound of a rare earth with iron, it is believed that the electric resistivity provides a tool for determining its Neel temperature.

The experimental procedure for this part of the study consisted in measuring the potential drop between two points on the surface of the sample with a constant current flowing through it. This was achieved by using the circuit shown in Fig. 5: the circuit current is determined by the resistance R, which is much larger than the sample resistance in series with it. Thus small variations of R_s do not affect the current and hence the potential drop. Potential drop and sample temperature were then simultaneously recorded by means of an X-Y recorder.

The results of one of the first runs are shown in Fig. 6. Even though to be considered preliminary, the shape of the curve agrees with the resistivity curve for the pure rare earth metal Tb shown in Fig. 4. The curve still contains a second, thus far unknown contribution, resulting in a small drift of the zero line. Therefore the decrease of the curve beyond the levelling off point is not real; instead, a small linear increase has to be assumed. It is hoped that by the

time of the conference a better curve will be available, from which also the exact value of the Néel temperature can be read. From the present measurements, a Néel temperature of about 300°C is inferred.

Summary and Conclusions

Both the specific heat and the electric resistivity measurements seem to indicate that the ferromagnetic phase in the RFe_7 compounds is followed by an antiferromagnetic phase, which in the case of $NdFe_7$ has a Néel temperature of slightly above 300°C.

Recent magnetic measurements of the Dayton group[6] with other compounds of the same type gave additional hints for the existence of Neel points in all these compounds (by exhibiting a second peak of the permeability curve), in agreement with our specific heat and resistivity studies.

Acknowledgments

References

(1) A.E. Ray, Strnat, K., Feldmann, D., "Proc. Third Rare Earth Conference," Gordon & Breach, 1964, 443.

(2) H. Weik, Fischer, P., Halg, W., Stoll, E., Rare Earth Research III, Gordon & Breach, 1964, 19.

(3) M. Griffel, Skochdopole, R.E., Spedding, F.H., J. Chem. Phys. 23, 2258 (1955).

(4) T. van Peski-Tinbergen, Dekker, A.J., Physica 29, 917 (1963).

(5) R.V. Colvin, Legvold, S.Spedding, F.H., Phys.Rev. 120, 741 (1960).

(6) G. Hoffer, Ray, A.E., Strnat, K., Paper No.11.6, Intern. Conf. on Magnetics, April 1966, Stuttgart, Germany.
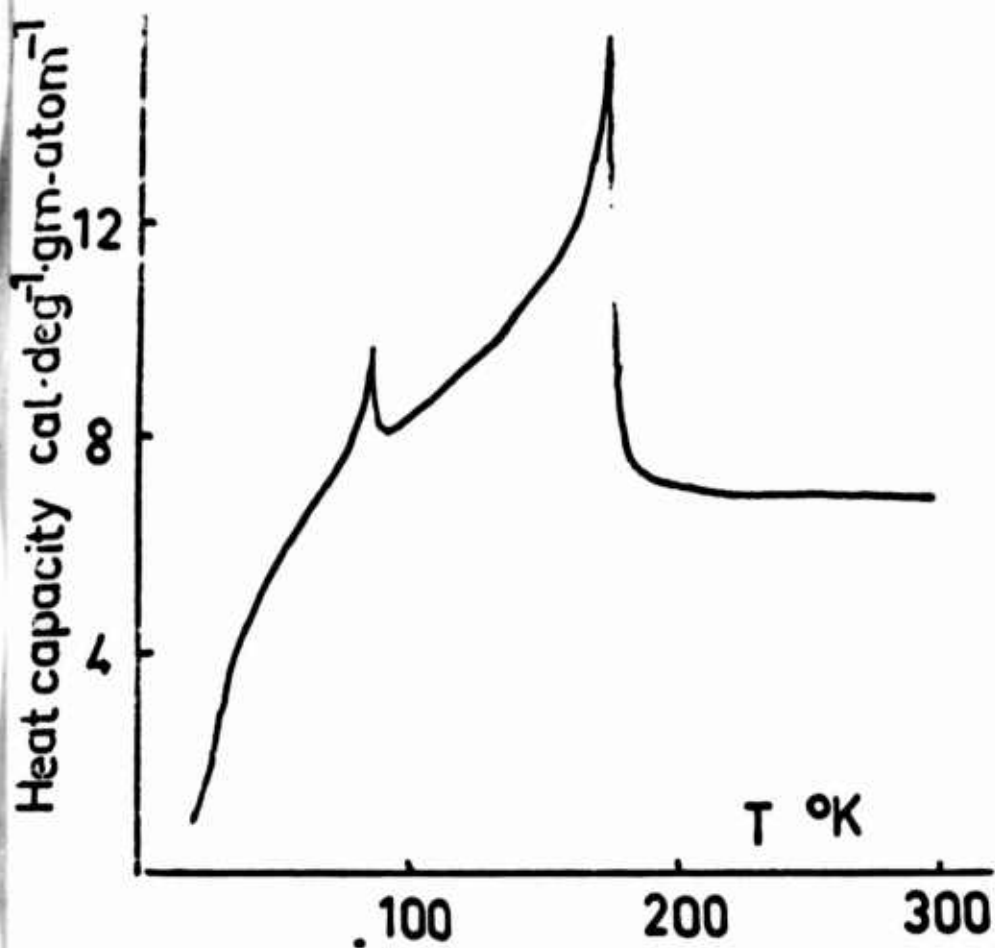
FIG. 1

Heat capacity
of Dy

FIG. 4

ς vs. T
for Tb

GROUND GLASS JOINT

METAL-TO-GLASS SEAL

TO VACUUM PUMP

THERMISTOR PROBE
.013 CM. DIA. COPPER
ND-FE$_7$ SAMPLE
THERMISTOR
HEATING COIL
.025 CM. DIA.
CONSTANTAN

SAMPLE ASSEMBLY

FIGURE 2

SPECIFIC HEAT (CALXGM)$^{-1}$(°C)

TEMPERATURE (°C)

SPECIFIC HEAT OF ND·FE$_7$
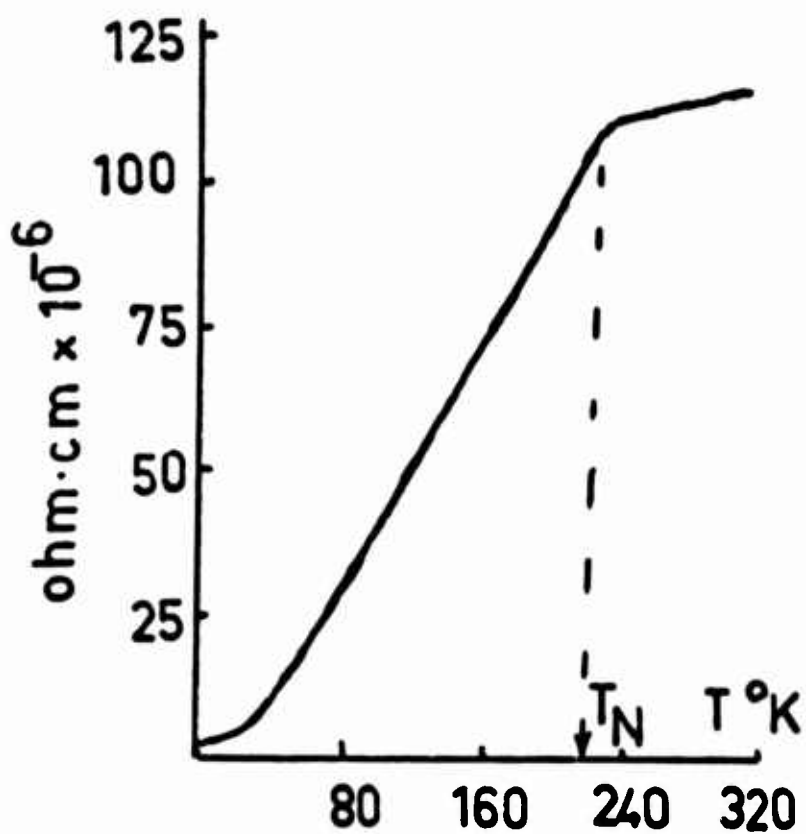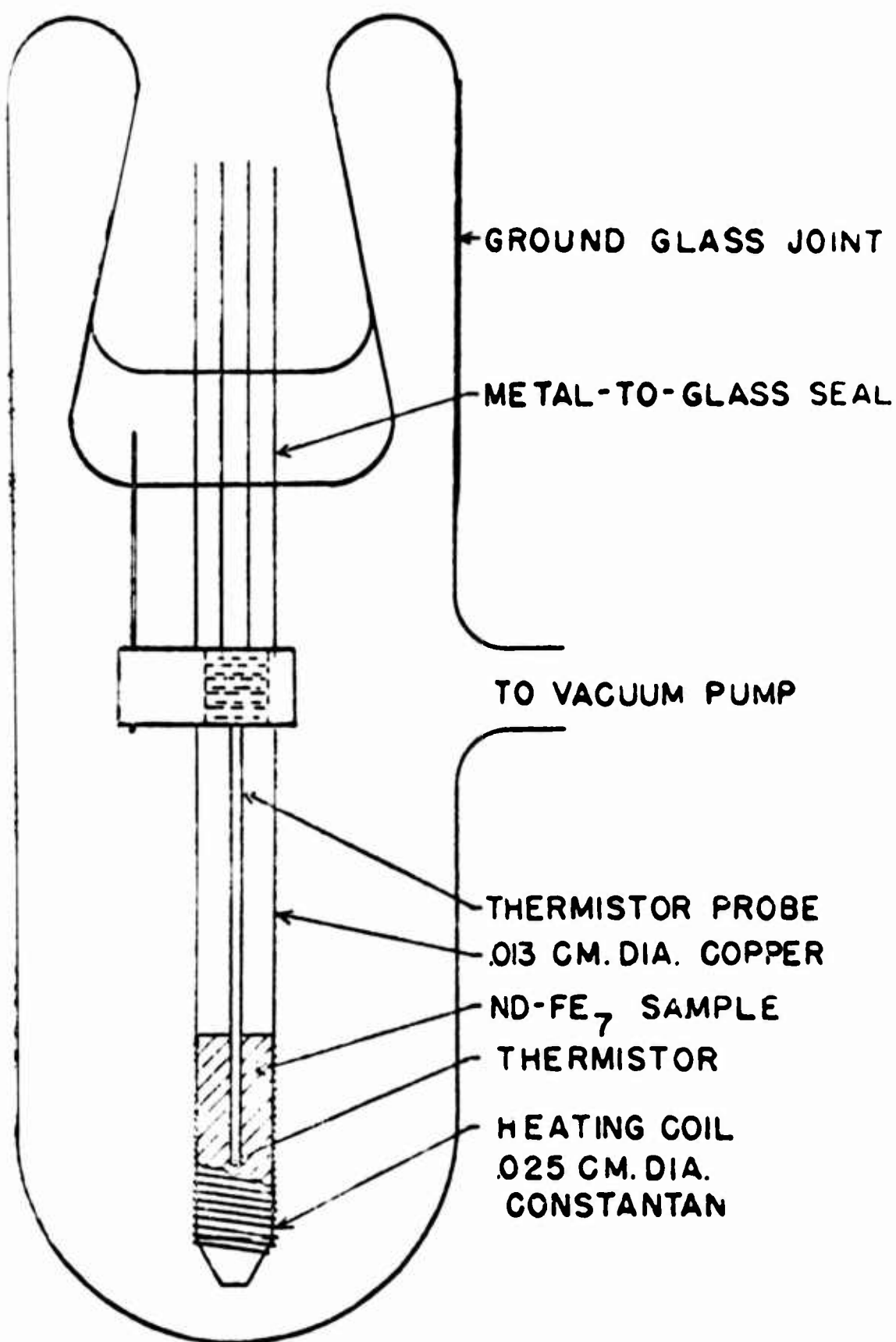
FIGURE 3
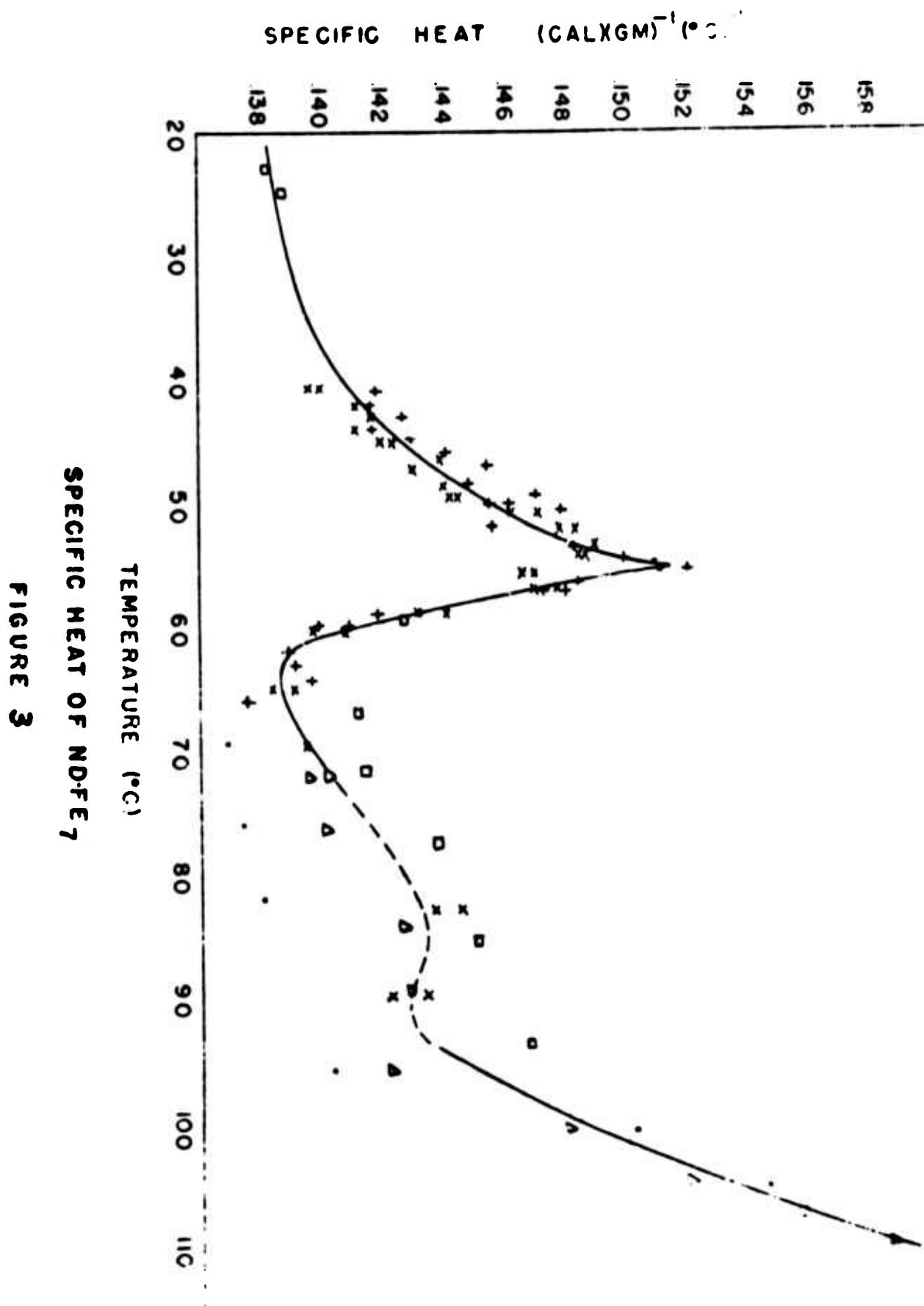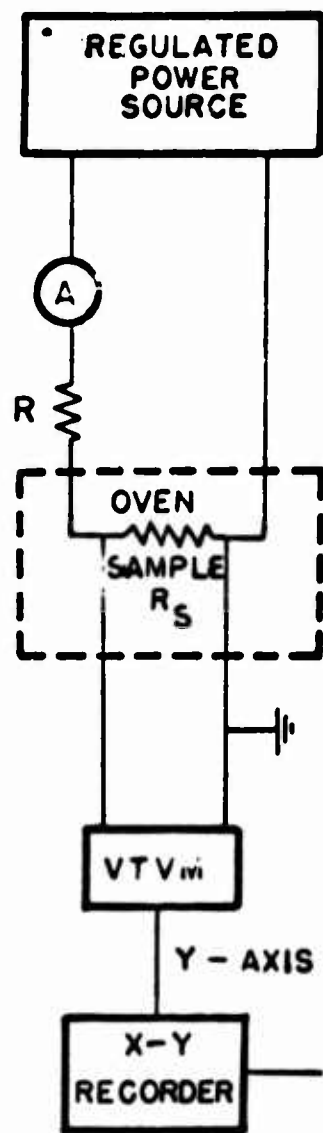
FIG. 5

Circuit for resistivity measurements
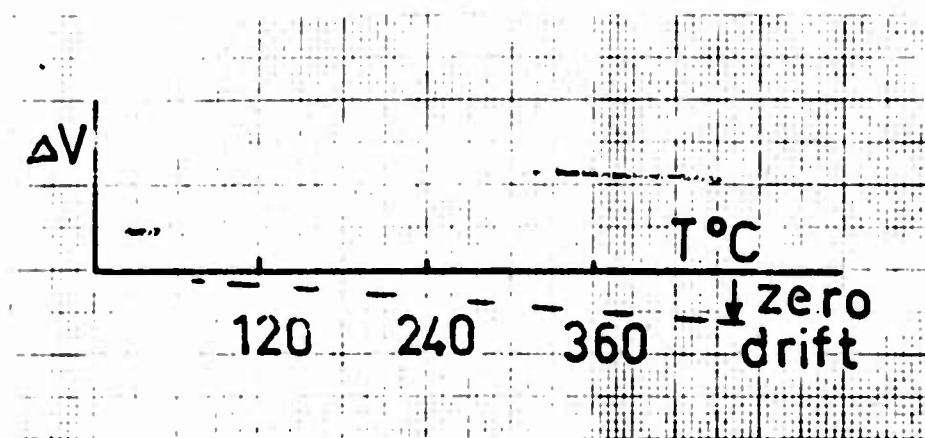
FIG. 6

ΔV vs. T

ANALYSES OF LOW-TEMPERATURE HEAT CAPACITIES OF
THE RARE-EARTH METALS

by J. A. Morrison and D. M. T. Newsham,

Division of Pure Chemistry,

National Research Council of Canada, Ottawa, Canada

ABSTRACT

Low-temperature heat-capacity data for the rare-earth metals have been reanalysed and somewhat different results have been obtained for individual contributions to the total heat capacity of several of the metals. Since the proportions of the different contributions vary from metal to metal, and with temperature, we stress the advantages of a graphical analysis as opposed to a standardised (computer) analysis such as that adopted by Lounasmaa et al. For each metal considered, the analysis gives the coefficient of the electronic contribution, and the coefficient of the leading term in the series expansion for the nuclear-hyperfine contribution, to an accuracy comparable to that of the experiments (a few percent at worst). For Yb and Lu, estimates of the lattice contributions have been obtained. For only four of the metals (Pr, Nd, Eu and Tm) is the magnitude of the magnetic contribution to the heat capacity large enough for its form to be determined. For these metals, the magnetic heat capacity seems to have an exponential temperature dependence.

I. INTRODUCTION

Extensive heat-capacity data for nearly all of the rare-earth metals have been obtained by Lounasmaa and colleagues[1-10] with an accuracy of about 1% in the temperature range $0.4 < T < 4°K$. We have reexamined the analyses of these data made by Lounasmaa et al. and derive somewhat different results for individual contributions to the total heat capacities of several of the metals.

For most of the rare-earth metals, there are at least four contributions to the low-temperature heat capacity. The general forms of three of them (the lattice [11], C_l, electronic[12], C_e, and nuclear-hyperfine[13], C_h) are well known:

$$C_l = aT^3 + bT^5 + cT^7 + \dots, \qquad (1)$$

$$C_e = \gamma T + \text{higher terms} \qquad (2)$$

and, at sufficiently high temperatures,

$$C_h = A/T^2 + B/T^3 + C/T^4 + \dots \quad . \qquad (3)$$

The higher terms in Eq. (2) are almost certainly negligible. Much less information is available for the fourth (i.e. magnetic, C_m) contribution to the heat capacity. Simple spin-wave theory[14] gives

$$C_m = KT^n \qquad (4)$$

where K is a constant and $n = 3/2$ for ferromagnetic and $n = 3$ for antiferromagnetic ordering. Detailed model calculations[15,16] give expressions of the form

$$C_m = f(T) \exp - (\Delta/kT), \qquad (5)$$

where Δ is an energy gap in the spin-wave spectrum arising from magnetic anisotropy.

In this contribution, we attempt to answer the following questions: given a set of experimental heat-capacity data of well-defined accuracy, (i) what can be deduced unambiguously from them? (ii) what is the best analytical procedure? (iii) what can be concluded about the general form of C_m?

II GENERAL STRATEGY OF ANALYSIS

Before attempting to analyse the heat-capacity data
in detail, it is in order to make a few general comments.
For the lattice and nuclear contributions, we must bear in
mind that Eq. (1) and (3) are not of closed form; they are
series that are convergent over limited temperature ranges
and it is not correct to truncate them arbitrarily. Their
usefulness is that they are results of general theory and,
as such, should be allowed to guide the analysis. They
should not be considered as a source of self-compensating
(adjustable) parameters for, say, a least-squares fit of the
data. The success of the analysis is not determined by how
well we can fit the experimental points with a single
equation but rather by the information that can be extracted
from the data, bearing in mind the probable accuracy of the
experiments. This information should be consistent with that
which can be deduced from other types of experiment. Since
the proportions of the different contributions to the heat
capacity vary from metal to metal, the standard (computer)
analysis applied to all of the metals by Lounasmaa et al.
has some severe disadvantages. Only in the simpler
examples (see next section) does it yield the correct
results.

III ANALYSIS OF THE DATA

A. Separation of electronic and lattice contributions.
   Ytterbium and Lutetium.

Lounasmaa[5,7] has measured the heat capacity of
ytterbium and lutetium between 0.4 and 4°K and, in
separate experiments[10], between 3 and 25°K for ytterbium.
Apart from small anomalies in each metal at the very lowest

temperatures, that have been fully discussed by Lounasmaa, there are only lattice and electronic contributions to C_p. We have analysed the data below 4°K, according to Eq. (1) and (2) by plotting C_p/T against T^2. In general, we would expect such plots to be curves with $\underset{T^2 \to 0}{Lt} \; C_p/T = \gamma$, the first derivative at $T^2 = 0$ equal to a and the second derivative equal to 2b. As it turns out, these plots are linear within the accuracy of the experimental data. For Yb, we find $\gamma = 2.90 \pm 0.05$ mj.deg^{-2}mole^{-1} and a = 1.18 ± 0.02 mj.deg^{-4} mole^{-1} and for Lu, $\gamma = 11.31 \pm 0.13$ mj.deg^{-2}mole^{-1} and a = 0.22 ± 0.04 mj.deg^{-4}mole^{-1}. While these results are in excellent agreement with the findings of Lounasmaa[7], they do not mean that the coefficients b,c ... of Eq. (1) are zero. Indeed, if we analyse the data for Yb over the temperature range 0.4-25°K, the effect of the higher order terms be omes quite apparent. We can see this in a plot of $(C_p - \gamma T)/T^3$ against T^2, as is shown in Fig. 1. The low-temperature

expansion for the lattice contribution appears to be valid up to about 5°K ($\sim\theta/25$). The smooth curve has been drawn taking due account of the probable accuracies of the points as indicated by the error bars. From the intercept, limiting slope and curvature at $T^2 = 0$ we find the following values for the coefficients in Eq. (1):

$$a = 1.162 \pm 0.01 \text{ mj.mole}^{-1}\text{deg}^{-4}$$
$$b = 1.5 \pm 0.5 \times 10^{-3} \text{ mj.mole}^{-1}\text{deg}^{-6}$$
$$c = 4 \pm 2 \times 10^{-5} \text{ mj.mole}^{-1}\text{deg}^{-8}$$

B. Separation of electronic and nuclear contributions.
Praseodymium, Samarium, Terbium, Holmium and Thulium.

The lattice and magnetic contributions to the heat capacity depend on positive powers of T (Eq. 1, 4, 5) although, as we have noted, there is some uncertainty as to the precise form of C_m. They tend to be small compared to the other contributions at very low temperatures where, for the metals praseodymium, samarium, terbium, holmium and thulium, the nuclear and electronic contributions predominate (i.e. they account for more than 90% of the total heat capacity). This means that the nuclear-electronic separation is best made by analysing data obtained at the lowest temperatures. We have made a separation of C_h and C_e for the above metals by making plots of $C_p T^2$ against T^3 from which we obtained A and γ from the intercept and limiting slope at $T^3 = 0$ respectively. A refined value for γ was then obtained from the intercept at $T^{-4} = 0$ of a plot of $(C_p - A/T^2)/T$ against T^{-4}. The limiting slope of this graph at $T^{-4} = 0$ gave B. Such a plot for thulium metal is shown in Fig. 2.

We interpret the rapid increase in the quantity $(C_p - A/T^2)/T$ as being due to the appearance of lattice and magnetic contributions in the region $T > 0.8°K$. The decrease of $(C_p - A/T^2)/T$ below the value of the intercept for higher values of T^{-4} undoubtedly results from contributions from higher terms in the expansion for C_h (Eq. 3)(we find $B = 0$ in this case). Similar plots were made for Pr, Sm, Tb and Ho, and all of the derived values for A, B and γ are given in Table I.
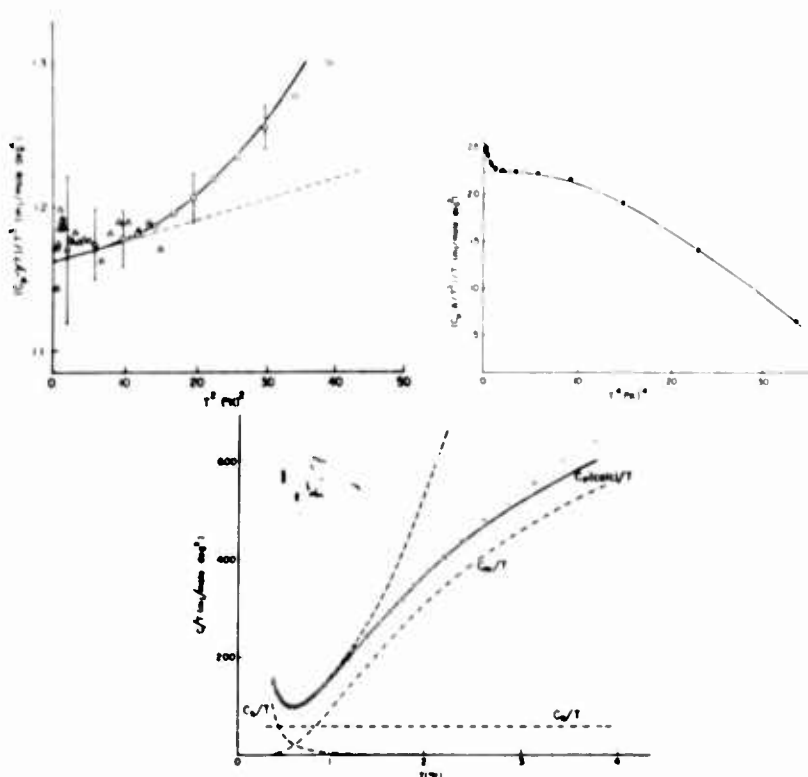
C. Magnetic contributions. Praseodymium, Neodymium, Europium and Thulium.

The analysis of data for higher temperatures presents greater difficulties for several reasons. The exact forms of the vibrational frequency distributions of the rare-earth metals are not known so that C_l may not be computed separately. Moreover, in the region where Eq. (1) is valid,

C_1 tends to be a minor component of the total heat capacity. On top of this, the general form of C_m is not known <u>a priori</u>. Nevertheless, for four of the rare earths (Pr, Nd, Eu and Tm), the lattice contributions to the heat capacity are very small in the region $0.4 < T < 4°K$ (in particular, not more than about 10, 2, 5 and 6% respectively). We can therefore estimate them with sufficient accuracy (For example, the characteristic temperatures probably lie in the range 100° to 200°K[7].)

For Nd, the lattice contribution is so small relatively that it can be neglected. For this metal, preliminary estimates of A and γ were obtained from the intercept and limiting slope of a plot of $C_p T^2$ against T^3 for $T < 0.8°K$. As a first approximation to C_m we took the quantity $(C_p - \gamma T - A/T^2)$. From the data between 1 and 4°K we found the best form for C_m by trial and error. This turned out to be

$$C_m = KT \exp(-\Delta/kT).$$

The data below 1°K were then corrected for the small magnetic contributions and refined values of γ and A were determined from plots of $(C_p - C_m)/T$ against T^3 and $(C_p - \gamma T - C_m)T^2$ against $1/T$. From the slope of the second of these plots we deduced the coefficient B. The refined values for γ, A and B were used to redetermine C_m and the procedure was repeated until consistent results were obtained; two iterations were sufficient. Somewhat similar analyses were made for Eu, Pr and Tm. The coefficients A, B and γ are given in Table I and the approximate forms which we have derived for C_m are given in Table II.

IV. RESULTS AND DISCUSSION

In Table I, we compare the values of A derived from the calorimetric data with those derived from other types of experiment (electron spin resonance and electron-nuclear double resonance on salts, and atomic beam measurements on free atoms) by Bleaney[13]. Table I also includes our estimates of B and γ, and the values for A, B and γ derived by Lounasmaa and colleagues. Agreement between the results of the different analyses is only achieved for the simpler examples (e.g. γ for Lu and Yb, or A for Sm and Dy). Except for the example of Pr, the magnitudes of A given in columns 2 and 3 of Table I are the same. The exception has been discussed by Bleaney[13].

In Table II we give the approximate forms that we have derived for the magnetic contributions to the heat capacities of Pr, Nd, Eu and Tm. The most striking feature of Table II is the constancy of the parameter Δ/k appearing in the exponent of Eq. (5). The pre-exponential terms in Nd and Eu depend on the first power of T within rather close limits. Pre-exponential terms in $T^{1/2}$ and $T^{3/2}$ are quite unacceptable. For Pr and Tm, however, we cannot definitely rule out pre-exponential factors in which the power of T differs by $\pm 1/2$ from that given in Table II. This is partly because of the uncertainties in making corrections for the lattice contributions and partly because of the much smaller magnetic contributions in these metals. At 4°K, the contribution of C_m to C_p is $\sim 60\%$ for Tm and $\sim 50\%$ for Pr compared with $\sim 90\%$ for both Nd and Eu. In Pr, there is a broad anomaly in C_p in the temperature region $2.5 < T < 4°K$.

The equation given in Table II for the magnetic heat capacity of Pr is intended to apply only in the region $T < 2.5°K$.

V. SUMMARY

We can now answer briefly the questions posed in the introduction. (i) Analysis of the low-temperature heat capacity data yields numerical values of A and γ of Eq. (2) and (3) to an accuracy comparable to that of the experiments (to a few percent at worst). The other coefficients in Eq. (3) are obtained either with poor accuracy or not at all. (ii) Because of the large variations from metal to metal, graphical analysis turns out to have many advantages. This is almost self-evident from an inspection of the variation with temperature of the different contributions to the total heat capacity of neodymium (see Fig. 3).

(iii) For four of the rare earth metals, C_m clearly seems
to have an exponential temperature dependence. Nothing cer-
tain can be deduced about the form of C_m for the other
metals.

All of the foregoing is not without controversy as
the following quotations[17] indicate: "Finally, a warning
might be in order for all future attempts to fit C_M
contributions in the rare earths by terms of the form
$T^n \exp(-Eg/kT)$. ----. If one allows himself the latitude
of adjusting C_E at will, then it is not too difficult to
make an exponential fit for some C_M so created." We leave
it to the reader to assess how much adjustment at will has
been made.

REFERENCES

1. O.V. Lounasmaa, Phys. Rev. 126, 1352 (1962).

2. O.V. Lounasmaa and R.A. Guenther, Phys. Rev. 126, 1357 (1962).

3. O.V. Lounasmaa and P.R. Roach, Phys. Rev. 128, 622 (1962).

4. O.V. Lounasmaa, Phys. Rev. 128, 1136 (1962).

5. O.V. Lounasmaa, Phys. Rev. 129, 2460 (1963).

6. O.V. Lounasmaa, Phys. Rev. 133, A211 (1964).

7. O.V. Lounasmaa, Phys. Rev. 133, A219 (1964).

8. O.V. Lounasmaa, Phys. Rev. 133, A502 (1964).

9. O.V. Lounasmaa, Phys. Rev. 134, A1620 (1964).

10. O. V. Lounasmaa, Phys. Rev. 143, 399 (1966).

11. T.H.K. Barron and J. A. Morrison, Can. J. Phys. 35, 799 (1957).

12. E.C. Stoner, Phil. Mag. 21, 145 (1963).

13. B. Bleaney, J. Appl. Phys. 34, 1024 (1963).

14. J. Van. Kranendonk and J.H. Van Vleck, Rev. Mod. Phys. 30, 1 (1958).

15. B.R. Cooper, Proc. Phys. Soc. 80, 1225 (1962).

16. A.R. Mackintosh, Phys. Letters 4, 140 (1963).

17. C. W. Dempesy, J. E. Gordon and T. Soller, Ann. Acad. Sci. Fenn. A. VI. 210, 204 (1966).

18. B. Bleaney and R. W. Hill, Proc. Phys. Soc. 78, 313 (1961)

19. M. Kalvius, P. Kienle, H. Eicher, W. Wiedemann and C. Schüler, Z. Physik 172, 231 (1963).

Table I. Coefficients of nuclear and electronic contributions to the heat capacities of the rare earth metals			
A(mj.deg.mole^{-1})		B(mj.deg^{2}mole^{-1})	γ(mj.deg.$^{-2}$mole^{-1})
from resonance expts[13]	from calorimetric data		
Pr 1064	21.0+0.4 (20.$\overline{9}$)[6]		26.6+0.2 (24.$\overline{4}$,26.1,10.5)[6]
Nd 14.3	4.7+0.2 (7)[6]	0.2+0.1	58+2 (2$\overline{2}$.5,10.5)[6]
Sm 8.90	8.56+0.1 (8.56)[1]		12.4+0.2 (12.$\overline{1}$2)[1]
Eu 4.2	2.30+0.05 (2.36)[8]	-0.03+0.03	12.1+0.5 (5.8)[8]
Tb 250[18]	223.0+1.5 (238)[3]	-1+4 ($\overline{-}$11.9)[3]	10.4+0.4 (9.0$\overline{5}$)[3]
Dy 26.6	24.9+0.5 (26.$\overline{4}$)[2]		17.9+0.4 (9.5)[2]
Ho 4220	3640+40 (445$\overline{6}$)[4]		50+2 (1$\overline{0}$)[4]
Tm 26.9 / 22.9[19]	19.6+0.3 (19.$\overline{1}$5,23.4)[9]	0+0.02 ($\overline{0}$,-1.79)[9]	22.3+0.2 (19.$\overline{2}$,17.94,10.5)[9]
Yb			2.90+0.05 (2.$\overline{9}$0)[5]
Lu			11.31+0.13 (11.2$\overline{7}$)[7]

The numerical results given in brackets are from the references indicated.

Table II. Magnetic heat capacity

$$C_m(\text{mj.deg}^{-1} \text{ mole}^{-1})$$

Pr	$41T^{3/2}\exp(-2.84/T)$
Nd	$1030T\ \exp(-2.44/T)$
Eu	$275T\ \exp(-2.51/T)$
Tm	$10T^{5/2}\exp(-3.0/T)$

THE OPTICAL AND ELECTRICAL PROPERTIES

OF YTTERBIUM THIN FILMS*

by

Ogba A. Okorie**
Southern University
Physics Department
Baton Rouge, Louisiana

and

Sohan Singh
Howard University
Physics Department
Washington, D. C.

Abstract

In addition to reflectance and transmittance, the thickness and the resistivity of Yb thin films deposited by vacuum evaporation were measured in the spectral region 0.5 to 6.8 microns. From these data, the refractive index n, the extinction coefficient k, the absorption coefficient $\mathcal{l}$, the carrier density and the types of carriers as well as their relaxation time were calculated. Drude theory applied well between 1 to 3.5 microns. Hagen-Ruben's relation also applied at intervals. The infinite wavelength index of refraction is 10.9 while the indirect transition is 1.8 ev. The mean free path of the carriers is 236A, the carrier velocity is 3.17×10^7 cm/sec, and the relaxation time is 7.45×10^{-14} sec. Empirically, the reflectance and the transmittance are related by an expression of the form $R = Ae^{-BT}$. Similar expression was determined for the reflectance and the wavelength.

Introduction

This study is an attempt to accumulate some useful data for the determination of the electrical and optical properties of some vacuum evaporated rare-earth thin films. The optical constants data may provide information on the band structure of the metals. Most of the work covers the spectral region 0.5 to 6.8 microns in the infrared spectrum. It is mainly between 10 microns and 0.01 microns that the classical concepts of the two optical constants, the refractive index n and the extinction coefficient k, apply best. In the region between 1 micron and 10 microns the simple theory of Drude is able to predict these constants, at least the extinction coefficient quantitatively. The predicted refractive index is generally small.

For most metals pronounced deviations from the Drude theory are observed mainly in the region shorter than 1 micron. These are due to the effect of the interband electronic transitions between the occupied bands and the higher empty bands. This volume effect is neglected in the classical theory of Drude.

It is the purpose here, to use the experimental data to test how well the classical Drude-Zener theory (and some of the simpler related theories) of free carriers may apply to the films studied. The least complicated and yet moderately accurate methods of determining the constants have been employed.

Experimental

The samples were prepared as thin films by evaporation of the bulk metal ytterbium 99.99% in a vacuum of the order of 5×10^{-5} mm Hg from a tantalum boat onto quartz glass slides. One of the main difficulties of depositing rare earth metals is that the metal pieces jump off the boat before deposition is completed. Therefore appropriate boat which can hold the source material in place during evaporation must be had. The open dimple-type of boats may not be useful. Cleaning of the substrate and the metals was carefully carried out, though a further cleaning was done by baking out the system including the mounted substrates. The experimental conditions were reliably controlled by keeping the cold-trap filled with liquid nitrogen, though the pressure generally rose slightly during the evaporation.

X-ray diffraction analysis of each series of films was continuously carried out to check whether or not the films oxidized during the study.

A Perkin-Elmer infrared spectrometer with an added reflectometer arm was used for the measurements. The film thickness was measured by interferometric method. The electrical resistivity was measured by four point probe method.[1,2]

The sign of the carriers was measured by thermal probe method. The absorption coefficient χ was calculated from the simple formula

$$\chi = \frac{1}{d} \ln \left(\frac{I_0}{I} \right)$$

where Io and I are the intensities of the light through the uncoated quartz substrate and a coated substrate respectively, d is the film thickness, and λ is the wavelength of the incident radiation in vacuum. The extinction coefficient was determined from the equation

$$k = \frac{\chi \lambda}{4\pi}$$

With k and R known, the values of n can be obtained from the numerical evaluation of $n = \dfrac{1-R}{1+R-2\sqrt{R}\cos\theta}$, $k = \dfrac{-2\sqrt{R}\sin\theta}{1+R-2\sqrt{R}\cos\theta}$

The theoretical reflectivity formula for normal incidence which is

$$R = \frac{(n-1)^2 + k^2}{(n+1)^2 + k^2}$$

was fully obeyed.

By graphical analysis of R and T, it is found that R and T are related by the expression

$$\ln R = 0.103 - 2.348T$$

or

$$R = \exp(-0.103 - 2.348T)$$

which is of the form

$$\log R = a + bT$$

in the spectral interval 0.7 micron to 2.5 microns.

The examination of the n,k data indicates that should remain constant at long wavelengths. By assuming that the lattice vibrational bands are not sufficiently strong to affect the dielectric constant appreciably, a straight line may be fitted to the long wavelength portion of the curve of n^2-k^2 versus λ^2. The infinite wavelength index of refraction obtained[3] from the intercept is 10.9.

The measured resistivity values are listed in Table 2. These values are higher than the published [4,5] resistivity of ytterbium by a factor of 2 to 3.

If it is assumed, as usual, that impurities added to a metal will increase the resistivity, our large values of resistivity may be attributed to contamination and possibility structural defects.

The study reveals that the electrical properties are those of degenerate semiconductor with holes as the majority carrier, and with very low mobility.

Graphical presentations of the transmittance T, reflectance R and the absorption coefficient $\mathcal{N}$ are given in Figures 1, 2, and 5 respectively.

The shapes of the R, and T curves are similar to those generally observed for most metals.

From the values of n and k we can calculate the real and imaginary parts of the dielectric constant.

Much work is generally devoted to the determination of $n^2 - k^2$ and 2nk since these quantities are of funamental significance in the study of the structure of matter. We have also computed the dielectric constant from

$$\epsilon = 1 - \frac{4\pi Z e^2}{m \omega^2}$$

The result is linear to λ^2 as expected from theory.

One of the ways of showing the existance of an absorption band in the infrared consists, after having computed n and k to draw the curve representative of

For quasi-free electron this should be a straight line. Theory and experiment agreed only in the range of 1 micron to 3 microns.

The square root of the absorption coefficient plotted against the incid t photon energy was extrapolated to obtain an absorption edge value of 1.83 ev.

The fundamental lattice dispersion frequency, was obtained from the plot $2nk\omega$ against frequency or wavelength. From the peak of the plot, ω_0 was determined, since $2nk\omega$ shows its maximum value at $\omega=\omega_0$

The plot of $\epsilon_1 = 1-n^2+k^2$ and $\epsilon_2 = n^2-k^2$ shows the range of frequency to which each of them contributes to the dielectric constant and where the effect of the other can be neglected.

In the solution of the equations of the motions of electrons that are subject to a periodic electric field, the damping constant is generally one of the significant quantities involved. This quantity has been calculated, following the method of Milton Gottlieb,[6] from the width of the imaginary dielectric constant curve at half-maximum. i.e.

$$\frac{\gamma}{\omega_0} = \frac{\omega_{\frac{1}{2}}^{+} - \omega_{\frac{1}{2}}^{-}}{\omega_0}$$

or $\frac{nk}{\lambda}$ plotted against λ .

Where $\omega_{\frac{1}{2}}^{+}$ and $\omega_{\frac{1}{2}}^{-}$ are the frequencies at half maximum on the high and low frequency sides; and where ω_0 is the fundamental transverse optical frequency obtained from the plot of $2nk\omega$ versus ω .

The results are $\omega_0 = 6.08 \times 10^{14}\, sec^{-1}$

and $\gamma = 0.161 \omega_0 = 0.98 \times 10^{14}\, sec^{-1}$

so γ is about 16% of ω_0.

An attempt has been made to check plasma oscillations in the films studied.

TABLE 1

$\lambda(A^o)$	R	T	n	k	α (cm-1)
0.5	0.150	0.722	2.2544	0.1334	2.33×10^4
0.7	0.155	0.714	2.2883	0.1385	2.41×10^4
0.9	0.170	0.689	2.3849	0.1893	2.66
1.0	.190	0.656	2.5175	0.2435	3.011
1.05	.200	0.640	2.5839	0.2740	3.188
1.1	.330	0.449	3.6263	0.4969	5.719
1.2	.42	0.336	4.5492	0.7617	7.79
1.4	.49	0.260	5.4587	1.0481	9.62
1.8	.505	0.245	5.5816	1.4275	10.05
2.00	.600	0.160	7.2514	2.1044	13.09
2.50	.650	0.122	8.1956	3.0174	15.03
3.10	.695	0.093	9.0541	4.2021	16.97
3.60	.700	0.090	8.3575	4.8857	17.20
4.00	.705	0.087	6.9997	5.5602	17.44
5.00	.710	0.084	5.9107	5.8111	17.69
6.00	.715	0.081	6.0877	5.9334	17.95×10^4 (cm-1)

TABLE 2

	Film Thickness d (A^o)	Resistivity ohm-cm ρ (ohm-cm	Type of Carrier
(1)	400	66×10^{-6}	Positive
(2)	500	49×10^{-6}	Positive
(3)	1400	86×10^{-6}	Positive
(4)	1500	61×10^{-6}	Positive
(5)	2000	61×10^{-6}	Positive

The average resistivity for the film is 68.5×10^{-6} (ohm-cm) corresponding to average conductivity of 1.459×10^4 mho cm^{-1} or (1.313×10^{16}/sec. in esu).

From the theory [6,7] of plasma oscillations, it is shown that when the plot of

$$\frac{2nk}{(n^2 + k^2 + 1)^2 + 4n^2k^2)}$$

versus photon energy in electron volts has a peak, tangential plasma oscillation exists; and then when

$$\frac{2nk}{(n^2 + k^2)^2}$$

has a peak, normal plasma oscillation exists. The energy values corresponding to the peak will be the plasma energy.

The results of these plots indicate plasma energy at 0.25 ev, 0.69 ev; 1.18 ev for tangential case; 1.05 ev; 1.8 ev for the normal case.

Anomalous skin effect was also investigated. The plots look rather reasonable in comparison to those published for silver and copper.

One of the quantities used frequently is the relaxation time τ, the complex relationship of energy and optical as well as electrical parameters. The relaxation time has been calculated and its dependence is shown graphically. The relaxation time has been calculated from the optical constants according to the formula:

$$\tau = \left(\frac{1 - n^2 + k^2}{2nk\omega}\right) \qquad \text{or} \qquad \tau = \left(\frac{1 - n^2 + k^2}{4\pi nkc}\right)\lambda$$
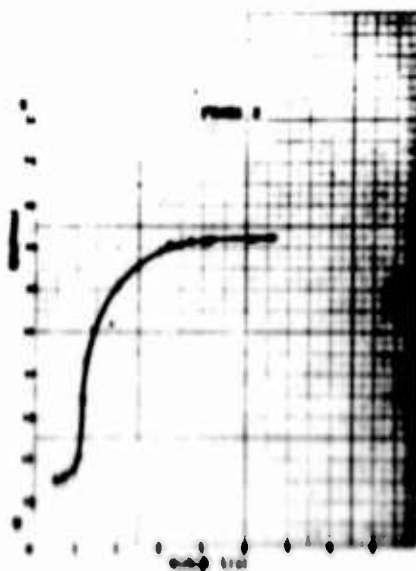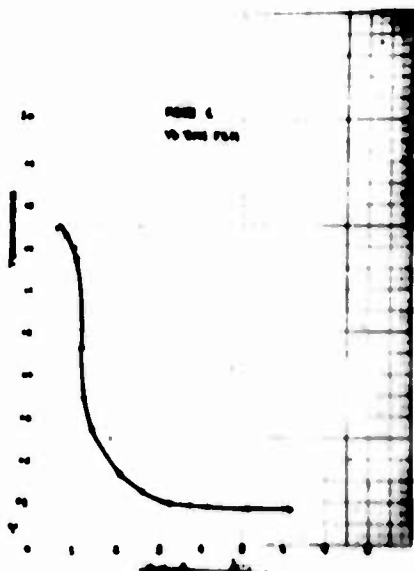
It can be observed from the graph that the relaxation time is linearly related to the wavelength only in the interval 0.5 microns to 3.6 microns. This can be understood if we assume that there are more than one type of carriers, though a particular carrier type may be predominant in some specific spectral range.

The experimental data indicate the majority carriers to be positive. The contribution of the conduction electrons to the absorption is about 9%. This is obtained from the formula [8-11]

$$A_{el} = \frac{1}{\sigma_c} \left(\frac{Ze^2}{\pi m} \right)^{\frac{1}{2}}$$

where σ_c = d.c. conductivity of the specimen (here
σ_c = 1.313 x 10^{16}/sec.),
e = electronic mass = 9.1 x 10^{-28} gm
Z = carrier density = 6.96 x 10^{20}/cm3
e = electronic charge = 4.8 x 10^{-10} esu

MEAN FREE PATH CALCULATION

The mean free path has been calculated by considering the Z carriers cm^{-3} as Fermi gas quasi-free electrons, then the resistivity

$$\rho = \frac{m v_f}{Z e^2 l} \quad ; \quad m v_f = h \left(\frac{3Z}{8\pi} \right)^{\frac{1}{3}}$$

v_f = velocity at Fermi surface.

l = mean free path

$\bar{\tau}$ = relaxation time.

From which equation we get

$$l = \frac{h}{\rho Z e^2} \left(\frac{3Z}{8\pi} \right)^{\frac{1}{3}} = \frac{\sigma h}{Z e^2} \left(\frac{3Z}{8\pi} \right)^{\frac{1}{3}}$$

The plasma oscillation angular frequency was calculated from

$$\omega_p = \left(\frac{4\pi Z e^2}{m} \right)^{\frac{1}{2}}$$

The change in optical properties of the thin films with time may be due to further agglomeration, recrystallization, chemical reaction and other structural changes.

The results of this work reveal that the rare-earth thin films of Yb, Sm and Nd increase on aging. X-ray analysis of samples of these films were carried out for days to find out if the increased transmittance could be due to oxidation. The x-ray analysis failed to reveal any oxidation of the films. Hence the transmittance variation must be due to effects other than oxidation.

The effect of prolonged x-radiation on the Yb films was qualitatively investigated. It was found that transmittance of the films increased when x-rayed for a few hours. A few hours x-irradiation produced transmittance increase equivalent to that which aging for days would produce. The shape of the T curve was also changed on x-raying the film.

The results of this study, show that very little is known about the Fermi surface of rare-earth metals. It should be possible to obtain some information about them from the optical properties of these metals.

Low temperature measurement of the dispersion of the real and imaginary parts of the complex dielectric permeability of a metal together with additional measurements of the electronic heat capacity or the paramagnetic sysceptibility will, evidently, be adequate to determine the total area of the Fermi surface and the velocity of electrons on this surface.

From this investigation one may make the following observations:

Films deposited slowly have more granular structures than rapidly deposited films; also the nature of the substrate and its temperature at the time of evaporation have considerable influence on the properties of the film.

The optical properties of the films vary strongly with thickness.

Film studies should employ methods, formulas, and techniques that take account of differences in structure, which are always possible as a result of aging or conditions of evaporation.

The studies of RE metal films may have more meaning when there has been no exposure to air.

Thin films begin to change as soon as they have been formed, even if left in the vacuum in which they had been prepared. This should provide valuable information on the influence of external factors such as residual gas in the bell-jar at the time of evaporation and gases and vapours absorbed in the film, changes in structure and other changes in the films.

The exposure of the films to the atmosphere changes the refractive index considerably.

More valuable information will be provided if accurate studies under highly controlled conditions could be done to evaluate the effect of structure , and the effects due to electronic transition and absorptions.
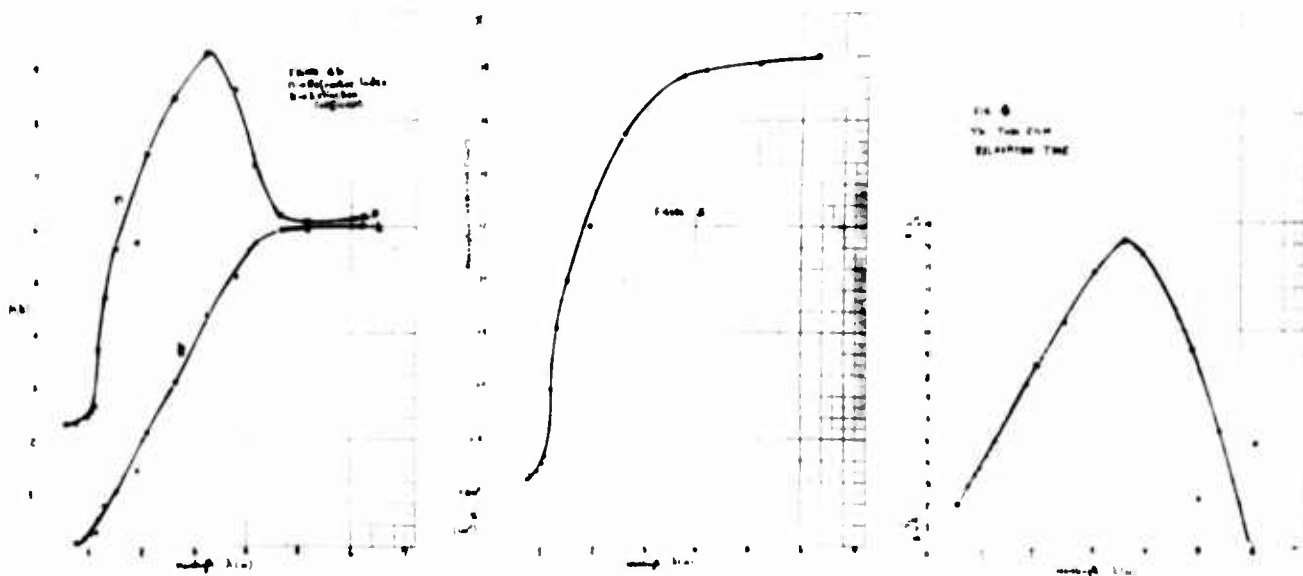
Acknowledgements

BIBLIOGRAPHY

1. Riso Kato, _Japanese_ J. _Phys_. _Soc_. 16, 2525 (1961).

2. Philips Res. Repts 19, 43-52 (1964).

3. R. E. Lindquist and A. W. Ewald, Phys. Rev. 135, A191 (1964).

4. F. H. Spedding, _Metallurgical_ _Review_, 1960, Vol. 5, No. 19, p. 297.

5. P. W. Bridgman, Proc. Amer. Acad. Arts Sc.; 1954, 83, p. 1.

6. Milton Gottlieb, J. O. Soc. _Am_. 50, 343 (1960).

7. Sasaki, T., Phys. Rev. 127, 1091, (1961).

8. M. N. Markov and A. S. Khaikin, Optics and Spectroscop 8, 253 (1960).

9. A. V. Bassewitz and G. V. Minnigerode, Zeitschrift fur Physik 181, p. 368 (1964).

10. M. Z. Kohler, Physik 125, p. 495 (1949).

11. H. Jones, Handbuch der Physik, Bd XIV S. 145ff. Berlin Gottinger-Heidelberg; Springer 1956.

12. J. Chem Soc. 10, 219, 1858; 11, p. 36 (1859).
    Prandtl and Scheiner, Z. Anorg. allgem. Chem. 220 107 (1934).

13. Vickery, _Chemistry_ _of_ _the_ _Lanthanons_, Butterworths, London, 1953.

14. _Chemistry_ _of_ _Ytterbium_ _V_. _Scandium_. Pergamon Press, London and New York, 1959.

15. F. Seitz, _The_ _Modern_ _Theory_ _of_ _Solids_, McGraw-Hill Book Company New York and London, (1940).

16. R. Weiss, _Solid_ _State_ _Physics_ _for_ _Metallurgists_, Pergamon Press, London and New York, 1963.

17. A. H. Wilson, _The_ _Theory_ _of_ _Metals_, Cambridge University Press, London and New York, 1936.

18. R. B. Dingle, _Physica_ 19, 729 (1953).

ELECTRICAL CONDUCTION AND DIELECTRIC BREAKDOWN IN THIN
EVAPORATED LAYERS OF SEVERAL RARE EARTH OXIDES

A. T. Fromhold. Jr., W. D. Foster, T. A. Hutchek, and R. B. Mosley

Department of Physics. Auburn University. Auburn. Alabama

Some electrical measurements at $300^{O}K$ are reported for
thermally-evaporated oxides 300 to 6000 $\AA$ in thickness of the
rare earth metals La. Ce. Pr. and Nd. Thin evaporated aluminum
electrodes were utilized to impress voltages in the range zero
to 80 volts across the oxide layers; electric fields as large
as 5 x 10^{6} volts/cm could be reached prior to destructive di-
electric breakdown. Low field ($E\lesssim 10^{4}$ volts/cm) current-
voltage characteristics are almost linear. High field ($E\gtrsim 10^{5}$
volts/cm) current-voltage behavior is initially quite erratic.
since the layers experience many nondestructive dielectric break-
downs. After voltage cycling. the current-voltage characteristics
tend to become stable. reproducible. and nonlinear. with current
densities ranging from one microampere/cm^{2} to one ampere/cm^{2}.
At 10^{-6} torr the initial current-voltage characteristics are less
erratic and can be stabilized by voltage cycling more readily than
those measured at ambient pressure. A reversible pressure effect
was observed in which the conductivity of the films increases
(e.g.. by a factor of 5 for neodymium oxide) as the pressure is
reduced from atmospheric to 10^{-6} torr. This indicates an oxygen
pressure-dependence of the stoichiometry and corresponding ionic
defect concentration of the oxide. Least-squares analysis using
the expressions for Schottky Emission, Frenkel-Poole Effect, and
Field-Induced Hopping ($I \propto \sinh \beta E$) indicates that the latter is
the more likely current-transport mechanism.

I. Air Measurements

The series of thermally-evaporated oxides (La, Ce, Pr, and Nd) for which measurements are herein reported have been grouped together because the thin-film electrical behavior is remarkably similar from oxide to oxide. Curves have been selected which are qualitatively typical of the entire group. Our measurements for the oxides of Gd and Er are also qualitatively the same as the measurements for the above 4 oxides. Attempts to fabricate metal-oxide-metal structures which yield both capacitance measurements and stable current-voltage characteristics for the oxides of Sm, Dy, Ho, and Yb were largely unsuccessful. Qualitatively different behavior was observed for the oxides of V, Sc, and Y, so these results will not be discussed.

Our experimental techniques are standard; the details of the evaporation procedure will be presented elsewhere. The oxides[1] had a nominal purity of 99.9%, except for lanthanum oxide, which was 99%. Oxide film thickness was measured to an accuracy of approximately 200 $\overset{o}{A}$ with a metallurgical microscope by means of the Tolansky method.[2] Dielectric constants ϵ were calculated from the capacitance, as measured with a 1000 Hz general purpose bridge, by means of the standard parallel-plate formula. The large variance in ϵ from sample to sample for films of approximately the same thickness illustrates the fact that the composition and structure of the film are affected markedly by the

evaporation conditons of source temperature. residual pressure.
evaporation pressure. and evaporation rate. This is in accordance
with the observation of Feldman and Hacskaylo[3] for CeO_2 and Yb_2O_3
films whenever the thickness is less than 10.000 Å. Huntley[4] has
also observed a large dependence of ϵ on porosity of bulk samples
of UO_2. In our measurements there was a tendency for ϵ of some
oxides to decrease with increasing thickness (e.g.. Gd). while
other oxides (e.g., Nd) showed a tendency for ϵ to increase with
increasing thickness.

The voltage necessary to produce dielectric breakdown increases
after an early series of low voltage dielectric breakdowns. Thus
the breakdown voltage depends upon the history of the capacitor
sandwich; it increases with increasing voltage-cycle number for
the oxides reported. A voltage cycle is defined herein as the
process in which the voltage across the film is increased from
zero to a value necessary for dielectric breakdown. and then de-
creased back to zero. Several breakdowns usually occur during
each voltage cycle. Each breakdown occurs over a highly localized
region. and is accompanied by the destruction of electrode material
and the emission of white light. The films usually recover their
pre-breakdown dielectric properties almost immediately after break-
down. The average value for the onset of local dielectric break-
down is initially low. but it increases to some higher value after
5 or 6 voltage cycles. After this initial series of voltage cycles,

the breakdown strength as a function of voltage cycle remains relatively constant. For example, a neodymium oxide film 955 $\overset{\circ}{A}$ in thickness had breakdown voltages above 50 volts following voltage cycling, which corresponds to breakdown fields above 5×10^6 volts/cm.

Figure 1 represents typical behavior of the current-voltage characteristics as observed for 14 samples of neodymium oxide after voltage cycling. The particular sequence of curves in the figure was measured at ambient pressure on a film 644 $\overset{\circ}{A}$ in thickness with an electrode area of 0.18 cm^2. Note that currents range up to 200 ma for voltages in the range 0 to 30 volts. Currents as large as 1100 ma were observed at atmospheric pressure for other neodymium oxide films. The voltage-cycle number is given in Fig. 1 for each current-voltage characteristic. These data at ambient pressure illustrate a tendency for the current at a given voltage to decrease with increasing voltage cycle. This behavior is believed to be due simply to the great number of dielectric breakdowns as manifested by the quite erratic behavior generally observed at ambient pressure; the large number of dielectric breakdowns simply destroys a significant area of the electrode material, thus resulting in a sample with a smaller effective area for current transport. Between unusually severe dielectric breakdown cycles, however, the characteristics are smooth, stable, and reproducible. For example, the center characteristic in Fig. 1 is virtually unchanged between cycles 8 and 15.
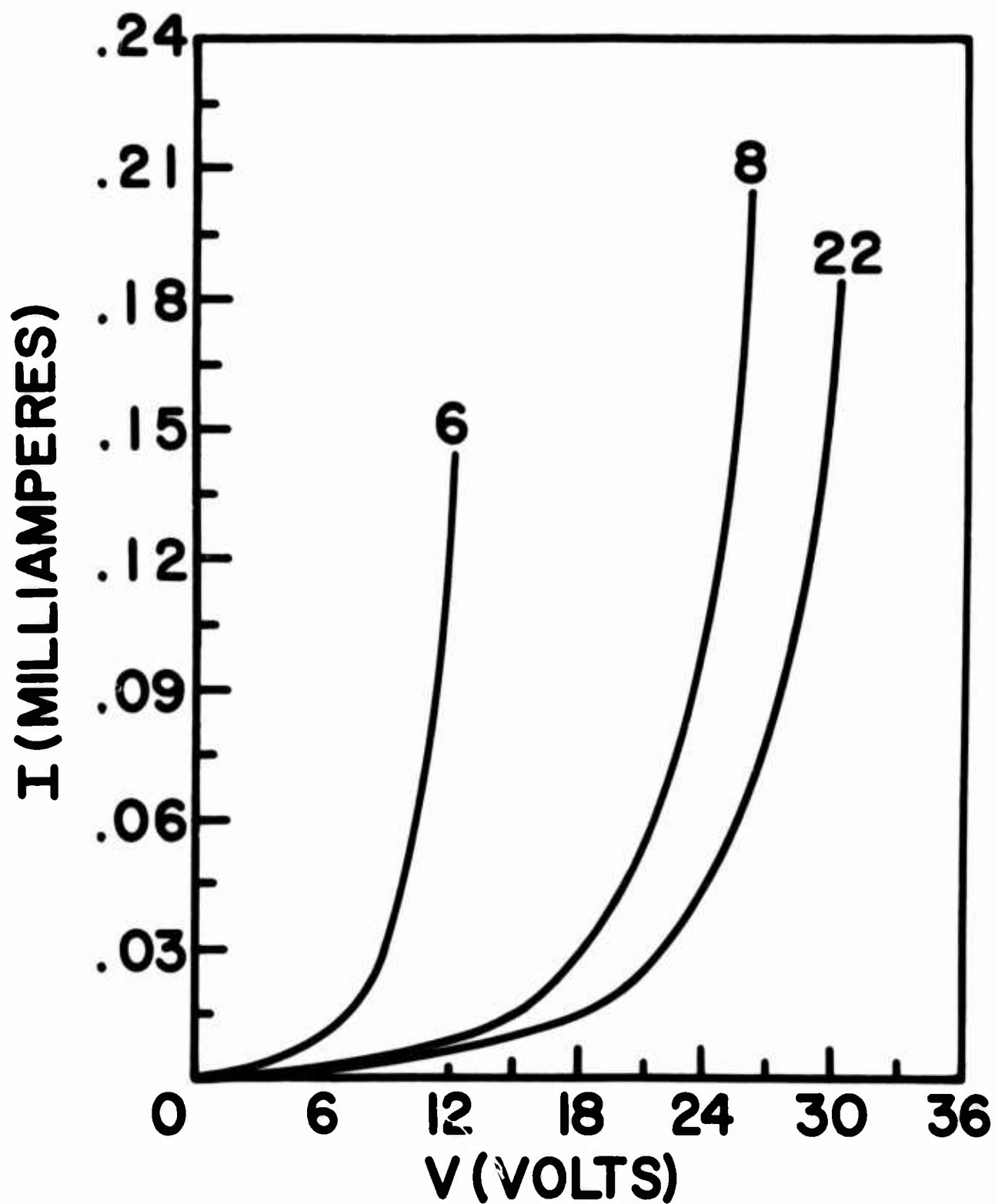
Fig. 1   Steady-state current-voltage characteristics for
neodymium oxide at atmospheric pressure.

A noteworthy feature is the characteristic shape of the curves, which remains unchanged with voltage cycling. The analytical expression and corresponding current transport mechanism providing the best least-squares fit to these curves is discussed in Section III.

Figure 2 illustrates the corresponding current-voltage characteristics for oxides of Ce, La, and Pr taken at ambient pressure. These smooth characteristics are atypical insofar as ambient pressure characteristics tend to be erratic because of the occurrence of many dielectric breakdowns. The thicknesses are 6440, 322, and 1288 $\overset{o}{A}$ for the oxides of Ce, La, and Pr, respectively. The electrode area was 0.20 cm^2 for the oxide of Ce, and 0.18 cm^2 for the oxides of La and Pr. Note that for cerium oxide, the conductivity decreases from voltage cycle 3 to voltage cycle 5, in agreement with the ambient pressure data illustrated for neodymium oxide in Fig. 1. The shape of the curves is of the same characteristic form for the three oxides illustrated in Fig. 2, although it can be seen that the pertinent constants for the appropriate analytical expression must be different. Preliminary structure studies (electron diffraction) on evaporated cerium oxide indicate that it is composed of fine-grained crystals with a cubic structure, the lattice parameters being within 5% of those for CeO_2. There is apparently little decomposition of this oxide during evaporation, in agreement with the observations of Feldman and Hacskaylo.[3] Evaporated oxides
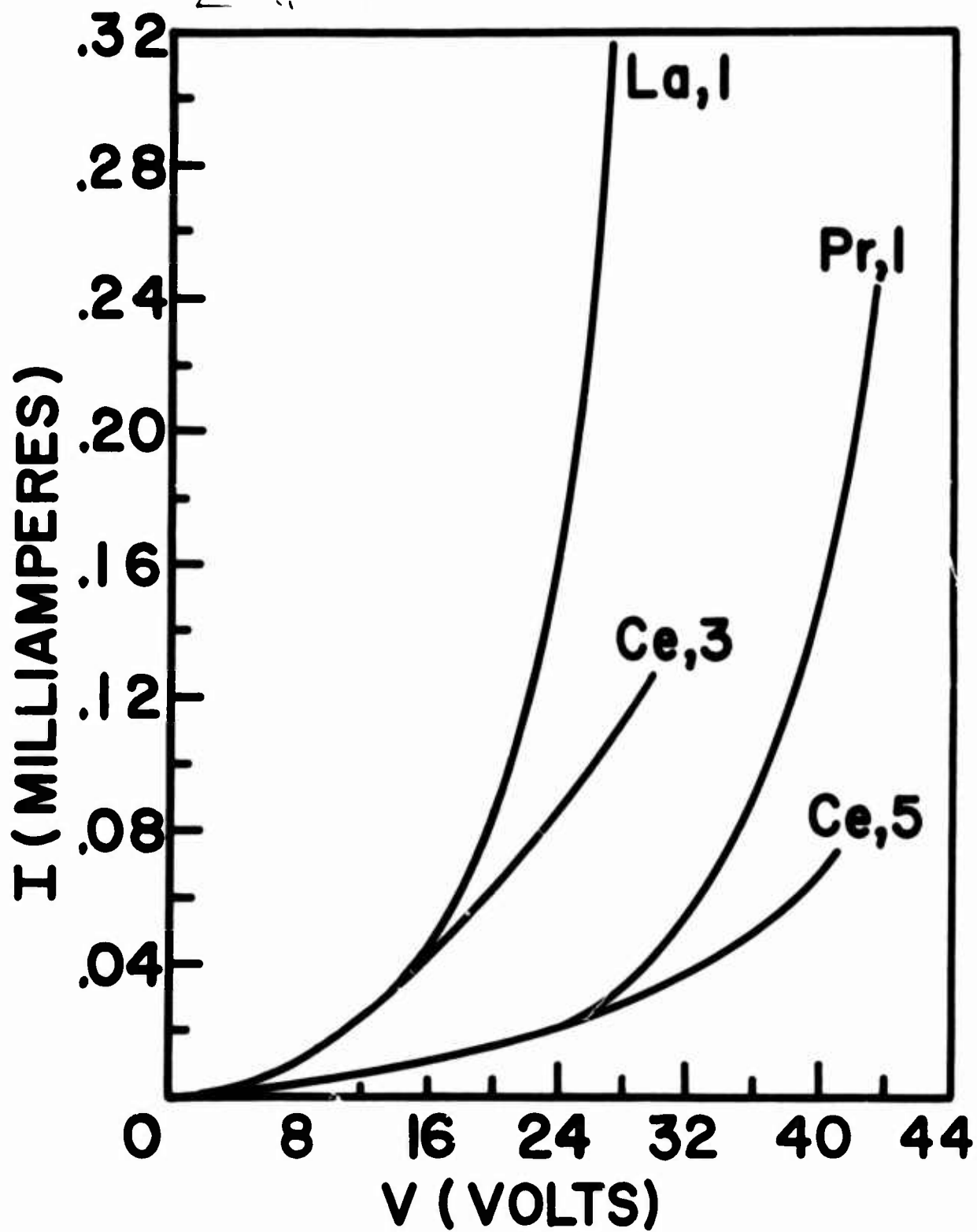
Fig. 2   Steady-state current-voltage characteristics for lanthanum oxide, cerium oxide, and praseodymium oxide at atmospheric pressure.

of neodymium and lanthanum were also found to be crystalline in
the present study.

II. Vacuum Measurements

The effects of air on the current-voltage characteristics
of neodymium oxide were studied by fabricating and measuring
metal-oxide-metal structures without removal from the evaporator
and without exposure to the atmosphere. The results of this study
can be summarized qualitatively as follows:

1. At 10^{-6} torr the initial current-voltage characteristics were
    less erratic and could be stabilized by voltage cycling more
    readily than corresponding characteristics measured in the
    atmosphere.

2. The functional form of the current-voltage characteristic
    seems to be the same for the vacuum and atmospheric pressure
    measurements; however, the nonlinear dependence of current
    on voltage becomes apparent at lower voltages for the vacuum
    data.

3. The current I at a given voltage is much larger (e.g., a
    factor of 5.4) at 10^{-6} torr than at atmospheric pressure;
    this effect, which is reversible, is attributed to an oxygen
    pressure-dependence of the oxide stoichiometry. This effect
    is remarkable in view of the fact that the evaporated aluminum
    electrodes are expected to protect the dielectric oxide from
    the ambient atmosphere everywhere except at the edges.

4. The current at a   voltage tends to <u>increase</u> with voltage cycling for vacuum measurements. in contrast to the results presented in Figs. 1 and 2 for the atmospheric pressure measurements. This vacuum behavior is in accordance with. though much less pronounced than. the "forming process" observed in Al_2O_3 by Hickmott.[5] where the "forming process" is defined[5] as the development of conductivity by the application of electrical potentials to thin-film metal-oxide-metal sandwiches. The increase of current with voltage cycling for the vacuum data is believed to be a true measure of the effect of voltage cycling on conductivity. whereas the severe dielectric breakdowns with corresponding destruction of electrode material is believed to be the predominant factor determining the behavior of current with voltage cycling at atmospheric pressure.

III. Interpretation of Results

Since the thickness of the oxides in this study should preclude electron tunneling[6] from one electrode to the other as a major current-transport mechanism. this mechanism is not considered to be very important in the present measurements. Space-charge-limited currents[7] can be important in thicker films. but the dependence of current on voltage ($I \propto V^n$. with $n \simeq 2$) is not as sensitive for this mechanism as is observed in our experiments. Therefore. three other mechanisms appear to be the more likely possibilities.

1. <u>Schottky Emission</u>. Schottky Emission[8,9] is an electrode-limited

process in which the current is determined by thermal excitation of electrons from the Fermi level of the electrode metal into the conduction band of the oxide. The metal-oxide work-function barrier is modified by the image potential and an applied electric field. The expression for the current is

$$I_S = A_S \exp(\beta_S V^{\frac{1}{2}}) \quad . \tag{1}$$

where V is the electrostatic potential impressed across the oxide. The constants A_S and β_S depend on the nature of the electrode metal and the oxide, the area and thickness of the oxide, and the temperature.

2. <u>Frenkel-Poole Effect</u>. In the Frenkel-Poole process[10,11] the electrical conductivity is limited by the field-enhanced thermal emission of electrons into the conduction band from a discrete trap level in the oxide. The expression for the current is

$$I_F = A_F V \exp(\beta_F V^{\frac{1}{2}}) \quad . \tag{2}$$

where the constants A_F and β_F depend upon the oxide and trap level in question, the area and thickness of the oxide, and the temperature.

3. <u>Field-Induced Hopping Process</u>. Ionic and electronic diffusion in insulators and in very narrow-band semiconductors is thermally activated; extremely large electric fields ($>10^4$ volts/cm) can result in modifications of the activation barriers for motion in the forward and reverse directions sufficient to yield a nonlinear dependence of current on field. The expression for

the current[12] for the case of equal diffusing defect concentrations at the electrodes is

$$I_H = A_H \sinh(\beta_H V) \quad . \tag{3}$$

where the constants A_H and β_H again depend on the metal-oxide-metal structure in question and the temperature.

The method of least-squares fitting to the analytical expressions was used to determine which of the above three current-transport mechanisms is the most probable one. The smallest standard deviation between experimental and theoretical points is given by the Field-Induced Hopping Process. The standard deviation for this process is generally a factor of 5 to 20 smaller than the next most likely mechanism, where in every case the two arbitrary parameters are chosen to minimize the standard deviation between experimental and theoretical points. A typical comparison between the standard deviations is 0.00096, 0.018, and 0.026 for the Field-Induced Hopping Process, Schottky Emission, and Frenkel-Poole Mechanism, respectively. These values are applicable to the curve for the oxide of Pr illustrated in Fig. 2. The Schottky Emission and Frenkel-Poole mechanims have standard deviations which usually differ by much less than a factor of 5, which reflects the fact that the exponential dependence on $V^{\frac{1}{2}}$ dominates a linear dependence on V.

No information was derived from the present studies pertaining to whether the Field-Induced Hopping Process is applicable to the ionic or to the electronic defect species. There is some published

evidence[13] that the oxide CeO_2 loses oxygen reversibly upon heating in vacuum to 485°C, which results in a decrease in the resistivity. the behavior being consistent with that expected of an n-type semiconductor. Further studies to determine the oxygen pressure-dependence and the temperature-dependence of the conductivity of these thin-film oxides are underway.

Acknowledgement

References

1. Source of lanthanum oxide: Electronic Space Products, Inc., Los Angeles. Source of the oxides of cerium, praseodymium. and neodymium: Bernard Ring, Inc., New York.
2. S. Tolansky, Multiple Beam Interferometry of Surfaces and Films (Oxford University Press, London, 1945) p. 224.
3. C. Feldman and M. Hacskaylo, Rev. Sci. Instr. 33, 1459 (1962)
4. D. J. Huntley, Can. J. Phys. 44, 2952 (1966).
5. T. W. Hickmott, J. Appl. Phys. 35, 2118 (1964).
6. T. E. Hartman and J. S. Chivian, Phys. Rev. 134, A1094 (1964).
7. A. Rose, Phys. Rev. 97, 1538 (1955).
8. P. R. Emtage and W. Tantraporn, Phys. Rev. Letters 8, 267 (1962).
9. A. T. Fromhold, Jr. and Earl L. Cook, Phys. Rev. Letters 17, 1212 (1966).
10. J. Frenkel, Phys. Rev. 54, 647 (1938).
11. T. E. Hartman, J. C. Blair, and R. Bauer, J. Appl. Phys. 37, 2468 (1966).
12. A. T. Fromhold, Jr. and Earl L. Cook, J. Appl. Phys., To be published, March (1967).
13. A. W. Czanderna and J. M. Honig, J. Phys. Chem. Solids 6, 96 (1958).

PERMANENT MAGNET PROPERTIES OF YCo$_5$ POWDERS

K.J. Strnat, J.C. Olson and G. Hoffer

Air Force Materials Laboratory (AFML/MAYE)
Wright-Patterson Air Force Base, Ohio 45433

ABSTRACT

The ferromagnetic intermetallic compounds of the type
RCo$_5$ between several rare earths and cobalt were found to be
promising candidates for a technological application as fine
particle permanent magnets. The theoretical upper limits for
the energy product of such magnets lie between 18 and 31.3
million Gauss-Oersted (28.1 MGOe for YCo$_5$), and coercive
forces in excess of those of any other magnets may be expected.
This paper describes experiments with powders of YCo$_5$ prepared
by mechanical milling. Intrinsic coercivities up to ~3000 Oe
were achieved for particle sizes near 5μ, but further size re-
duction unexpectedly lowers H$_c$ again. This is explained as
the result of plastic deformation damage in the crystallites.
Initial experiments suggest that two measures can reduce the
"overmilling effect" and may allow attainment of higher coercive
forces and consequently higher energy products: grinding below
room temperature and high-vacuum annealing of the powders.
Oxidation of the smallest particles seems to occur during
grinding unless air is excluded and this results in a further
reduction of H$_c$. However, particles in an epoxy matrix and
powder compacts did not change their properties appreciably
during several months of aging at room temperature. Magneti-
zation curves are presented for a 64 % dense compact having an
energy product of 1.2 MGOe.

INTRODUCTION

A study[1] of the anisotropic magnetization behavior of a single crystal of the intermetallic phase YCo_5 led to the conclusion[2] that this substance is a very promising candidate material for a practical application in permanent magnets. YCo_5 crystals exhibit a uniaxial magnetic symmetry, the crystallographic c-axis being the easy axis of magnetization, and have an extremely high magnetocrystalline anisotropy. Because of this feature, according to the theory of small-particle magnetism, fine powders of YCo_5 should exhibit very high coercive forces. In view of the other previously known[3,4] favorable magnetic properties of high saturation and Curie temperature, one could expect to make good permanent magnets from such powders by the simple method of compacting them with a binder in a magnetic field. The latter has to align the c-axes of the crystal particles. The theoretical upper limits for the energy product of YCo_5 are $(BH)_{max} = 28.1 \times 10^6$ Gauss-Oersted for the case of a 100% dense magnet, 13.7 MGOe for a compact of well-aligned particles occupying 70% of the total volume, a packing density one should be able to achieve in practice. This figure is higher than the energy product reported for the best laboratory magnets of the Alnico type, and it is a multiple of that for good magnets of any kind now commercially available with the exception of an extremely expensive PtCo alloy which has up to 9.5 MGOe. YCo_5 furthermore compares favorably with the commercial crystal anisotropy-type magnets, barium and strontium ferrite, and with the compound MnBi which has been considered for magnet use, in that its spontaneous magnetization[5] and anisotropy constant[6] change only slightly with temperature near room temperature. All this, and the prospect of simple fabrication, makes it appear definitely worthwhile to study the properties of YCo_5 powders.

Further anisotropy studies[7] showed that several other RCo_5 compounds, where R is a light rare earth metal or a mixture thereof, show similar or even higher promise for permanent magnet use. Especially noteworthy are $PrCo_5$ which has the highest potential energy product (31.3 MGOe), $SmCo_5$ which has the largest crystal anisotropy and rather readily yielded record coercive force values[8] and the alloy where R is cerium-rich mischmetal because of its relatively low price. However, the initial powder experiments reported here were done on YCo_5 as the substance about which more basic information is available than for other RCo_5 compounds, and as the first of the group known to be of technological interest.

THE PERTINENT PHYSICAL PROPERTIES OF YCo_5

Summerized below are what we consider the best available data for those basic properties of YCo_5 which are of significance for the permanent magnet application. They are taken from the references 1, 5 - 7 and 9 - 11.

STRUCTURE: hexagonal, $CaCu_5$ $(D2_d)$-type

$\left. \begin{array}{l} a = 4.931\overset{o}{A}, \quad c = 3.980\overset{o}{A} \end{array} \right\}$ at 25^oC

DENSITY: $d = 7.59$ g/cm^3

SATURATION: $\quad \sigma(O) = 118$ emu/g $\qquad$ at 0^oK

$\left. \begin{array}{l} \sigma(RT) = 111.5 \text{ emu/g} \\[2mm] 4\pi M_S = 10,600 \text{ G} \end{array} \right\}$ at 25^oC

CURIE POINT: $t_c \approx 703^oC$

An initial-permeability maximum whose significance is as yet unclear was observed at 630^oC.

ANISOTROPY CONSTANTS: $K_1 = 7.1 \times 10^6 erg/g$, $K_2 < 2 \times 10^5$, $K_4 \approx 0$

ANISOTROPY FIELD: $H_A = 127$ kOe $\qquad$ all at 25^oC

PERITECTIC TEMPERATURE: $t_p = 1,352^oC$ (Ref. 10)

$\qquad\qquad\qquad$ or $t_p = 1,420^oC$ (Ref. 11)

SAMPLE PREPARATION

The alloys were made by arcmelting stoichiometric amounts of cobalt (99.9% nominal purity) and nuclear-grade yttrium sponge followed by vacuum annealing, typically for 168 hours at 1000^oC. Fig. 1 shows metallographic sections of three ingots used in the milling experiments.

The buttons were usually crushed, mortar-ground to -250μ particle size, and then milled by means of a vibratory mill (SPEX MIXER/MILL Model 8000) using a 60 cm^3 toolsteel jar, three $\frac{1}{2}$" diameter balls and n-hexane as the grinding fluid.

In one milling experiment (see Fig. 2 and Table I) rotary "ball"-milling was employed using a 5" I.D. alumina ceramic jar and 12 ceramic cylinders 3/4" diameter by 1" as the grinding medium.

Samples for the coercive force measurements were made by imbedding 2-5 vol.% of powder in Allaco 20/20 epoxy cement which was cured for >30 minutes at ~70°C. For all "aligned" samples a field of ~15 kOe was applied during hardening.

MILLING EXPERIMENTS

Since YCo_5 is a rather brittle substance, mechanical milling offers itself as the simplest method of producing powders having average particle sizes in the micron range. J.J. Becker ground milligram amounts in an extremely high-speed vibratory mill and observed that the coercive force of randomly oriented powders rose to a peak of 2200 Oe for a particle size of ~4μ and then decreased again on prolonged milling even though the particle size continued to decrease. We ground larger amounts in three different mills under various conditions and observed always basically the same behavior. However, it is obvious that the method and scale of grinding and the amount of liquid added not only strongly influence the grinding time but also affect the peak coercivity and the degree to which the particles can be oriented by a magnetic field.

Figures 2 - 4 show the dependence of the intrinsic coercive force, $_MH_c$, and of the ratio of remanence to peak magnetization, M_r/M_p, upon the milling time. Unless otherwise noted, the measurements were made on the as-milled powders. $4\pi M$ vs. H-magnetization curves were measured with a D.C. hysteresigraph employing induction coils and two Miller integrators;[12] the peak field strength was usually 16.9 kOe. All other conditions are noted in the figure captions.

Figure 2 shows the results of "ballmilling" 50 grams of YCo_5 powder to which 100 cm^3 hexane were added to make a slurry. The grinding proceeded very slowly and the experiment was in this respect the opposite extreme of Becker's vibration milling in which the peak of H_c was reached after 40 seconds. It is remarkable that, nevertheless, the particle size (maximum of the distribution, judged from photomicrographs) corresponding to the peak is very nearly the same in both experiments. Fig. 3 shows the results of vibration grinding in our (larger) vibratory mill. Here, small but equal quantities of a thin slurry (1 gram YCo_5 in 2 cm^3 hexane) were milled without interruption for the periods indicated and used to make a field-oriented and a random-particle sample each time. The coercivities of the

oriented samples are lower than those of the random ones.

Scaling up the vibration milling to 25g with 20 cm³ hexane in the same jar reduced the milling speed drastically but increased the coercivity and improved the loop squareness slightly (Fig. 4, curves a). In an attempt to produce more powder with maximum H_c, this experiment was closely duplicated except that the jar was opened for the first time after 7 hours (curves b). It became obvious that under these conditions the peak had shifted toward shorter grinding time and increased to $H_c \approx 3000$ Oe. This made one suspect that in the first run the air introduced every time the jar was opened for sampling may have oxidized and thus effectively removed a part of the finer, high-coercivity particles as they formed. After ca.15 minutes of mill operation the jar becomes too warm to touch, a fact which would tend to accelerate any oxidation.

DISCUSSION OF THE RESULTS

The behavior of coercive force and remanence ratio as a function of milling time may be qualitatively explained as the result of several physical effects which act concurrently but alternately dominate in different portions of the curves. We start with definitely polycrystalline coarse particles which cannot be aligned by a field because they have no well-defined easy axis and in which magnetization reversal proceeds by domain wall motion. In the very early stages of the milling the particles fracture mostly along grain bounderies, the approach to a single-crystal powder being evidenced by the rapid rise of M_r/M_p, but there is some plastic deformation within the crystallites causing local stresses which impede the domain wall motion and consequently increase the coercive force. Then a range follows in which more and more crystals are crushed into fragments of single-domain size which causes a further increase of H_c. However, an increasing number of dislocations are created within the particles. The atomic order or the "degree of crystallinity" gets slowly lost or, possibly, local twinning or even a transformation to an hitherto unknown polymorph of the $CaCu_5$ structure may take place. Any of these events will cause the easy axis to become less well defined again, or even introduce a multitude of local easy directions, and will thus make particle alignment by a magnetic field more difficult. This is experimentally observed as the slow decrease of M_r/M_p following its peak. The same mechanisms will, of course, reduce and may eventually destroy the uniaxial crystal aniso-tropy of each particle. This leads to the drastic drop of

H_c on prolonged grinding, even though in this stage the majority of the particles may already be of single-domain size.

With the values for M_r/M_p ranging from 0.5 to 0.8, the alignment achieved by application of a magnetic field is relatively poor even at the peak of the curve. It appears that M_r/M_p is the lower the faster the grinding rate. The reason for this could be a higher average temperature of the powder during faster grinding causing a greater plasticity of the particles which would accelerate the detrimental effects of plastic deformation discussed above.

Kneller[13] found electron-microscopic evidence of plastic deformation in strongly "overmilled" YCo_5 powder (final point of Fig. 2) and reports that in this sample the normal x-ray diffraction lines of YCo_5 are replaced by an as yet unidentified different set.

LOW-TEMPERATURE GRINDING AND ANNEALING

If the "overmilling effect" is indeed attributable to the effects of plastic deformation of the particles upon the crystal anisotropy, two remedies should be possible: (1) One may accomplish the milling at a lower temperature where the alloy is presumably more brittle. (2) A properly conducted heat treatment of the powder after grinding promotes a healing of the deformation damage to crystal perfection. Some initial experiments along both lines were performed.

Three sieve-fractions of relatively coarse powders were produced by mortar grinding, once dry at room temperature and again at $77^{\circ}K$ under liquid nitrogen, and made into field-aligned coercive force samples. H_c of the cold-ground powders was approximately twice that of those prepared at room temperature (Fig. 5). This indicates that milling at reduced temperature may be a quite effective means of increasing H_c above ca. 2000 Oe.

First attempts to anneal overmilled powders in quartz bulbs evacuated with a mechanical pump resulted in a drastic further loss of coercive force. However, more careful high-vacuum annealing for 2 hours at $420^{\circ}C$ raised the coercivity of the powder (9-hour point on curve b, Fig. 4) from 2630 Oe to 2900 Oe and improved M_r/M_p slightly (0.58 to 0.6).

PERMANENT MAGNET PROPERTIES OF COMPACTS

A few attempts were made, using quite inadequate improvised equipment, to produce dense magnets by compacting powders in a magnetic field without a binder or after coating the particles with an acrylic lacquer. Cylindrical magnets of 60 to 65 % packing density were made in a nonmagnetic die between steel plungers exerting pressures of 13,000 to 51,000 psi with a hydraulic press in the direction of a field which increased during pressing to maxima between 9000 and 15,000 Oe. Prismatic samples were produced with a screw press in the 16.7 kOe field of an electromagnet, the latter being transverse to the force. Densities of 55 to 64 % (binder included) of the theoretical $d = 7.59$ g/cm^3 were achieved with unknown pressures. Figures 6 and 7 show the magnetization curves of a magnet prepared by the latter method from the as-ground powder corresponding to the 9 hour point on curve b, Fig. 4. No compacts have as yet been made from powders milled to an optimum combination of H_c and M_r/M_p and experiments with such dense magnets are only at a beginning.

STUDIES OF AGING

In view of the observed apparent sensitivity of YCo_5 to oxidation during ballmilling and the well-known chemical instability of many rare earth metals and alloys, one may expect that the properties of YCo_5 magnets exposed to air change with time even at room temperature. Becker[8] has indeed observed appreciable aging effects on very high-coercivity powders prepared by a chemical technique. We have remeasured the magnetization curves of various representative samples of oriented powders in epoxy and found no appreciable changes.

1. As an example we compare in Table I some properties of our oldest reliably measured samples first prepared in mid-1966 and remeasured after 7 months.

2. From other powder (9 hour point, Fig. 4b) oriented epoxy-matrix samples were made right after the milling and again after 6 weeks during which the powder was kept in air slightly moist with hexane. H_c and M_r/M_p were unchanged.

3. A magnet of 55 % packing density weighing ~4 grams was also remeasured 6 weeks after its preparation. The properties are listed in Table II.

In this case, the coercive force remained practically unchanged while a relatively small reduction of the saturation, remanence and energy product indicate that an oxidation of particles near the surface may have occured.

Our results to date indicate that the corrosion of YCo_5 at room temperature is no serious problem. However, in view of the practical importance of magnet stability systematic investigations of this nature must continue.

ACKNOWLEDGEMENTS

REFERENCES

1. G. Hoffer and K. Strnat, IEEE Trans. Magnetics, MAG-2 (1966) 487.

2. K. Strnat and G. Hoffer, Air Force Technical Report AFML-TR-65-446(1966).

3. K. Nassau, L.V. Cherry and W.E. Wallace, J. Phys. Chem. Solids 16(1960) 123 and 131.

4. E.A. Nesbitt, H.J. Williams, J.H. Wernick and R.C. Sherwood, J. Appl. Physics 33(1962) 1674.

5. R. Lemaire, Cobalt 32(1966) 132.

6. G. Hoffer and K. Strnat, J. Appl. Physics 38(1967) March Supplement(in press).

7. K. Strnat, G. Hoffer, J.C. Olson, W. Ostertag and J.J. Becker, J. Appl. Physics 38(1967) March Supplement (in press).

8. J.J. Becker, Air Force Technical Report AFML-TR-67-28 (1967) on contract AF33(615)-1490.

9. W. Ostertag, Air Force Technical Report AFML-TR-64-343 (1965).

10. K. Strnat, W. Ostertag, N.J. Adams and J.C. Olson, Proc. 5th Rare Earth Res. Conf., Book V, p. 67.

11. J. Pelleg and O.N. Carlson, J. Less Common Metals 9 (1965)281.

12. R. Kubach, M.S. Thesis (E.E.), Univ. of Dayton, Ohio (1966)

13. E. Kneller, Max Planck-Institute, Germany. Personal communication.

TABLE I: Aging Behavior of Aligned Powders in Epoxy
(ballmilled, see Fig. 2)

Milling Time Hours	June-July 1966		February 1967		Change %	
	$_MH_c$ Oe.	M_r/M_p	$_MH_c$ Oe.	M_r/M_p	δH_c	$\delta \frac{M_r}{M_p}$
125	1,550	0.76	1,525	0.76	-1.7	0
250	1,680	0.73	1,716	0.72	+2.1	-1.4
400	1,740	0.68	1,750	0.69	+0.6	+1.5
800	1,190	0.56	1,141	0.55	-4.1	-1.8

TABLE II

	$_MH_c$	$4\pi M_p$	$4\pi M_r$	M_r/M_p	$(BH)_{max.}$
9 Jan.	2,020	4,990	2,960	0.594	1.0
21 Feb.	2,030	4,650	2,770	0.595	0.95
Change %	+ 0.5	- 6.8	- 6.4	0	- 5
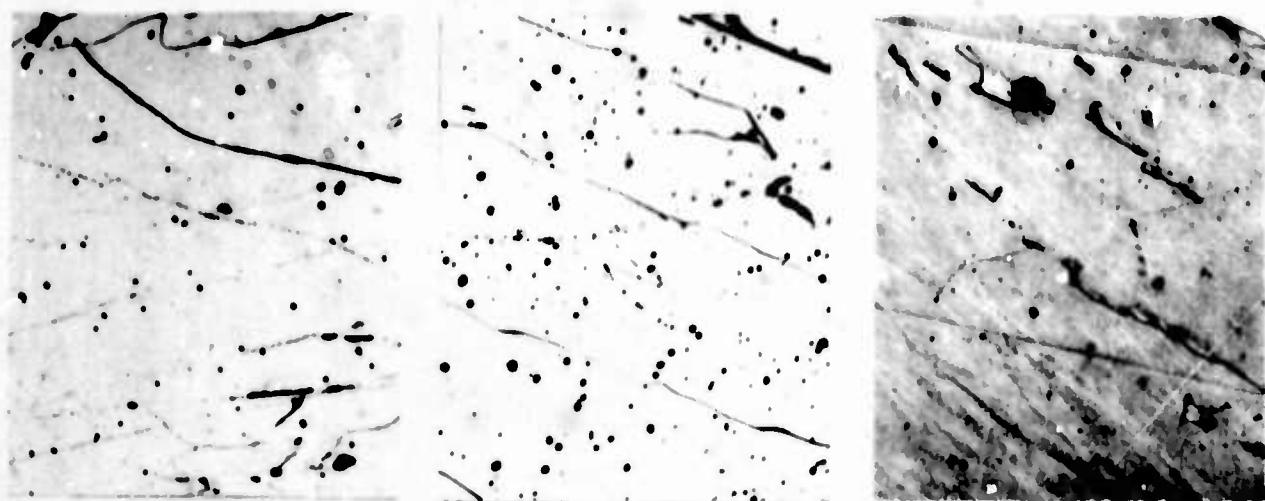
Ingot: Co-Y-9g   Co-Y-9h   Co-Y-9e

See: Fig.4, curve a   Fig. 4, curve b   Figure 3

Figure 1: PHOTOMICROGRAPHS OF THREE ALLOYS USED IN GRINDING EXPERIMENTS (250x).
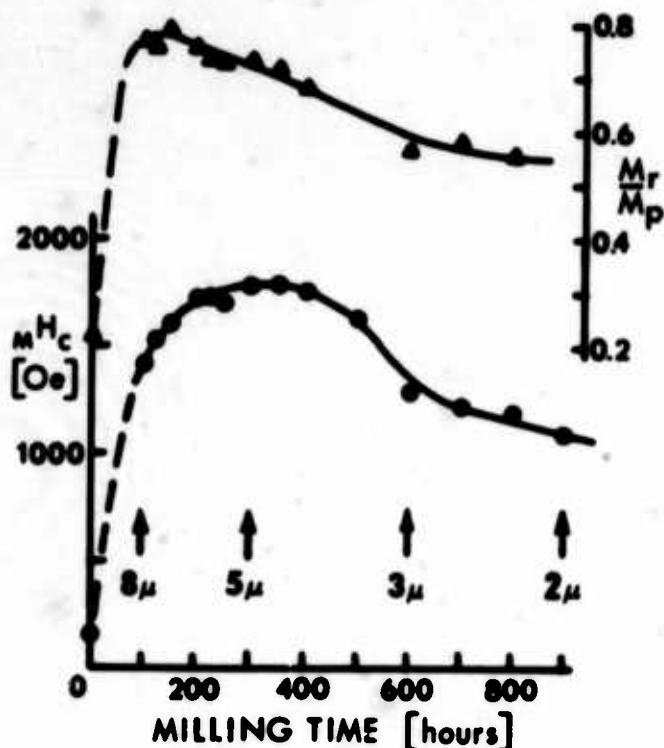
Figure 2: SLOW BALLMILLING.

Initial 50 grams of YCo$_5$ reduced by ~1 g for each sample

Oriented particles.
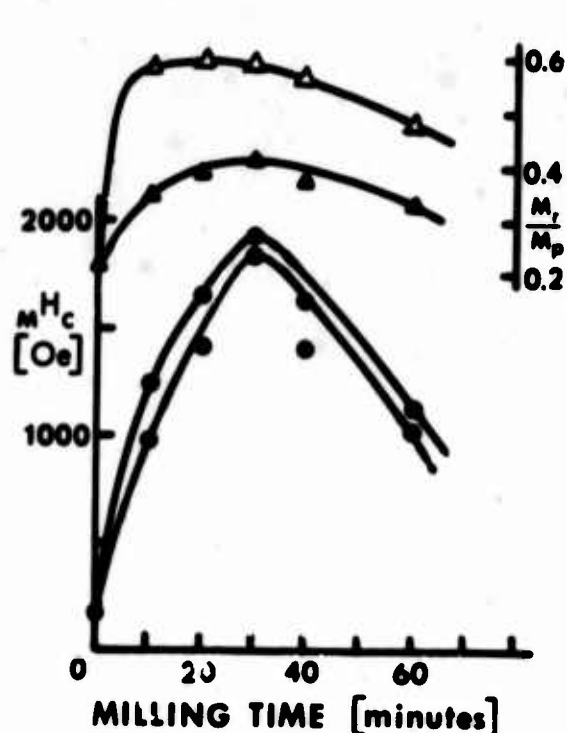
Figure 3: VIBRATION GRINDING.

1 gram in 2 cm^3 hexane ground uninterrupted for each time period indicated.

●▲ Oriented particles
●▲ Random particles

Ingot Co-Y-9e
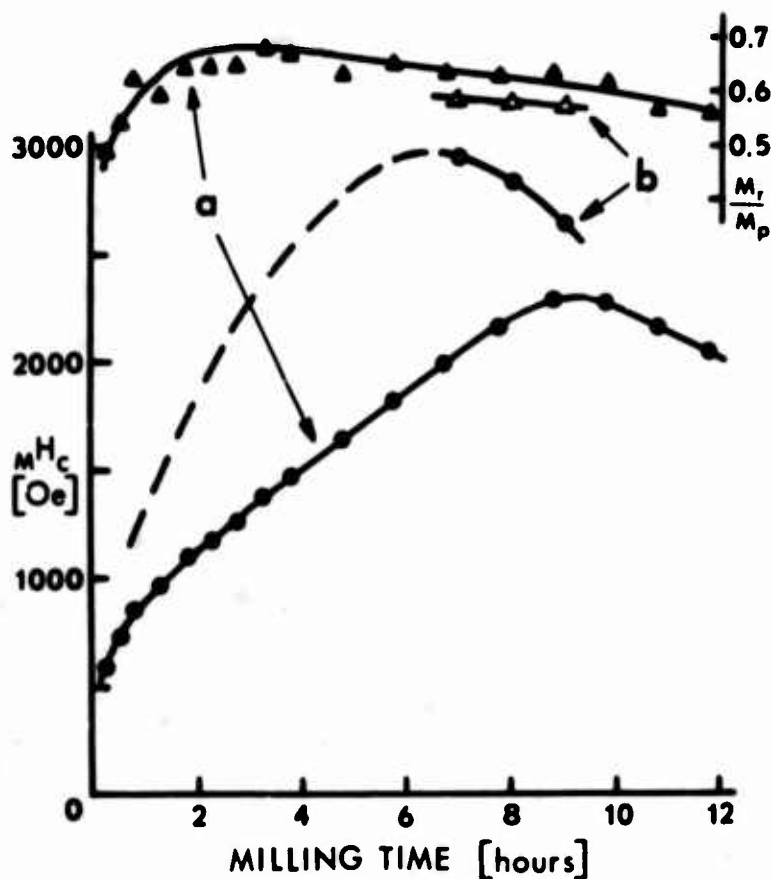
Figure 4:
VIBRATION GRINDING.

Initial 25 grams, in 20 cm^{-3} hexane, reduced by ∼0.1 g for each sample.

Oriented particles

●▲(a) Ingot Co-Y-9g
●▲(b) Ingot Co-Y-9h

Figure 5: COLD GRINDING

Coercive forces of three sieve fractions of powders mortar-ground at room temperature and under liquid nitrogen
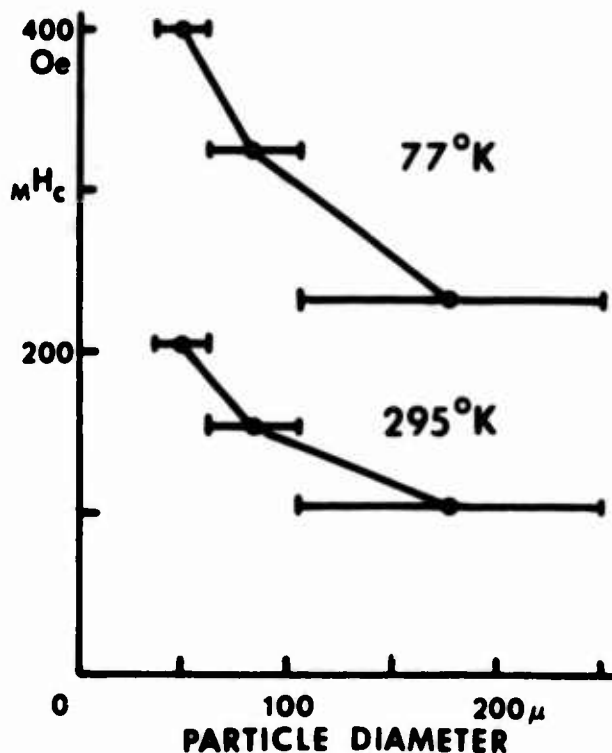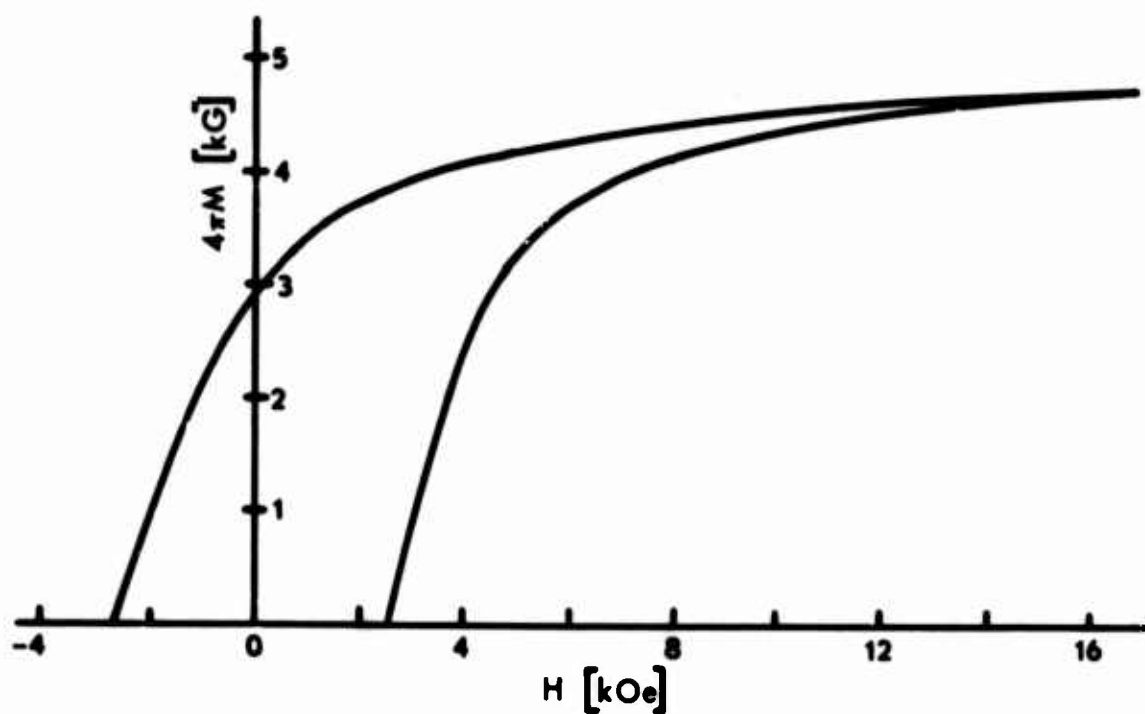
Figure 6: HYSTERESIS LOOP OF COMPACT YCo$_5$ MAGNET

Ingot Co-Y-9h, milled 9 hours, 0.64 vol. packing fraction
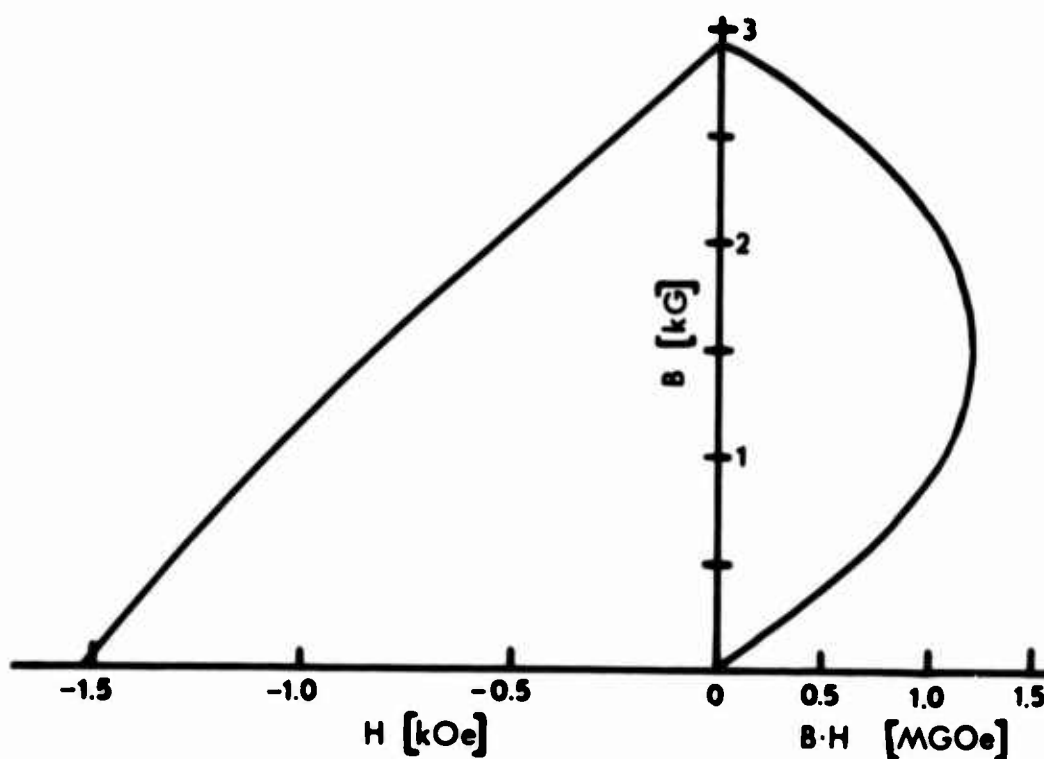
Figure 7: DEMAGNETIZATION CURVE OF COMPACT MAGNET.

Same as Fig. 6

High Field Magnet Moment Measurements in Single
Crystal Rare-Earth Metals

S. Foner, National Magnet Laboratory,[†] Massachusetts
Institute of Technology, Cambridge, Mass. 02139

In this paper we summarize the status of our recent high field
magnetic moment measurements in a number of single crystal rare-earth
metals. A brief discussion of measurements in Gd, Ho, Er and Dy was pre-
sented earlier.[1] A more detailed series of studies[2] has continued on
various crystals prepared by other techniques in order to determine effects
of crystal preparation, strain, etc. on the magnetic properties. Measure-
ments as a function of temperature and field (dc to 170 kG so far - 220 kG
experiments are scheduled) have been made along all principal axes. The
simplest case is Gd which saturates at low fields (< 60 kG) for all principal
directions. Ho, Dy and Er approach saturation along the easy axis in most
cases, but complete saturation is not achieved along the hard axes for the
fields available. The detailed results are complex, show large hysteresis
effects in some cases, and often show several magnetic transitions as a
function of field. There is a large anisotropy in Dy as expected from earlier
data. Our results extend a number of the earlier investigations by the Ames
group at much lower magnetic fields. The results of our experiments will
be compared with the magnetic data of the Ames group as well as with the
extensive neutron diffraction investigations by the Oak Ridge group.[3] The
saturation moment, the approach to magnetic saturation, and various high

field transitions will be discussed.

Single crystals of Eu, Sm and Tm have been grown at NML by Dr. M. Schieber and these have also been examined at high fields. The lack of single crystals and high fields has apparently resulted in some speculation particularly in Tm and Eu. We find that the Tm moment along the easy axis approaches that expected for saturation of the Tm^{3+} ion at high fields, and that the low values of magnetic moment even at 70 kG[4] can be attributed mainly to a very high anisotropy rather than to impurity effects. On the other hand impurity effects may be the determining factor in the complex behavior presented earlier for Eu.[5] Our data to 150 kG at 4.2°K show a constant susceptibility rather than a field dependent one in contrast to earlier low field polycrystalline data.[5] The implications of our results on the Eu problem will be summarized. The data for Sm shows a small susceptibility consistent with antiferromagnetic ordering.

Because saturation has not been observed along the hard axes for many of these rare-earth metals, we have initiated pulsed field studies up to about 400 kG. Some of these results will be discussed.

The combination of extremely high anisotropy and high magnetic moments in these rare-earths make reliable measurements in high fields difficult. Methods which avoid these problems will be briefly mentioned. The status of research on other rare-earth metals at high fields will also be summarized.

The above brief summary covers a broad program of high field rare-earth studies at NML and elsewhere. Participants in these experiments

include J.J. Rhyne of the U.S. Naval Ordnance Laboratory, Washington,

D.C., E.J. McNiff, Jr., M. Schieber, (now at the Hebrew University,

Jerusalem, Israel), and R. Doclo.

(1) S. Foner and E.J. McNiff, Jr., 12th Conference on Magnetism and Magnetic Materials 1966.

(2) S. Foner, J.J. Rhyne, E.J. McNiff, Jr., and R. Doclo, to be presented at Am. Phys. Soc. Meeting, Toronto, Canada.

(3) An up-to-date (June 1966) summary is given by R.M. Bozorth and C.D. Graham, Jr., Rare-Earth Metals, Compounds, and Solid Solutions, to appear as a Chapter in Handbook of Magnetic Materials, edited by F.E. Luborsky and P.A. Albert (Reinhold Press).

(4) W.E. Henry, J. Appl. Phys. Suppl. $\underline{31}$, 323S (1960).

(5) R.M. Bozorth and J.H. Van Vleck, Phys. Rev. $\underline{118}$, 1493 (1960).

FREQUENCY DEPENDENCE OF MAGNETIC LOSSES IN Ho IN THE NEIGHBORHOOD OF THE CURIE TEMPERATURE[*]

B. C. GERSTEIN AND F. OLANDER

Institute for Atomic Research and Departments of
Chemistry and Metallurgy

Iowa State University Ames, Iowa 50010

Abstract - The frequency dependence of the imaginary and real suscep-
tibilities of polycrystalline Ho has been measured in the neighborhood
of the ferromagnetic ordering temperature. The nature of the χ'-ω-T
and χ''-ω-T surfaces has been defined in the range $10 \leq T \leq 25°K$ $22 \leq
\omega \leq 110$ Hz. For the sample measured, the resonant frequency for do-
main wall motion lies below 22Hz indicating that ac susceptibilities
of Ho measured above 10Hz will not agree with dc measurements. The
results were fitted to a driven oscillator model and were found to cor-
relate more closely with a model in which effective mass is ignored
than with one in which it is not, but the agreement is not completely
satisfactory.

INTRODUCTION

While there has been a great deal of work devoted to investigating

magnetic behavior of ordered systems in the neighborhood of their

ordering temperatures[1] and some work in investigating ac losses in

ferromagnetically ordered systems well below their ordering temper-

atures,[2] the majority of the former has been in fields in excess of

1000 Oe, and the latter in 3 - d transition metals and alloys, and in-

deed, not near the Curie "pernts".[3] The investigation of magnetic

behavior of rare earths via ac techniques near their Curie pernts has

been to date almost untouched.[4]

In previous work in this Laboratory,[5] we had measured the real and imaginary susceptibilities of Ho at 33Hz and a field of 10 Oe. It was desirable to extend the frequency range of the measurements to determine if the lack of agreement with dc measurements in the ferromagnetic region was due to the magnitudes of the fields or to the fact that appreciable losses were occurring. The instrument making this possible was a newly acquired tunable oscillator amplifier supplied by E. S. I. of Portland, Oregon.

While the primary purpose of the measurements was to define the nature of the frequency - temperature - susceptibility surfaces for polycrystalline Ho near the Curie pernt, it was hoped that the measurements would also yield a measure of parameters relatable to a first principles calculation of interactions between moments in domain walls of Ho.

EXPERIMENTAL

The ac susceptibilities were obtained using a low field mutual inductance technique of the type previously described[6] but modified so that the susceptibility could be obtained as a function of frequency. Continuous single control tuning of both the generator and the detector made it possible to measure the frequency dependence of the losses. The tunable oscillator-amplifier, an Electro Scientific-Industries Model 861-A ac generator detector, consists of a variable frequency generator and a low noise, high gain, tuned detector.

The circuitry and cryostat system have been previously described,[5] but the system for mounting and for supporting the coils was redesigned for this experiment. The sample, the thermocouple, and

the sample coils were placed inside a temperature controlled copper cylinder to assure that these components would be in thermal equilibrium.

All the susceptibilities were measured at fields of 2.10 ± 0.5 Oe, calculated from the number of turns and the current of the primary.

The polycrystalline sample of holmium was in the form of a cylinder 0.77 cm long and 0.072 cm in diameter. The sample was prepared by the calcium reduction of the anhydrous fluoride as previously described, [7, 8] and contained <500 ppm Er as the major impurity.

RESULTS

The results of the frequency dependence studies in which the experimental frequencies were 21, 33, 50, 75 and 100 Hz, are shown in Figs. 1a, and b. The χ''-ω-T surface in the neighborhood of the Curie pernt is shown in Fig. 2a. The most notable feature of these curves is that below the Curie temperature the magnitude of ' ... components of the susceptibility vary inversely with f- ...y. From the isothermal plots it is clear that th ... .ability is being measured on the high side of t' ... sonant frequency. It follows that ac measurements above ... .al not agree with static susceptibility results.

DISCUSSION

In a ferromagnet the application of a small external field H_o $\cos \omega t$ results in small displacements of the domain walls. The equation of motion describing the displacement of a 180° domain wall under an applied field parallel to the wall is [1]

$$m\ddot{z} + \beta\dot{z} + \alpha z = 2M_s H_o e^{j\omega t} \tag{1}$$

where

    m = the mass of the wall
    z = the displacement
    β = the damping parameter
    α = the resistance parameter
    M_s = the saturation magnetization.

For a polycrystalline sample, we write

$$m\ddot{z} + \beta\dot{z} + \alpha z = \Gamma M_s H_o e^{j\omega t} \tag{2}$$

where Γ accounts for random wall orientation. The steady state solution of this equation is

$$Z = \frac{\Gamma H_o M_s e^{j\omega t}}{(\alpha - m\omega^2)} \left[\frac{1 + j\delta'}{1 + \delta'^2} \right] \tag{3}$$

where

$$\delta' = \frac{\beta\omega}{\alpha - m\omega^2} \tag{4}$$

and the resonance frequency is $\omega_o = (\alpha/m)^{1/2}$. The analagous solutions for the case m = 0 are

$$Z = \frac{\Gamma M_s H_o e^{j\omega t}}{\alpha} \left[\frac{1 - j\delta}{1 + \delta^2} \right] \tag{5}$$

where

$$\delta = \frac{\beta\omega}{\alpha} . \tag{6}$$

Relating the ac susceptibility to the domain wall motion, we find

$$\chi_m^u = \frac{\Gamma''}{(\alpha - m\omega^2)} \frac{(1 - j\delta')}{(1 + \delta'^2)} \tag{7}$$

in the case of non negligible domain wall mass, and

$$\chi_m^u = \frac{\Gamma''}{\alpha} \frac{(1 - j\delta)}{(1 + \delta^2)} \tag{8}$$

for the case $m = 0$, where χ_m^u is the unrationalized cgs molar suscepti-
bility, and Γ'' is a constant for a given number of moles and a given
measuring coil.

Non Negligible Domain Wall Mass

If $m\omega^2$ is not negligible compared to α, Eq. (7) yields

$$\chi' = \frac{\Gamma''}{(\alpha - m\omega^2)} \frac{1}{(1 + \delta'^2)} \text{ and } \chi'' = \frac{\Gamma''}{(\alpha - m\omega^2)} \frac{\delta'}{(1 + \delta'^2)} \quad (9)$$

from which we see

$$\frac{\chi''}{\chi'} = \delta' \quad (10)$$

and

$$\frac{\alpha}{\Gamma''} - \frac{m\omega^2}{\Gamma''} = \pm \frac{\chi'}{\chi''^2 + \chi'^2} . \quad (11)$$

To the extent that the model is correct, a plot of $\dfrac{\chi'}{\chi''^2 + \chi'^2}$ vs ω^2
should yield two straight lines, one with positive slope m/Γ'' for
$\omega > \omega_e$, and one with negative slope $- m/\Gamma''$ for $\omega < \omega_e$, the respective
intercepts being $\mp \alpha / \Gamma''$.

$m\omega^2$ Negligible Compared α

In this case, the same manipulations as above but applied to (10)
rather than (9) yield

$$\frac{\chi'}{\chi''^2 + \chi'^2} = \frac{\alpha}{\Gamma''} = \text{const, all } \omega. \quad (12)$$

Our values of $\chi'/(\chi''^2 + \chi'^2)$ vs ω^2 are shown in Fig. 2b. The
lack of an intercept on the ω^2 axis clearly indicates that we are dealing
with the case $m\omega^2 << \alpha$.

It is interesting to speculate how the resonant frequency might be related to the ordering temperature, and why the value for Ho is so low relative to systems such as ferrites[9] with resonant frequencies of the order of kilocycles. We do so using the theory of Kittel & Galt for cubic lattices[1] as a guide. The ratio of resonance frequencies of two systems will be proportional to the ratios $(\alpha/m)^{1/2}$. Using Eqs. (29.3) and (30.6) of Ref. 1, we find

$$\omega_0 \sim \frac{T_c S^2}{K^{3/2}} \tag{13}$$

where T_c is the ordering temperature and K is the anisotropy energy. This proportionality ignores the stress-saturation magnetostriction product relative to the anisotropy energy, and considers the stress to be the same in both systems. Anisotropy energies in hexagonal rare earths are generally higher than those in cubic ferrites, and ordering temperatures are lower, so with Eq. (13) as a guide, we would expect the resonance frequencies for domain wall motion in Ho to be lower than that of ferrites.

ACKNOWLEDGMENTS

LITERATURE CITED

1. Kittel, C. and Galt, J.K., Solid State Physics 3, 439 (1956).

2. Bozorth, R.M., "Ferromagnetism", D. Van Nostrand Co., Inc., New York, N.Y., (1951).

3. Giauque, W.F. Brodale, G.E. Fisher, R.A. and Hornung, E.W., J. Chem. Phys. 42, 1 (1965).

4. Pake, G.A., "Paramagnetic Resonance" Benjamin Inc., New York (1962) p. 29.

5. Jelinek, F.J., Hill, E.D. and Gerstein, B.C., J. Phys. Chem. Solids 26, 1475 (1965).

6. Gerstein, B.C., USAEC Rept. IS-331 [Iowa State University of Science and Technology, Ames, Iowa, 1960].

7. Daane, A.H., Dennison, D. and Spedding, F.H., J. Am. Chem. Soc. 78, 2272 (1953).

8. Spedding, F.H. and Daane, A.H., J. Am. Chem. Soc. 74, 2783 (1952).

9. Galt, J.K., Andrus, J., and Hopper, H.G., Rev. Mod. Phys. 25, 93 (1953).
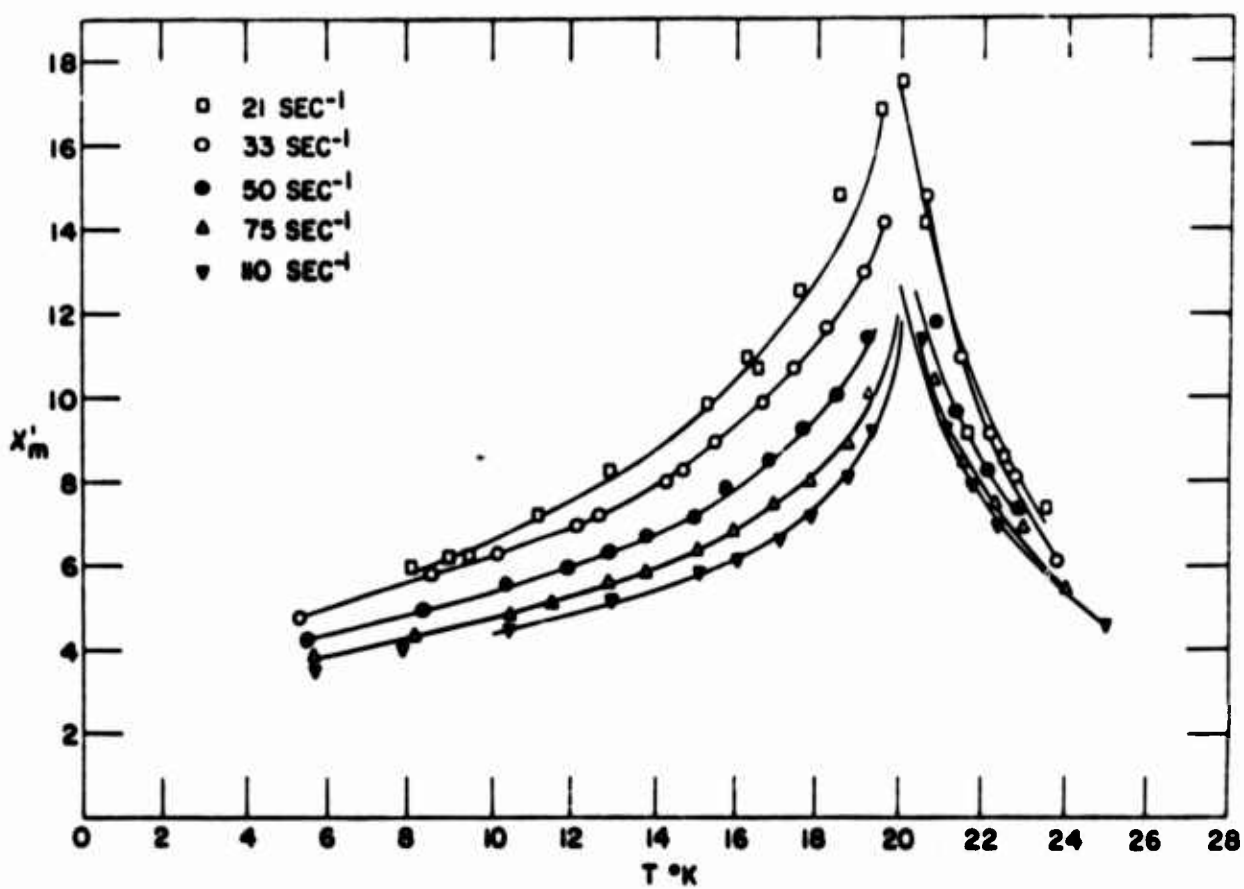
Fig. 1a. Magnitude of X'_m versus T.
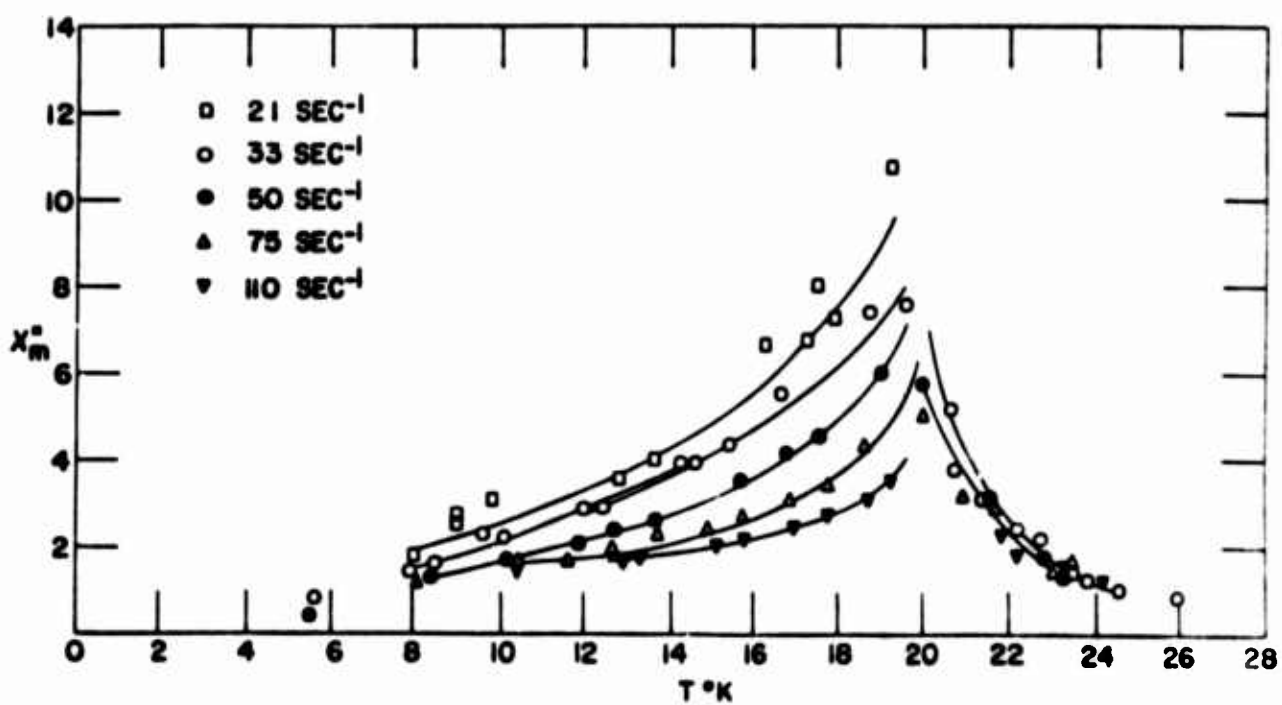
Fig. 1b. Magnitude of the imaginary component versus T.
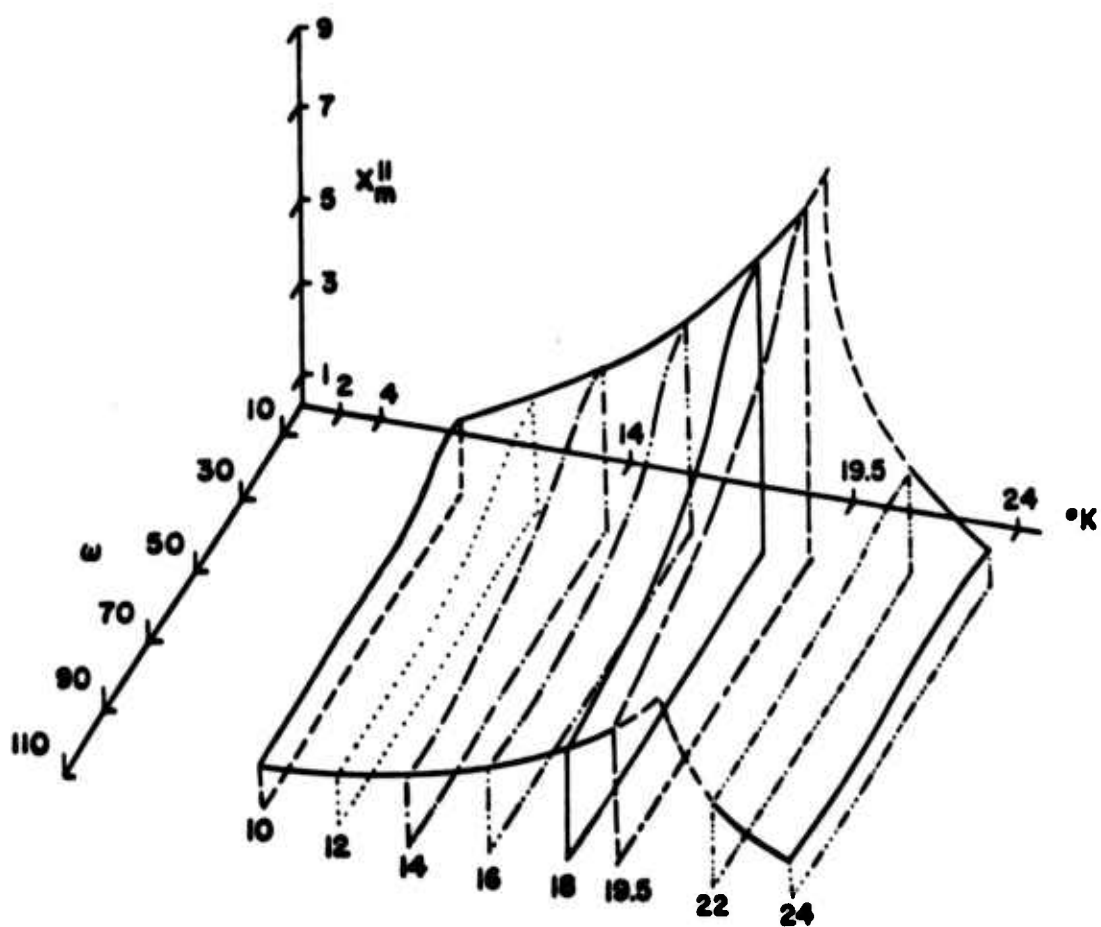
Fig. 2a. Nature of χ'_m versus T versus ω surface.
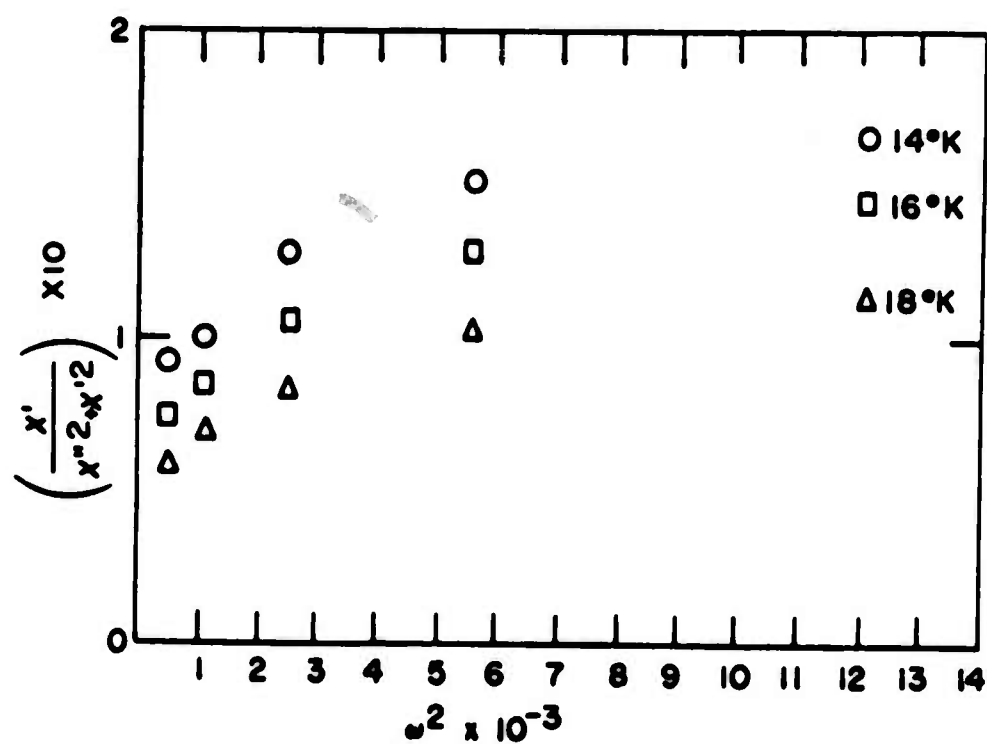
Fig. 2b. Results showing ω^2 versus $\dfrac{\chi'}{\chi'^2 + \chi'^2}$.

ELECTRICAL RESISTIVITY and SEEBECK
EFFECT of THULIUM SINGLE CRYSTALS

Sam Legvold and L. Roger Edwards

Institute for Atomic Research and Department of Physics
Iowa State University, Ames, Iowa 50010

L-10
Legvold

Abstract

Single crystals of Tm have been grown by the strain anneal tech-
nique. The electrical resistivity and the Seebeck coefficients have been
measured along the three crystallographic directions $<11\bar{2}0>$, $<10\bar{1}0>$,
and $<0001>$ as a function of temperature from 4° to 300°K. The elec-
trical resistivity results indicate a Néel temperature of 57.5°K with no
evidence for other magnetic transitions.

The Seebeck coefficients also indicated a Néel temperature of 57.5°K
However, the Seebeck coefficient of the $<0001>$ crystal showed a second
transition at 32°K, which is in good agreement with low field magnetic
susceptibility measurements on polycrystalline Tm[3]. Neutron diffrac-
tion data of Koehler et al.[8] indicated the transition to be about 38°K.

Both measurements exhibited a significant anisotropy between the
$<0001>$ direction and the basal plane. Magnetic measurements on these
samples are anticipated.

Introduction

Magnetic and transport properties of polycrystalline Tm have been
measured[1-5]. Because of the magnetic and crystalline anisotropy of
Tm, single crystal data is necessary for the understanding of these
physical properties. Here we report the electrical resistivities and
Seebeck coefficients of Tm single crystals.

Tm has twelve 4-f electrons of which two are unpaired. It is the
direct exchange[6] between the conduction electrons and the localized
4-f electrons which gives rise to the anomalous transport properties,
while it is the indirect exchange[7] between 4-f electron shells which
causes the magnetic ordering. Koehler et al.[8] have shown that Tm
goes from a paramagnetic structure to a sinusoidally modulated

antiferromagnetic structure below 57°K and then from the antiferro-
magnetic structure to a ferrimagnetic structure below about 38°K.

Experimental

The Tm used in this experiment was separated from the other rare
earths by the ion-exchange process at the Ames Laboratory. The sin-
gle crystals were grown by the strain anneal technique as described by
Nigh[9]. Because Tm has a high vapor pressure the arc-melted button
was suspended and sealed under a $\frac{1}{2}$ atmosphere of He in a Ta "bomb"
for the annealing program. Single crystals $\sim\frac{1}{2}$ inch were obtained. The
crystals were oriented by Laue back-reflection and cut to 1 x 1 x 10 mm
by the spark errosion technique.

The electrical resistivity was measured by the standard 4-probe
technique[4]. Temperatures between 1.2° and 4.2°K were obtained by
pumping on liquid He, while automatically controlled heaters were
used for the 4.2°to 300°K range.

The Seebeck coefficients were measured by a technique described
by Sill[10].

Results and Discussion

Resistivity

The results of the electrical resistivity measurements are shown
in Figure 1. Above the Neel temperature (T_N) the resistivity of both
the basal plane and the <0001> crystals behaves linearly with tempera-
ture. Below T_N the resistivity of the <0001> crystal increases suddenly,
goes through a maximum and then decreases smoothly to the impurity
scattering level. The resistivity of the basal plane crystals, however,
just goes through a change of slope at T_N. The experimental data pre-
sented here agrees well with the qualitative prediction of Freeman
et al.[11] for Tm. These authors' argue that the periodic variation of
the magnetic moment below T_N introduces extra superzone planes of
energy discontinuity perpendicular to the k_z direction. These planes
destroy large portions of the Fermi surface in the k_z direction and
hence the conductivity in the <0001> direction decreases suddenly be-
low T_N. Thus the resistivity should suddenly increase below T_N.

Now the resistivity should also decrease below T_N because of the change in magnetic order. Hence we get the maximum in the <0001> direction. These authors also show that the superzone planes have little effect on the Fermi surface in the kx, ky directions. Hence the resistivity of the basal plane crystals just goes through a change in slope due to the change in magnetic order.

Elliot and Wedgewood[12], using an ellipsoidal Fermi surface intersected by superzone planes, have obtained theoretical expressions for the resistivities of the heavy rare earths. We have applied their theory to the experimental data of Tm. The results are shown in Figures 2A and 2B. The poor fit at low temperatures is probably due to the neglect of spinwave scattering and to other approximations made in the theory[12]

It is interesting to explore the theory of electron scattering at temperatures above T_N. Let ρ_M be the spin disorder resistivity and $d\rho/dT$ be the slope of the resistivity curve for $T > T_N$. From Figure 1 we see that

$$\rho_M^{<10\bar{1}0>} > \rho_M^{<0001>}$$

(1)

$$(d\rho/dT)^{<10\bar{1}0>} > (d\rho/dT)^{<0001>}$$

In terms of a relaxation time τ, which is independent of energy, the conductivity tensor is

$$\sigma_{ij} = \frac{e^2 \tau}{4\pi^2 \hbar} \int_{F.S.} v_i \, dS_j$$

where v_i is the velocity of the electron and the integral is taken over the Fermi surface. Neglecting the impurity scattering we can write for the relaxation

$$1/\tau = 1/\tau_s + cT$$

where τ_s is the spin scattering relaxation time[12] and $(cT)^{-1}$ is the high temperature phonon scattering relaxation time.

If we approximate v_x and v_z by some average velocity $\bar{v}$, we get the following expressions for the resistivity

$$\rho_{xx} \propto \frac{c}{\bar{v} \int dS_x} T + \frac{1}{\tau_s \bar{v} \int dS_x} = (d\rho/dT)^{<10\bar{1}0>} T + \rho_M^{<10\bar{1}0>}$$

(2)

$$\rho_{zz} \propto \frac{c}{\bar{v} \int dS_z} T + \frac{1}{\tau_s \bar{v} \int dS_z} = (d\rho/dT)^{<0001>} T + \rho_M^{<0001>}$$

From the complete Fermi surface of Tm[11] we see that

$$\int dS_x < \int dS_z$$

and hence equation (1) follows.

It is interesting to note that equations (1) holds for Gd, Er, Dy, H ,
and Tb. This, however, is not surprising because all these elements
have a similar Fermi surface in the paramagnetic region.

Seebeck Coefficients

The results of the Seebeck measurements are shown in Figure 3.
At T_N all the Seebeck coefficients exhibit sharp maxima. The <0001>
coefficient, however, goes through a sharp minimum at 32°K. It is
this minimum which we interpret as the antiferromagnetic-ferrimag-
netic transition. This is supported by Jelinek's et al.[3] susceptibilit
measurements on polycrystalline Tm.

Presently there is no theory which accounts even qualitatively for
the temperature dependence of the Seebeck coefficients. Besides the
ordinary diffusion and phonon drag, there is magnon drag, two carriers
(6s and 5d electrons), and magnetic superzones.

Acknowledgments

References

(1) B. L. Rhodes, S. Legvold, and F. H. Spedding, Phys. Rev., <u>109</u>, 1547 (1958).

(2) D. D. Davis and R. M. Bozorth, Phys. Rev., <u>118</u>, 1543 (1960).

(3) F. J. Jelinek, E. D. Hill, and B. C. Gerstein, J. Phys. Chem. Solids, <u>26</u>, 1475 (1965).

(4) R. V. Colvin, Sam Legvold, and F. H. Spedding, Phys. Rev., <u>120</u>, 741 (1960).

(5) H. J. Born, Sam Legvold, and F. H. Spedding, J. Appl. Phys., <u>32</u>, 2543 (1961).

(6) S. H. Liu, Phys. Rev., <u>121</u>, 451 (1961).

(7) M. A. Ruderman and C. Kittel, Phys. Rev., <u>96</u>, 99 (1954).

(8) W. C. Koehler, J. W. Cable, E. O. Wollan, and M. K. Wilkinson, J. of Appl. Phys., <u>33</u>, 1124 (1962).

(9) H. E. Nigh, J. Appl. Phys., <u>34</u>, 3323 (1963).

(10) L. R. Sill and S. Legvold, Phys. Rev., <u>137</u>, A1139 (1965).

(11) A. J. Freeman, J. O. Dimmock and R. E. Watson, Phys. Rev. Letters, <u>16</u>, 94 (1966).

(12) R. J. Elliot and F. A. Wedgewood, Proc. Phys. Soc., <u>81</u>, 846 (1963).

ELECTRICAL RESISTIVITY OF THULIUM SINGLE CRYSTALS
AS A FUNCTION OF TEMPERATURE
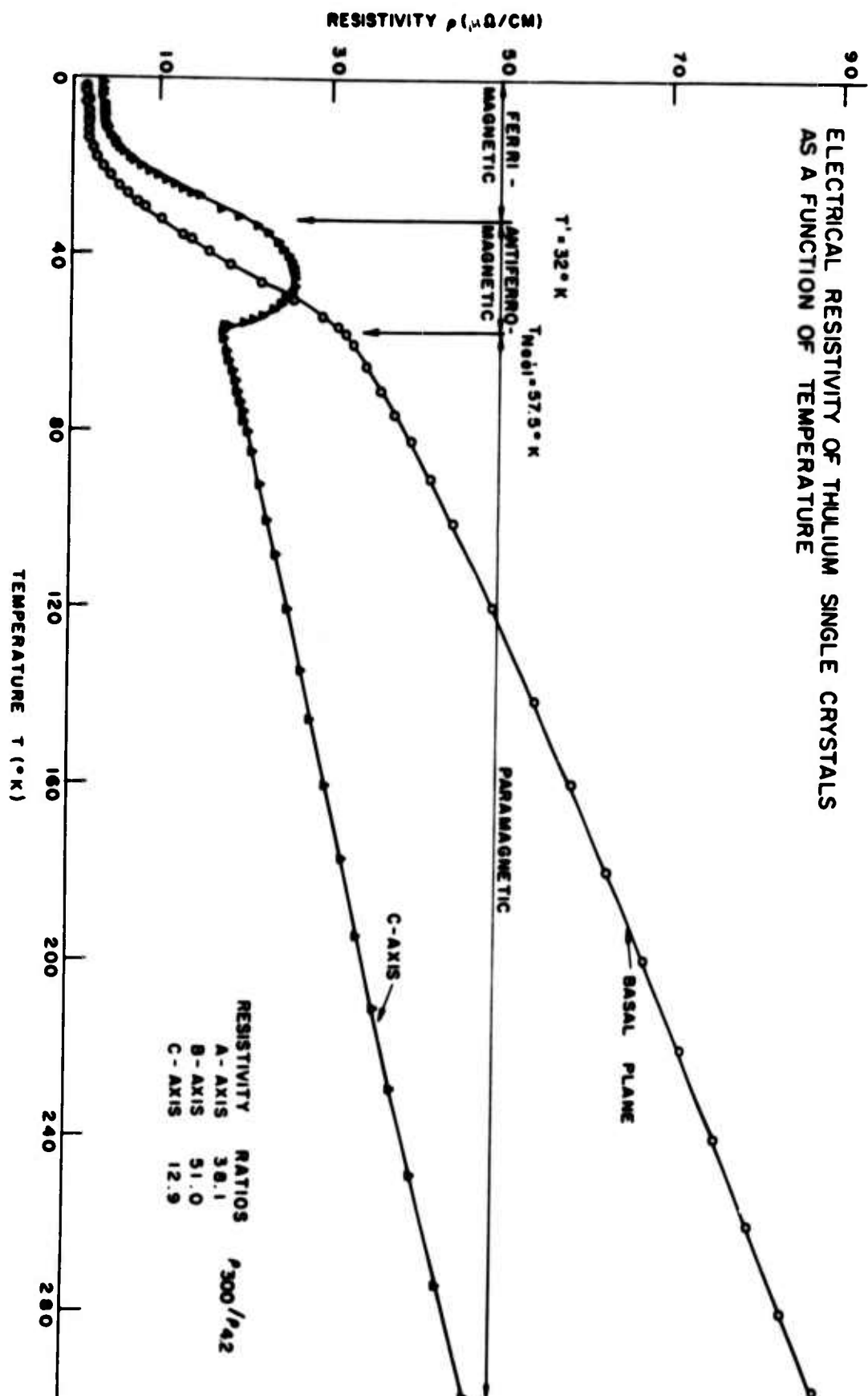
Fig. 1.
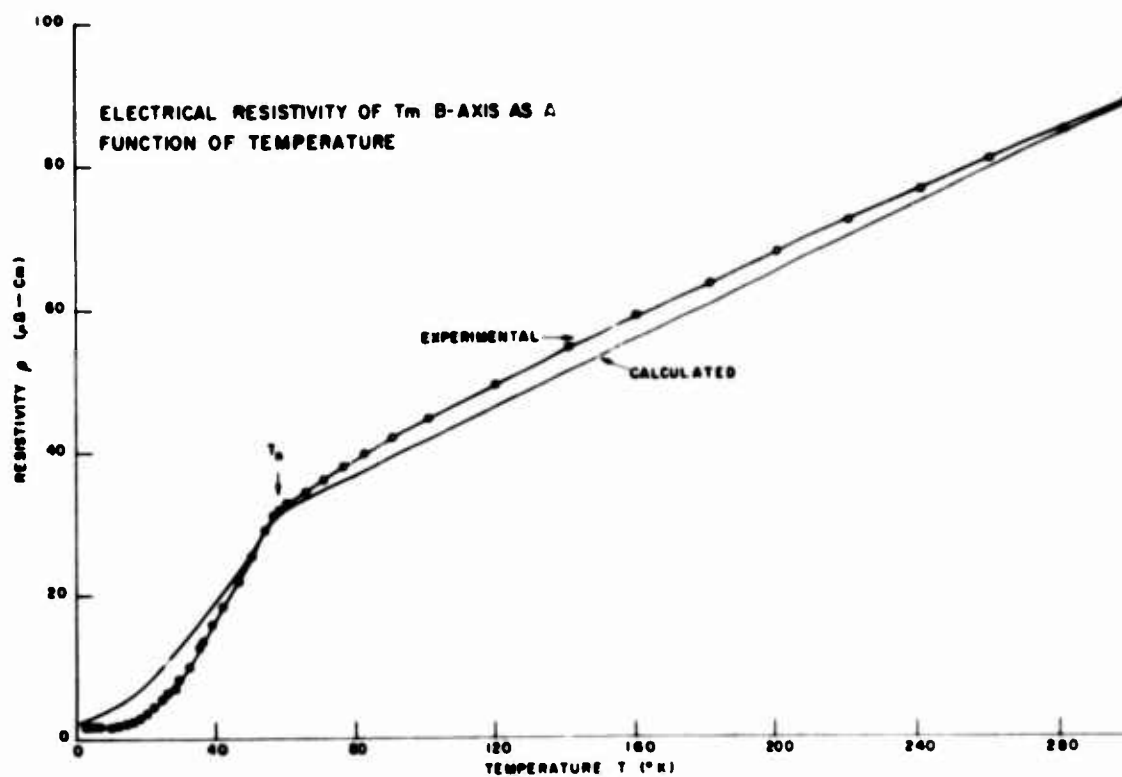
Fig. 2A.
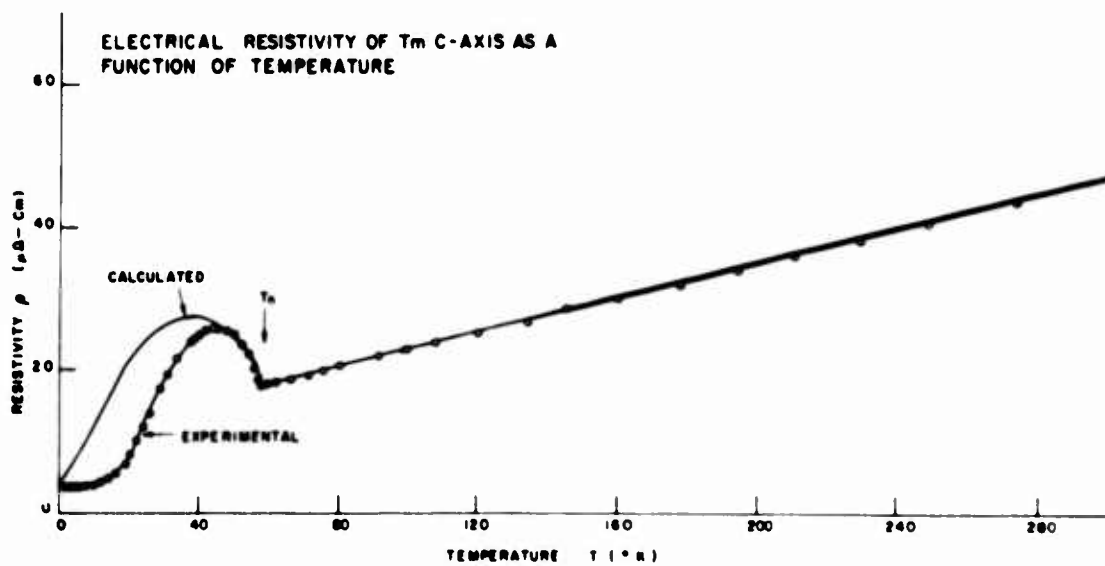
Fig. 2B.

ABSOLUTE SEEBECK COEFFICIENTS OF THULIUM
SINGLE CRYSTALS AS A FUNCTION OF TEMPERATURE
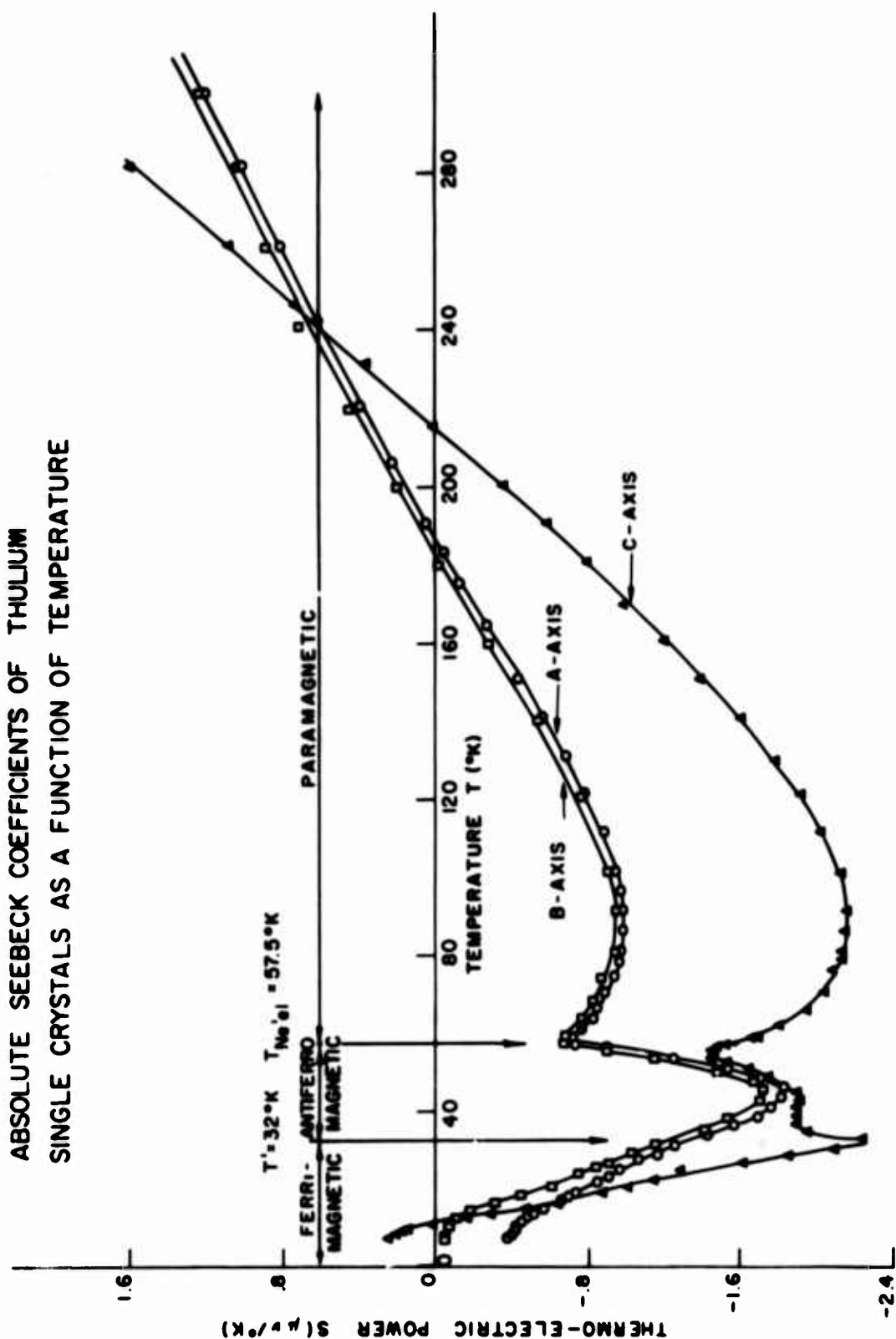
STRUCTURE ELECTRONIQUE DES MONOCARBURES DE TERRES RARES

par R. LALLEMENT

C.E.N.F.A.R. France

Résumé : Nous avons étudié la résistivité électrique, le pouvoir thermoélectrique, la susceptibilité magnétique et la chaleur spécifique électronique des carbures de terres rares.

L'analyse des résultats conduit à adopter une structure de bande pour les carbures déduite très simplement de la structure de bande des métaux.

I - INTRODUCTION.

La structure électronique des composés interstitiels comme les hydrures, les borures, les carbures et les nitrures, fait l'objet de nombreuses études, tant théoriques que pratiques. [1 à 5]. Plusieurs théories peuvent être avancées à leur sujet et les expériences ne permettent pas de choisir entre elles avec certitude. Ces composés, généralement cubiques à faces centrées, fragiles, à haut point de fusion, sont-ils caractérisés par de fortes liaisons covalentes entre métal et métalloïdes ? [1, 2]. Ces corps, généralement bons conducteurs de l'électricité et de la chaleur, à l'éclat métallique, sont-ils plutôt caractérisés par de fortes liaisons entre les atomes métalliques ? [3, 4, 5].

A la suite de nos études sur les propriétés électriques et magnétiques des monocarbures de terres rares [6], il nous a semblé utile d'examiner dans quelle catégorie ces carbures se plaçaient.

II - EXISTENCE DES MONOCARBURES.

Nous n'insisterons pas sur les méthodes de carburation et frittage classiques que nous avons utilisées [7]. Rappelons

simplement que, si le diagramme terres-rares carbone n'est
pas encore établi de façon absolue, certains points peuvent
être considérés comme sûrs :

- les monocarbures de La, Ce, Nd, Pr n'existent pas $\underline{/}\bar{8}, \underline{9}\underline{/}$

- en plus du dicarbure et du sesquicarbure, il existe deux
types de monocarbures $\underline{/}\bar{6}, 10, 1\underline{1}\underline{/}$: - l'un est cubique à fa-
ces centrées, de formule MC_x - l'autre est dérivé du premier
par une mise en ordre des atomes de carbone; sa formule est
M_2C. Il est rhomboédrique $\underline{/}\bar{1}\underline{2}\underline{/}$.

III - ETUDE DES PROPRIETES PHYSIQUES.

Nous avons étudié les deux types de carbure sans rencontrer
de différences fondamentales dans les propriétés physiques.
Il est vraisemblable que le modèle de structure électronique
auquel nous aboutirons est valable pour les carbures MC_x
comme pour les carbures M_2C.

Nous examinerons successivement les résultats des mesures de
résistivité, de pouvoir thermoélectrique, de susceptibilité
magnétique et de chaleur spécifique électronique, dans la me-
sure où ces expériences donnent des renseignements qualita-
tifs ou quantitatifs sur la structure électronique des car-
bures.

1°. Résistivité.

Les résistivités sont de type métallique pour les corps étu-
diés, elles présentent toutes des anomalies caractéristiques
des transitions ordre-désordre magnétique. L'analyse des
courbes de résistivité, dont l'allure générale est celle de
la figure 1, est classique $\underline{/}\bar{1}\underline{3}\underline{/}$. On peut tirer des résultats
une valeur pour la résistivité résiduelle ρ_i, une valeur de
la résistivité magnétique ρ_m, une valeur de la résistivité
due aux phonons ρ_{ph}, une température de transition approxi-

mative T_c. Pour certains des carbures, nous noterons l'existence d'un maximum de la résistivité au voisinage de la température T_c.

L'ensemble des résultats est porté dans le tableau 1.

Nous noterons trois points :

a) la résistivité est de type métallique

b) les résistivités dues aux phonons $\dfrac{d\rho_p}{dT}$ sont fortes et analogues à celles des métaux (tableau 1, colonnes 4 et 5)

c) les résistivités magnétiques sont voisines de celles des métaux

	Sm	Gd	Dy	Ho	Er
ρ_m carbure	45	110	75-90	45-55	45-50
ρ_m métal	30	106	58	32	24

2°. Pouvoir thermoélectrique.

Les pouvoirs thermoélectriques sont forts et négatifs. Ils présentent des anomalies assez nettes au voisinage des températures de transition T_c, comme le montre la figure 2.

Nous avons rassemblé dans le tableau 2 l'ensemble des résultats ainsi obtenus. La valeur du changement de pente à la température T_c est intéressante, car elle se prête à un calcul théorique, comme nous le verrons plus loin.

3°. Susceptibilités magnétiques.

D'une façon générale la susceptibilité magnétique des carbures suit bien, au moins à température suffisamment haute, une loi de Curie-Weiss $\chi = \dfrac{C}{T-\theta}$, et les moments que l'on déduit

des constantes de Curie sont en bon accord avec les valeurs calculées pour des ions libres (tableau 3). Les seules exceptions sont le carbure de samarium et le carbure d'ytterbium. Pour le premier, on sait que pour l'ion Sm^{3+} l'écart entre le multiplet fondamental et le premier multiplet excité n'est pas grand devant kT et qu'en conséquence les susceptibilités ne suivent pas la loi de Curie-Weiss $\underline{/14/}$. Pour le second, la faible valeur du moment déduit des constantes de Curie laisse supposer la présence d'un certain pourcentage d'ions divalents.

La figure 3 met en évidence à quel point les valeurs de θ pour les carbures sont voisines de celles des métaux.

Le tableau 3 montre que les températures θ diminuent quand la teneur en carbone augmente.

4°. Chaleur spécifique électronique.

Nous avons, enfin, mesuré la chaleur spécifique électronique γ de plusieurs carbures de terres rares (fig. 4).

Nous avons trouvé des valeurs de γ fortes : 5 à 6 $mj/mole°K^2$ voisines de celles des métaux (8 à 10 $mj/mole°K^2$).

IV - INTERPRETATION

Nous avons maintenant à notre disposition tous les éléments pour faire une détermination semi-qualitative de la structure de bande des carbures.

Deux résultats sont très nets :

a) la densité d'état est certainement forte, du même ordre que celle des métaux (cf valeurs de γ)

b) les carbures ressemblent beaucoup aux métaux (résistivités magnétiques, résistivités dues aux phonons, températures $θ_p$).

Il est donc très tentant de donner aux carbures une structure de bandes analogue à celle des métaux :

classiquement la structure de bandes des métaux des terres rares se décrit ainsi : c'est une bande hybride s-d, contenant trois électrons presque libres de masse effective m* $\simeq$ 3 $\overline{\angle 15 \angle}$

En second lieu nous pourrons adopter, pour décrire les couplages magnétiques, le modèle antérieurement proposé par de Gennes dans le cas des métaux de terres rares $\angle \overline{16}, 1\underline{7}\angle$. Dans ce modèle les ions de terres rares trivalents sont couplés entre eux par l'intermédiaire d'environ 3 électrons de conduction de masse effective voisine de 3 masses électroniques, la fonction de couplage étant la fonction oscillante de Ruderman-Kittel : $F(x) = \dfrac{x \cos x - \sin x}{x^4}$.

Avec ces deux hypothèses de travail, nous pouvons analyser rapidement les résultats expérimentaux obtenus pour les carbures.

1°) Résistivités magnétiques.

Nous avons vu plus haut que nous pouvions tirer des résultats expérimentaux une contribution magnétique ρ_m à la résistivité.

Au dessus de T_c, ρ_m tend vers la valeur ρ_{mo} indépendante de la température. Au voisinage de T_c, on observe une légère anomalie qu'il nous semble raisonnable d'attribuer aux effets de l'ordre local. Si on se limite aux interactions entre ions magnétiques plus proches voisins, il a été montré que l'on a, pour une structure cubique à faces centrées $\angle \overline{13}, 1\underline{5}\angle$

$$\frac{\rho_m (T_c)}{\rho_{mo}} = 1 + \frac{4}{3} f (k_F d)$$

d est la distance entre ions magnétiques plus proches voisins et la fonction $f (k_F d)$ est représentée figure 5.

Des valeurs expérimentales de $\dfrac{\rho_m(T_c)}{\rho_{mo}}$ on déduit que k_F d ne peut prendre que des valeurs voisines de 2, de 4, ou de 5,5.

2°) <u>Pouvoir thermoélectrique</u>. Dans le même modèle, on montre que le pouvoir thermoélectrique subit un changement de pente au voisinage de T_c /15/ avec

$$\left(\frac{dS}{dT}\right)_{T > T_c} - \left(\frac{dS}{dT}\right)_{T < T_c} = -\frac{19}{8}\ \frac{\pi^2 k_B^2}{e}\ \frac{k_F d}{E_F}\ \frac{d(f(k_F d))}{d(k_F d)}$$

Les changements de pente observés expérimentalement sont positifs. Parmi les valeurs possibles de k_Fd nous ne retiendrons donc que celles qui rendent $\dfrac{d(f(k_F d))}{d(k_F)}$ négatif, soit k_F d $\sim$ 2 et k_F d $\sim$ 5,5. Mais de faibles variations de k_Fd au voisinage de la valeur 2 entraîneraient de fortes variations du rapport $\dfrac{\rho_m(Tc)}{\rho_{mo}}$. Expérimentalement on constate que ce rapport n'est guère sensible à la teneur en carbone. Dès lors, la valeur k_Fd $\sim$ 5,5 semble la plus probable. Le nombre d'électrons de conduction par atome métallique serait alors $\xi = 3,5$ à 4.

3°) <u>Températures de Curie</u>. Nous avons vu que les températures de Curie paramagnétiques θ_p sont très voisines de celles des métaux et qu'elles décroissent quand la teneur en carbone augmente. Les théories développées à propos des métaux de terres rares donnent /16/ :

$$k_B\ \theta_p = -\frac{3\pi}{4}\ \xi^2\ \frac{\Gamma^2 (g_J - 1)^2}{v^2\ E_F}\ J\ (J+1)\ \sum_j F\ (k_F\ R_{oj})$$

On s'attend à ce que la constante de couplage Γ varie peu dans la série et qu'elle soit sensiblement égale à la valeur qu'elle prend dans les métaux /16/. Dans ces conditions les variations de θ_p avec la teneur en carbone sont principalement commandées par la variation de la quantité $\xi^2 \sum_j F\ (k_F\ R_{oj})$. La somme $\sum_j F\ (k_F\ R_{oj})$ a été calculée pour un réseau cubique à faces centrées /6, 18/. Elle s'annule pour $k_F d = 3,5$, ce

qui correspond à $\xi = 3,7$. L'extrapolation de la courbe expérimentale qui donne la variation de θ_p avec la teneur en carbone pour les carbures d'holmium donne $\theta_p = 0$ pour le composé de formule Ho $C_{0,7}$. Sachant que, dans le métal pur, $\xi = 3$, <u>tout se passe donc comme si chaque atome de carbone cédait un électron à la bande de conduction du métal</u>. On prévoit alors que θ_p doit diminuer quand on passe de Ho $C_{0,4}$ à Ho $C_{0,7}$, ce qui est conforme à l'expérience.

Dans le cas particulier du carbure Ho $C_{0,5}$ on trouve alors $\xi = 3,5$ soit $k_F d = 5,30$. Pour cette valeur de $k_F d$ la théorie prévoit un changement de pente du pouvoir thermoélectrique à T_c de l'ordre de $+ 0,05 \times 10^{-8}$ volt deg^{-2}, en bon accord avec l'expérience. On peut encore calculer la somme $\sum_j F (k_F R_{oj})$ et, à partir des deux équations

$$k_B \theta_p = - \frac{3\pi}{4} \xi^2 \frac{\Gamma^2 (g_J - 1)^2}{v^2 E_F} J(J+1) \sum_j F(k_F R_{oj})$$

$$\text{et} \quad \rho_{mo} = \frac{3\pi}{8} \frac{m^*}{He^2} \frac{\Gamma^2 (g_J - 1)^2 J(J+1)}{V E_F}$$

les valeurs expérimentales de ρ_{mo} et θ_p permettent de déterminer les quantités m^* et Γ. On trouve

$$\begin{cases} m^* = 2,3 \text{ masses électroniques} \\ \Gamma = 9,6 \text{ eV.Å}^3 \end{cases}$$

Dans l'holmium pur les valeurs de ces paramètres sont voisines $\overline{/11/}$:

$$\begin{cases} m^* = 3 \text{ masses électroniques} \\ \Gamma = 6 \text{ eV.Å}^3 \end{cases}$$

4°) <u>Chaleur spécifique électronique</u>. Dans le modèle simple qui ressort de ces considérations, l'insertion de carbone

dans la matrice métallique a pour principale conséquence d'augmenter la population de la bande de conduction du métal. L'expérience donne $\gamma \sim 10$ mJ x mole^{-1} x deg^{-2} pour les métaux de terres rares et $\gamma \sim 6$ mJ x mole^{-1} x deg^{-2} pour les carbures.

A partir de ces données expérimentales on peut encore obtenir une nouvelle estimation de m* dans les carbures. En effet γ est proportionnel à $\xi^{1/3}$ m*. Si on adopte les valeurs $\xi = 3$ et m* = 3 pour le métal et $\xi = 3,5$ pour le carbure, on obtient m* = 1,8 pour le carbure en assez bon accord avec la valeur m* = 2,3 obtenue précédemment.

Si l'on se réfère, d'autre part, aux plus récents calculs de la structure de bande du gadolinium métallique $\underline{/19/}$, d'après lesquels la structure de bande est analogue à celle d'un métal de transition, avec une bande d étroite chevauchant une large bande s au niveau de Fermi, on peut constater que l'augmentation du nombre d'électrons dans la bande d conduit à une diminution de la densité d'états en accord avec nos mesures de γ.

V - CONCLUSION

Au total, l'ensemble des résultats expérimentaux que nous avons décrits s'interprètent bien dans le cadre d'un modèle très simple :

La structure de bande des carbures et celle des métaux sont très voisines. On peut les décrire classiquement comme une bande hybride s-d où les électrons de conduction ont une masse effective de 3 masses électroniques environ. Le nombre d'électrons de conduction augmente lorsque l'on passe du métal au carbure, le carbone cédant environ 1 électron par atome à la bande de conduction. Les liaisons restent de type métallique

ce qui n'est pas trop surprenant, étant donné que le nombre
d'atomes de carbone en insertion reste relativement faible.

Les couplages magnétiques dans les carbures sont, comme pour
les métaux, des couplages indirects par les électrons de con-
duction, et les conclusions simples auxquelles nous avons
abouti permettent de comprendre dans leurs grandes lignes les
propriétés magnétiques.

Il est vraisemblable que cette description est en fait trop
simple et que, comme pour les métaux, les calculs de structu-
re de bande conduiraient plutôt à une structure voisine de
celle des métaux de transition.

Quoi qu'il en soit l'analogie entre les carbures et les mé-
taux de terres rares et la nature métallique des liaisons
dans ces composés nous semble bien établie.

BIBLIOGRAPHIE

1) BILZ H.,   Z. für Phys. $\underline{153}$, 338, (1958)

2) RUNDLE R.E. Acta cryst. I; $\underline{180}$, (1948)

3) DEMPSEY E. Phil. Mag. $\underline{8}$, 285, (1963)

4) ERN. V. et SURTENDICK A.C. Phys. Rev. $\underline{137\ A}$., 1927,
              (1965)

5) COSTA P. et CONTE R.E.
   International symposium on compounds of interest
   in nuclear reactor technology. Boulder (1964)

6) LALLEMENT R. Thèse Orsay 1966
        Rapport CEA 1966. R.3043

7) PASCARD R. 4th Plansee Seminar, Juin 1961

8) SPEDDING F.H., GSCHNEIDNER K., DAANE A.H.
    J. Amer. Chem. Soc. $\underline{80}$, 4499, (1958)

9) PALENICK G.J. Thèse UCCLA (1960)

10) CHUBB W. et KELLER D.L.
    Symposium on carbides in nuclear energy.
    Harwell (1963)

11) DEAN G., LALLEMENT R., LORENZELLI R., PASCARD R.
    C.R. Acad. Sc. Paris, $\underline{259}$, 2442, (1964)

12) BACCHELLA G.L., MERIEL P., PINOT M., LALLEMENT R.
    Bull. Soc. Franc. Miner. Crist. LXXXIX, 226,
              (1966)

13) DE GENNES P.G. et FRIEDEL J.
    J. Phys. Chem. Solids, $\underline{4}$, 71, (1958)

14) VAN VLECK J.H. et FRANCK A.
    Phys. Rev. $\underline{34}$, 1494, (1929)

15) ROCHER Y.A. Adv. in. Physics. $\underline{11}$, 43, (1962)

16) DE GENNES P.G. C.R. Ac. Sc. $\underline{247}$, 1836, (1958)

17) DE GENNES P.G.
    J. Phys. Radium. $\underline{23}$, $\underline{630}$, (1962)

18) MATTIS D., ANTHONY N. et HORWITZ L.
I.B.M. Research report RC. 945 (1963)

19) DIMMOCK et FREEMAN
Phys. Rev. Letters $\underline{13}$, 25, 750, (1964)

- **tableau 1 -**

	P_m	P_i	T_c	$\dfrac{d\rho_o}{dT}$	$\dfrac{d\rho_o}{dT}$ métal	$(\dfrac{d}{dT})_{T_c}$	ordre local
Sm C_x + traces de Sm_2C_3	45	85	35	$28\ 10^{-2}$		1,45	non
Gd C_x + traces de métal	105	36	400	$25\ 10^{-2}$		0,38	oui
Gd C_x + traces de métal	60	110	400	$6\ 10^{-2}$	$7,5\ 10^{-2}$	0,26	oui
Gd $C_{0,5}$	110	60	400	$12\ 10^{-2}$		0,28	oui
Dy $C_{0,35}$	90	40	160	$23\ 10^{-2}$	$12\ 10^{-2}$	0,62	oui
Dy C	75	75	165	$30\ 10^{-2}$		0,66	non
Ho $C_{0,35}$	55	150	70-80	$23\ 10^{-2}$	$13\ 10^{-2}$	0,70	oui
Ho_2 C	45	90	90	$22\ 10^{-2}$		0,53	non
Er $C_{0,4}$	50	80	50	$23\ 10^{-2}$	$20\ 10^{-2}$		oui
Er_2C	45	65	70	$24\ 10^{-2}$		0,86	non

- tableau 2 -

	S 300°K $\mu V/°K$	S métal $\mu V/°K$	$(\frac{dS}{dT})Tc$ $\mu V/°K^2$	Tc
Sm $C_{0,65}$ + traces $Sm_2 C_3$	- 7	+ 1	+ 0,04	25°K
Gd $C_{0,4}$ Gd_2C	- 6 - 7	- 2	+ 0,02	330°K
Dy $C_{0,4}$ Dy_2C	- 3,5 + 1,5	- 2	+ 0,05 + 0,07	135°K 140°K
Ho_2C	- 7	- 2	+ 0,07	100°K
Er $C_{0,4}$ Er_2C	- 7 - 14	- 1	+ 0,09 + 0,08	30°K 80°K

- tableau 3 -

Carbures	Θ	moment expérimental	moment théorique
Gd $C_{0,35}$ Gd $C_{0,65}$	373°K 313°K	pas mesuré	
Dy_2 C	175°K	11.3	10.6
Ho $C_{0,5}$ Ho $C_{0,65}$ Ho_2 C	75°K 17 °K 105°K	10.9 9.5 10.5	10.6
Er $C_{0,35}$ Er $C_{0,45}$	24°K 0°K	7.5 8.5	9.6

- figure 1 -
. . . .
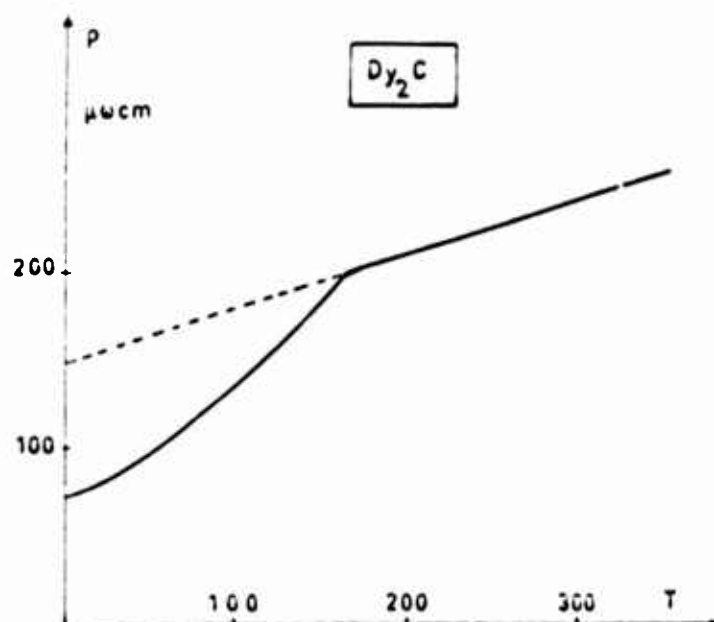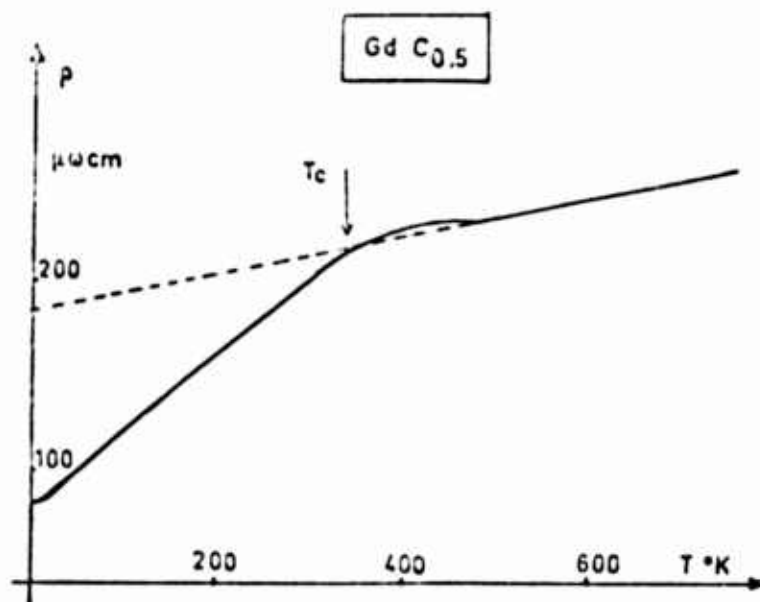
- figure 2 -
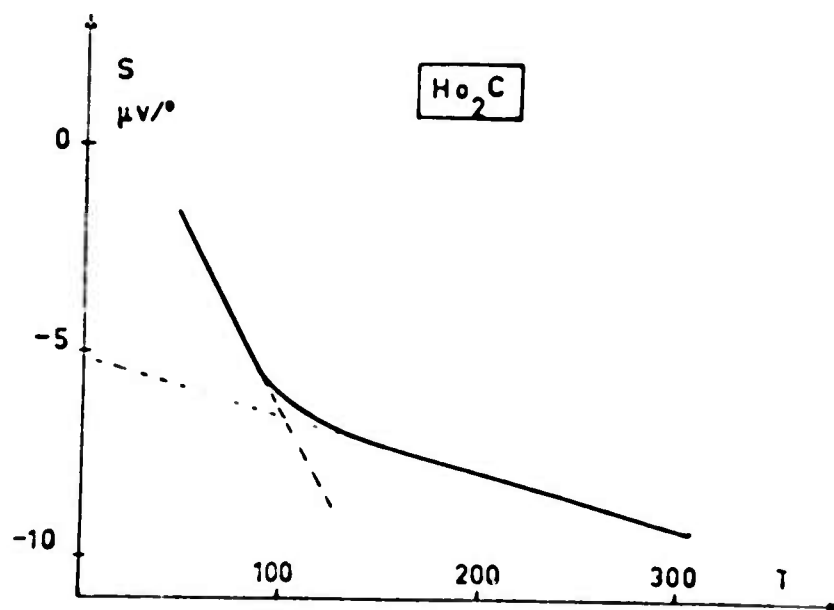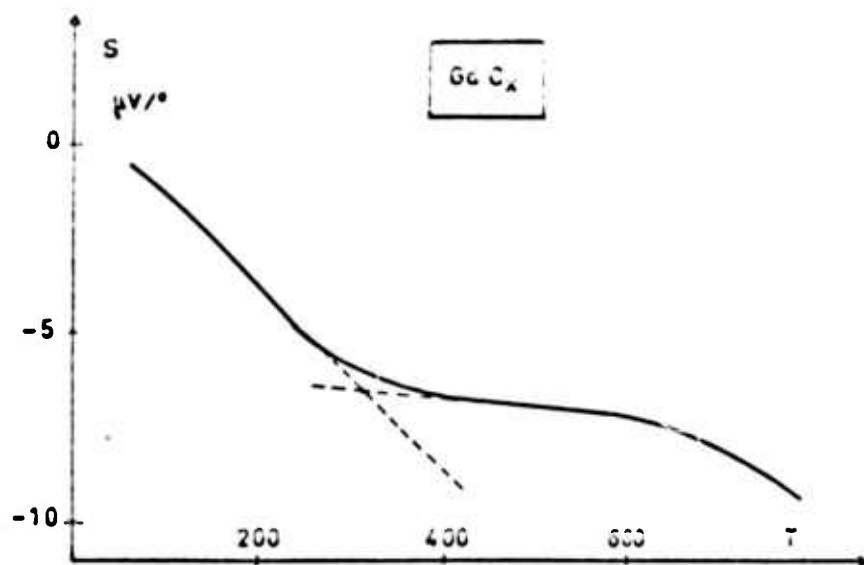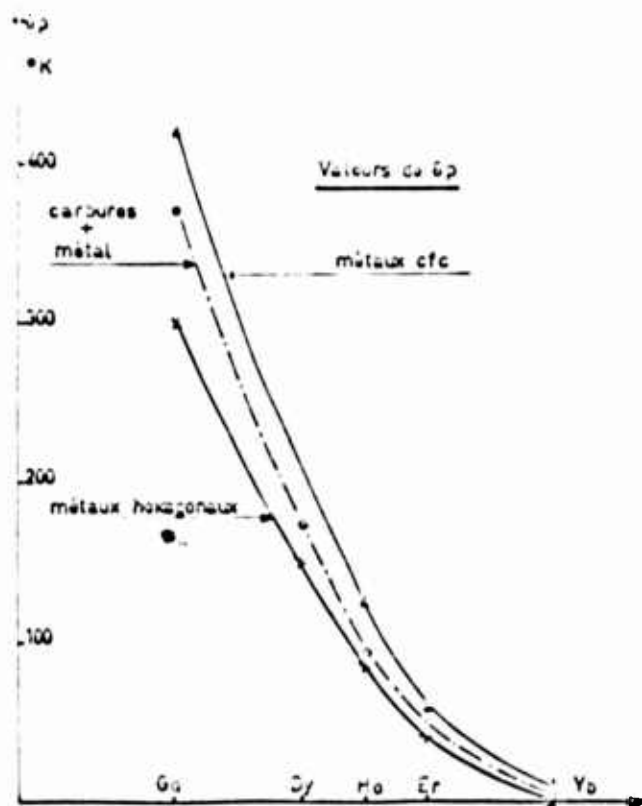
- figure 4 -
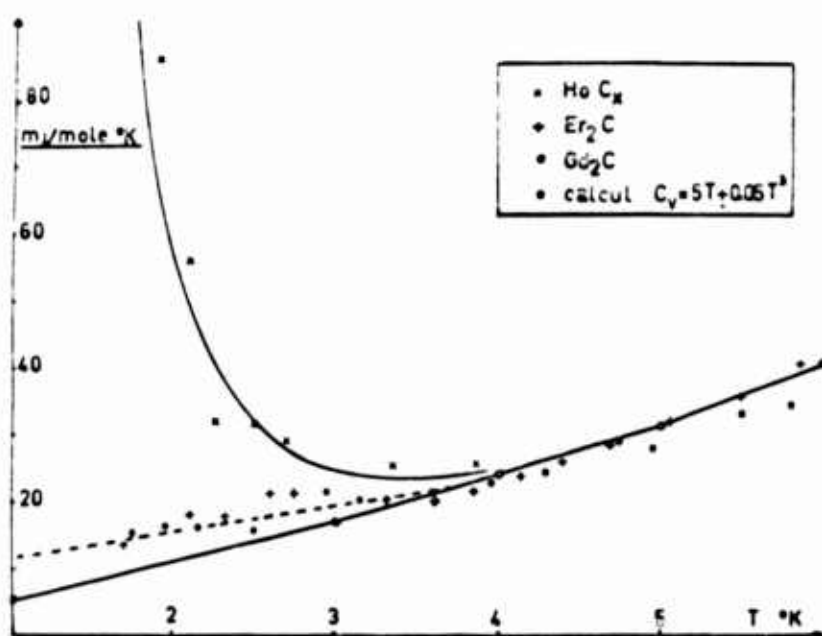
- figure 5 -
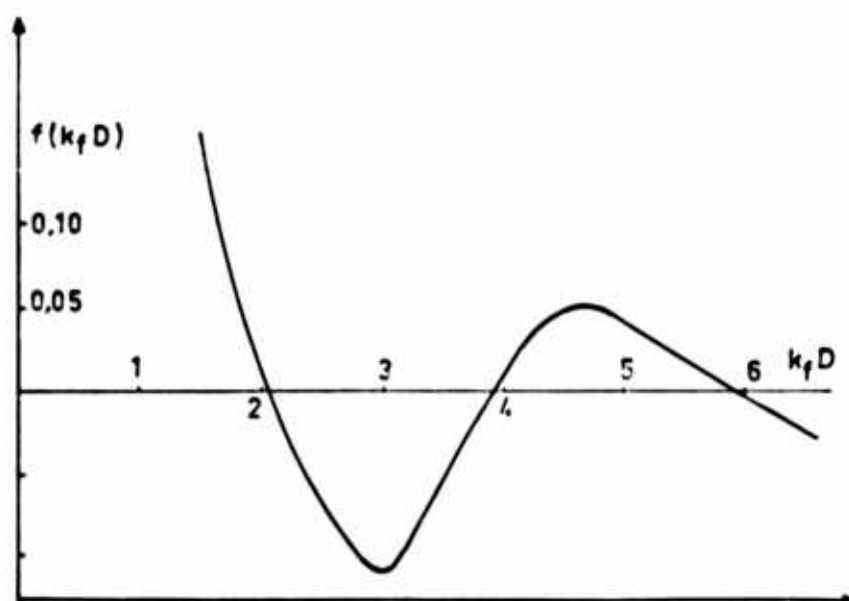
CHEMICAL ASPECTS OF INDUSTRIAL PREPARATION OF THE RARE EARTH METALS

by

J. L. Moriarty
Lunex Co., P isant Valley, Iowa

ABSTRACT

This paper is intended to be a review covering more than ten years experience with the industrial process chemistry involved in producing rare earth metals. Fluoride and chloride preparatory methods are discussed along with tabular presentations of some physical property data. Metallothermic reduction techniques as applied to both processes are shown. Also a comparison of representative metal microstructures and analyses is made. Employing the chloride process one can expect oxide conversions in excess of 97 per cent and yields of recovered metal to range from 77 to 86 per cent of theoretical. Average typical Spectrographic and gas analyses indicate that a final product purity of 99.9+ per cent is common for the metals prepared. The thermodynamic and vapor pressure characteristics of several of the rare earths permits direct reduction of their oxide to metal. High purity metals behave nicely and can be readily cast, rolled and machined under the appropriate conditions. In producing the rare earth elements on a commercial scale numerous factors such as optimum purity, availability, marketability, demand, economics, and equipment requirements must be carefully considered.

THE FLUORIDE PROCESS

For a number of years rare earth fluorides have been employed as the reactant salts in the preparation of free rare earth elements. Advantages of their use are stability in air, ease of preparation from the oxides and quantitative reduction to the metals.

There are four primary procedures for hydrofluorination (1).

I - Direct reaction of R_2O_3 with anhydrous HF

$$R_2O_3 + 6HF \xrightarrow{700^\circ C} 2RF_3 + 3H_2O$$
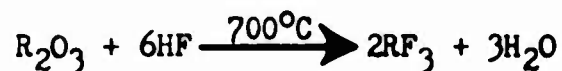
Rotary batch, fluidized bed and vibrating tray methods have all been successful with reported conversions in excess of 99 per cent.

II - Direct reaction of R_2O_3 with $NH_4F \cdot HF$

$$R_2O_3 + 6NH_4F \cdot HF \xrightarrow{300^\circ C} 2RF_3 + 6NH_4F + 3H_2O$$
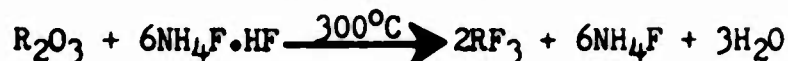
This is a batch process carried out in a platinum boat inside an Inconel chamber with conversions as high as 99.99 per cent.

III - Precipitation of RF_3 from aqueous solution

$$R_2O_3 + 6HCl \text{ (aq.)} \longrightarrow 2RCl_3 \cdot XH_2O \qquad X \text{ usually} = 6$$

$$RCl_3 \cdot XH_2O + HF \overset{48\%}{\text{(aq.)}} \longrightarrow RF_3 \cdot X'H_2O \qquad X' \text{ is } 1/2 \text{ to } 1$$

$$RF_3 \cdot X'H_2O \xrightarrow[600^\circ C \text{ in HF gas}]{300^\circ C \text{ in Vacuo}} RF_3 + X'H_2O$$
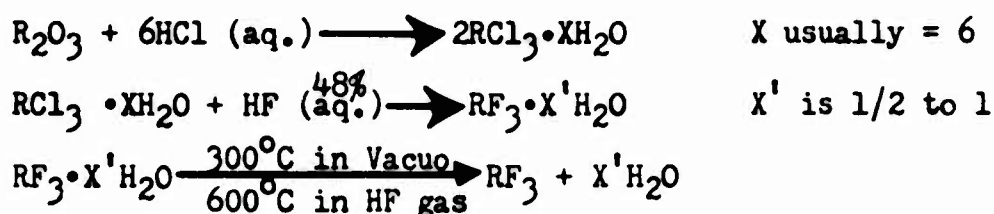
This is also a batch method, but more complex than the two previous procedures since it involves precipitation and dehydration.

IV - Molten - Salt purification of RF_3

$$RF_3 \cdot 1/2H_2O \xrightarrow[\substack{1000^\circ C \text{ bubble} \\ \text{in HF gas}}]{LiF} RF_3 - LiF \text{ (fused mixture)} + 1/2H_2O$$
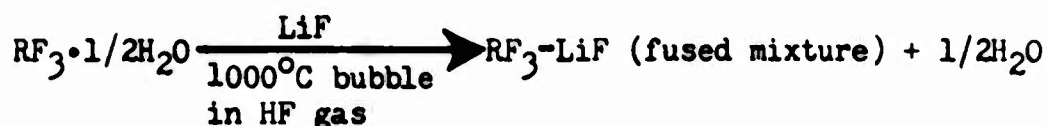
The lower melting salt mixture is purified in a large platinum crucible and cast into a suitable mold, with the dehydration 99 per cent or better completed.

These preparative procedures have been widely accepted for producing large quantities of rare earths, in particular yttrium. Some physical property data for the fluorides are shown in Table I. On occasion methods I and II were followed for relatively small production lots. The Fluoride Process Flowsheet (Figure 1.) displays the scheme used by ourselves for metallothermic reductions of rare earths prior to 1959. Ingots of the rare earth metals thus produced represented yields 95 to 97 per cent of theorical.

It was our experience that the rare earth fluorides could not be completely dehydrated for industrial scale operations. Consequently

TABLE I

Some Physical Properties of Rare Earth Trifluorides

Compound	Appearance[1]	Crystal[2] Structure	M.P.(°C)[1]	Trans. Temp.(°C)[2] Hex - Ortho
YF_3	White	Dimorp.	1152	1052
LaF_3	White	Hex	1493	none
CeF_3	White	Hex	1430	none
PrF_3	Green	Hex	1395	none
NdF_3	Violet	Hex	1374	none
SmF_3	White	Dimorp.	1306	555
EuF_3	White	Dimorp.	1276	700
GdF_3	White	Dimorp.	1231	900
TbF_3	White	Dimorp.	1172	950
DyF_3	Light Green	Dimorp.	1154	1030
HoF_3	Brownish Pink	Dimorp.	1143	1070
ErF_3	Pink	Dimorp.	1140	1075
TmF_3	White	Dimorp.	1158	1030
YbF_3	White	Dimorp.	1157	985
LuF_3	White	Dimorp.	1182	945

during the reduction a hydrolysis product (oxyfluoride) would form. This compound along with unconverted oxide remained dispersed throughout the metal as a deleterious non-metallic inclusion.

THE CHLORIDE PROCESS

Due to the rare earths great chemical affinity, especially for non-metallic elements and metalloids, impurity elements easily contaminate them. Subsequent purification is very difficult, if not impossible in some cases. It is therefore, judicious to exercise considerable care during all stages of rare earth metal production.

The reduction of yttrium trichloride by lithium to yield a pure crystalline product was initially developed at General Electric-ANPD(3). The process was studied in detail by the U.S. Bureau of Mines (Albany, Oregon) and by ourselves. The method used in preparing anhydrous rare earth chlorides is that reported by Reed, et.al. (4).

$$R_2O_3 + 6NH_4 \, Cl \xrightarrow{350^{\circ}C} 2RCl_3 + 3H_2O + 6NH_3$$
$$\text{(excess)}$$

Employing this procedure conversions of 97 to 99.9 per cent are readily obtained.

Although the trichlorides have the distinct disadvantage of being very hydroscopic, this problem can be largely overcome by handling the materials hot, in lump form, and shielded from the atmosphere. Purification of these lower melting chlorides can be accomplished by _in situ_ distillation prior to reduction to metal. The vapor pressures and some physical properties of the chlorides are given in Table II. The Chloride Process Flowsheet is shown in Figure 2 and represents the method used for metallothermic reductions. Yields of recoverable crystal sponge range

TABLE II

Some Physical Properties Rare Earth Trichlorides

Compound	Appearance[8]	Crystal[5][6] Structure	M.P.(°C)[7]	Temp °C @ 2 torr[8] Vapor Pressure
YCl_3	White	Mono	709	975
$LaCl_3$	White	Hex	862	997
$CeCl_3$	White	Hex	817	1125
$PrCl_3$	Green	Hex	786	1085
$NdCl_3$	Violet	Hex	758	1106
$SmCl_2$	Brown	----	562	1229
$EuCl_3$	Yellow	Hex	623[8]	930
$GdCl_3$	White	Hex	602	995
$TbCl_3$	White	----	582	1068
$DyCl_3$	Yellow Green	Mono	647	939
$HoCl_3$	Rose Brown	Mono	705[8] 720	953
$ErCl_3$	Pink	Mono	760[8] 824	1076
$TmCl_3$	Light Green	Mono	830[8] 865	925
$YbCl_3$	White	Mono	860[8]	1039
$LuCl_3$	White	Mono	925	959

from 77 to 86 per cent of theorical values depending upon the rare
earth being produced.

Microstructures of yttrium arc-melted ingots made by both the
fluoride and chloride processes are compared in Figure 3. Photo A
shows lower purity metal prepared from slightly hydrated YF_3 via a
lithium-magnesium alloy contact reduction. Photo B shows high purity
metal prepared from anhydrous YCl_3 via a lithium vapor reduction.
Major impurity element analyses of the two metal ingots are given in
Table III. In our experience, metals made by the chloride process
represent a substantial improvement over those produced by the fluoride
method.
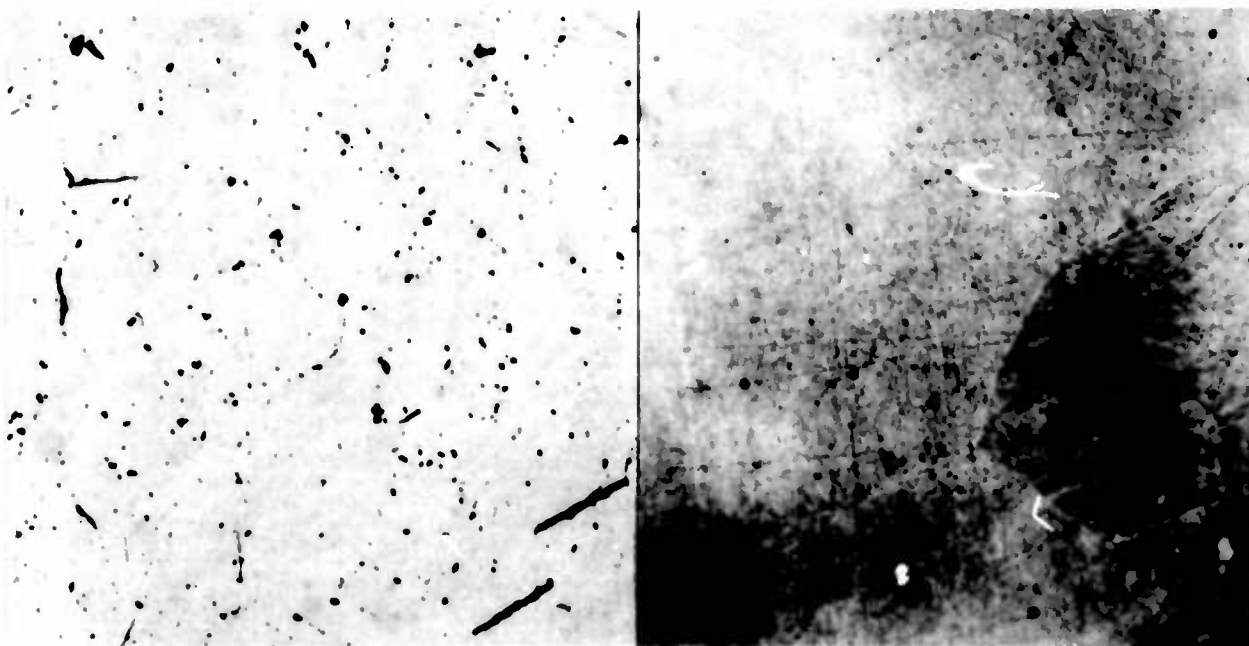
PHOTO A - as polished R-54, 100X   PHOTO B - as polished R-61, 100X

FIGURE 3 - Microstructures of yttrium ingots

TABLE III

Yttrium Ingot Analyses (ppm)

	C	S	Mo	Kjel. N_2	Leco O_2
R-54	21	5	47	37	2650
R-61	ND	ND	trace	27	370

DIRECT REDUCTION

The above metallothermic reductions do not work for samarium, europium and ytterbium because lower valent halides form (RX_2); these will not quantitatively reduce with either lithium or calcium. The volatility of some of the heavier rare earths suggested that these elements could be prepared directly from their oxides by reduction-sublimation with lanthanum (9), thereby eliminating the reduction of the halides. Rare earth oxides are blended with chips of lanthanum or vacuum purified misch metal and the mixture is reacted according to the Direct Reduction Flowsheet (Figure 4).

$$R_2O_3 + 2La \xrightarrow{\quad 1000^\circ - 1300^\circ C \quad} 2R\uparrow + La_2O_3$$
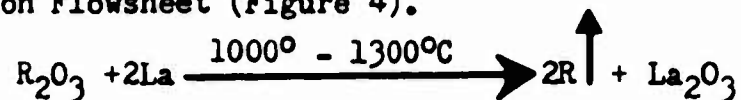
Information useful in establishing conditions for vacuum melting, purification, and distillation or sublimation of the rare earths can be found in a summary article by Gschneidner (10).

Since 1959 we have employed either the chloride process or direct reduction procedures to produce 99.9+ per cent pure (Nuclear Grade) rare earth metals. Table IV records average typical emission spectrographic analysis for tramp elements found in the end-product. Average typical gas analysis for the metals is given in Table V. Often during reduction the crystal sponge is not melted, therefore the rare earths in this form are consistantly the highest in purity.

PRODUCT HANDLING CONSIDERATIONS

The rare earths are either induction or arc-melted in a vacuum (10^{-4} torr) or under an inert gas blanket depending upon the melting point and vapor pressure of the particular element. Both tantalum and tungsten are suitable melting crucible materials and the metals can be cast into a variety of shapes in chilled copper molds. The success or failure realized in fabrication and forming the metals is largely dependent on the nature and quantity of the contained impurities. Rare earths of good purity (99.9 per cent) are easily cut with a hacksaw, free-machined with a lathe tool or milling cutter, and rolled into sheets at room or warm temperatures.

Caution should be exercised in the handling of rare earths to avoid their contamination and possible pyrophoric reactions. A good grade of mineral oil serves well to protect exposed metal surfaces from the atmosphere during machining. High flash point oil is also a satisfactory medium in which to store and ship the air corrodible metals, however a leak tight container filled with dry argon is recommended.

TABLE IV

RARE EARTH METAL

Average Typical Analysis (★)
(Spectrographic)

Element	ppm	Element	ppm
Aluminum	1*	Magnesium	5*
Beryllium	10*	Manganese	1*
Boron	50*	Nickel	1*
Cadmium	5*	Niobium	50*
Calcium	200**	Potassium	1*
Chromium	1*	Silicon	50*
Cobalt	1*	Sodium	5*
Copper	1*	Tantalum	10*
Iron	1*	Titanium	1*
Lead	10*	Vanadium	1*
Lithium	1*	Zinc	50*
		Zirconium	20*
Cerium	50*	Lutetium	5*
Dysprosium	5*	Neodymium	50*
Erbium	100*	Praseodymium	50*
Europium	5*	Samarium	5*
Gadolinium	5*	Terbium	50*
Holmium	50*	Thulium	5*
Lanthanum	10*	Ytterbium	50*

(★) - Representative 1960 to date

* - No persistant line was found, value reported is the detection limit.

** - Calcium reported as 200 ppm due to the electrode compartment containing Calcium bearing material.

TABLE V
RARE EARTH METAL (★)

Average Typical Analysis

(gases)

	Leco Oxygen ● (ppm)	Kjel. Nitrogen (☆) (ppm)
Yttrium Sponge	480	8
Ingot	782	20
Lanthan Ingot	588	8
Praseodymium Ingot	508	12
Neodymium Ingot	537	14
Samarium Ingot	300	20
Europium Ingot***	~1200	23
Gadolinium Sponge	409	3
Ingot	570	12
Terbium Ingot***	~1600	21
Dysprosium Sponge	503	7
Ingot	597	14
Holmium Sponge	225	3
Ingot	566	4
Erbium Sponge	413	3
Ingot	623	7
Thulium Ingot***	400	19
Ytterbium Ingot***	<500	<1
Lutetium Ingot***	>2000	38
Cerium Ingot***	<500	<1

(★) — Representative 1960 to date

● — Inert gas fusion

(☆) — Micro Kjeldahl - colorometric

*** — One ingot only

INDUSTRIAL PROCESS OPTIMIZATION

An excellent comprehensive report covering the rare earth industry appeared about one year ago (11). Insofar as the demand for high purity individual rare earth metals is concerned it has been, in recent years, largely confined to research applications. Scientists interested in conducting both fundamental and applied studies almost invariably require the best possible purity metals. Albeit the quantities are quite small by most industrial standards. The questions of availability and high price of several rare earths have occurred from time to time.

When one considers that only a limited number of applications have thus far been developed for these metals, it is little wonder that marketability remains a major problem. In this situation we must weigh the optimum purity of the product which can be obtained from well established routine production procedures, against new equipment expense and improved chemical and metallurgical process development costs. In other words, it would conceivably require considerable time and capital to prepare 99.999 per cent pure rare earths, and yet realize a final demand for only one pound or less of the product metals. It does not appear to be economically justified, at this juncture, for industrial producers to expend the necessary effort to achieve an ultimate purity product to meet every research requirement.

Investigations of electrowinning and electro-refining (1a) have been varied and interesting even though the preparation of a strictly high purity metal has been elusive. There are several important processes useful in end-product purification of some rare earths, these have been reviewed (10) or described in detail elsewhere (12, 13).

ACKNOWLEDGEMENT

REFERENCES

(1) Spedding, F.H. and Daane, A.H. ed. "The Rare Earths", 77, J. Wiley & Sons, Inc., New York, (1961).

(1a) Loc. Cit., 126 & 146.

(2) Thoma, R.E. and Brunton, G.D., Inorg. Chem., 5, no. 11, 1927, (1966).

(3) Nolting, H.J., Simmons, C.R., and Klingenberg, J.J., J. Inorg. & Nuclear Chem., 14, 208, (1960).

(4) Reed, J.B., Hopkins, B.S., and Andrieth, L.F., "Inorganic Synthesis", H.S. Booth, ed., Vol 1, 28, McGraw-Hill Book Co., New York, (1939).

(5) Templeton, D.H. and Dauben, C.H., J. Am. Chem. Soc., 76, 5237, (1954).

(6) Templeton, D.H. and Carter, G.F., J. Phys. Chem., 58, 940, (1954).

(7) Spedding, F.H. and Daane, A.H., Met. Rev., 5, 297, (1960).

(8) Moriarty, J.L., J. Chem. & Eng. Data, 8, no. 3, 422, (1963).

(9) Daane, A.H., Dennison, D.H. and Spedding, F.H., J. Am. Chem. Soc., 75, 2272, (1953).

(10) Gschneidner, Jr., K.A., "Trans. Vac. Met. Conf.", L. M. Bianchi, ed., 99, Amer. Vac. Soc., Boston, Mass., (1966).

(11) Special Report, Chem. & Engr. News, 43, 78, May 10, (1965).

(12) Williams, J.M. and Huffine, C.L., Nucl. Sci. Eng. 9, 500, (1961).

(13) Carlson, O.N., Schmidt, F.A. and Peterson, D.T., J. Less-Comm. Met., 10, 1, (1966).

Metallothermic Reduction – Y, Nd, Pr, Gd, Dy
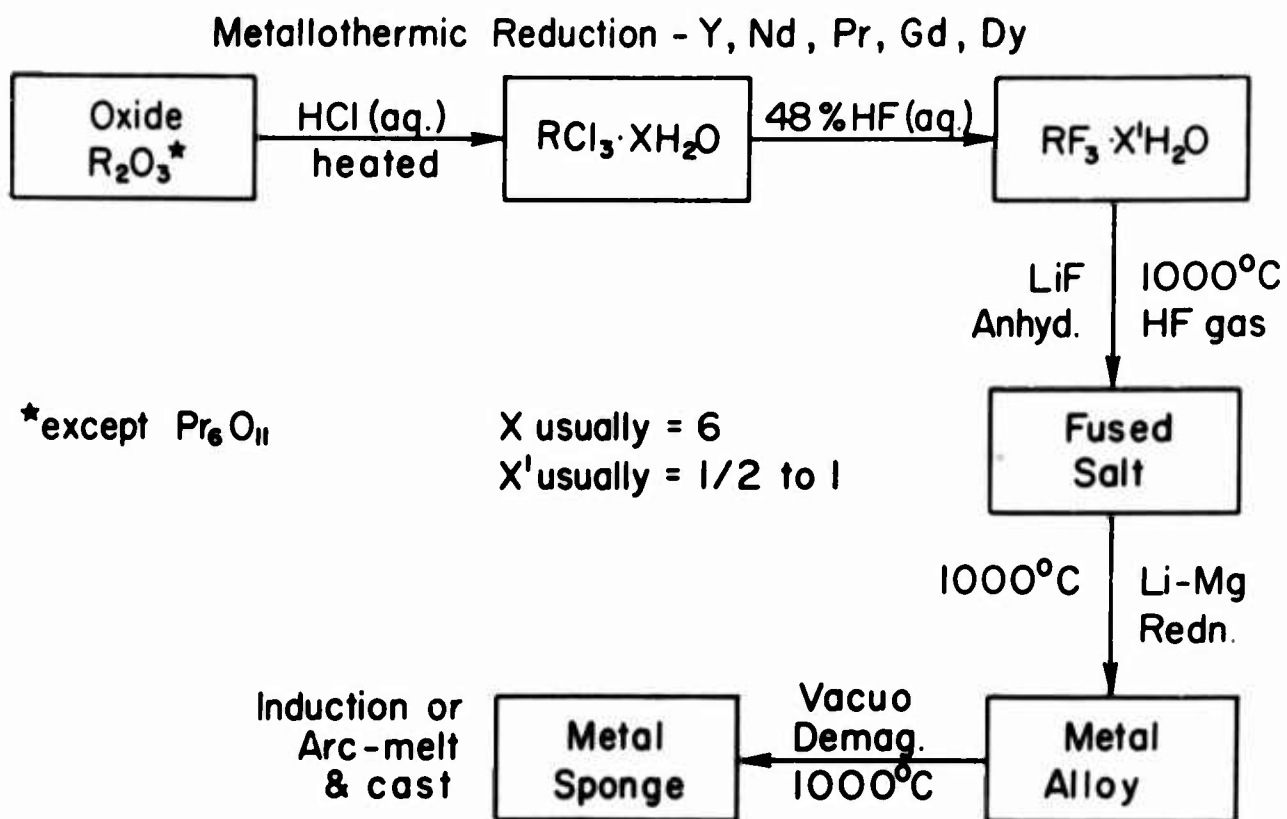
FIGURE 1 – Fluoride Process Flowsheet

664a
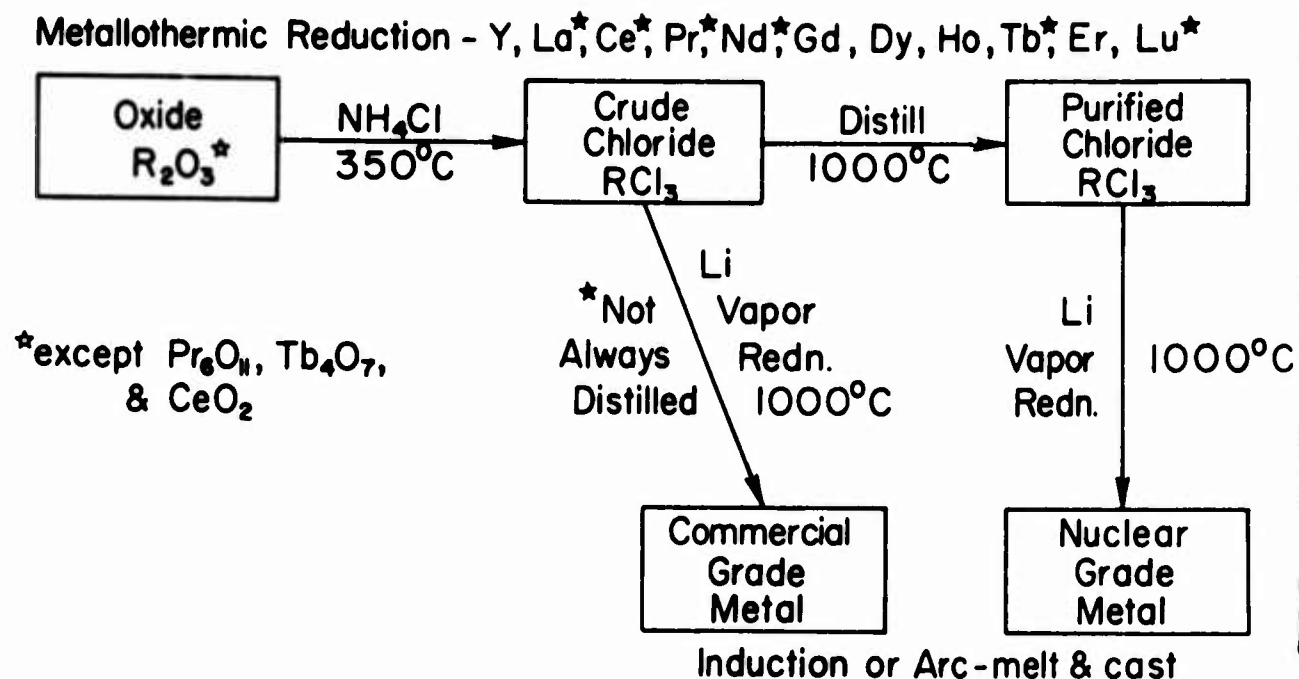
FIGURE 2 - Chloride Process Flowsheet

Direct Reduction — Sm, Eu, Yb, Tm

Oxide
R_2O_3

Purified La or Mischmetal
$1000-1300°C$

Crude
Metal

Distill
or
Sublime

$1250°C$

Purified
Metal

Induction melt
and cast
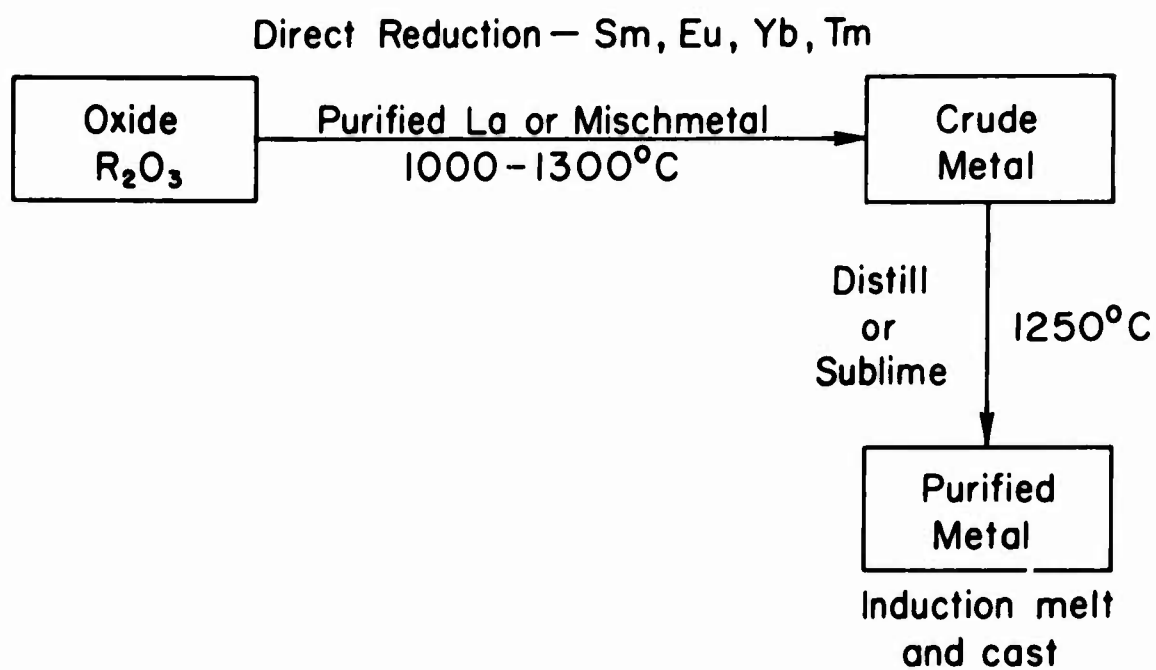
FIGURE 4 - Direct Reduction Flowsheet

RARE EARTH SEPARATION SOLVENT: TBP vrs. D2EHPA?

G. A. Elias, R. F. Sebenik and M. Smutz

Institute for Atomic Research and Department of
Chemical Engineering, Iowa State University, Ames, Iowa

Summary

A computer program has been written for the TBP-Rare
Earth Nitrate-HNO_3 acid system that predicts the return on
the investment for a processing plant as a function of the
operating conditions and the cost assumptions. The results
of these calculations will be shown and the optimization
technique explained. It is not possible at this time
to develop a similar calculation procedure for the D2EHPA-
Rare Earth Chloride-HCl system because no techniques have
yet been developed for calculating equilibrium concentrations
of two phases for the D2EHPA system. A small scale continuous
extractor is therefore being operated using D2EHPA to estimate
the optimum operating conditions for the desired separation.

The two solvents are being compared for the recovery
of 99.0% of the La fed in a didymium mixture at a purity
of 99.9% in a continuous multistage countercurrent extractor
at an arbitrarily selected production rate of 2.5 tons of
didymium oxide feed per day. At this time, it has not been
demonstrated in the laboratory that such separations can
actually be achieved.

Preliminary results indicate that both solvents have certain advantages. TBP has a significantly higher distribution coefficient for rare earths and thus less volume of solvent is needed for a given production rate. D2EHPA has a significantly higher separation factor for Pr with respect to La. This means fewer stages are required. Since, at the production rate assumed, the cost of the extractor is small relative to other costs, other factors such as the cost of recovery of the acid and the cost of corrosion resistant apparatus may decide the eventual winner.

The optimum amount of diluent, if any, to be used with the two solvents has not been determined. Although TBP can be used without a diluent, it may be more economical to do so in view of phase separation problems at low solute concentrations. Most equilibrium data for D2EHPA have been obtained with one mole of extractant per liter, but this may or may not be the optimum amount tc use in a given extractor.

The paper to be presented at the meeting will give the status of the study at that time. A conclusive answer will not be known until after both processes have been studied in pilot plant tests.

EFFECT OF TEMPERATURE ON THE HEDTA- AND EDTA-ELUTION
POSITIONS OF YTTRIUM IN THE RARE-EARTH SEQUENCE

J. R. Morton and D. B. James
Michigan Chemical Corporation
Saint Louis, Michigan

ABSTRACT

Varying the elution temperature in the ion-exchange separation of
an yttrium-lanthanide mixture shifts the elution position of yttrium.
With HEDTA as the eluant the position of yttrium at room temperature
is slightly ahead of neodymium, at 90-95°C it is between terbium and
gadolinium, and at 45-50°C it is in the vacant promethium position. A
practical scheme for the purification of yttrium has been devised using
this shift of position.

With EDTA the elution position of yttrium is always between terbium
and dysprosium; but increasing temperature decreases the dysprosium-
yttrium separation factor, possibly negating any increased separation
efficiency resulting from the decreased theoretical plate height.

INTRODUCTION

The separation of the rare earths has been demonstrated using many

different chelating agents in combination with cation-exchange resins[1].

The two chelating agents which have stood the test of time and indus-

trial practicability are ethylenediaminetetraacetic acid (EDTA) and

hydroxyethylethylenediaminetriacetic acid (HEDTA).

EDTA is in greatest industrial use, while HEDTA runs a poor second.

One of the reasons EDTA is so widely used is that it will efficiently

separate all of the rare earths and yttrium from each other with the

exception of the europium-gadolinium pair. This pair can be readily

separated by conventional chemistry.

HEDTA finds its main use in the separation of thulium, ytterbium and lutetium and the light rare earths (lanthanum through praseodymium or neodymium if yttrium is absent).

The increasing demand for yttrium has renewed interest in the evaluation of more rapid and economical ion-exchange separations of yttrium from the other rare earths. Lindstrom and Winget[2] showed that hydrogen ion could be used as the retaining ion in rare-earth separations with EDTA if the system were operated at 90-95°C. It appeared that the separation of dysprosium and yttrium was more difficult in this temperature range. This indicated that a study of the variation of the separation factor between dysprosium and yttrium with temperature would be rewarding.

No systematic investigation of the use of HEDTA in rare-earth separations at various temperatures between 25 and 95°C has been reported.

EXPERIMENTAL

Solutions - The yttrium-lanthanide solution for loading the feed columns contained 22.1% rare-earth oxides, which analyzed 65.6% yttrium oxide.

The HEDTA eluant was a 5.0-g/l solution. The pH was 6.5.

Reagent-grade materials were used to prepare the saturated copper sulfate solution and the 2N hydrochloric acid for conditioning the separation columns.

A 10-g/l EDTA solution (pH 8.5) was used to remove dysprosium and yttrium from the resin in the separation-factor, temperature-variation experiments.

The dysprosium-yttrium-EDTA solutions used in these studies were prepared from dysprosium- and yttrium-EDTA solutions generated by elutions with 10-g/l EDTA. Equal volumes of these solutions were mixed and diluted to half their original concentration.

Resin - The ion-exchange resins used in this work were Rohm and Haas IR-120 and Permutit Q. The crosslinkage was a nominal 8%, and the screen size of the dry beads was 40-50 mesh.

Apparatus - The two-inch inside diameter, 60-inch columns were housed in a large, steam-heated box. A controlling pyrometer maintained the proper temperature by means of an air-activated steam valve and a blower which re-circulated the air over the steam coils and columns. A four- to six-°C temperature differential existed between the tops and bottoms of the columns, depending on the temperature of operation. The eluant system in order of flow consisted of the following parts: a stainless-steel eluant tank, deaerator, cooler, surge tank, filter, preheater, ion-exchange columns, cooler, and a fraction-collection system.

Methods - In the work involving HEDTA the feed columns were loaded by passing through them a 2,260-g portion of the feed solution, diluted to seven liters. Excess solution was washed from the columns, and the contained rare earths were precipitated as the oxalates and ignited to the oxides. The separation columns were converted to the hydrogen ion state with 2N hydrochloric acid, the excess removed with

deionized water. The loaded rare earths were eluted through two band lengths with deaerated, 5.0-g/1 HEDTA solution at 2.66 ml/cm^2/min. The rare-earth-containing eluant was collected in consecutive fractions and precipitated with oxalic acid. The oxalates were ignited to the oxides and analyzed.

The method used to determine the separation factor variation with temperature was similar to that used by Spedding, Powell, and Svec[3] for nitrogen isotopes. A two-inch inside diameter, 60-inch column, containing 30 inches of cupric-state, ion-exchange resin was washed with deaerated water and brought to the desired temperature. Heated, deaerated, dysprosium-yttrium-EDTA solution was percolated through the column at 1.33 ml/cm^2/min, and the rare earths were collected in fractions until the dysprosium-yttrium ratio of the column effluent returned to that of the solution entering the column. After washing with deaerated, deionized water at the same rate of flow and temperature, the rare earths in the resin were removed with the EDTA stripping solution. The precipitated oxalates were ignited to oxides and analyzed for dysprosium and yttrium by X-ray fluorescent spectrometry. The separation factor was calculated using the equations of Spedding, Powell, and Svec[3].

RESULTS AND DISCUSSION

Figure 1 shows the separations resulting from two band lengths of elution with HEDTA at various temperatures. The room-temperature experiment shows the expected separation of lutetium, ytterbium, thulium, and erbium, and of praseodymium, cerium and lanthanum, but little separation of dysprosium through samarium and the very poor separation of

yttrium and neodymium.

At $92\pm3°C$ the elution position of yttrium has shown an apparent shift from just in front of neodymium to between gadolinium and terbium. The separation of elements lutetium through dysprosium and neodymium through lanthanum was excellent, reflecting the much improved kinetics of the system; but the gadolinium-europium-samarium separation remains poor, and the yttrium is badly contaminated with terbium.

At $62\pm2°C$ yttrium assumed an elution position just behind samarium, but gadolinium and samarium (and europium) badly contaminate the yttrium band.

Lowering the temperature to $47\pm2°C$ apparently positioned yttrium midway between samarium-gadolinium and neodymium, producing many fractions of high purity yttrium.

The elution position of the rare earths is determined, for the most part, by the relative magnitudes of their stability constants for chelate formation with HEDTA. These constants were determined as a function of temperature by Moeller and Ferrus[4]. Their data are presented in Figure 2. One must apply a correction factor (assumed temperature independent) of 0.245 log units in order to move yttrium to the observed positions just ahead of neodymium at room temperature and equidistant between neodymium and gadolinium at 47°C. This factor might be due to a resin effect since the ionic radius of yttrium is more like those of erbium or holmium than like neodymium. Since the separation factor between yttrium and gadolinium or neodymium is the ratio of stability constants, from Figure 2 we obtain a value of $\alpha=1.5$. Applying the classic equation of Powell and Spedding[5]

$$V = \frac{1 + (\alpha - 1) \ No}{\alpha - 1}$$

we find a steady-state separation of a 1/3-gadolinium, 1/3-yttrium, 1/3-neodymium mixture should be achieved in 2 1/3 band lengths of elution.

Elevated-temperature elutions with EDTA indicated poorer yttrium-dysprosium separations. This prompted an investigation of the variation of the separation factor between these elements with varying temperature. The results are shown in Figure 3 as log α verses reciprocal temperature. The slope yields a value of -0.28 kilocalories for the enthalpy of the reaction

$$Dy(Resin)^{+3} + Y(EDTA)^{-} \longrightarrow Y(Resin)^{+3} + Dy(EDTA)^{-},$$

if we assume that these are the only significant rare-earth species in either phase and that the activity coefficient ratios are unity.

Figure 4 shows the drastic effect of elevated temperature upon the elution distance required to reach steady state. Because of improved kinetics and therefore shortened steady-state overlap regions, elevated temperature elution has been advocated as a means of improving efficiency. Without quantitating the effect of temperature upon theoretical-plate height the net result cannot be predicted, but Figure 4 suggests that raising the temperature could adversely effect yttrium productivity.

permission to publish this work.

REFERENCES

1. J. E. Powell, Section I, Chap. 5, 55-73 in "The Rare Earths", F. H. Spedding and A. H. Daane Editors, John Wiley and Sons, Inc., New York (1961).

2. R. E. Lindstrom and J. O. Winget, U.S. Bur. Mines Rept. 6131 (1961).

3. F. H. Spedding, J. E. Powell, and H. J. Svec, J. Am. Chem. Soc., 77, 6125 (1955).

4. T. Moeller and R. Ferrus, J. Inorg. Nucl. Chem., 20, 261 (1961).

5. J. E. Powell and F. H. Spedding, USAEC Rept. ISC-617 (1955) and Chem. Eng. Progr. Symp. Series, 55, No. 24, 101 (1959).

PERCENT COMPOSITION

HEPTA -- VARIOUS TEMPERATURES
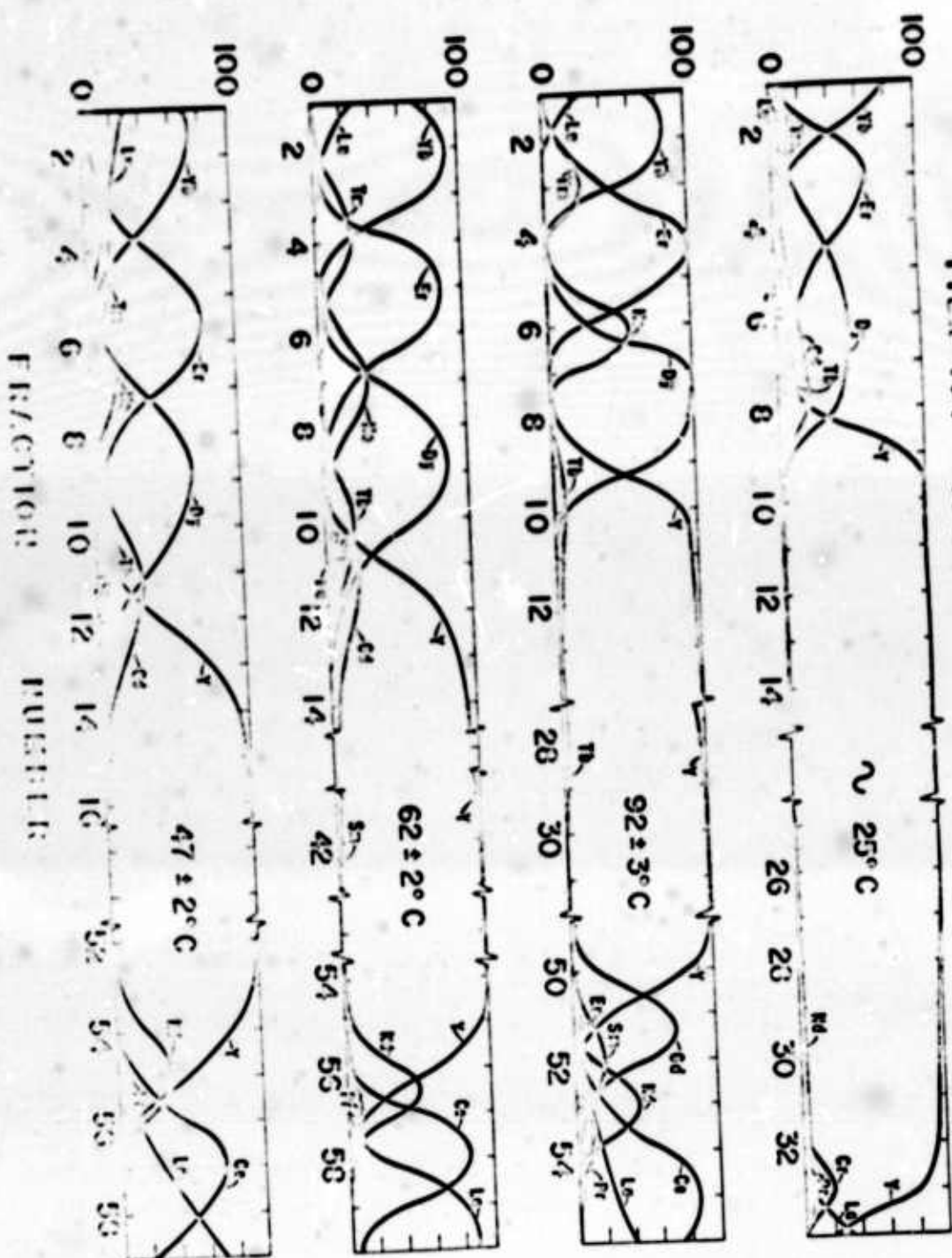
TEMPERATURE- ELUTION POSITION

LOG STABILITY CONSTANT
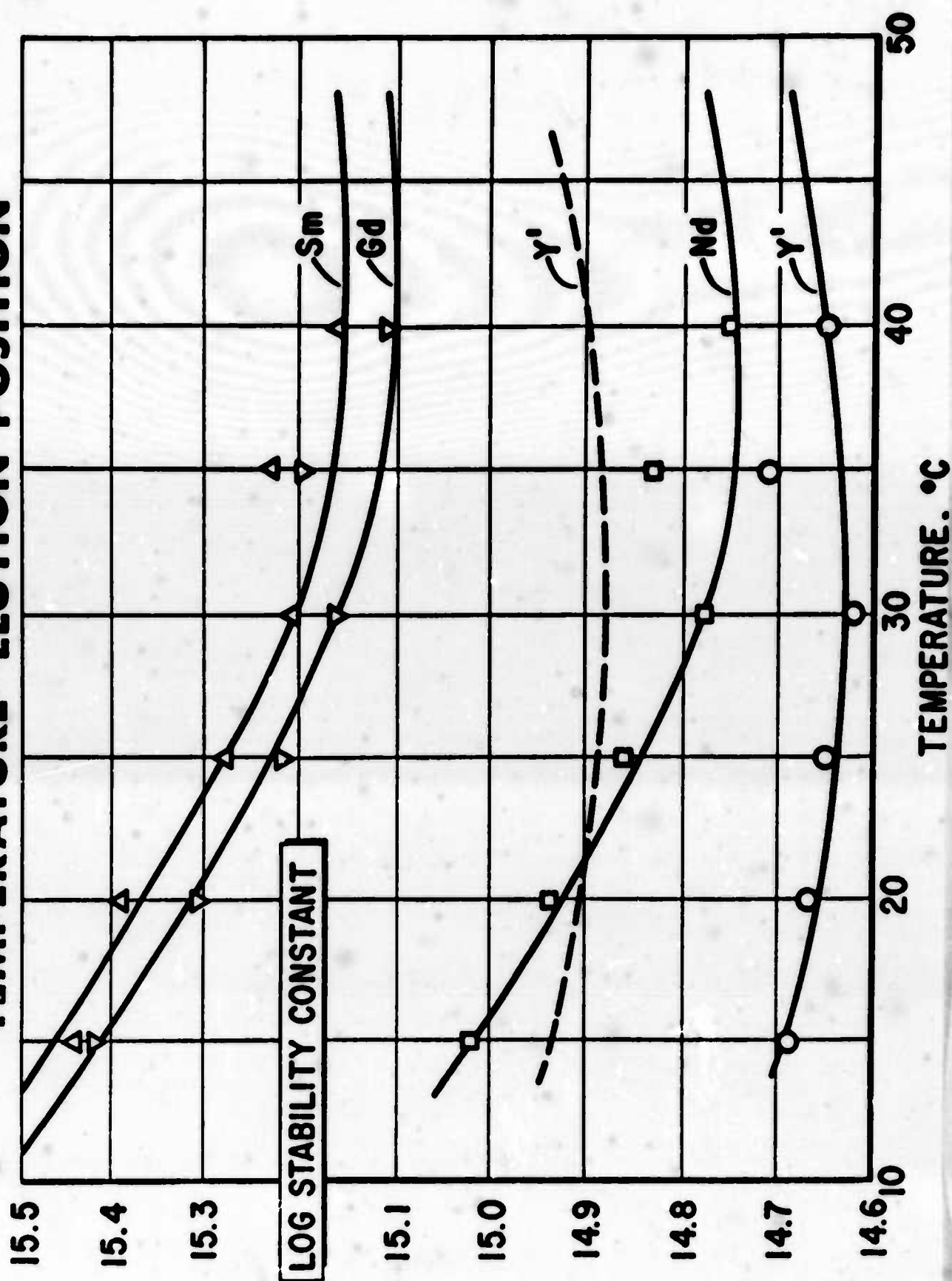
TEMPERATURE, °C

α TEMPERATURE VARIATION
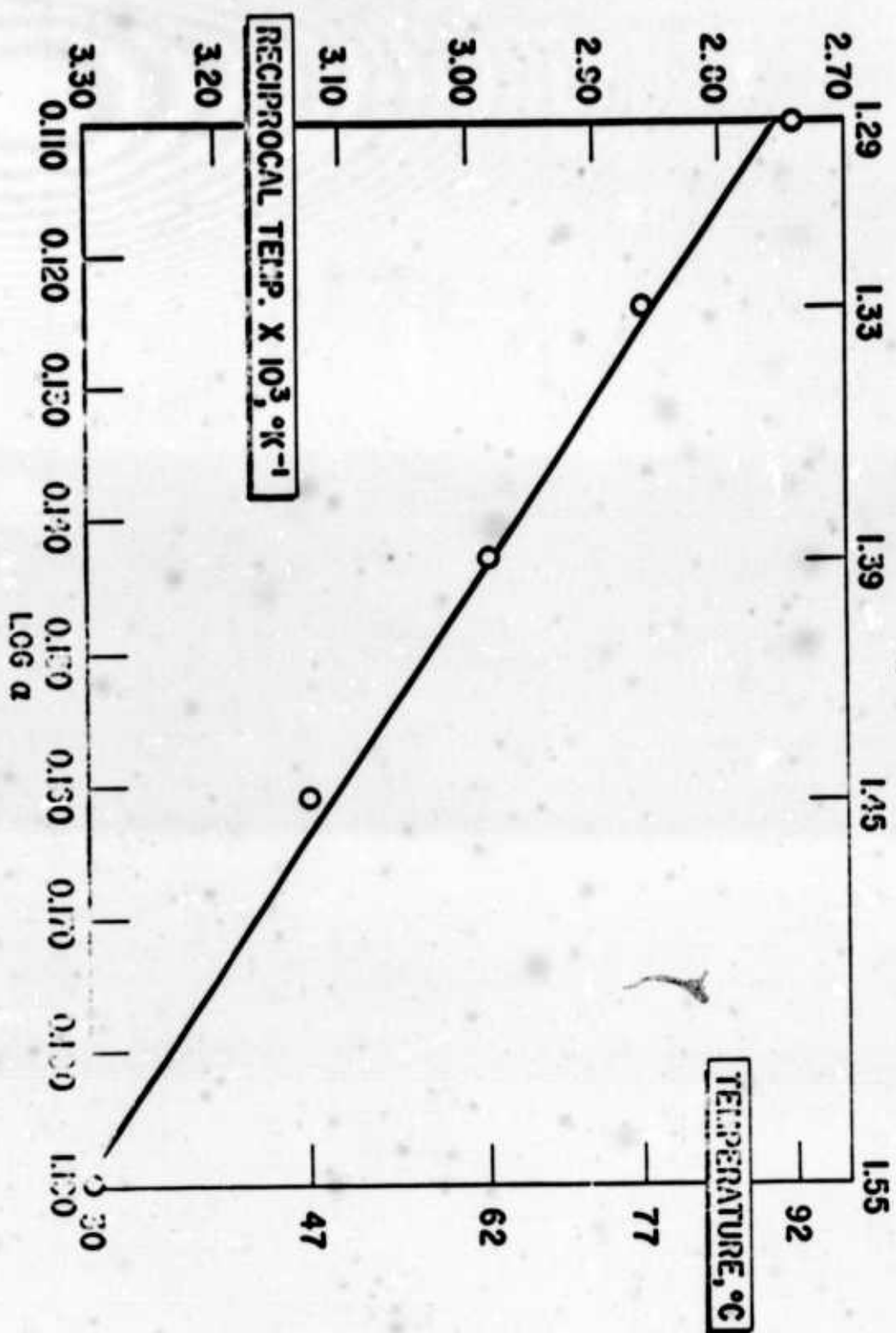
TEMPERATURE AND ELUTION DISTANCE
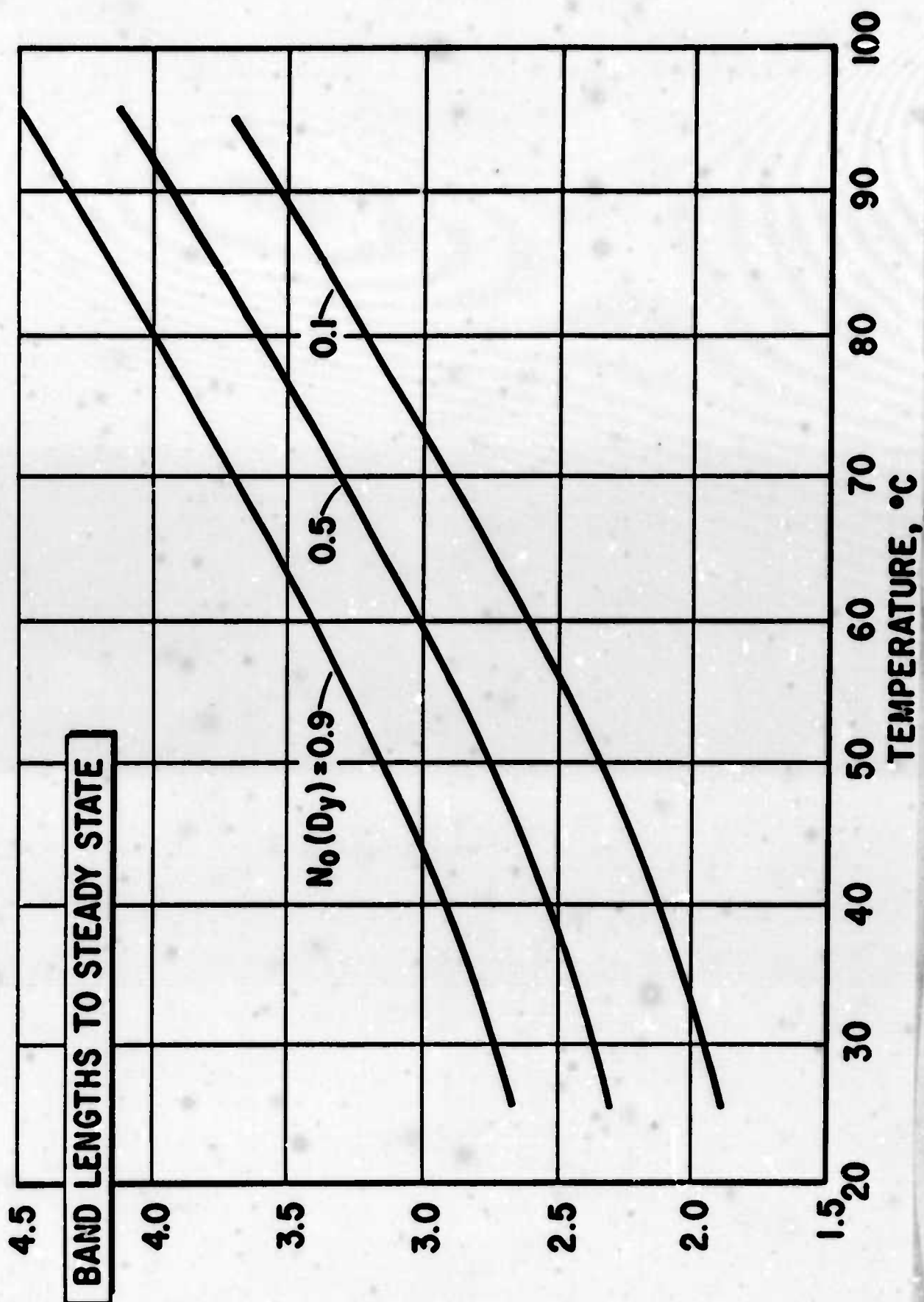
COMMERCIAL ION EXCHANGE SEPARATION OF THE RARE EARTHS

W. L. Silvernail and M. M. Woyski

American Potash & Chemical Corporation
Los Angeles, California

ABSTRACT

Rapid production of yttrium is achieved by making use of the different positions of yttrium in the elution sequence with different eluting agents. Elution with HEDTA is used to separate the heavy elements. This is followed by elution with EDTA to separate the lights. Elution with EDTA is carried out with a pre-prepared solution of rare earth chelate. This permits operation at much higher concentration and facilitates the recovery of EDTA. The use of non-rare earth retainers is eliminated. In actual operation, columns loaded with crude material are introduced into the elution train at suitable intervals resulting in almost continuous production of purified product.

The use of pre-prepared solutions of rare earth chelates is also applicable to the separation of other rare earths with a gain in operating efficiency. Some fundamentals of commercial ion exchange operation are considered.

INTRODUCTION

Commercial ion exchange separation of the rare earths utilizes displacement chromatography. In the simplest case, the separation of a binary mixture, the two species to be separated, A and B, are sorbed on a resin bed originally loaded with C, a species having a lesser affinity for the resin than A or B. The sorbed bed A-B is then eluted with an eluant DV where D is a fourth species and V is a chelating agent. D is chosen so that AV and BV are more stable than DV. The over-all result is that D replaces A and B on the resin, and A and B are transported downstream as the complexed species AV and BV. If AV is more stable than BV, further exchange takes place and A moves ahead of B. In order to keep the over-all band from spreading, the solution is passed into another column of resin loaded with a fifth species E, a so-called "retainer", chosen so that EV is more stable than AV. A then replaces E on the resin. If elution is continued, a steady-state condition finally results in which the original band is separated into two parts, A and B.

The rate and degree of separation depend on two parameters: the separation factor (S), and the height equivalent to a theoretical plate (HETP). The separation factor S is defined as the ratio of the respective distribution coefficients of the species on the resin and in solution. For similar ions having nearly identical distribution coefficients the separation factor for the two species A and B approximate the ratio of the respective stability constants, that is

$$S = \frac{K_{AV}}{K_{BV}} \tag{1}$$

where K_{AV} is the stability constant for the reaction $A + V \longrightarrow AV$. Although the values reported by different investigators vary in absolute value, the ratios for various pairs of elements agree fairly well and it is from these that the separation factors are calculated.

FUNDAMENTAL CALCULATIONS

ν, ϵ, N Relationships

In 1955, Spedding, Powell, and Svec[1] showed how equilibrium constants can be used to calculate the number of displacements required to separate the isotopes of nitrogen by an ion exchange process. In a later publication Powell and Spedding[2] extended the method to the separation of rare earths. The very simple basic equation derived by these authors has been exceedingly useful in designing ion exchange systems. Furthermore, by examining the relationships of the factors in the equation, subsidiary relationships which further aid in understanding ion exchange and designing systems emerge.

Spedding's equation states that the number of band displacements required to separate two elements A and B is given by:

$$\nu = \frac{1 + \epsilon N_A^o}{\epsilon} = \frac{1}{\epsilon} + N_A^o \tag{2}$$

where ϵ is the separation factor minus one ($\epsilon = S-1$) and N_A^o is the mole fraction of element A, the leading element in the binary mixture to be separated. Figures 1 and 2 illustrate the fundamental characteristics of ion exchange separation which, though obvious from an inspection of the equation, are more easily interpreted with the aid of the charts.

Figure 1 shows the effect of starting composition on the distance, ν, required to effect the separation. Since $\nu = \frac{1}{\epsilon} + N_A^o$, the maximum difference in ν is one band length as N_A^o varies from 0 to 1. The significance of this is that element B, the trailing element, can be freed of a trace of element A which moves forward more rapidly than nearly pure A can be purified with respect to B. This fact can be of economic importance. The reason for this difference is that in the first case only the small amount of impurity ($N_A^o \sim 0$) need be transported forward but in the latter, the major constituent ($N_A^o \sim 1$) must be transported to leave behind the impurity which was initially distributed uniformly along the whole band.

Figure 2 shows the effect of ϵ. It will be noted that increasing above about 5 produces relatively little effect on ν. However, in the case of difficult time-consuming separations ($\epsilon < 1$), a small increase in ϵ produces a large decrease in ν and, if efficiency is a factor, must be sought diligently.

PRODUCTION RATE

A. Linear Rate of Separation

In ion exchange production, a major cost determining factor is the elution distance required to obtain a product. For making comparisons and also for design calculations, it is useful and convenient to express productivity (φ) in terms of the feet (band length) of product produced per foot of band travel (band advance or elution distance). To purify a band, it must travel ν displacements:

$$\nu = \frac{1}{\epsilon} + N_A^o \qquad (3)$$

If the working band is one foot, $\left| N_A^o \right|$ will be the feet of band occupied by element A after separation is complete. It follows that N_A^o/ν is the feet of A produced per foot of travel. Therefore

$$\varphi_A = \frac{N_A^o}{\nu} = \frac{\epsilon N_A^o}{1 + \epsilon N_A^o} \qquad (4)$$

$$\varphi_B = \frac{N_B^o}{\nu} = \frac{(1 - N_A^o)}{1 + \epsilon N_A^o} \qquad (5)$$

and

$$\varphi_A + \varphi_B = \varphi_T = \frac{\epsilon}{1 + \epsilon N_A^o} \qquad (6)$$

Figure 3 shows the amount of A produced per foot of band advance (φ_A) from mixture containing varying amounts of A for various values of ϵ. Figure 4 shows the same data (φ_B) for element B. Again, it will be noted that the purification of B, the trailing element, can be very rapid if the content of A is relatively low and ϵ is moderately high. That is, as N_A^o approaches 0, the rate of production of B approaches ϵ. On the other hand, the production rate of A is at most one foot per foot of band travel as when N_A^o approaches 1, φ_A approaches $\dfrac{\epsilon}{1 + \epsilon}$ which approaches 1 for large values of ϵ.

B. Time Rate of Separation

If the permissible rate of elution (feet of band advance per day) for near perfect separation is known, the rate of increase in the length of band of purified material can be calculated.

$$\varphi_{tA} = \varphi_A \times \rho$$

$$\varphi_{tB} = \varphi_B \times \rho \tag{7}$$

C. Mass Rate of Separation

Production rate in lbs/day (P) is given by the product of linear rate of separation (φ), the elution rate (L), the cross sectional area of the column (α) and the resin capacity in lb/cu ft (W):

$$P_A = \varphi_A \times L \times \alpha \times W_{AR}$$

$$P_B = \varphi_B \times L \times \alpha \times W_{AR} \tag{8}$$

Conversely, the size of column required for a desired production rate can be calculated from knowledge of the composition of starting material, the separation factor, and permissible elution rate.

In Table I are given the separation factors for adjacent elements using EDTA and HEDTA respectively as the eluant anions.

TABLE I

SEPARATION FACTORS AND 1/ϵ VALUES FOR ADJACENT PAIRS OF RARE EARTHS CALCULATED FROM AVERAGE VALUES OF STABILITY CONSTANTS FOR EDTA AND HEDTA AS ELUANT ANIONS[3]

R-R'	EDTA		HEDTA	
	S	$1/\epsilon$	S	$1/\epsilon$
La-Ce	3.7	0.37	5.0	0.25
Ce-Pr	2.5	0.67	2.8	.55
Pr-Nd	1.8	1.25	1.8	1.25
Nd-Sm	3.2	0.46	2.6	.63
Sm-Eu	1.5	2.0	Ca 1.0	-
Eu-Gd	1.05*	Ca 5	0.7*	-
Gd-Tb	4.2	0.30	Ca 1.0	-
Tb-Dy	2.3	0.77	Ca 1.0	-
Dy-Ho	2.6	0.63	Ca 1.0	-
Ho-Er	1.8	1.25	1.2	5
Er-Tm	3.1	0.48	2.0	1.0
Tm-Yb	1.8	1.25	1.6	1.7
Yb-Lu	1.9	1.11	1.3	3.3
Tb-Y	1.5	2.0	3.5	0.40
Y-Dy	1.6	1.7	3.5	0.40
Nd-Y	30.2	.04	1.5*	2.0
Y-Sm	8.7	.13	4.5	0.3

*In these cases the calculated separations do not agree with observed elution behavior.

D. Graphical Representation of the Progress of Separation

A conventional representation of the progress of separation of two elements is given in Figure 5. At the start, the band (50 feet) is uniformly loaded with a mixture containing 31 m/o Pr and 69 m/o Nd. As elution proceeds, neodymium moves forward and accumulates at the head of the band. Praseodymium lags and accumulates at the tail. Until the separation is complete or nearly complete, a zone of the original composition is present between the bands of leading and trailing elements.

The dotted lines in Figure 5 represent the idealized form on which the Spedding equation and the developments in this discussion are based. To further visualize this ion exchange elution process, two methods of charting the progress of separation are illustrated. In the first (Figure 6) the frame of reference is the band undergoing separation; in effect, the observer travels with the rare earth band and sees only the relative travel of the elements being separated. In the second (Figure 7) the reference is the system of columns being used for the separation. The observer then sees the entire band moving forward as well as the relative motions of the individual elements. Such a chart is useful in planning maximum utilization of columns.

Example - Separation of a mixture of 31 m/o Pr and 69 m/o Nd by elution with EDTA

The separation factor for this pair of elements is 1.82. For the mixture in question, the number of band lengths to obtain complete separation will be:

$$\nu = \frac{1}{\epsilon} + N_A^o = \frac{1}{.82} + .69 = 1.91$$

For a loaded band of 50 feet (as shown in Figures 10 and 11) the required elution distance will be 95.5 feet. During the period of elution pure Pr and Nd will accumulate at rates of .16 and .36 feet per foot of band travel respectively since

$$\varphi_{Nd} = \frac{0.69}{1.91} = .36 \quad \text{and} \quad Pr = \frac{.31}{1.91} = .16$$

- 684 -

The length of band of each element present at any time during the elution may be determined from the relationships

$$f_A = \rho\varphi_A \qquad\qquad f_B = \rho\varphi_B \qquad (9)$$

Calculations based on this relationship are accurate only for the hypothetical perfect system; that is, a system in which the height equivalent to a theoretical plate is zero. The HETP is defined as the distance measured along the bed in which the ratio of A to B differs by one separation factor, or

$$h = \frac{\log S}{\dfrac{\log \dfrac{(A/B)x}{(A/B)y}}{D}} \qquad (10)$$

where:

    h = HETP
    S = separation factor
    (A/B)x = ratio of components A and B at some point x in the band
    (A/B)y = ratio of components A and B at some point y further along the band
    D = distance between points x and y

HETP is a function of the contact time and rates of exchange and hence depends on such factors as the flow rate, concentration, pH, temperature, resin particle size, etc. In practice an HETP of zero is approached only at very low elution rates on very fine resin. Operation of practical ion exchange systems involve corrections which must be applied to calculate performance. A convenient parameter for this purpose is the D_{1000}, or impurity gradient, which is defined as the distance along the band in which the concentration of a component decreases from C_0 to $0.001\ C_0$. This is useful in comparing the effects of changing various operating conditions within a given system. The effect on production of pure material is shown in Figure 8.

A second limitation, also not inherent in the method of calculation, is the accuracy of separation factors. Although the absolute values of the association constants show some variance, the separation

factors which are calculated from the differences are in fair agreement.

In practice, binary mixtures of rare earths are seldom encountered. Moreover, conditions are usually imposed by the composition of the feed stock available. Nevertheless, it is convenient as a first approxima- tion to treat a given system as a binary one by applying the relation- ships given above to the pair of adjacent components having the smallest separation factor. All the species that move ahead of the separation point are then considered to have the concentration N_A^O and those that hold back, the concentration N_B^O or $1-N_A^O$.

Consider now the purification of yttrium. In the processing of monazite, yttrium concentrates in certain streams and can be recovered from these in concentrations ranging from about 35% to 75% of the total rare earths present. A typical composition is 60 w/o Y_2O_3 - 30% heavies (Sm through Lu) and 10% lights (La through Nd). Examination of Table I shows that in an EDTA system yttrium lies between Tb and Dy, while in HEDTA it lies close to Nd. In the former case, if we assume that all the heavies are represented by Dy and all the lights by Tb, we get the values shown in the following table:

REO	Wt %	Mole %	S_{EDTA}	ν (Band Length)
Tb	10	7.9		
			1.45	3.1
Y_2O_3	60	70.6		
			1.6	1.88
Dy_2O_3	30	21.4		

In other words, in an EDTA system slightly over 3 band lengths would be required to purify yttrium. With HEDTA purification is even slower. Experience shows that in excess of five band lengths are re- quired to separate yttrium from neodymium.

Consider now a two-stage elution in which the system is first eluted with HEDTA to separate the heavies. This will require 0.61 band lengths inasmuch as the separation factor Y-Dy is 3.5 whence $\nu = 1/2.5 + 0.21 = 0.61$. The remaining Y-Nd fraction having the composition 90 m/o Y_2O_3 and 10 m/o Nd_2O_3 is then eluted with EDTA to separate Y from Nd. For this separation $\nu = 1/29.2 + 0.9 = 0.96$ band lengths. Thus the total elution distance is 1.6 band lengths compared to 3.1 for EDTA alone or about 5.0 for HEDTA alone.

In practice ytrrium concentrate is loaded onto columns in the NH_4^+ cycle. After washing and backwashing, the columns are eluted with HEDTA buffered with ammonia to a pH of about 8.0. Because HEDTA free-acid (H_3V) is sufficiently soluble, a hydrogen ion retainer column is used. The progress of the elution is shown in Figures 8 and 9 in which the concentration gradients of Dy are used to follow the separation. It is to be noted that the concentration gradient quickly assumes a nearly constant slope and that the gradient initially moves at a rate faster than the band is traveling. However, after a time the rate at which the Dy is moving forward decreases and finally approaches a steady state moving at the same rate as the band is traveling. The maximum production rate is reached before the steady state is, and is also shown in Figure 9. At this point the band is split into two parts. The head section containing the heavies plus the Y-heavies overlap is made the lead column in the next run for which loaded columns have been made ready.

The tail section consisting of heavies-free Y and lights is washed free of HEDTA and is then eluted with EDTA complexed with La or Ca. Because EDTA free-acid (H_4EDTA) is relatively insoluble, a hydrogen ion retainer cannot be used and must be replaced with one containing a metal which forms a complex with EDTA equal to or stronger than that formed by Y. Copper or zinc is suitable or, in the particular case at hand where heavies have been removed in the HEDTA cycle, yttrium itself may be used as the retainer. Therefore, as elution proceeds, the first eluant coming off the columns is collected in tanks until sufficient

yttrium is obtained to load a new column. The Y-EDTA solution is then acidified to a pH of about 1.5 which releases the Y^{+3} and causes the H_4EDTA to precipitate. This is filtered and the filtrate containing Y^{+3} is used to load the first retainer column. Elution is then recommenced and the solution coming from the retainer column again is collected and made acidic to recover the EDTA. The filtrate is treated with oxalic acid to precipitate yttrium oxalate which is washed, filtered, dried, and ignited to Y_2O_3.

The La-EDTA eluant is conveniently prepared by stripping the tail columns in the band with $NH_4 \cdot EDTA$ which then leaves the columns in the ammonia cycle ready to be loaded with yttrium concentrate feed. In practice, these feed columns may be introduced into the next run operating on the HEDTA cycle, thus making the operation essentially continuous.

REFERENCES CITED

1. Spedding, F. H., J. E. Powell and J. J. Svec, "A Laboratory Method for Separating Nitrogen Isotopes by Ion Exchange", J. Am. Chem. Soc., 77, 6125 (1955)

2. Powell, J. E. and F. H. Spedding, "Basic Principles Involved in the Macro-Separation of Adjacent Rare Earths from Each Other by Means of Ion Exchange", Iowa State College, ISC-857 for U.S.A.E.C. (1959)

3. Powell, J.E., "Progress in the Science and Technology of the Rare Earths", L. Eyring, editor, 78-81, MacMillan Co., New York (1964)
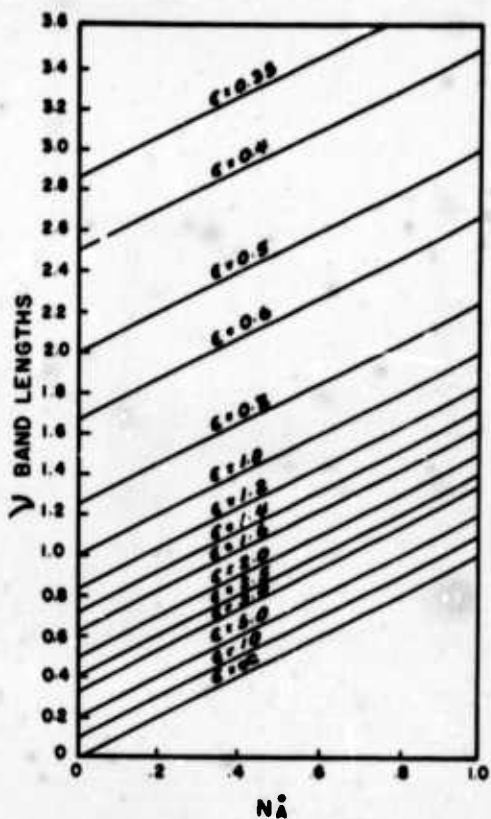
FIG. 1 EFFECT OF STARTING COMPOSITION ON ELUTION DISTANCE REQUIRED TO SEPARATE TWO ELEMENTS

FIG. 2 EFFECT OF ε ON ELUTION DISTANCE REQUIRED TO SEPARATE TWO ELEMENTS

FIG. 3 PRODUCTION RATE FEET OF A PER FOOT OF BAND ADVANCE

FIG. 4 PRODUCTION RATE FEET OF B PER FOOT OF BAND ADVANCE

FIG. 5 PROGRESSIVE COMPOSITION PROFILES DURING SEPARATION OF TWO ELEMENTS (IDEALIZED)

FIG. 6 PROGRESS OF A SEPARATION (RELATIVE TO LOADED BAND)

FIG. 7 PROGRESS OF A SEPARATION (RELATIVE TO RESIN BED)

FIG. 8 SEPARATION OF YTTRIUM AND DYSPROSIUM SUCCESSIVE DYSPROSIUM PROFILES

A D:1000 = 0.0
B D:1000 = 130
C D:1000 = 3.0

FIG. 9 PRODUCTION OF YTTRIUM WITH LESS THAN 100 PPM DY
A - ACTUAL
B - IDEAL

RECOVERY OF CERIUM AND LANTHANUM BY OZONATION OF LANTHANIDE SOLUTIONS

By D. J. Bauer and R. E. Lindstrom

* * * * * * * * * * * * * * oral presentation and preprinting
by rare earth conference committee

RECOVERY OF CERIUM AND LANTHANUM BY
OZONATION OF LANTHANIDE SOLUTIONS

D. J. Bauer and R. E. Lindstrom

Reno Metallurgy Research Center, Bureau of Mines,
U. S. Department of the Interior,
Reno, Nevada

ABSTRACT

Oxidation of lanthanide solutions with ozone at pH 4.5 and ambient temperature results in precipitation of 98 percent of the original cerium present. Corresponding cerium purity is increased from 50 to 98 percent.

Alternatively, ozonation at pH 6.5 and 85° C differentially precipitates cerium and heavier elements, and leaves 89 percent of the original lanthanum in solution at a purity of 95 percent. Subsequent recovery of cerium from the heavier elements is accomplished by dissolving the precipitate and reoxidizing the cerium with ozone at pH 4.5 and ambient temperature. The filtrate contains an enriched praseodymium-neodymium-samarium-europium mixture that is amenable to separation by ion exchange or solvent extraction.

INTRODUCTION

Cerium and lanthanum are among the most abundant of the rare-earth elements, and cerium in particular is important from an economic standpoint.

The separation of cerium and lanthanum from various source materials has been accomplished by a variety of methods, including fractional crystallization (4, 6), basicity precipitation (3), ion exchange (5), and solvent extraction (2, 7). Probably the best known and most widely used techniques for cerium purification are those which are based on oxidation of cerium in solution to the tetravalent state. The cerium can be recovered by precipitation of the comparatively insoluble tetravalent cerium by pH control (3) or by extraction of the ceric salt into an organic extractant (7). Persulfates, permanganates, and hypochlorites are frequently used for oxidation of cerium in

solution to the ceric state. Alternatively, cerous hydroxide is readily oxidized to hydrated ceric oxide by heating in air. Leaching of this material under controlled pH conditions will dissolve the trivalent hydroxides, whereas the cerium remains insoluble.

The oxidizing capabilities of ozone are well known for organic systems, including water purification, waste treatment, and organic synthesis (1); however, relatively little work has been done on inorganic systems. The use of ozone for oxidizing cerium in solution would appear to offer several potential advantages over present oxidation techniques. Extensive inventories of chemicals would be largely avoided. The absence of contaminating ions could eliminate an additional processing step, and operating costs may be lower, depending on other factors in the system.

MATERIALS, APPARATUS, AND PROCEDURE

Charge solutions were prepared by dissolving bastnasite-type oxides in sulfuric, nitric, or hydrochloric acid and diluting to a final concentration of 12 grams rare-earth oxides (RE_2O_3 basis) per liter. Higher concentrations were feasible with nitrate and chloride solutions, but concentrated sulfate solutions precipitated on extended storage. A typical feed solution consisted of 36 percent La_2O_3, 50 percent CeO_2, 3. 5 percent Pr_6O_{11}, 9. 7 percent Nd_2O_3, 0. 7 percent Sm_2O_3, and 0. 1 percent Eu_2O_3, in weight percentages, oxide basis.

Ozone was produced in a conventional generator using dry oxygen feed. The generator was controlled to deliver approximately 2. 5 grams of ozone per hour with an oxygen flow of 0. 02 cfm at 8 psi. Toxic ozone fumes were confined in a hood.

Individual experiments were conducted with 800-ml quantities of feed solution in 1-liter, open-top, glass reaction vessels. Solutions were stirred and were heated during selected experiments with a stirring hotplate. Ozone and ammonia gas were introduced into the lanthanide solution through fritted glass tubes. The ammonia was added to neutralize acid formed in the oxidation reaction. Addition of ozone was continued until essentially all of the cerium had precipitated or until a predesignated reaction time was reached. Precipitation of cerium was complete when the pH of the solution remained constant. The CeO_2 was recovered by filtration.

Cerium precipitation was followed with a Ce^{144} tracer for initial reaction-time studies. Lanthanide product fractions were analyzed by X-ray fluorescence.

RESULTS AND DISCUSSION

Since cerium compounds are known to be oxidized under certain conditions by oxygen, preliminary experiments were run with air and oxygen to establish a baseline for comparison with subsequent results obtained with ozone. Negative results were obtained with pH values as high as 5.5 at ambient temperature. As expected, precipitation started to occur on increasing the temperature to 85° C and the pH to 6.5. Under these conditions, considerable quantities of trivalent hydroxides are coprecipitated with the tetravalent cerium.

Initial experiments with ozone were conducted to determine the variation of CeO_2 precipitation with time at different pH values and temperatures in chloride solutions. Figure 1 shows that CeO_2
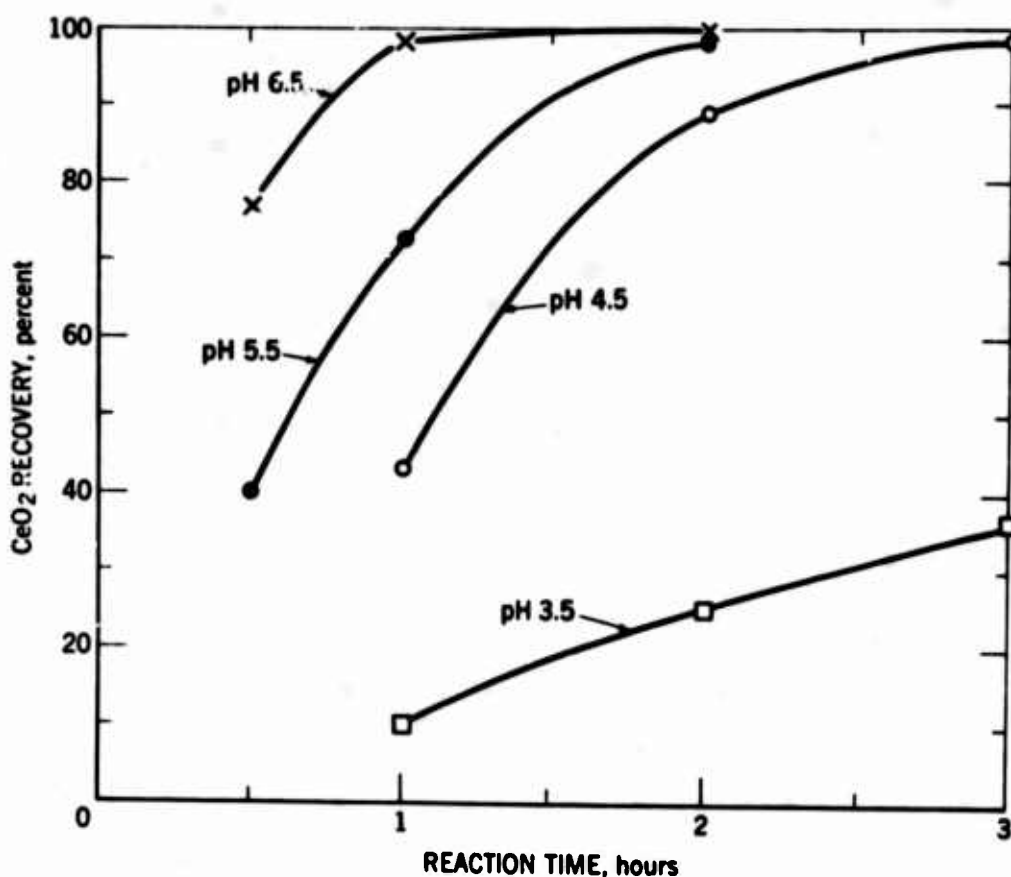
FIGURE 1. - Effect of Reaction Time on CeO_2 Recovery From Lanthanide Chloride Solution at Ambient Temperature.

precipitation increases both with reaction time and pH. At ambient temperature and a 3-hour reaction period, CeO_2 precipitation increased from 36 percent to 98 percent when the pH was increased from 3.5 to 4.5. Ninety-nine-plus-percent precipitation of CeO_2 occurred in 2 hours at pH 5.5, whereas only 1 hour was required for 99-percent precipitation at pH 6.5. The same general trend is observed in figure 2 for operation at 85° C; however, the higher
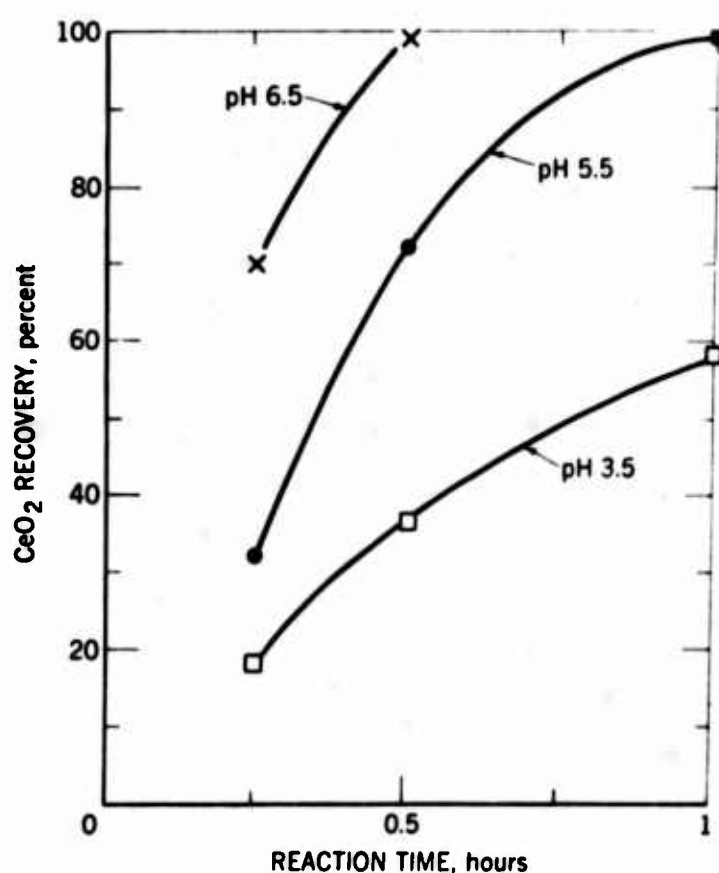
FIGURE 2. - Effect of Reaction Time on CeO_2 Recovery From Lanthanide Chloride Solution at 85° C.

temperature increases the rate of CeO_2 precipitation considerably. Complete precipitation of CeO_2 occurred in 1 hour at pH 5.5, and only one-half hour is required at pH 6.5.

Subsequent experiments with ozone were conducted in lanthanide sulfate, nitrate, and chloride solutions to obtain recovery and purity data for cerium and lanthanum. The three anion species were included in the study because it was not known if differences in their

abilities to form complex ions with the lanthanides would affect the recovery and purity of the ceric oxide precipitate. Table 1 summarizes CeO$_2$ recovery and purity obtained with the sulfate, nitrate, and chloride solutions at ambient temperature. A maximum

TABLE 1. - Precipitation studies at ambient temperature

Anion	pH	Reaction time, hr	CeO$_2$ in precipitate		La$_2$O$_3$ in filtrate	
			Recovery, percent	Purity, percent	Recovery, percent	Purity, percent
	(1.5	3	93	79	88	63
	(2.5	2	97	86	92	67
SO$_4$	(3.5	2	99.3	85	93	69
	(4.5	2	99.8	86	93	70
	(5.5	2	99.6	92	95	75
	(3.0	3	73	93	(1/)	(1/)
NO$_3$	(4.5	3	99.2	93	97	75
	(5.0	2	99.1	93	98	73
	(5.5	1	98.8	89	(1/)	(1/)
	(3.5	3	36	89	(1/)	(1/)
Cl	(4.5	3	98	98	98	70
	(5.5	2	99.2	92	94	75
	(6.5	1	99.8	76	90	88

1/ Not determined.

CeO$_2$ purity of 98 percent was obtained with the chloride solution, whereas the sulfate and nitrate solutions gave maximum purities of 92 to 93 percent. Recovery values of approximately 99 percent were common to all three anion species with pH values above 4.5. However, with pH values below 4.5, precipitation from the sulfate solution resulted in recovery values markedly superior to those obtained in chloride or nitrate solutions.

The effect of temperature on cerium recovery was determined at 85° C in nitrate and chloride systems. Solubility limitations prevented investigation of sulfates under these conditions. Table 2 shows that the reaction time required to reach a given percentage recovery of ceric oxide is substantially less at 85° C; however, purity of the cerium product is less. A cerium purity of 95 percent was reached in 1 hour in the chloride system, but the recovery was only 58 percent.

TABLE 2. - Precipitation studies at 85° C

Anion	pH	Reaction time, hr	CeO$_2$ in precipitate		La$_2$O$_3$ in filtrate	
			Recovery, percent	Purity, percent	Recovery, percent	Purity, percent
NO$_3$	(5. 5	1/2	99. 4	72	78	90
	(6. 5	1/2	99. 9	70	80	96
	(3. 5	1	58	95	94	51
Cl	(4. 5	1	99. 9	90	97	75
	(5. 5	1	99. 3	80	90	82
	(6. 5	1/2	99. 7	72	88	94

Complete precipitation of pure cerium would leave a filtrate containing a theoretical maximum of 72 percent lanthanum. However, the lanthanum recovery-purity data obtained during recovery of cerium (tables 1 and 2) show that at pH values of 4. 5 and above, the praseodymium, neodymium, and samarium start to precipitate selectively with cerium, thereby leaving a purified lanthanum product in the filtrate. Lanthanum purity in the filtrate increases with increasing pH up to the maximum value investigated, pH 6. 5. The increase in purity occurs at ambient temperature as well as at 85° C, although the highest lanthanum purity values are obtained at the higher temperature. Operating at 85° C and pH 6. 5 resulted in 80-percent recovery of 96-percent-pure lanthanum (oxide basis) in the nitrate system and 88-percent recovery of 94-percent-pure lanthanum in the chloride system. At ambient temperature, the best result obtained was 90-percent lanthanum recovery at 88-percent purity. The advantage would seem to be with operation at elevated temperature, especially since the reaction time is decreased from 1 to 1/2 hour by heating the solution to 85° C.

Isolation of both cerium and lanthanum would require a two-step operation in which the primary precipitation of cerium and heavier lanthanides at 85° C, to recover lanthanum, was followed by filtration and a second precipitation of CeO$_2$ from the redissolved cerium and heavier fraction at ambient temperature. Data given in table 3 are typical of the results obtained in the two-step process. The first filtrate analyzed 95-percent-pure lanthanum for both the chloride and nitrate systems. Corresponding lanthanum recovery amounted to 89 percent in the nitrate system and 83 percent in the chloride system. Subsequent recovery of cerium from the heavier lanthanides by a

second ozonation step at pH 4.5 was in the 95-percent range for both the nitrate and chloride systems, and the cerium product purity averaged 97 percent. Inasmuch as results appear to be largely independent of the anion species, the anion used could be varied according to other considerations.

TABLE 3. - Two-step precipitation studies

Treatment	Anion	Temperature	pH	Reaction time, hr	Recovery, percent	Purity, percent
Step 1 - lanthanum	NO_3	85°C	6.5	1/2	89	95
recovery	Cl	85°C	6.5	1/2	83	95
Step 2 - cerium	NO_3	Ambient	4.5	3	94	98
recovery	Cl	Ambient	4.5	3	97	96

Production of high-purity cerium was shown to be feasible by dissolving the 98-percent-purity cerium ozonation product in hydrochloric acid and reozonating it at a pH of 4.5. The purity of the resulting cerium product was in excess of 99.9 percent and recovery was essentially complete.

STOICHIOMETRY

The stoichiometry of the reaction occurring between ozone and the cerium in solution was investigated by oxidizing high-purity cerous nitrate, chloride, and sulfate solutions at ambient temperature. No ammonia was added during the tests, and the pH dropped from an initial value of 6 to 2.5 for the chloride solution and to 2.0 for the nitrate and sulfate solutions. No precipitation occurred in the nitrate solution, possibly because of the stability of the anionic cerium nitrate complex at low pH. For the chloride and sulfate solutions, the ratio between the CeO_2 recovered, the ozone consumed, and the hydrogen ions produced at ambient temperature corresponds to the following equation for the chloride system:

$$2CeCl_3 + O_3 + 3H_2O \rightleftharpoons 2CeO_2 + 6HCl + O_2. \quad (1)$$

The experimental data checked within 5 percent for equation 1.

COSTS

Major factors in the costs of ozone are the plant size, cost of power, and the plant depreciation cycle. Based on power at 1 cent per kwhr and a 4-percent-per-year depreciation, a 2,000 pound-per-day plant would produce ozone at approximately 14 cents per pound. By way of comparison, the price of sodium hypochlorite is approximately twice that of ozone on a pound basis, and something like 3 times that of ozone on a mole basis. Precipitation tanks and filtration equipment would be expected to be much the same for oxidation with either ozone or sodium hypochlorite. Ozonation would have the added advantage of obviating a sodium removal step for the trivalent lanthanide liquor.

CONCLUSIONS

Cerium can be effectively recovered from complex lanthanide mixtures in solution by a simple oxidation-precipitation process utilizing ozone to precipitate CeO_2. Alternatively, recovery of both cerium and lanthanum can be effected by a two-step ozonation at pH 6.5 and pH 4.5. The technique is simple, relatively rapid, and produces good yields of commercial-grade cerium and lanthanum compounds. In addition, separation is accomplished without introducing contaminants into the system.

REFERENCES[1]

1. American Chemical Society. Ozone Chemistry and Technology. 1959, 465 pp.

2. Dyrssen, David. Phenylbenzohydroxamic Acid. Acta Chem. Scand., v. 10, 1956, pp. 353-359.

3. Moeller, Therald, and Howard E. Kremers. The Basic Characteristics of Scandium, Yttrium, and the Rare Earth Elements. Chem. Rev., v. 37, 1945, pp. 97-159.

4. Patkin, P. N. (Separation of Cerium From Natural Mixtures and Extraction of Its Compounds in a High Degree of Purity.) Doklady Moskov. Sel'skokhoz. Akad. im K. A. Timiryazeva, Nauch. Konf. 1, No. 30, 1957, pp. 222-227.

5. Powell, J. E., and F. H. Spedding. Basic Principles Involved in the Macro-Separation of Adjacent Rare Earths From Each Other by Means of Ion Exchange. Iowa State College, ISC-617, Oct. 26, 1955, 28 pp.

6. Vickery, R. C. Chemistry of the Lanthanons. Academic Press, Inc., New York, 1953, 296 pp.

7. Warf, J. C. Extraction of Cerium (IV) Nitrate by Butyl Phosphate. J. Am. Chem. Soc., v. 71, No. 9, 1949, pp. 3257-3258.

---

[1] Titles enclosed in parentheses are translations from the language in which the item was originally published.

"COMMERCIAL PRODUCTION OF EUROPIUM OXIDE"

Paul R. Kruesi

Molybdenum Corporation of America

Abstract:

In response to the sudden demand for commercial quantities
of europium oxide, Molybdenum Corporation of America de-
veloped and placed in operation a plant for europium recovery.
The technical and economic aspects of this plant are discussed.
Of special significance to the future of the rare earths, are
the availability of large amounts of co-products from this
operation and the development of techniques to isolate the
individual rare earths on a large scale.

Papers will be available at the Conference.

A CRACKING PROCESS FOR RARE EARTH ORES BY DIRECT CHLOR-INATION AT HIGH TEMPERATURES ON A PRODUCTION SCALE

W. Brugger and E. Greinacher
Th. Goldschmidt A.G., Essen, West Germany

ABSTRACT

The direct chlorination of rare earth ores without re-sorting to carbides or similar compounds is described. Complete chlorination of all non-volatile components of the ore results between 1000°C and 1200°C in a special electrically heated furnace. The furnace is so constructed that it is possible to replace the most vital parts quickly and in a hot furnace, thereby bringing under control the unavoidable effects of corrosion. The flow sheet of the process is presented. The process permits a large productive capacity in a small space at low investment and low labor output. It is possible to process the most varied ores such as Bastnasite, Monazite, Allanite, Cerite, Xenotime, Euxenite, Fergusonite, Gadolinite, etc. in the same installation. Reference will be made to the problems of conversion of off-gases. As final product one obtains fused anhydrous chlorides of the rare earths without thorium chloride and without oxychloride content. These chlorides are very well suited for the production of the corresponding metals. With a similar process one can also convert pure rare earth oxides to the corresponding anhydrous chlorides.

INTRODUCTION

During the last two decades, numerous processes for chlorination of rare earth bearing ores have been published in the literature (1-10); none of the processes found application, however, in the production of rare earth chlorides. The disadvantage of most of the described chlorinations is due to the fact that the reaction product after reaction with chlorine must be extracted with water since the reaction could not be taken fully to completion and therefore the unconverted ore residues contaminated the chloride produced. This aftertreatment cancels the advantages of direct chlorination so that the wet processes run more economically.

To achieve complete chlorination in an economically acceptable reaction time, higher temperatures are necessary than those described in the literature. In the following there is described a practical process which avoids the disadvantages of incomplete reaction through higher reaction temperatures.

THE CHLORINATION PROCESS

Figure 1 presents the flowsheet for a complete rare earth chlorination. The process is simple and problems concentrate themselves on the crucial element of the installation: the chlorination furnace, which will for this reason be thoroughly described.

The ore is ground with no serious restrictions with respect to grain size, which must be less than 80 mesh ASTM. If the ore is in the form of sand as for example with monazite or xenotime, or comes from a flotation, then it is not in general necessary to regrind it. The powdery or sandy ore is mixed thoroughly with activated carbon powder with an aqueous binder (sulfite liquor, sugar, starch, etc.) and with some water. The somewhat dry brew is compressed through a briquetting machine into small briquettes which pass through a band drier; finally the fine fraction is screened off, so that it is not blown out of the furnace later on due to the high gas velocity. The fine fraction is returned to the mixer. The briquettes pass continuously or batchwise into the chlo - ination furnace.

In the furnace the ore-carbon mixture is completely converted with gaseous chlorine.

There follows a separation of the resulting reaction products according to their volatility. The rare earth chlorides are tapped from the bottom of the furnace from time to time as a non-volatile fluid melt. The alkali and alkaline earth chlorides go likewise into the melt chamber. All other reaction products are carried off with the off-gases.

The tapped chloride melt is allowed to solidify in steel pans and the resulting crystal cake is crushed. The rare earth chloride so produced serves as the raw material for the production of mischmetal and other rare earth compounds

THE CHLORINATION FURNACE

The most important requirement for complete chlorination
is a temperature in the reaction zone of the furnace in
the range of $1000^\circ C$ to $1200^\circ C$, the exact temperature
depending upon the nature of the ore used. At these tem-
peratures practically all metals and refractory materials
react with the chlorine and carbon and/or carbon monoxide.
Even natural graphite and amorphous carbon cannot resist
these conditions for any length of time. For this reason,
a special furnace with inserts was developed (13), whose
hot reaction zone could be kept small and whose corrodable
parts are made of amorphous carbon inserts, which may be
rapidly replaced.

At the available temperatures, the rare earths and impuri-
ties react extraordinarily fast according to the equations
of Table 1. The reaction of chlorine and carbon with the
rare earths, alkalies, and alkaline earths, iron and
aluminum in the ore is exothermic at these high tempera-
tures, while SiO_2 and P_2O_5 react endothermically. Although
the exact enthalpy values at these high temperatures were
not determined, experience shows that the entire reaction
runs slightly exothermically even with phosphates and
silicates.

If the reaction temperature drops significantly below
$1000^\circ C$, carbon dioxide forms in a strongly exothermic re-
action, so that the temperature in the reaction zone tends,
within certain bounds, to be self-regulating.

The liberated reaction heat is not sufficient, however, to
compensate for the heat losses from radiation and from
heat transport by the off-gases. For this reason, the
system must be supplied with auxiliary energy. For this
purpose, an electric resistance furnace meeting the follow-
ing three prerequisites is employed:

1.) The electric energy must be almost entirely converted
     into heat within the small reaction zone.

2.) The electric resistance consists of loose layers of
     coke and of the ore-carbon briquettes, which can be
     replaced by direct addition.

3.) The chlorine flows directly into the hottest zone
     and reacts there with the ore-carbon mixture.

The construction of the furnace is represented by
Figure 2. A steel shell is so lined that the innermost
layer of brick consists of dense corrosion-resistant
material; the outer layers on the other hand consist of
highly insulating light brick. This lining has the purpose
of confining the heat in the furnace and allowing the
collection in the liquid state of the melted chlorides
from the bottom layer or the reaction zone. The lining is
provided at the bottom with a tapping canal, through which
the liquid chloride is drawn off from time to time.

In the lining, which is about two meters high, there is a
hollow amorphous carbon cylinder designated as the "insert."
Between the carbon cylinder and the brick layer there is
a gap of several centimeters so that the insert can be
quickly installed and removed. At the lower end of the
insert there lies, on a vertical graphite rod, a screen-
plate, which separates the reaction zone from the melt
collection zone. On the screenplate there lies loosely
dumped coke and on the coke are the ore-carbon briquettes.

A central hollow graphite rod reaches from the top into
the coke layer in the insert and serves as the so-called
central electrode.

The furnace is enclosed at the top by a steel hood lined
with ceramic material. At the top of the furnace hood
are two closable input funnels for the ore-carbon bri-
quettes and at the side there is an outlet for the off-
gases. The gap from the furnace hood to the graphite in-
sert and to the central electrode is sealed and electri-
cally insulated. Likewise the hood and the graphite in-
sert are sealed with respect to the lining and the steel
shell.

The central electrode is supported at the top in a mov-
able manner. It serves both as the current conductor as
well as the chlorine pipeline. The alternating current
for heating of the furnace flows from a transformer via
the central electrode through the coke and ore-carbon
briquettes to the graphite insert. The main resistance
is in the layer of coke and briquettes, where as a re-
sult the greatest heat is liberated. The metal-graphite
contacts lie in the relatively cold zone at the upper
end.

The furnace is designed for high thermal loads; the
temperature of the reaction zone can be extensively
varied to match the different ores. One requires

higher temperatures for silicates and phosphates than for oxidic ores or niobates and tantalates of the rare earths. The chlorine gas flows from tank storage via a flowmeter to the upper end of the central electrode, streams through the bore of the central electrode directly into the reaction zone, distributes itself through the entire cross-section of the coke layer and reacts with the ore-carbon briquettes on top of it. The resulting liquid chlorides flow through the coke layer and the screen plate into the melt chamber. On this path, over which carbon is always available, the last oxide residues are converted to chlorides. It is necessary, however, to operate with an excess of chlorine so that the off-gases still contain free chlorine. This results in maintaining the iron in the trivalent stage so that it may be separated with the off-gases.

The liquid reaction products are collected in the lower part of the furnace and released from time to time through the tapping canal.

THE FURNACE OFF-GASES

By means of an exhauster, the furnace is kept at a slightly negative pressure. The carbon monoxide which forms and the volatile chlorides are together drawn off with excess chlorine into a purification system.

If it is not necessary to separate any volatile substances as, for example, the chlorides of niobium, tantalum, thorium, tin, etc., the off-gases may be converted in a combustion chamber directly behind the furnace, first with city gas and steam and finally with air. As a result, from the chlorine, HCl is produced and from the chlorides, either oxides or strongly basic insoluble chlorides. Finally the carbon monoxide and the excess city gas are burned off. The off-gases from the combustion chamber are washed with water; the residual small quantities of HCl remaining in the off-gas are absorbed in a tower with caustic solution. The acidic water from the first wash tower is neutralized with limestone. The gases finally released into the atmosphere contain only carbon dioxide and air.

If valuable chlorides are recovered from the off-gases, a substantially larger installation is required.

OPERATION OF THE FURNACE

The chlorination furnace is operated with alternating current at low voltage of approximately 10-20 volts in order to avoid arcing and thereby non-uniform heating of the reaction zone. Along with the low voltage, high currents of 2000-3000 amperes are involved, which leads to contact difficulties. These difficulties could, however, be overcome.

If the furnace lining is consumed, i.e. has been perforated through the wall either by reaction or by friction, the furnace hood is removed, the hot lining is pulled out, a new lining is inserted into the still hot furnace, the hood is replaced and after a short heat-up time, chlorination proceeds again. Interruption of production amounts to about 10-14 hours.

Some operating data of a furnace with an amorphous carbon liner of about 700 mm diameter are presented in Table 2. These data are concerned with the chlorination of bastnasite ore. For other ores the data would be significantly different. The production capacity of the relatively small furnace is astonishingly high and is limited only by the fact that, at still higher throughputs, such high gas velocities arise that too much dust is carried out of the furnace, leading to losses.

THE FINAL PRODUCTS

The final products of chlorination may be classified according to their vapor pressures or according to their boiling points into three groups. In Table 3 are presented a number of possible reagents, arranged according to their boiling points.

The first group includes all reaction products which are so volatile at the high reaction temperature that their content in rare earth chlorides lies under 0.01%. This group includes all the important heavy metal chlorides and the chlorides of the non-metals.

The second group includes the chlorides which, because of their low vapor pressures, can be partially separated. This includes, above all, the alkali chlorides. Iron-II-chloride is of little significance. Since operation is with an excess of chlorine, all the iron is in the form of $FeCl_3$. If too little chlorine is employed, one finds

immediately a rising iron content in the rare earth chlorides. The manganese content in ores can, under some circumstances, be quite disturbing.

The third group of chlorides is found almost entirely in the liquid chloride. To these belong, naturally, all of the rare earth chlorides, of which only the first and last members ($LaCl_3$ and $LuCl_3$) are shown in the Table. In addition, one finds here the alkaline earth chlorides with the exception of $MgCl_2$. This means that the alkaline earth chlorides cannot be separated from the rare earth chlorides. This sets a limit on the feed for the chlorination process. If an ore contains so much alkaline earth content as to reduce the usefulness of the chloride, it is better to utilize a wet chemical process. According to our experience, however, this is rarely the case.

In Table 4 are shown the analyses of two rare earth chlorides produced by the chlorination of bastnasite from the Mt. Pass Mine and from Madagascar. The relatively high content of $BaCl_2$, $SrCl_2$ and $CaCl_2$, typical of Mt. Pass quality, is in general, acceptable. A better grade of chloride results from use of bastnasite from Madagascar.

ECONOMIC ASPECTS

The economic advantage of the process is due to the low labor component of the simple process, the small space requirement and the low capital costs. On the other hand, the costs for the chlorine depend strongly on the nature of the ore; if the ore contains many impurities which make volatile chlorides (i.e. SiO_2), the costs for the chlorine can become prohibitive. Energy costs are very small. Only the cost of development was unusually high, since there were many difficult and time-consuming problems to solve.

CONCLUSION

The direct chlorination process, as today successfully employed by Th. Goldschmidt A.G. in Essen, West Germany, has the following advantages:

1. Practically all rare earth ores can be utilized without alteration of the process or the equipment.

2. The process yields an anhydrous chloride of the rare earths, without oxide or oxychloride content, which

is suited for conversion to the rare earth metals.

3. The installation requires little space, equipment and labor since it works at high concentrations, namely with anhydrous chloride melts. Consequently, very high specific throughputs result.

4. Through chlorination all impurities, with the exception of the alkali and alkaline earth chlorides, are cleanly separated from the rare earths.

The difficult problems of materials and corrosion were solved over a period of many years, so that today the system is reliable and operates economically.

REFERENCES

1. Aleksandrov, G. P., Russ. Pat. 57 668 (1940)

2. Hartley, F. R., J. Appl. Chem. (London) 2 (1952) 24

3. Sarma, B., and I. Gepta, J. Sci. Ind. Research (India) 14 B (1955) 82.

4. McIntosh, A. B., Ind. Chemist 32 (1956) 195

5. Henderson, A. W., S. L. May, and K. B. Higbie, Ind. Engng. Chem. 50 (1958) 611

6. Zimmermann, I. B., and I. C. Ingles, Analytical Chem. 32 (1960) 241.

7. Gokhale, Y. W., R. Manocha, and D. Sen. J. Sci. Ind. Research (India) 19 B (1960) 422

8. Meersou, G. A., A. N. Zelikman, L. V. Belyaevskaya, N. Y. Tseitima, and G. F. Kirillova, Sb. Nauchn. Tr.. Inst. Tsvetn. Metal. 33 (1960) 175 (Russian).

9. Hilal, O. M., and F. A. El Gohary, Ind. Engng. Chem. 53 (1961) 99Z.

10. Jordanov, N., and Khr. Daiev, Zhurnal Analit. Khim. 17 (1962) 431.

11. Isao Tanabe, and coworkers, Denki Kagaku, 29 (1961) 461 (Japan)

12. Th. Goldschmidt A.-G., German Patent 956.993

13. Th. Goldschmidt A.-G., German Patent 1.110.876

    "   "   "   U.S. Patent 2.755.325

    "   "   "   U.S. Patent 3.147.331

Table No. 1

Equations for the Most Important Reactions in the Chlorination Furnace (Bastnasite)

$$2\ CeO_2 + 4\ C + 3\ Cl_2 \longrightarrow 2\ CeCl_3 + 4\ CO + x\ kcal$$

$$Ln_2O_3 + 3\ C + 3\ Cl_2 \longrightarrow 2\ LnCl_3 + 3\ CO + x\ kcal$$

$$CaO + C + Cl_2 \longrightarrow CaCl_2 + CO + x\ kcal$$

$$Fe_2O_3 + 3\ C + 3\ Cl_2 \longrightarrow 2\ FeCl_3 + 3\ CO + x\ kcal$$

$$2\ FeO + 2\ C + 3\ Cl_2 \longrightarrow 2\ FeCl_3 + 2\ CO + x\ kcal$$

$$SiO_2 + 2\ C + 2\ Cl_2 \longrightarrow SiCl_4 + 2\ CO - x\ kcal$$

$$P_2O_5 + 3\ C + Cl_2 \longrightarrow 2\ POCl_3 + 3\ CO - x\ kcal$$

$$\left[\begin{array}{l} P_2O_5 + 5\ C \longrightarrow 2\ P + 5\ CO - x\ kcal \\ CO_2 + C \rightleftarrows 2\ CO - x\ kcal \end{array} \right]$$
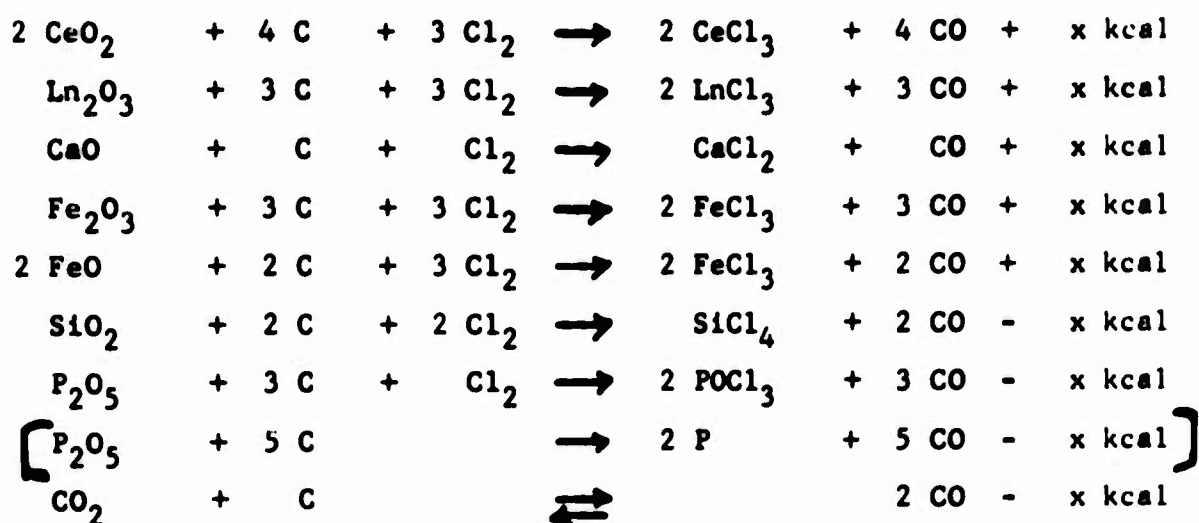
Table No.2

Operating Data of a Furnace With Synthetic Carbon Lining of About 700 mm Diameter During Chlorination of Bastnasite Ore

Capacity of Furnace — ca. 100 tons/mo. RE Chloride

Capacity of Carbon Liner — ca. 200 tons RE Chloride

Capacity of Inner
Refractory Lining — ca. 2000 tons RE Chloride

Consumption

Chlorine — 0.9-1.0 kg/kg RE Chloride

Energy — 0.4-0.6 kwh/kg RE Chloride

Melting - Boiling Point and Vapor Pressure of Chlorides

Name	Formula	Melting Point (°C)	Boiling Point (°C)	Temperature (°C) at (mm Hg)					Remarks
				1	10	40	100	400	
Chlorine	Cl$_2$	-118	- 33	-118	- 102	- 84	- 72	- 47	
Phosgene	COCl$_2$	-104	+ 8	- 93	- 69	- 50	- 36	- 8	
Boron-Trichloride	BCl$_3$	-107	+ 13	- 91	- 67	- 48	- 32	- 4	
Silicon-Tetra-Chloride	SiCl$_4$	- 69	+ 57	- 63	- 34	- 12	+ 5	+ 38	
Phosphorus-Tri-Chloride	PCl$_3$	-112	+ 74	- 52	- 21	+ 2	+ 21	+ 52	
Carbon-Tetra-Chloride	CCl$_4$	- 23	+ 77	- 50	- 20	+ 4	+ 23	+ 58	
Germanium-Tetra-Chloride	GeCl$_4$	- 49	+ 84	- 45	- 15	+ 8	+ 27	+ 64	
Phosphorus-Oxychloride	POCl$_3$	+ 2	+ 105	-	+ 2	+ 27	+ 47	+ 84	
Tin-Tetra-Chloride	SnCl$_4$	- 30	+ 113	- 23	+ 10	+ 35	+ 55	+ 92	
Chromium Oxychloride	CrO$_2$Cl$_2$	- 96	+ 117	- 18	+ 14	+ 38	+ 58	+ 95	
Vanadium Oxychloride	VOCl$_3$	- 77	+ 127	- 23	+ 12	+ 40	+ 62	+ 103	
Titanium-Tetra-Chloride	TiCl$_4$	- 30	+ 136	- 14	+ 21	+ 48	+ 71	+ 113	
Vanadium-Tetra-Chloride	VCl$_4$	- 28	+ 148						
Phosphorus-Penta-Chloride	PCl$_5$	Subl.	+ 162	- 55	+ 83	+ 102	+ 117	+ 147	
Aluminum-Tri-Chloride	AlCl$_3$	+192	+ 180	+100	+ 123	+ 140	+ 152	+ 172	
Niobium-Penta-Chloride	NbCl$_5$	+174	+ 240						
Tantalum-Penta-Chloride	TaCl$_5$	+221	+ 242						
Molybdenum-Penta-Chloride	MoCl$_5$	+194	+ 268						
Phosphorus	P	+ 44	+ 280	+ 77	+ 128	+ 167	+ 197	+ 251	
Iron-Tri-Chloride	FeCl$_3$	+304	+ 319	+194	+ 235	+ 257	+ 272	+ 298	
Zirconium-Tetra-Chloride	ZrCl$_4$	+437	+ 331	+190	+ 230	+ 259	+ 279	+ 312	Sublimes
Hafnium-Tetra-Chloride	HfCl$_4$	+432							
Tungsten-Hexa-Chloride	WCl$_6$	+275	+ 347						
Niobium-Oxy-Chloride	NbOCl$_3$	Subl.	+ 400						Sublimes
Beryllium-Di-Chloride	BeCl$_2$	+291	+ 488	+346	+ 384	+ 411	+ 461	+ 487	
Thorium-Tetra Chloride	ThCl$_4$	(820)	+ 730						Sublimes
Lead-Di-Chloride	PbCl$_2$	+501	+ 954	+547	+ 648	+ 725	+ 784	+ 893	
Iron-Di-Chloride	FeCl$_2$	-	+1026		+ 700	+ 779	+ 842	+ 961	
Manganese-Di-Chloride	MnCl$_2$	+650	+1190		+ 778	+ 879	+ 960	+1108	
Lithium-Chloride	LiCl	+614	+1382	+783	+ 932	+1045	+1129	+1290	
Potassium-Chloride	KCl	+790	+1407	+821	+ 968	+1078	+1164	+1322	
Sodium-Chloride	NaCl	+800	+1465	+865	+1017	+1131	+1220	+1379	
Lutetium-Tri-Chloride	LuCl$_3$	+892	+1480						
Yttrium-Tri-Chloride	YCl$_3$	+700	+1510						
Barium-Tri-Chloride	BaCl$_2$	+962	+1560						
Calcium-Di-Chloride	CaCl$_2$	+772	+1600						
Lanthanum-Tri-Chloride	LaCl$_3$	+852	+1750						

Typical Analysis of Rare Earth Chlorides from the
Chlorination Furnace Using Bastnasite from Mountain Pass
hine in California and from Madagascar

	Produced from Bastnasite from:	
	Mountain Pass (%)	Madagascar (%)
Total Oxide	66	69
CeO_2	49 - 50	47.5 - 48.5
Pr_6O_{11}	3.8 - 4.3	4.6 - 4.9
Nd_2O_3	11 - 12	16 - 17
Sm_2O_3	0.6 - 1.0	1.4 - 1.6
La_2O_3 + Other REs	32 - 35	28 - 31
Fe_2O_3	< 0.01	< 0.01
P_2O_5	< 0.01	< 0.01
NaCl	0.2 - 0.4	0.2 - 0.4
$MgCl_2$	0.1 - 0.2	∅
$CaCl_2$	3.4 - 3.6	0.6 - 0.8
$SrCl_2$	0.4 - 0.6	0.1
$BaCl_2$	2.6 - 4.2	0.1
Acid Insoluble-Fluoride	13 - 15	8

(Note: CeO_2 through La_2O_3 + Other REs: TO = 100)
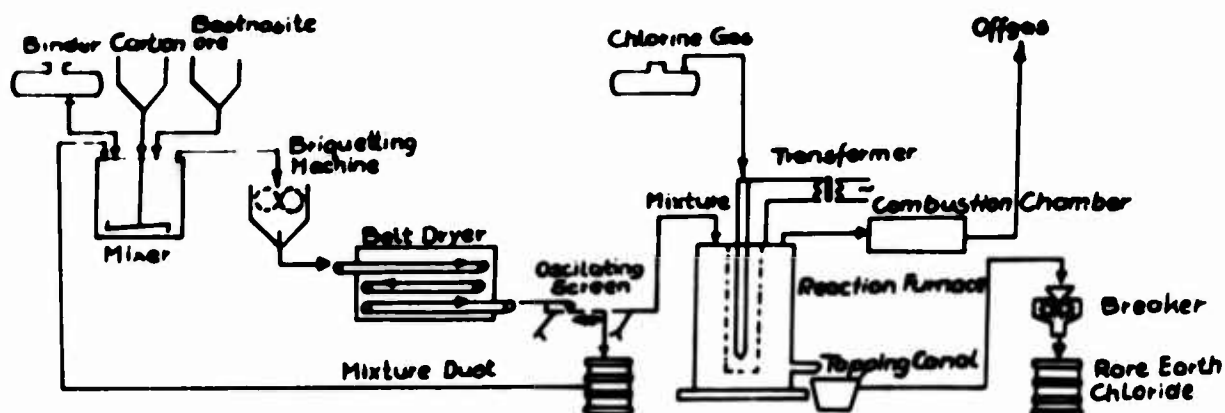
Diagrommatic Flow Sheet for Production of Rare Earth Chloride
from Bastnasite Ore

Figure 1.
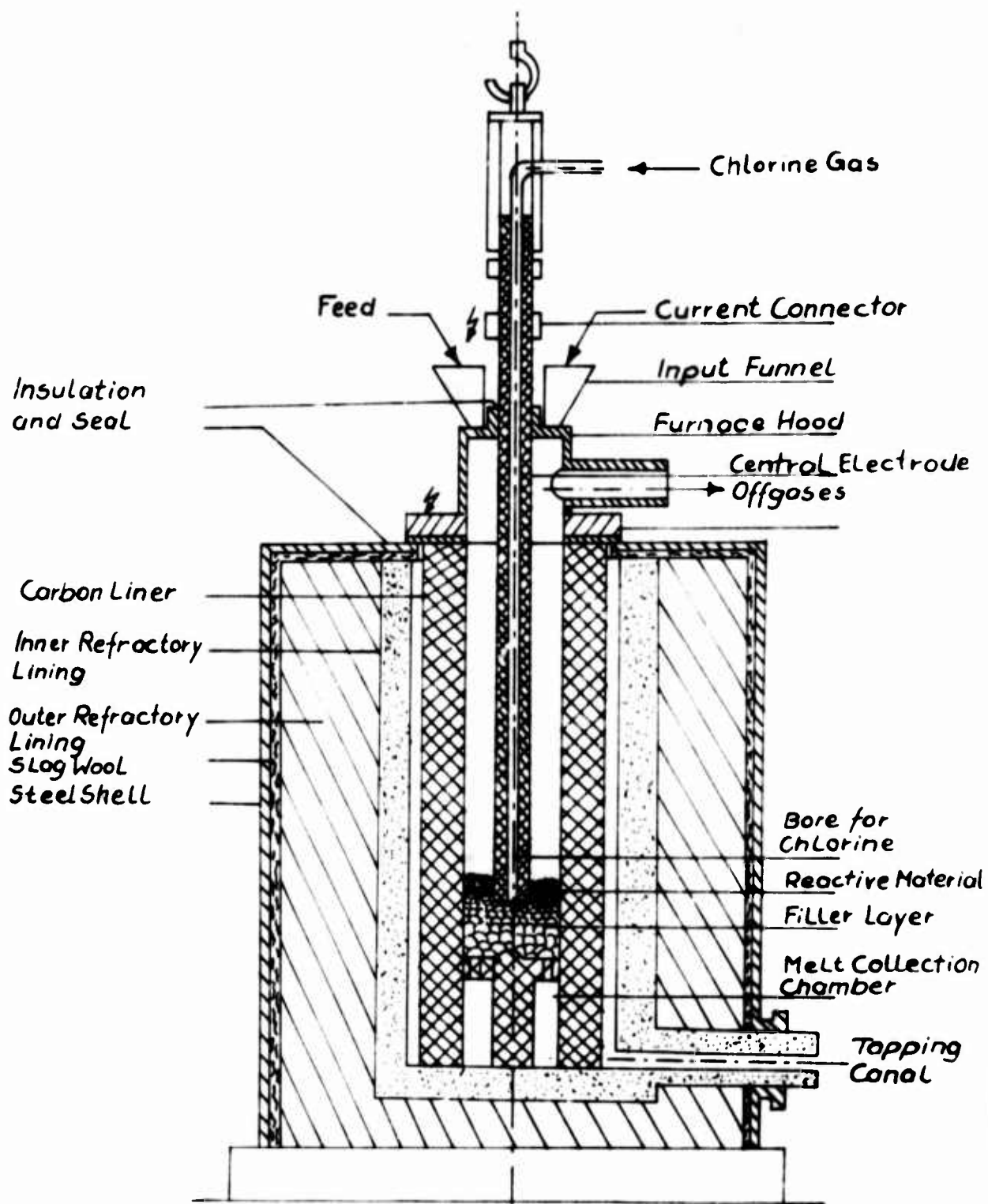
Figure 2. Diagram of the Chlorination Furnace

DIRECT ELECTROLYSIS OF RARE-EARTH OXIDES
TO METALS AND ALLOYS IN FLUORIDE MELTS

By E. Morrice, E. S. Shedd, and T. A. Henrie

* * * * * * * * * * * * * oral presentation
and preprinting by conference

(For presentation at the Sixth Rare-Earth
Research Conference, May 3-6, 1967,
Gatlinburg, Tennessee)

DIRECT ELECTROLYSIS OF RARE-EARTH OXIDES TO
METALS AND ALLOYS IN FLUORIDE MELTS

E. Morrice, E. S. Shedd, and T. A. Henrie

Reno Metallurgy Research Center, Bureau of Mines,
U. S. Department of the Interior,
Reno, Nevada

ABSTRACT

Techniques developed by the Federal Bureau of Mines for the prepara-
tion of high-purity rare-earth metals and their alloys by electrolysis
of the oxides in fluoride media are discussed. Individual cerium,
lanthanum, neodymium, praseodymium, dysprosium, gadolinium, and
yttrium metals, as well as the mixture "didymium", and specific alloy
compositions of these metals and samarium with iron, nickel,
chromium, and cobalt, were prepared. Individual metals were
electrodeposited in the liquid state on tungsten or molybdenum
cathodes. Alloys were prepared by electrodepositing the rare-earth
metal on a consumable base metal cathode at a temperature above the
melting point of the eutectic formed between the rare-earth element
and the cathode material. Cells for electrowinning metal products in
gram and pound quantities, along with methods for the continuous
electrowinning of cerium and lanthanum, are described.

INTRODUCTION

Preparation of high-purity rare-earth metals and their alloys by
electrowinning is part of a comprehensive research program by the
Federal Bureau of Mines for recovery of reactive metals from oxides
or naturally occurring compounds. Studies are directed toward winning
the metal products in the liquid state rather than preparing high-surface-
area dendritic products, thus minimizing contamination and facilitating
metal-electrolyte separation.

The rare-earth oxides are very stable as evidenced by the average
free energy of formation that is in excess of -110 kcals per gram atom
of oxygen at $1,500^{\circ}$ K. This value can be compared with values for
aluminum oxide of -96 kcals and magnesium oxide at about -102 kcals.
In the reduction of rare-earth oxides by carbon, thermodynamic calcu-
lations and metallurgical practice show that formation of the carbides
is favored instead of reduction to metal. Methods for preparing the rare-
earth metals, therefore, are limited to electrowinning procedures or to re-
ducing the oxides or salts with energy-expensive metals, such as calcium.

Most of the earlier work on the electrowinning of rare-earth metals was done on a laboratory scale, utilized chloride salts, and has been summarized in a historical review (3). Cerium, lanthanum, and mischmetal are now produced commercially by electrolysis of anhydrous chlorides in alkali or alkaline-earth chloride melts at relatively low temperatures. Many of the rare-earth metals, however, have melting points above 1,000° C. Electrolytic reductions to the liquid metal phase require an electrolyte with special properties not met by chloride electrolytes. These properties are low vapor pressure at high temperatures, ability to readily dissolve rare-earth oxide, and a cation that will not be co-reduced with the rare-earth ion. With these factors in mind, the electrolytes chosen for winning Nd, Pr, Sm, Gd, Y, Dy, and didymium metals contained 50 mole-percent LiF, the remainder being the rare-earth fluoride. The cerium and lanthanum electrolytes were ternary mixtures including barium fluoride. The solubility of the rare-earth oxides in fluoride electrolytes was determined to be from 2 to 4 percent by a method described previously (5).

It was believed that problems such as carbon contamination and reaction of the higher melting rare-earth metals (>1,300° C) with the electrolyte could be minimized by electrowinning alloys of these metals. Certain alloys have potential uses in industry and in nuclear technology, as well as serving as intermediates for preparation of the reactive metals. A few examples are Y-Fe for nodularizing cast iron; Gd and Dy alloys with Fe, Ni, and Cr for the control of nuclear reactors.

CELL DESIGN AND OPERATION

Studies on the direct electrowinning of the rare-earth elements and their alloys resulted in the design and development of three electrolytic cells. Two cells, each approximately 6 inches in diameter, were used for determining operating parameters, such as bath composition, oxide feed rate, and electrolysis temperature, for preparation of high-purity metallic products by a batch-type process. The third cell, approximately 12 inches in diameter, was used to determine optimum conditions for continuous cell operation and removal of molten Ce and La metals. The metal or alloy formed on the cathode in the liquid state and collected in the form of nodules or a liquid pool in another portion of the cell. One of the 6-inch-diameter cells was used for investigations of the cerium-group metals and on rare-earth alloys melting below 1,300° C, and the other cell was operated at temperatures up to 1,700° C for preparing liquid yttrium-group metals.

Certain features were common to each of the cells: (1) Each was enclosed in an inert-atmosphere chamber to prevent reaction of the liquid rare-earth metal or alloy with air and moisture. This chamber was similar to that described previously (4). (2) Each cell was internally heated, the necessary heat in the reaction zone of the 12-inch cell being provided solely by the electrolysis current and being supplemented in the 6-inch cells by alternating current. (3) The anodes and the crucible for containing the molten electrolyte were fabricated from AGX-grade graphite stock. For electrowinning individual rare-earth metals, the cathode was tungsten or molybdenum. For preparing alloys, the cathode was a consumable rod of the non-rare-earth constituent of the alloy. (4) The crucible was placed inside a shell fabricated from heat-insulating mullite brick and alumina. The removable top of the shell was also made of mullite brick and had a graphite facing to protect the brick from erosion.

Electrowinning Lower Melting Point Rare-Earth Metals

The 6-inch cell for electrowinning Nd, Pr, and didymium metals is illustrated in fig. 1. To maintain the requisite bath temperature for
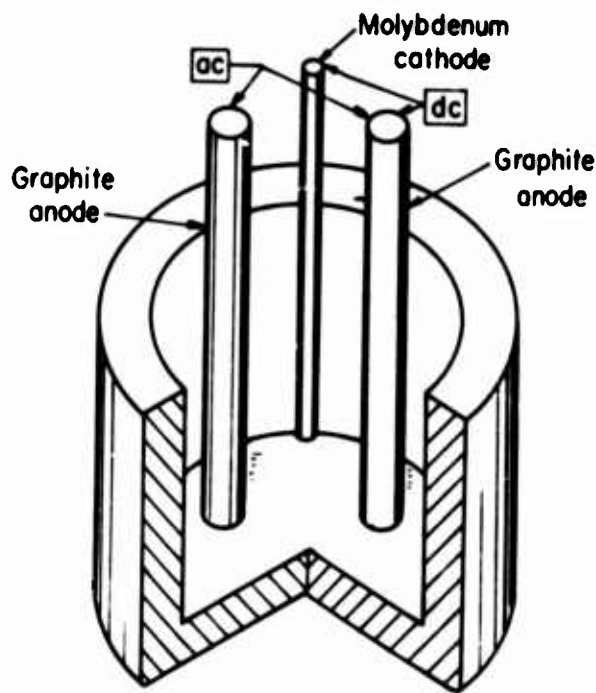
FIGURE 1. - Basic Features of Electrowinning Cell.

electrolysis, more heat was required than could be supplied by direct current power. The cell, therefore, was provided with auxiliary heat by passing alternating current between the anodes.

Contamination of the rare-earth metal by the graphite crucible was prevented by collecting the liquid metal on a frozen electrolyte skull. The skull was maintained by carefully controlling the temperature of the electrolyte, cooling the bottom of the crucible to balance the heat input when necessary.

Before starting electrowinning, an inert atmosphere was obtained in the cell chamber by pumping and backfilling with helium. The fluoride electrolyte was charged to the cell and meltdown was started at the top of the electrolyte container by striking an arc to the cathode with a tungsten probe. After a molten pool of electrolyte was obtained, the probe was removed, alternating current was applied to the anodes, and heating continued until the required cell temperature was attained. Electrolysis was then started and the rare-earth oxide was intermittently fed to the cell. After the electrowinning experiment was completed, the electrolyte was allowed to freeze and the metal was subsequently recovered.

Operational data for typical Nd, Pr, and didymium experiments are given in table 1. Analysis of the atmosphere in the cell chamber during

TABLE 1. - Operational data for typical neodymium, praseodymium, and didymium electrowinning in a 6-inch-diameter cell

Operational parameter		Numerical Values		
		Nd	Pr	Didymium[1]
Rare-earth oxide added to fluoride bath . . grams		312	196	97
Average direct current. . . . . amp .		55	50	60
Average dc voltage . . . . volts		27	19	24
Average alternating current [2] . . . . . amp .		89	130	136
Average ac voltage [2] . . . . volts		52	38	45
Initial anode current density (dc) . . amp/cm^2 .		.6	.3	.6
Initial cathode current density. . . . amp/cm^2 .		6.9	6.0	9.6
Initial anode current density (ac) . . amp/cm^2 .		2.0	1.9	2.5
Average electrolyte temperature . . . . $^{\circ}$C .		1,098	1,030	1,115
Average cell-bottom temperature . . . . $^{\circ}$C .		740	800	770
Duration of electrolysis . . . . hr . .		2.0	1.1	1.4
Rare-earth metal recovered . . . . . gram		151	85	82
Current efficiency. . . . . pct. .		77	88	55

1/ Effective molecular weight of didymium assumed to be 142.1.
2/ Supplemental power applied to the anodes.

TABLE 1. - Operational data for typical neodymium, praseodymium, and didymium electrowinning in a 6-inch-diameter cell.

electrolysis showed that a $CO-CO_2$ gas mixture was evolved from the anodes. Good coalescence of the metal products was obtained, and nodules weighing up to 170 grams were recovered. Current efficiencies up to 88 percent were a ined.

Preparation of Alloys by Direct Electrolysis

The cell for electrowinning rare-earth alloys had the same design as the cell for preparing Nd, Pr, and diaymium metals, except that the cathode consisted of a consumable rod of Fe, Ni, Cr, or Co. The rare-earth metal was reduced from its oxide dissolved in the melt and deposited on the consumable cathode. Electrolyte compositions were the same as those used in electrowinning the individual metals. The cell was operate at temperatures below the melting point of the ferrous metal and above th melting point of the eutectic formed between the rare-earth and ferrous metals. As the alloy formed on the cathode and dripped off, the cathode pencilled down and was lowered into the electrolyte.

Operation data for electrowinning typical alloys of gadolinium with iron and chromium, samarium with iron, and dysprosium with cobalt, are given in table 2. Current efficiencies based on trivalent reactions,

TABLE 2. - Operational data for typical rare-earth ferroalloy electrowinning experiments

Operational parameter	Values for specific alloys			
	Gd-Cr	Gd-Fe	Dy-Co	Sm-Fe
Average direct current . . . . amp.	87	66	77	45
Average dc voltage. . . . . volts	28	27	27	26
Average alternating current[1] . . . . . amp.	181	100	112	66
Average ac voltage[1] . . . . volts	56	47	49	43
Initial anode current density (dc) . amp/cm^2 .	1.2	1.1	1.0	1.1
Initial cathode current density. . . amp/cm^2 .	22.1	12.2	7.7	10.1
Initial anode current density (ac) . amp/cm^2 .	5.0	3.3	3.0	3.2
Average electrolyte temperature. . . . °C .	1,291	935	1,020	887
Average cell-bottom temperature . . . °C .	815	660	741	719
Duration of electrolysis . . . . hr. .	1.1	1.2	1.0	1.5
Alloy recovered . . . . grams	69	106	89	67
Rare-earth metal content . . . . wt pct	96	85	82	87
Current efficiency . . . . pct .	36	58	47	46

[1] Supplemental power applied to anodes.

TABLE 2. - Operational data for typical rare-earth ferroalloy electrowinning experiments.

ranged from 36 to 58 percent. The major off-gases were carbon oxides, with carbon monoxide predominating at the higher cell operating temperatures. Alloy nodules weighed from 2 to 100 grams and were easily separated from the frozen electrolytes. The composition of the nodules was temperature-dependent and comparable to compositions given by the solidus-liquidus line on the ferrous metal side of the binary phase diagram. In table 3, the compositions of electrowon alloys are compared

TABLE 3. - Compositions of electrowon alloys as compared to compositions given by the solidus-liquidus line in the phase diagrams

Alloy composition	Cell operating temperature, ° C	Ferrous metal content, weight-percent	
		Experimental	Theoretical [1]
Fe-Dy. .	1,064	12	30
-Gd. .	935	15	18
-La. .	964	6	10
-Nd. .	985	28	20
-Sm .	887	13	28
-Y . .	984	24	30
Ni-Sm. .	876	19	(2/)
-Y . .	1,140	49	55
Cr-Gd. .	1,291	4	6
-Y . .	1,376	15	20
Co-Dy. .	1,020	18	30

1/ Properties of the Rare Earth Metals and Compounds. Ed. by John A. Gibson and Gifford S. Harvey, AFML-TR-65-430, January 1966, 354 pp.
2/ No data.

TABLE 3. - Compositions of electrowon alloys as compared to compositions given by the solidus-liquidus line in the phase diagrams.

with the value expected from the phase diagrams.

Of particular interest was the electrowinning of a Sm-Fe alloy. Previous investigators have been unable to prepare Sm either by electrolysis or by metallothermic reduction of its halides because of the stability of the divalent ion (2). By producing a Sm-Fe alloy, back reaction of Sm with its fluoride was inhibited, and alloy nodules weighing as much as 15 grams and containing 87 weight-percent Sm were recovered.

Electrowinning Higher Melting Point Rare-Earth Metals

Certain problems encountered in the lower temperature cell were greatly magnified in attempts to electrowin the yttrium group elements as liquid metals at temperatures up to 1,700° C (1). The main problem areas were: (1) The energy required to deposit the metal at temperatures above its melting point, (2) control of the temperature in the metal collection zone, and (3) refractories and materials of construction capable of withstanding both the elevated temperatures and the corrosive nature of the salts. The essential features of the high-temperature cell are given in fig. 2.
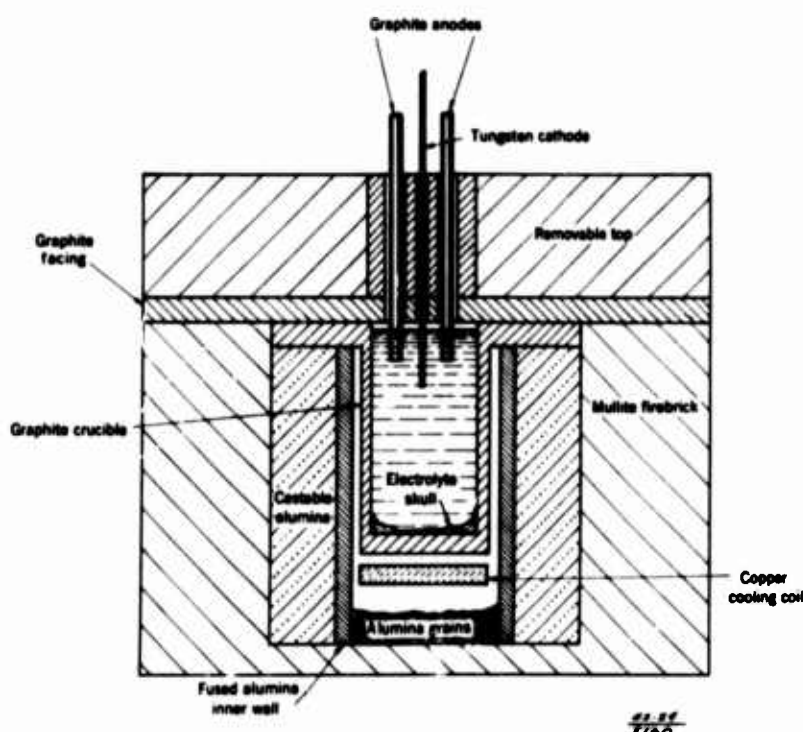
FIGURE 2. - High-Temperature Electrowinning Cell.

The necessary heat in the reaction zone of the cell was obtained by applying alternating current to two graphite anodes which supplied approximately three-fourths of the total power. Considerably more energy was required to maintain the temperature in the high-temperature cell than in the cell for winning cerium-group metals. For example, the power requirement for electrowinning Pr was 6 kw, whereas in preparing Gd, 14 kw were used. The anode reaction (formation of CO) appears to be one important rate-controlling factor in the operation of the cell. Therefore, the graphite anodes were fluted to provide as large a surface area as practicable. The larger surface area also permitted shallower immersion of the anodes, thereby facilitating escape of the carbon oxides from the bath.

Experience indicated that a relationship exists between the temperature of the metal collection zone and the recovery and purity of the product. To minimize back reaction with the electrolyte and contamination of the metal, nodules were collected on a frozen electrolyte skull in a portion of the cell maintained at approximately 500° C below the melting point of the reactive metal. The conditions for operating the thermal gradient cell were obtained by internally heating the electrolyte and, at the same time, cooling the bottom of the crucible by passing helium or air through a copper coil placed below the crucible.

Materials necessary for construction and operation of the high-temperature cell were extended nearly to their limits, and only by use of a combination of materials could a satisfactory cell be designed. The graphite crucible was placed inside a shell fabricated from layers of various heat-insulating refractory materials. The inner wall of the shell was made from fused alumina. Castable alumina, 2 inches thick, was then placed around the inner wall. Finally, there was an outer wall 4 inches thick made from mullite brick. Granular alumina was placed below the graphite crucible to a depth of about 1-1/2 inches.

Operation of the high-temperature cell was demonstrated by preparing liquid Gd, Dy, and Y metals in the temperature range of 1,370° to 1,700° C. Good coalescence of the metal products was obtained, and nodules weighing from 1 to 20 grams were recovered. Operational data for a typical Gd experiment are given in table 4.

TABLE 4. - Operational data for a typical gadolinium
electrowinning cell

Operational parameter	Numerical value
Average direct current . . . . amp.	95
Average dc voltage . . . . volts	27
Average alternating current[1] . . . . amp.	202
Average ac voltage [1] . . . . volts	57
Initial anode current density (dc). .amp/cm^2.	1.0
Initial cathode current density. . .amp/cm^2.	31.4
Initial anode current density (ac). .amp/cm^2.	4.3
Average electrolyte temperature . . .° C..	1,370
Average cell-bottom temperature . . .° C.	810
Duration of electrolysis. . . . . . . .hr ..	0.7
Gadolinium metal recovered . . . . .grams	65
Current efficiency . . . . .pct ..	50

[1] Supplemental power applied to the anodes.

TABLE 4. - Operational data for a typical gadolinium electrowinning cell.

Continuous Electrowinning of Cerium and Lanthanum

A 12-inch-diameter cell was designed and operated to demonstrate the feasibility of preparing Ce and La metals by a continuous process. Both metals were collected on molybdenum and tungsten hearths and tapped from the cell into ladles in an inert-atmosphere casting chamber ($\underline{6}$-$\underline{7}$).

The basic cell design for electrowinning Ce is given in fig. 3. The
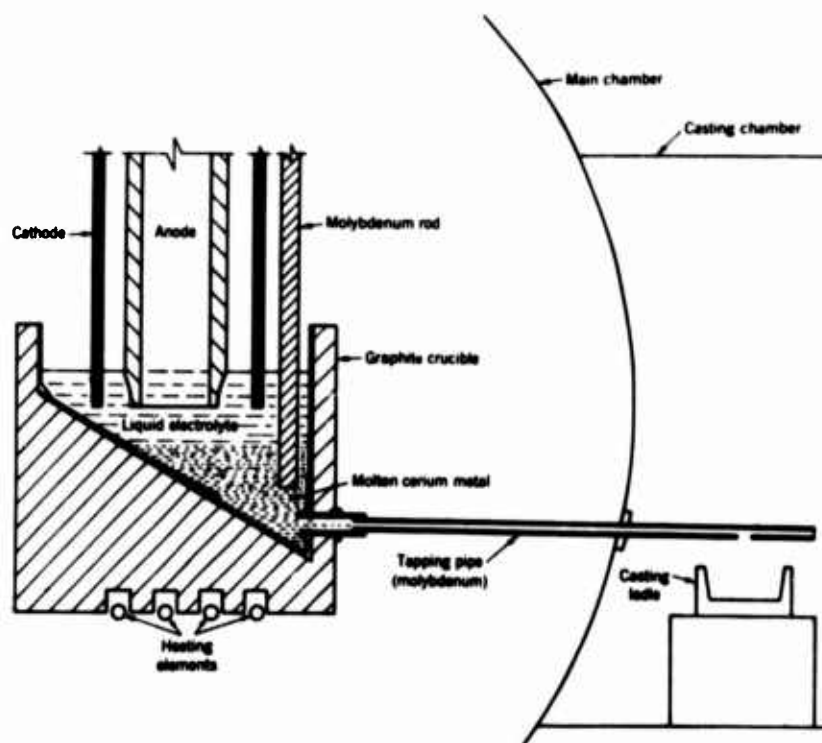
FIGURE 3. - Cell Used for Continuous Operation and Tapping.

graphite crucible had a 60° sloping bottom completely lined with molybdenum sheet. A 1/2-inch-diameter molybdenum tapping pipe was connected to the bottom of the molybdenum-lined crucible and extended into the casting chamber, which was an integral part of the cell chamber. The single anode was a graphite tube 4-3/8 inches in outside diameter, 3 inches inside diameter, and 22 inches long. The tubular anode also served as a feed tube for adding electrolyte or oxide. Molybdenum or tungsten rods, 0.4 inch in diameter, were used for the nine cathodes that were evenly spaced in a circle 1-1/8 inches from the anode surface.

The following description is typical of cerium experiments: The liquid electrolyte consisted of 63 weight-percent CeF_3, 16 percent BaF_2, and 21 percent LiF. Electrolysis was carried out at a bath temperature of 850° C, with the necessary heat provided by the electrolysis current of 785 amperes at 8.5 volts. Cerous oxide was fed to the cell at a rate of 30 grams per minute. After four hours, electrolysis was stopped, alternating current was applied to heat the molybdenum tapping pipe, and the liquid Ce metal was tapped into ladles. Electrolysis was continued in a similar manner for 3 consecutive days. During this time, several tappings of metal were made.

The electrode arrangement for electrowinning Ce, employing a central tubular anode, was not satisfactory for La because sufficient current could not be maintained to sustain the cell operating temperature. The difference between the ability in Ce electrowinning and the inability in La electrowinning to sustain the requisite bath temperature may be explained by the different valence species that can exist in the two electrolytes. In the case of the cerium electrolyte, both +4 and +3 valent Ce species were present. If the anolyte did not contain sufficient oxide to sustain the anode reactions, the Ce^{+3} was oxidized to Ce^{+4}, and the cell continued to operate at the same amperage. As the Ce^{+4} accumulated in the electrolyte, the oxide became more soluble, and a balance between oxide availability and anode reaction was reached. Lanthanum, however, has only the trivalent species. If the oxide is not available to the anode at a surface concentration sufficient to support the imposed anode reaction, the electrolysis rate slows and the temperature decreases. Intuitive reasoning resulted in reversing the electrode arrangement to have one central molybdenum cathode surrounded by eight graphite anodes. This placed the anodes on the outside and allowed a greater proportionate volume of the electrolyte to serve as anolyte. Using this electrode arrangement, La metal was electrowon and tapped for 4 consecutive days.

PRODUCT QUALITY

Examination of rare-earth metal nodules, after recovery from the 6-inch-diameter cells, showed small amounts of bath adherent to the nodule surfaces. The bath was removed and the nodules were sampled for analysis

The purity of typical nodules of Nd and Pr is given in table 5.   Most of

TABLE 5. - **Analyses of neodymium and praseodymium-**
            metal nodules

Element	Nodule analysis, weight-percent	
	Nd	Pr
Aluminum	0. 002	0. 010
Calcium	. 005	. 005
Carbon	. 014	. 010
Fluorine	. 040	. 030
Iron	. 012	. 012
Lithium	. 013	(1/)
Magnesium	. 005	. 003
Nitrogen	. 001	. 002
Oxygen	. 015	. 018
Other rare earths 2/	. 020	. 060
Silicon	. 005	. 003
Tungsten	. 020	. 020
Total	0. 150	0. 170

1/ Not determined.
2/ Less Nd or Pr.

TABLE 5. - Analyses of neodymium and praseodymium -
                metal nodules.

the metallic impurities, except for tungsten from the cathode, originated
in the electrolyte and feed materials.   Microscopic examination showed
that some of the nodules contained small amounts of interspersed electro-
lyte, a possible source of the fluorine contamination.   Analyses of
didymium and ferroalloy nodules gave comparable results to those ob-
tained for Nd and Pr.

The carbon and oxygen impurity levels in Gd, Dy, and Y metals were
considerably higher than those in Nd and Pr.   The high values were
attributed to the reaction of the metals at elevated temperatures, with
carbon oxides produced at the anodes and with the oxide sludge in the bath.
The design of the high-temperature cell, incorporating shallow immersion
of fluted anodes and the maintenance of a thermal gradient between the
zones of metal deposition and collection, helped to minimize contamination
of the metals.   For example, Gd metal won at 1,400° C and collected at
860° C contained 500 ppm carbon and 100 ppm oxygen, whereas metal won
at the same temperature and collected at 1,000° C contained 10 times the
amount of oxygen and carbon.

Analysis of the impurities in Ce and La metal ingots cast during continuous electrolysis experiments is given in table 6. Molybdenum,

the c   n

TABLE 6. - **Analysis of impurities in tapped cerium and**
lanthanum metals

Element	Ingot analysis, weight-percent	
	Ce	La
Aluminum	0.040	0.030
Barium	(1/)	(2/)
Calcium	(2/)	(1/)
Carbon	.010	.033
Copper	.001	(2/)
Iron	.007	.027
Molybdenum	.076	.028
Oxygen	.016	.016
Silicon	.008	.055
Tungsten	.002	(2/)
Total	0.160	0.189

1/ Not determined.
2/ Not detected.

TABLE 6. - Analysis of impurities in tapped cerium
and lanthanum metals.

the major impurity in the Ce metal, came from the molybdenum hearth and electrodes. Lanthanum metal collected on a tungsten hearth contained <100 ppm tungsten.

SUMMARY

Cells were designed and successfully operated on a practical laboratory scale for electrowinning high-purity Nd, Pr, and didymium, as well as the higher melting point metals - Gd, Dy, and Y. The elements were prepared generally from their oxides dissolved in fluoride melts and deposited as liquid metals on a tungsten cathode. Similarly, specific alloy compositions of these metals and Sm, with selected ferrous metals, were prepared by electrodepositing the rare-earth metals on consumable cathode fabricated from the ferrous metals.

A cell was designed for winning Ce and La metals from their oxides in pound quantities by a continuous process. The liquid metals were tapped from the cell and cast into ingots.

INTRODUCTION

The only rare earth metal product currently produced in
tonnage quantities by fused salt electrolysis is mischmetal,
which is composed chiefly of cerium, lanthanum, neodymium
and praseodymium. In addition, several thousand pounds
per year of cerium, lanthanum and didymium (Nd + Pr) are
also electrowon by methods basically the same as those em-
ployed for production of mischmetal.

Since the commercial operation of fused salt electrolytic
cells involves considerable "know how", which is not dis-
closed in the published literature, this paper must be
limited in scope to avoid disclosure of proprietary informa-
tion. For this reason, all references herein are based on
presently available published data.

RAW MATERIALS

Commercial production of mischmetal is based on the use of
mixed rare earth chloride, which will be designated "LnCl$_3$"
in this paper. This compound has been traditionally pro-
duced from monazite sand, a rare earth and thorium phosphate
found in India, Brazil, South Africa, Australia and the
United States. In recent years it has been produced in
growing quantities from bastnasite, a rare earth fluocarbon-
ate found in California, in Central Africa and in Madagascar.

In the past, all mixed rare earth chloride was produced by
wet chemical treatment of monazite and bastnasite to yield a
hydrated product. In the last several years, Th. Gold-
schmidt A.G. of Essen, West Germany has chlorinated these
ores to produce an anhydrous rare earth chloride suitable
for electrolysis without further processing. Typical anal-
yses of these chlorides are presented in Table I.

DEHYDRATION OF HYDRATED RARE EARTH CHLORIDE

If hydrated rare earth chloride is used, it must be processed
to yield an anhydrous product with low oxychloride content.
This is accomplished by using methods which minimize oxida-
tion or hydrolysis. The hydrated chloride contains about
30% H$_2$O.

Typical dehydration techniques include vacuum heating or
heating in air with the admixture of non-rare earth salts
to reduce hydrolysis. The Auergesellschaft in Berlin
during World War II used rotary iron vacuum drum driers,
steam heated to 350° C at a vacuum of 700 mm to yield a
product with an oxychloride content of about 1.5%.

Commercial Production of Rare Earth Metals
by Fused Salt Electrolysis

I. S. Hirschhorn
Ronson Metals Corporation
Newark, N.J.

ABSTRACT

The commercial production of rare earth metals by fused salt electrolytic methods is described. These methods are used to make mischmetal, cerium, lanthanum and didymium (Nd+Pr).

The feed materials consist essentially of anhydrous chlorides of the metal to be produced, augmented by additions of non-rare earth salts to yield an electrolyte with satisfactory properties for reduction. The rare earths are derived either from monazite or from bastnasite ores. The anhydrous chlorides are manufactured from the hydrated chlorides by methods which minimize oxidation or hydrolysis. Alternatively, anhydrous chlorides may be used which result from the direct chlorination of rare earth ores by the Goldschmidt process. These are particularly suitable for electrolysis due to their very low oxychloride content. Fluorides and oxides of the rare earths are produced by wet chemical methods to provide the relatively small quantities of these compounds now used for commercial fused salt electrolysis.

Reduction cells in use today are constructed mainly from (a) ceramics (b) graphite or (c) iron. The advantages and disadvantages of these types of cells are described together with the typical products which result from their use.

Primary attention is given to production of mischmetal (mixed rare earth metal), which is the rare earth metal produced on the largest scale today. Brief reference is made also to production of cerium, lanthanum and didymium (Nd + Pr) metal.

Finally, a resume of the current uses of these metals is presented with reference to recent trends in the industrial applications of the rare earth metals.

Prometheus in Bavaria heated a mixture of rare earth chloride with $CaCl_2$ in air for 2 to 2.5 hours with a typical yield of 62%, which would indicate substantial oxychloride content. Treibacher Chemische Werke of Austria were reported to use a two-stage vacuum drying process, in which the hydrate was heated first at 170° C and then at 350° C (3).

Other commercial dehydration techniques involve addition of ammonium chloride to reverse hydrolysis according to the following reactions:

$$LnCl_3 + 3H_2O \longrightarrow Ln(OH)_3 + 3\overline{HCl}$$

$$Ln(OH)_3 + 3NH_4Cl \longrightarrow LnCl_3 + 3\overline{NH_3} + 3\overline{H_2O}$$
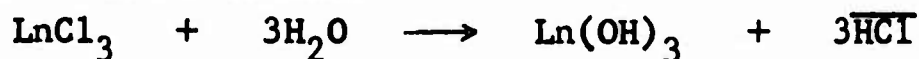
Some commercial producers employ sodium or calcium chloride to retard hydrolysis on the basis of the common chloride-ion mass action effect. Since addition of NaCl and/or $CaCl_2$ to the electrolyte is often desirable, these compounds may be conveniently incorporated in the feed during dehydration.

FLUORIDES AND OXIDES

Mixed rare earth fluorides and oxides are of minor importance in the production of mischmetal. However, these are significant raw materials for the electrolytic production of some of the pure rare earth metals such as cerium and lanthanum. The anhydrous fluorides and oxides are produced by air-drying or vacuum-drying the compounds. The oxides are derived from dehydration of precipitated hydroxides or by decomposition of precipitated carbonates or oxalates. The fluorides are generally precipitated from a mixed rare earth chloride solution, or produced from the oxides by reaction with ammonium bifluoride at 500-600° C according to the following reaction:

$$Ln_2O_3 + 3NH_4HF_2 \longrightarrow 2LnF_3 + 3\overline{NH_3} + 3\overline{H_2O}$$
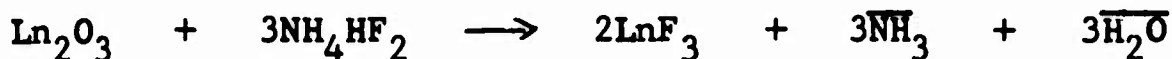
The literature also refers to fluorination with H_2F_2 or ClF_3.

Recently, the U.S. Bureau of Mines published a method for the production of stable cerous oxide, which involves the reduction of ceric oxide with graphite in an helium atmosphere at 900 to 1250° C (7). The use of this oxide results in improved current efficiencies in electrolytic reduction to cerium metal. The reaction involved is as follows:

$$2CeO_2 + C \longrightarrow Ce_2O_3 + \overline{CO}$$

This process may prove eventually to have commercial value.

REDUCTION

Representative electrolytic reduction cells described in the literature include two types of ceramic cells (9) (3) and one graphite cell (7). The operating characteristics of these cells are summarized in Table II. The designs of these cells are reproduced in Figures 1, 2 and 3.

The ceramic cells of the type shown in Figure 1 are usually operated in series, which facilitates semi-continuous production since molten electrolyte can be transferred from one cell to another for rapid start-up. During operation the metal collects at the bottom of the cell, where it is maintained in the molten state by the flow of direct current through it to the cathode. At convenient intervals, the metal, covered with a layer of molten electrolyte, is ladled out and poured into molds, where it solidifies under a protective layer of electrolyte. After cooling, the metal may be separated from the solidified electrolyte by breaking off the salt layer and washing.

Contamination of the product due to iron and silica may be reduced by constructing cells of graphite, which also serves as the cathode. The anodes are usually either carbon or graphite. The electrolyte consists of mixtures of $LnCl_3$ with NaCl, KCl, $CaCl_2$ or other salts as preferred by the various producers. The cells may be enclosed to exclude air, thereby resulting in reduced gas content in the mischmetal produced.

Bath temperatures are approximately 800-900° C. The metal collects at the bottom of the cell, where it may be maintained in the molten state by resistance heating, or allowed to solidify by use of a cooled cathode. In the latter case, it is necessary to remelt the metal by internal resistance heating, sometimes supplemented by external sources of heat, before it can be removed from the cell. This type of cell may be stationary like the one described above, or, as in Figure 2, tiltable, which simplifies pouring of the product into molds.

These cells are run either singly from rectifiers or in series by use of motor-generator sets. Operation is batchwise or continuous, depending upon the preference of various producers.

Sometimes, iron pots are used instead of graphite crucibles in this type of commercial cell, when rare earth metals contaminated with iron are acceptable, as for example, for mischmetal intended for ferrous alloy applications.

In all cases, the gaseous products of the electrolytic reaction, consisting mainly of chlorine, contaminated with gaseous carbon compounds, are drawn off and absorbed in a suitable system to control air pollution.

The graphite cell of Table II and Figure 3 was developed by the U.S. Bureau of Mines. Similar cells with controlled atmosphere, pressure and temperature have successfully produced semi-commercial quantities of cerium, lanthanum and yttrium with purity better than 99.9% (2). These cells use an electrolyte similar to that previously employed by Gray (1) The compound reduced to metal is Ln_2O_3.

Such cells are reported to yield current efficiencies ranging from 75 to 95%. In the instance shown in Table II, the current efficiency is 96% due primarily to the use of Ce_2O_3 rather than CeO_2. It must also be recognized that in these experimental cells, supplementary alternating current is employed for metal melting prior to tapping.

The lower current efficiencies reported for commercial cells are due in part to energy consumption for maintenance of melt temperature. Another important reason for reduced current efficiencies in commercial cells producing mischmetal is the accumulation of compounds of samarium, europium and other non-reducible rare earth compounds in the electrolyte. For this reason, the spent electrolyte must be removed and replenished with fresh electrolyte as necessary to maintain good operating conditions.

The ultimate economic advantage of cells like these, developed by the Bureau of Mines, over commercial cells based on use of chlorides still remains to be demonstrated.

Table III provides data on the quality of electrowon rare earth metals available today. This confirms the fact that metals of high purity can be produced by fused salt electrolysis if carefully purified feed materials are used and if cell atmosphere composition is controlled.

CURRENT APPLICATIONS FOR ELECTROLYTIC RARE EARTH METALS

Mischmetal, which sells for less than $3.00 per pound, is the lowest cost rare earth metal product. Its oldest, and still one of the most important uses, is in the manufacture of sparking metal alloys for cigarette lighter flints and welding gas igniters. These contain 70 to 80% mischmetal.

In recent years, important metallurgical applications for mischmetal have been developed. In ductile iron (sometimes called nodular iron), mischmetal reduces the effect of subversive elements, helps desulfurization, increases magnesium

recovery and ladle fluidity. It may be added either separately or contained in silicon-magnesium-mischmetal or other alloys. Mischmetal increases the oxidation resistance of nickel-chromium alloys and improves the ductility and impact properties of cast steel, and the hot workability of stainless steels. In magnesium alloys, mischmetal improves pressure tightness and high temperature creep resistance. In secondary aluminum alloys, it enhances fluidity, inhibits surface oxidation and refines grain structure. Mischmetal inhibits inverse segregation in lead bronzes and deoxidizes copper alloys. In the precision casting industry, small additions of mischmetal are made to improve the castability of superalloys, stainless and tool steels.

While mischmetal is actually the predominant rare earth metal used in industry today, there is growing interest in cerium, lanthanum, didymium ($Nd + Pr$), yttrium and cerium-free mischmetal. Some of the applications for these metals currently under investigation include additives for the improvement of alloys of copper, cobalt, beryllium, tantalum, aluminum, magnesium, and other non-ferrous metals. In addition, the individual rare earth metals have received renewed consideration as desirable additives for ductile iron, heat resistant stainless steels, and refractory metals.

Other applications being studied include new cathode emitters, new getters for electronic tubes and other devices, and new materials including intermetallics for solid state devices, such as transistors and thermoelectric elements.

Cerium and yttrium metal have been successfully employed as starting materials for production of hydrides for use as moderators in high temperature nuclear reactors. Alloys of cerium with cobalt and plutonium have been used effectively as liquid neutronic reactor fuels.

During 1966, it was reported that a new permanent magnet composed of YCo_5 promises to surpass the energy product of the best magnets available today by a factor of three. This could lead to important commercial uses for yttrium, or possibly for some of the other rare earth metals whose compounds with cobalt have suitable magnetic characteristics.

CONCLUSION

It may be concluded from the facts presented in this report that suitable raw materials for electrolytic production of the major rare earth metals are readily available, that practical cells for production are in use and better ones under development, so that the rare earth metal producers should have no difficulty in meeting the growing needs of industry for these important metals, both with respect to quantity and quality.

Table I
Typical Analyses of Rare Earth Chlorides

Type	Hydrated	Hydrated	Anhydrous
Source	Monazite	Bastnasite	Chlorinated Bastnasite
Total Oxide	46.2 %	46.0 %	66.0 %
CeO_2	47.6	50.3	49.1
Pr_6O_{11}	5.0	4.2	4.7
Nd_2O_3	17.3	11.2	12.7
Sm_2O_3	2.9	1.3	1.6
La_2O_3 + Other REs	27.1	32.8	29.5
H_2O	28.5	29.0	0.5
Fe_2O_3	0.04	0.002	<0.01
P_2O_5	<0.01	<0.03	<0.01
Na_2O	0.1	0.15	0.16
MgO	0.1	0.1	0.09
CaO	0.9	0.19	1.3
SrO	-	0.2	0.3
BaO	-	0.24	1.1
Insoluble Residue	0.05	0.04	5.4 *

Note: CeO_2, Pr_6O_{11}, Nd_2O_3, Sm_2O_3, La_2O_3 + Other REs → TO=100

* Consists mainly of rare earth fluoride

Table II

Characteristics of Some Fused Salt Electrolytic Cells for Production of Rare Earth Metals

Cell Type	Ceramic	Ceramic	Graphite
Reference	(9)	(3)	(7)
Cell Material	Firebrick	Fireclay and Cement	Graphite
Anode	Carbon	Graphite	Graphite
Cathode	Iron	Iron	Tungsten
Electrolyte	$LnCl_3$	$LnCl_3$	Ce_2O_3
	NaCl	$CaCl_2$	CeF_3
			BaF_2
			LiF
Bath Temp.(Avg.)	850° C	850° C	850° C
Cell Atmosphere	Cell Gases + Air	Cell Gases + Air	Cell Gases + Helium
DC Amps. (Avg.)	2300	1500	785
DC Volts (Avg.)	14	12	8.5
Kwh/lb. (DC)	7.1	6.2	2.5
Current Eff. %	45	50	96
$LnCl_3$/Metal Ratio	2.3	2.8	-
Lbs. Metal/Hour	4.1	2.9	2.8

Table III

Typical Analysis of High Purity Rare Earth Metals
Commercially Produced by Fused Salt Electrolysis
(Weight Percent)

Grade*	Mischmetal 99.9	Cerium 99.9	Lanthanum 99.9
Ce	53	N.D.	.10
La	23	.03	N.D.
Nd	16	.07	.05
Pr	5	-	.12
Dy	Tr	-	-
Er	-	-	-
Eu	-	-	-
Gd	2	-	-
Ho	-	-	-
Lu	-	-	-
Sm	-	-	-
Tb	-	-	-
Tm	-	-	-
Y	Tr	-	-
Yb	-	-	-
Al	-	-	.007
Ba	-	-	.011
Ca	-	-	-
Cr	.034	-	.002
Cu	-	.016	-
Fe	.035	.014	.043
Mg	.032	.030	.010
Mn	.006	.023	.004
Mo	-	-	.001
Ni	-	-	-
Si	.010	.005	.029
Th	-	-	-
Ti	-	-	= =
C	.008	.006	.001
O	.002	.004	.002
N	.003	.002	.003

N.D. = Not Determined
－ = Not Detected
Tr = Trace

＝ Based on nominal total rare earth metal content

Figure 1

Reduction Cell at Treibacher Chemische Werke (Austria)
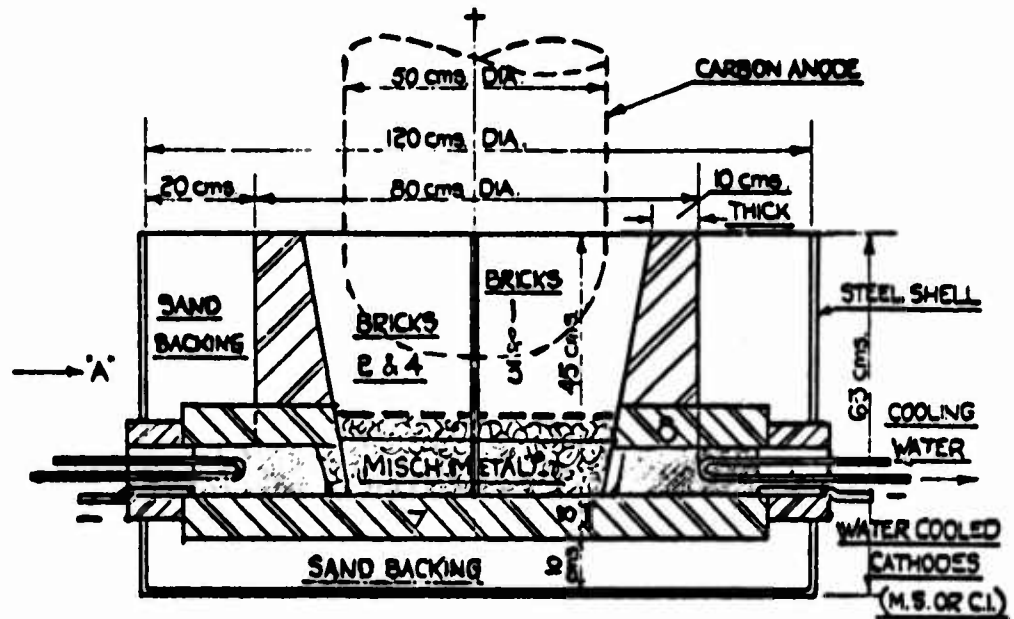### After B.I.O.S. Report (9)

Figure 2

Reduction Cell at Prometheus (Bavaria)
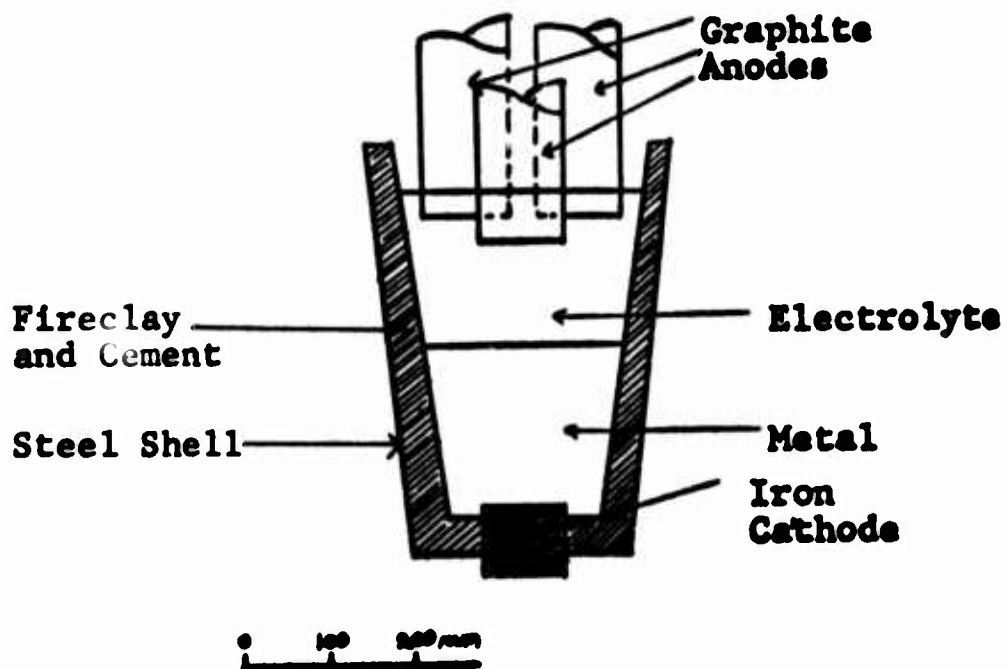### After FIAT Report (3)

Figure 3

Reduction Cell at Reno Laboratory
of U.S. Bureau of Mines (7)